**THESE de DOCTORAT DE L'INSA LYON,
membre de l'Université de Lyon**

Ecole Doctorale N° 162
MEGA (Mécanique, Energétique, Génie civil, Acoustique)

Spécialité : Génie mécanique

Soutenue publiquement le 29/09/2023, par :
Gabriel LANASPEZE
Ingénieur INSA Lyon

Contribution to roller chain drive quasi-static modelling for efficiency optimisation. Application to track cycling.

Devant le jury composé de :

BAIETTO Marie-Christine	Directrice de Recherche, INSA Lyon	Présidente du jury
BURGESS Stuart	Professor, University of Bristol	Rapporteur
RENAUD Franck	Maitre de Conférences – HDR, ISAE-SUPMECA	Rapporteur
CLANET Christophe	Directeur de Recherche, Ecole Polytechnique	Examinateur
GUILBERT Bérengère	Maitre de Conférences, INSA Lyon	Co-directrice de thèse
VILLE Fabrice	Professeur des Universités, INSA Lyon	Directeur de thèse

Definitive version
07/11/2023

Référence : TH0991_ Gabriel LANASPEZE

L'INSA Lyon a mis en place une procédure de contrôle systématique via un outil de détection de similitudes (logiciel Compilatio). Après le dépôt du manuscrit de thèse, celui-ci est analysé par l'outil. Pour tout taux de similarité supérieur à 10%, le manuscrit est vérifié par l'équipe de FEDORA. Il s'agit notamment d'exclure les auto-citations, à condition qu'elles soient correctement référencées avec citation expresse dans le manuscrit.

Par ce document, il est attesté que ce manuscrit, dans la forme communiquée par la personne doctorante à l'INSA Lyon, satisfait aux exigences de l'Etablissement concernant le taux maximal de similitude admissible.

Département FEDORA – INSA Lyon - Ecoles Doctorales

SIGLE	ECOLE DOCTORALE	NOM ET COORDONNEES DU RESPONSABLE
CHIMIE	**CHIMIE DE LYON** https://www.edchimie-lyon.fr Sec. : Renée EL MELHEM Bât. Blaise PASCAL, 3e étage secretariat@edchimie-lyon.fr	**M. Stéphane DANIELE** C2P2-CPE LYON-UMR 5265 Bâtiment F308, BP 2077 43 Boulevard du 11 novembre 1918 69616 Villeurbanne directeur@edchimie-lyon.fr
E.E.A.	**ÉLECTRONIQUE, ÉLECTROTECHNIQUE, AUTOMATIQUE** https://edeea.universite-lyon.fr Sec. : Stéphanie CAUVIN Bâtiment Direction INSA Lyon Tél : 04.72.43.71.70 secretariat.edeea@insa-lyon.fr	**M. Philippe DELACHARTRE** INSA LYON Laboratoire CREATIS Bâtiment Blaise Pascal, 7 avenue Jean Capelle 69621 Villeurbanne CEDEX Tél : 04.72.43.88.63 philippe.delachartre@insa-lyon.fr
E2M2	**ÉVOLUTION, ÉCOSYSTÈME, MICROBIOLOGIE, MODÉLISATION** http://e2m2.universite-lyon.fr Sec. : Bénédicte LANZA Bât. Atrium, UCB Lyon 1 Tél : 04.72.44.83.62 secretariat.e2m2@univ-lyon1.fr	**Mme Sandrine CHARLES** Université Claude Bernard Lyon 1 UFR Biosciences Bâtiment Mendel 43, boulevard du 11 Novembre 1918 69622 Villeurbanne CEDEX sandrine.charles@univ-lyon1.fr
EDISS	**INTERDISCIPLINAIRE SCIENCES-SANTÉ** http://ediss.universite-lyon.fr Sec. : Bénédicte LANZA Bât. Atrium, UCB Lyon 1 Tél : 04.72.44.83.62 secretariat.ediss@univ-lyon1.fr	**Mme Sylvie RICARD-BLUM** Institut de Chimie et Biochimie Moléculaires et Supramoléculaires (ICBMS) - UMR 5246 CNRS - Université Lyon 1 Bâtiment Raulin - 2ème étage Nord 43 Boulevard du 11 novembre 1918 69622 Villeurbanne Cedex Tél : +33(0)4 72 44 82 32 sylvie.ricard-blum@univ-lyon1.fr
INFOMATHS	**INFORMATIQUE ET MATHÉMATIQUES** http://edinfomaths.universite-lyon.fr Sec. : Renée EL MELHEM Bât. Blaise PASCAL, 3e étage Tél : 04.72.43.80.46 infomaths@univ-lyon1.fr	**M. Hamamache KHEDDOUCI** Université Claude Bernard Lyon 1 Bât. Nautibus 43, Boulevard du 11 novembre 1918 69 622 Villeurbanne Cedex France Tél : 04.72.44.83.69 hamamache.kheddouci@univ-lyon1.fr
Matériaux	**MATÉRIAUX DE LYON** http://ed34.universite-lyon.fr Sec. : Yann DE ORDENANA Tél : 04.72.18.62.44 yann.de-ordenana@ec-lyon.fr	**M. Stéphane BENAYOUN** Ecole Centrale de Lyon Laboratoire LTDS 36 avenue Guy de Collongue 69134 Ecully CEDEX Tél : 04.72.18.64.37 stephane.benayoun@ec-lyon.fr
MEGA	**MÉCANIQUE, ÉNERGÉTIQUE, GÉNIE CIVIL, ACOUSTIQUE** http://edmega.universite-lyon.fr Sec. : Stéphanie CAUVIN Tél : 04.72.43.71.70 Bâtiment Direction INSA Lyon mega@insa-lyon.fr	**M. Jocelyn BONJOUR** INSA Lyon Laboratoire CETHIL Bâtiment Sadi-Carnot 9, rue de la Physique 69621 Villeurbanne CEDEX jocelyn.bonjour@insa-lyon.fr
ScSo	**ScSo*** https://edsciencessociales.universite-lyon.fr Sec. : Mélina FAVETON INSA : J.Y. TOUSSAINT Tél : 04.78.69.77.79 melina.faveton@univ-lyon2.fr	**M. Bruno MILLY** Université Lumière Lyon 2 86 Rue Pasteur 69365 Lyon CEDEX 07 bruno.milly@univ-lyon2.fr

*ScSo : Histoire, Géographie, Aménagement, Urbanisme, Archéologie, Science politique, Sociologie, Anthropologie

Remerciement

Les travaux présentés dans ce manuscrit ont été menés au laboratoire LaMCoS[1] au sein de l'INSA Lyon. Ils ont été financés par l'INSA Lyon dans le cadre d'un contrat doctoral et s'inscrivent dans le projet THPCA 2024 et le programme Sciences[2024].

Je tiens tout d'abord à remercier toutes les personnes qui ont rendu possible ce projet de recherche, et en particulier :

- Mes tuteurisses de thèse : Fabrice VILLE, Lionel MANIN et Bérengère GUILBERT. Merci à tous les trois de m'avoir donné l'opportunité de mener ce projet de recherche. J'aimerais avoir une pensée particulière pour Lionel que la vie a empêché de voir la fin de ce projet. Merci à Fabrice pour avoir accru son implication après le départ de Lionel nous permettant ainsi de mener le projet à bien. Un grand merci à Bérengère qui a su prendre, avec brio, le vélo en marche.
- Les référents scientifiques du projet THPCA et de la Fédération Française de Cyclisme (FFC), Jean-Christophe PERAUD, Phillipe ODIER et Emmanuel BRUNET. Ce fut un plaisir de vous rencontrer régulièrement pour partager les avancées du projet. Ma culture cycliste en est ressortie fortement grandie.
- Les membres du jury pour avoir accepté de participer à l'évaluation de mon travail. Christophe CLANET, directeur du programme Sciences[2024], que je remercie également pour son suivi du projet ainsi que ses questions toujours pertinentes qui ont orienté mon travail. Merci à Marie-Christine BAIETTO d'avoir accepté de présider mon jury de thèse. Un merci grand aux rapporteurs, Franck RENAUD et Stuart BURGESS, pour leur lecture attentive et leurs remarques pertinentes. J'ai également été très sensible à l'effort fait par tous les membres du jury, et en particulier Stuart BURGESS, pour s'être déplacé en personne le jour de la soutenance.

Je tiens ensuite à remercier Martin BEST pour son travail de grande qualité sur le banc d'essai, mais aussi pour l'excellente relation que nous avons su construire. Merci à Jérôme CAVORET pour ses réflexions toujours justes que ce soit au sujet de ma thèse ou en dehors. Un merci particulier pour les séances de réparation de vélo parfois tardives. Merci Sophie DE OLIVEIRA et Zahia ACHOUI qui ont grandement facilité mon travail grâce à leur accompagnement, et plus largement à tous les personnels de l'INSA qui m'ont accompagné durant ce projet.

Merci à tous les doctorantes et doctorants qui ont croisé mon parcours durant ma thèse. Notamment au sein de l'équipe SMC : Thomas, Augustin, Lucas, Marie, Aude, Elias, Paul, Julien, Aurore, Sebastian, Gabriel, Wassim. Merci pour l'ambiance conviviale au laboratoire et en dehors. Un merci particulier aux personnes avec qui j'ai eu l'honneur de partager mon bureau : Pierre, Nicolas et Büşra. Merci pour votre constante bonne humeur ainsi que pour les discussions, parfois profondes, parfois moins, concernant la tribologie, mais pas que. Merci également pour les suggestions scientifiques qui ont constamment stimulé mon travail. Un merci tout particulier à Gladys pour son accompagnement, sa gentillesse et sa patience, en particulier pendant la rédaction du manuscrit. S'il reste des fautes d'orthographe, adressez-vous à elle.

Merci à mes parents et mes frères, pour leur présence, leurs suggestions pertinentes, et surtout pour avoir su m'apporter un recul bienvenu lors des moments les plus difficiles de ce projet.

---

[1] http://lamcos.insa-lyon.fr/

Merci à mes amis qui ont toujours été là pour m'entourer. La bande de l'INSA, du lycée, de l'impro. Merci notamment à mes colocs durant cette aventure : Niconil et La bête. J'espère ne pas vous avoir trop fatigué avec mes dissertations sur les chaines de vélos parfois trop tard le soir.

Merci à l'INSA Lyon. Cette école m'a pris en sortant du bac et en 8 formidables années m'a fait grandir sur de très nombreux points, évidemment scientifiquement, mais surtout humainement.

Enfin merci à toi qui s'apprêtes à lire ce manuscrit. J'espère que tu trouveras un intérêt au travail qui y est présenté. Si jamais tu as l'occasion de le réutiliser, j'en serai très heureux.

Voici maintenant venu le moment où je peux écrire ce que je veux ! Je me permets donc d'ajouter une figure en format non-vectoriel, comme ça, pour le plaisir.
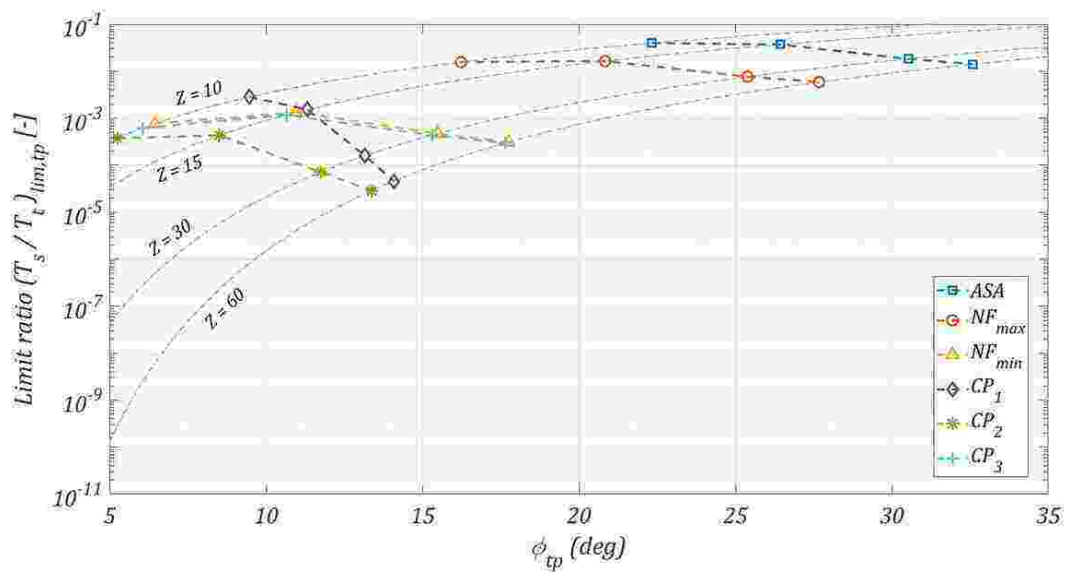
Tu trouves ça moche ? Eh bien moi aussi. Alors j'espère que tu apprécieras le travail fourni pour éviter cette bouillie de pixels à chaque illustration 😉. J'en profite d'ailleurs ici pour adresser un appel aux gens de chez Microsoft : s'il vous plait, faites en sorte que l'on puisse utiliser directement des fichiers .svg dans word sans problème de conversion. De très nombreux doctorants vous seraient reconnaissant.

Pour enfin finir ces (trop) longs remerciements, j'ai moi aussi choisi une citation pour faire classe. En plus, elle est parfaitement adaptée au contexte de rédaction d'un manuscrit de thèse et à son indispensable besoin de vulgarisation.

« Ce qui est simple est faux.
Ce qui ne l'est pas est inutilisable. »

Paul Valéry

Abstract

The intense competition between high-level athletes in track cycling requires research in order to make optimisation possible. In this context, the energetic efficiency of roller chain drives is studied to improve understanding of loss sources and propose paths of optimisation.

Losses in chain drives are known to be mostly caused by the meshing/un-meshing process of chain links on the sprockets. However, a preliminary study shows that losses caused by the motion of rollers along their associated tooth profile have a significant influence. The aim of this work is therefore to explore this phenomenon.

First, an original 2D quasi static model of a two-sprocket drive is presented. The global drive kinematics (including transmission error) is determined using specific sub-models for the tight and slack strands. A local sprocket sub-model is then introduced to calculate link tension, roller/sprocket contact force and roller location. This model can be used for different tooth profile geometries.

Following a specific validation process, the quasi-static model is used to explore the influence of tooth profile geometry on the interdependent evolutions of loads and roller location. Significant differences are reported. Its application to typical a track cycling drive shows that the specific constraints involved can only be overcome by dedicated tooth profiles.

A second model is then presented. Based on the results provided by the quasi-static model, it calculates drive efficiency, considering the losses caused by meshing and roller motion. Comparisons with experimental measurements are carried out to validate the approach proposed.

The efficiency model is then used to conduct a parametric study on track cycling roller chain drives. The influences of tooth profile geometry, applied torque, tension setting, number of sprocket teeth, chain pitch and friction coefficient are assessed and interactions between parameters identified. Based on the results, guidelines for future optimisations are given.

Keywords: Mechanical transmission, roller chain, kinematics, tension model, tooth profile geometry, roller motion, power losses, efficiency

Résumé

L'importante compétition entre cyclistes sur piste de très haut niveau pousse les travaux de recherches à explorer toutes les possibilités d'optimisations. Dans ce contexte, le rendement énergétique des transmissions par chaine à rouleaux est étudié dans le but d'améliorer la compréhension des puissances dissipées et d'en déduire des possibilités d'optimisations.

Dans les transmissions par chaine, les pertes sont majoritairement causées par l'engrènement/dégrènement des maillons sur les pignons. Toutefois, une étude préliminaire a montré que les pertes dues au mouvement des rouleaux le long de leur profil de dent ont une influence significative. Le but de ce travail est donc d'explorer ce phénomène.

Un modèle 2D quasi-statique est tout d'abord présenté. La cinématique générale (comprenant les erreurs de transmission) est déterminée en utilisant des sous-modèles spécifiques aux brins tendu et mou. Un modèle local de pignon est ensuite introduit afin de calculer les tensions dans les maillons ainsi que les forces de contact entre rouleaux et pignons. Le modèle peut être utilisé avec différentes géométries de denture.

Après un processus de validation, le modèle quasi-statique est utilisé pour étudier l'influence du profil de denture sur les évolutions corrélées des charges et des positions de rouleaux. Des différences significatives sont observées. L'application du modèle à une transmission de cyclisme sur piste montre que des géométries de denture dédiées sont indispensables pour faire face aux contraintes spécifiques induites par cette utilisation.

Un second modèle est ensuite proposé. En se basant sur les résultats du modèle quasi-statique, il calcule le rendement d'une transmission en prenant en compte les pertes causées par l'engrènement ainsi que les mouvements de rouleaux. Des comparaisons avec des résultats expérimentaux sont menées pour valider l'approche proposée.

Le modèle de rendement est ensuite utilisé pour mener une étude paramétrique sur des transmissions par chaines de cyclisme sur piste. L'influence de plusieurs paramètres est explorée : géométrie de denture, couple appliqué, réglage de la tension, nombres de dent des pignons, pas de la chaine et coefficient de frottement. Les interactions entre paramètres sont identifiées. En se basant sur les résultats, des lignes directrices pour de futures optimisations sont proposées.

Mots clefs : Transmission mécanique, chaine à rouleaux, cinématique, modèle de tension, géométrie de denture, mouvement de rouleau, puissances dissipées, rendement

Table of Contents

List of Figures

Nomenclature

Symbol	Units	Description
a	m	Transition of friction correction parameter (tanh width)
$C_{1,2}$	[-] and m	Chainette fitting contants
C_j	$N.m$	Torque associated with sprocket j
d	m	Absolute roller displacement
$\bar{d}$	[-]	Proportional roller displacement
$D_{x,y}$	m	Horizontal and vertical distance between the slack strand tips
ΔX	m	Horizontal distance between the axes of the driving and driver sprockets
ΔY	m	Vertical distance between the axes of the driving and driver sprockets
$E_{0,i,ij,ii}$	[-]	DOE factor effect
F	N	Generic letter for forces
f	[-]	Parameter for tight strand length (from Fuglede & Thomsen [1])
g	$kg.s^{-2}$	Acceleration of gravity
K, K'	rad / deg	Constants for calculation of ϕ_{tp} (specific to each tooth profile family)
L	m	Distance between the axes of the driving and driver sprockets
M_j	[-]	Tangency points for the tight strand common tangent
m_{link}	kg	Chain link mass
$n_{j,s,t,tot}$	[-]	Number of links
N_j	[-]	Tangency points for the slack strand common tangent
$P_{loss,mesh,roller}$	W	Dissipated powers
p	m	Chain pitch
$P_{i,k}$	N	Roller sprocket contact force
r	m	Chainette parameter
R/D_{bush}	m	Chain bush radius/diameter
R/D_{pin}	m	Chain pin radius/diameter
R/D_{roller}	m	Chain roller radius/diameter
$R_{1,2,etc.}$	m	Radius of tooth profile circle arc portion
R_{curve}	m	Local tooth profile curvature radius
R_j, R_{pitch}	m	Pitch radius of sprocket j
R_{tb}	m	Tooth bottom radius
R_{tip}	m	Tip radius for a given tooth profile
$slack$	[-]	Mid-span movement as a fraction of L
SS	[-]	DOE sum of square

$T_{i,j,k,s,t}$	N	Link tension force
T_s/T_t	[-]	Tension ratio
$(T_s/T_t)_{lim,tp}$	[-]	Limit ratio in good working conditions (excluding tooth climbing regime)
V	[-]	DOE variance
W	J	Generic letter for mechanical work
$x_{i,j}, X_{i,j}$	[-]	DOE coded units
x_t	m	Length of the tight chain strand
Z	[-]	Number of teeth

Greek letters

α^*	rad	Angles between two consecutive links
α_j	rad	Angular pitch of sprocket j
$\alpha_{s,t,j}$	rad	Angle between a chain strand and the closest link with both rollers contacting sprocket j
β	rad	Tilt angle of the pitch circles common tangent relatively to the centre direction
β_t	rad	Tilt angle of the tight chain strand relatively to the centre direction
δ	rad	Friction correction angle
$\|\delta(\infty)\|$	rad	Correction angle outside
η	[-]	Chain drive efficiency
γ	[-]	Non-dimensional roller location coordinate
$\gamma_{tp}^{A,B}$	[-]	Non-dimensional roller location coordinate at transition points A and B
κ	rad	Angle between the direction of the preceding link a the local $\vec{x}$ axis
λ_i	rad	Tilt angle for a slack strand link relatively to the horizontal direction
$\bar{\mu}$	[-]	Global friction coefficient
μ_{br}	[-]	Friction coefficient for the bush/roller contact
μ_δ	[-]	Friction coefficient associated with the friction correction angle δ
μ_{pb}	[-]	Friction coefficient for the pin/bush contact
μ_{rp}	[-]	Friction coefficient for the roller/profile contact
ν	rad	Angle between the direction of the following link a the local $\vec{x}$ axis
ϕ	rad	Roller contact angle
$\psi_{s,t,j}$	rad	Angle between a strand tip on sprocket j and the point of tangential contact
$\psi_{t,I,init}$	rad	Initial value for angle $\psi_{t,I}$
s_c	m	Curvilinear abscissa of the roller/profile contact point along its trajectory
s_r	m	Curvilinear abscissa of the roller centre along its trajectory
τ	rad	Tilt angle of the drive centre direction relatively to the horizontal

θ	rad	Generic letter for angles
ζ	rad	Driving sprocket rotation angle

Indices

	Description
i	Rollers and links spatial numbering
j	Sprocket numbering. I for the driving sprocket/chainring, II for the driven sprocket/rear cog.
k	Drive sub-positions "per component"
m	Explored sub-positions within a drive period. Varies between 1 and nb_{pos}.

Subscripts

A, B	Relative to kinematic cases A and B (used in CDEM)
br	Relative to Bush/Roller chain interface
$fol/prev$	Designate following and previous link with respect to a given chain articulation (used in the CDEM)
$init$	Use for variables related to the starting position of the kinematic calculation ($m = 1$)
pb	Relative to Pin/Bush chain interface
rp	Relative to Roller/Profile chain interface
s	Attribute of the slack chain strand
t	Attribute of the tight chain strand
tp	Attribute of the roller location transition points

Superscripts

A, B	Used to denote transition points A and B

Abbreviations

QSCDM: Quasi-Static Chain Drive Model, see Chapter II.
CDEM: Chain Drive Efficiency Model, see Chapter III.
GPLD: Geometric Progressive Load Distribution, see Naji & Marshek [2], see Chapter I.
tp: transition point
CP: Cycling Profiles, see Chapter IV.
LC: Loading Condition, see Chapter V.
EEU: Everything Else Unchanged, see Chapter VI.
RCD: Real Chain Dimension, see Chapter VI.
DOE: Design Of Experiments, see Chapter VI.
ANOVA: ANalysis Of VAriance, see Chapter VI.

En hommage à Lionel MANIN

General introduction

Following the awarding of the 2024 Olympic Games to Paris, French researchers have mobilised to play a role in this national event. Grandes écoles, universities and research centres gathered in the collective Sciences[2024] research program[1]. The aim of the project is to provide support to the French athletes in their quest for Olympic medals.

Part of the Sciences[2024] program, the THPCA 2024[2] (high performance in cycling and rowing) research project is supported by the French National Research Agency (ANR), see Figure 0-1. This project groups the French Cycling Federation (FFC) and the French Rowing Federation (FFA) with the aim of aiding the performances of athletes of both disciplines. This project is transdisciplinary as researchers from various fields (engineering, mechanics, physiology, computer science, *etc*.) each play a role. In parallel with this project, INSA Lyon founded this thesis whose objective is to develop a numerical model dedicated to the study of track cycling roller chain drive efficiency.

(a) *(b)*
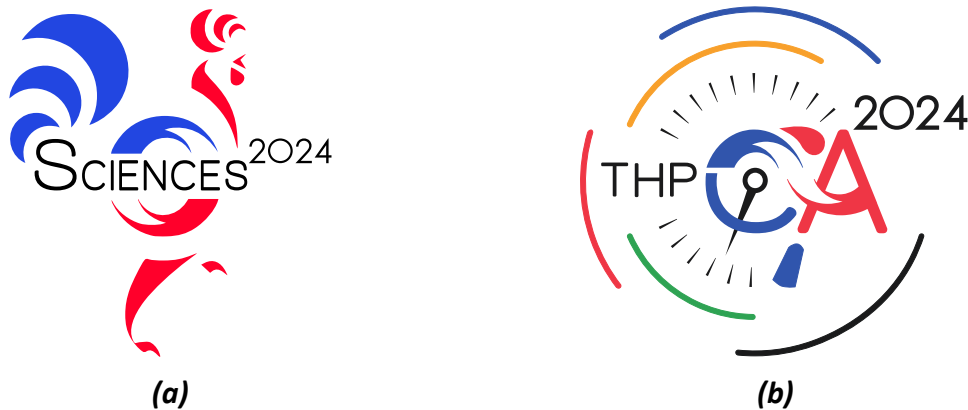
Figure 0-1: (a) Sciences[2024] (b) THPCA 2024 logo

In this thesis, Chapter I gives an overview of the previous works regarding the modelling of power losses in roller chain drives. The evolution of quasi-static tension models used to calculate loads in an operating chain (*i.e.*, link tension and roller/profile contact force) is detailed. The evolution of the connection between loads and roller location (along its associated tooth profile) is presented. Finally previous works regarding chain drive efficiency (mostly based on the quasi-static models mentioned) are introduced alongside experimental measurements.

In Chapter II, an original Quasi-Static Chain Drive Model (QSCDM) is presented. This model is used to calculate loads and roller location simultaneously. Any tooth profile geometry can be tested. The effect of friction introducing differences between driving and driven sprockets is considered.

Chapter III presents elements of validation of the QSCDM. Comparisons to both experimental measurements and previous numerical studies are carried out with satisfactory results.

In Chapter IV, the QSCDM is used to study the influence of the tooth profile geometry for industrial and track cycling drives. Analysis methods are proposed to facilitate characterising the influence of tooth profile geometry on chain drive behaviour, particularly on the evolution of loads and roller location. It is shown that the specific constraints of track cycling drives require dedicated tooth profiles to ensure satisfactory operations.

---

[1] https://sciences2024.polytechnique.fr/projet
[2] THPCA: Très Haute Performance en Cyclisme et Aviron. Grant number: 20-STHP-0006, https://anr.fr/ProjetIA-20-STHP-0006

In Chapter V, a Chain Drive Efficiency Model (CDEM) is introduced. Using the results provided by the QSCDM detailed in Chapter II, this model calculates the drive efficiency. Validation elements are presented based on measurements from both the literature and from a dedicated test rig specifically deigned to study track cycling drive efficiency.

Finally, in Chapter VI, using the CDEM, a parametric study of track cycling drive efficiency is carried out. The influence of tooth profile geometry is tested. The effects of various other parameters such as chain pitch and external torque are explored. The most influential parameters are identified using a Design Of Experiments (DOE) analysis. Based on the results obtained, guidelines for possible optimisation are proposed.

Chapter I

Context and literature review

I.1 General context

I.1.1 Roller chain

A chain is an arrangement of links able to rotate relatively to each other. It is used with sprockets to transmit power between two or more shafts, for instance from a motor to a receptor. Power transmission can also be carried out simultaneously with the reduction/increase of rotational speed using sprockets with different numbers of teeth. The first sketches of modern chains can be traced back to Leonardo da Vinci (see Figure I-1.a).

(a)   *(b)*
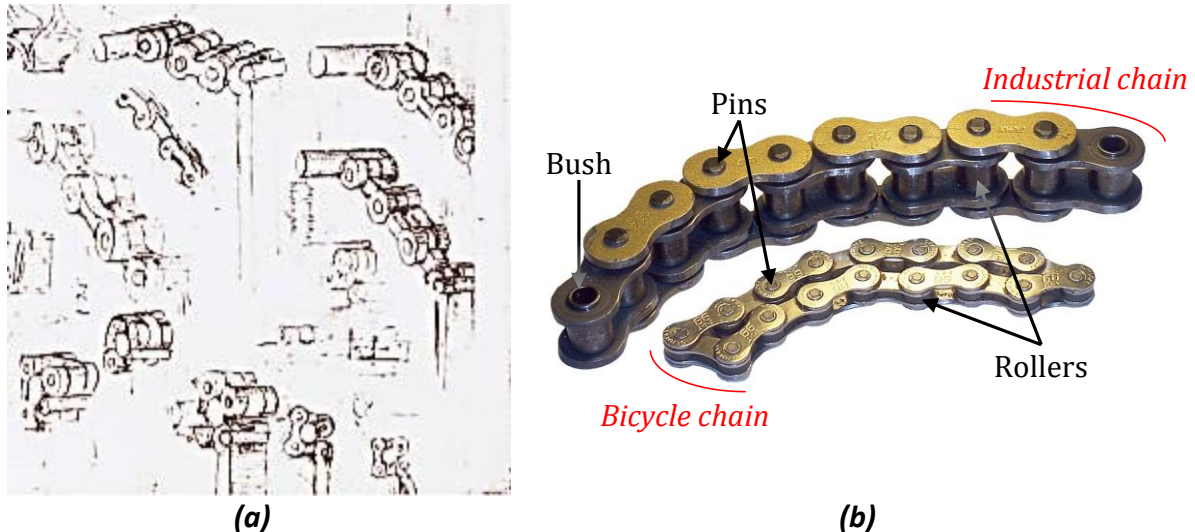
Figure I-1: (a) Sketches of chains by Leonardo Da Vinci, cropped and modified from [3] *(b) Comparison of industrial and bicycle chains* [4]

Chains remained ideas and drawings until Hans Renold invented the bush roller chain in the late 19th century [5]. The addition of bushes and rollers (see Figure I-1.b) reduces wear and leads to a significant improvement of chain life, allowing the mechanism to be widely used. Indeed, the free rotation around the bush distributes the contact stress over the entire roller circumference therefore increasing fatigue life compared with a situation where the contact point is always at the same location. A nomenclature of a modern roller chain is presented in Figure I-2.

(a)   *(b)*
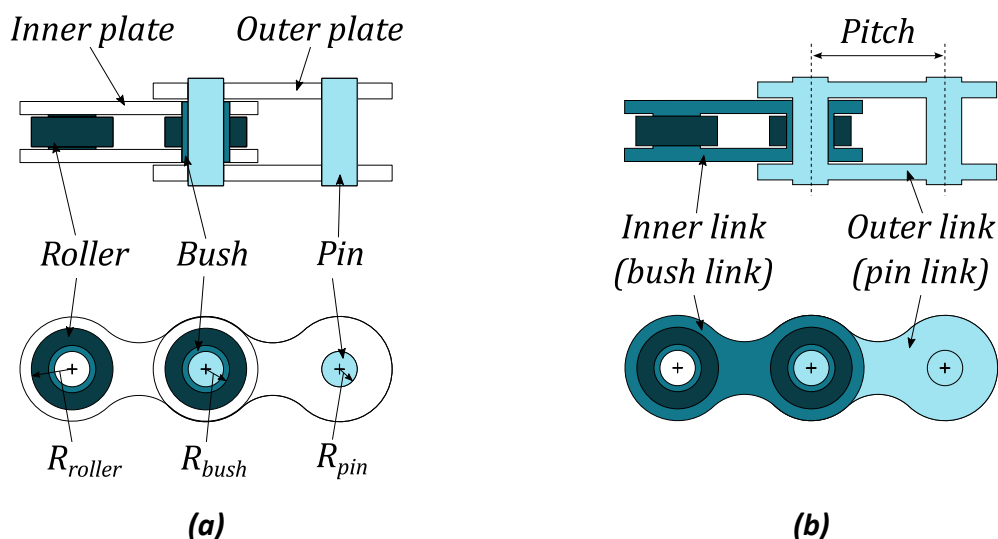
Figure I-2: Nomenclature of a modern roller chain: (a) part names, (b) sub-assemblies

Chains are composed of an alternance of inner and outer links (see Figure I-2.b). The outer links are constituted by pins in interference fit with outer plates. The inner links are formed by bushes, in interference fit with inner plates. Articulations between consecutive links are possible as a pin can rotate in its associated bush. The rollers are located around the bushes. Each roller rotates freely around its associated bush and makes contact with a sprocket. The pin, bush and roller are cylindrical parts whose radii are denoted R_{pin}, R_{bush} and R_{roller}, respectively (see Figure I-2.a). The distance between the axis of two consecutive bushes is called the chain pitch. The pitch is also the distance between the axis of two consecutive pins for new chains (the pin link pitch increases as the chain wears [6] due to the removal of material). The inner and outer links can be designated indifferently as bush and pin link, respectively.

Nowadays, roller chains are widely used in various applications. They are for instance present in internal combustion engines (timing chains) [7], [8], lifting machines [9], escalators [10], *etc*. With various applications come different constraints. Rotational speeds can reach thousands of rpm in internal combustion engines, while more than tens of thousands of newtons can be carried at slow rotational speeds in lifting applications [9].

To face all these challenges, numerous types of chains are proposed by manufacturers [11]. Among them, double pitch chains (see Figure I-3.a) allow weight reduction thanks to increased pitch. Cranked link chains (see Figure I-3.b) are formed by a single link type which eases potential length adjustments. Roller chains are also used in bicycle applications which constitute the core of this manuscript.

(a)   *(b)*

Figure I-3: (a) Double pitch chain (b) Cranked link chain [12]

I.1.2 Utilisation for cycling

In bicycle applications, chains are used to transmit the power supplied by the cyclist (through the pedals) from the chainring to the rear wheel. This transmission is usually performed with rotational speed modification. Rotational speed is usually increased for a road bike to reach high velocity while it can be reduced in cross country cycling. Cycling chains use a pitch of $1/2'' = 12.7mm$.

For most applications, modern bikes use a derailleur system (see Figure I-4.a). This mechanism allows modifications of the rear wheel's rotational speed, compared to that of the crankshaft, by changing the number of teeth of the chainring and rear cog engaged. The ratio between the number of teeth of the chainring and rear cog is called gear ratio (see §I.2.2). The use of bicycles for daily trips is expanding which obliges public transport to adapt [13]. New modes of bike use encourage manufacturers to constantly improve the derailleur system to enable easier gear shifting [14]–[17] and increasing reachable ratios [18], [19].

Substantial work has been done on road bike drives to optimise their efficiency. Many websites of amateur cyclists discuss the best drive arrangement and lubrication [20], [21]. Some manufacturers have proposed innovations such as the oversized derailleur [22] using bigger sprockets.

(a) **(b)**
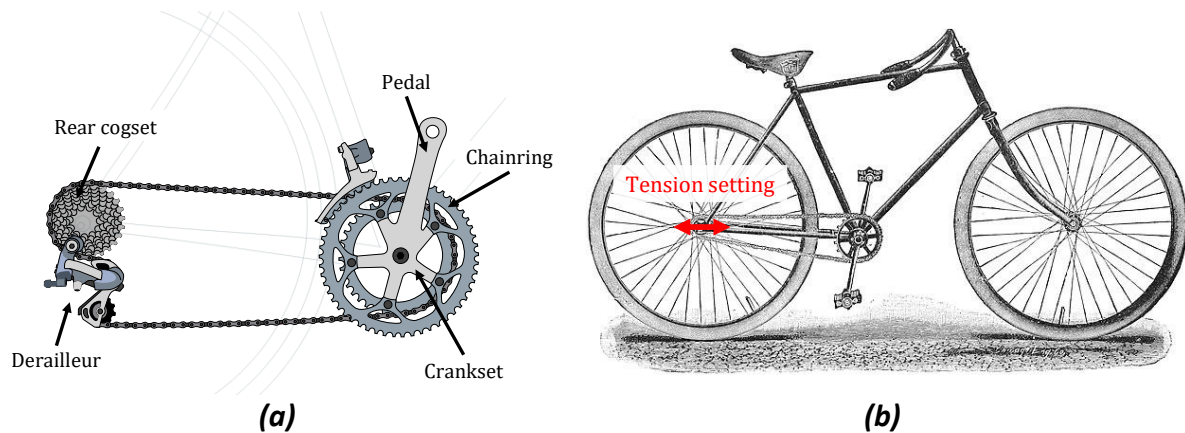
Figure I-4: Bicycle drives using (a) the modern derailleur system, adapted from [23] *(b) the single speed drive (on old bicycle)* [24]

However, this manuscript focuses on track cycling applications. Track bicycles use single speed drives (see Figure I-4.a). Such drives do not use a derailleur, resulting in a fixed gear ratio that cannot be changed while riding the bike. Consequently, the rotational speed ratio between the crankset and the rear wheel is also fixed. Moreover, due to the absence of freewheel (contrary to most bicycles using a derailleur), the cyclist is required to pedal as long as the bike is moving. In the absence of a derailleur, chain tension adjustments are achieved by changing the centre distance between the chainring and the rear cog (see Figure I-4.b). Optimisation is also carried out by the manufacturers of track bike drives [25], [26]. In particular, a specific chain using a smaller pitch of $3/8'' = 9.525mm$ was used by the Great Britain team at the last Olympic games [27].

Track cycling is a sport practised internationally mainly developed in Europe and Japan. It has been an Olympic sport since the beginning of the modern Olympic games for men (in 1896) in since 1988 for women [28]. Track cycling is practised in circular arenas called velodromes. Various types of race exist. Some are team events, some are individual. Some events such as the pursuit (see Figure I-5.a) require endurance skills. Others, such as the sprint (see Figure I-5.b) require explosivity.

(a) **(b)**

Figure I-5: Track cycling races: (a) Team pursuit (b) Individual sprint (© P. Pichon / FFC)

Endurance races are relatively long (about 4 minutes for a typical pursuit) and are characterised by high and almost constant speed (about $60km/h$). Conversely, sprint races are usually shorter and more speed variations are encountered. In such races, athletes usually start slowly (sometimes in track stand) before quickly accelerating to reach speeds of up to $70km/h$. The most extreme conditions for the chain drive are encountered in high intensity sprints where the chainring rotational speed can reach $130\ rpm$. The torque applied on the chainring can reach $500N.m$ at peak effort and up to $300N.m$ sustained for several drive rotations.

In track cycling races, final time differences between athletes are usually very close. Table I-1 shows the results of the individual men's sprint final of the Tokyo 2021 Olympic games where the two first races were decided by a margin of 1/100 seconds. These reduced gaps justify the interest of chain drive optimisation as little improvements can decide the race winner.

	Race 1	Race 2	Race 3
Harrie Lavreysen	$+0.012s$	Winner	Winner
Jeffrey Hoogland	Winner	$+0.015s$	$+0.208s$

Table I-1: Men's individual sprint, results of the final at Tokyo 2021 Olympic games [29]

Compared to industrial chain drives, track cycling drives are characterised by:

- Moderate rotational speed. The maximal speed encountered is $130\ rpm$ in high intensity sprints.
- High torques. Torques up to $300N.m$ can be sustained by top level athletes during high intensity sprints.
- Light chains. Track drives use lighter chains than the usual industrial standard. A typical track cycling link of pitch $p = 1/2'' = 12.7mm$ weighs about $3.6g$[1] (see Figure I-1.b).
- High gear ratio. In track cycling applications, gear ratios are typically between 3 and 5 which is usually higher than values encountered for industrial applications. Consequently, the number of chainring teeth is usually much higher than that of the rear cog.
- Safety. To preserve the athlete's safety, the risk of chain breakage must be reduced as much as possible. Chain standards [30] should prevent such events as the breaking load must be at least $8000N$ (no more than $4100N$ has been observed for track cycling chains[2]). Chain drop must also be avoided. This question is related to tension setting and will be addressed in the manuscript.

Due to these characteristics, the centrifugal force applied on a roller meshed with a 70 tooth chainring (highest possible number of teeth on current track bicycles) rotating at $130\ rpm$ reaches a maximum of about $0.09N$ (compared to up to $4100N$ in link tension). Therefore, quasi-static modelling is well adapted to such drives as the computational cost will be limited without significant loss of precision.

In track cycling applications, strand vibrations are known to occur. These are probably mainly caused by the varying torque applied at the chainring due to preferential pedal direction (more torque is applied with horizontal pedals). This study is limited to constant torque and rotational speed. Therefore, strand vibrations are neglected.

---

[1] Compared to about $7.6g/link$ for industrial chains of the same pitch [11].
[2] Corresponding to $500N.m$ at the chainring for a $Z_I|Z_{II} = 60|15$ drive.

Considering the boundaries of the analysis, a corresponding literature review is presented in the following parts.

First, an overview of a roller chain drive is given. The definition of sprocket geometry is detailed and different tooth profile standards are presented. Then, the polygonal effect, a perturbation inherent to any chain drive, is described. Its kinematic consequences are detailed. Although not studied in this thesis, a brief summary of the dynamical implications of the polygonal effect is also given.

Then, a review of existing quasi-static tension models is provided. Such models are used to determine the loads encountered in a chain drive (mainly link tension and roller/sprocket contact force). Progressive efforts to explore the dependency between roller locations along the associated tooth profile and link tension evolution are detailed.

Then, previous works dedicated to chain drive efficiency are presented. Models and experimental studies are detailed. Orders of magnitudes of drive efficiency are given.

Finally, the objectives of the thesis are set out considering the detailed literature review.

I.2 Overview of roller chain drives

The following part gives an overview of roller chain drives. Sprocket construction is first detailed. Standards regarding tooth profile definition are also presented. Then, the kinematic and dynamical consequences of the polygonal effect are explored.

I.2.1 Sprocket definition

To define the geometry of a given sprocket, the pitch polygon is first constructed [31] (see Figure I-6.a). This polygon has the same number of sides as the desired number of teeth Z. The side of the polygon is equal to the desired pitch $p_{sprocket}$. The circumscribed circle of this polygon is called pitch circle. The radius of the pitch circle is given by eq.(I-1).

$$R = \frac{p_{sprocket}}{2\sin(\alpha/2)}$$
(I-1)

with:

- $\alpha = 2\pi/Z$, the pitch angle

Each vertex of the pitch polygon is associated with an angular sector of width α. The tooth profile geometry of each angular sector is given using the summit as local origin O (see Figure I-6.b). Angular sectors are usually identical and therefore the definition of only one of them is sufficient to give the entire sprocket geometry.
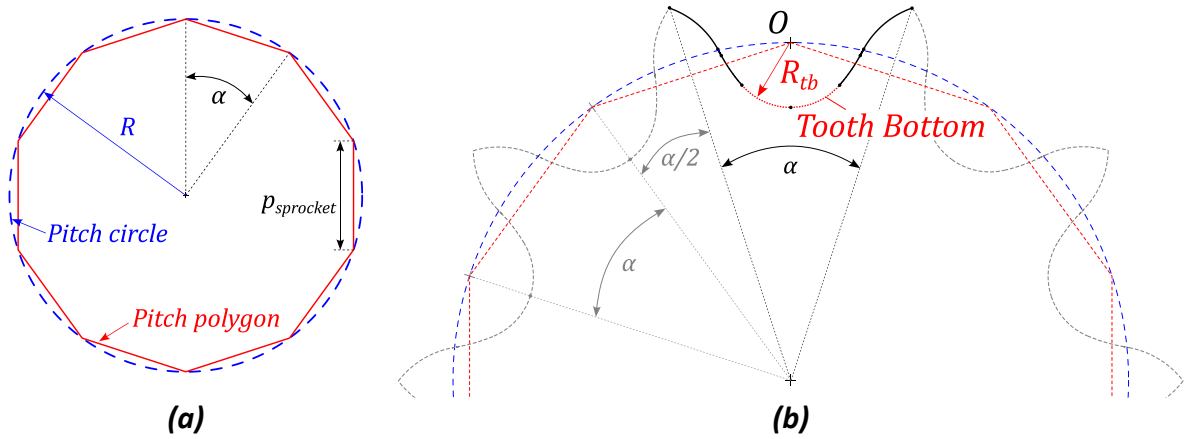
Figure I-6: (a) Pitch circle and polygon (b) tooth profile definition

Typical definitions of tooth profile are given in by ASA [32] and ISO [31] standards (see Figure I-7). For both standards, the local tooth profile is defined using circle arcs and/or straight lines. Both standards propose symmetrical profiles. Therefore, only one half is defined and the second one is obtained by symmetry with respect to $(O, \vec{y})$.
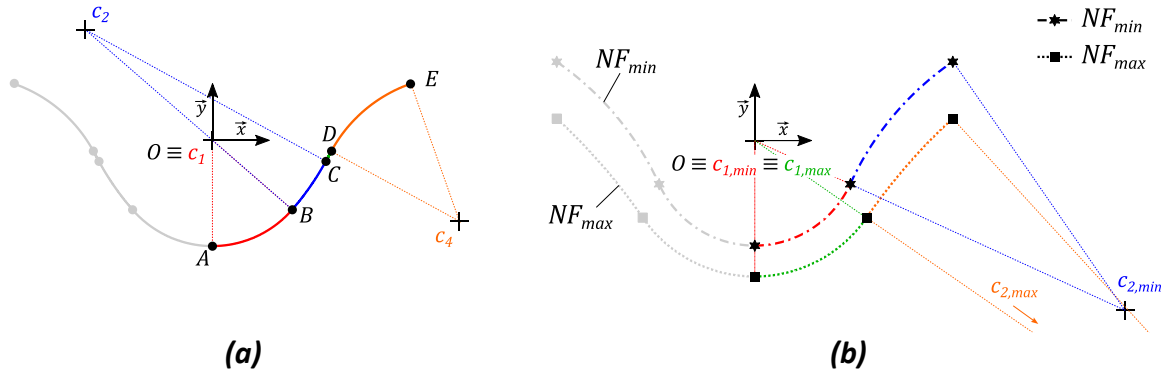
Figure I-7: (a) ASA tooth profile [32] **(b) NF profile from ISO standard** [31]

For ASA and ISO standards, tooth profile parameters are given by equations depending on the number of teeth Z, the roller radius R_{roller} (expected to be used with the sprocket) and the sprocket pitch $p_{sprocket}$. These definitions are given in Appendix A.

For one set of Z, R_{roller} and $p_{sprocket}$, the ASA standard [32] gives a single tooth profile. It is defined by three circle arcs and one straight portion (see Figure I-7.a).

- Between A and B, the first circle arc defines the tooth bottom (centre c_1). This arc is also called *seating curve*. Its centre coincides with the local origin O and its radius is strictly larger than the roller radius R_{roller}
- Between B and C, the second circle arc is called the *working curve* (centre c_2)
- Between D and E the last circle arc called the *topping curve* defines the tooth tip (centre c_3)
- Points C and D are linked by the *straight portion*

Curve portion parameters are always such that the slope is continuous along the tooth profile (*i.e.*, curve portions are tangent at B, C and D). This profile geometry is denoted as ASA profile for the rest of the manuscript.

For one set of Z, R_{roller} and $p_{sprocket}$, the ISO standard [31] gives a range of acceptable profiles. The boundaries of the acceptable zone are delimited by two extreme tooth profiles: NF_{min} and NF_{max}[3]. Therefore, any profile whose geometry lies between the two extreme ones satisfies the standard (see Figure I-7.b). For the rest of the manuscript, both NF_{min} and NF_{max} geometries are considered. Their definition is more straightforward than the ASA one as it is based on only two tangent circle arcs.

For both standards, the bottom of the tooth profile (called tooth bottom) is circular (see Figure I-6.b). The centre if this circle arc coincides with the local origin O and its radius R_{tb} is larger than R_{roller}. It can be noted that the ASA profile satisfies the ISO standard as it lies in between the NF_{max} and NF_{min} profiles.

---

[3] The ISO standard is based on a previous NF standard.

I.2.2 Polygonal effect

A typical chain drive is represented in Figure I-8. The driving sprocket is at the right-hand side with index I while the driven sprocket is on the left with index II. The driving sprocket rotates clockwise. Therefore, the tight strand is the higher one and transmits loads. The slack one is at the bottom. The strand tips mark the transition between the links in the chain strands and those meshed with a sprocket (see Figure I-8). Each time the driving sprocket meshes a new link, another one is removed from the driven sprocket. Therefore, the mean rotational speed ratio of the drive is equal to the gear ratio $Z_I/Z_{II} = R_I/R_{II}$.
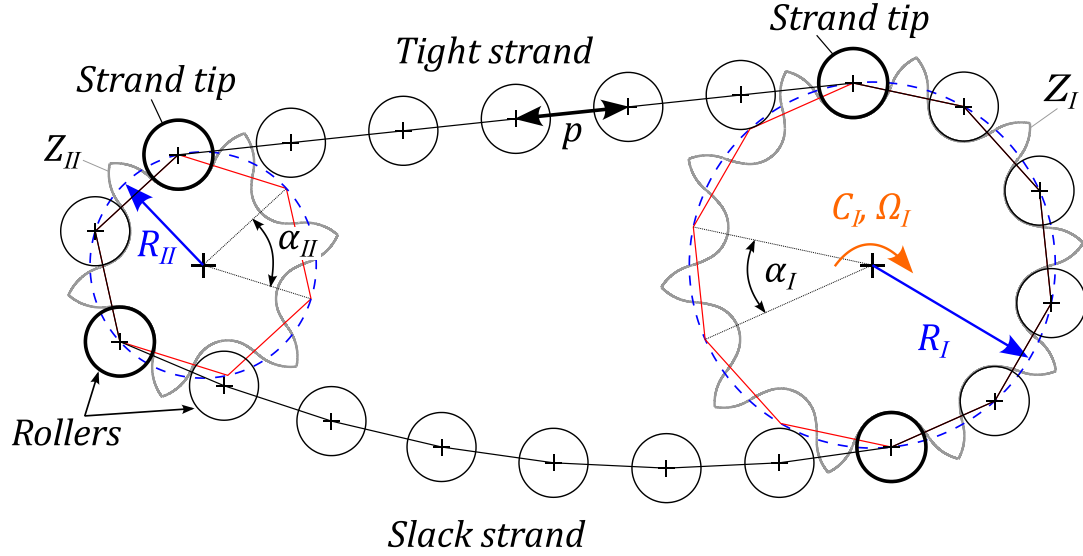
Figure I-8: Diagram of chain drive principle

For chain and sprockets of matching pitch (*i.e.*, $p_{sprocket} = p_{chain} = p$), in a first approximation, the radius difference between the roller and the tooth bottom can be neglected (the radius difference is about 4.3% for NF_{max} profile[4]) [33]. Thus, the centre of the rollers in contact with a sprocket lies at the vertices of the pitch polygon (see Figure I-8). Consequently, as the drive rotates, strand tips move along the pitch circle. Figure I-9 shows the two extreme strand tip positions for a given sprocket (assuming a horizontal strand).

(a)   *(b)*
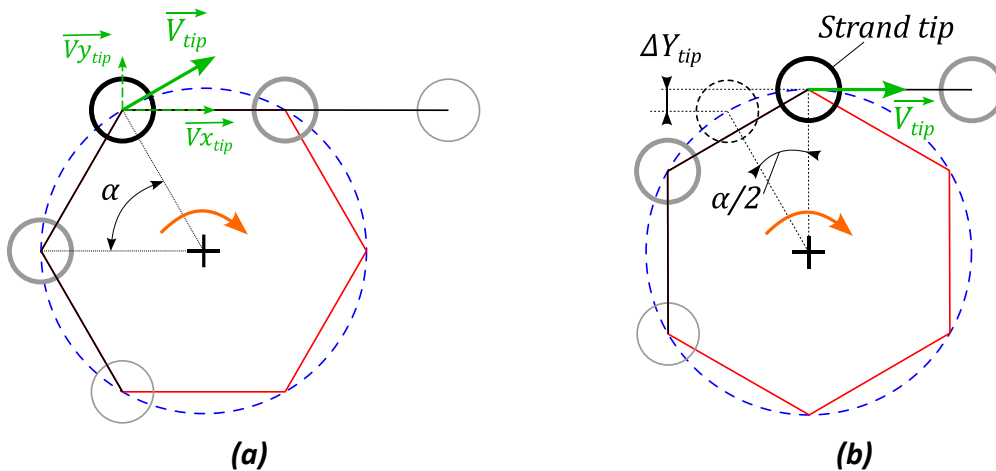
Figure I-9: Extreme strand tip positions

---

[4] With $D_{roller} = 7.75mm$ which gives $R_{tb} = 4.05mm$ (see Appendix A).

The strand tip movement along the pitch circle causes the projections of the strand tip speed $\overrightarrow{V_{tip}}$ along the horizontal and vertical directions to vary (see Figure I-9). Moreover, the height of the strand tip is also modified by an amount ΔY_{tip}, given by eq.(I-2) (see Figure I-9.b).

$$\Delta Y_{tip} = R \left(1 - \cos\left(\frac{\alpha}{2}\right) \right) \qquad \textbf{\textit{(I-2)}}$$

The variation of the strand tip positions is a consequence of the discrete nature of the chains. Indeed, contrary to belts, the relative rotation between links can only occur at the chain articulations. This phenomenon, and all the consequences that it induces, are generally denoted polygonal effect, due to the shape taken by a chain wrapping around a sprocket, approximately following the pitch polygon (see Figure I-8).

The polygonal effect induces periodical variations of the rotational speed ratio, causing transmission error. Moreover, it acts as a dynamical excitation which generates possible vibration problems. Both subjects (*i.e.*, kinematics and dynamics) are discussed separately below.

a) *Kinematic consequences of the polygonal effect*

Binder [32] was the first to propose a kinematic model of a chain drive. Assuming that all the parts are rigid, he proposed to consider the dependency between the rotation of the driving and driven sprockets using a four-bar mechanism (see Figure I-10). Thus, the strand tip positions move along the pitch circles, making it possible to model the polygonal effect.
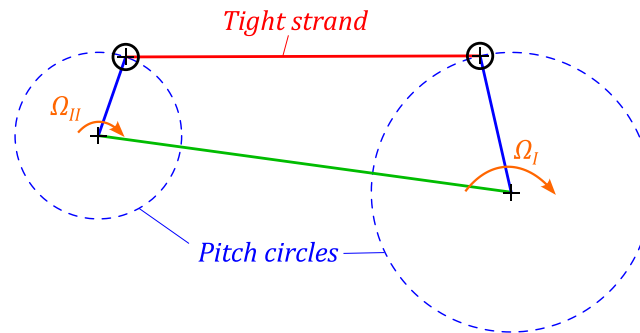
Figure I-10: Tight strand model using a four-bar mechanism

Binder [32] reported that the behaviour of the four-bar mechanism depends on the centre distance between the driving and the driven sprockets. He limited his study to drives with a horizontal tight strand common tangent (*i.e.,* upper tangent common to both pitch circles, see Figure I-11.b). Two extreme cases were considered depending on the length of the common tangent being equal to a multiple of the chain pitch (Figure I-11.a) or an odd multiple of a half pitch (Figure I-11.b). These two cases correspond to the variation of strand tip positions of both sprockets occurring in simultaneous or opposing phase, respectively. It can be noted that, depending on the phasing of both sprocket rotations, the number of links in the chain strands can vary (*e.g.*, between 5 and 6 in Figure I-11.a and Figure I-11.b, respectively).
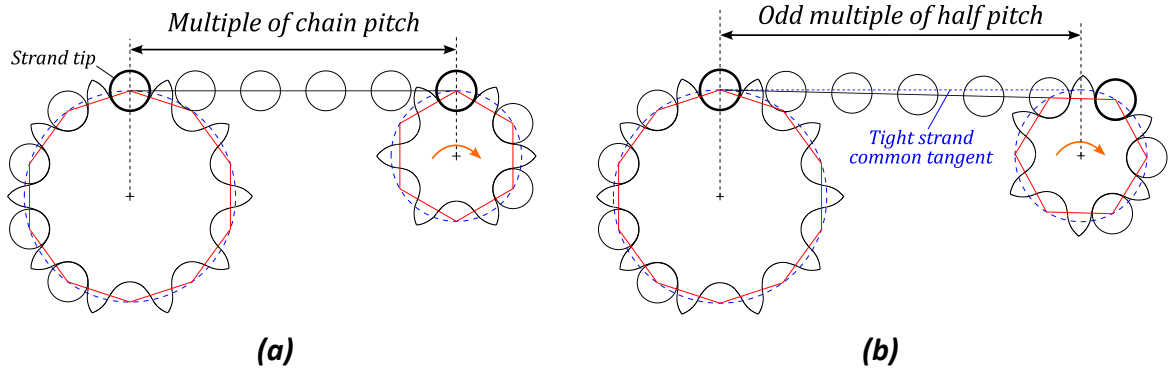
Figure I-11: Drive with tight strand common tangent being (a) a multiple of the chain pitch, (b) an odd multiple of half pitch

For the two extreme cases of Figure I-11, the ratio between the rotational speed of the driving and driven sprockets was calculated using the four-bar mechanism shown in Figure I-10. The deviation of this instantaneous ratio from its mean value Z_I/Z_{II} (*i.e.*, transmission error) was characterised using the parameter ΔR according to eq.(I-3). The results, with ΔR expressed in %, are presented in Figure I-12. The drives studied were for driving sprockets with less teeth than the driven one (*i.e.*, $Z_I < Z_{II}$).

$$\Delta R = \frac{\left(\frac{\Omega_I}{\Omega_{II}}\right)_{max} - \left(\frac{\Omega_I}{\Omega_{II}}\right)_{min}}{\left(\frac{\Omega_I}{\Omega_{II}}\right)_{min}} \qquad \textbf{(I-3)}$$
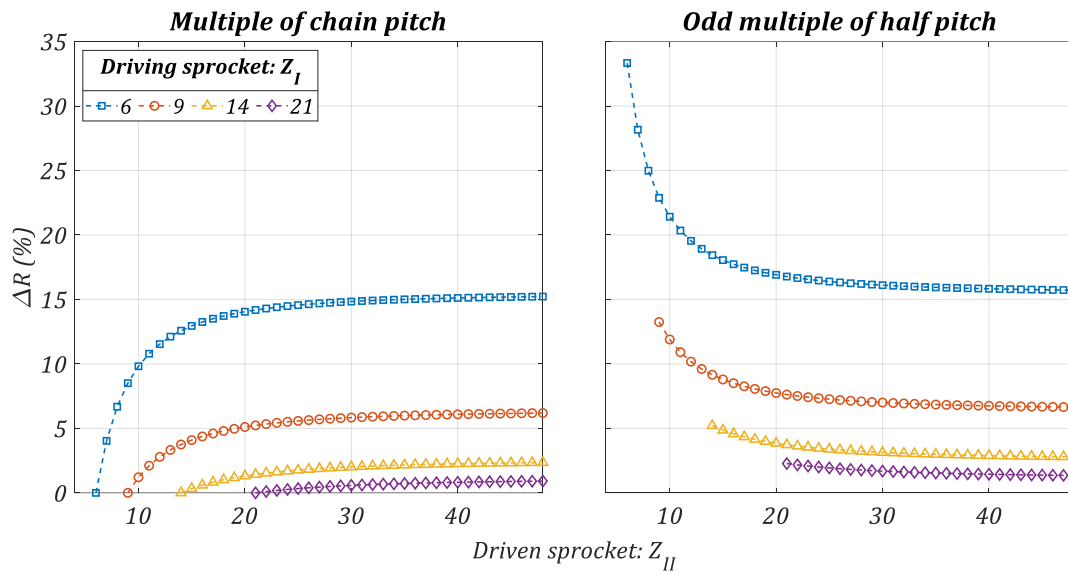
Figure I-12: Variation of ΔR for various numbers of teeth. Adapted from [32]

For a high driven sprocket number of teeth Z_{II}, the two extreme centre distance cases tend toward the same deviation ΔR. However, for a smaller Z_{II}, the odd multiple of half pitch case diverges whereas the multiple of half pitch converges to zero. For the multiple of chain pitch case, drives with $Z_I = Z_{II}$ show a constant speed ratio (*i.e.*, $\Delta R = 0$). On the contrary, a $Z_I|Z_{II} = 6|6$ drive for the odd multiple of half pitch case undergoes a variation of about 35%. The results also show that the influence of the polygonal effect decreases as the numbers of teeth increase. Variations of less than 1% are predicted for drives with high numbers of teeth such as $Z_I|Z_{II} = 21|48$. This undesirable instantaneous speed ratio variation is the main reason why chain manufacturers recommend avoiding excessively small

numbers of teeth (sprockets with less than $Z = 19$ are usually not recommended for industrial applications) [34].

Mahalingam [35] and Morrison [36] proposed similar studies and also found that multiple number of pitch case should be preferred to limit kinematic perturbations. Mahalingam later used his kinematic modelling as boundary conditions for a study of strand vibration (see §b) below). In [37], Bouillon & Tordion tested experimentally the kinematic theory based on a four-bar mechanism. They measured the transmission error as well as the angular acceleration of the sprockets. Their results showed that the four-bar mechanism gives a good approximation of sprocket movements for small numbers of teeth where polygonal action is dominant (the theory shows good predictions up to $Z = 18$ [37]). Above this number of teeth, dynamical effects can no longer be neglected (see §b) below). In [1], [38] Fuglede & Thomsen also modelled the kinematic consequences of the polygonal effect using a four-bar mechanism. They proposed an analytical solution for transmission error and sprocket acceleration. A generalisation of the two extreme cases "multiple of chain pitch" and "odd multiple of half pitch" was proposed using parameter f. This parameter was used to define the length of the tight strand common tangent according to eq.(I-4).

$$L_{ct} = (N + 1 + f)p \qquad\qquad \textbf{\textit{(I-4)}}$$

with:

- L_{ct}, the length of the tight strand common tangent (see Figure I-11.b)
- $N \in \mathbb{N}$, the minimal number of links in the tight strand
- $f \in [0\,,1[$

For $f = 0$, the tight strand common tangent equals a multiple of the chain pitch and the drive is in the "multiple of chain pitch" case. For $f = 0.5$, the drive is situated in the "odd multiple of half pitch" case. Using their kinematic solution, Fuglede & Thomsen also calculated the required chain length for the drive to operate (the slack strand trajectory was assumed to be straight). They showed that polygonal action causes this theoretical length to vary. This variation produces fluctuations of link tension during drive operations. As for Mahalingam [35], the kinematic study was used as input for a more complex analysis of strand vibration (see §b) below).

To compensate the consequences of polygonal action, Radzimovsky [39] proposed to add an original mechanism at the drive input to vary the rotational speed of the driving sprocket. The mechanism parameters are adjusted to compensate for the kinematic perturbations to obtain an overall mechanism with a constant speed ratio (*i.e.*, $\Delta R = 0$).

b) *Dynamical consequences of polygonal effect*

Kinematic studies of the polygonal effect are usually carried out to obtain boundary conditions for more complex dynamical studies (*e.g.*, Mahalingam [35], Fuglede [38]). Indeed, the periodical variation of the speed ratio acts as a dynamical excitation, causing longitudinal and transverse strand vibrations. Strand vibrations will not be considered in this manuscript. However, the following section gives a brief overview of the literature on the subject.

Transverse vibration of a chain strand were studied by Binder [32], [40]. The chain strand was represented as articulated masses linked to massless bars. The strand boundaries were assumed to be fixed (see Figure I-13). Binder [41] also studied impacts occurring between the chain and sprocket at each capture of a new roller by the driving sprocket. Sack [42] studied the transverse vibrations considering the strand as a string with uniformly distributed mass. The string boundaries were

assumed to move at constant speed. Mahalingam [43] used its kinematic study to apply boundary speeds caused by polygonal action. All the studies showed that resonance occurs when the meshing frequency (frequency of polygonal effect) meets the natural strand frequencies. The addition of moving boundaries reduces the predicted natural strand frequencies. Consequently, the drive rotational speeds to be avoided in order to prevent large vibrations are also modified.
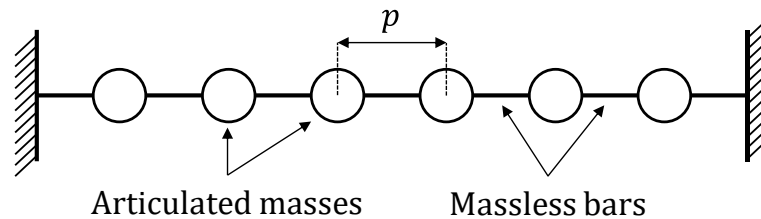
Figure I-13: Strand modelling with fixed boundaries. Adapted from [40]

Turnbull [44] studied strand vibration using a 2D dynamic model of chain drive. The torsional vibration of the sprockets was included. Experimental measurements were also performed. The results showed that the tortional natural frequencies of the sprockets are of the same order as the strand natural frequencies. Therefore, they should also be considered and care must be taken to maintain the meshing frequency far from them. However, these frequencies depend, for instance, on the properties of the shafts, the position of the bearings, *etc*. Therefore, they must be determined by considering the entire system and not only the chain drive. It was proposed to reduce the chain pitch to limit the excitation caused by polygonal action (pitch radius R can be kept constant by increasing the number of teeth, see eq.(I-1)). Moreover, experimental results showed that large transverse strand vibrations occur more easily for "multiple of chain pitch" case (*i.e.*, $f = 0$, see eq.(I-4)) despite polygonal excitation being less significant. Measurements of the noise caused by roller/sprocket impacts were also performed. It was shown that this noise decreases for higher numbers of teeth and smaller chain pitch (*i.e.*, less polygonal action).

*L*ongitudinal strand vibrations was studied by Fawcett *et al.* studied in [45]–[48]. These vibrations can cause significant link tension oscillations. It was shown that changing the centre distance (*i.e.*, parameter f) does not significantly modify these oscillations. Roller/sprocket impacts were also studied. It was shown that the addition of lubricant at the roller/sprocket interface reduces the noise. An apparatus constraining the tight strand trajectory close to the driving sprocket meshing point was also proposed to reduce the noise caused by impacts. A review of this subject from 1981 can be found in [49].

Strand models were later improved by Chen *et al.* [50], who considered the chain strand as a travelling string (like Mahalingam [43]) but introduced the possibility of varying the string length to account for the varying number of links in a chain strand (see Figure I-11). Choi & Johnson studied in [51] the influence of a tensioner on strand dynamics. It was shown that the tensioner could be used to reduce vibrations.

More recently, the dynamical behaviour of chain drive was studied using multibody dynamical models. Such models can be found for instance in [52]–[57]. In [58], [59] Omar proposed a multibody formulation to study bicycle chain drive dynamics including the derailleur system. Examples of link tension and acceleration were given.

The question of the dynamical behaviour of the drive is mainly addressed in industrial applications where high rotational speed (thousands of rpm can be reached) makes it more likely to encounter natural frequencies and therefore trigger significant vibrations. Patents on this subject can for instance

be found in [60], [61] which propose varying the sprocket pitch from one tooth to another to divide the excitation caused by the polygonal effect between more frequencies.

This part gave on overview of roller chain drives. Tooth profile standards and sprocket definition were described after which the polygonal effect, inherent to any chain drive, was presented. Previous works, using four-bar mechanisms to explore the kinematic consequences on transmission were also described. Such models give a good approximation of the dependency between driving and driven sprocket rotation. Although not considered in this manuscript, a brief review of the dynamical implications of the polygonal effect was also given. This subject is indeed quite complex and requires dedicated models which is not in the scope of the study.

The following part details the evolution of quasi-static tension models which fall within the scope of this thesis.

I.3 Quasi-static tension models

The evolution of quasi-static tension models is now presented. These models play an important role in modelling drive efficiency as they calculate the loads involved in a chain drive which is necessary to ultimately obtain the power losses (see §I.4 below).

The loads considered are usually link tension and roller/sprocket contact forces. They are determined through varying assumptions. The evolution of roller motion modelling is also presented. Its connection with load variations is also discussed

The first model of loads between the chain (including rollers) and sprockets was introduced by Binder in 1953 [32]. Binder considered the equilibrium of a chain articulation (*i.e.*, a set of pin, bush and roller, see Figure I-14.a) subjected to three external forces (see Figure I-14.b and Figure I-15.a):

- T_i, the tension in the link preceding the articulation considered
- T_{i+1}, the tension in the link following the articulation
- P_i, the contact force between the tooth profile and the roller

Roller/profile clearances were neglected (*i.e.*, $R_{roller} = R_{tb}$) and all the rollers were assumed to lie at the tooth bottom (*i.e.*, the roller centre coincides with the centre of the tooth bottom circle). In this specific position, the rollers are called seated.
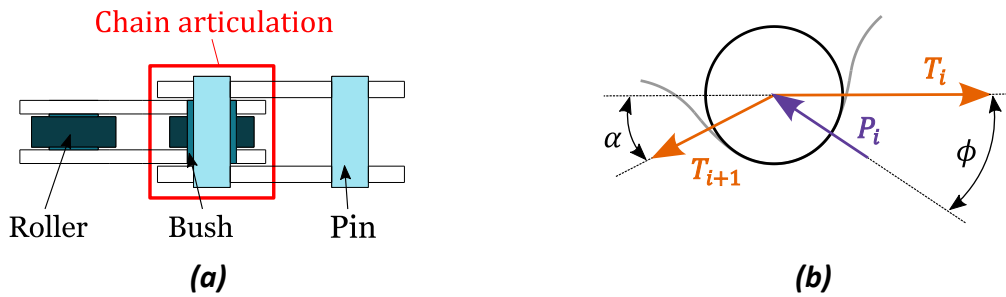
Figure I-14: Equilibrium of chain articulation according to Binder [32]

The tensions in the tight and slack strands (T_t and T_s, respectively) were assumed to be constant and known. Parameters in Figure I-14 are:

- $i \in [\![1 , n + 2]\!]$ such that $T_1 = T_t$ and $T_{n+2} = T_s$ (see Figure I-15.a). n is the number of links in contact with the sprocket considered
- ϕ, pressure angle between the directions of T_i and P_i
- α, angle between the directions of T_{i+1} and T_i. As all the rollers are seated, this angle equals the pitch angle

For the ASA profile, the pressure angle ϕ is estimated in the standard assuming that P_i acts along the profile normal direction and that roller/profile contact occurs at point B (see Figure I-7.a).

The articulation equilibrium shown in Figure I-14.b leads to the following relation between T_i and T_{i+1}.

$$T_{i+1} = T_i \frac{\sin(\phi)}{\sin(\phi + \alpha)} \tag{I-5}$$

Considering the equilibrium of every articulation in contact with the sprocket considered gives a relation between the tight strand tension T_t and the tension in link i (eq.(I-6)).

$$T_i = T_t \left(\frac{\sin(\phi)}{\sin(\phi + \alpha)} \right)^{i-1} \tag{I-6}$$

This first tension model calculated the tension in each link in contact with a considered sprocket, assuming that the tight strand tension T_t is known. Howerver, this approach suffered from several drawbacks. First, link tension does not depend on the instantaneous sprocket orientation since as the articulation is meshed it is considered to carry the same amount of load as any other. Secondly, the link tension was independent from the slack strand tension T_s. Binder's model therefore constitutes a good approximation for the tensions in links close to the tight strand. Finally, roller location and link tension were independent as all the rollers were assumed to be seated independently of any loading considerations. Later studies will resolve these open questions.
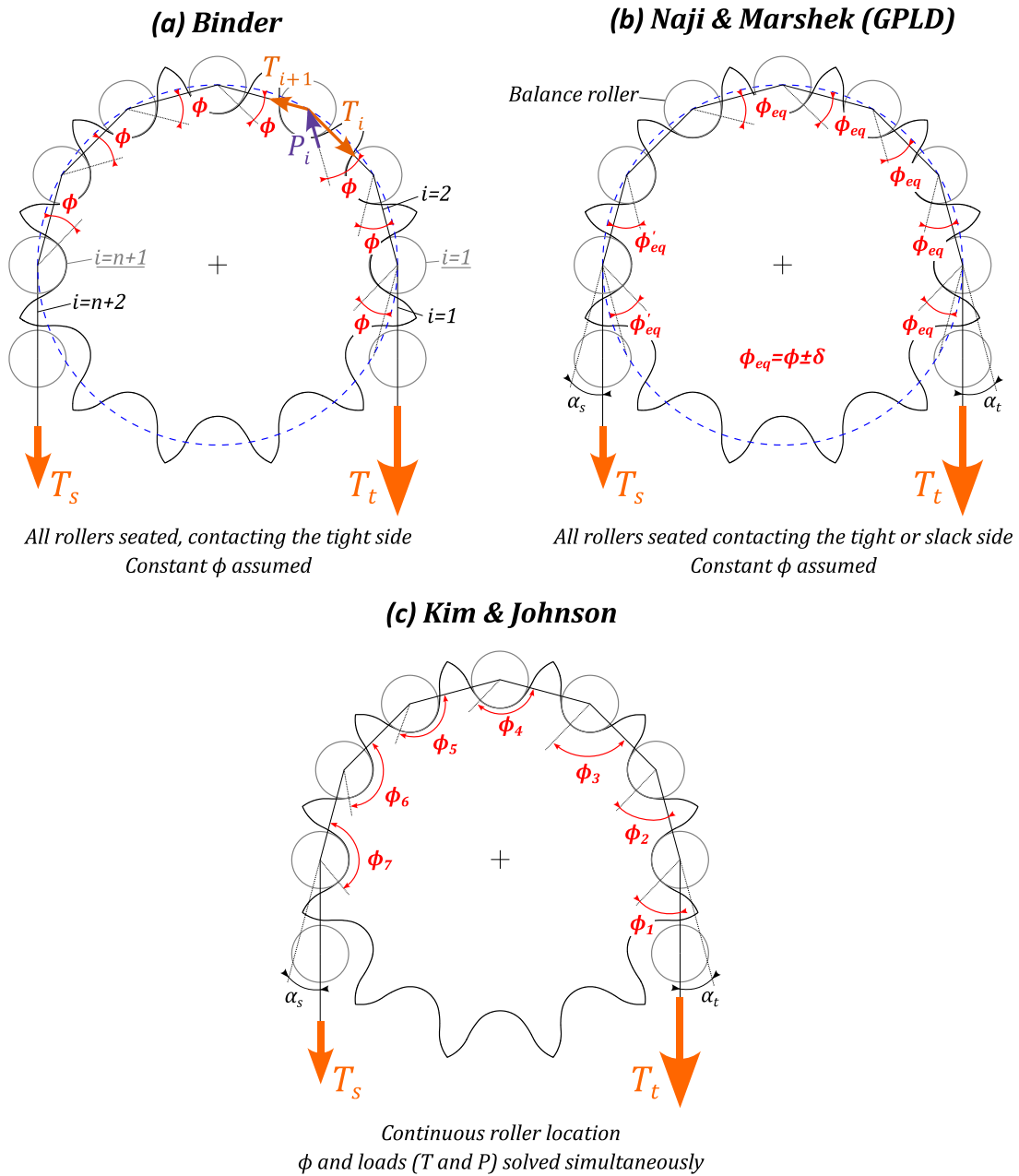
Figure I-15: Evolution of pressure angle modelling (adapted from [52]*): (a) Binder (b) GPLD model from Naji & Marshek (c) Kim & Johnson*

In the 1980s, Naji & Marshek produced numerous studies aimed at improving the first approach introduced by Binder. They presented measurements of link tensions performed using an instrumented link [62], [63]. Using weights to prescribe strand tension, several tension ratios T_s/T_t were tested. Due to the constraints of the experimental apparatus, measurements were carried out at quasi-static speed. The results were presented as relative tension T_i/T_t. Similar tension ratios T_s/T_t were tested for different absolute tensions. It was shown that, for the loads explored (up to $850N$), the evolution of relative tension does not depend on the magnitude of absolute tension. Driving and driven sprockets were studied and differences in load evolutions were reported (see Figure I-17 below).

Based on the experimental results, they introduced the Geometric Progressive Load Distribution (GPLD) tension model which significantly improved Binder's model [2]. Sprocket orientation was considered thanks to the addition of angles α_t and α_s (for the roller marking the transition with the tight and slack strands, respectively, see Figure I-15.b). These angles correct eq.(I-5) for articulations in the process of meshing and un-meshing. To account for the slack strand tension T_s, Naji & Marshek proposed that each roller can contact either the tight or the slack side of its associated tooth profile (see Figure I-16) while remaining seated. A roller contacting the tight side of the profile corresponds to Binder's approach (see Figure I-14.b).

(a)   *(b)*
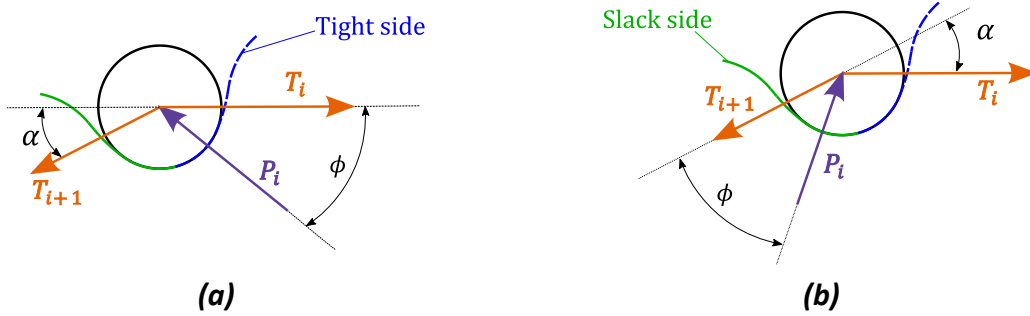
Figure I-16: Roller contacting the (a) tight (b) slack side of the tooth profile

From the tight to the slack strand, the rollers first contact the tight side of the tooth profile before switching to contact the slack one. The switch between the two positions was assumed to be instantaneous. The last roller to contact the tight side of the profile was called the balance roller (see Figure I-15.b). The index i of the balance roller depends on the tension ratio T_s/T_t (see Figure I-15.a for index i). The higher the slack strand tension, the further the transition from the slack strand (*i.e.*, the lower the index i of the balance roller). Variations of the balance index introduced a dependency between the location of the rollers along the associated tooth profile and loading conditions.

The differences measured between the driving and driven sprocket were attributed to the effect of friction (see Figure I-17). To account for this effect, Naji & Marshek proposed to correct the pressure angle ϕ with a friction correction angle $\delta = \text{atan}(\mu_\delta)$. This angle depended on μ_δ, the static friction coefficient between the roller and the tooth profile. The correction can be either positive or negative depending on the sprocket being driving or driven and the roller contacting the tight or the slack side.

Considering all these improvements, the tension in link i can be expressed according to eq.(I-7) for a driven sprocket (the equation for the driving sprocket is obtained by switching the sign before the correction angle δ).

$$T_i = \max\left[T_t \frac{\sin(\phi - \delta + \alpha - \alpha_t)}{\sin(\phi - \delta + \alpha)}(q_-)^{i-2};\right.$$

$$\left. T_s \frac{\sin(\phi + \delta + \alpha - \alpha_s)}{\sin(\phi + \delta + \alpha)}(q_+)^{n+1-i}\right]$$

(I-7)

with:

- $i \in [\![2, n+1]\!]$. $T_1 = T_t$ and $T_{n+2} = T_s$
- $q_- = \frac{\sin(\phi - \delta)}{\sin(\phi - \delta + \alpha)}$ and $q_+ = \frac{\sin(\phi + \delta)}{\sin(\phi + \delta + \alpha)}$ accounting for seated rollers
- n, the number of links in contact with the considered sprocket

Figure I-17 shows a comparison of experimental measurements and the GPLD model for driving and driven sprockets.
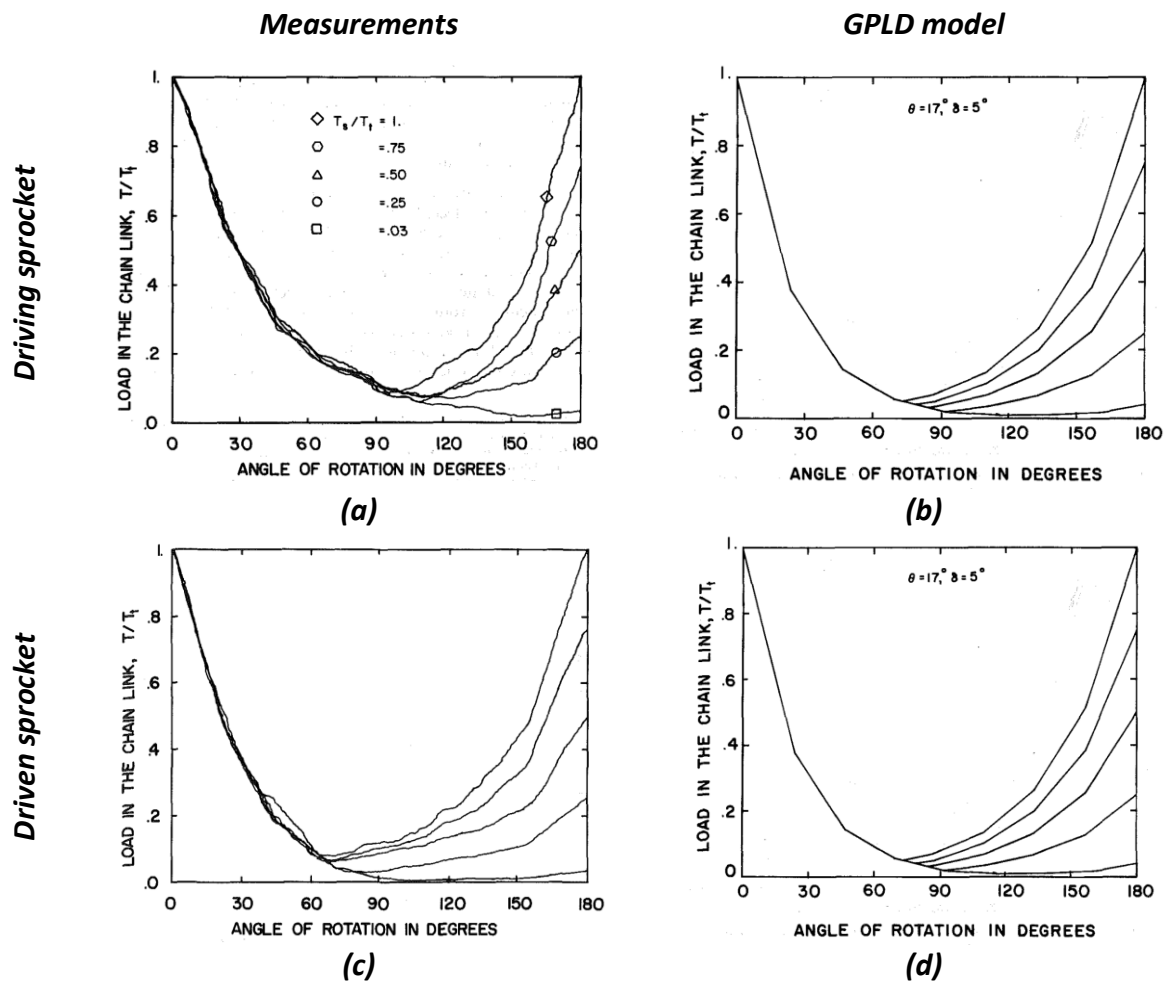
Figure I-17: Evolution of relative link tension (a) experimental measurements, driving sprocket (b) GPLD model driving sprocket (c) experimental measurements, driven sprocket (d) GPLD model driven sprocket [62]

Slope breaks are visible (mostly on the model curves, see Figure I-17.b). They mark the capture of a new roller by the sprocket considered. Between these breaking points, link tension evolution is mostly linear. The agreement between the experimental measurements and model results is very good, supporting the GPLD tension model.

Again in [2], Naji & Marshek proposed a model of part deformations due to the loads carried. Both link elongation and tooth profile deflection were considered. The results showed that both effects mostly cancelled each other and that they can be neglected for steel chains meshed with steel sprockets.

In following studies [64], [65], Naji & Marshek extended the possibilities of roller location along its associated tooth profile. Dependency between the position of each roller was introduced considering two constraints: each roller should contact its associated tooth profile and the centres of adjacent rollers should be separated by a chain pitch p (see Figure I-18). Based on roller location, the pressure angle ϕ could be determined considering the profile normal direction at the roller/profile contact point (it was assumed that P_i acts along the normal direction). However, roller/profile clearances were still neglected. Thus, the new approach was only applied to un-seated rollers. Therefore, rollers lying at the tooth bottom were still considered seated and their pressure angle were still assumed to be constant and given by ASA profile geometry. This model was used to assess the influence of inner link (pin link) elongation due to the impact of wear on link tension evolution. This more advanced approach proposed greater dependency between roller location and link tension.

Later, Kim & Johnson [52] completed the process started by Naji & Marshek and proposed a link tension model with full dependency between roller location and loads. To do so, they used the same approach as Naji & Marshek (*i.e.*, consecutive rollers distant by a chain pitch p) but roller/profile clearances were no longer neglected (*i.e.*, $R_{tp} \neq R_{roller}$). This allowed locating the roller at any curve portion even when contacting the tooth bottom. This new approach is denoted full roller location. The pressure angle was therefore only determined according to the normal direction at the roller/profile contact.
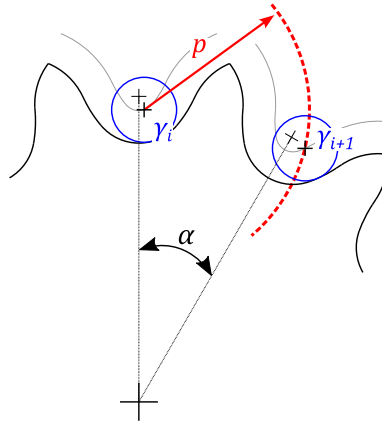
Figure I-18: Dependency between the location of two adjacent rollers (the clearance between roller and profile is exaggerated)

Rollers were located along their tooth profile using a dimensionless coordinate γ (see Figure I-19.b). Using this coordinate, the dependency between consecutive roller positions was presented in a curve showing the location of the following roller γ_{i+1} as a function of the preceding one γ_i (see Figure I-19.a). To facilitate comprehension, the notations of this manuscript are used in Figure I-19 in place of the original ones presented in [52].
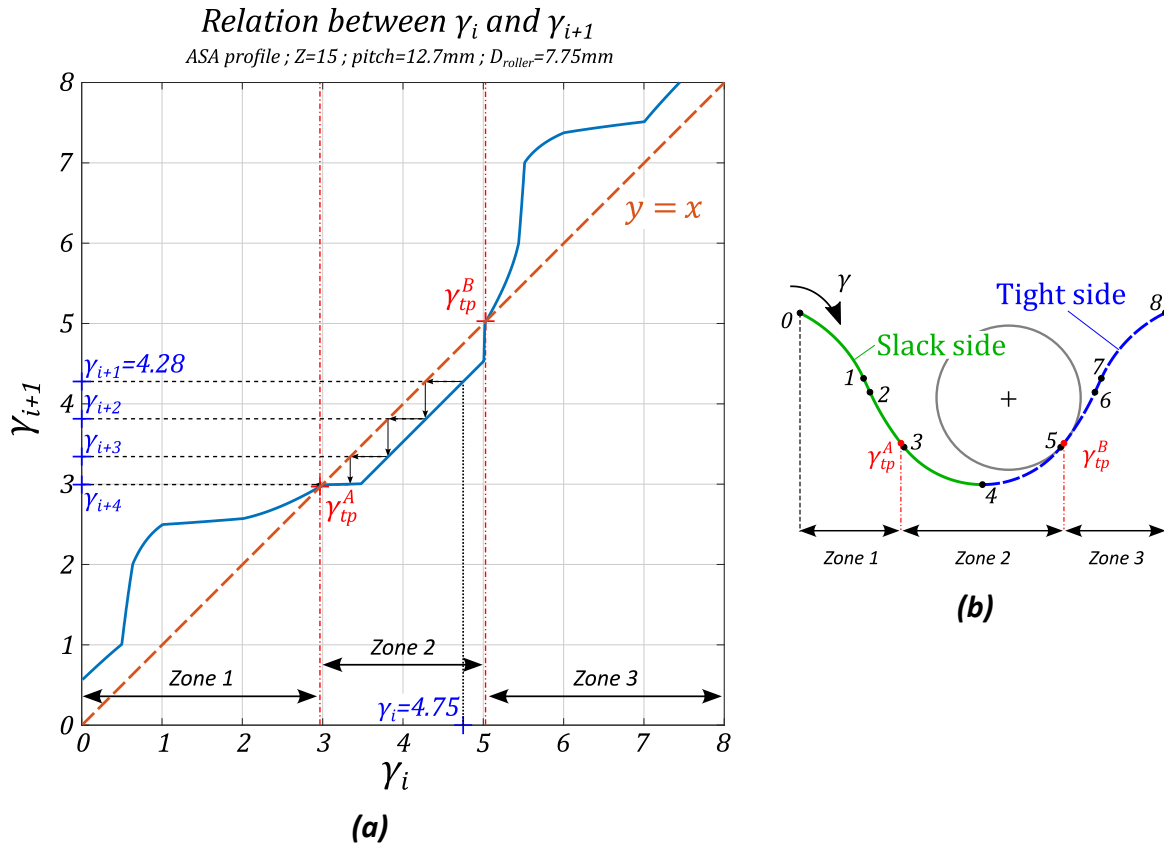
Figure I-19: (a) Relation between consecutive roller locations, adapted from [52] **(b) coordinate γ (the clearance between roller and profile is exaggerated)**

This curve exhibits two intersection points with the first bisector $y = x$. These points are called transition points (denoted tp). As shown in Figure I-19.b, transition point B (*i.e.*, γ_{tp}^B in Figure I-19) lies at the tight side of the profile while transition point A lies at the slack one. The transition points correspond to stable roller locations. Therefore, if roller i lies at a transition point, all the rollers will also lie at this point (following and preceding). Moreover, consecutive roller locations can be graphically determined following back and forth travel between the first bisector and the characteristic curve. An example with $\gamma_i = 4.75$ is given in Figure I-19. It can be noted that the configurations where all the rollers lie at a transition point represent a limit. This limit can be approached as close as desired (*i.e.*, consecutive γ_i can approach $\gamma_{tp}^{A,B}$) but can never be reached unless all the roller locations are exactly equal to $\gamma_{tp}^{A,B}$. In addition, for high values of γ_i (above $\gamma_i \approx 7.5$ in Figure I-19.a), the consecutive roller location γ_{i+1} cannot be defined. For such roller locations, no intersection between the consecutive tooth profile and the circle of radius p can be found (see Figure I-18). In concrete terms, when a roller is located too high on the tooth profile, the following one cannot contact the sprocket within its associated tooth profile.

As the transition points cannot be crossed, the graph is split into three distinct zones:

- $\gamma \in [0 \,, \gamma_{tp}^A[$. The adjacent roller relation is such that $\gamma_{i+1} < \gamma_i$ and the roller locations tend to zero. However, roller locations in this zone induce impossible link tension evolution. Therefore, in practical cases, no rollers lie in this zone (more details are given in §II.2.2).
- $\gamma \in]\gamma_{tp}^A \,, \gamma_{tp}^B[$. As the transition points cannot be crossed, the roller locations tend to γ_{tp}^A more or less quickly depending on the initial γ. This zone represents stable drive operations and is encountered in most practical cases.

- $\gamma \in]\gamma_{tp}^B , \gamma_{max}]$. In this zone, $\gamma_{i+1} > \gamma_i$, therefore, the roller location proceeds until a position such that γ_{i+1} is undefined is reached (*i.e.,* a roller will eventually miss a tooth resulting in dysfunction of the drive). Coordinates γ rising above γ_{tp}^B correspond to rollers climbing the tooth flank of the profile. This zone does not represent desirable working conditions as it is associated with possible chain drop. However, it is physically possible to reach this zone (unlike the first one) for drives under extreme loading conditions.

The tension model used by Kim & Johnson was distinct from the GPLD and considered pin and bush link differently. Moreover, friction was no longer considered only at the roller/profile interface (using correction angle δ) but rather at all articulation interfaces (*i.e.*, pin/bush, bush/roller and roller/profile). Using this specific tension model combined with the full roller location introduced, Kim & Johnson proposed a numerical procedure to solve link tension and roller location simultaneously. Typical roller locations results are presented in Figure I-20. The two plateaux correspond to transition points tp^A and tp^B. They can be interpreted as the equivalent roller location corresponding to a roller contacting the slack and tight side of the tooth profile, respectively. The results agreed with the experimental link tension measurements of Naji & Marshek [62]. Moreover, it was shown that friction at pin/bush and bush/roller interfaces does not significantly influence link tension predictions.
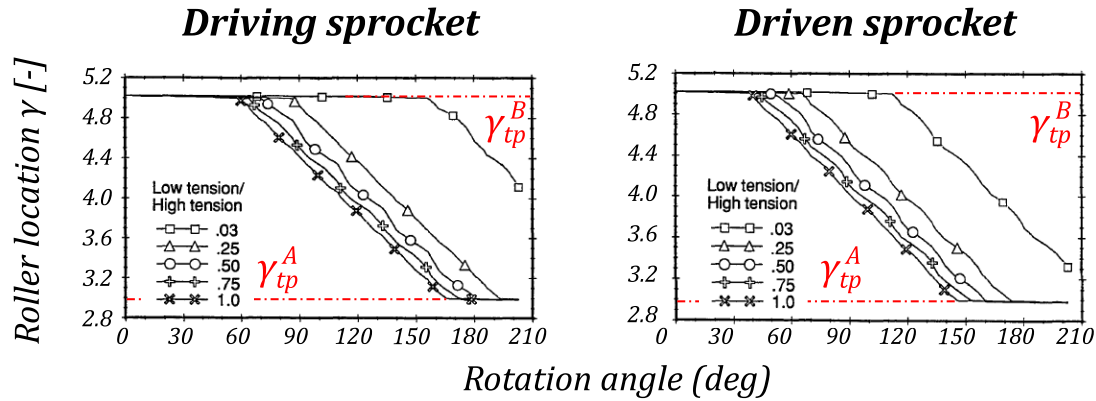
Figure I-20: Roller location during sprocket rotation for driving and driven sprockets (0° corresponds to tight strand meshing/un-meshing). Adapted from [52]

To achieve full roller location, the computational cost was high. Moreover, this new model still considered only one sprocket rather than a full transmission. Strand tensions T_s and T_t had to be assumed. Only the ASA profile was considered.

The evolution of roller location and pressure angle modelling between Binder [32] and Kim & Johnson [52] is shown in Figure I-21 and Figure I-15 respectively.
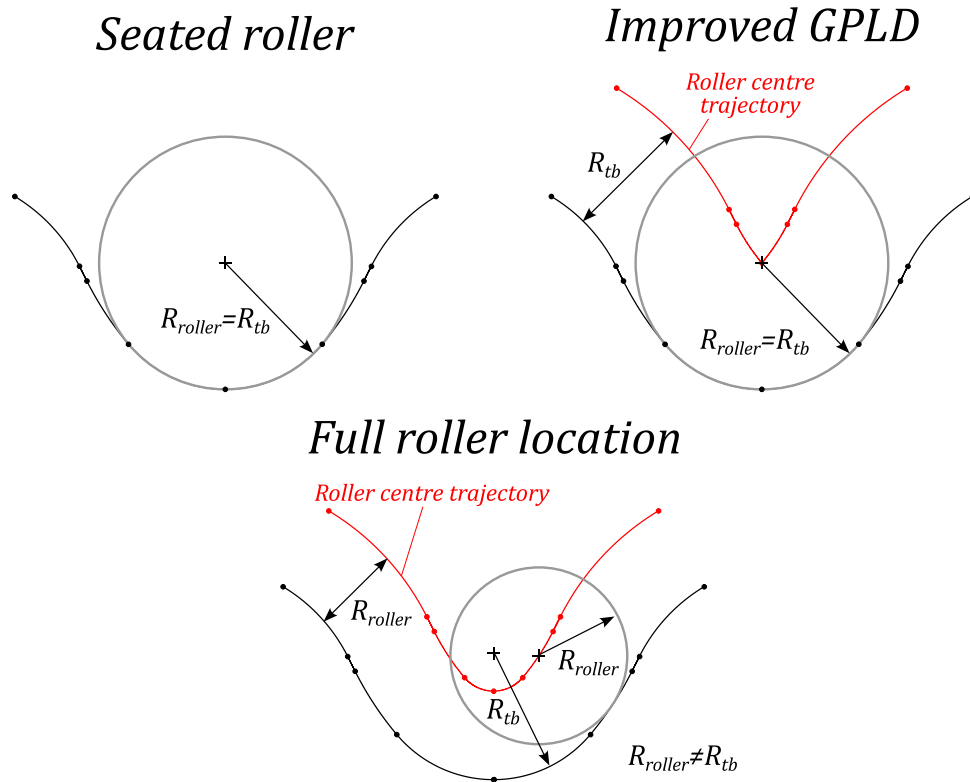
Figure I-21: Evolution of roller location modelling between seated roller to full roller location (clearance between roller and profile is exaggerated for full roller location)

Verne [66] applied the full roller location methodology of Kim & Johnson to the GPLD model. Eq.(I-7) was adapted as angles α and ϕ were no longer assumed but rather determined from the roller location and the tooth profile normal direction, respectively. Numerical search was also used to calculate loads and roller locations simultaneously. This model was then applied to entire drives (*i.e.*, not only for one sprocket) but strand tensions were still assumed. The influence of tooth profile geometry was also studied as comparisons between ASA and NF tooth profiles (see Figure I-7) were carried out. Contrary to Naji & Marshek, both link elongation and tooth deflection were considered. As strand tensions were assumed, the model resolutions for each sprocket were independent and carried out sequentially. Therefore, roller locations for both sprockets were both dependent on the strand tensions but independent from each other. The resulting drive model was mostly used for dynamical studies.

With a similar approach, Troedsson & Vedmar proposed static and dynamic drive models [67], [68]. The full roller location approach of Kim & Johnson was also used. This time, only the ISO tooth profile was studied. Link elongation was considered but tooth deflection was neglected. Moreover, Troedsson and Vedmar introduced a specific sub-model for the slack strand. This model calculates the tension in the slack strand links assuming that they are subjected only to gravitation. Thanks to this new component, the slack strand tension T_s no longer needs to be assumed and dependency between sprockets was introduced. Therefore, a single resolution was carried out for the entire drive. The authors however reported numerical challenges associated with this resolution [69].

Lodge & Burgess later proposed a different approach in [70], [71] to investigate cycling and industrial drives. Indeed, in their study, roller location was not relevant. Moreover, the agreement of Kim & Johnson's model with Naji & Marshek's experimental measurements (see Figure I-17.a) was similar to what was obtained using the GPLD model (as mentioned above, see [52]). Therefore, they opted for a less computationally intensive study. Instead of using full roller location, they proposed three sub-

models meant to represent three possible sprocket behaviours. The choice between sub-models was done based on the tension ratio T_s/T_t applied on the sprocket considered. Going from the highest ratios to the smallest, the three sub-models were:

- The GPLD model as presented by Naji & Marshek in [2] (see eq.(I-7)). This sub-model represents the sprocket behaviour where rollers tend to cross the tooth profile going from one transition point to the other (*i.e.*, zone 2 in Figure I-19). Friction modelling based on the correction of the pressure angle ϕ by δ was used.
- The static roller sub-model. In this sub-model, based on Binder's approach [32] (see eq.(I-6)), all the rollers are assumed to be seated and contacting the tight side of the tooth profile (see Figure I-16). The pressure angle ϕ is assumed to be equal for all rollers and its value is adjusted between $\phi - \delta$ and $\phi + \delta$ for a driven sprocket (switch sign before δ for driving sprocket) to transition towards the nest sub-model.
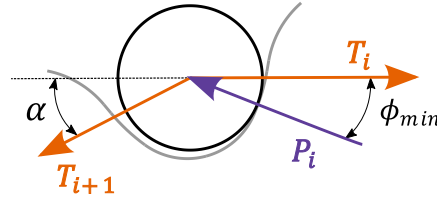
Figure I-22: Roller climbing the tooth flank to reach ϕ_{min} [70]

- The low slack tension sub-model. In this sub-model, a new roller position is assumed. Instead of being seated and contacting either the tight or the slack side of the profile, rollers can also climb the tooth flank (*i.e.*, zone 3 in Figure I-19). It is assumed that this new position reduces the pressure angle to ϕ_{min} (see Figure I-22), without changing α, making it possible to reach smaller tension ratio T_s/T_t. For the ASA profile, ϕ_{min} is estimated in the standard assuming that roller/profile contact occurs at point D (see Figure I-7.a).

  To account for the changing direction of roller motion (*i.e.*, from tp^B toward the tooth tip), the sign of the correction angle is switched in this sub-model. As with the GPLD model, a transition roller can be defined between the first ones (close to the tight strand) being seated (see Figure I-14) and the last ones climbing the tooth flank. As the applied ratio decreases, this transition roller moves toward the tight strand until all the rollers climb the tooth flank. Beyond this limit case (*i.e.*, all rollers climbing the tooth flank), it is assumed that chain drop occurs.

  The resulting expression for link tension T_i is given for a driven sprocket in eq.(I-8).

$$T_i = \min\left[T_t \frac{\sin(\phi + \delta + \alpha - \alpha_t)}{\sin(\phi + \delta + \alpha)} (q_+)^{i-2} \right.$$
$$\left. T_s \frac{\sin(\phi_{min} + \delta + \alpha_s)}{\sin(\phi_{min} + \delta)} (q_{+,min})^{i-n-1} \right] \quad \textbf{(I-8)}$$

with:

- $i \in [\![2, n+1]\!]$. $T_1 = T_t$ and $T_{n+2} = T_s$
- ϕ_{min}, given by the ASA standard for rollers climbing the tooth flank [32]
- $q_{+,min} = \frac{\sin(\phi_{min}+\delta)}{\sin(\phi_{min}+\delta+\alpha)}$

This sprocket model was then used along an improved formulation of the slack strand model proposed by Troedsson & Vedmar [67] to model two-sprocket drives. The slack strand tension T_s was therefore given by the dedicated model while the tight strand one was assumed to match torque requirements on the drive.

The complete drive model was validated using new experimental data proposed by Stephenson *et al.* [72]. These data were obtained for a drive operating at real rotational speed thanks to an original experimental apparatus. However, the results obtained exhibited more noise measurements than the quasi-static measurements from Naji & Marshek [62].

The three sub-models approach drastically reduces computational cost as analytical formulations replaced numerical search. However, roller motion was no longer precisely assessed. Moreover, this model is applicable only for the ASA tooth profile (values of ϕ are not given in the ISO standard [31]).

For all the tension models detailed in this part, friction coefficients, when needed, were assumed constant and given as inputs.

More broadly, it is known that chain dimensions can deviate from the nominal ones (*e.g.,* pitch, part radii). Such deviation can be caused by manufacturing imperfections resulting, for instance, in uneven chain and/or sprocket pitch. The assembly process can also cause distortions of the parts which can potentially create asymmetrical links and therefore contacts between plates (even for perfectly aligned drive). Moreover, under loading, chain parts distort mainly through tooth deflection and link elongation (comprising pin bending) [2]. Finally, wear can be modelled as an increase in pin link pitch [65] potentially reaching several percent [73]. The effect of such dimension modifications has been taken into account in previous tension models such as link elongation in [65], [66], [69] and show an influence on load distribution. However, all these deviations from the nominal dimensions probably vary in the same order of magnitude which makes it difficult to considered one without considering all.

This part was dedicated to the introduction of quasi-static tension models. These models calculate the link tension of roller/sprocket contact force, providing varying hypotheses. Works have been carried out to model the dependency between roller location and loads. This movement culminated with the models of Kim & Johnson and Troedsson & Vedmar where full roller location was determined simultaneously with loads. Lodge & Burgess later proposed another approach based on three sub-models. Computational cost was reduced as numerical search was replaced by analytical formulations. However, precise roller location could no longer be determined outside of three assumed locations: seated in contact with the tight or slack side of the profile (see Figure I-16) and climbing the tooth flank (see Figure I-22).

I.4 Chain drive efficiency

This part is dedicated to the previous works regarding chain drive efficiency. It includes modelling and experimental measurements, both considering industrial and bicycle drives. Models of drive power losses usually use one of the tension models introduced in the previous part (see §I.3).

The first model of chain drive efficiency was carried out by Binder [32]. Expressions for power loss due to link meshing were proposed. The meshing phenomenon designates the rotational motion undergone by each link during its meshing/un-meshing from/to a given sprocket. Indeed, let us consider for instance a link coming from the tight strand to be meshed on the driving sprocket. Links constituting the tight strand are arranged along a straight line (*i.e.*, with no change of orientation between each other). However, once both rollers are in contact with the driving sprocket, the link direction follows in a first approximation the side on the pitch polygon (see §I.2). Therefore, the angle between consecutive links (*i.e.*, angle α_t, see Figure I-23) goes from zero (link in the tight strand) to the pitch angle α (link with both rollers in contact with the sprocket). This angular variation causes friction in the chain articulation and therefore energy dissipation. The same phenomenon also occurs at the slack strand but usually under significantly lower link tension.
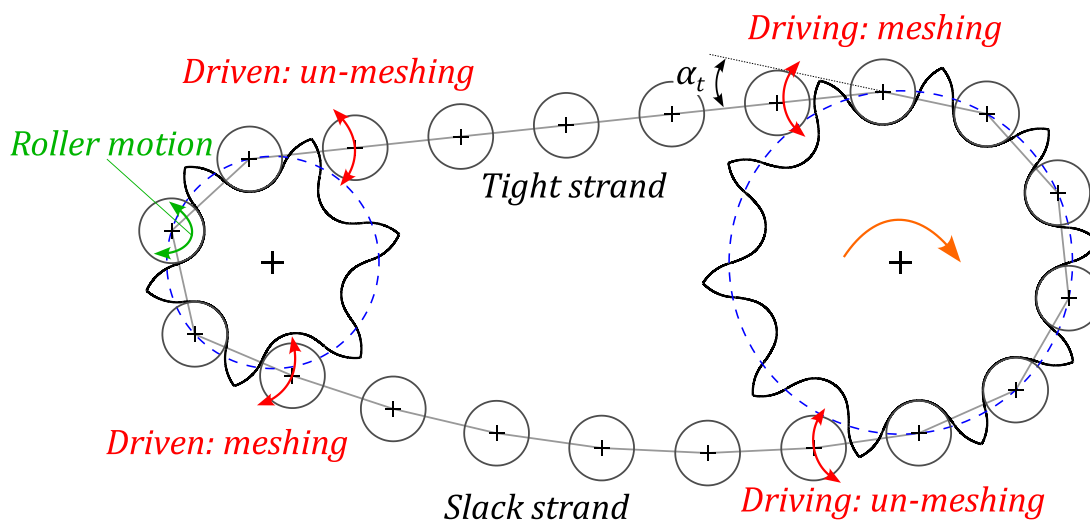
Figure I-23: Losses due to friction at chain articulations in chain drive
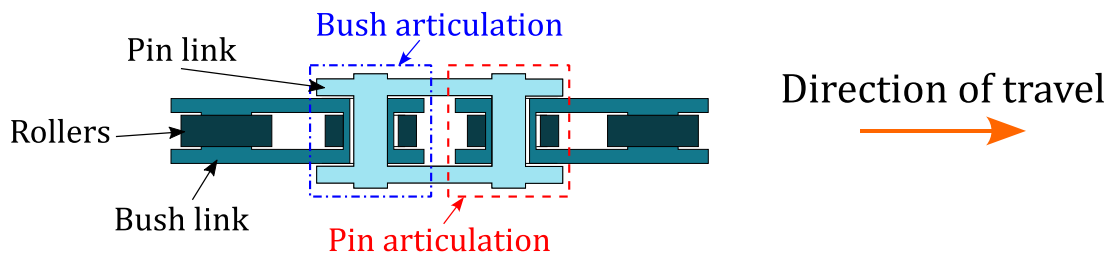
Figure I-24: Pin and bush articulations

In his study of the meshing phenomenon, Binder introduced a distinction between pin and bush articulations (see Figure I-24). In roller chains, pin and bush links alternate. However, the meshing of a pin or a bush link produces different power losses. Indeed, the meshing of a pin link causes friction mainly at the interface between the pin and the bush (see Figure I-25.a). When a bush link meshes, friction additionally occurs at the bush/roller interface (see Figure I-25.b). Moreover, the loads

associated with this relative motion between parts are different depending on whether a pin or a bush link is meshing (see Figure I-25).
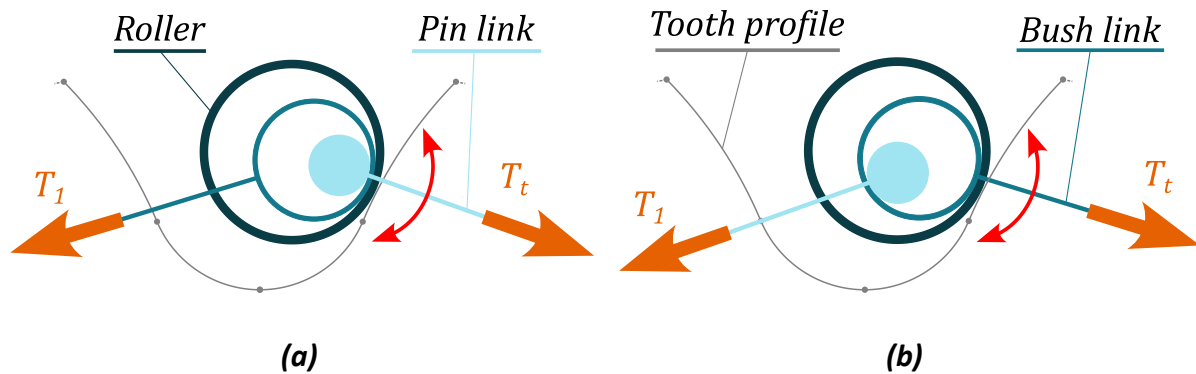
Figure I-25: Meshing from the tight strand of (a) pin (b) bush articulation, side view

Therefore, pin articulation designates an articulation such that meshing occurs for a pin link. Similarly, bush articulation designates an articulation such that a bush link is meshing. It can be noted that for a pin (bush) articulation, un-meshing is undergone by the bush (pin link).

The implication of the proposed power loss relations in terms of drive efficiency was not discussed by Binder [32]. However, the results show that the dissipated work is proportional to the pitch angle α. This first suggests that larger sprockets (with smaller pitch angle) could exhibit better efficiency.

Hollingworth & Hills [74], [75] proposed a study of chain drive efficiency dedicated to cranked link chains (see Figure I-3.b). They assumed that only link meshing contributes to chain drive power losses. For a cranked link chain, all articulations have the same type (pin or bush articulation) but this type can be reversed by changing the set-up direction. The two types of articulation were designated as "open end forward" and "narrow end forward" in this specific context. Coulomb friction was assumed at all chain interfaces. The prediction of drive efficiency depending on the articulation type (*i.e.*, the set-up direction) was proposed. The results showed that open end forward direction (*i.e.*, pin articulation) should be favoured for drives such that $Z_{II} > Z_I$. However, the proposed power loss expressions could not be derived by the author. The same difficulties of reproducing calculations were already reported by Logde in [71].

Kidd studied the efficiency of chain drives applied to road bicycles [76]. Experimental measurements were carried out to assess the effect of various parameters (lubricant, input power, sprocket size, *etc.*). It was shown that the derailleur system is responsible for a large share of the power losses for a road bike drive. Experimental measurements from [76] with and without a derailleur system are presented in Figure I-26. The results show efficiencies between 95 and 98.5% for drives with a derailleur while 99% is reached for simple two-sprocket drives without a derailleur.

$Z_I = 48 \,; Z_{II} = 21 \,; \Omega_I = 130rpm$
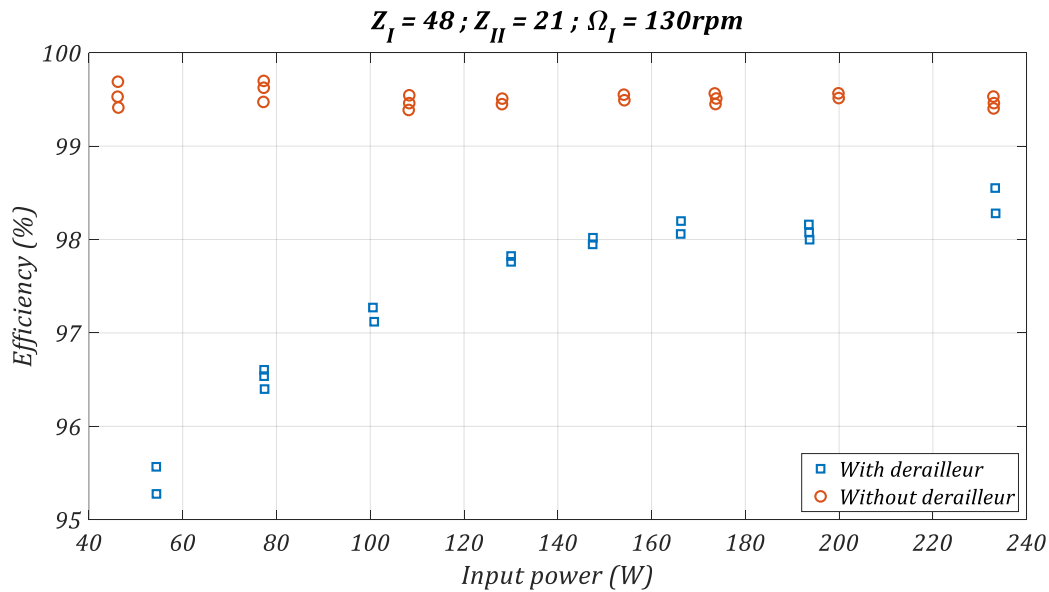
Figure I-26: Chain drive efficiency measurements with and without a derailleur system. Adapted from [76]

The results showed that drive efficiency (with and without a derailleur) rises with increasing input power. As the measurements were carried out at constant speed, higher input powers were achieved by increasing the transmitted torques. This increase in drive efficiency was attributed to a decrease of the proportional contribution of slack strand meshing losses. Indeed, increasing the applied torque mostly increases the tight strand tension while maintaining the slack one constant. Therefore, the relative contribution of the slack strand decreases as the input power increases, resulting in higher efficiency. This effect is particularly visible in the presence of a derailleur system (see Figure I-26). Indeed, this system applies significant tension in the slack strand and adds articulation points at both idler sprockets (see Figure I-4.a). A linear relation between reciprocal tight strand tension and chain drive efficiency was proposed on the basis of the results presented. Smaller reciprocal tensions, associated with higher torques, tight strand tensions, and power, resulted in higher drive efficiencies. The effect of the number of sprocket teeth was also tested and the results showed higher efficiency for drives with larger sprockets.

Kidd [76] also proposed a model of chain drive efficiency. Meshing losses were considered with distinction between pin and bush articulations. Potential drive misalignments caused by the derailleur system (*i.e.*, shift between rear cog and chainring planes) were also modelled through friction between chain plates. The model results also exhibited higher efficiencies for increasing input powers (*i.e.*, higher torques) and sprocket sizes. The analysis of each sprocket contribution to losses highlighted the dominant contribution of the rear cog. This higher contribution (compared the chainring one) was attributed to the smaller number of rear cog teeth (and therefore larger pitch angle α) encountered in usual cycling drives.

At the same time, Spicer *et al.* [77] also studied bicycle chain drives. Experimental measurements were carried out using a test rig dedicated to road bike drives. The results confirmed the linear relation between reciprocal tight strand tension and drive efficiency. However, the efficiencies measured by Spicer *et al.* [77] were significantly lower than those of Kidd [76]. Efficiencies fell to about 85% whereas Kidd reported efficiencies systematically above 90%. The interest of bigger sprockets was also reported experimentally.

A model was also proposed. Meshing losses were considered along lateral friction between plates due to the offset introduced by the derailleur system. The difference between pin and bush articulation was neglected. However, no comparison with the experimental data was proposed.

In [78], Spicer *et al.* suggested that possible non-linearities in the tensile behaviour of the links could be responsible for limiting drive efficiency. This new possible source of loss was proposed as an explanation for the lower drive efficiencies measured in [77].

Later, Lodge & Burgess also proposed an experimental and theoretical study of drive efficiency [70], [71]. Experimental results confirmed that bigger sprockets exhibit higher efficiency. The increasing efficiency for higher applied torque was also reported. Two-sprocket drives (close to track cycling drives) were studied with an efficiency of around 98%.
An efficiency model based on the tension model detailed in the previous part (see §I.3) was also proposed. As with the preceding studies, meshing losses were assumed to be the only source of losses. As only two-sprocket drives were considered, losses due to the offset introduced by the derailleur were neglected. The distinction between pin and bush articulation was considered. The dissipated work was calculated by integrating the loads given by each sub-model (see §I.3) between $\alpha_t = 0$ and $\alpha_t = \alpha$. For instance, for a pin articulation leaving or entering the tight strand (for the driving and driven sprocket, respectively), the work dissipated at the pin/bush interface is calculated as shown by eq.(I-9).

$$W_{pin/bush,pin\ art} = \frac{\mu}{\sqrt{1+\mu^2}} R_{pin} \int_0^\alpha T_t d\alpha_t$$

$$= \frac{\mu}{\sqrt{1+\mu^2}} T_t R_{pin} \alpha$$

(I-9)

The dependence on pitch angle α is clear for this specific case. However, relations can be more complex. Eq.(I-10) gives the development for the bush/roller interface, again for a pin articulation. For this interface, the force to be considered is now T_1 (see Figure I-25.a) which varies as α_t goes from 0 to α.

$$W_{bush/roller,pin\ art} = \frac{\mu}{\sqrt{1+\mu^2}} R_{pin} \int_0^\alpha T_t \frac{\sin(\phi + \delta + \alpha - \alpha_t)}{\sin(\phi + \delta + \alpha)} d\alpha_t$$

$$= \frac{\mu}{\sqrt{1+\mu^2}} T_t R_{pin} \frac{\cos(\phi + \delta) - \cos(\phi + \delta + \alpha)}{\sin(\phi + \delta + \alpha)}$$

(I-10)

The model proposed was able to capture the increasing efficiency for rising torque as well as the interest of larger sprockets. However, discrepancies between the model and the experimental measurements were reported for low torque and heavy chains. These differences were attributed to neglected loss phenomena such as vibrations and impacts between rollers and sprockets.

More recently, Zhang & Tak [79] proposed a model considering meshing losses as well as damping in the chain links. Sgamma *et al.* [80] conducted an experimental study on chain efficiency. Based on the results obtained, they proposed a phenomenological model to predict drive efficiency. The range of parameters tested (particularly the slack strand tension) applied to motorcycle drives.

In [81], the author proposed to consider the contribution of losses caused by roller motion along the corresponding tooth profile. This type of loss was denoted roller losses (see Figure I-23). Preliminary results were obtained providing simplifying hypotheses (the difference between pin and bush articulation was neglected, roller motion was independent from the applied torque). These results

suggested that roller losses could be as influential as meshing losses (see Figure I-27). This conclusion highlighted the interest of any potential model of chain drive efficiency considering roller motion.

$$Z_I|Z_{II} = 60|15; \ T_s/T_t = 0.1$$
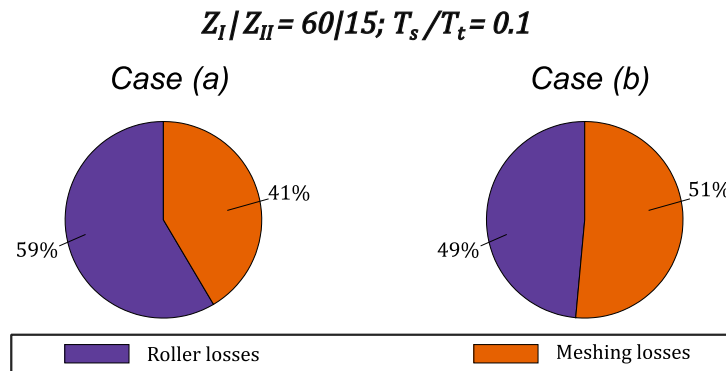
Figure I-27: Contribution of roller and meshing losses to global losses for different kinematic conditions (case a and b) [81]

The dependencies of drive efficiency on sprocket size and driving torque call into question the optimisation of the full system containing the chain drive (even regardless of the influence of roller losses). Indeed, favouring for instance bigger sprockets increases the weight of the drive which can be detrimental to the whole mechanism (*e.g.*, mountain bikes). Of course, the answer requires optimisation studies specific to each application considered (moving or static drive, fixed or varying rotational speed, *etc*.). Guidelines regarding global optimisations were proposed by Lodge & Burgess in [82]. Similarly, considering the cycling context, the relation with applied torque causes drive efficiency to vary along a race depending on the power supplied by the cyclist. This dependency was explored by Barnaby *et al.* in [83], [84].

All the models presented in this part assumed Coulomb law of friction [85]. The friction coefficients are always input variables. Their values are usually assumed and constant. Possible dependences of the friction coefficient on tribological conditions (*e.g.*, roughness, sliding speed, *etc*.), such as proposed for instance in [86], are neglected.
It can also be noted that the influence of vibrations on drive efficiency has never been studied.

Further remarks on test rigs

All the experimental studies presented by Kidd [76], Spicer *et al.* [77], Lodge & Burgess [70], Zhang & Tak [79] and Sgamma *et al.* [80] were based on test rigs reproducing the architecture of a usual chain drive. These test rigs had two shafts, for the driving and driven sprockets. These shafts were instrumented to measure torque and rotational speed and ultimately calculate drive efficiency (see Figure I-28.a).
The advantage of this approach is its similarity to the real application. Measurements can be carried out for instance at fixed torque and/or rotational speed, for various sprockets, *etc*. The potential addition of a derailleur system is also facilitated by the architecture.

(a) *(b)*
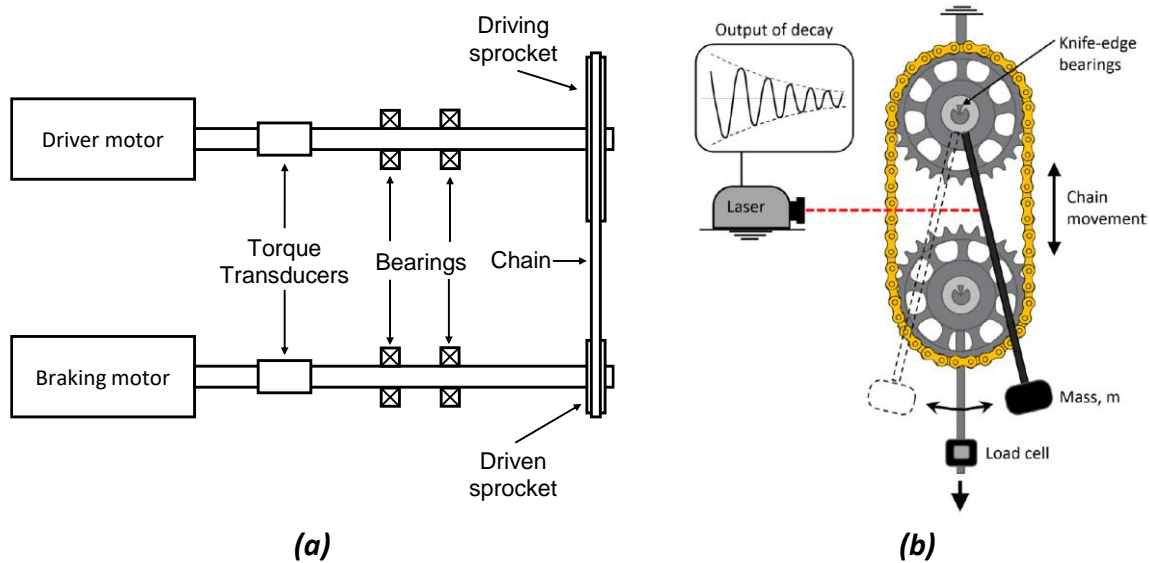
Figure I-28: (a) Usual test rig for efficiency measurements, adapted from [70] ***(b) pendulum test rig*** [87]

However, the main drawback of this approach lies in the measurement uncertainties. Indeed, chain drives are very efficient mechanisms (about 98% for two sprocket drives [70]). Therefore, any test rig must have high accuracy to measure potential variations between drive configurations. Moreover, chain drives can transmit considerable powers (up to $1600W$ for track cycling[5]). Therefore, expensive sensors are usually required to match the required accuracy. To get round this challenge, alterative test rigs have been proposed.

Egorov *et al.* [88] proposed to measure the deceleration of the drive. Providing that the inertias of both shafts are well known beforehand, the deceleration time allows measuring drive efficiency with high precision. The disadvantage of this architecture is that the efficiency obtained represents an average over the entire deceleration. Therefore, it does not allow assessing the efficiency for fixed conditions (*e.g.*, fixed torque or rotational speed).

Wragge-Morley *et al.* [87] proposed to build a pendulum with a chain drive (see Figure I-28.b). Measuring the oscillation decay characterises the dissipations occurring in the drive. This architecture reduces uncertainties [87] as time decay can be measured more easily and with better accuracy compared to torque. However, as with the inertia based measurement [88], such a test rig does not enable easily testing drive efficiency in fixed conditions. Moreover, any change of the sprocket tested might be difficult.

This part was dedicated to a review of experimental and modelling works on chain drive efficiency. Experimental measurements showed that the efficiency of two sprocket drives used in track cycling applications is relatively high (about 99%). Higher efficiencies were also reported for larger sprockets and higher torques. Several models have been presented. Most of them are based on one of the tension models detailed in the previous part (§I.3) to calculate link tension T and contact force P. Coulomb friction was assumed for all the models and constant friction coefficients were considered. Previous efficiency models were mostly based on meshing losses caused by the articulation of chain links during their meshing and un-meshing from sprockets (none considered the effect of strand vibrations). Based on this loss type, the beneficial effect of bigger sprockets and higher torques on drive efficiency was reproduced. Indeed, bigger sprockets reduce the pitch angle α which limits meshing losses. As for higher torques, they cause the slack strand meshing losses to become less influential, which increases drive efficiency. However, meshing-loss based models failed to explain all

---

[5] For $300N.m$ applied at $130rpm$ at the chainring.

the experimental measurements, particularly for low torques [70]. A possible explanation is given by a preliminary study presented by the author [81]. The results suggest that losses caused by roller motion along the associated profile (called roller losses) can contribute as much to global dissipation as meshing losses.

I.5 Conclusion and thesis objectives

This chapter was dedicated to the introduction of the research context and literature review.

First, the specificities of track cycling chain drives were detailed. The latter are mainly: light chains, moderated rotational speeds and high loading torques. These constraints led to a quasi-static modelling approach.

An overview on roller chain drive was then given. The definition of standard sprockets was detailed. The polygonal effect, a phenomenon inherent to any chain drive, was presented. This phenomenon is important to consider when studying chain drive operation as it introduces transmission error resulting in a complex relation between the instantaneous speeds of the driving and driven sprocket The literature on the subject showed that kinematic models using four-bar mechanisms are an interesting approach when dynamical effects are neglected.

The evolution of quasi-static tension models (dedicated to the calculation of link tensions and roller/sprocket contact forces) was then presented. The successive models improved the connection between loads and roller location. However, this connection was introduced along with numerical challenges which resulted in computationally intensive models. The successive results agreed with the link tension measurements performed on industrial drives (mainly, Naji & Marshek [62] and Stephenson *et al.* [72]).

Finally, previous models and experimental measurements dedicated to chain drive efficiency were presented. Most models were based on meshing losses caused by the relative articulation between consecutive links during meshing and un-meshing. These models generally agreed with experimental data with a notable exception for low torques. Recently, the author highlighted that losses caused by roller motion along the associated tooth profile might have a significant influence on drive efficiency. However, the results were only preliminary and deeper studies are required to get rid of the simplifying hypotheses. This importance of roller losses also raised the question of the tooth profile as it might change the roller motion evolution.

Thesis objectives

Considering the previous works on the subject, the main objective of this thesis is to study chain drive efficiency, taking into account the influence of losses caused by roller motion along the associated tooth profile. To do so, a parametric model of chain drive efficiency is developed. The model will be able to consider different tooth profile geometries both from standards or created for the study (*e.g.*, ASA, NF_{min} and NF_{max}). It will be used to test the influence of various parameters such as tension settings, loading conditions (*i.e.*, driving torque), chain pitch, sprocket number of teeth, *etc*.

Efficiency modelling will be carried out in two steps. First an original Quasi-Static Chain Drive Model (QSCDM) will be presented. Compared to previous works, its formulation is general such that any tooth profile geometry can be considered. This first model will compute loads (*i.e.*, link tension and roller/sprocket contact force) and displacements (*i.e.*, roller motion and link orientation). Elements of previous studies by Lodge & Burgess [70], Troedsson & Vedmar [69] and Kim & Johnson [52] will be reused. An original architecture based on dedicated sub-models for chain strands and sprocket is proposed to facilitate the numerical resolution and therefore limit the possible issues reported by Troedsson & Vedmar [69]. Validation will be presented based on industrial drives. The quasi-static model presented will then be used to study the influence of tooth profile geometry on both cycling and industrial chain drive behaviour (load evolution, roller motion, *etc*.). In the second step, an original Chain Drive Efficiency Model (CDEM) will be presented. Compared to previous studies, the influence of losses caused by roller motion is considered. Combined with the Quasi-Static Chain Drive Model (QSCDM), it will calculate chain drive efficiency considering roller motion and tooth profile geometry. Finally, the CDEM will be used to carry out a parametric study of track cycling drive efficiency

considering the influence of roller losses. Guidelines for possible optimisations will be discussed on the basis of the results obtained.

Considering the track cycling application (light chain, moderate speed, see §I.1.2), dynamical effects, including strand vibrations, will be neglected. However, the proposed quasi-static model (QSCDM) is general and can be applied to any two-sprocket drive as long as the hypotheses are met (*e.g.*, dynamical effects can be neglected). It can therefore be used for industrial drives[6] with moderate rotational speed. Considering that the literature on quasi-static tension models (see §I.3) is mainly composed of industrial examples, the QSCDM will be validated on such industrial drives. The same reasoning stands for the efficiency model (CDEM). The latter will however be used to conduct a parametric study only on track cycling drives.

---

[6] Compared to track cycling drives, industrial ones usually have a smaller gear ratio Z_I/Z_{II}. Chains can have a pitch different to $1/2''$ (higher or lower) and the slack to tight tension ratio T_s/T_t is usually higher due to higher slack strand tension (tensioners are often used).

Chapter II

Quasi-Static Chain Drive Model

This chapter introduces an original Quasi-Static Chain Drive Model (QSCDM). This model, dedicated to two-sprocket chain drives, calculates the location of each roller along its corresponding tooth profile simultaneously to the link tension and roller/sprocket contact force (generally designated as *the loads*). It consists of the first step of the Chain Drive Efficiency Model (CDEM), introduced later in Chapter IV. The QSCDM considers a whole drive with relations between the chain strands and the sprockets. The drive studied is characterised by its geometry (centre distance, vertical shift between the sprockets), the chain properties (pitch, link mass and roller diameter) as well as the 2D tooth profile of each sprocket (tooth geometry and sprocket pitch). Dependency on the external loading conditions (*e.g.*, driving torque) and the drive geometry (*e.g.*, slack strand tension setting) is investigated. The model has the ability to run using different tooth profile geometries.

Although being as general as possible, this model is meant to study single-speed bicycle drives. The hypotheses chosen are therefore adapted to this context. As no derailleur system is present for single speed drive, the model is assumed to be planar (2D). Cycling drives are used with relatively light chains ($\approx 3.6 \ g/link$) and moderate rotational speed ($130 rpm$ at most on the driving sprocket, see Chapter I). Thus, all dynamical effects are neglected hence the quasi-static model. Variations in chain dimensions are neglected (including wear and manufacturing imperfections) as all dimensions are assumed to be nominal. Moreover, based on the work of Naji & Marshek [2], which states that part deformations do not significantly influence load distribution, all the components are assumed to be rigid. Link elongation and tooth deflection are therefore not considered. Friction is introduced using a correction angle as presented by Naji & Marshek [2], [62], [64].

The Quasi-Static Chain Drive Model (QSCDM) consists of three sub-models connected to each other: the first two are for each chain strand (tight and slack) and the last one is used for both the driving and the driven sprocket. The slack strand is considered with a similar approach to that of Troedsson & Vedmar [67] and Lodge & Burgess [70], assuming that only gravitation applies on the strand. The tight strand is considered to be straight and modelled as a four bar mechanism [1], [35]. An original numerical procedure is presented to calculate the strand trajectories and the number of links in each sub-model (denoted as global kinematics). The global kinematics is assumed to be independent from the tooth profile geometry as all the rollers in contact with a sprocket are considered to lie on the pitch circle. Moreover, as part deformations are neglected, this global kinematics is also independent from the loading conditions applied on the drive. The local sprocket sub-model (used for the driving and the driven sprocket) is based on the approach presented by Kim & Johnson [52]. However, instead of being assumed and constant, imposed link tensions are based on the kinematics and external loading conditions determined. Roller locations are therefore calculated considering the influence of the previous part of the model. Compatibility issues occurring at the transition between each sub-model are also addressed. As the model is quasi static, each consecutive drive sub-position is solved independently.
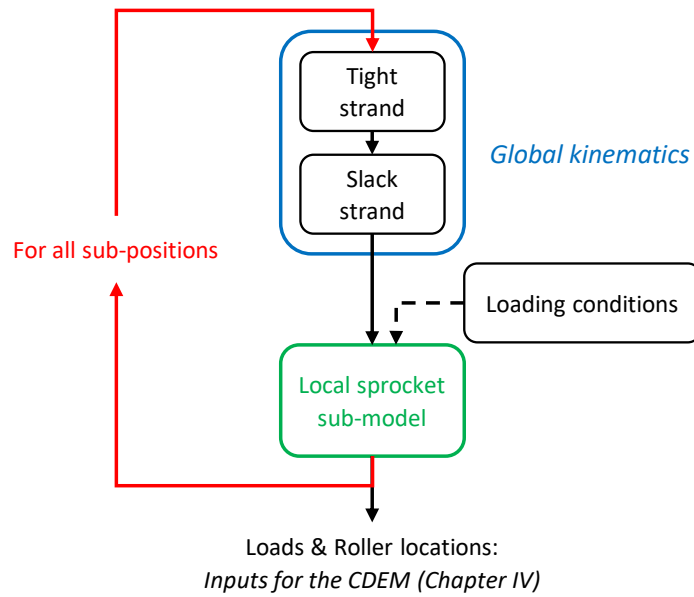
Figure II-1: General Quasi-Static Chain Drive Model (QSCDM) solving procedure

The general solving procedure is presented in Figure II-1. This chapter details the different steps. First, the global kinematics is introduced including the tight and slack strand modelling. The local sprocket sub-model is then presented. It details the dependency between roller locations and loads and determines each simultaneously. Finally, the procedure used to solve the entire model is presented.

II.1 Global drive kinematics

For the sake of convenience, in the entire manuscript, unless otherwise stated, the driving sprocket rotates clockwise (angle ζ) and is represented on the right-hand side of the drive. Thus, the tight strand, transmitting power, is always the one above. Links and rollers are numbered spatially according to Figure II-2 using index i. Roller $i = 1$ is the first roller in contact with the driving sprocket then i increases in the rotation direction of the drive (clockwise direction). Link i is always located before roller i (in the direction of rotation). The driving and driven sprockets are denoted $j = I$ and $j = II$, respectively (see Figure II-2). Except for ζ monitoring the driving sprocket rotation, all angles are positive counter-clockwise.
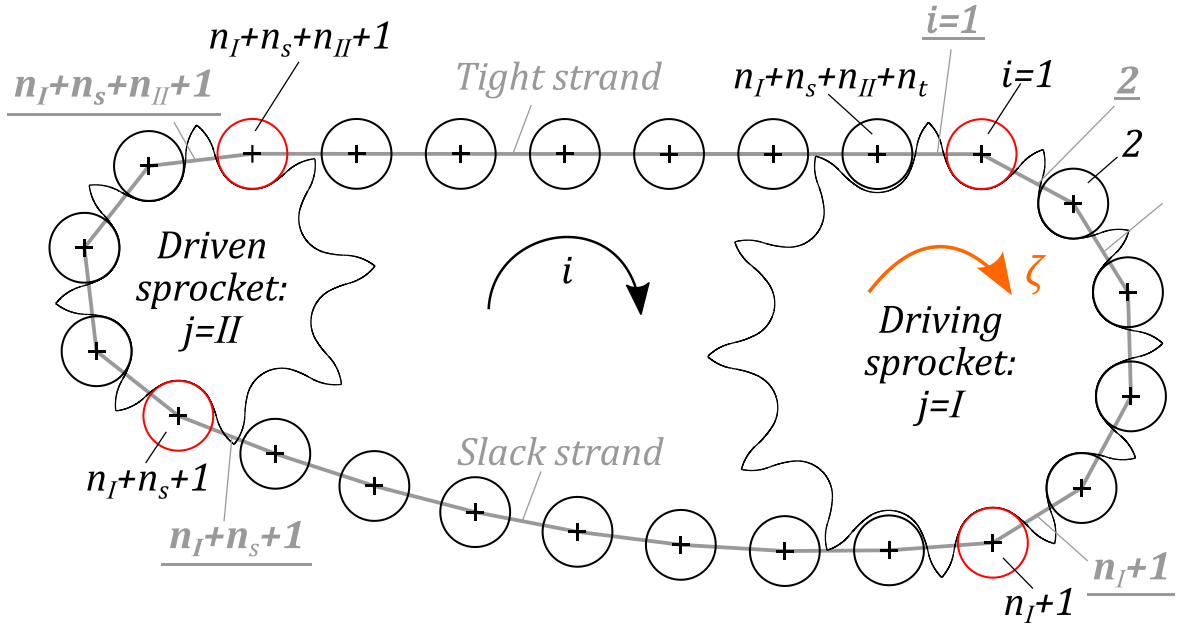
Figure II-2: Link and roller spatial numbering

The number of links with both rollers in contact with the driving and the driven sprockets are denoted n_I and n_{II}, respectively. The number of links in the tight and slack strand are n_t and n_s, respectively. Therefore, the total number of links and rollers in the chain n_{tot} is given by eq.(II-1).

$$n_{tot} = n_I + n_{II} + n_s + n_t \qquad \text{(II-1)}$$

For the global kinematics, the clearance between the roller and the tooth profile is neglected. Therefore, it is assumed that the centres of the rollers in contact with a sprocket lie on the corresponding pitch circle. Based on [33], Figure II-3 shows the parameters used to characterise a given drive.
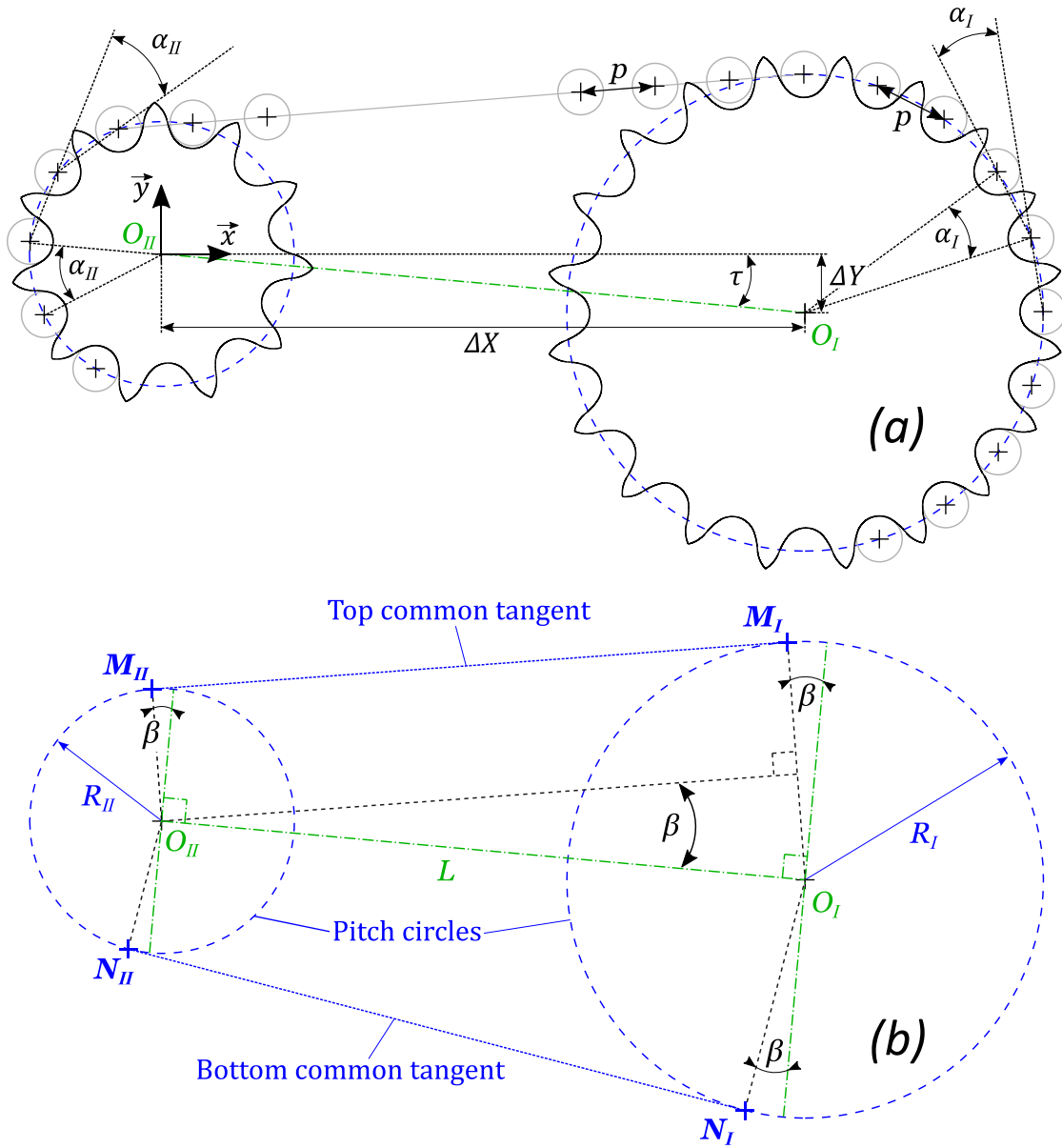
Figure II-3: Definition of the global drive geometry (a) drive spatial parameters (b) pitch circles and common tangents

The parameters in Figure II-3 are:

- $\alpha_j = 2\pi/Z_j$, the angular pitch of sprocket j. Z_j being the number of teeth of sprocket j,
- p, the chain and sprocket pitch (assumed to be equal),
- $L = \left\| \overrightarrow{O_{II}O_I} \right\|$, the centre distance between the driving and driven sprocket axes,
- $\tau = (\vec{x}, \overrightarrow{O_{II}O_I})$, the tilting angle between the centre axis $\overrightarrow{O_{II}O_I}$ and the horizontal direction $\vec{x}$,
- $\Delta Y = \overrightarrow{O_{II}O_I} \cdot \vec{y}$, the vertical signed distance between the sprocket axes,
- $\Delta X = \overrightarrow{O_{II}O_I} \cdot \vec{x}$, the horizontal signed distance between the sprocket axes,
- $R_j = p/\left[\sin(\alpha_j/2)\right]$, the radius of the pitch circle for sprocket j,
- $\beta = (\overrightarrow{O_{II}O_I}, \overrightarrow{M_{II}M_I}) = \sin^{-1}\left(\frac{R_I - R_{II}}{L}\right)$, the angle between the centre axis $\overrightarrow{O_{II}O_I}$ and the top common tangent. The bottom common tangent is symmetrical to the top one with respect to $\overrightarrow{O_{II}O_I}$. The tangency points for the top and bottom common tangent are denoted M_j and N_j, respectively.

II.1.1 Tight strand sub-model

This part details the sub-model used for the tight strand of the chain drive.

The tight strand is assumed to be a straight line between the first and last roller (in terms of index i) contacting the driving and driven sprocket, respectively (*i.e.*, rollers $i = 1$ and $i = n_I + n_{II} + n_s + 1$ see Figure II-4). These two specific rollers are called strand tips, and link articulations are assumed to occur only at these points.
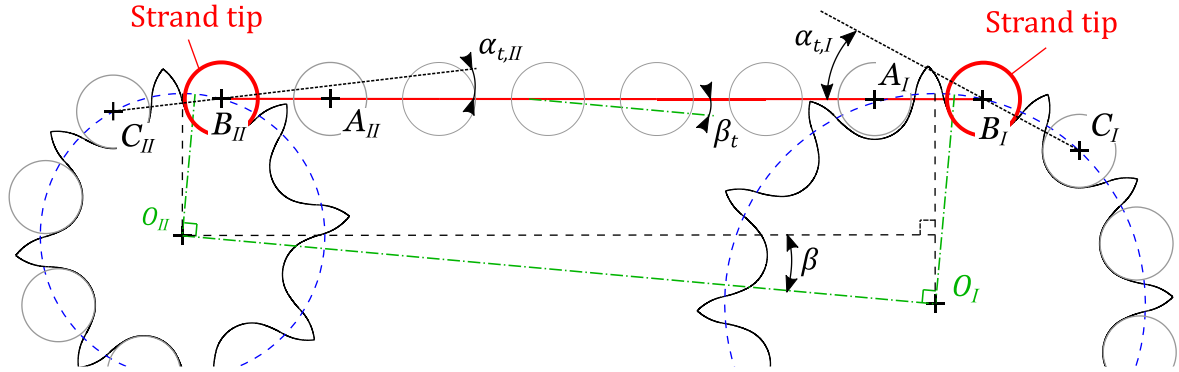
Figure II-4: Tight strand definition

The strand tips-roller centres are called B_j ($j = I$ or II for the driving and driven sprocket, respectively). The centres of the adjacent rollers are called A_j and C_j (Figure II-4). The rollers of centre C_j are in contact with the sprocket while the rollers of centre A_j lie in the tight strand.

Angles $\alpha_{t,I}$ and $\alpha_{t,II}$ are introduced in eqs.(II-2) between the directions of the tight strand and the closest link with both rollers in contact with the driving and driven sprockets, respectively (as in [2], [64], [70]).

$$
\begin{aligned}
\alpha_{t,I} &= \left(\overrightarrow{C_I B_I}, \overrightarrow{B_I A_I} \right) && \text{(a)} \\
\alpha_{t,II} &= \left(\overrightarrow{B_{II} A_{II}}, \overrightarrow{C_{II} B_{II}} \right) && \text{(b)}
\end{aligned}
\qquad \textbf{(II-2)}
$$

These angles will be used the check the validity of the drive kinematics and for load calculation (see §II.1.3 and §II.2.2).

As the transmission rotates, the positions of the strand tips move along the pitch circles. Thus, the tight strand direction varies during the drive operation and is therefore distinct from the common tangent direction β which is constant for a given drive. To monitor these variations, angle β_t (Figure II-4) is introduced to measure the direction of the tight strand while angles $\psi_{t,j}$ (Figure II-5) track the position of the strand tips relatively to the tangency points (M_j), see eq.(II-3) and (II-4).

$$
\beta_t = \left(\overrightarrow{O_{II} O_I}, \overrightarrow{B_{II} B_I} \right) \qquad \textbf{(II-3)}
$$

$$
\begin{aligned}
\psi_{t,I} &= \left(\overrightarrow{O_I B_I}, \overrightarrow{O_I M_I} \right) && \text{(a)} \\
\psi_{t,II} &= \left(\overrightarrow{O_{II} M_{II}}, \overrightarrow{O_{II} B_{II}} \right) && \text{(b)}
\end{aligned}
\qquad \textbf{(II-4)}
$$
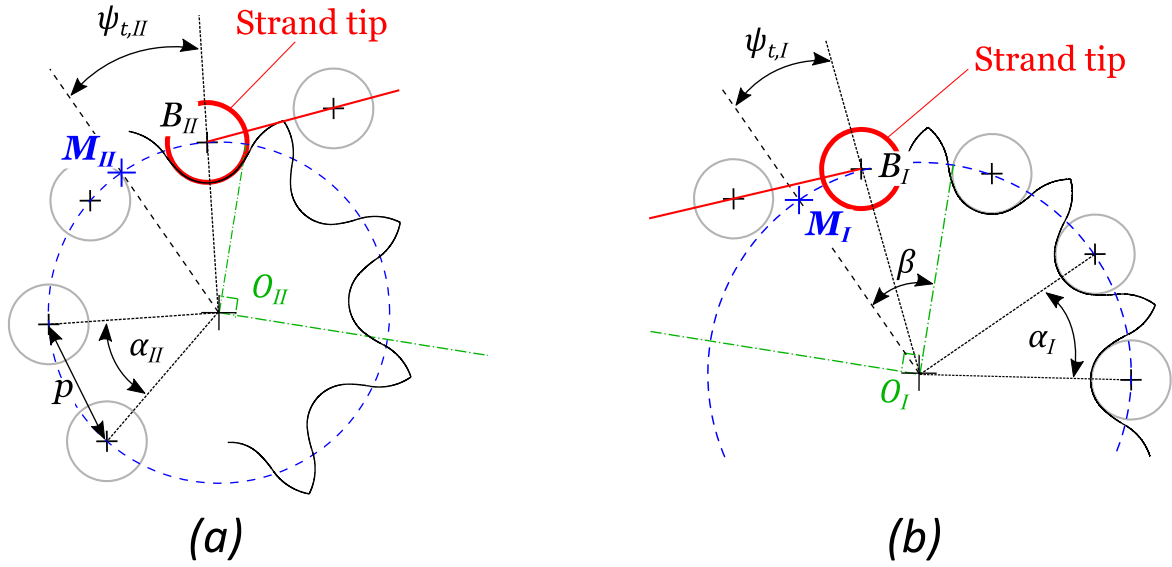
Figure II-5: Definition of (a) $\psi_{t,II}$ (b) $\psi_{t,I}$ (b)

The tight strand induces a dependency between the rotation of the driving and driven sprockets. This dependency is expressed using a four bar mechanism [1], [32], [35]–[37] (see Chapter I, §I.2.2) illustrated in Figure II-6.
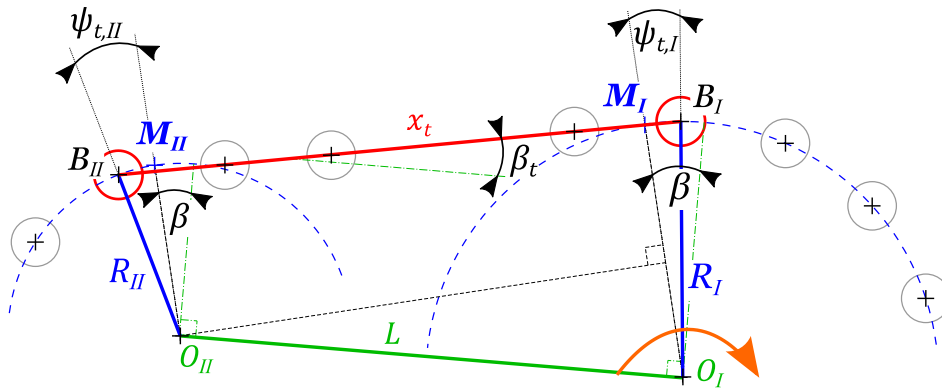
Figure II-6: Four bar model of the tight strand

The chain closure condition involves the following equations between β, $\psi_{t,I}$, $\psi_{t,II}$ and β_t.

$$\begin{cases} x_t \cos(\beta_t) - R_{II} \sin(\psi_{t,II} + \beta) + R_I \sin(\beta - \psi_{t,I}) = L \\ x_t \sin(\beta_t) + R_{II} \cos(\psi_{t,II} + \beta) - R_I \cos(\beta - \psi_{t,I}) = 0 \end{cases} \qquad \text{(II-5)}$$

with:

$$x_t = p n_t \qquad \text{(II-6)}$$

Once the tight strand is fully defined (*i.e.*, $\psi_{t,j}$ and β_t are known), angles $\alpha_{t,I}$ and $\alpha_{t,II}$ can be calculated using eqs.(II-2). Figure II-7 shows a zoom-in and these two angles.
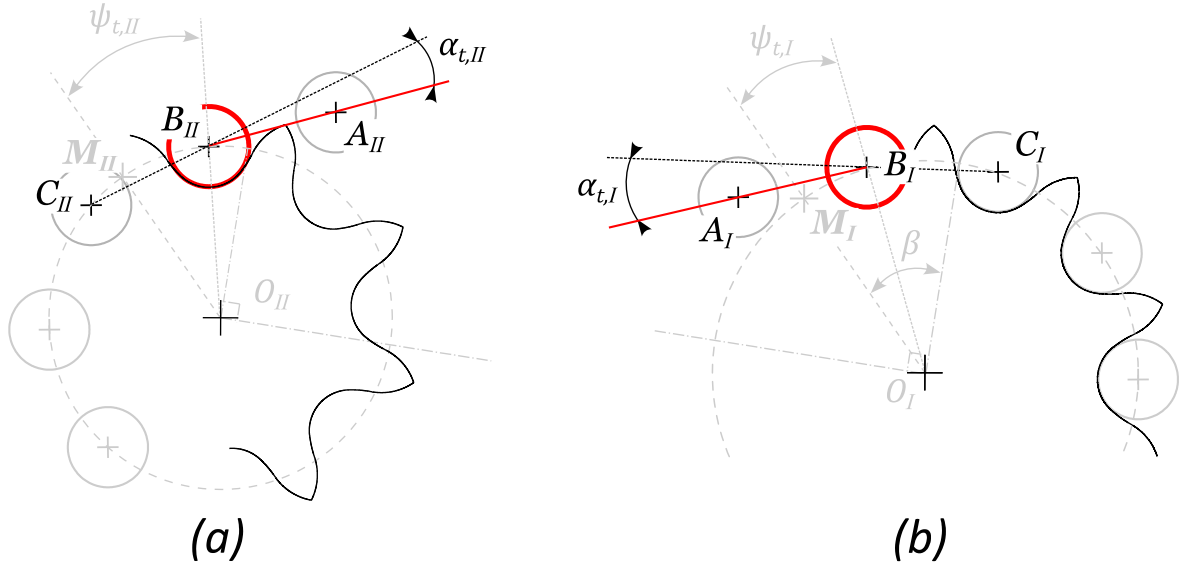
Figure II-7: Definition of angles (a) $\alpha_{t,II}$ (b) $\alpha_{t,I}$

As the tight strand is assumed to be straight, the tension is the same for all the included links. This particularly stands for the boundary link tensions $T_{i=1}$ and $T_{i=n_I+n_s+n_{II}+2}$ denoted $T_{t,I}$ and $T_{t,II}$, respectively (see eq.(II-7), link numbering is given in Figure II-2).

$$
\begin{aligned}
T_{t,I} &= T_{i=1} & (a)\\
T_{t,II} &= T_{i=n_I+n_s+n_{II}+2} & (b)\\
T_{t,I} &= T_{t,II} & (c)
\end{aligned}
\qquad \textbf{(II-7)}
$$

II.1.2   Slack strand sub-model

As with the tight strand, the slack strand tips are the centres of the first and last contacting rollers of the driven and the driving sprockets, respectively (*i.e.*, roller $i = n_I + n_s + 1$ and $i = n_I + 1$ in Figure II-2). Their roller centres are designated as E_j and the centres of the adjacent rollers are D_j and F_j (see Figure II-8).
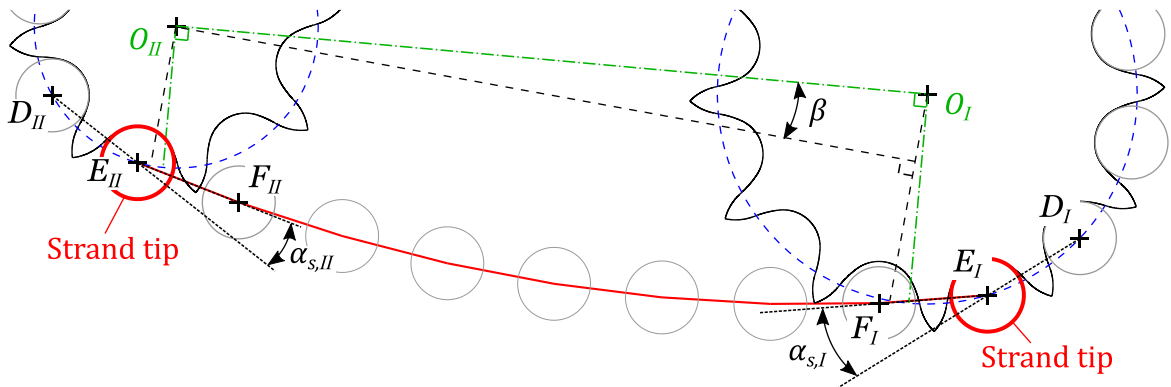
Figure II-8: Slack strand definition

Angles $\alpha_{s,j}$ (Figure II-8) and $\psi_{s,j}$ (Figure II-9) are also defined in a similar way to the tight strand in eqs.(II-8).

$$\alpha_{s,I} = \left(\overrightarrow{E_I F_I}, \overrightarrow{D_I E_I} \right) \qquad (a)$$
$$\alpha_{s,II} = \left(\overrightarrow{D_{II} E_{II}}, \overrightarrow{E_{II} F_{II}} \right) \qquad (b)$$

(II-8)

$$\psi_{s,I} = \left(\overrightarrow{O_I N_I}, \overrightarrow{O_I E_I} \right) \qquad (a)$$
$$\psi_{s,II} = \left(\overrightarrow{O_{II} E_{II}}, \overrightarrow{O_{II} N_{II}} \right) \qquad (b)$$

(II-9)

(a) (b)
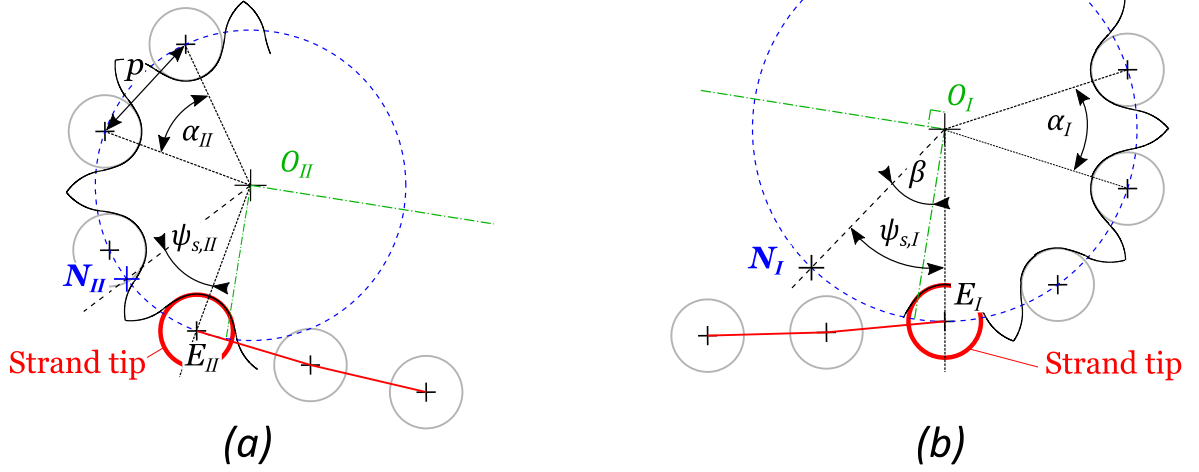
Figure II-9: Definition of (a) $\psi_{s,II}$ (b) $\psi_{s,I}$

As the slack strand does not transmit load, its tension is significantly lower than the tight one. As such, the effect of gravity on the strand trajectory is preponderant. To consider this effect, the model presented by Troedsson & Vedmar [67] and improved by Lodge & Burgess [70] is used. The load in the strand is assumed to be due solely to gravitation and the link masses are considered to be lumped at the roller centres. The slack strand is therefore modelled as a set of punctual masses (each with mass m_{link}) linked with massless bars (see Figure II-10). The centre of roller i is designated as R_i.
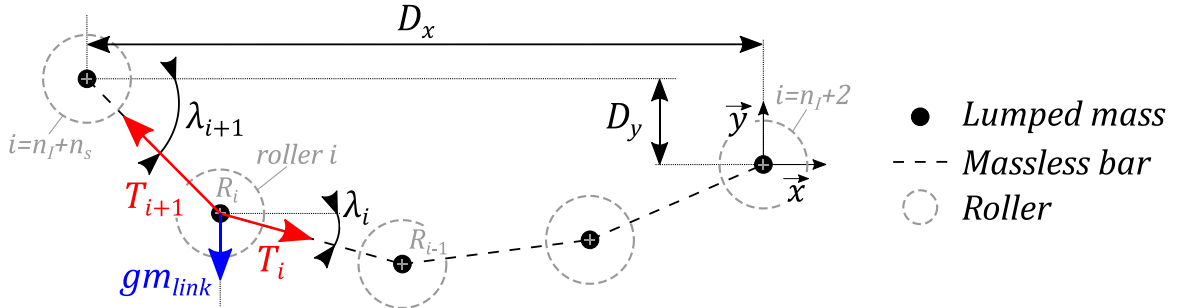
Figure II-10: Slack strand modelling

A given roller is subjected to three external forces (Figure II-10). The tension in the preceding and following links (respectively T_i and T_{i+1}) and the weight (corresponding to the weight of one chain link of mass m_{link}). The spatial direction of link i is given relatively to the horizontal direction ($\vec{x}$ in Figure II-10) by angle λ_i. The equilibrium of a roller leads to the following equations.

$$\begin{cases} T_{i+1} = T_i \dfrac{\cos(\lambda_i)}{\cos(\lambda_{i+1})} \\[3mm] \tan(\lambda_{i+1}) = \dfrac{m_{link}g + T_i \sin(\lambda_i)}{T_i \cos(\lambda_i)} \end{cases} \qquad \textbf{(II-10)}$$

with:

- $i \in [\![n_I + 2, n_I + n_s]\!]$
- $\lambda_i = \left(\vec{x}, \overrightarrow{R_i R_{i-1}} \right)$

Equations (II-10) connect the characteristics of one roller/link pair (*e.g.*, λ_i and T_i) with the following one (λ_{i+1}, T_{i+1}). Therefore, if a set of values (T_i, λ_i) is known, it is possible to calculate all the tensions and link orientations considering all the rollers step by step.

Moreover, as presented by Lodge & Burgess in [70], a valid slack strand must fulfil the following equations (eqs.(II-11), see Figure II-10), ensuring that a set of angles λ_i is consistent with the positions of the strand boundaries.

$$\sum_{i=n_I+2}^{n_I+n_s+1} p\cos(\lambda_i) - D_x = 0 \qquad \text{(a)}$$

$$\textbf{(II-11)}$$

$$\sum_{i=n_I+2}^{n_I+n_s+1} p\sin(\lambda_i) - D_y = 0 \qquad \text{(b)}$$

Therefore, once the slack strand tips' locations are known (*i.e.*, angles $\psi_{s,j}$), distances D_x and D_y are deduced and the corresponding slack strand can be calculated. Numerical search is used to find a set of values (*e.g.*, $T_{n_I+2}, \lambda_{n_I+2}$) resulting in the smallest residual value on eqs.(II-11). Similarly with the tight strand, once the slack strand trajectory is known (angles λ_i for all rollers), the values of angles $\alpha_{s,I}$ and $\alpha_{s,II}$ can be computed using eqs.(II-8).

The tension in the boundary links ($T_{i=n_I+2}$ and $T_{i=n_I+n_s+1}$) are denoted $T_{s,I}$ and $T_{s,II}$, respectively. Unlike the tight strand (see eqs.(II-7)), they do not necessarily have the same value.

$$\begin{aligned} T_{i=n_I+2} &= T_{s,I} & \text{(a)} \\ T_{i=n_I+n_s+1} &= T_{s,II} & \text{(b)} \end{aligned} \qquad \textbf{(II-12)}$$

The slack strand sub-model can only be used in conditions where the number of links in the strand is sufficient. As no link elongation is modelled, the condition translates in eq.(II-13), ensuring that the distance between strand tips is smaller than the strand length.

$$\sqrt{D_x^2 + D_y^2} < p n_s \qquad \textbf{(II-13)}$$

In order to study the influence of the tension setting on drive behaviour and efficiency, it is necessary to quantify strand looseness. A representation of the chain tension is usually obtained with a measure of the mid-span movement (*i.e.*, the peak to peak slack strand deflection) expressed as a proportion of L [73] (Figure II-11). The mid-span recommendation is 4-6% of L for regular industrial drives [73]. For sensitive transmissions (high speed, impulse, reversing) the setting can be reduced to 2-3% [73].
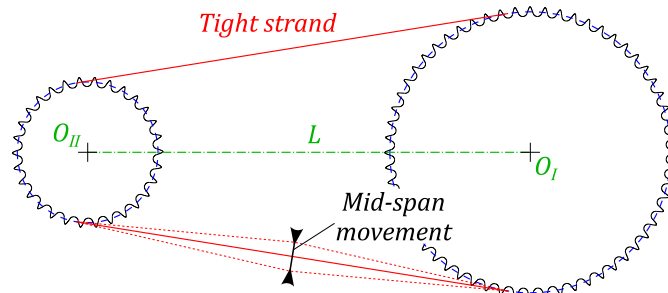
Figure II-11: Mid-span movement of the slack strand, adapted from [73]

The procedure to geometrically calculate the mid-span movement for a given drive sub-position is given in the Appendix E. As its value changes for each sub-position (*i.e.*, for each driving sprocket orientation), the looseness setting of a given drive is calculated as the mean mid-span movement value on ten linearly spaced sub-positions within the drive movement studied. For the rest of the manuscript, the looseness setting will be given as a proportion of L expressed in % for each drive studied.

II.1.3   Global kinematics: numerical procedure

The models for the tight and slack strand have been introduced. The numerical procedure to solve the global kinematics is now detailed.

Both strands have been introduced as independent systems. However, they are connected by the driving and driven sprockets. The centre of every roller in contact with a sprocket is assumed to lie on the related pitch circle at a distance p apart from each other. Therefore, the tight and slack tips on a given sprocket are intertwined by the following equation (see Figure II-12 and eqs.(II-4) and (II-9)).

$$\pi - 2(-1)^j\beta = \psi_{t,j} + \alpha_j n_j + \psi_{s,j} \tag{II-14}$$
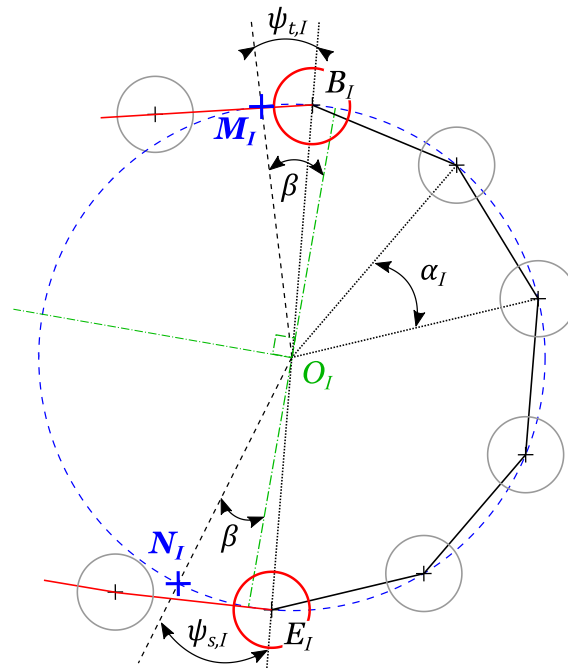
Figure II-12: Relation between $\psi_{s,I}$ and $\psi_{t,I}$

Angles $\alpha_{t,j}$ and $\alpha_{s,j}$, introduced in the previous sections, are now used to assess the validity of any proposed kinematics [81] as they are restricted to the interval $]0, \alpha_j]$ (with $j = I, II$). Indeed, let us

consider the meshing at the driving sprocket (roller coming from the tight strand to be captured by the driving sprocket). When a new roller comes into contact with the sprocket (roller B in Figure II-13.a), angle $\alpha_{t,I}$ equals 0^+. Angle $\alpha_{t,I}$ increases as the driving sprocket continues its rotation. Assuming that the following roller comes into contact when its centre hits the pitch circle, the next capture occurs when $\alpha_{t,I} = \alpha_I$ (Figure II-13.b). At the following instant, the strand tip jumps to roller A and the same procedure is repeated.
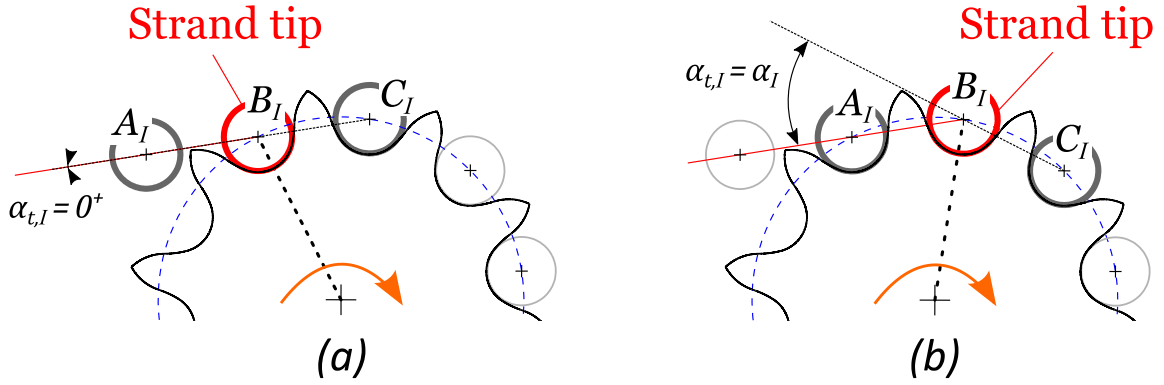
Figure II-13: Extreme satisfactory tight strands at the driving sprocket with (a) $\alpha_{t,I} = 0^+$, (b) $\alpha_{t,I} = \alpha_I$

The global kinematics is independent from the loading conditions and cyclic. The angular period corresponds to a driving sprocket rotation of α_I (inducing an α_{II} rotation of the driven one). Calculations are therefore only carried out for one drive period (*i.e.*, the driving sprocket rotation angle ζ goes from $\zeta = 0$ to $\zeta = 1$). The period considered is divided into sub-positions upon which the following numerical procedure is applied.

The tight strand is solved first following the flow chart presented in Figure II-14.a. The algorithm is initialised with values for $\psi_{t,I}$ and n_t. Values for β_t and $\psi_{t,II}$ are then computed using equations (II-5) and angles $\alpha_{t,I}$ and $\alpha_{t,II}$ are calculated using eqs.(II-2). The values obtained are compared to the interval $]0, \alpha_j]$ to check the validity of the kinematics proposed. If the conditions are not fulfilled, the initial predictions are changed. Indeed, if $\alpha_{t,I}$ exceed α_I, it means that the roller assumed to be the strand tip is in fact the second meshed roller (see Figure II-15.a). Therefore, the number of links in the tight strand as well as the value of $\psi_{t,I}$ must be adjusted (a link is removed from the tight strand and $\psi_{t,I}$ is reduced by α_I). Similarly, a negative value of $\alpha_{t,I}$ signifies that the roller assumed to be the strand tip is in reality part of the tight strand (see Figure II-15.b). The same reasoning applies to the driven sprocket with α_{II} except that $\psi_{t,II}$ is not adjusted as its value is calculated using the four-bar mechanism relation (eqs. (II-5)). When the conditions on $\alpha_{t,j}$ are met, the tight strand is solved.

(a)

(b)
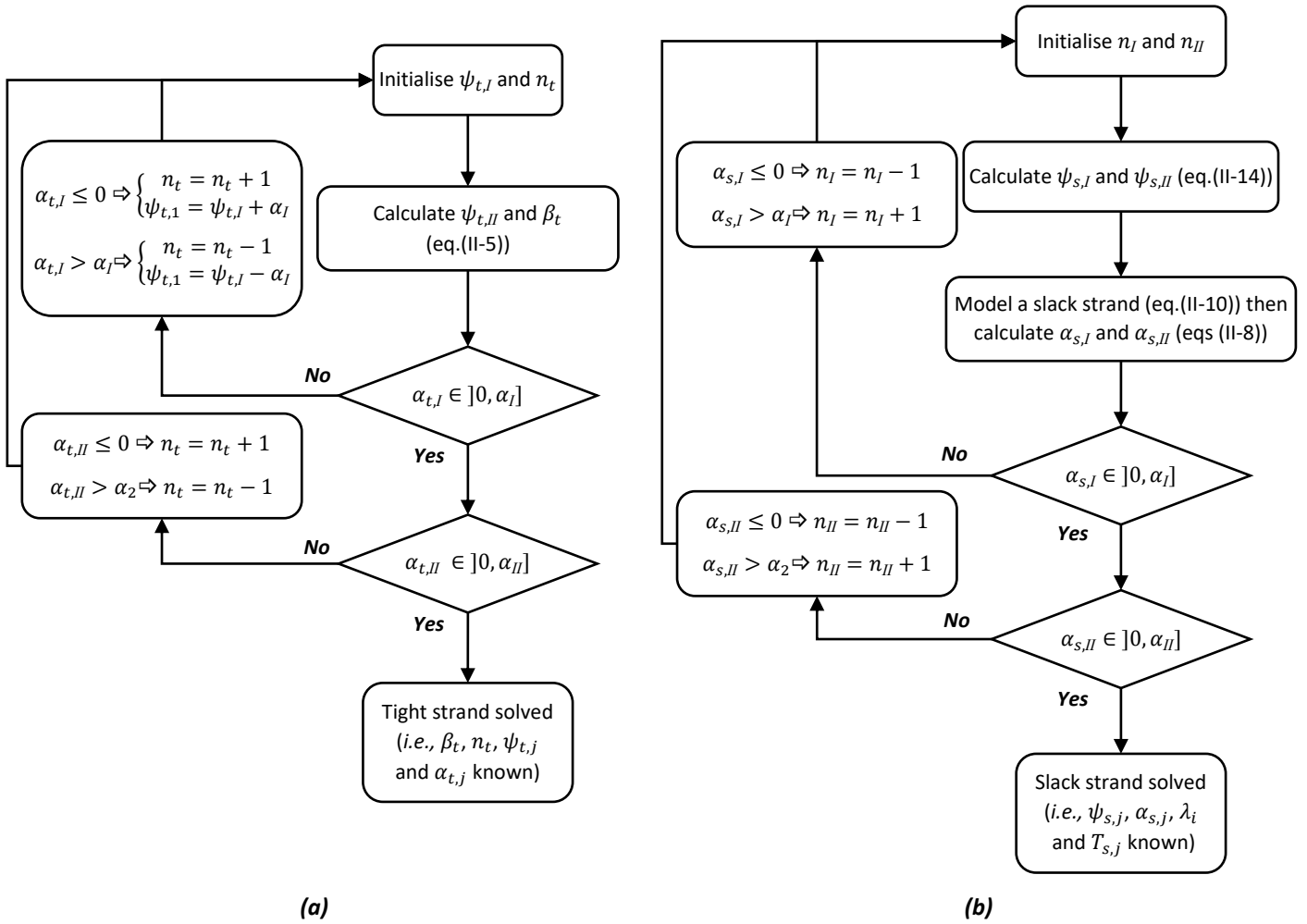
Figure II-14: Flow chart for (a) tight and (b) slack strand numerical calculation

The slack strand is then determined using the algorithm presented in Figure II-14.b. The method is similar to that used for the tight strand except for the initializing variables. The values for n_I and n_{II} are first predicted. The locations of the corresponding slack strand tips (*i.e.,* $\psi_{s,j}$) are then determined using equation (II-14). Based on these locations, a slack strand is modelled and the corresponding $\alpha_{s,j}$ angles are calculated and compared to $]0, \alpha_j]$ to check the validity of the proposed geometry. As with the tight strand, if the conditions are not met, the initial predictions are changed until an acceptable proposal is found.
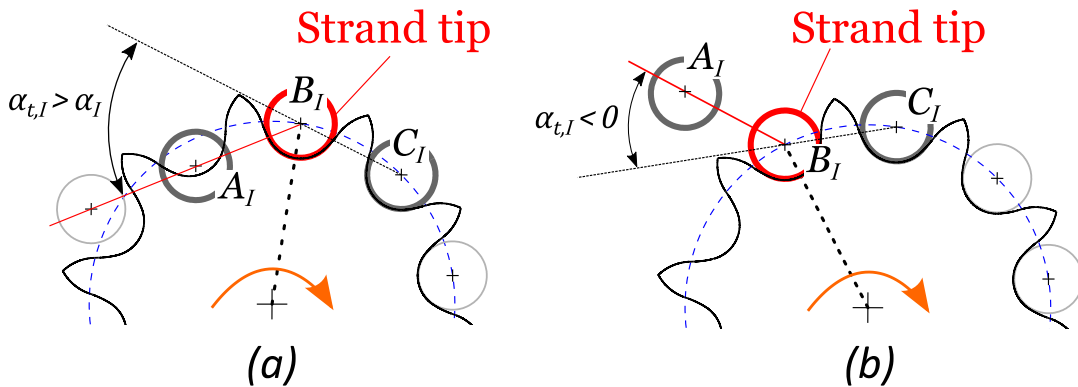
Figure II-15: Unsatisfactory tight strand at the driving sprocket (a) $\alpha_{t,I} > \alpha_I$ (b) $\alpha_{t,I} < 0$

The first sub-position to be solved is characterised by the initial driving sprocket orientation $\psi_{t,I}\big|_{init}$ (given as input parameter). Any initial value for $n_t\big|_{init}$ and $n_j\big|_{init}$ can be provided. However, to limit the number of steps and improve computation time, the following initial values are used. The initial value of n_t is obtained considering that the length of the common tangents equals $L\cos(\beta)$ (see Figure II-3). Similarly, initial values of n_j (see eq.(II-16)) are based on the theoretical wrapping angle of sprocket j $(\overrightarrow{O_jN_j}, \overrightarrow{O_jM_j})$ being equal to $\pi \pm 2\beta$ depending on the sprocket being driving or driven (see Figure II-12).

$$n_t\big|_{init} = \text{round}\left(\frac{L\cos(\beta)}{p}\right) \qquad\qquad \textbf{(II-15)}$$

$$n_j\big|_{init} = \text{round}\left(\frac{\pi - 2(-1)^j\beta}{\alpha_j}\right) \qquad\qquad \textbf{(II-16)}$$

with:

- round, function giving the nearest integer

The global kinematics numerical procedure presented in Figure II-14 stops when an acceptable geometry is found. Therefore, if two (or more) acceptable geometrical solutions coexist for the same drive position (*i.e.*, same ζ), the procedure can stop on either one depending on the initialisation values. In the preliminary study presented in [81], no such issue was reported. This was probably because the slack strand was assumed to be a straight line like the tight one. However, using the more developed non-linear model presented in §II.1.2, the coexistence of two simultaneous geometrical solutions was observed for the slack strand.
The two possible solutions can be generated using either the results of the preceding or following drive sub-position as the initialisation value (respectively called forward and backward calculation, see Figure II-16).
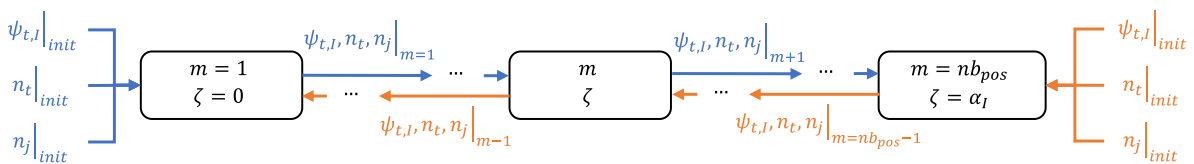
Figure II-16: Kinematic procedure for forward and backward calculation

Figure II-17 shows the evolution of the number of links in the slack strand during one drive period (from $\zeta = 0$ to $\zeta = \alpha_I$) for two slack strand settings to appreciate the two simultaneous solutions. It can be seen that the two solutions agree on the most part of the drive period. The two solutions differ on "non-determined zones". Elsewhere, they are in accordance on "agreement zones". The differences between the two solutions are caused by different predictions of the roller capture and release events at the slack strand. It is observed that the width of the non-determined zones increases with the slackness of the strand. (*i.e.*, the looser the strand, the larger the non-determined zones, see Figure II-17).
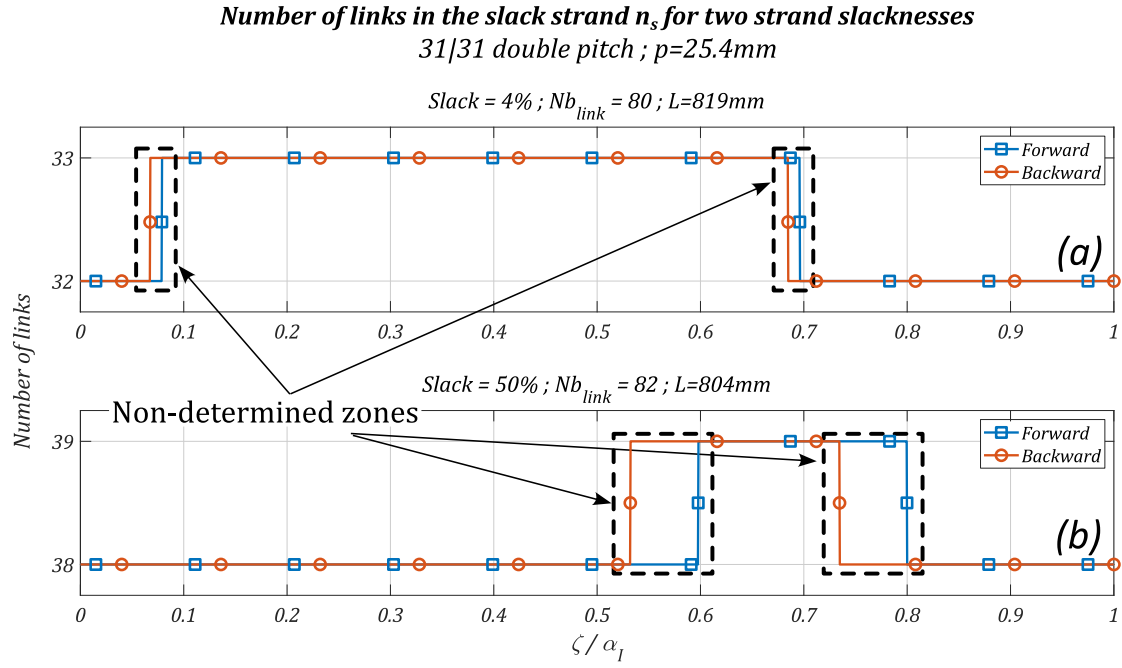
Figure II-17: Non-determined zone for (a) slack=4% (b) slack=50%

In real life cases, the backward calculation would represent a backward rotation of the driving sprocket (counter-clockwise according to the convention of this manuscript) but still with the upper strand being tight. Such drive operations are non-physical and therefore not considered here. Consequently, the forward calculation solution is always considered. However, to ensure that the forward branch is chosen, the initial position (given by $\psi_{t,I}\big|_{init}$) must be in an agreement zone. Therefore, a specific check is added at the initialisation of the procedure. If the starting position prescribed by $\psi_{t,I}\big|_{init}$ lies in one of the non-determined zones, the global kinematics calculation is initialised with the closest unambiguous drive sub-position. The cyclic properties of the model are then used to obtain the kinematics with the phasing prescribed by $\psi_{t,I}\big|_{init}$.

The global drive kinematics giving both strands' trajectories as well as the numbers of links in each sub-model (*i.e.,* n_t, n_s, n_I and n_{II}), has been presented. The slack tensions for each sprocket ($T_{s,I}$ and $T_{s,II}$) are also determined. The results are independent from the loading conditions and tooth profiles as the rollers in contact with a sprocket are assumed to lie on each pitch circle. The tight strand sub-model has been detailed. It consists of a four-bar mechanism and expresses the dependency between the rotation of the driving and driven sprockets. The slack strand sub-model, based on the works of Troedsson & Vedmar [67] and Lodge & Burgess [70] is also presented. It calculates the trajectory of a hanging chain strand subjected only to its weight. Finally, the original numerical procedure used for the calculation of the global kinematics is introduced. The question of simultaneous solutions due the non-linear slack strand model is treated. The solution obtained with the recursive algorithm is always preferred (each sub-position is initialised using the results of the preceding one).

II.2 Local sprocket sub-model, roller location and load calculation

This part details the local sprocket sub-model used for the simultaneous calculation of loads and roller locations. This sub-model can be used on either the driving or the driven sprocket.

In this part, as only one sprocket is considered at a time, the subscript j is not specified unless essential for understanding. For instance, notations α, α_t, α_s are used to designate variables α_j, $\alpha_{t,j}$, $\alpha_{s,j}$, respectively. All indexes i refer to the driving sprocket. In particular roller $i = 1$ corresponds to the first roller in contact with the sprocket, while roller $i = n + 1$ corresponds to the last roller in contact (marking the transition with the tight and slack strand respectively). The developments for the driven sprocket are obtained by changing these indexes according to Figure II-2

II.2.1 Location of a roller along its corresponding tooth profile

a) Tooth profile definition

The definition of sprocket geometry has been detailed in Chapter I. In this model, it is assumed that all sprocket angular sectors are identical. Therefore, a sprocket is fully defined by one angular sector in the local coordinate system $(O_i, \vec{x_i}, \vec{y_i})$ (see Figure II-8.b). The angular sector is defined as a piecewise curve where each portion is either a circle arc or a straight line. The definition of the portions must ensure the continuity of the slope (*i.e.,* the derivative of the curve). Moreover, the defined geometry must be such that it is not possible for a roller to contact the profile at more than one point. This implies that the radius of any convex circle portion (especially the tooth bottom circle of radius R_{tb}) must be greater than the roller radius (*e.g.*, $R_{tb} > R_{roller}$ in Figure II-18).
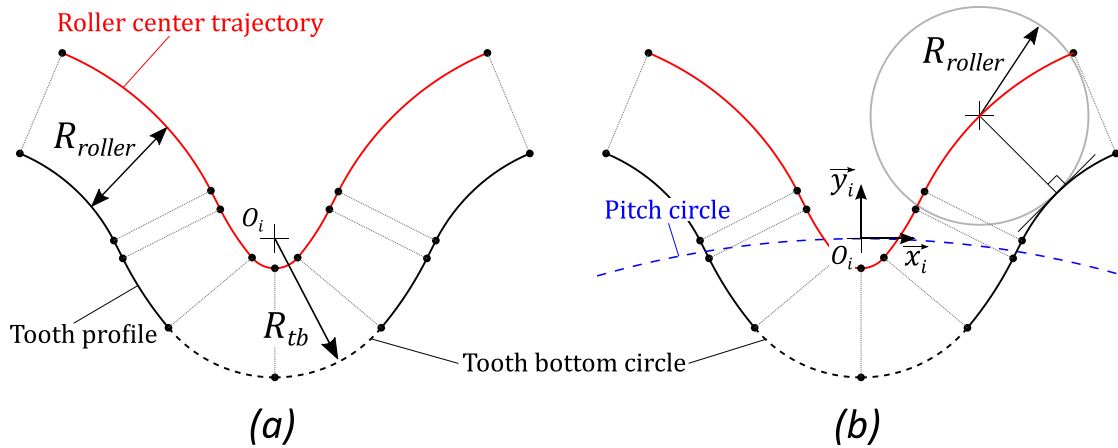
Figure II-18: Tooth profile (a) roller centre trajectory (b) local coordinate system (the clearance between roller and profile is exaggerated)

Axes $\vec{x_i}$ and $\vec{y_i}$ can be seen in the radial and tangential directions to the pitch circle at the local origin respectively (see Figure II-18). The local origins of two adjacent tooth profiles are α_j apart (see Chapter I and Figure II-20 below).

Knowing the roller radius and the definition of the tooth profile, it is possible to determine the roller centre trajectory. This curve is composed of all the possible locations for the centre of a roller in contact with the defined profile. In practice, this curve is defined as the parallel to the tooth profile (toward O_i), shifted by R_{roller} (Figure II-18). It therefore has the same number of circle arcs and lines as the tooth profile. A procedure to calculate the roller centre trajectory based on R_{roller} and the tooth profile definition is detailed in the Appendix B.

To locate the roller along its corresponding tooth profile, three different coordinates are used (see Figure II-19). These three coordinates are intertwined and knowing only one of them is sufficient to calculate the remaining two. The conversion methodology is detailed in the Appendix C.

- γ is a dimensionless coordinate. The definition is similar to coordinates η and ξ in [67] and [52] respectively. γ starts at 0 and is an integer at each point of transition between two portions of the curve. Therefore, γ ranges between $[0, Nb_{portion}]$, with $Nb_{portion}$ being the number of curve portions defining the tooth profile. Between integers, γ varies linearly with the sweeping angle θ for circle sectors and with x for the straight parts (see Figure II-19).
- s_c is the curvilinear abscissa of the contact point between the roller and its corresponding tooth profile (along the tooth profile).
- s_r is the curvilinear abscissa of the roller centre along the roller centre trajectory.

Coordinate γ is easier to interpret than the curvilinear abscissas but it also distorts reality. A distance of *e.g.*, $\Delta\gamma = 0.5$ does not correspond to the same distance in mm depending on the curve portion considered. On the contrary, the curvilinear abscissas will be used for calculations but their interpretation in terms of roller position along the tooth profile is more difficult.
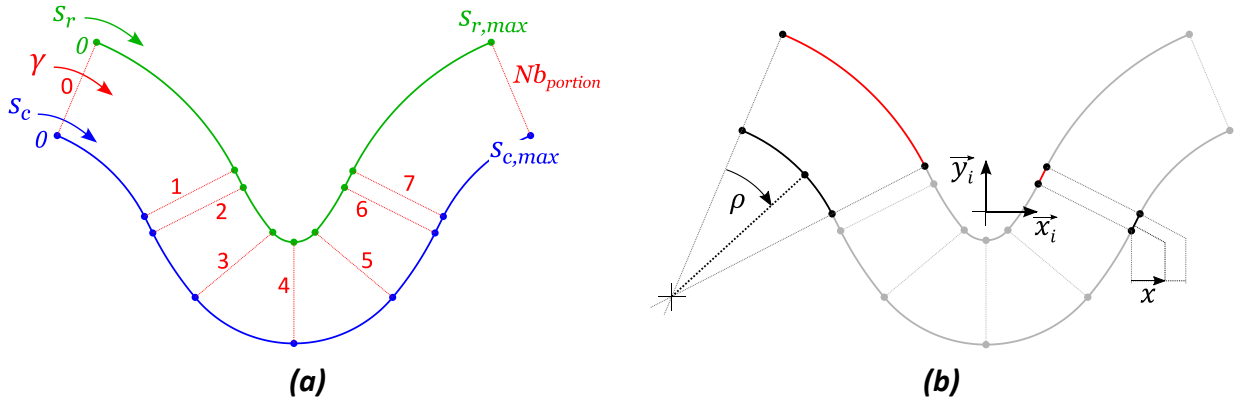
Figure II-19: (a) Roller location coordinates (b) Definition of circle arc and line profile portion (the clearance between roller and profile is exaggerated)

b) Relation between consecutive roller locations

The relation between consecutive roller locations is considered in a way similar to that of Kim & Johnson [52] and Troedsson & Vedmar [67] (see Chapter I). Therefore, adjacent rollers on a given sprocket are distant by a chain pitch p. Therefore, knowing the location of a roller, the adjacent one will lie on the roller centre trajectory of the adjacent profile at a distance p. The problem can therefore be treated as finding the intersection between a circle of radius p centred at the known roller position and the adjacent roller centre trajectory (see Figure II-20)
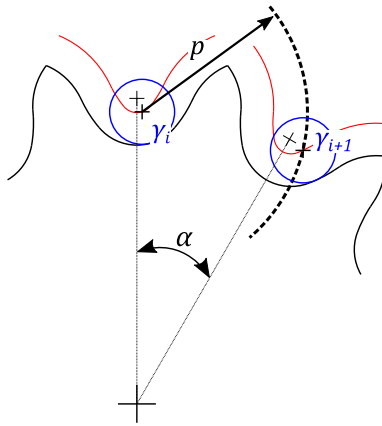
Figure II-20: Dependency between the location of two adjacent rollers (the clearance between roller and profile is exaggerated)

A detailed procedure (based on [52]) to calculate the location of the following roller (from the tight to the slack strand) based on the adjacent one is given in the Appendix D. This procedure is general and can be applied to any tooth profile.

As proposed by Kim & Johnson [52] and Troedsson & Vedmar [67] (see Chapter I, §I.3), the relation between two consecutive roller locations is visualised by plotting γ_{i+1} as a function of γ_i. This representation is called the roller location characteristic curve. The same relation can also be plotted for the two additional coordinates s_c and s_r. Examples of curves obtained using s_r and s_c as roller location variables are presented in Figure II-21. The general image of the curves is affected but the intrinsic relation is the same. Transition points and the three zones presented in §I.3 are visible. As for γ, the curves using s_c or s_r also exhibit values for articulation i which results in a non-defined roller location for articulation $i+1$ (see Figure II-21.b).
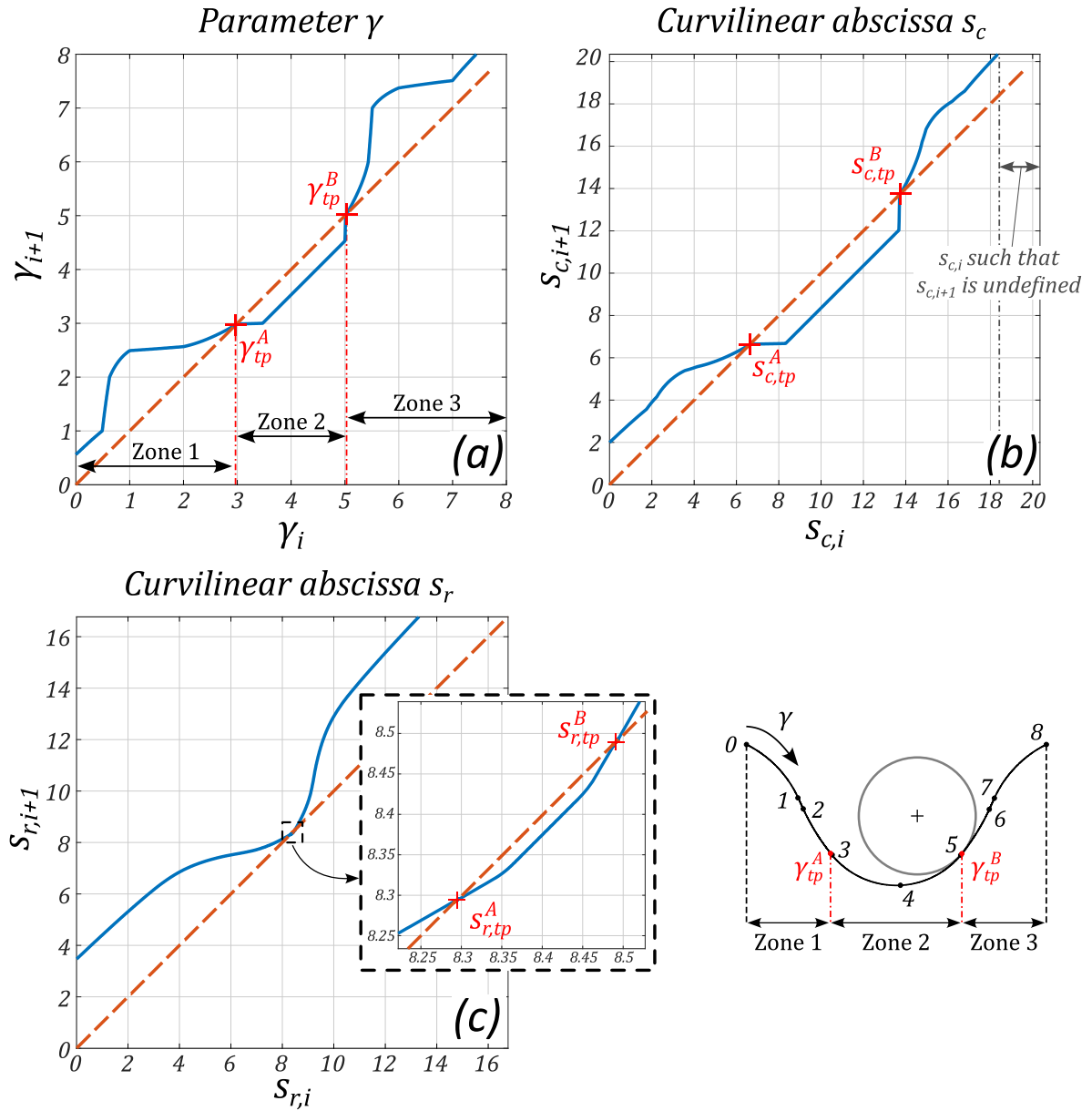
Figure II-21: Example of roller location characteristic curves for (a) γ, (b) s_c, (c) s_r

In practice, the loading conditions applied will force the roller locations to lie close to γ_{tp}^B (see Chapter IV). Therefore, the notation γ_{tp} (without superscript) can be used to designate γ_{tp}^B (similarly for $s_{c,tp}$ and $s_{r,tp}$).

The characteristic adjacent roller location curve is specific to each tooth profile, it varies with respect to the geometry definition, number of teeth, *etc*. A library of curves for several tooth profiles families (*e.g.*, ASA, NF_{max}, NF_{min}) is available in Appendix A.

This section highlights that there is a direct relation between a roller location and the locations of the adjacent ones. ***Therefore, the location of a single roller defines the locations of all the rollers on the sprocket considered.***

c) Angles between links

Depending on the location of each roller along its corresponding tooth profile (represented by coordinate γ), the relative position of consecutive links is not the same. However, these positions will prove useful to link roller locations to loading conditions (see §II.2.2, Tension model) and later to calculate the efficiency of a chain drive (see Chapter V) and must therefore be tracked.

To do so, four angles are defined for each roller (Figure II-22).

- α_i^*, angle between the directions of the following and preceding link (link $i+1$ and i respectively). This angle equals α if the three roller centres lie on the pitch circle (as assumed for the global kinematics, see §II.1)

$$\alpha_i^* = \left(\overrightarrow{R_i R_{i+1}}, \overrightarrow{R_{i-1} R_i}\right) \qquad \text{(II-17)}$$

- ϕ_i, angle between the direction of the preceding link (link i) and the profile normal at the contact point between the roller and the profile.

$$\phi_i = \left(\overrightarrow{R_{i-1} R_i}, \vec{u}\right) \qquad \text{(II-18)}$$

- κ_i, angle between the direction of the preceding link (link i) and the $\overrightarrow{x_i}$ direction in the local profile axis system.

$$\kappa_i = \left(\overrightarrow{R_i R_{i-1}}, \overrightarrow{x_i}\right) \qquad \text{(II-19)}$$

- ν_i, angle between the direction of the following link (link $i+1$) and the $\overrightarrow{x_i}$ direction in the local profile axis system.

$$\nu_i = \left(\overrightarrow{R_i R_{i+1}}, \overrightarrow{x_i}\right) \qquad \text{(II-20)}$$

Parameters in Figure II-22 are:

- $\vec{u}$, the outgoing normal at the contact point between tooth profile and roller i
- R_i, the centre of roller i
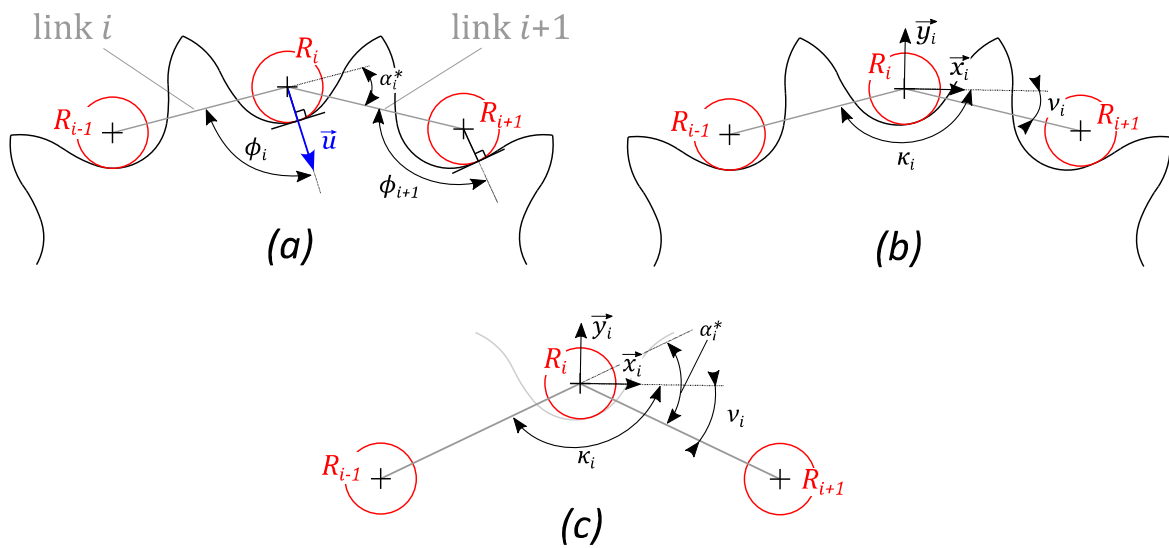
Figure II-22: Angles between consecutive links (a) ϕ and α^* (b) ν and κ (c) relation between the angles (the clearance between roller and profile is exaggerated)

Moreover, angles κ, ν and α^* are connected by eq.(II-21) (see Figure II-22.c).

$$\kappa_i - \nu_i = \pi - \alpha_i^*$$ (II-21)

At this point, compatibility issues arise at the interfaces between the global kinematics (used to calculate angles $\alpha_{t,s,j}$, see §II.1) and the local sprocket sub-model. Indeed, for the global kinematics, all roller centres are assumed to lie on their related pitch circle while the local sprocket sub-model locates the rollers more accurately (using coordinate γ). Questions arise especially for angles α_1^*, α_{n+1}^*, κ_1, ν_{n+1} and ϕ_1 (with n being the number of links in contact with the sprocket considered). Calculating them involves the location of rollers both in a chain strand (whose trajectory is determined using the global kinematics) and in contact with the sprocket considered. These compatibility issues are represented in Figure II-23. The roller location as assumed in the global kinematics calculation (see §II.1) is represented in Figure II-23.a while the precise roller location allowed by the local sprocket sub-model is represented in Figure II-23.b.
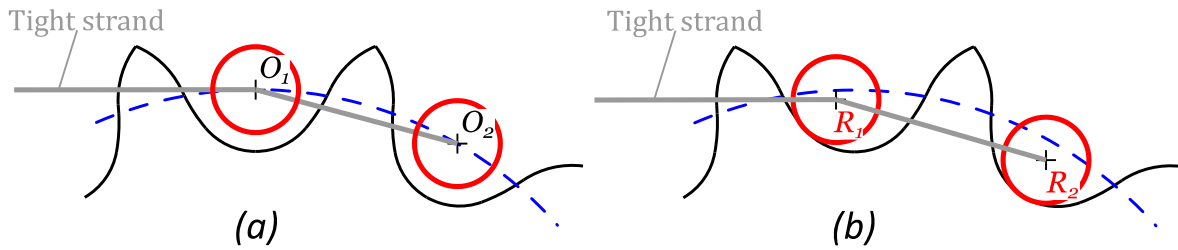
Figure II-23: Roller locations according to (a) global kinematics (b) local sprocket sub-model (the clearance between roller and profile is exaggerated)

Compatibility is solved using the following hypotheses. It is first assumed that angles α_1^* and α_{n+1}^* are equal to angles α_t and α_s, respectively, as calculated through the global kinematic study.

$$\alpha_1^* = \alpha_t$$ (II-22)
$$\alpha_{n+1}^* = \alpha_s$$ (II-23)

For angles κ_1 and ν_{n+1}, equation (II-21) is considered to be fulfilled, therefore, the angles are calculated from ν_1 and κ_{n+1}, respectively, as follows (eqs.(II-24) and (II-25)).

$$\kappa_1 = \pi - \alpha_1^* + \nu_1 = \pi - \alpha_t + \nu_1$$ (II-24)
$$\nu_{n+1} = \kappa_{n+1} - \pi + \alpha_{n+1}^* = \kappa_{n+1} - \pi + \alpha_s$$ (II-25)

The tight strand span is significantly larger than the roller/profile clearance (*i.e.*, $L\cos(\beta) \gg R_{tb} - R_{roller}$). Therefore, it is assumed that the tight strand direction calculated in the global kinematics is not affected by the roller/profile clearance. Therefore, ϕ_1 is calculated using the following relation (see Figure II-24).

$$\phi_1 = \theta - \alpha_t$$ (II-26)

with:

- $\theta = (\vec{u}, \vec{v})$. Vector $\vec{u} = \overrightarrow{O_2 O_1}$ gives the direction of link 2 and vector $\vec{v}$ is the outgoing profile normal at the roller profile contact point.
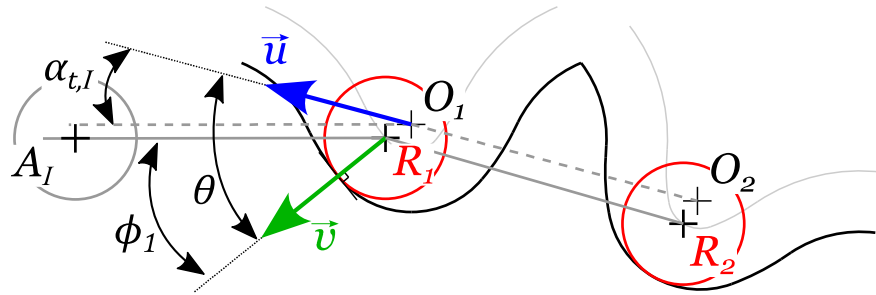
Figure II-24: Calculation of ϕ_1 (the clearance between roller and profile is exaggerated)

The assumptions stated to solve the compatibility issue (eqs. (II-22) to (II-26)) are justified by the small roller/profile clearance in real cases (about 4.3% between R_{roller} and R_{tb} for NF_{max} profile[1]). For specific drives with a bigger roller/profile clearance, these assumptions might have more influence.

The values of all the link angles are directly related to the roller locations, themselves directly related to the location of one roller. **_Therefore, all the link angle values can be calculated from the location of one roller in contact with the sprocket considered._**

II.2.2 Tension model

All the parameters introduced to locate the rollers and describe their relative orientations are now used to express the equilibrium conditions of a chain in contact with a given sprocket. This results in a relation between roller locations, loads (link tension and roller-profile contact force) and external loading conditions (*e.g.*, strand tensions).

As with previous tension models [2], [32], [70] detailed in Chapter I, the equilibrium of a chain articulation (*i.e.*, a set of pin, bush and roller) is considered. The effect of gravity is neglected with respect to the other forces considered. Therefore, a chain articulation with its roller in contact with a sprocket is subjected to three external forces (Figure II-25):

- T_i, the tension force in the preceding link,
- T_{i+1}, the tension force in the following link,
- P_i, the total (*i.e.*, tangential plus normal) contact force between the roller of articulation i and its corresponding tooth profile.

It is assumed that the tension forces act along the direction of their related link. Contact force P_i acts along a roller radius and its direction is given by angle ϕ_i. As with the approach of Kim & Johnson [52] and Verne [66], angles ϕ_i and α_i^* are not assumed but calculated from the locations of rollers along their associated tooth profile.
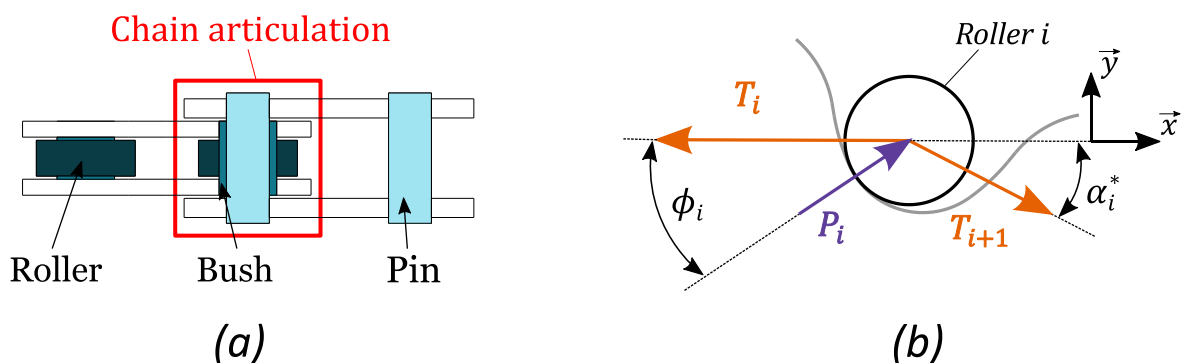
Figure II-25: Equilibrium of a chain articulation in contact with a sprocket

---

[1] With $D_{roller} = 7.75mm$ which gives $R_{tb} = 4.05mm$ (see Appendix A)

The three forces are concurrent at the roller centre; therefore, the torque equilibrium is always verified. The equilibrium along the two planar directions ($\vec{x}$ and $\vec{y}$ in Figure II-25) leads to the following relations. These relations are similar to those presented by Binder in [32] (see eq.(I-5)).

$$\begin{cases} T_{i+1} = T_i \dfrac{\sin(\phi_i)}{\sin(\phi_i + \alpha_i^*)} \\[4mm] P_i = T_i \dfrac{\sin(\alpha_i^*)}{\sin(\phi_i + \alpha_i^*)} \end{cases} \qquad \textbf{(II-27)}$$

Friction is introduced in the model in a similar way to that presented by Naji & Marshek in [2] (see Chapter I). According to this method, also used in [6], [62], [70], [81], the moment induced by the tangential friction force (F_i in Figure II-26) is neglected. The effect of friction is therefore equivalent to a correction of the angle ϕ_i by a factor δ (Figure II-26). Angle δ is calculated based on μ_δ representing the static friction coefficient at the roller/tooth interface [2].
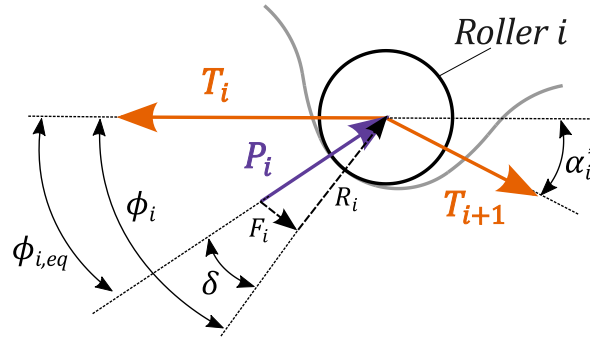
Figure II-26: Articulation equilibrium with friction

In the original formulation [2], the value of the correction angle had only two possibilities; $\delta = + \operatorname{atan}(\mu_\delta)$ and $\delta = - \operatorname{atan}(\mu_\delta)$ with no intermediate values. The correction sign must be such that the tangential friction force (F_i in Figure II-26) opposes the roller motion along its corresponding tooth profile. Consequently, this sign depends on the direction of roller motion and the sprocket studied being driving or driven [2], [70]. In this model, the same principle is used. However, the correction factor can now range between $[- \operatorname{atan}(\mu_\delta), + \operatorname{atan}(\mu_\delta)]$ as a tanh type function is used to connect the two extreme values (see Figure II-27). The interest of this continuous connection will be highlighted in Chapter IV. Moreover, it is assumed that all the rollers have the same correction angle δ and that its value is related only to the position of the first roller in contact with the sprocket considered (γ_1 or equivalently $s_{c,1}$). The sign switches at the transition point $s_{c,tp}$ as it marks the transition between zone 2 and zone 3 (see Figure II-21) where the direction of roller motion along the tooth profile changes (from one transition point to the other in zone 2 and toward the tooth tip in zone 3). The correction angle is therefore calculated as follows.

$$\delta(s_{c,1}) = (-1)^j \operatorname{atan}(\mu_\delta) \tanh\left(\frac{3(s_{c,1} - s_{c,tp})}{a}\right) \qquad \textbf{(II-28)}$$

The width of the tanh function is characterised by the parameter a (see eq.(II-28)) such that the transition between the two extreme values $\pm \operatorname{atan}(\mu_\delta)$ occurs between $\pm a$ according to eqs.(II-29).

$$\begin{aligned} \delta(a) &= 0.99 \operatorname{atan}(\mu_\delta) &\text{(a)} \\ \delta(-a) &= -0.99 \operatorname{atan}(\mu_\delta) &\text{(b)} \end{aligned} \qquad \textbf{(II-29)}$$

Since a is a numerical parameter, its value has therefore been chosen to avoid interferences with the results. A sensitivity study was carried out and a value of $a = 1e^{-10}m = 0.1nm$ chosen for this work (details are given in Appendix F).
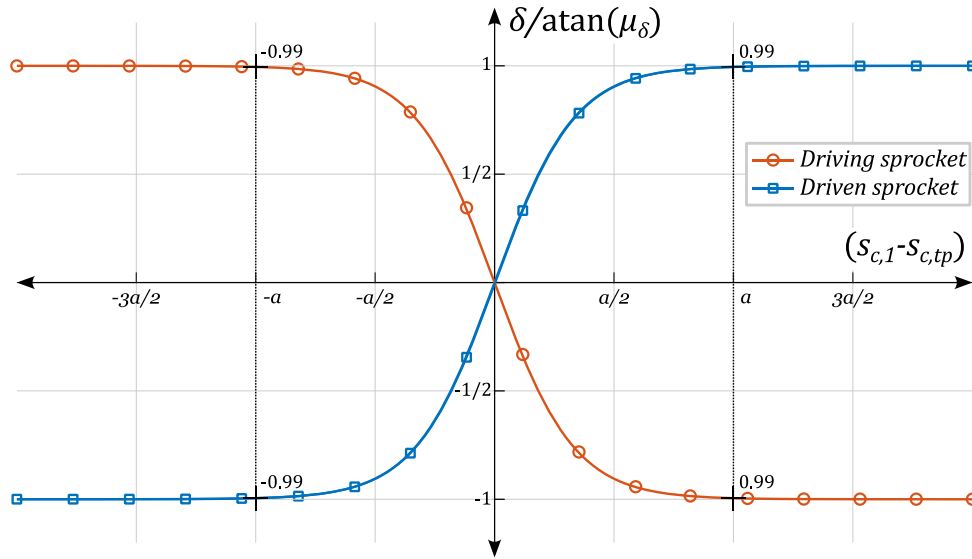
Figure II-27: Correction factor δ as a function of $s_{c,1}$

Adding the influence of friction to equation (II-27) leads to the new articulation equilibrium relation expressed in eq.(II-30).

$$
\begin{cases}
T_{i+1} = T_i \dfrac{\sin(\phi_i + \delta)}{\sin(\phi_i + \delta + \alpha_i^*)} \\[4mm]
P_i = T_i \dfrac{\sin(\alpha_i^*)}{\sin(\phi_i + \delta + \alpha_i^*)}
\end{cases}
\tag{II-30}
$$

Finally, the ratio between the tight and slack strand tensions is expressed in eq.(II-31) considering the consecutive equilibrium of all the articulations in contact with the sprocket (see Figure II-28).

$$
\frac{T_s}{T_t} = \prod_{i=1}^{n+1} \frac{\sin(\phi_i + \delta)}{\sin(\phi_i + \delta + \alpha_i^*)}
\tag{II-31}
$$
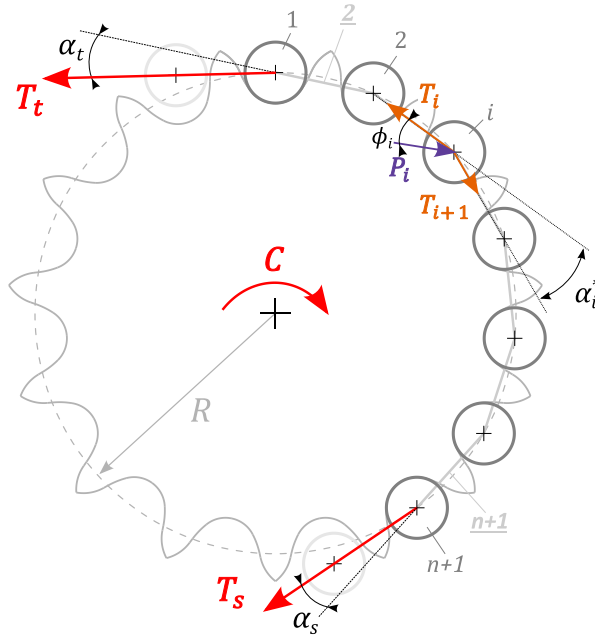
Figure II-28: Sprocket equilibrium

Eq. (II-31) highlights the direct relation between the tension ratio (ratio of the slack to tight strand tension) and angles ϕ_i and α_i^*; themself directly related to the location of one roller. **Thus, the position of one roller is directly related to the tension ratio.** In practice, the tension ratio is expressed as a function of the location of the roller marking the transition with the tight strand (*i.e.*, roller $i = 1$). Figure II-29 shows the evolution of the slack to tight tension ratio (T_s/T_t) as a function of the location of the first roller $s_{c,1}$. This relation is plotted for $|\delta(\infty)| = 5°$ and $0°$ (corresponding to $\mu_\delta = 0.087$ and 0, respectively) to appreciate the effect of friction. The value of a is set at $1e^{-6}m$ for illustration purposes.
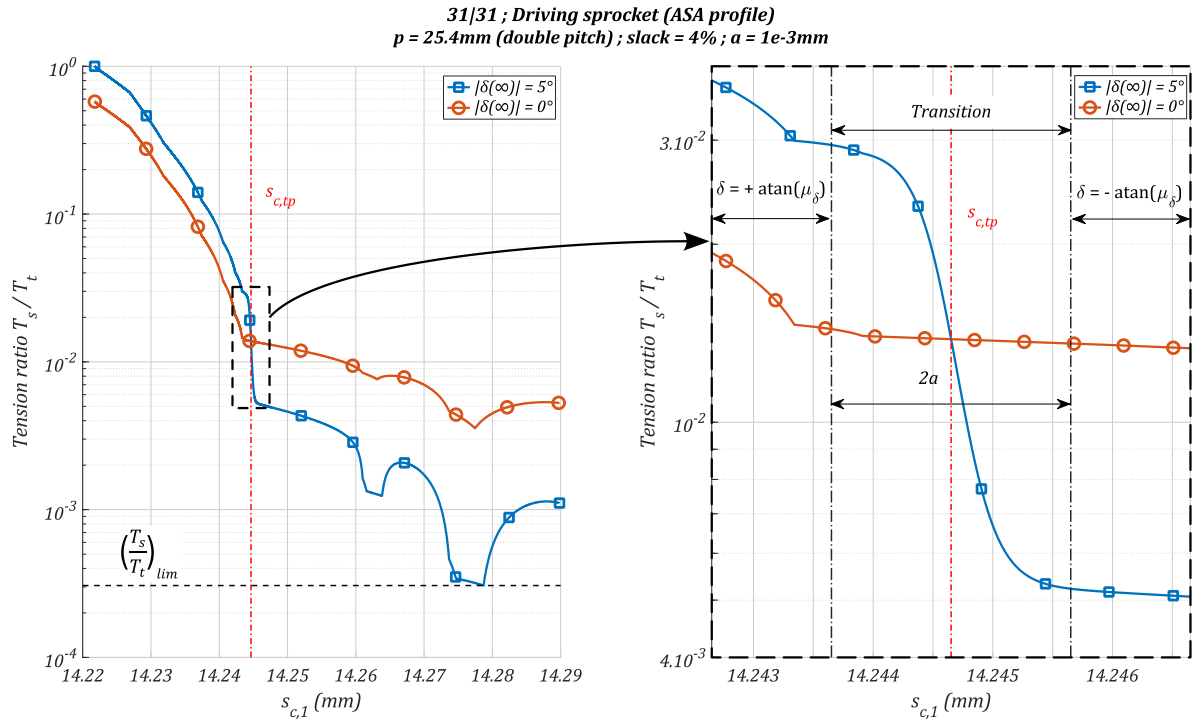
Figure II-29: Example of relation between the tension ratio and the location of the first roller

Figure II-29 shows that the effect of friction on a driving sprocket results in a higher (lower) tension ratio for a given roller location before (after) the transition point. The effect on a driven sprocket is reversed. Deeper analysis of the relation between tension ratio and roller location will be carried out in Chapter IV. The curves in Figure II-29 exhibit a minimum value for the tension ratio called $\left(\frac{T_s}{T_t}\right)_{lim}$. The existence of this minimum value signifies that not all ratios can be reached. If a ratio is too small (*i.e.*, the external loading conditions are too severe), no solutions are possible, meaning that the chain cannot wrap around the sprocket while carrying the prescribed load.

Furthermore, a global relation between the tight and slack tensions and the torque applied on the sprocket can be developed (see eq.(II-32)). This relation is obtained considering the equilibrium of the system constituted by the sprocket and all the articulations in contact with it (articulation from $i = 1$ to $i = n + 1$, see Figure II-28).

$$C = R\left[T_t \cos\left(\alpha_t - \frac{\alpha}{2}\right) - T_s \cos\left(\alpha_s - \frac{\alpha}{2}\right)\right] \qquad \textbf{\textit{(II-32)}}$$

Equations (II-31) and (II-32) are combined to express a direct relation between the location of the first roller (*i.e.*, $s_{c,1}$) and the external loading conditions. The latter are fully defined by two out of the three variables T_t, T_s and C.

Going back to Chapter I, §I.3, it was stated that rollers cannot lie in zone 1 (see Figure II-21). Indeed, when rollers lie in zone 1, the induced angles α_i^* and ϕ_i injected in eq. (II-30) are such that T_{i+1} is smaller than T_i for all i. This results in a drive where the tight strand tension T_t is lower than the slack one T_s. Such a case implies an inversion between the driving and driven sprocket with the tight strand being at the bottom of the drive. These drives are not within the scope of this study.

The local sprocket sub-model has been introduced. It takes into account the dependency between roller locations introduced by Kim & Johnson [52] and Troedsson & Vedmar [67] with a tension model close to what Verne used in [66]. Friction is introduced thanks to a correction angle as proposed by Naji & Marshek in [2]. The sub-model obtained shows that the location of roller $i = 1$ (expressed as $s_{c,1}$) is interdependent with the external loading conditions applied on the sprocket.

All the sub-models constituting the QSCDM have been detailed. Their combination in the general solving procedure is now explained (this general procedure includes the global kinematics solved in §II.1.3).

II.3 Solving of the entire chain drive model

II.3.1   Resolution of all the sub-positions

The cyclic property of the global kinematics has already been presented in §II.1.3. Its period corresponds to a driving sprocket rotation of α_I (inducing an α_{II} rotation of the driven one). The external loading conditions are also assumed to have the same cyclic property making it possible to solve the model for only one period before generalising the results.

As only one period is explored, the driving sprocket rotation angle ζ ranges between the interval $[0, \alpha_I]$. The explored interval is divided into a given number of sub-positions nb_{pos} numbered by index m ($m \in [\![1, nb_{pos}]\!]$). The initial orientation of the driving sprocket, for sub-position $m = 1$, is given by $\psi_{t,l}|_{init}$. The external loading conditions are given as inputs by specifying either the torque applied on one sprocket C_j or the tight strand tension T_t.
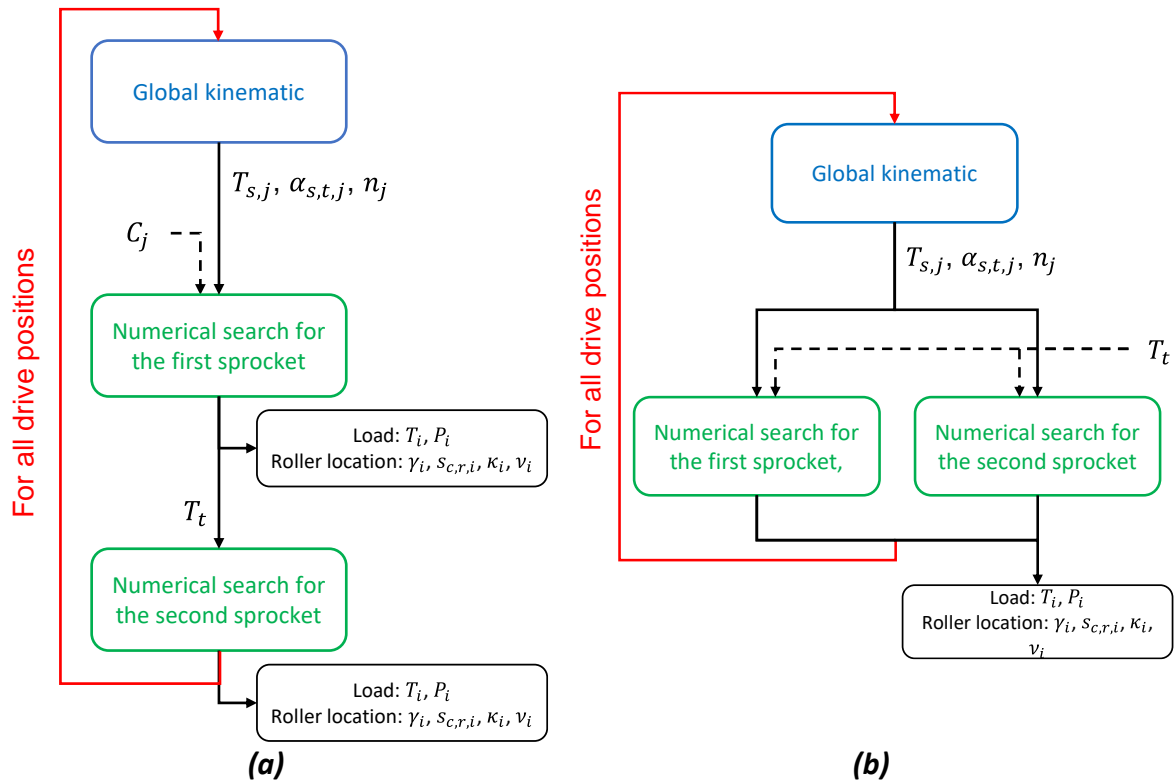
Figure II-30: Flow chart for solving the entire model for loading conditions given as (a) torque on one sprocket (b) tight strand tension

The global kinematics is first solved as detailed in §II.1 giving values for the slack strand tension for each sprocket ($T_{s,I}$ and $T_{s,II}$ for the driving and driven sprocket, respectively) as well as angles $\alpha_{s,t,j}$ and the number of links in each sub-model of the drive (*i.e.*, n_j and $n_{s,t}$). At this point, the procedure differs depending on the external loading conditions applied (see Figure II-30). If a torque is prescribed, the sprocket on which the torque is applied is solved first. Based on the slack strand tension, the value of $s_{c,1}$ matching the loading conditions is determined by numerical search. Solving the first sprocket gives the value of the tight strand tension $T_{t,j}$ (equal for both sprockets, see eqs.(II-7)). Therefore, the tension ratio is known for the remaining sprocket and it can then be solved *via* numerical search as well. If the loading conditions are given as a tight strand value, the two sprockets can be solved simultaneously, still *via* numerical search, as the tension ratio is prescribed for both (Figure II-30.b).

The numerical search problem consists in finding the value of $s_{c,1}$ in accordance with the prescribed loading conditions. Unlike the work by Kim & Johnson in [52], the relation presented between the roller locations and the tension ratio (*i.e.*, relation between $s_{c,1}$ and T_s/T_t or C) as described in this work is not always monotonous (see Figure II-29 or Figure II-31). This is caused by either the influence of the friction correction (*i.e.*, angle δ) or the profile geometry. The main consequence being that it is possible for several roller locations $s_{c,1}$ to satisfy the imposed loading conditions. When multiple solutions coexist, the smallest suitable $s_{c,1}$ is preferred to favour the continuity of the roller motion obtained coming from the stable drive operation (closer to the transition point, Figure II-31).
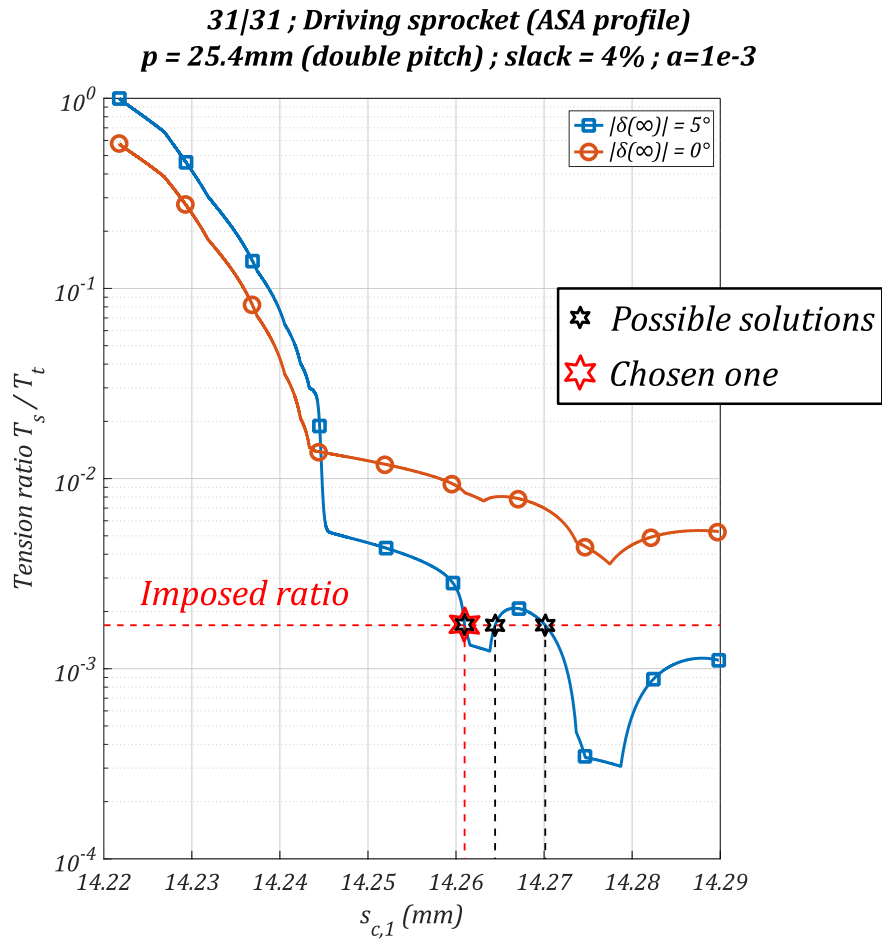
Figure II-31: Simultaneous numerical solutions

Moreover, it should be noted that the relation between the loading conditions and roller location is specific for one drive sub-position (*i.e.*, one driving sprocket orientation ζ). Indeed, the number of links n_j, the angles $\alpha_{s,t,j}$ and the slack strand tension $T_{s,j}$ vary within the studied period. Figure II-32 illustrates this variation. The tension ratio/roller location relation is plotted right before and right after the capture of a new roller by the driving sprocket. The $s_{c,1}$ interval plotted is such that its minimum results in $T_s/T_t = 1$ and its maximum corresponds to the maximal $s_{c,1}$ value that does not result in a roller missing a tooth (see Figure II-21.b).
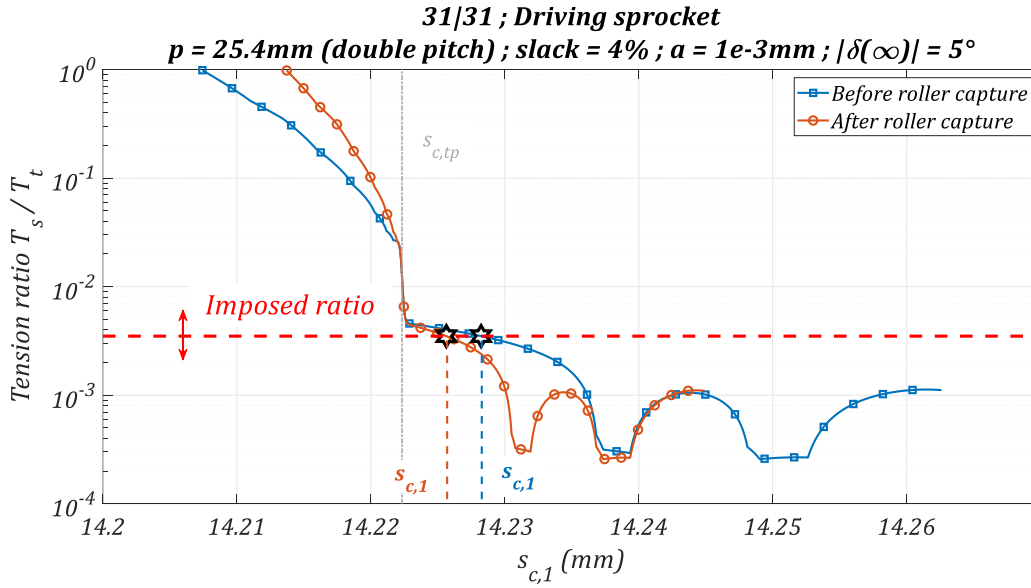
Figure II-32: Example of extreme relations between tension ratio and roller location

The interval of possible roller location $s_{c,1}$ is reduced when an additional roller is captured (*i.e.*, after roller capture). Indeed, smaller $s_{c,1}$ values are sufficient for a roller to miss the tooth when the number of rollers in contact increases (positions such that γ_{i+1} is not defined are reached sooner, see Figure II-21.b). Combined with the modification of the tension ratio imposed by the loading conditions, the resulting roller location $s_{c,1}$ changes (*i.e.*, $s_{c,1}$ is not constant for any ζ).

The solving procedure presented is sequential. The global kinematics is solved first before using its results for the sprocket sub-model. This strategy takes advantage of the hypothesis stating that the global kinematics is independent from the external loading conditions. This approach is different from that used by Troedsson & Vedmar [67] where all the sub-models were solved together.

The strategy used in this study allows easier solving of each sub-model. However, compatibility issues are introduced at the interfaces between the global kinematics and the local sprocket sub-model (see Figure II-23). Indeed, the first assumed that all rollers lie on the pitch circle while the second make it possible to locate them more precisely along their corresponding tooth profile (see §II.2.1).

II.3.2   Resolution for one chain component

Up to now, the procedure used to spatially solve (following spatial index i, see Figure II-2) the roller locations ($\gamma, s_c, s_r, \kappa, \nu$) and the loads ($T, P$) for all the explored sub-position m has been given. These spatial results are denoted "per position". However, to ultimately calculate power losses (see Chapter IV), it is interesting to know the evolution of loads and roller locations following a single chain component (*e.g.*, a roller or a link). As the model is periodic, the spatial information obtained can be rearranged into evolutions following a specific chain component (link or roller) during its contact with a given sprocket. These new results "per component" are denoted with index k. The challenge to be overcome here is that the spatial numbering introduced in Figure II-2 changes each time a new roller is captured by the driving sprocket. Therefore, to track a given chain component (*e.g.*, a roller in Figure II-33) the results of each sub-position must be combined in the correct order. In Figure II-33, $\zeta_{capture}$ corresponds to the value of ζ right before roller capture by the driving sprocket.
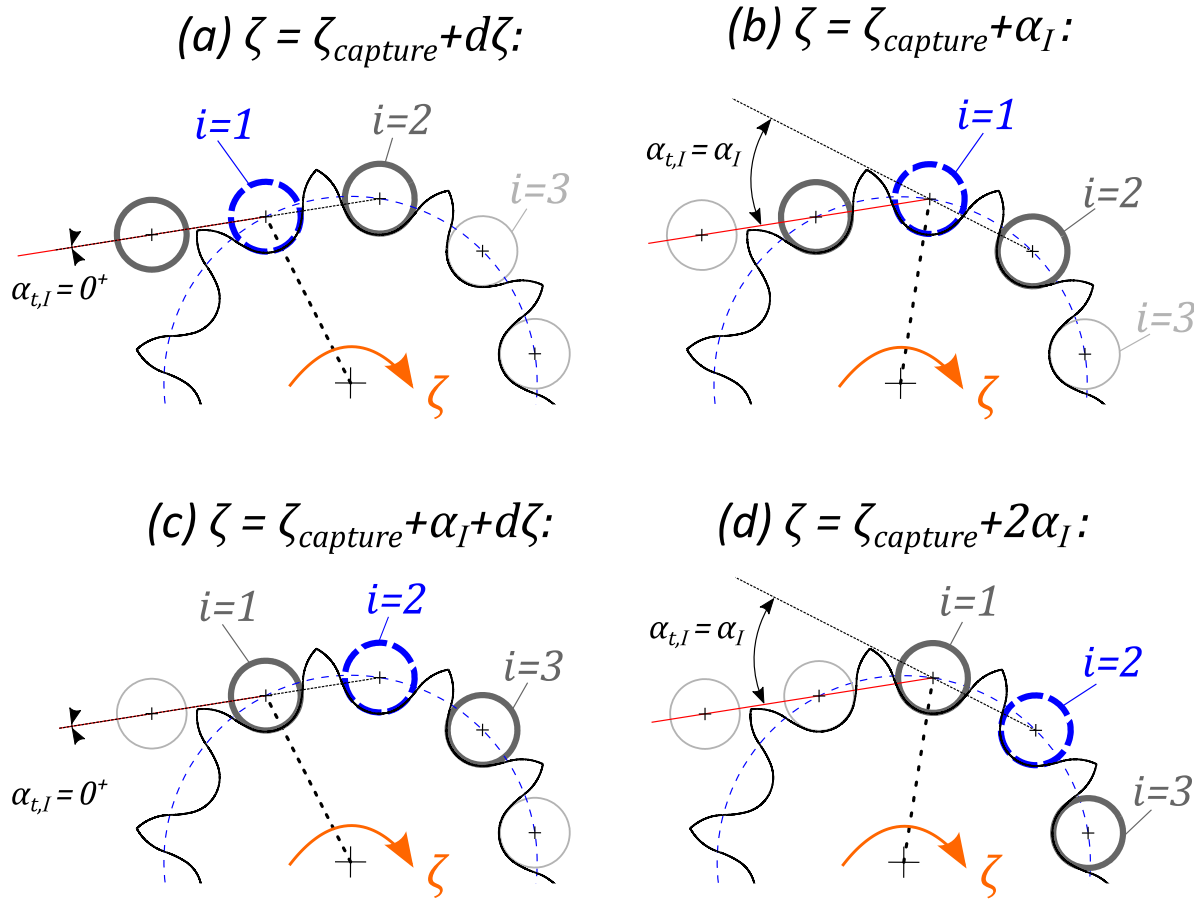
Figure II-33: Evolution of index i of a given roller throughout the drive operation (a) right after roller capture by the driving sprocket (b) right before the capture of a new roller (c) right after the capture of a new roller (a drive period away from (a)) (d) right before the capture of a second roller (one drive period away from (b))

The values "per position" are identified by indexes m and i. $P(m, i)$ designates the value of the contact force at roller i for sub-position m. The evolution "per component" $P(k)$ is obtained by going through all the possible (m, i) values, and applying eqs.(II-33) on each.

$$for\ m \leq m_{capture}: \quad k = i(nb_{pos} - m_{capture}) + m \qquad (a)$$

$$(II-33)$$

$$for\ m > m_{capture}: \quad k = (i - 1)(nb_{pos} - m_{capture}) + (m - m_{capture}) \qquad (b)$$

with:

- $m_{capture}$ the index of the sub-position immediately before roller capture by the driving sprocket (corresponding to $\zeta_{capture}$, see Figure II-34).

The index rearrangement characterised by eqs.(II-33) is represented graphically in Figure II-34. Each row corresponds to a given sub-position m while each column corresponds to all the contact forces on roller i. The evolution of force P "per component" starts with the values corresponding to $P_{i=1}$ after the capture of a new roller ($m > m_{capture}$). It continues with the P_1 value before the roller capture ($m \leq m_{capture}$). The same principle is repeated for all i until the roller is released by the sprocket ($i = n_I + 1$).

$$P(\zeta = 0) \quad = \quad (P_{i=1} \quad P_2 \quad P_3 \quad \cdots \quad P_{n_I} \quad P_{n_I+1}) \qquad m = 1$$

$$P(\zeta = \zeta_{capture}) \quad = \quad (P_{i=1} \quad P_2 \quad P_3 \quad \cdots \quad P_{n_I} \quad P_{n_I+1})$$

m

Roller capture by the driving sprocket

$$P(\zeta = \zeta_{capture} + d\zeta) \quad = \quad (P_{i=1} \quad P_2 \quad P_3 \quad \cdots \quad P_{n_I} \quad P_{n_I+1})$$

$$P(\zeta = \alpha_I) \quad = \quad (P_{i=1} \quad P_2 \quad P_3 \quad \cdots \quad P_{n_I} \quad P_{n_I+1}) \qquad m = nb_{pos}$$

$$P(k) = [P_1 \quad \cdots \quad P_1 \quad P_1 \quad \cdots \quad P_1 \quad P_2 \quad \cdots \quad P_2 \quad P_2 \quad \cdots \quad P_2 \quad \cdots$$
$$P_3 \quad \cdots \quad P_3 \quad P_{n_I} \quad \cdots \quad P_{n_I} \quad P_{n_I+1} \quad \cdots \quad P_{n_I+1} \quad P_{n_I+1} \quad \cdots \quad P_{n_I+1}]$$
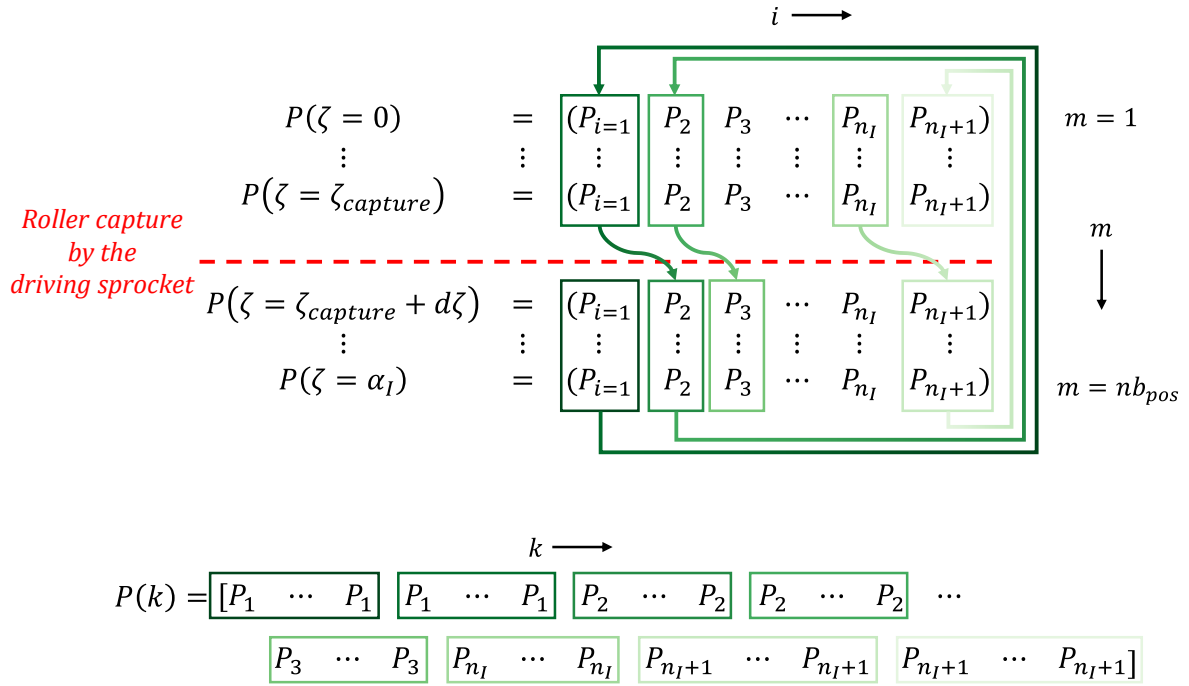
Figure II-34: Rearrangement of a variable "per position" to its evolution "per component"

An analogue procedure is applied to rearrange the values of all roller locations ($\gamma, s_c, s_r, \kappa, \nu$) and loads ($T, P$) from "per position" into "per component".

The differences between "per position" and "per component" representation can be appreciated in Figure II-35. "Per position" curves are given for 4 distinct sub-positions (indexes m and correcponding ζ are given in the figure). Calculations were carried out with $\psi_{t,I}|_{init} = 0$. The ζ pitch is non-even. More details are given in Appendix I. The evolution of force P will be commended later in Chapter IV.

31/31 double pitch (ASA) ; p=25.4mm ; slack=4% ; C_I=10N.m
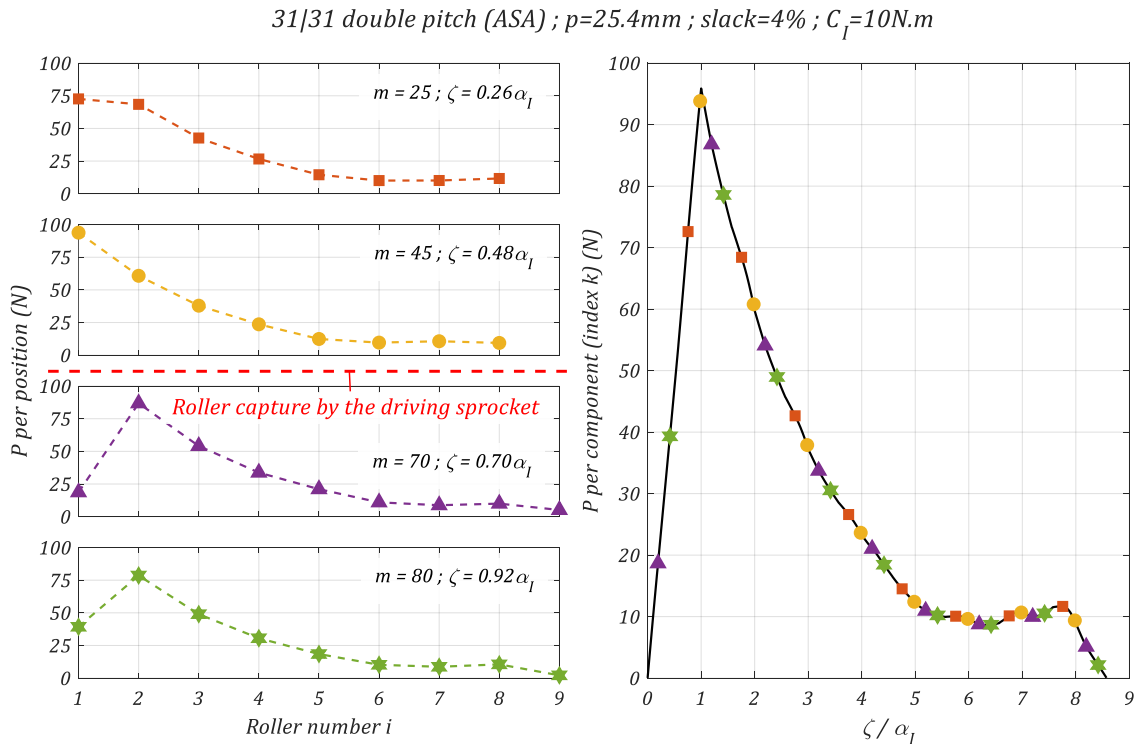
Figure II-35: Evolution of the contact force P, "per position" and "per component"

The curves "per position" constitute a capture of the spatial force distribution at a given driven sub-position. Therefore, each curve gives crossing points without the evolution of *e.g.*, force P between them. The real evolution of the force can only be appreciated by combining the information included in all the "per position" curves. Doing so allows for example appreciating the maximum reached after the initial increase at $\zeta/\alpha_I = 1$. It can be noted that the number of rollers in contact with the sprocket considered is not constant for all drive positions (varies from 8 to 9). This is due to the phase shift between the roller capture and release by the sprocket.

The resolution procedure for the whole chain drive model has been detailed. It depends on the external loading conditions being given as torque C_j or tight strand tension T_t. In both cases, the global kinematics is solved first to obtain the slack strand tension for both sprockets. Then, based on these slack tensions and the loading conditions, the location of the first roller $s_{c,1}$ is determined *via* numerical search. Due to the complexity of the relation between $s_{c,1}$ and tension ratio, it is possible for several roller locations to match the imposed conditions. In such cases, the smaller $s_{c,1}$ solution is preferred to favour continuity coming from the stable drive operation zone. The conversion of the results from the "per position" to the "per component" arrangement is then presented.

II.4 Conclusion

In this chapter, the Quasi-Static Chain Drive Model (QSCDM) was introduced. This 2D model studies a chain drive considering the connections between strands and sprockets, each represented by specific sub-model. Calculations can be carried out using different tooth profile geometries.

The global kinematics of the drive (*i.e.*, strand trajectories, number of links in each sub-model) is assumed to be independent from the external loading conditions and sprocket tooth profile. It is determined using the sub-models presented for the tight and slack strand using an original numerical procedure. The strand trajectories obtained give angles $\alpha_{s,t,j}$ and slack strand tensions $T_{s,j}$, used later in the local sprocket sub-model.

The local sub-model used for the sprockets was detailed. It is used to calculate the loads (*i.e.*, link tension and roller/profile contact force) and roller locations along their corresponding tooth profile simultaneously, as both are intertwined. The direct relation between roller locations and loading conditions was presented. The compatibility issues at the interfaces between strands and local sprocket sub-models were addressed.

The general solving procedure for the whole QSCDM was then introduced. The global kinematics was solved first before its results were used in the local sprocket sub-model. The external loading conditions can be prescribed *via* a torque applied on either sprockets or *via* the tight strand tension. This sequential approach facilitates the solution of each sub-model but introduces compatibility issues. Cases where several roller locations $s_{c,1}$ are suitable were treated.

Chapter III

Quasi-Static Chain Drive Model: elements of validation

The Quasi-Static Chain Drive Model (QSCDM) has been introduced. It is now compared to both numerical and experimental results from the literature to test its aptitude to correctly predict chain drive behaviour. Validation in carried out in different steps. Sub-parts of the model are considered separately before analysing the predictions of the entire QSCDM.

The global kinematics is first considered alone. The tight strand numerical solution is validated using the analytical solution proposed by Fuglede & Thomsen [1]. The slack strand model predictions are analysed and compared to known analytical results for hanging cables [89].

The sprocket sub-model is then considered in two steps. First, roller location and link angle calculation are studied without considering the loads involved. Roller location characteristic curves (see Chapter II, §II.2.1) are compared to those presented by Kim & Johnson in [52]. Then, consecutive roller locations and resulting link angles (articulation angle α^* and pressure angle ϕ) are compared to the numerical results of Naji & Marshek [64] and the graphical[1] results of Binder [32].

In the second step, the local sprocket sub-model is studied, without the connection to the global kinematics to match the literature case studies. Link tension and roller location "per position" are compared to the experimental results of Stephenson *et al.* [72] and the numerical model of Lodge & Burgess [70]. Then, link tension and roller location "per component" are compared with the numerical results presented by Kim & Johnson in [52].

Finally, the whole QSCDM (*i.e.*, global kinematic, roller location and loads calculation "per component") is compared to the numerical results of Troedsson & Vedmar [67].

---

[1] Obtained measuring link angles on large size sketches.

III.1 Global drive kinematics

III.1.1 Tight strand

The tight strand sub-model is compared to the analytical results presented by Fuglede & Thomsen [1]. The same validation was also presented by the author in [81].

In [1], Fuglede & Thomsen presented an analytical analysis of a tight chain strand (see §I.2.2). They proposed an analytical solution for the relation between the rotation of the driving and driven sprockets (*i.e.*, relation between $\psi_{t,I}$ and $\psi_{t,II}$). Expressions for the associated rotational speed ($\dot{\psi}_{t,j}$) and acceleration ($\ddot{\psi}_{t,j}$) were also given. As with the model presented in this manuscript, Fuglede & Thomsen assumed an equal pitch for the chain and the sprockets and no clearance between the roller and tooth profile (*i.e.*, $R_{roller} = R_{tb}$, see Figure II-18).

In [1], the drives considered are such that the tight strand common tangent is horizontal (*i.e.*, $\beta + \tau = 0$, see (see Figure II-3). The drive centre distance (*i.e.*, distance L) is characterised by the parameters N and f as prescribed by eq.(III-1) (see §I.2.2, eq (I-4)).

$$L \cos(\beta) = (N + 1 + f)p \qquad \textbf{\textit{(III-1)}}$$

with:
- $N \in \mathbb{N}$, the minimal number of links in the tight strand
- $f \in [0,1[$

Three drive configurations are studied (see Table III-1), each for three values of f, resulting in a total of nine cases. For each configuration, the numerical procedure presented in §II.1.3 for the calculation of the global kinematics is used.

$Z_I|Z_{II}$	N
6	9	4
12	18	11
21	63	34

Table III-1 : Drive configurations compared with results from Fuglede & Thomsen [1]

Figure III-1 shows comparison with the results from Fuglede & Vedmar. The evolution of the driven sprocket rotation $\psi_{t,II}$, the rotational speeds ratio $\dot{\psi}_{t,II}/\dot{\psi}_{t,I}$ and the driven sprocket acceleration $\ddot{\psi}_{t,II}$ are shown. In the article, Fuglede & Thomsen presented curves. Sample points have been digitised for comparison. In Figure III-1, solid lines are calculated using the tight strand sub-model presented in §II.1.1. Instantaneous derivatives are computed numerically from the displacements using a central difference. The initial chainring orientation $\psi_{t,I}\big|_{init}$ is set at the position of roller capture by the driving sprocket, calculated according to [1], allowing direct comparison with similar curve phasing. The driving sprocket rotational speed is set at 100rpm.
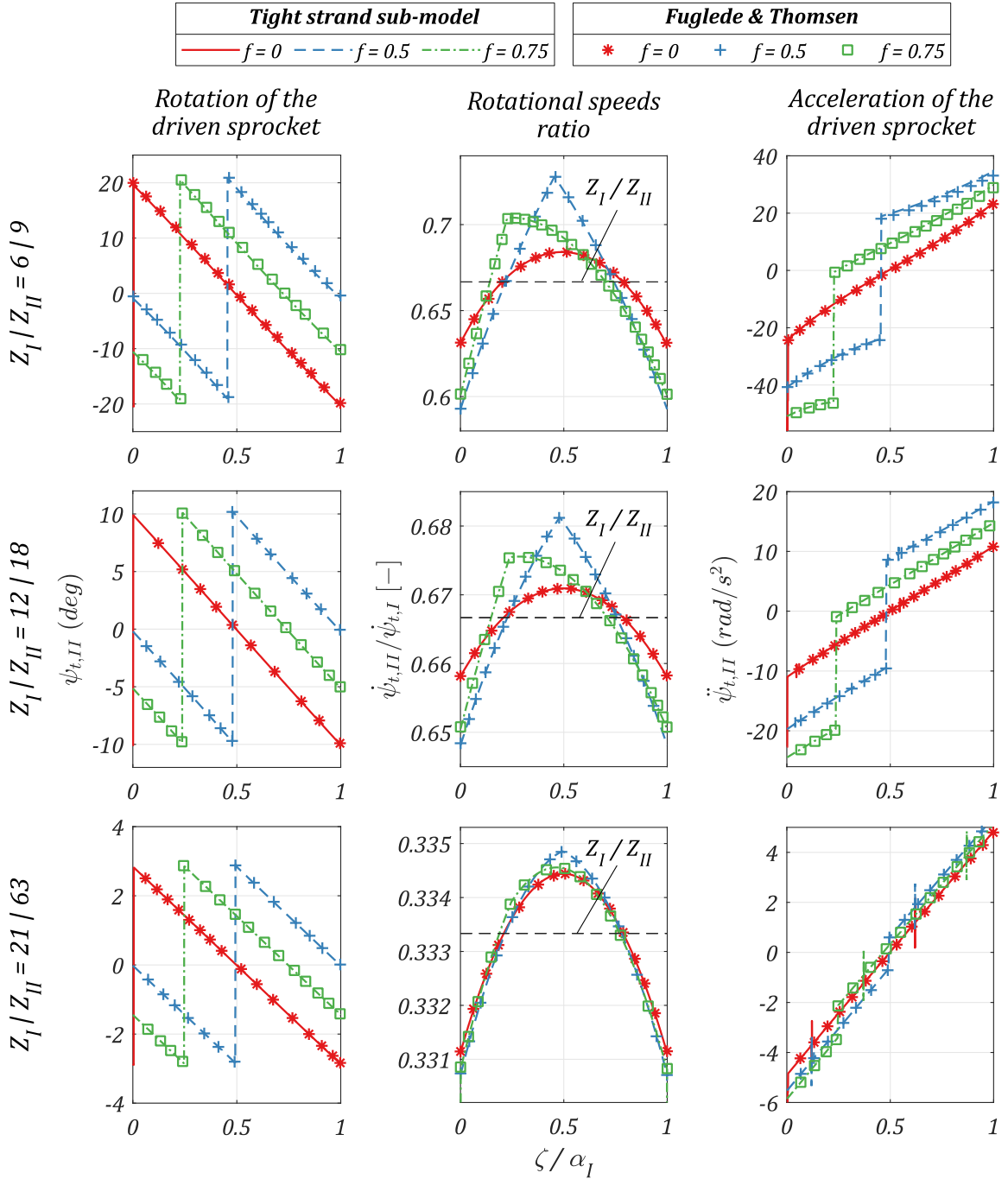
Figure III-1: Comparison of the tight strand kinematics with Fuglede & Thomsen [1]

Both models are in agreement for all the drive configurations tested. The positions of roller capture and release by the driving and driven sprocket, respectively, are particularly well predicted. These particular drive sub-positions are associated with discontinuities in $\psi_{t,II}$ and $\ddot{\psi}_{t,II}$ plots in Figure III-1 as the strand tips are considered to jump instantaneously. The $\psi_{t,II}$ curves show that the roller capture and release are simultaneous for $f = 0$ (*i.e.*, common tangent with a length equal to a whole number of pitches). For other values of f, both events do not occur in phase. They are in opposing phase for $f = 0.5$. The velocity ratio curves ($\dot{\psi}_{t,II}/\dot{\psi}_{t,I}$) highlight that the rotational velocity ratio varies during a meshing period and is therefore not exactly equal to the mean value $Z_I|Z_{II}$ (*i.e.*, transmission error). This variation is caused by the change in the tight strand orientation (see angle β_t §II.1.1) and is part of the polygonal effect (see §I.2.2). The highest deviation (compared to $Z_I|Z_{II}$) occurs for $f = 0.5$.

Higher numbers of teeth are associated with lower deviation of the velocity ratio and consequently lower discontinuities in rotation acceleration (see $\ddot{\psi}_{t,II}$ curves in Figure III-1). The results are consistent with the literature stating that polygonal effect and vibration issues are higher for small number of teeth [33], [44], [90]. Moreover, drives with a tight strand common tangent length equal to an odd number of a half pitch (*i.e.*, $f = 0.5$) have already been associated with higher kinematic perturbations [44], [48], [49], [90] (see §I.2.2).

The results of the numerical procedure used for tight strand calculation are consistent with the analytical results of Fuglede & Thomsen [1] for a wide range of tooth numbers. The tight strand predictions (*i.e.*, angles β_t, $\psi_{t,j}$ and n_t) are therefore validated. Compared to analytical approaches, the numerical modelling presented could be more easily adapted with different hypotheses (*e.g.*, elongated chain pitch, *etc.*).

III.1.2 Slack strand

The slack strand sub-model is compared to the known catenary results for hanging cables [89]. Then the prediction in terms of link orientation and tension are analysed.

The catenary (or chainette) result is an analytical solution known in the literature for hanging cables subjected only to gravitational field and with continuous mass distribution [89]. For such cases, the trajectory of the hanging cable is governed by the following generic equation (called catenary or chainette).

$$f(x) = r.\cosh\left(\frac{x}{r} + C_1\right) + C_2 \qquad \textit{(III-2)}$$

with:

- $r = T_h/gw$, the ratio between the horizontal tension (T_h) at the strand tips and the gravitational acceleration g multiplied by the linear density of the solid considered $w = m_{link}/p$ (with p the chain and pitch), respectively.
- $(C_1, C_2) \in \mathbb{R}^2$, two constants to be adjusted to make the general curve compatible with each particular case.

To fit eq.(III-2) to any particular case, parameter r is first calculated using the tension prediction of the slack strand model for T_h. The values of both constants (C_1 and C_2) are determined considering the conditions imposed on the trajectory at both extremities (the local origin O_{local} is set at the left strand tip, see Figure III-4).

$$f(0) = 0 \Leftrightarrow C_2 = -r.\cosh(C_1) \qquad \textit{(III-3)}$$

$$f(Dx) = D_y \Leftrightarrow r.\cosh\left(\frac{D_x}{r} + C_1\right) + C_2 = Dy \qquad \textit{(III-4)}$$

Combining eqs. (III-3) and (III-4) gives the following relation for C_1.

$$r.\cosh\left(\frac{D_x}{r} + C_1\right) - r.\cosh(C_1) - D_y = 0 \qquad \textit{(III-5)}$$

Eq. (III-5) is solved numerically to obtain the catenary curve adapted to the prescribed mass (w), tension (T_h) and geometrical conditions D_x and D_y (Definition of D_x and D_y are recalled in Figure III-4). Differences between the slack strand model presented (with discreet mass distribution) and the corresponding catenary are shown in Figure III-2. As the results are independent of the scale of the

chain, they are given relatively to the chain pitch p (scaled variables are given with a bar, e.g., $\bar{X} = X/p$). The link mass and roller diameter are given for a standard track cycling chain[2].

$$\bar{m}_{link} = 0.28g/m \; ; \bar{D}_{roller} = 0.61$$

(a)   *(b)*
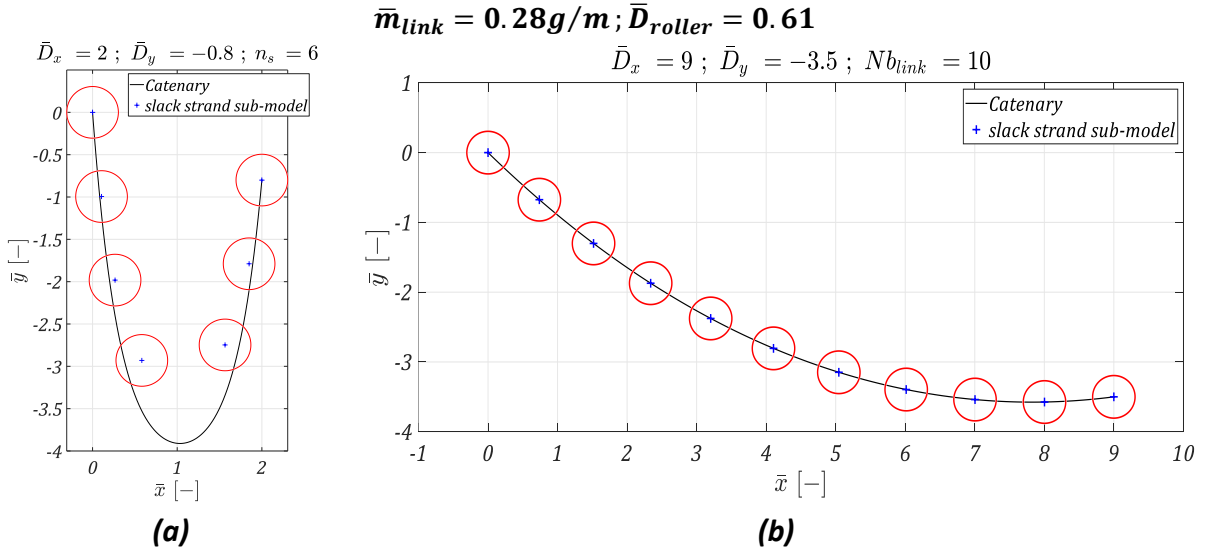
Figure III-2: Comparisons between the slack strand sub-model and the catenary curve (a) $\bar{D}_x = 2$, $\bar{D}_y = -0.8$, $n_s = 6$ (b) $\bar{D}_x = 9$, $\bar{D}_y = -3.5$, $n_s = 10$

Both models show the same trend. The trajectories obtained exhibit a bell shape tending toward a straight line as the distance between the tips increases. Comparisons with the catenary curve show notable differences for small x spans. In Figure III-2.a, the small number of links in the strand results in sharp changes in link orientation, causing considerable deviation from the smooth catenary curve. For values of $\bar{D}_x$ and $\bar{D}_y$ more compatible with a real chain strand (Figure III-2.b), the difference becomes negligible. The discreet approach used in the model presented §II.1.2 therefore shows greater interest for strands with a high number of links (longer chain) and small spans.

The prediction of the model in terms of link tension is now analysed. Figure III-3 shows the evolution of the tension in the first link of the strand for various values of $\bar{D}_x$. Tensions are scaled by the chain pitch. Examples of the strand trajectories obtained are inserted in the figure. $\bar{D}_y$ is set at zero and the number of links is constant and set to 6. The ratios for mass and roller diameter are again taken from the standard track cycling chain.

---

[2] $p = 12.7mm \; ; m_{link} = 3.6g \; ; D_{roller} = 7.75mm$
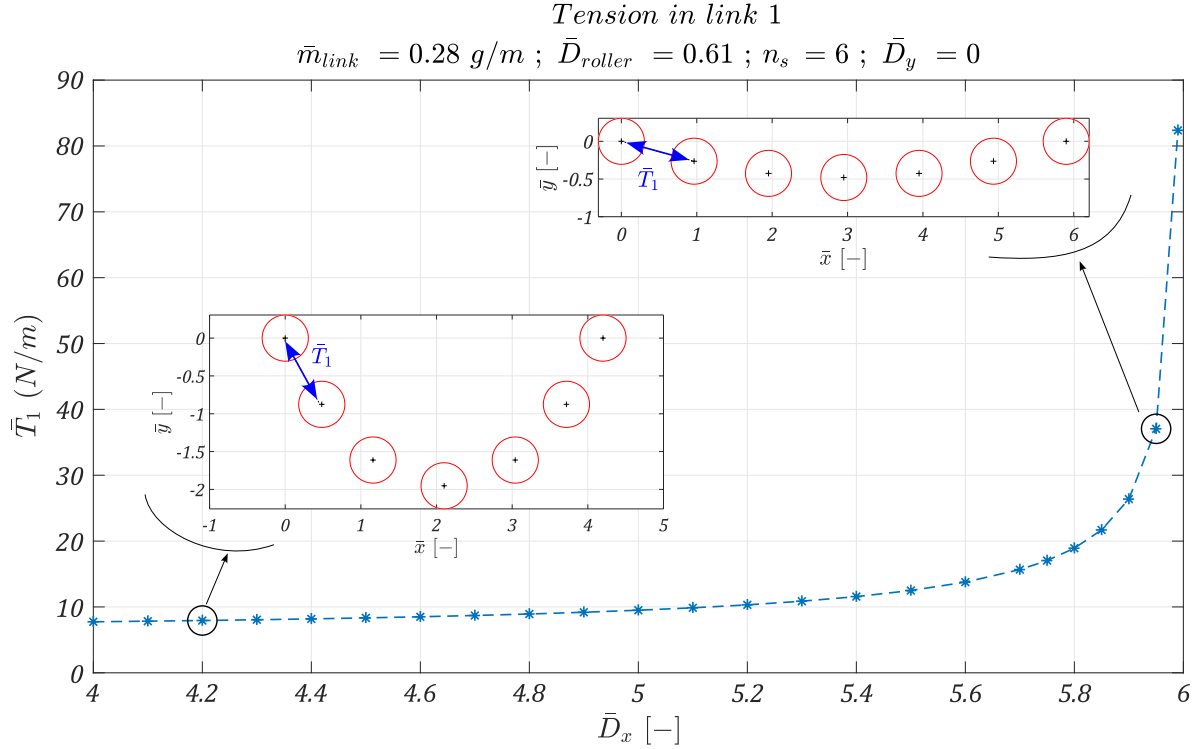
Figure III-3: Tension (scaled by chain pitch) in the first strand link in strand trajectories for various $\overline{D}_x$ values

As the number of links in contact is constant, increasing the x span $\overline{D}_x$ stretches the chain strand. Therefore, tension $\overline{T}_1$ increases with $\overline{D}_x$. The rise is firstly moderate and then goes asymptotically to infinity as the distance between the strand tips tends to $n_s \cdot p$ (*i.e.*, $\overline{D}_x$ tends to n_s). This quick increase for very stretched strands might have consequences on the drive behaviour as a small change in strand span results in a significant change in tension. The loading conditions could therefore drastically change within a given angular period α_I. Nevertheless, the increase is expected as the tension in the tip links must compensate the purely vertical strand weight. The magnitude must then increase as the force directions tend toward the horizontal for an increasingly stretched strand.

The slack strand model is now applied to a chain drive. The tooth numbers are $Z_I | Z_{II} = 31 | 31$ (*i.e.*, 31 teeth for both the driving and driven sprocket) meshed with double pitch chain ($p = 25.4mm$). The link mass is set at $12.7g$ (from the No 2040 chain in [11]). The strand trajectory is studied for a particular drive sub-position where a theoretical straight slack strand would be horizontal[3] (i.e., $D_y = 0$). Different strand loosenesses are tested (see §II.1.2 for the looseness measurement). It must be noted that the looseness cannot reach 0% as the value given is a mean value for one drive period (computed from 10 linearly spaced values of ζ within a drive period α_I). For that number to exist, the strand must be defined for each drive position (i.e., fulfilling eq.(II-13)), therefore forcing the mean value to be strictly positive.

The slack strand model prediction in terms of link orientation λ_i is presented in Figure III-4. The link numbers are given in the local numbering system as specified in the figure.

---

[3] $\zeta \approx 0.88\alpha_I$ with $\psi_{t,I}\big|_{init} = 0$
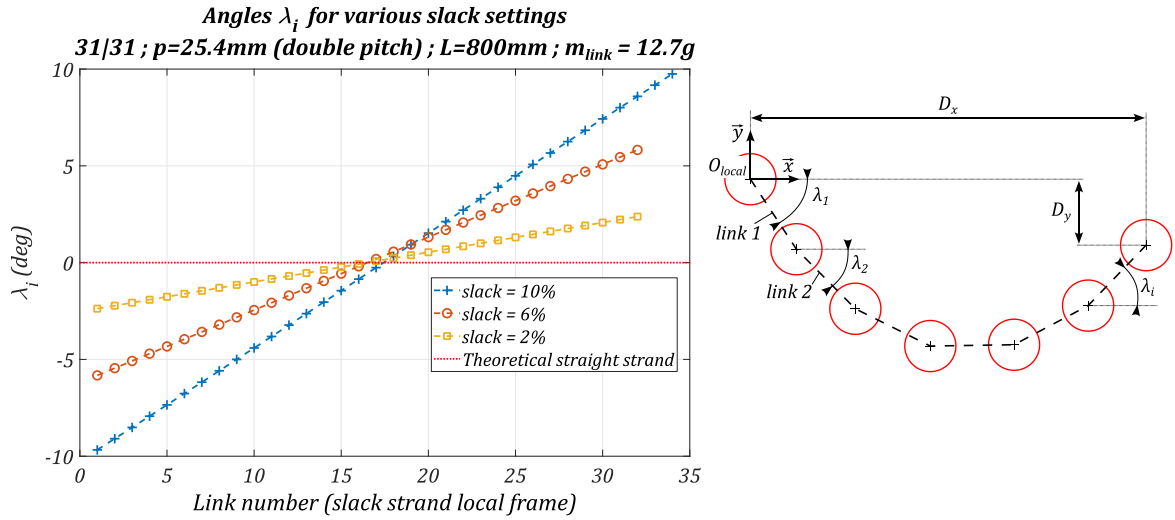
Figure III-4: Angles λ_i for various slack settings

As the strand is stretched, the number of links n_s decreases (two links are added for $slack = 10\%$ compared to the 6 and 2% cases, see Figure III-4). It can also be observed that the magnitudes of link orientations λ_i decrease with the slack value tending to zero for a straight strand. Angles λ_i are symmetric with respect to the middle of the strand, with negative values at the strand beginning and positive ones for the second half. This is consistent with the bell shape trajectory applied to particular cases where $D_y = 0$ (the angles would not be symmetric for $D_y \neq 0$).

It was demonstrated that the slack strand model presented shows consistent behaviour. The trajectories obtained are similar to the known results of catenary curves, especially for high strand spans as in chain drives. The link tension increases as expected as the strand is stretched. When used on a chain drive, the slack strand model still exhibits consistent results as the predicted link orientation decreases with the slack setting.

III.2 Local sprocket sub-model: relation between roller locations

The specific sub-models used for the tight and slack strand for the global kinematics calculation have been analysed. This part compares the sprocket sub-model predictions in terms of roller location and link angle. Connections between roller location and loads are presented in the following section.

III.2.1 Roller location characteristic curves

As mentioned in Chapter I, Kim & Johnson [52] introduced the notion of the roller location characteristic curve. This curve represents the location of a given roller as a function of the location of the previous one (*i.e.*, γ_{i+1} as a function of γ_i).

Figure III-6.a shows roller location characteristic curves calculated by Kim & Johnson in [52]. Figure III-6.b shows the same curves using the QSCDM. The curves are plotted for ASA profiles with $Z = 12$, 24 and 36. The sprocket pitch is $p = 1/2'' = 12.7mm$ and the roller diameter is $D_{roller} = 8.51mm$. The resulting dimensions for the ASA profile are calculated according to the standard given in [32], [52], [64] (see Appendix A).

Kim & Johnson's curves are given for coordinates ξ. It is equivalent to γ but ranges between $[-4,4]$ instead of $[0,8]$ for the ASA profile (Figure III-5).

Figure III-5: Roller location coordinate for ASA profile according to (a) Kim & Johnson [52] (b) this model
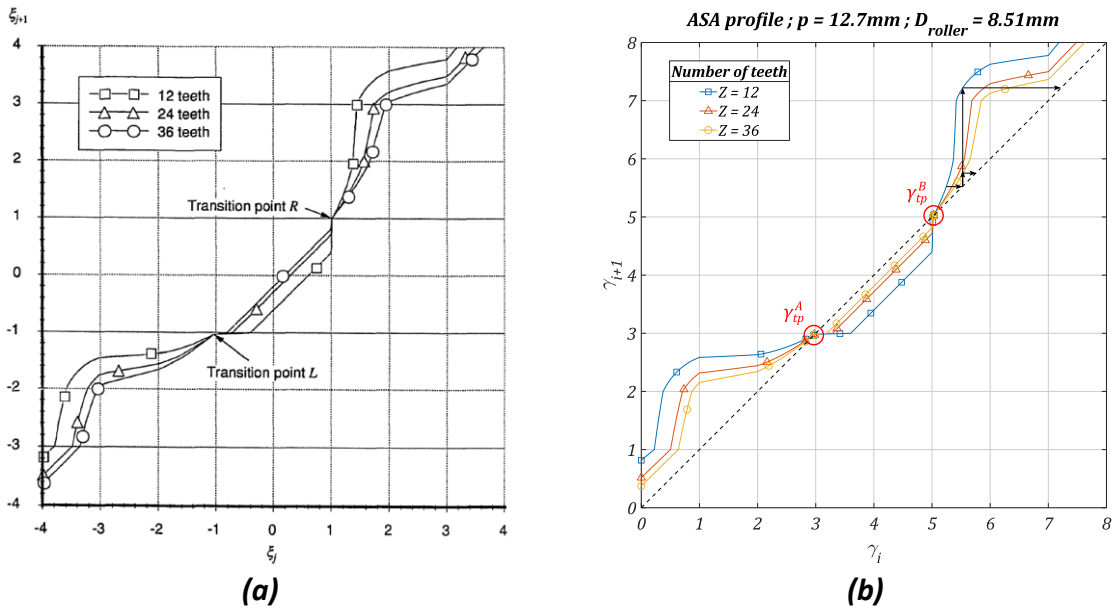
Figure III-6: Adjacent roller location characteristic curve according to (a) Kim & Johnson [52] (b) QSCDM

Figure III-6 shows that the curves obtained are identical for all numbers of teeth tested, therefore validating the procedure presented.

All the curves are symmetric with respect to the line $y = -x$ consistently with the profile being symmetric. Their shape is modified with the number of teeth Z. The smaller the number of teeth, the greater the deviation from the first bisector. Consequently, it takes fewer rollers to cross the zone between the transition points ($\gamma \in \left[\gamma_{tp}^A, \gamma_{tp}^B \right]$) for small Z. Similarly, starting from the same γ beyond the transition points (*i.e.*, $\gamma > \gamma_{tp}^B$), it takes fewer rollers for a small number of teeth before skipping a tooth. However, one cannot directly conclude that sprockets with small number of teeth will result in easier chain drop. Indeed, the link angles (*e.g.*, α^* and ϕ) and therefore the implications in terms of load calculation are different depending on Z (see Chapter IV below).

III.2.2 Consecutive roller location and link angles

Roller locations are related to the link angles ϕ (called pressure angle), α^* (articulation angle), κ and ν (see §II.2). Calculation of link angles are compared to the studies presented by Binder [32] and Naji & Marshek [64]. No chain strand nor load is considered as the studies focused only on consecutive roller locations imposed by the geometry of the sprocket (*i.e.*, the 2D tooth profile) and the chain pitch. As no load is applied, the location of one roller must be prescribed (see below).

In 1956, Binder proposed a purely graphical study of consecutive roller locations. Using large size sketches of sprockets, he measured the articulation and pressure angles (α^* and ϕ, respectively), stating that the centre of two consecutive rollers should be a chain pitch p apart. In [64], Naji & Marshek proposed a numerical procedure to automate the work of Binder (see Chapter I). This provides better precision and repeatability. Similarly, angles ϕ and α^* were calculated. In both studies, the clearance between the roller and tooth bottom was neglected (*i.e.*, $R_{roller} = R_{tb}$). This assumption leads to a slight shift of the roller centre trajectory compared to the procedure presented as the distance to the tooth profile is R_{tb} instead of R_{roller} (see Figure III-7, see Figure I-21). Consequently, for rollers in contact with the tooth bottom curve (*i.e.*, seating curve in [64]), the pressure angle ϕ could not be calculated/measured from the geometry. Moreover, all the cases where the contact point with the tooth profile lies at the seating curve (*i.e.*, $\gamma \in [3,5]$ for ASA profiles, see Figure III-7) are combined in one roller location condition called "seated roller" (see Chapter I).
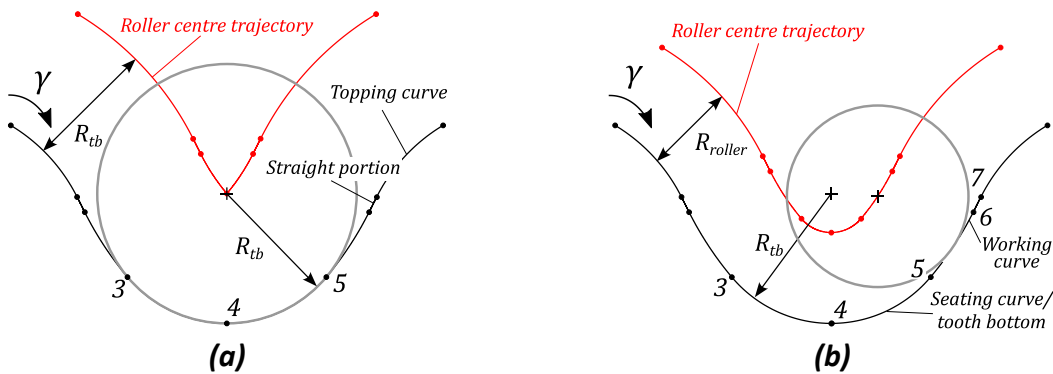
Figure III-7: Roller location according to (a) Naji & Marshek and Binder's assumptions (b) the model presented (the clearance between roller and profile are exaggerated)

For all the cases presented, the ASA profile is still used but with a sprocket pitch $p = 1'' = 25.4mm$ and roller diameter $D_{roller} = 15.88mm$. Various numbers of teeth are tested with variations of the chain pitch to simulate wear. For all the sprockets considered, the number of rollers in contact is assumed to be $(Z/2) + 1$ (only even numbers of teeth Z are tested). The numbering used is given in Figure III-8. Angles α_1^*, ϕ_1 and $\alpha_{(Z/2)+1}^*$ cannot be calculated as the chain strands are not considered. The location of the last roller (roller $(Z/2) + 1$) is assumed and the resulting locations of the other ones are calculated.
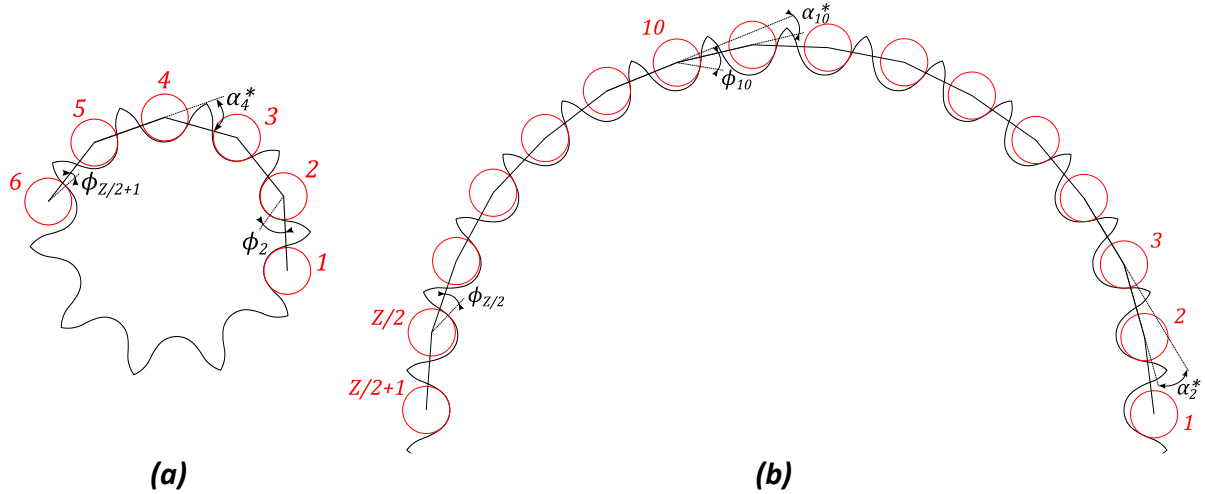
Figure III-8: Roller location according to the QSCDM (a) $Z = 10$ no elongation (b) $Z = 30$ 3% pin-links elongation

The first case is for a sprocket of $Z = 10$ teeth with the chain pitch equal to the sprocket one. According to [32] and [64], the last roller in contact (*i.e.*, roller $(10/2) + 1 = 6$) is set at the highest point of the working curve, corresponding to $\gamma = 6$ (see Figure III-7.b). The comparisons are shown in Figure III-9.
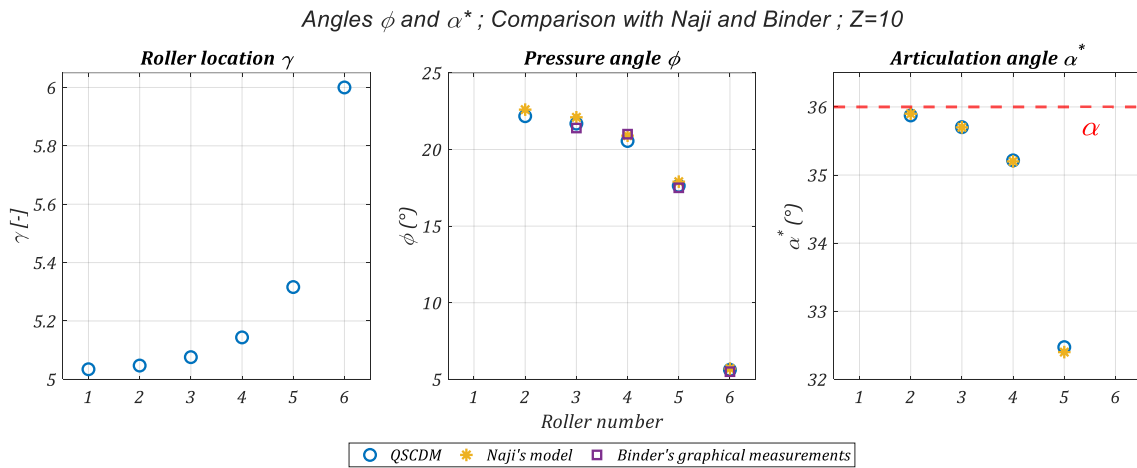
Figure III-9: Comparison of pressure angle ϕ and articulation angle α^* with Naji & Marshek [64] and Binder [32] ; $Z = 10$, no link elongation

The location for the initial roller (*i.e.*, roller 1) resulting in roller 6 lying at $\gamma = 6$ is close, but still greater than the transition point ($\gamma_1 \approx 5.03$, $\gamma_{tp}^B \approx 5.024$ for the profile considered). The evolution of roller location exhibits an exponential aspect as the first rollers almost lie at the same contact point before a fast increase in γ occurs for the last ones (particularly for rollers 5 and 6). For the pressure and articulation angles, the evolution obtained shows the same trend and values comparable with the results of Naji & Marshek and Binder. The pressure angles ϕ decrease as the rollers climb the tooth flank starting from $\phi_1 \approx 22°$ to $\phi_6 \approx 6°$. Similarly, the articulation angles obtained also decrease while staying relatively close to the value obtained with all the rollers seated $\alpha = 36°$ (corresponding to the pitch angle for $Z = 10$). The smaller value is $\alpha_5^* = 32.4°$. All the values of α^* are smaller than α. Overall, the results obtained do not exactly match these of Naji & Marshek and Binder. The differences are certainly related to the method used (Binder's results were obtained from purely graphical means) and the assumption stated (no clearance between the roller and the tooth bottom).

For the second test, the influence of chain pitch variation was tested (the results are shown in Figure III-10).

To simulate wear, the pin link lengths are assumed to be elongated by 3% (the length of the bush links remains equal to the sprocket pitch). Four numbers of teeth are tested ($Z = 10, 20, 30$ and 60). For all cases, Binder and Naji & Marshek assumed that roller $(Z/2) + 1$ is "seated" (*i.e.*, in contact with the seating or tooth bottom curve). In the model presented, this corresponds to all $\gamma \in [3,5]$. For the sake of comparison, it was considered that roller $(Z/2) + 1$ lies at $\gamma = 5$ for all cases. Pin and bush links alternate, and the last link (*i.e.*, link $(Z/2)$ between roller $(Z/2)$ and $(Z/2) + 1$) is a pin link.

The images of the roller locations obtained for the two case studies are presented in Figure III-8.

Similarly to the preceding case, the values obtained are not equal but have similar trends, compared to Naji & Marshek and Binder's results. The deviations are still probably caused by the different assumptions. The alternation between elongated and non-elongated links results in the rollers arranging themselves along two distinct curves reaching an asymptote when a sufficient number of rollers are in contact. For $Z = 60$, these asymptotes are around $\gamma \approx 6.5$ and $\gamma \approx 5.9$. The pressure angles are also arranged in two curves, both decreasing as the rollers move away from the transition point. For the link angle, two distinct values emerge above and below the pitch angle α. The distance between the values obtained and α can be relatively important (up to $\pm 5°$ with $\alpha = 6°$ for $Z = 60$).

The comparison between the cases with and without pin link elongation shows that the consecutive roller locations greatly depend on the chain pitch as a 3% variation is sufficient to greatly modify the link angles obtained. The consequence in terms of drive behaviour may also be considerable as the loads are computed based on these angles (see eq.(II-27)).

Based on the comparison presented with the results of Naji & Marshek [64] and Binder [32], the method used for the link angle calculations is considered validated.
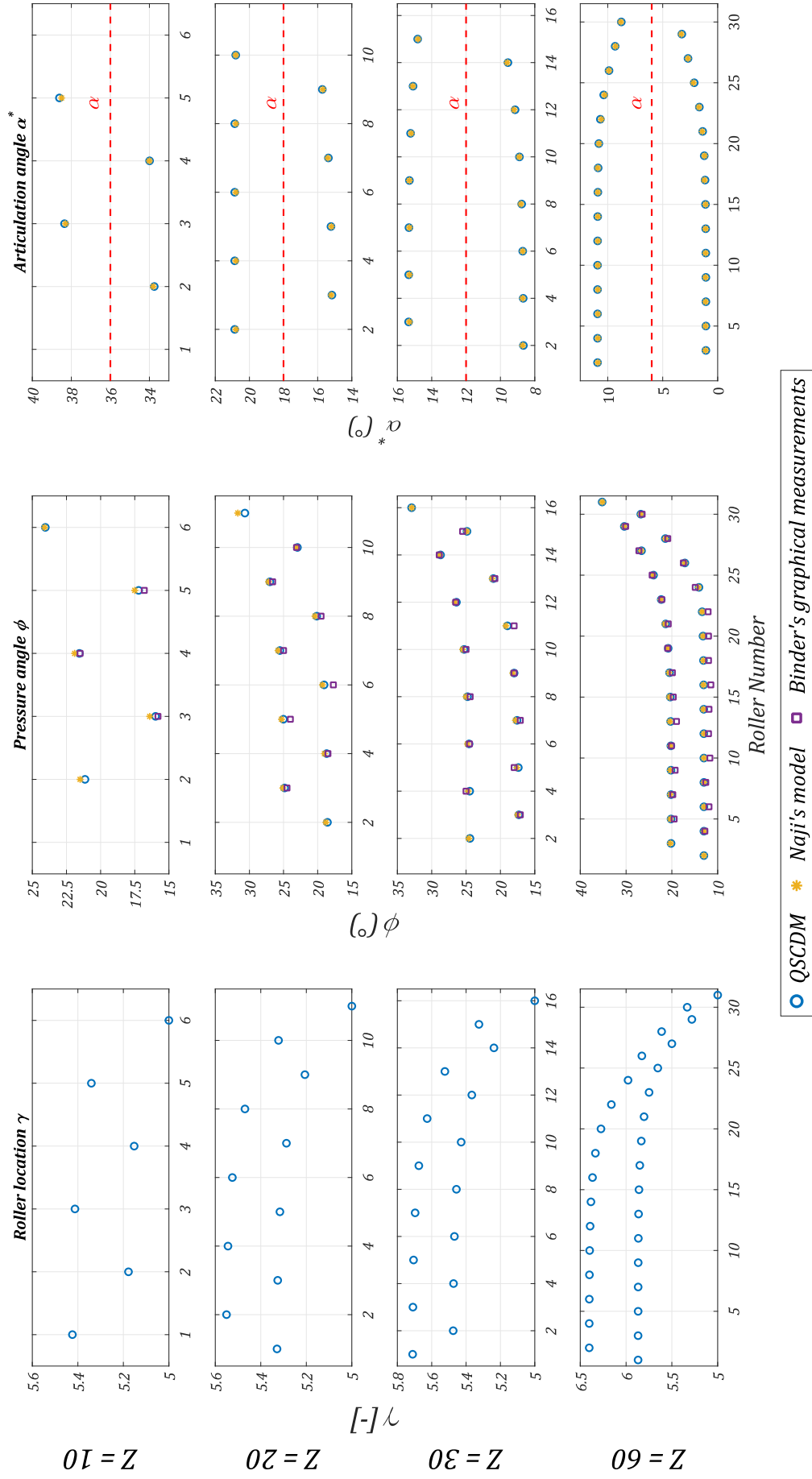
Figure III-10: Comparison of pressure and articulation angle with Naji & Marshek [64] and Binder [32] ; Z = 10, 20, 30, 60 ; 3% pin-link elongation

III.3 Local sprocket sub-model: connection between loads and roller location

In the previous part, the sprocket sub-model prediction in terms of adjacent roller location and resulting link angles was compared to the literature and proven to be reliable.

In this part, the relation between roller location and loads (link tension and contact forces see Chapter II) is explored. The local sprocket sub-model is still considered alone (without connection to the global drive kinematics) to match the conditions of the comparison cases. The local sprocket sub-model predictions "per position" are compared to the model of Lodge and Burgess [70] and the experimental data of Stephenson *et al.* [72]. Then, the results "per component" are compared to the model presented by Kim and Johnson [52].

III.3.1 Loads and roller location "per position"

The load predictions of the local sprocket sub-model (see §II.2.2) are first compared to the work of Stephenson *et al.* [72] and Lodge & Burgess [70]. Due to the specificity of the case studied here, the model results are presented "per position".

Stephenson *et al.* presented an original experimental apparatus allowing real time measurements of the tension force in a chain link. Lodge & Burgess presented an enlarged tension model based on the GPLD model originally introduced by Naji & Marshek [2] (see Chapter I). In the GPLD model, it is assumed that a roller can only have two positions: in contact with the tight side of the tooth profile or in contact with the slack side of the tooth profile (see Figure III-11, Chapter I). The switch between these two positions is assumed to be instantaneous. The principle of this model is detailed by the author in [81].
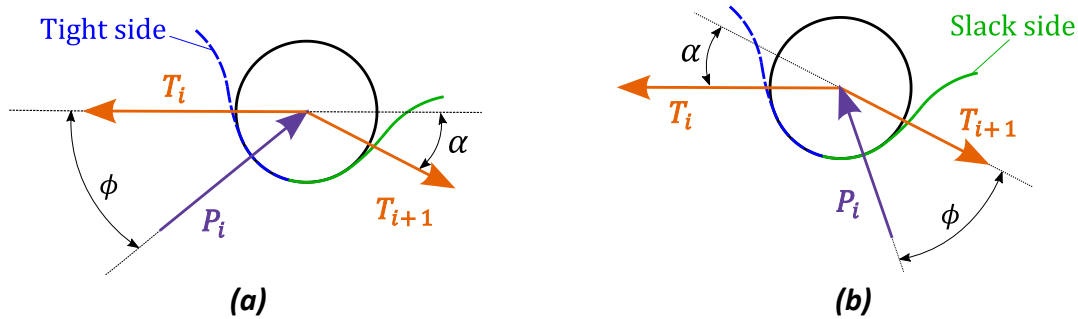
Figure III-11: Roller position in the GPLD model; roller in contact with the (a) tight (b) slack side of the tooth profile [2], [70], [81]

Lodge & Burgess studied the same drive as Stephenson *et al.* Validation is therefore carried out on both simultaneously. The numbers of teeth of the drive studied are $Z_I|Z_{II} = 18|36$. The chain and sprockets pitches are identical ($p = 3/8''$). Three loading conditions are explored as the driving sprocket undergoes a torque of $53N.m$, $33N.m$ or $23N.m$. Due to the specificities of the drive studied, tension mechanisms compelled both strand trajectories and slack strand tension. Therefore, the model presented for the global kinematics cannot be used.

To allow comparison, the model is modified as follows. As the global kinematics cannot be calculated, only one drive position is studied. Angles $\alpha_{t,j}$ and $\alpha_{s,j}$ are therefore constant and their value is assumed to be $\alpha_j/2$. The number of links in each part of the drive are set based on the paper of Stephenson *et al.* [72] (see Figure III-12). The slack strand tension is set at $T_s = 200N$ as prescribed in [72]. A friction correction angle $|\delta(\infty)| = 5°$ is considered (see Table III-2, other drive parameters are not needed). Neither the roller diameter nor the tooth profile are specified in either study [70], [72].

For these calculations, the roller diameter is set according to the American standard (see Table III-3) and the *ASA* tooth profile is used. As a consequence of the modifications applied, link meshing (*i.e.,* variation of angles $\alpha_{s,t,j}$, part of the polygonal effect) is not modelled.

$Z_I|Z_{II}$	L	ΔY	$slack$	$|\delta(\infty)|$
18|36	-	-	-	5°

Table III-2: Drive parameter for comparison with Lodge & Burgess [70] *and Stephenson et al.*

Pitch p	D_{roller}	m_{link}
$3/8'' = 9.525mm$	$5.08mm$	-

Table III-3: Chain parameters [11] *for comparison with Lodge & Burgess* [70] *and Stephenson et al.*

For each loading condition, the tight strand tension T_t is calculated based on the slack one and the torque applied on the driving sprocket using eq.(II-32). The link tension obtained for the drive position studied is then calculated using the local sprocket tension model (see §II.2). The comparison of the results obtained with the experimental data of Stephenson *et al.* and the model of Lodge & Burgess are presented in Figure III-13. The x-coordinate is given as specified in Stephenson's paper [72]. The instrumented link is in contact with the driving sprocket between position 94 and 104. It is then part of the slack strand until position 35 (a full drive rotation is completed at position 108). It contacts the driven sprocket until position 57 and finally completes its rotation as part of the tight strand. The corresponding link and roller numbering is given in Figure III-12.
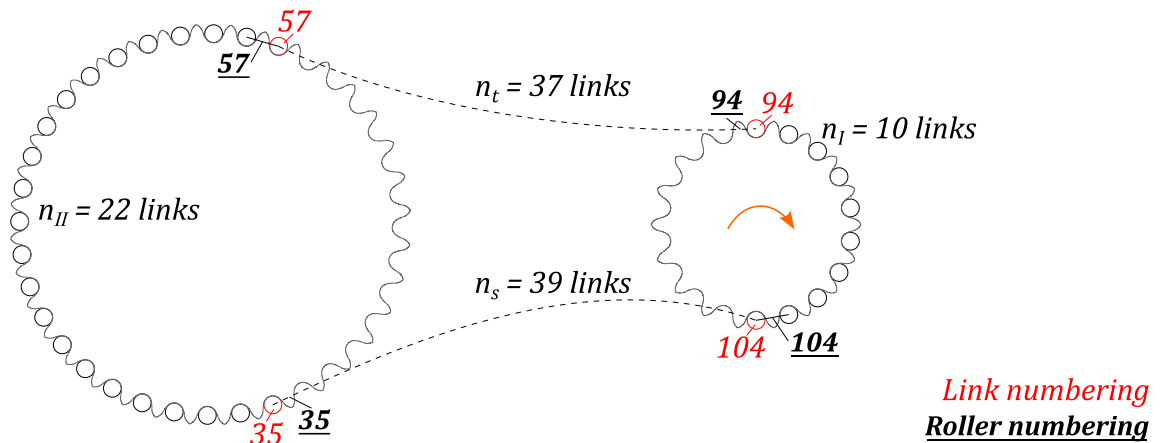
Figure III-12: Link position in the drive presented by Stephenson et al. [72]
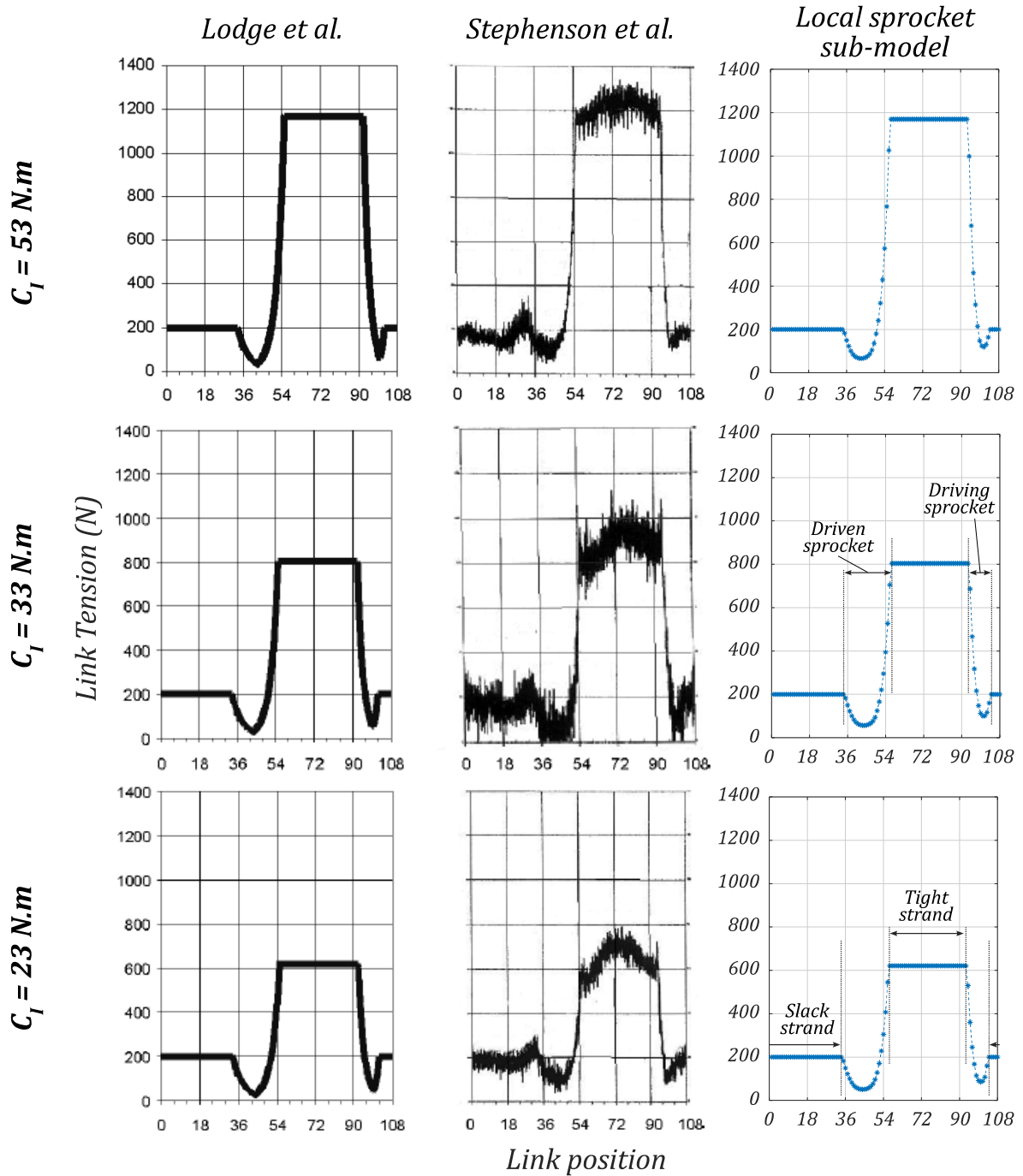
Figure III-13: Comparison of link tension with Lodge & Burgess [70] **and Stephenson et al.** [72] **for several torques**

Despite the noise in the experimental data, the local sprocket sub-model and the measurements agree regarding the general link tension evolution. The variation in the measured strand tensions is probably a consequence of the tensioning rail (not modelled here). For the sprocket sub-model, the sharp transition between sprockets and strands is probably caused by the absence of the link meshing (constant $\alpha_{s,t,j}$ and number of links $n_{s,t,j}$). The sprocket sub-model also agreed with the model of Lodge & Burgess. The main difference is observed for the links in contact with both sprockets. Lodge & Burgess's model predicted a sharp change at the link tension minima as the rollers are assumed to switch instantaneously from contacting the tight side to the slack side of the tooth profile. Conversely,

the model presented in this manuscript considers a gradual process. The link evolution obtained is less angular, resulting in better agreement with the experimental measurements.

The gradual transition of the roller from contacting the tight to the slack side of the tooth profile is represented in Figure III-14. It shows the locations of the rollers in contact with the driving and driven sprocket (still "per position"). The roller numbering is still according to Figure III-12. The GPLD model does not directly give any information on the roller locations. However, these are extrapolated from the tension curves presented in Figure III-13. It is considered that a roller in contact with the tight or slack side of the profile lies at the transition points (respectively γ_{tp}^B and γ_{tp}^A for the tight and slack side). The transition roller is that marking the border between decreasing and increasing tension and the side switch is instantaneous.
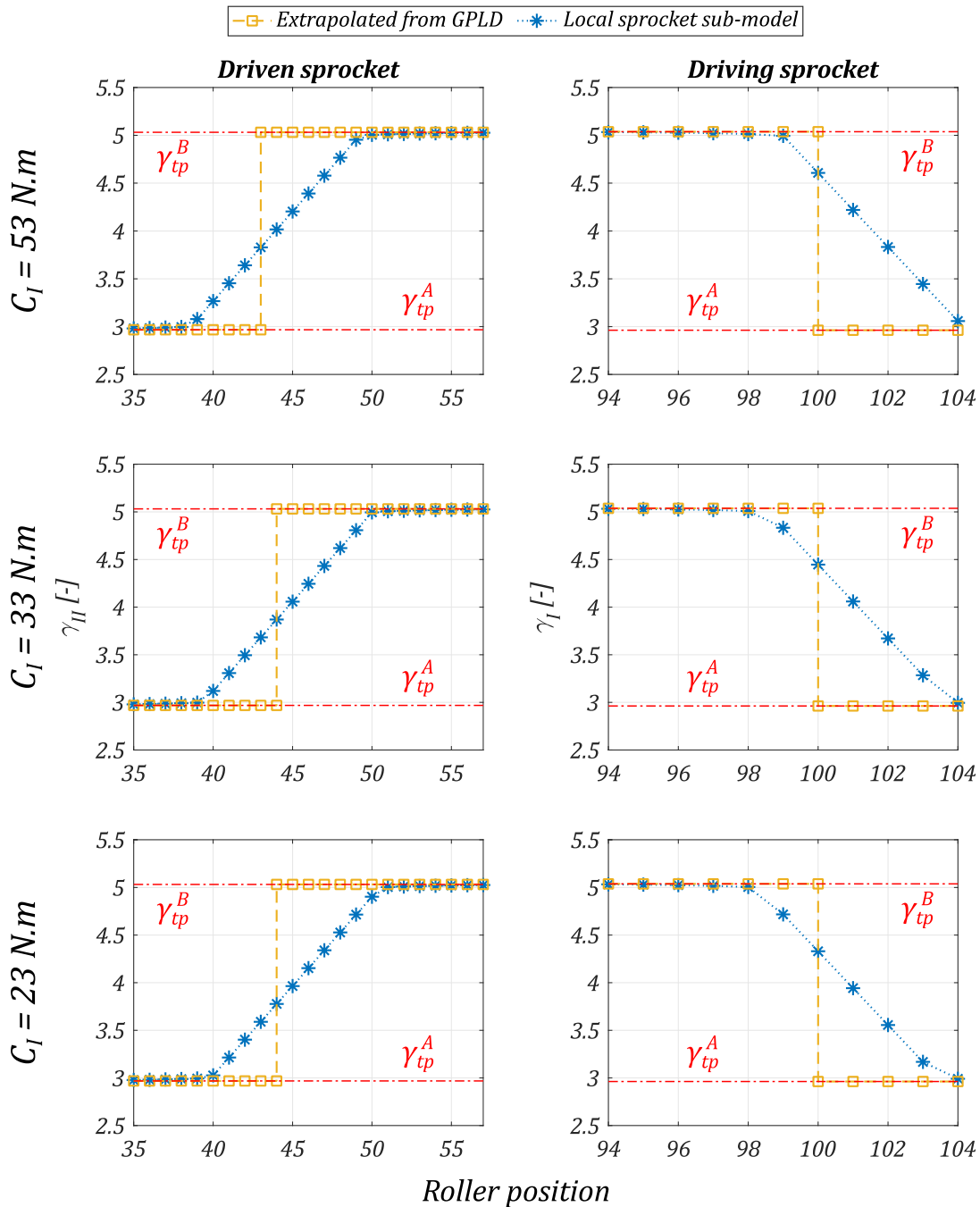
Figure III-14: Roller location for the driving and driven sprocket, comparison with extrapolated locations from the GPLD model

Predictions of both models have low dependences on the loading conditions tested. For the GPLD model, the transition roller on the driven sprocket is at position 43 for $C_I = 53N.m$ and 44 for the remaining conditions. It is always at position 100 for the driving one. For the model presented, the roller location changes slightly for the first roller to cross the profile but the curve shapes are almost the same. For the driven sprocket, the rollers tend to cross the entire profile, from one transition point to the other, while they barely reach the second transition point for the driving sprocket. The differences between driving and driven sprockets are due to the different numbers of rollers in contact and to the effect of friction (details on differences between driving and driven sprockets are given in Chapter IV). The comparisons with the roller locations extrapolated from the GPLD are consistent as the instantaneous switches between the profile sides occur within the gradual transitions predicted by the model presented for all the cases tested. It should be noted that the side switching dynamics, ignored in the GPLD approach, approximately involves half of the rollers in contact. These differences in the side switching dynamics are responsible for the divergence in link tension.

III.3.2   Loads and roller location "per component"

"Per component" predictions of the local sprocket sub-model are now compared to the work presented by Kim & Johnson [52].

Kim & Johnson [52] presented a sprocket model to calculate the evolution of link tension, contact force and roller location. No strand was considered and tensions T_t and T_s (tensions in the tight and slack strand, respectively) were assumed to be constant and known. The approach presented in this manuscript for the calculation of consecutive roller locations is similar to that proposed by Kim & Johnson (see §II.2). However, the tension model is different. In [52], Kim & Johnson distinguished pin and bush links and studied their equilibrium considering friction at all the chain articulation interfaces (*i.e.*, pin/bush, bush/roller and roller/profile) whereas in the QSCDM, the differences between pin and bush links are neglected and friction is considered only at the roller/profile interface.

The results presented by Kim & Johnson were for a 31 tooth double pitch sprocket meshed with the standard No 2040 chain ($p = 25.4mm$). The friction coefficient at the roller/profile interface was assumed to be 0.08 (corresponding to $|\delta(\infty)| \approx 4.57°$). The tension in a pin link as well as roller locations were calculated for various tension ratios (T_s/T_t). The sprocket wrapping angle (as introduced in [65]) was assumed to be 180° (*i.e.*, both strands are assumed to be parallel, see Figure III-15). Both driving and driven sprockets were studied to explore the influence of friction. In [52], Kim & Johnson carried out a comparison of their results with the experimental measurements of Naji & Marshek [62] (see §I.3) with good agreement. Therefore, this comparison with the results of Kim & Johnson indirectly applies to the experimental measurements of Naji & Marshek.

A 31|31 drive is studied to enable the comparison with the local sprocket sub-model. The slack strand is assumed to be straight using the method presented in [81] therefore forcing the wrapping angle of each sprocket to 180°. The two strand directions are then used to calculate angles $\alpha_{s,t,j}$. As both strands are parallel, the conditions in terms of number of links n_j and meshing angle $\alpha_{s,t,j}$ are identical for the driving and driven sprockets. The tension of both the slack and the tight strand is set to match the ratios tested. The chain parameters are set according to [11] for a No 2040 standard chain and $|\delta(\infty)|$ is chosen to match a friction coefficient of 0.08. The parameters used for this case study are summarised in Table III-4 (other drive parameters are not needed) and Table III-5.

(a)

(b)

Figure III-15: (a) general view of 31|31 double pitch drive (b) Driving sprocket at the positions of roller capture and release

$Z_I\|Z_{II}$	L	ΔY	$slack$	$\|\delta(\infty)\|$
31|31 (double pitch)	-	0	-	4.57°

Table III-4: Drive parameters for comparison with Kim & Johnson [52]

Pitch p	D_{roller}	m_{link}
$25.4mm$	$7.92mm$	-

Table III-5: Chain parameters for comparison with Kim & Johnson [52]

A comparison of both models for the link tension and roller location is presented in Figure III-16. Sub-figures (a-d.1) are from Kim & Johnson [52] while (a-d.2) are from the local sprocket sub-model. Five different tension ratios are explored ($T_s/T_t = 1$, 0.75, 0.5, 0.25 and 0.03). The results are given as a function of the sprocket rotation angles. The tracked link leaves the tight strand at $0°$ which also corresponds to the capture of the tracked roller (see Figure III-15.b). For the driven sprocket, curves are shown from the tight to the slack strand to match Kim & Johnson's representation.

Driving sprocket
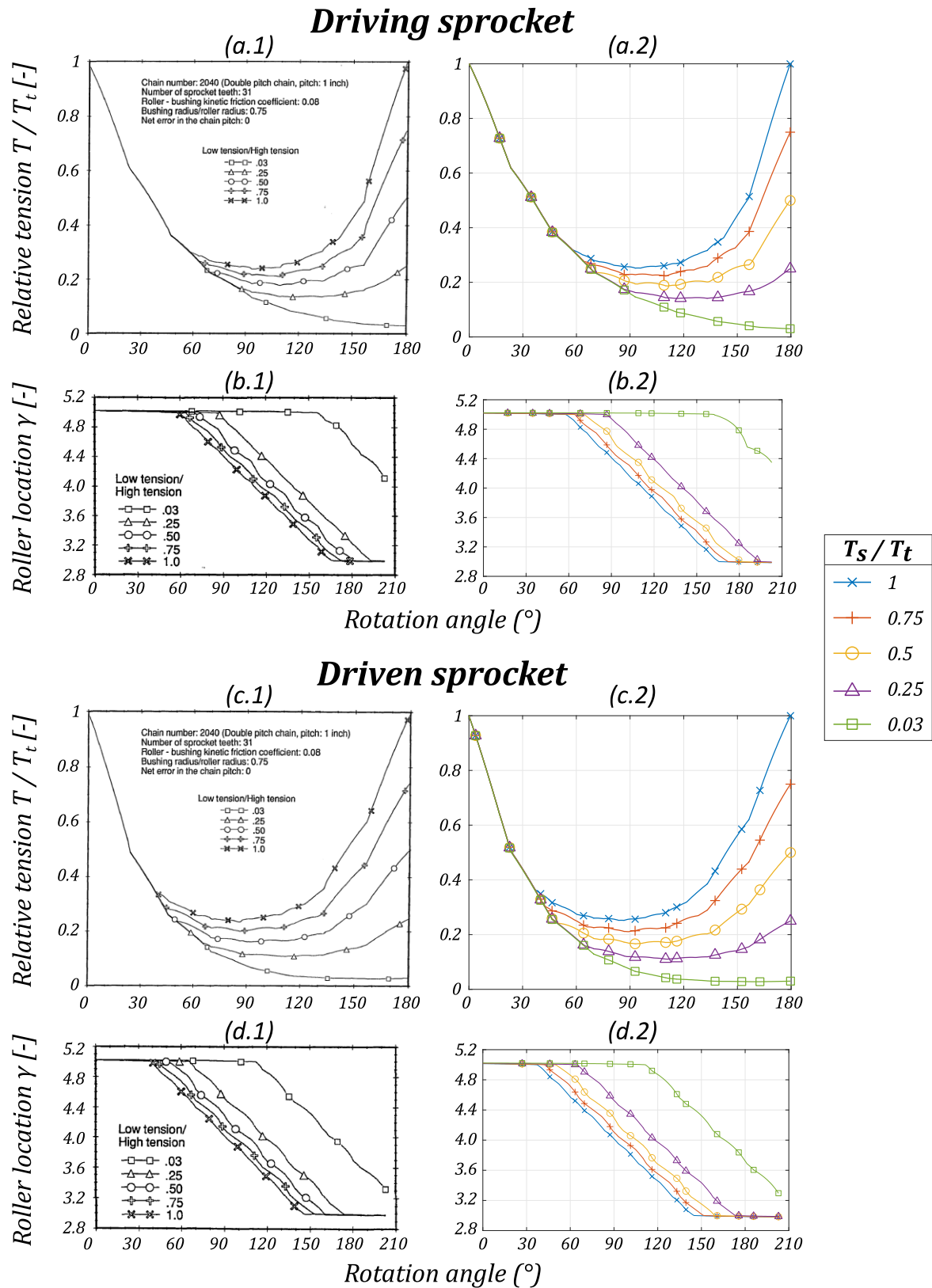
Driven sprocket

Figure III-16: Comparison with Kim & Johnson [52] **in link tension and roller location for driving and driven sprockets**

The roller location from Kim & Johnson was originally presented in terms of coordinate ξ. To compare them, they have been converted to γ using eq. (III-6) (see Figure III-5, only valid for ASA profiles).

$$\gamma = \xi + 4 \qquad\qquad\qquad \textbf{\textit{(III-6)}}$$

with:

- $\xi \in [-4,4]$, the roller location coordinate as presented by Kim & Johnson in [52]
- $\gamma \in [0,8]$, the roller location coordinate for the presented model.

The roller location curves show rotation angles greater than 180° as the tracked articulation remains in contact with the sprocket for another angular period (angle α_I) after the link has been released. The articulation therefore leaves the sprocket at a rotation angle of $180 + \alpha_I \approx 203°$ (see Figure III-15.b). Both models agreed on the evolution of link tension and roller location for all the tension ratios tested and for both driving and driven sprockets. In terms of link tension, both models exhibit superimposed curves at the beginning of the sprocket rotation for all the ratios tested. Then, the curves start to split up at the same rotation angles for both models, with the curves related to higher tension ratios leaving the common trajectory first. Depending on the ratio, tension reaches its minimum before increasing again or simply decreases all the way to the slack strand. The differences between the driving and driven sprockets (due to the effect of friction, see §I.3) are similar. The driving sprocket shows a slower decrease in link tension than the driven one for all ratios. Naji & Marshek [62] reported the same behaviour observed experimentally with superimposed curves at the beginning of rotation regardless of the loading conditions. In terms of roller location, the results also exhibit superimposed curves as all the roller locations start at the first plateau where $\gamma_i \approx \gamma_{tp}^B$. The curves then diverge with the more loaded cases showing less roller displacement. For the lowest ratio ($T_s/T_s = 0.03$), the rollers do not reach the second plateau associated with transition point A ($\gamma_i \approx \gamma_{tp}^A$), regardless of the sprocket being driving or driven. For the driven one the rollers tend to start "crossing the profile" sooner and therefore reach the second plateau before compared to the rollers in contact with the driving sprocket under the same loading conditions. Detailed analysis of the differences between driving and driven sprockets will be given in Chapter IV.

For both models, slope breaks are visible in the link tension evolution. They are caused by the fluctuations of angles $\alpha_{s,t}$ and indicate the roller captured (released) on the driving (driven) sprocket. Their angular period is therefore $\alpha_I \approx 23°$. These slope breaks are also visible in both the experimental results [62] and in the GPLD model [2] from Naji & Marshek.

The good agreement of the two models suggests that the effect of friction at the pin/bush and bush/roller interface, as modelled by Kim & Johnson, does not significantly influence the link tension and roller location. However, friction at the roller/profile interface greatly influences the results obtained, exhibiting differences between the driving and driven sprockets. Considering the good agreement of Kim & Johnson's model with the experimental results of Naji & Marshek [2] (the comparison is shown in [52]), this suggests that the approach used in this work for the friction model (correction angle δ) is sufficient to represent loads and roller location evolution with limited complexity.

III.4 Complete drive model

The global kinematics (*i.e.*, tight and slack strand sub-models) and local sprocket sub-model have been considered independently and compared to the literature. The QSCDM (*i.e.*, global kinematics, roller location, load calculation and transition from "per position" to "per component") is now compared to the work presented by Troedsson & Vedmar in [67].

In their work, Troedsson & Vedmar presented a complete chain drive model, including a specific model for the slack strand (used as a basis for the sub-model presented in this work, see §II.1.2). The effect of gravity was considered for the load computation but friction was neglected. The elongation of the links under the action of link tension was also taken into account (contrary to the model presented) but tooth deflection was ignored. A mock test for a 10|20 drive was presented. The total number of links Nb_{link} equalled 40 and a torque of $C_I = 5N.m$ was applied on the driving sprocket. The centre distance L was 196.8mm. The sprocket and chain pitch were assumed not to be equal, their values being respectively $p_{sprocket} = 15.875mm$ (5/8″) and $p_{chain} = 15.95mm$. The tooth profile used was not given in detail in the paper but was from the standard DIN 8187. However, this standard has been replaced by the ISO 606 [31] (defining NF_{min} and NF_{max} profiles, see §I.2.1) and the author could not obtain the precise definition of the geometry mentioned.

Changes had to be carried out to enable the comparison with the QSCDM presented in the manuscript. The global kinematics calculation method cannot be used with different pitches for the chain and sprockets. Therefore, it is considered that both pitches equal $15.875mm$. To fit the smaller chain pitch, the centre distance must be adapted and is set to $196.5mm$ to match the slack strand tension. Neither the mass of the links nor the roller diameter were given in in the paper [67]. Based on the pitch, their values are taken from a catalogue [91] (chain No 500, see Table III-7). As the tooth profile used in the paper could not be found by the author, the profile NF_{max}, from the standard ISO 606 [31] is used. Finally, the correction angle $\delta(\infty)$ is set to 0 as friction was neglected in the paper. The parameters used for this case study are summarised in Table III-6 and Table III-7

$Z_I|Z_{II}$	L	ΔY	*slack*	$|\delta(\infty)|$
10|30	196.5mm	0	7.46%	0°

Table III-6: Drive parameters used for comparison with Troedsson & Vedmar [67]

Pitch p	D_{roller}	m_{link}
$15.875mm$	$10.16mm$	$12.38g/link$

Table III-7: Chain parameters for comparison with Troedsson & Vedmar [67]. ***Based on chain No 500 in*** [91]

The chain drive is solved using the QSCDM with the above parameters. The evolution of loads (link tension and contact force) as well as roller locations (*i.e.*, γ) are calculated "per component" and compared to the results of the paper. Figure III-17 shows the evolution of the contact force at articulation i (during its contact with the driving and driven sprocket) and link tension for link $i + 1$ (see Figure III-19 and Figure II-2). These forces are denoted F_{i+1} and F_c respectively for Troedsson & Vedmar. The x-axis coordinate is the driving sprocket rotation expressed as a fraction of the driving sprocket pitch angles (ζ/α_I).
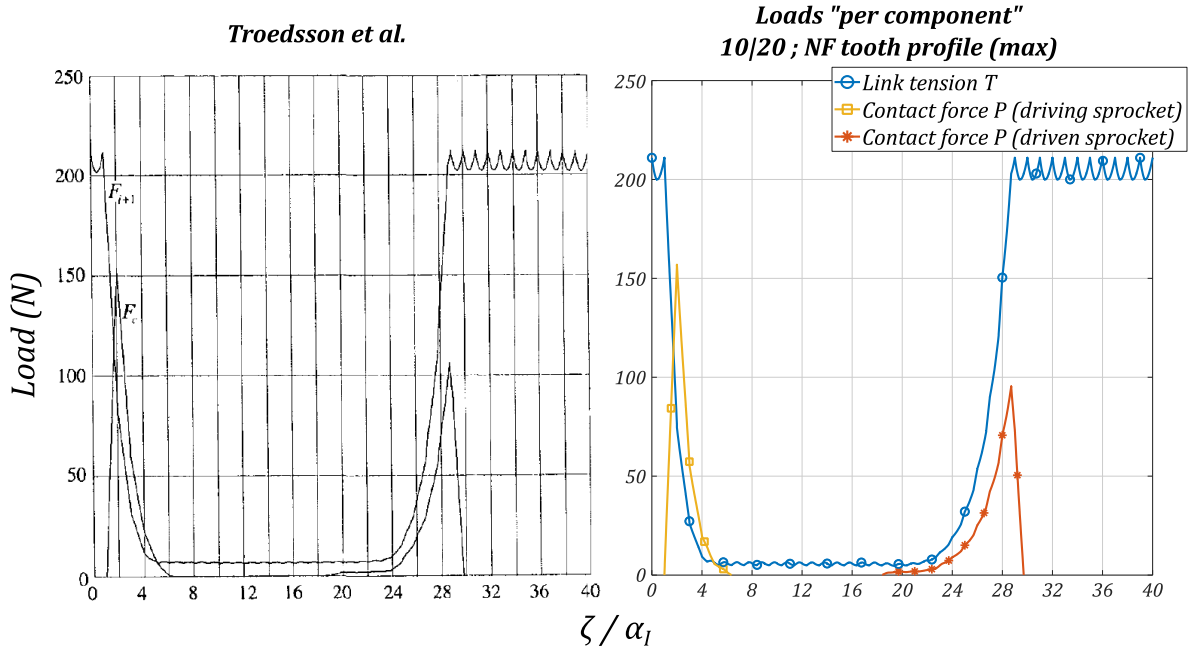
Figure III-17: Comparison of link tension and contact force with Troedsson & Vedmar [67]

The curves look similar for both models. The tracked roller first comes into contact with the driving sprocket, resulting in the link tension going from the tight to the slack one. After a period in the slack strand, the articulation comes into contact with the driven sprocket which takes it back to the tight strand. Both models show oscillations in the strand tensions. These oscillations are caused by two main phenomena: the slack tension variation and the meshing angles variation. Indeed, as the slack strand tips move, the slack strand tension varies (see Figure III-18.a) and meshing angles $\alpha_{s,t,j}$ also vary at the same time (see roller capture and release sub-positions in Figure III-18). These parameters all intervene in the relation between torque and strand tension (see eq.(II-32)). As a consequence, the tight strand tension adjusts to maintain a constant driving torque resulting in the variation shown in Figure III-18.b. The oscillations in the slack strand tension seem higher for the model presented, compared to the results of Troedsson & Vedmar, which results in higher oscillations in the tight tension as well. This difference is probably caused by the chain mass. Indeed, the higher slack strand oscillations in the model presented suggest that the link mass used is higher than in the paper. The contact forces exhibit the same trend for both models as the first peak occurs during the link meshing before the force rapidly decreases. However, the reached peak values differ, as they are a little higher for the driving sprocket and a little lower for the driven one in the QSCDM compared to that of Troedsson & Vedmar. The higher strand tension oscillations might reflect the contact force, probably explaining some of the differences observed. The possible different tooth profiles used for both models could also have an influence. Despite these discrepancies, the general force evolutions are very similar for both models.

Figure III-18 represents the tight and slack strand tension at the driving sprocket (respectively $T_{t,I}$ and $T_{s,I}$) during a model period. The sub-positions of roller capture and release by both sprockets are represented. The adaptive angular pitch used in the model is visible. The discretisation pitch is reduced around each event of roller capture or release and specifically around those concerning the tight strand. This allows capturing with improved precision these significant instants with limited consequences on computation time (see Appendix I). The slack tension varies for each sub-position, reaching about $5N$ to $6.6N$ at its lowest and highest points, respectively. The maximal slack tension occurs at about $\zeta/\alpha_I = 0.3$ between the roller release by the driven sprocket and the roller capture by the driving one. The minimum is reached immediately before the release of a new roller by the

driving sprocket into the slack strand. As the release (capture) of a roller at the driving (driven) sprocket is assumed to be instantaneous, the slack strand tip position also changes instantaneously. This results in discontinuities in the slack strand tension with the one resulting from the roller release at the driving sprocket being the most significant. The resulting variation of the tight strand tension $T_{t,I}$ (to ensure constant torque) is shown in Figure III-18.b. The phasing is different compared to the slack one. The maximum tension (about $211N$) is reached around the position of roller capture by the driving sprocket while the lowest one (about $200N$) lies close to the position of roller release from the driven sprocket. The magnitude of the discontinuity caused by the roller release from the driving sprocket is similar in the tight tension but its relative importance is reduced as the magnitude of the tight strand variation is greater than that of the slack one.
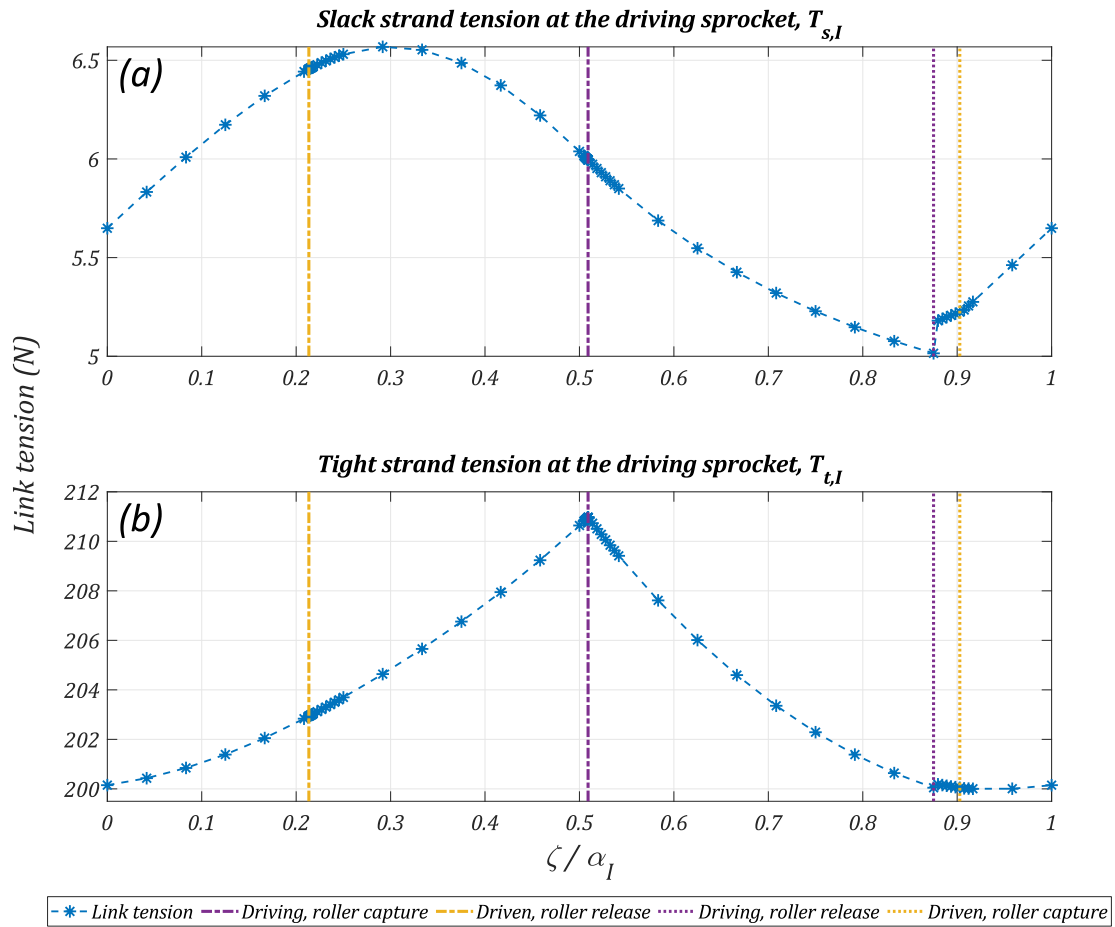
Figure III-18: link tension at the driving sprocket: (a) slack strand, (b) tight strand

In order to compare the prediction in terms of roller location, the normal directions at the roller/profile contacts are shown in Figure III-19. As for the roller locations, these normal directions depend on the drive position considered. However, this information was not given by Troedsson & Vedmar. For the model presented, the normals are shown for the drive position immediately before the capture of a new roller by the driving sprocket (*i.e.*, $\zeta \approx 0.52\alpha_I$ with $\psi_{t,I}\big|_{init} = 0$).

(a) **(b)**
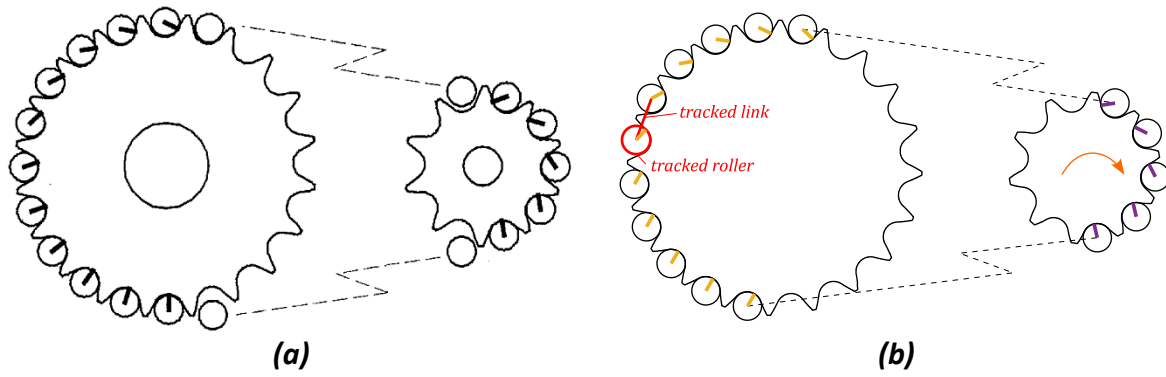
Figure III-19: Roller-profile contact normal direction according to: (a) Troedsson & Vedmar** [67]**, (b) QSCDM. The strands are shortened for visualisation

As friction is neglected (*i.e.*, $|\delta(\infty)| = 0$), the normal directions are also the directions of the contact forces. In both models, all the rollers in contact with the driving sprocket carry loads: the closer to the tight strand, the greater the load carried. Indeed, the normal direction tends to the radial direction (*i.e.*, no load carried) as the rollers move their way to the slack strand. The same trend is observed for the driven sprocket. However, according to the QSCDM, the normal direction of the last roller in contact is oriented towards the slack strand (*i.e.*, the contact point has moved to the slack side of the profile, see Figure III-11). The transition from a roller contacting the tight to the slack side of its profile is much quicker in the QSCDM than in the paper [67]. Indeed, in Troedsson & Vedmar, the five rollers closer to the slack strand (for the driven sprocket) carry almost no loads but do not "cross the profile". Conversely, in the model presented, the transition from contact with the tight to the slack side of the profile is completed by the two rollers closer to the slack strand (still for the driven sprocket). It is interesting to note that despite these differences in terms of normal direction, the evolutions of the contact forces are similar for the two models (as shown by Figure III-17). The differences are therefore probably caused by the drive position studied. It is also possible that the roller diameter is different for both models resulting in different adjacent roller relations therefore causing the differences in normal direction.

To conclude, despite the parameters being slightly different (*i.e.*, chain pitch, tooth profile and link mass), the results of both models are very similar, both in load evolution and in normal direction (*i.e.*, related to roller location). The QSCDM presented in its entirety therefore seems able to predict the behaviour of a given chain drive. The similar results suggest that the link elongation (considered by Troedsson & Vedmar but neglected in the presented model) does not significantly affect the drive behaviour. However, the loads applied on this case study are moderate (up to $200N$ compared to a maximum of $4000N$ in track cycling drives, see §I.1.2) so this conclusion should to be tested in more extreme loading conditions. Similarly, the effect of gravity, considered by Troedsson & Vedmar in the tension model of a roller in contact with a sprocket, but neglected in the tension model presented, does not seem to significantly influence the results.

III.5   Conclusion

This chapter was dedicated to the validation of the Quasi-Static Chain Drive Model (QSCDM). The process was carried out on the different sub-parts and finally on the whole QSCDM.

The global kinematics was first reviewed. The comparison of the tight strand sub-model was in agreement with the analytical predictions of Fuglede & Thomsen [1]. The predictions of the roller capture and release positions are similar, likewise for the sprocket rotation speed and acceleration. The numerical procedure presented has the advantage of accommodating the addition of new hypotheses more easily (*e.g.*, replacing the condition on $\alpha_{s,t}$ with a detection of roller sprocket collision). The slack strand sub-model was then analysed and compared to the known results for a catenary curve. Its behaviour proved to be consistent and its application to a chain drive also exhibited predictable results.

The local sprocket sub-model was then analysed in two steps. First, the relation between adjacent rollers was considered regardless of the impact on loads. Its successful comparison with the roller location characteristic curves presented by Kim & Johnson [52] was detailed. The calculation of link angles was then compared to the graphical measurements performed by Binder [32] and the numerical predictions of Naji & Marshek [64]. The comparison showed similar trends despite exhibiting little variations imputed to the different hypotheses stated.

In the second step, the relation between roller location and loads, as predicted by the local sprocket sub-model, was studied. The sub-model was tested alone without the connection to the global kinematics. The predictions were compared to the model developed by Lodge & Burgess [70] and the experimental results of Stephenson *et al.* [72]. Due to the specificity of the cases studied (strand trajectories compelled by guide rails), the evolution of the meshing angles $\alpha_{s,t,j}$ could not be calculated. Therefore, the results were presented "per position". The results are consistent for link tension evolution. Compared to the model of Lodge & Burgess, assuming instantaneous roller location variation, the QSCDM is able to capture the progressive switching between the two transition points (between the slack and tight side of the tooth profile). "Per component" predictions were compared to the model of Kim & Johnson [52] for the classical case study of a 31|31 double pitch chain. Both models agreed on the evolution of link tension and roller location. This agreement suggests that friction at the pin/bush and bush/roller interfaces (considered by Kim & Johnson but neglected in this manuscript) do not significantly influence the drive behaviour. The correction angle approach used in this manuscript therefore seems sufficient to model the effect of friction.

The whole QSCDM (*i.e.*, global kinematic and sprocket sub-model) was then compared to the results presented by Troedsson & Vedmar [67]. Despite uncertainties on the precise tooth profile geometry and chain characteristics, the predictions were in accordance. This result supports the hypothesis stating that part deformations, and specifically link elongation, do not significantly influence the drive behaviour (*i.e.*, loads and roller locations). Similarly, the choice of neglecting gravity in the sprocket sub-model is backed.

The whole QSCDM as well as its constitutive sub-models were compared successfully to the results of the literature from both numerical models and experimental measurements. Although meant to study track cycling drives, the model hypotheses are general enough to cover industrial cases. Thanks to this flexibility, the model was validated using industrial chain drive literature as no appropriate results for cycling drives could be found. The similarity between the industrial drives tested and cycling cases (*e.g.*, negligible dynamical effect) ensures the validity of applying the method specifically to track cycling.

Chapter IV

Chain drive behaviour, influence of tooth profile for industrial and track cycling drives

The Quasi-Static Chain Drive Model (QSCDM) has been presented and validated against numerical models and experimental results from the literature. In this chapter, it is used to analyse the influence of tooth profile on the chain drive behaviour, for both industrial and cycling applications.

First, the influence of the standard tooth profiles (ASA, NF_{min} and NF_{max}) on chain drive behaviour is tested. Industrial drives are considered in order to analyse the impact of these profiles on their dedicated application. The loads (*i.e.*, link tension and roller/profile contact force) are calculated using the three profiles. The specificities of the QSCDM presented are explored and compared to single sprocket models of Naji & Marshek [2], [6] and Kim & Johnson [52]. The influence of the connection between strands and sprockets on loads and roller location oscillations is characterised. This first section demonstrates the interest of the QSCDM presented for industrial drive applications. Moreover, it provides a first assessment of the influence of tooth profile on drive behaviour.

Based on the results of the first part, analysis methods are presented. These original methods are focused on characteristic pressure angle values. The latter characterise each tooth profile. These methods also enable easier analysis and prediction of the influence of a given profile on the drive behaviour. A global analysis of the main drive behaviours is presented. Parallels with other models presented in the literature are also given.

Finally, the analysis methods presented are applied to track cycling drives. Their interest is demonstrated through easier interpretation of the results. The specificities inherent to track cycling applications are explored. The interest of dedicated tooth profiles is demonstrated and original geometries are proposed. Finally, the influence of the new tooth profile geometries is tested on a typical track cycling drive and a comparison with the industrial case is carried out.

IV.1   Analysis of industrial drives

The influence of the standard profiles is tested considering the typical $Z_I|Z_{II} = 31|31$ double pitch drive [52], [62] already broached in the validation process (see §III.3.2).

Both the driving and the driven sprockets have 31 teeth. They are used with the double pitch chain ANSI C2040R, as in the work of Naji & Marshek [62] and Kim & Johnson [52]. The chain characteristics are taken from a catalogue [11] and summarised in Table IV-1. The chain has a number of links $Nb_{link} = 80$ and the distance L is set to obtain a slack strand looseness of $slack = 4\%$ to match the recommendation for industrial drives [73]. As in Naji & Marshek in [62], a correction angle $|\delta(\infty)| = 5°$ is chosen. The drive parameters are summarised in Table IV-2.

Pitch p	D_{roller}	m_{link}
$1'' = 25.4mm$	$7.92mm$	$12.7g$

Table IV-1: Characteristics of the ANSI C2040R chain, based on [11]

$Z_I|Z_{II}$	L	ΔY	$slack$	$|\delta(\infty)|$
$31|31$	≈ 819mm	0	4%	$5°$

Table IV-2: Parameters **of the $31|31$ double pitch drive**

Parameters $\psi_{t,I}|_{init}$ and a are set to 0 and $1e^{-10}m$, respectively. A general view according the global kinematics of the drive studied (generated with the QSCDM) is presented in Figure IV-1 according the global kinematics. The results of the global kinematics analysis are presented for one drive period in Figure IV-2.
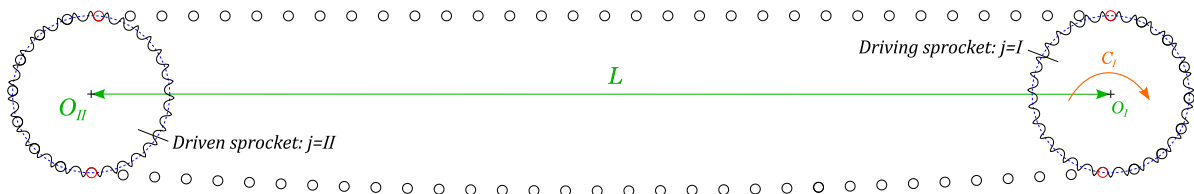
Figure IV-1: General view of the $31|31$ double pitch drive ($slack = 4\%$)
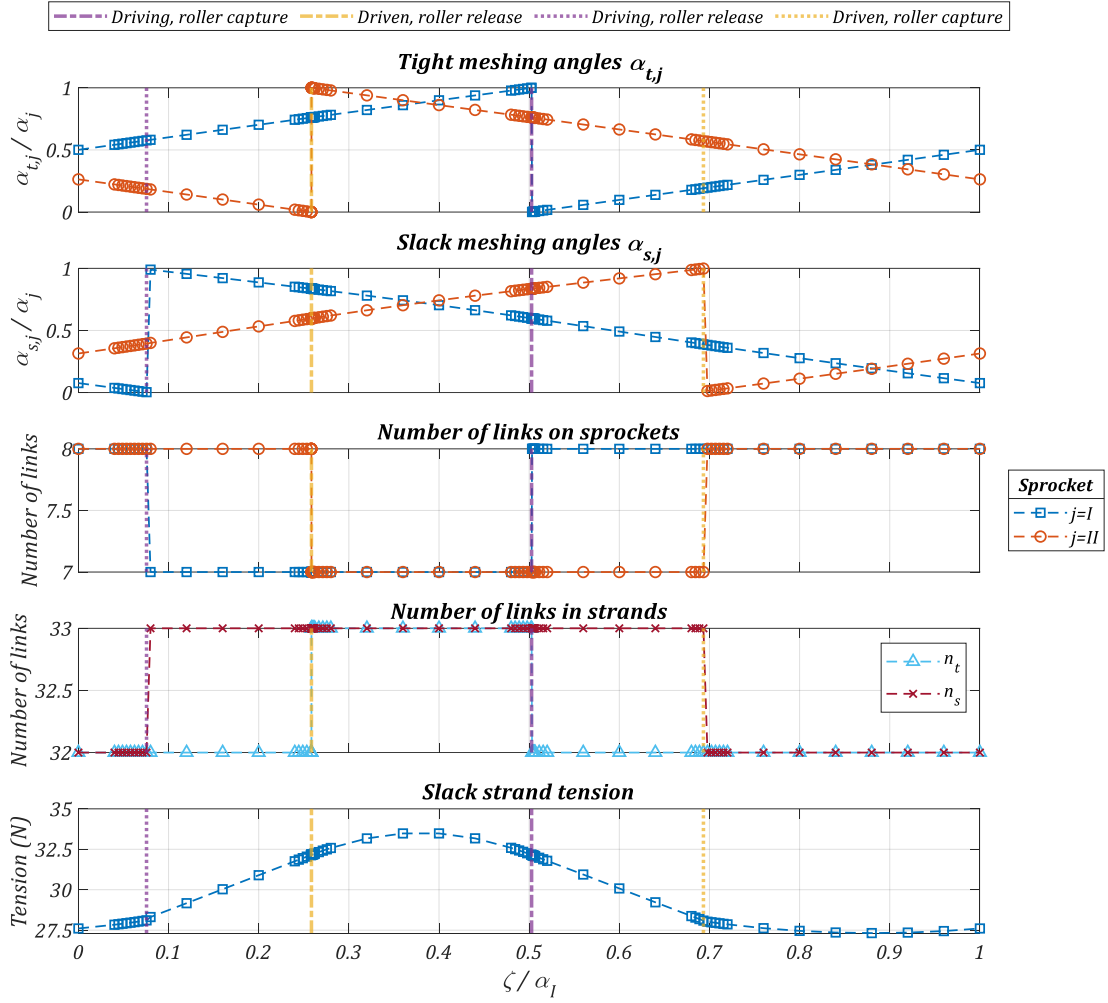
Figure IV-2: Global kinematics of the 31|31 double pitch drive

The variation of the meshing angles $\alpha_{t,j}$ and $\alpha_{s,j}$ is shown. They vary between $]0, \alpha_j]$ (with $j = I$ or II for the driving and driven sprocket, respectively). The discontinuities in the curves mark roller capture and release events. For both sprockets, the roller capture and release do not occur simultaneously. Therefore, the number of links in contact with each sprocket is not constant and varies between 7 and 8. Consequently, the numbers of links in the strands also vary between 33 and 32. Indeed, the looseness setting of the slack strand (4%) is tight enough to obtain the same extreme number of links in both strands. As shown previously in §III.4, the moving tips cause the slack strand tension to vary within a drive period. Only the driving sprocket slack tension $T_{s,I}$ is plotted as the driven one is almost equal due to the strand being almost symmetric ($Dy \ll p.n_s$). The slack tension increases from about $27N$ at its minimum to about $33N$ at its maximum. Discontinuities in the tension occur at the roller release (capture) by the driven (driven) sprocket. This is due to the compatibility between the global kinematics and the local sprocket sub-model (see Chapter II). Indeed, for slack strand calculation, the rollers marking the strand tips are assumed to lie on the pitch circle. Therefore, they cannot leave (come into contact with) the sprocket gradually. As the drive is symmetric (*i.e.*, $Z_I = Z_{II}$ and $\Delta Y = 0$), the global kinematics for the driving and driven sprockets is the same (the ranges of the meshing angles and number of links are in the same intervals). The only difference is a shift in phase caused by the top common tangent not being equal to a whole number of pitches. Consequently, the slack strand tension has the same value at the events of roller capture (release) by the driving sprocket and release (capture) by the driven one. The kinematics presented is the same for all the profiles tested (see §II.1).

Comparison of the three industrial profiles is presented in Figure IV-3. Markers are set at the boundary points between the curve portions in Figure IV-3.a.
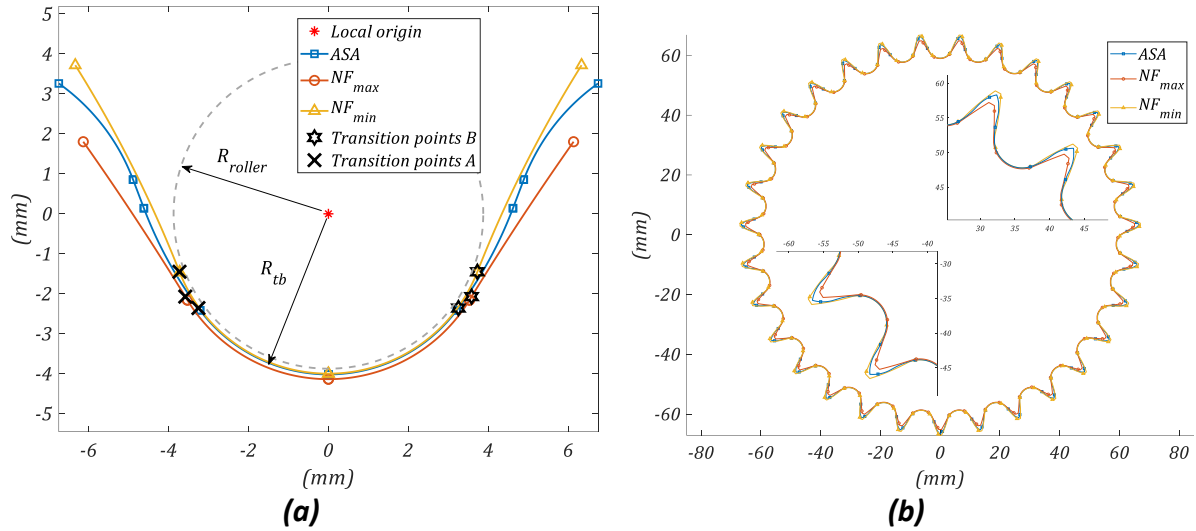
Figure IV-3: Comparison of ASA, NF_{max} and NF_{min} profiles: (a) in the local profile coordinate system, (b) for a whole sprocket (31 teeth double pitch sprocket)

In the local coordinate system view (Figure IV-3.a), the differences of tooth bottom radius (R_{tb}) can be appreciated. The NF_{min} profile is that with the smallest clearance with the roller. Along the tooth flank, the NF_{min} profile exhibits the steepest slopes while the NF_{max} has the shallowest. The slope of the profile flank does not significantly vary for the NF profiles as it is defined by a circle with a large radius (compared to the other dimensions). The ASA profile slopes lie between the two preceding profiles with significant changes along the curve. Going from the transition point to the tooth tip, the slope first lies close to the NF_{max} one before catching up with the NF_{min} and finally decreasing at the topping curve (last portion of the ASA profile). One can note that the ASA profile satisfies the ISO standards as its definition always lies between the two NF ones. The positions of the transition points are not the same for each profile. However, it is interesting to note that these specific points lie almost at the borders of the tooth bottom portion (*i.e.*, close to $\gamma = 3$ and $\gamma = 5$ for NF and ASA profiles, respectively, see Appendix A).

The different tip diameters can be appreciated in the global view (Figure IV-3.b). However, this parameter will have limited influence on the profile properties (see §IV.2 and IV.3).

IV.1.1 Tooth profile influence

Beforehand, it is important to remember the general dynamics of roller location. It was demonstrated by Kim & Johnson in [52] that rollers marking the transition with the tight strand always contact the tooth profile close to the transition point B (tp^B). Then, depending on the loading conditions, $s_{c,1}$ is located before or after tp^B. Consequently, rollers tend to cross the profile going toward transition point A (tp^A) or tend to climb the tooth flank with a high risk of chain drop (see Chapter I and Chapter II). Therefore, roller location always starts at the transition point tp^B (or simply tp). An example of typical roller location evolution for the ASA profile is given in Figure IV-4.a.
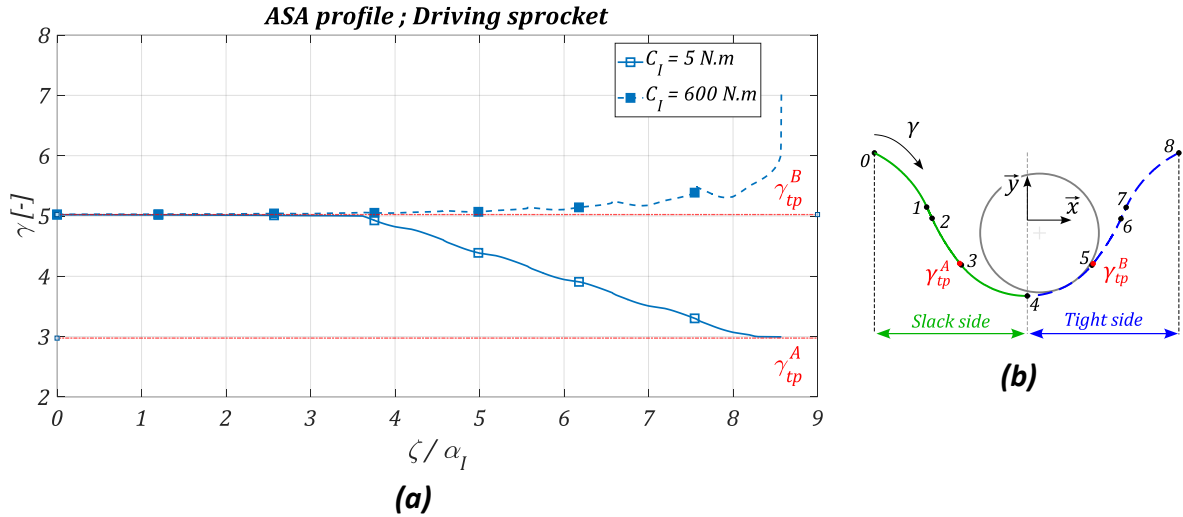
Figure IV-4: ASA driving sprocket (a) example of roller location (b) tight and slack side of the profile

Taking advantage of this *a priori* known roller motion, new parameters allowing roller location comparisons between several tooth profiles are introduced. Indeed, the different coordinates used for roller location (*i.e.*, γ, s_c and s_r) are dependent on the profile considered and do not necessarily fall within the same intervals, thereby preventing direct comparison.

The first parameter is the contact point displacement d. It represents the displacement of the roller/profile contact point starting at the capture of articulation i (*i.e.*, at index $k = 1$, see eq.(IV-1)). d_i is positive when the roller tends to cross the tooth profile while it is negative when the roller location tends to infinity (see Figure IV-5).

$$d_i(k) = s_{c,i}(k = 1) - s_{c,i}(k) \qquad (IV\text{-}1)$$

The second parameter of roller location is $\bar{d}_i$. It represents the evolution of d_i scaled by the distance between the two transition points along the tooth profile. The proportion, expressed in percentage, represents the length covers by the roller/profile contact point between the two points. When $\bar{d}_i = 0\%$, the roller lies at $s_{c,tp}^B$ and it reaches $s_{c,tp}^A$ for $\bar{d}_i = 100\%$ (eq.(IV-2)). $\bar{d}_i$ can also exhibit negative values when the roller tends to climb the tooth profile. For these cases, the scaling allows appreciating this motion in relation to the inter transition points distance.

$$\bar{d}_i(k) = \frac{d_i(k)}{s_{c,tp}^B - s_{c,tp}^A} \qquad (IV\text{-}2)$$

This representation is interesting as the distance between the two transition points along the tooth profile (called inter-tp distance, see Figure IV-5) differs for all profiles (see Table IV-3). Therefore,

different profiles might exhibit the same displacement d_i for different proportions of inter-tp distance $\bar{d}_i$.
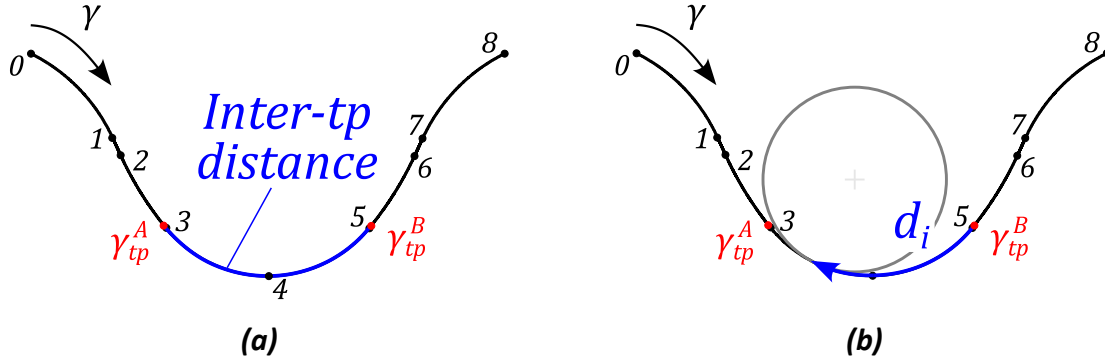
Figure IV-5: (a) inter-tp distance, (b) absolute contact displacement d

	ASA	NF_{max}	NF_{min}
Inter transition points distance (mm)	7.58	8.66	9.60

Table IV-3: Inter transition points distances for industrial tooth profiles

Similarly to what Naji & Marshek proposed in [2], the half tooth profile with positive x values (*i.e.*, right half of the profile in Figure IV-4.b) is designated as the tight side of the tooth profile. Conversely, the second half, with negative x values, is called the slack side of the tooth profile. Therefore, tp^B and tp^A are located on the tight and slack sides of the profile, respectively (see Chapter I).

The results for the driving sprockets at torque $C_I = 5N.m$ are given in Figure IV-6. The evolution of the link tension T_{i+1} and contact force P_i (numbering according to Figure II-2) is given "per component" as a function of the driving sprocket rotation angle ζ expressed in fraction of α_I. For driving sprockets, the origin $\zeta = 0$ marks the capture of articulation i from the tight strand.

$31/31 \ (double \ pitch) \ ; \ Driving \ sprocket \ ; \ C_I = 5N.m \ ; \ slack = 4\%$
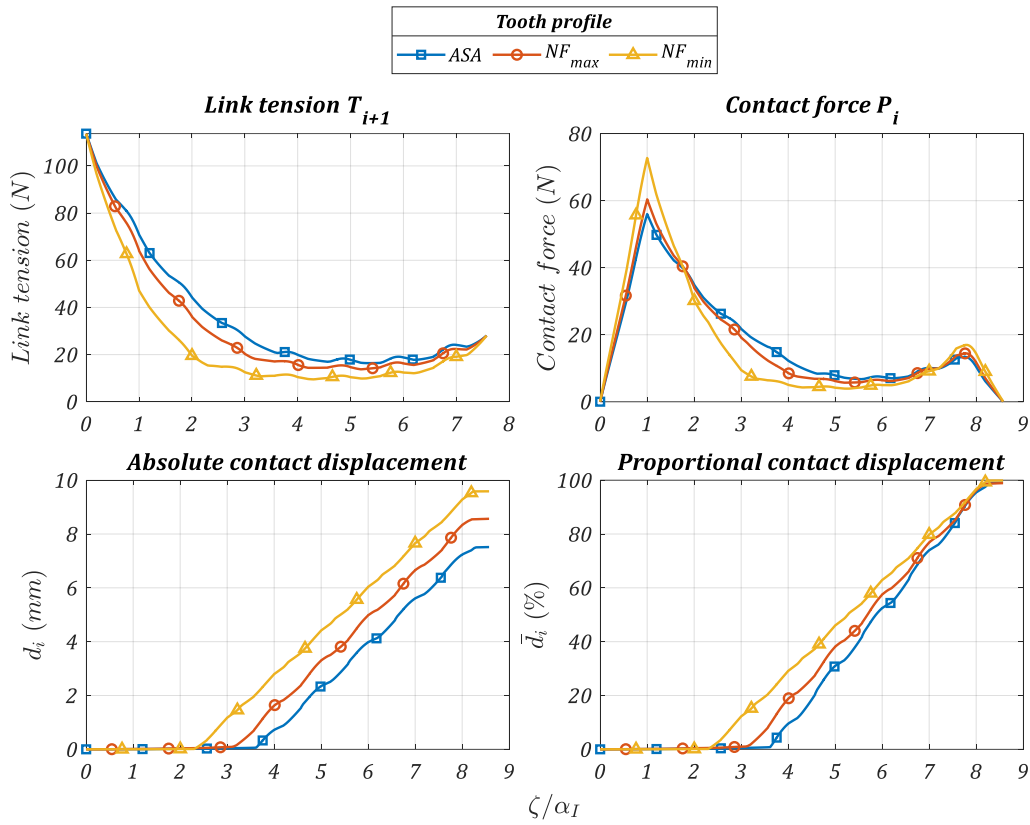
Figure IV-6: Link tension, contact force and roller location for $C_I = 5N.m$, driving sprocket

The link tension and contact force evolution show expected evolution. As presented in the literature (*e.g.*, [2], [52], [62], [64], [70]), the link tension first decreases to a minimum around $\zeta/\alpha_I = 5$ before re-increasing slightly to reach the slack strand tension (about $30N$ in this example, see Figure IV-2). The contact force first increases quickly during the meshing of the articulation (up to $\zeta/\alpha_I = 1$) before decreasing regularly to reach its minimum at the same time as the link tension. It then increases again, still along the link tension before dropping to zero after the un-meshing of the articulation.

The influence of the tooth profile geometry is visible on all the plotted results. For the link tension, the curve slopes are different depending on the profile. Moreover, quick initial decreases are associated with equally quick final re-increases. The NF_{min} profile exhibits the steeper slopes. For the contact force, steep slopes are associated with bigger initial and final maxima. The decrease after the first maximum (after $\zeta/\alpha_I = 1$) also follows the same trend as the link tension slopes (*i.e.*, the steeper the link tension decrease, the steeper the contact force decrease). All these differences are associated with a tooth being able to withstand different loads. Profiles able to withstand more load on each tooth (associated with high peak value on the contact force curve) also exhibit steeper slopes on the link tension evolution. The maximal contact force value reaches about 56, 60 and $72N$ for the ASA, NF_{max} an NF_{min} profiles, respectively. During the first period, the link tension decreases from around $112N$ to approximately 71, 64 and 47 for the ASA, NF_{max} an NF_{min} profiles, respectively.

Concerning the roller location, d_i is positive for all the profiles meaning that all display behaviour in which rollers tend to cross the profile from tp^B to tp^A (see eq.(IV-1)). For all the profiles, the roller remains at the transition point (*i.e.*, at $s_{c,tp}^B$) during the decrease in link tension. Depending on the tooth profile, the distance d travelled by the roller differs with the NF_{min} profile associated with the biggest travel distance. However, this difference is caused by the different inter-tp distance (see Table IV-3) as the distance between the transition points is fully crossed for all profiles (*i.e.*, $\bar{d}_i = 100\%$ is

reached for all the profiles). However, the rollers tend to stay longer at the transition point for profiles with moderate slopes in link tension and contact force (*e.g.*, *ASA* profile).

Compared to the curves presented in the literature, *e.g.*, Naji & Marshek [62] (see Figure I-17) or Kim & Johnson [52] (see §III.3.2), the link tension curves exhibit oscillations. These oscillations are mainly visible closer to the slack strand (for high values of ζ/α_I). Consequently, the slope breaks at each whole value of ζ/α_I (marking the capture of a new roller) are less visible compared to the results of Naji & Marshek [62] and Kim & Johnson in [52]. This subject will be discussed in the next section (see §IV.1.2). The intrinsic relation between loads and roller location must be noted. As long as the roller contacts the tight side of the tooth profile (corresponding to $\bar{d}_i < 50\%$ for symmetric profiles), T_{i+1} is smaller than T_i and the tension decreases (see eq.(II-27)). Once the roller reaches the slack side of the profile (corresponding to $\bar{d}_i > 50\%$ for symmetric profiles), tension T_{i+1} becomes greater than T_i and the tension re-increases. The minimum in link tension is therefore reached at $\bar{d}_i = 50\%$ for symmetric profiles. The same reasoning applies to the contact force.

The same results are plotted in Figure IV-7 for a driving torque of $C_I = 50N.m$, again for the driving sprocket.

31/31 (double pitch) ; Driving sprocket ; C_I =50N.m ; slack = 4%
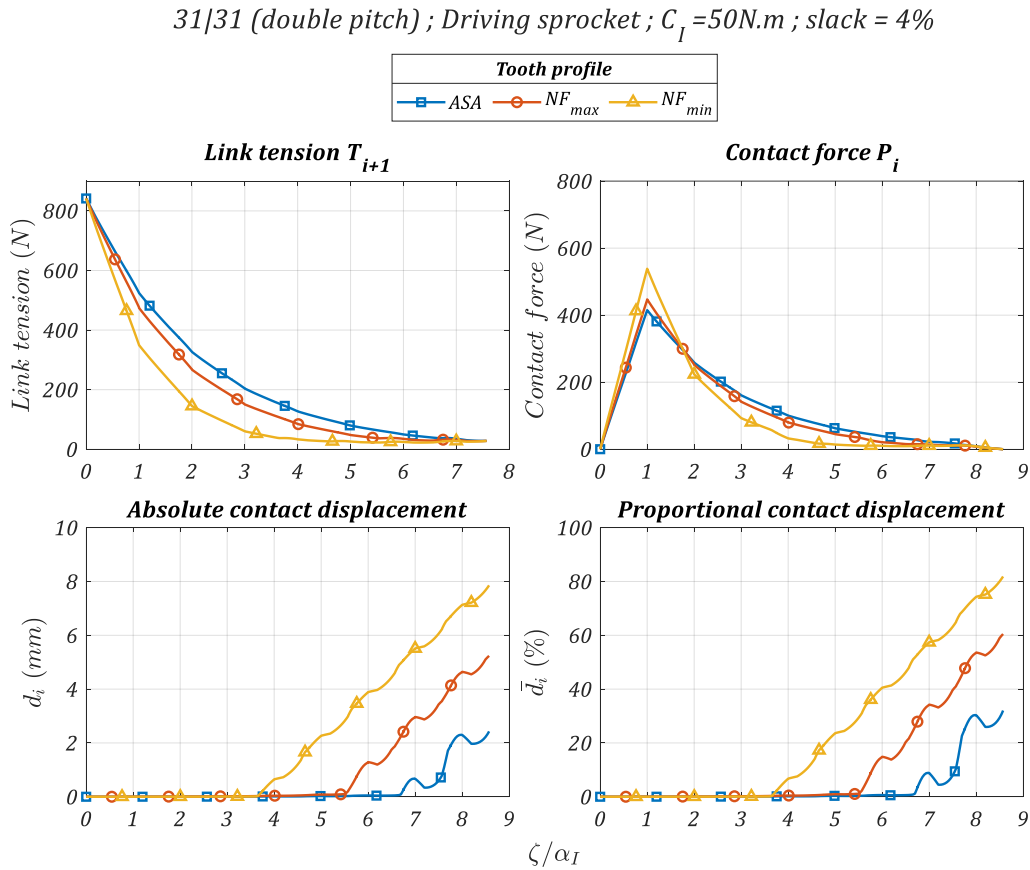
Figure IV-7: Link tension, contact force and roller location for $C_I = \mathbf{50N.m}$, driving sprocket

The link tension reaches higher values than in the previous case as the tight tension increases to match the new torque condition (the tight tension now reaches about $820N$). The contact force also increases accordingly. However, the general shape of both curves remains identical with a strong link tension decrease until a minimum is reached around $\zeta/\alpha_I = 6$. For the ASA profile, the tension now decreases all the way down to the slack strand value (as $\bar{d}_i < 50\%$). As for the previous case ($C_I = 5N.m$), the NF_{min} profile exhibits the steeper slopes both in link tension and contact force.

In terms of roller location, all the profiles show rollers starting close to tp^B before tending to tp^A. However, the rollers tend to stay longer nearby tp^B compared to the preceding case. As a consequence, they do not entirely cross the profile. The greatest roller motion is observed for the NF_{min} profile where about 80% of the inter-tp distance is travelled (representing $\approx 8mm$ along the tooth profile). For the ASA profile the roller barely moves from the tp as it starts its crossing only around $\zeta/\alpha_I = 7$ to reach about 30% of the inter-tp distance.

The oscillations, observed in the previous case, are less visible for link tension and contact force as their magnitude is less significant compared to the amplitude of each curve. However, they are visible in the roller location curves. Their influence is particularly significant for the ASA and NF_{max} profile where they cause the roller motion to be non-monotonic. This subject is discussed in §IV.1.2.

The differences between driving and driven sprockets are now presented. The results obtained for a driven sprocket, again for $C_I = 50N.m$, are shown in Figure IV-8. As in the work of Naji & Marshek [2], [6], [62] and Kim & Johnson [52] the results are given from the tight to the slack strand. The abscissa is again the angle ζ/α_I. However, articulations contacting a driven sprocket go from the slack to the tight strand. Therefore, $\zeta/\alpha_I = 0$ is associated with the roller release into the tight strand while the articulation meshing (from the slack strand) occurs at $\zeta/\alpha_I|_{max}$.
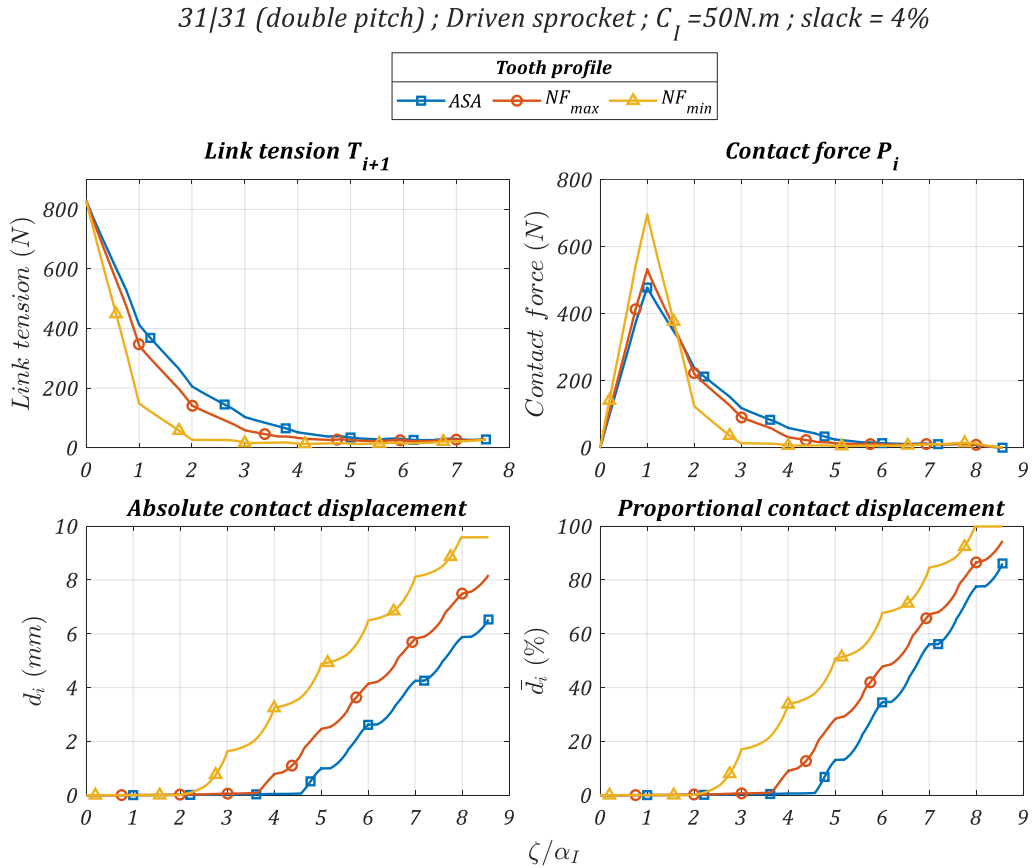
Figure IV-8: Link tension, contact force and roller location for $C_I = 50N.m$, driven sprocket

Compared to the driving sprocket in the same loading conditions (see Figure IV-7), the slopes for the link tension and contact force are steeper. Thus, the minimal link tension is reached earlier (around $\zeta/\alpha_I = 3$) and the maximal contact force is higher. Consequently, the rollers leave the tp sooner and also tend to travel further along the tooth profile. $\bar{d}_i$ reaches at least 80% for all the profiles, with the NF_{min} profile even reaching tp^A (i.e., $\bar{d}_i = 100\%$). These observations are consistent with the results

presented by Kim & Johnson [52] (see §III.3.2). The oscillations in the roller location curves are less significant compared to the driving sprocket. Non-monotonic motion is only slightly observed for the ASA profile. It is interesting to note that the results obtained for the driven sprocket with NF_{max} profile are very similar to those for a driving NF_{min}. Both show a link tension of about $350N$ at $\zeta/\alpha_I = 1$ and a maximal associated contact force of about $530N$. They also both exhibit roller travel between 80 and 90% of the inter-tp distance. This indicates that the differences between tooth profiles behave in the same manner as the differences between driving and driven sprockets.

IV.1.2 Loads and roller location oscillations, the interest of relative tension

On all studied examples, the curves show oscillations (in link tension, contact force and roller location). These oscillations are not always discernible depending on their magnitude. However, it was observed that load variation and roller location are coupled. Therefore, oscillations in one necessarily mean oscillation in the other. These oscillations are not present on the model results by Kim & Johnson [52] (see §III.3.2) or in the measures from Naji & Marshek [62] (see Figure I-17). Figure IV-9 shows a comparison of the link tensions obtained in this part using the whole model ($C_I = 5N.m$) and the results of the validation process (see §III.3.2), both for driving sprockets. The curves from the validation (obtained using the local sprocket sub-model alone, see Figure IV-9.b) are representative of the results of Kim & Johnson and Naji & Marshek (see Figure I-17 and §III.3.2). Only slope breaks at each capture of a new roller ($\zeta = \alpha_I \approx 23°$) are visible while the curves for the QSCDM (Figure IV-9.a) show oscillations. This part is dedicated to the explanation of this oscillation phenomenon.
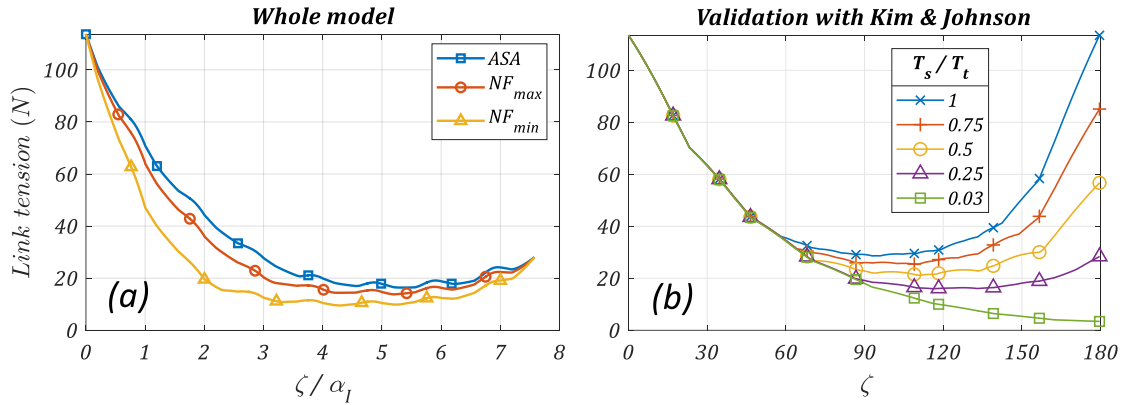
Figure IV-9: Comparison between link tensions using (a) the whole model (from Figure IV-6) (b) the validation curves presented at §III.3.2 (from Figure III-16)

a) *Effect on the tight strand tension variation*

In the results presented in the previous part, a whole chain drive is studied. Strand tensions result from a specific slack strand model, and a condition of constant torque on the driving sprocket is applied. Therefore, the following differences are apparent between this work and that of Kim & Johnson and Naji & Marshek.

- Non-parallel strands resulting in different phasing in the roller capture and release,
- Variation of slack strand tensions $T_{s,j}$,
- Variation of tight strand tension T_t (resulting from the constant torque condition).

However, both works considered the variation of angles $\alpha_{s,t,j}$ allowing to model the meshing of the sprocket considered. However, in this study, as the strand trajectories result from the drive kinematics, they are not necessarily parallel. This implies different phasing in the roller capture and release events compared to Kim & Johnson and Naji & Marshek. Figure IV-2 showed the variation of the slack strand tension and meshing angles $\alpha_{s,t,j}$ during a drive period. As the driving torque is forced to be constant, the tight strand tension has to adjust according to eq.(II-32). The same phenomenon was already reported in the validation process with the results of Troedsson & Vedmar (see §III.4). The resulting tight strand tension for $C_I = 5$ and $50 N.m$ is shown in Figure IV-10.
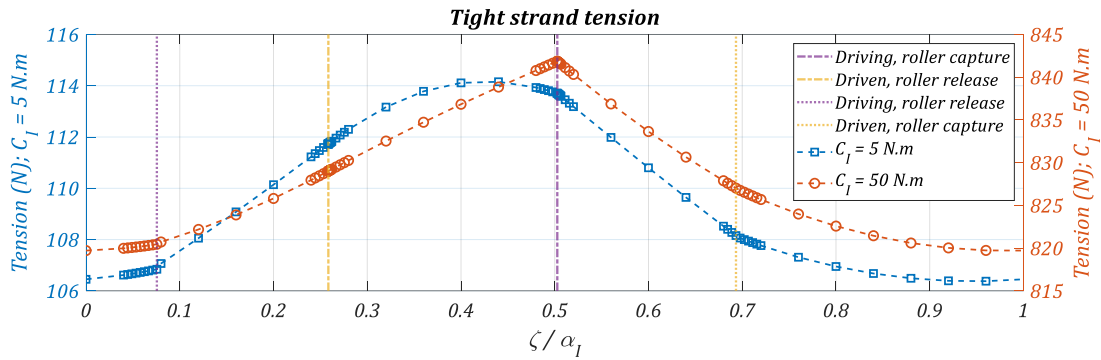
Figure IV-10: Driving sprocket tight strand tension for $C_I = 5$ and $50 N.m$

The more highly loaded the drive, the more the tight strand variation differs from that of the slack one. This is due to the relative influence of the two causes responsible for tight strand variation: slack strand variation and meshing angles. The more the drive is loaded, the less significant the slack strand variation becomes compared to the effect of the meshing angles. Consequently, the tight strand tension maximum progressively distinguishes from the slack tension maximum. For $C_I = 50 N.m$, the maximal tight strand tension occurs at the driving sprocket roller capture. The discontinuities in the slack strand variation occurring at the roller capture (release) by the driven (driving) sprocket are still visible in the tight strand variation. However, their relative influence reduces as the magnitude of tight strand tension variation increases.

To cancel the influence of the tight strand tension variation, the relative load (scaled by T_t) can be plotted. Examples of results expressed in relative tension (T_{i+1}/T_t) are presented in Figure IV-11. Plots in relative tension were also presented in Kim & Johnson and Naji & Marshek as they also allow generalising the results to any tight strand tension.
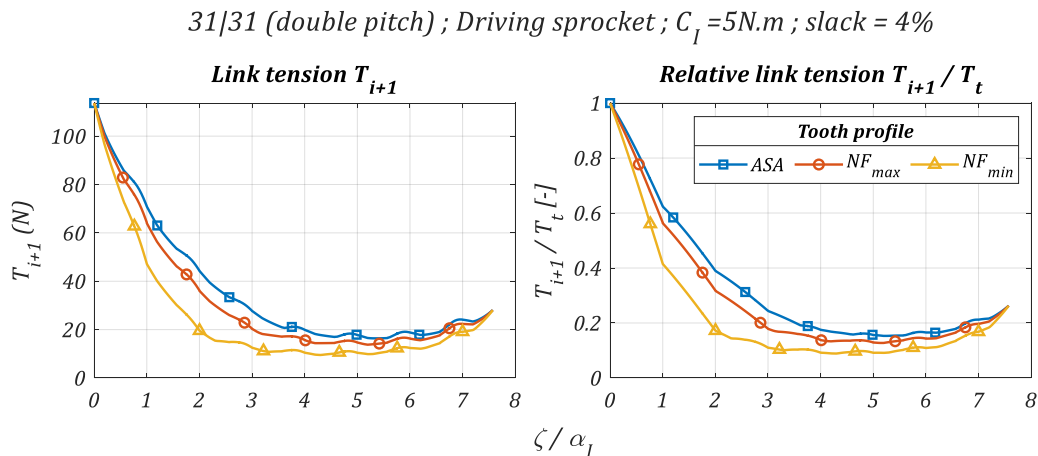
Figure IV-11: Absolute versus relative link tension evolution

Figure IV-11 shows that fewer oscillations are present on the relative tension plots compared to the initial absolute representation. In particular, the slopes for the first periods became constant and the capture of a new roller (for each whole ζ/α_I value) is more visible. The superposition of relative tension curves for the different driving torque and for each tooth profile is presented in Figure IV-12 (for the driving sprocket).
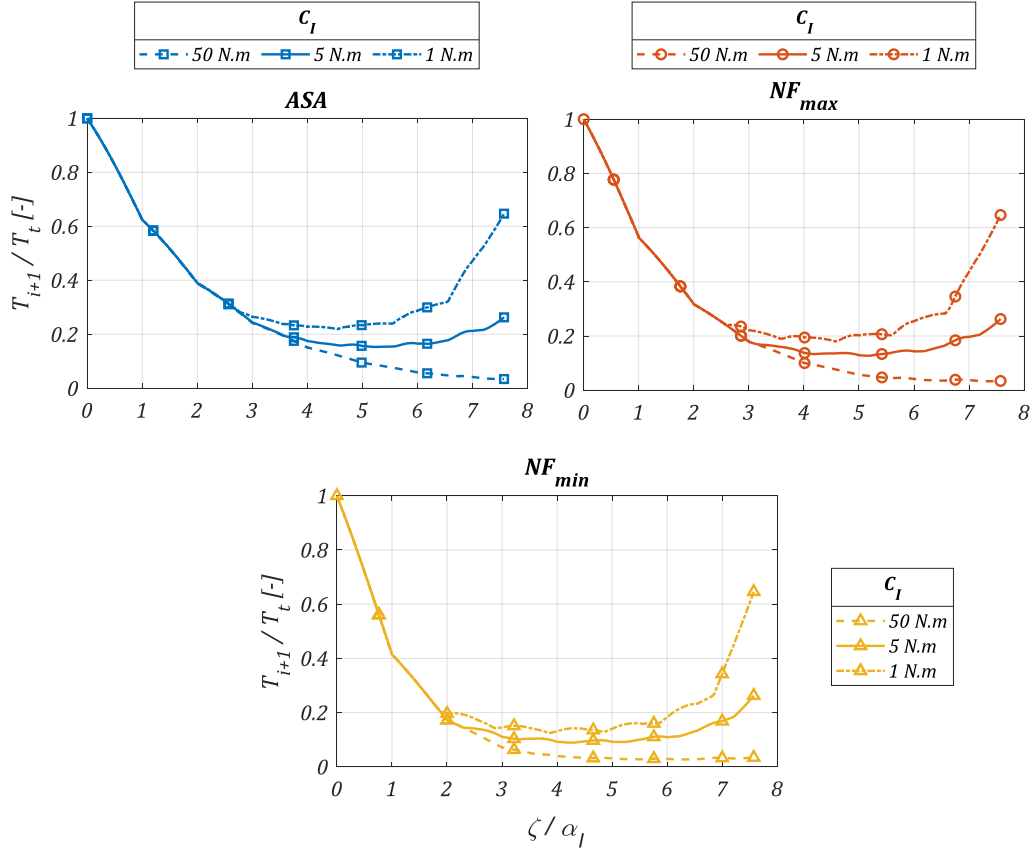
Figure IV-12: Relative link tension for three loading conditions, driving sprocket

The curves are superimposed for the first model period. This indicates that the tension decay follows the same trend for a given profile, independently of the loading conditions. For instance, the link tension falls by approximately 60% during the meshing for the NF_{min} profile (40% for the ASA). However, oscillations are still present as the link goes to the slack strand. Therefore, another phenomenon, apart from the tight strand variation, is responsible for these oscillations.

b) Effect of the tension ratio variation

Knowing both strand tensions allows calculating the tension ratio $T_s/T_{t,j}$ which also varies along a drive period (see Figure IV-13).
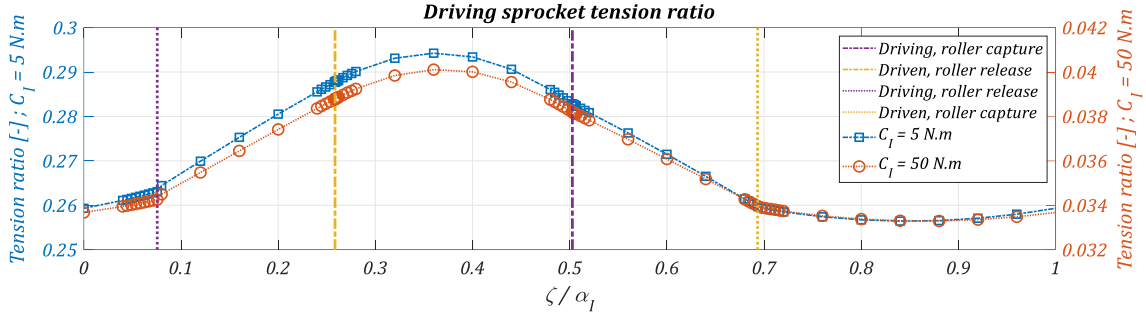
Figure IV-13: Driving sprocket tension ratio for $C_I = 5$ and $50 N.m$

As for the slack tension in Figure IV-2, the tension ratio is plotted only for the driving sprocket. The phasing of the tension ratio variations follows the variations of the slack tension (as $T_s/T_t \propto T_s$). The ratio varies significantly during one drive period, going for instance from about 0.26 to 0.29 for a driving torque of $C_I = 5N.m$. The variation of the tension ratio causes the deviations from the literature.

Figure IV-14 shows a 3D plot of relative tension (T/T_t) as a function as the rotation angle (ζ/α_I). The third dimension shows the slack to tight tension ratio (T_s/T_t). The red curve highlights the path followed by the link studied in this 3D space. The case considered is for a driving sprocket at $C_I = 5N.m$ with NF_{min} profile. The colour scale shows the differences with the slice corresponding to the median tension ratio.
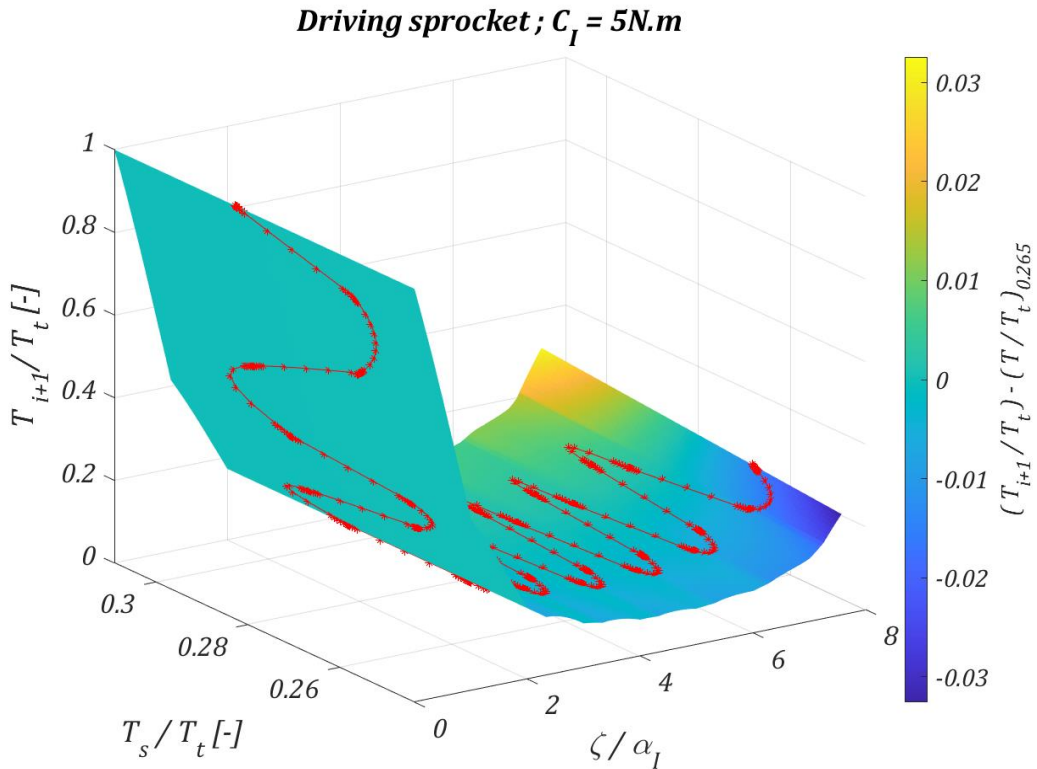
Figure IV-14: 3D plot of relative link tension depending on the rotation angle (ζ/α_I) and the tension ratio (T_s/T_t)

This representation clearly shows the variation of tension ratio during the roller sprocket contact. The model period is visible in the periodical oscillations of the red curve. Each slice of the 3D plot represents a constant tension ratio condition, similar to the works presented by Kim & Johnson and Naji & Marshek. Differences between the constant ratio conditions (highlighted by the colour) become significant close to the slack strand. Figure IV-15 shows a similar plot in a 2D space. The two dotted curves show the relative link tension plot for the two extreme ratios. The solid line plot shows the path followed with a varying tension ratio.
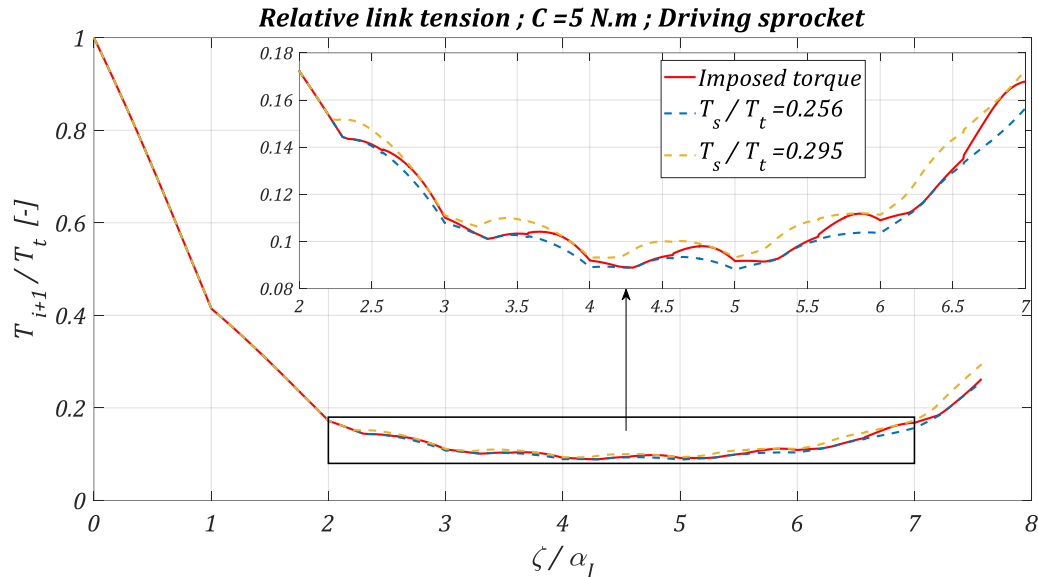
Figure IV-15: Relative link tension bounded by the two extreme tension ratio conditions

The solid line travels back-and-forth between the two extreme ratio conditions resulting in link tension oscillations. Consistently with Figure IV-12, Figure IV-15 also shows superimposed curves for the first drive periods.

The oscillations in the link tension and contact force curves have multiple sources. The loading conditions imposed in this work cause variations of the tight and slack strand tensions. Consequently, the tension ratio also varies. Because of these specific constraints, the roller location can exhibit non-monotonic motion (called back-and-forth motion). In the model definition (see §II.2), it was assumed that the sign of the friction correction angle δ is dependent only on the location of the first roller $s_{c,1}$. This assumption implies that the motion of every roller is monotonic and depends only on the zone in which the first roller lies (zone 2 or 3, see §II.2). Therefore, the back-and-forth roller motions are in contradiction with this hypothesis. Indeed, the friction force should oppose the roller motion and therefore switch sides (*i.e.*, the friction angle should switch signs) each time the roller motion changes direction. However, no satisfactory model for this phenomenon could be developed in this work. It is therefore still assumed that the correction angle depends only on the location of the first roller even in the presence of back-and-forth roller motion. More details about the condition of appearance of this non-monotonic roller motion are given in the Appendix G.

Typical examples of industrial drives have been analysed. The results show that roller location and load (link tension and contact force) are intertwined. The influence of the tooth profile geometry was tested. The results show that the decreasing and increasing slopes both in link tension and contact force vary depending on the profile, steep slopes being associated with higher maximum contact forces and longer roller displacements. The comparison of driving and driven sprockets show that the slopes

associated with the driven sprocket are steeper, with the same correlations with maximum contact force and roller displacement (longer roller displacement and higher maximum).

Significant oscillations are present in all the curves analysed. These oscillations were not reported in the work of Kim & Johnson [52] and Naji & Marshek [2], [62]. The source of this phenomenon comes from the differences between the models. In this manuscript, the model considers a whole drive with the dependency between strands and sprockets. Therefore, both strand tensions vary resulting in variations of the tension ratio. The influence of the variation of T_t and T_s/T_t on the oscillations has been studied. Not all the profiles (*i.e., ASA, NF_{max} and NF_{min}*) react to this perturbation in the same way. The significance of the oscillations in loads decreases as the driving torque increases. The opposite is observed for roller location. In some cases, back-and-forth roller motions have been reported. These specific non-monotonic motions are in contradiction with the hypotheses stated for friction correction (monotonic roller motion with direction given by the first roller location $s_{c,1}$).

The analysis of industrial drives demonstrates the influence of tooth profile geometry on chain drive behaviour. Based on this first assessment, the following part proposes original methods to characterise tooth profile properties.

IV.2   Tooth profile analysis methods

IV.2.1   Pressure angle at the transition point ϕ_{tp}

For the loading conditions explored in the previous part, and for both driving and driven sprockets, the rollers first lie at the tp before starting to cross the profile at different instants depending on the tooth profile (*i.e.*, ASA, NF_{max} and NF_{min}), loading conditions, *etc*. Similarities have been observed in the differences between tooth profiles and between driving and driven sprockets, suggesting that the same phenomenon could explain both.

Figure IV-16 shows plots of the pressure angle ϕ_i for the driving and driven sprocket (at $C_I = 50N.m$).
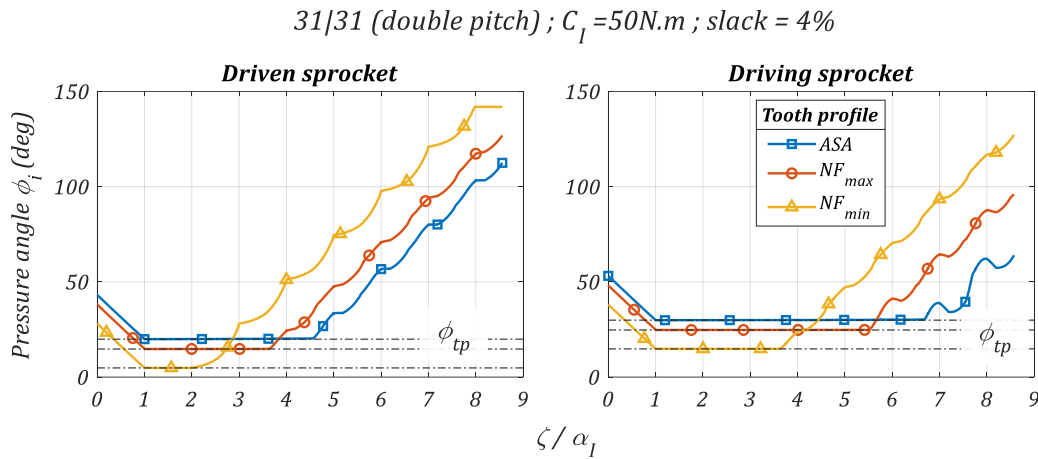
Figure IV-16: Pressure angle ϕ_i for driving and driven sprocket

The evolution of ϕ_i is consistent with the roller location variations (see Figure IV-7 and Figure IV-8). Indeed, the pressure angle depends on the directions of the previous link and profile normal at the roller/profile contact point (see §II.2). When the rollers lie at the transition point, both directions are almost unchanged. Consequently, the pressure angle ϕ_i obtained is also constant. As soon as the roller starts crossing the tooth profile, the normal direction changes and the pressure angle increases. When the profile is entirely crossed (*e.g.*, for NF_{min} driven sprocket) the pressure angle stabilises at a new plateau as the roller reaches the second transition point tp^A. The link meshing is visible between $\zeta/\alpha_I = 0$ and 1 where an initial decrease occurs as α_t is increasing (see Figure IV-16).

Similarly, the evolution of the articulation angle α_i^* is shown in Figure IV-17. The link meshing and un-meshing are clearly visible as α_i^* goes from 0 (roller capture) to about α_j when a new roller is captured ($\zeta/\alpha_I = 1$). The un-meshing shows the inverse variation. Apart from this, the articulation angle remains almost constant and very close to the pitch angle α_j despite the roller location variations. Small angle variations are visible with the greatest deviation from the pitch angle value occurring one drive period before the roller starts to cross the profile. This corresponds to the following roller (*i.e.*, roller $i+1$) starting to cross the profile. The biggest deviation is observed for the NF_{max} profile, certainly because this profile has the biggest roller/tooth bottom clearance, therefore resulting in the biggest gap between roller centres and pitch circle (see Figure IV-3).
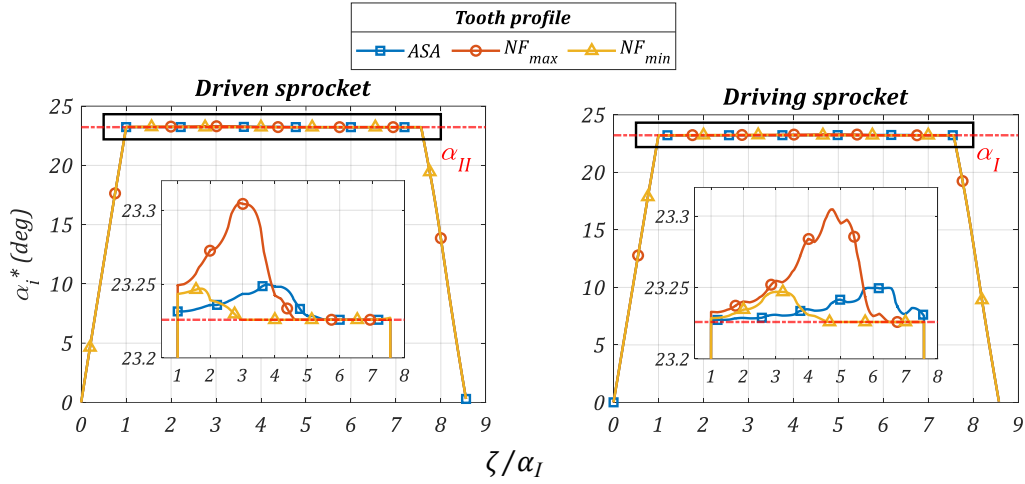
Figure IV-17: Articulation angle for the driving and driven sprockets

Besides the meshing and un-meshing process, the articulation angle α_i^* is nearly constant and only the pressure angle ϕ_i varies in first approximation.

The value of ϕ_i at the transition point is characteristic of a given tooth profile and called ϕ_{tp}. The difference between driving and driven sprockets is exactly $2|\delta(\infty)| = 2 \times 5° = 10°$ (see Figure IV-16). It is therefore due to the influence of the friction correction angle δ. A pressure angle can be associated with both transition points. Their values are obtained numerically knowing the tooth profile definition. Table IV-4 shows the value of $\phi_{tp}\big|_B$ and $\phi_{tp}\big|_A$ for the three profiles studied before the friction correction. As for the other transition point properties, ϕ_{tp} (without mentioning A or B) designates $\phi_{tp}\big|_B$.

	ASA	**NF_{max}**	**NF_{min}**
$\phi_{tp}\big|_B$	24.87°	19.73°	9.83°
$\phi_{tp}\big|_A$	131.9°	137.0°	146.9°

Table IV-4: ϕ_{tp} without friction correction for ASA, NF_{max} and NF_{min} tooth profiles

The eq.(II-27) showed that the ratio between T_{i+1} and T_i depends on the pressure angle ϕ_i and the articulation angle α_i^*. Considering in first approximation that the articulation angle equals α_j, smaller values of ϕ result in smaller T_{i+1}/T_i ratios (*i.e.*, a tooth caring more load). The contact force shows the same trend (see eq.(II-27)). Therefore, the differences observed between profiles can be analysed considering parameter ϕ_{tp}. Profiles with smaller ϕ_{tp} value (*e.g.*, NF_{min}, see Table IV-4) are associated with steeper slopes both in link tension and contact force slopes, and greater roller location variations. Due to friction, the value of ϕ_{tp} is corrected by $\pm|\delta(\infty)|$ depending on the sprocket being driving or driven. The similarities observed between a driving NF_{min} and driven NF_{max} profile are therefore explained by the similar corrected pressure angle $\phi_{tp} \pm |\delta(\infty)|$ (about 14.7°, see Figure IV-16).

$\phi_{tp}\big|_B$ is associated with the decreasing link tension slope. Similarly, $\phi_{tp}\big|_A$ is associated with the renewed increase in link tension (and contact force) when the rollers reach the slack side of the tooth profile. As the industrial profiles are symmetrical, $\phi_{tp}\big|_A$ is as large as the pressure angle at tp^B (*i.e.*, $\phi_{tp}\big|_B$) is small (see Table IV-4).

$\phi_{tp}\big|_B$ corresponds to the "tooth pressure angle for a new chain" given in the ASA standard [32]. This angle is calculated analytically for the ASA profile assuming that the two rollers (roller $i-1$ and i needed to calculate ϕ_i) are seated and that the contact point lies at the transition between the seating and working curve (*i.e.*, at point B, see Appendix A corresponding to $\gamma = 5$).

The pressure angles $\phi_{tp}\big|_{A,B}$ change with the number of teeth according to a function specific to each tooth profile. However, hierarchy between tooth profiles, in terms of ϕ_{tp}, is usually respected. For instance, a NF_{min} profile always has smaller ϕ_{tp} than an ASA one with the same teeth number. More information about this point will be given in §IV.3.1.

IV.2.2   Pressure angle characteristic curve

In the previous part, the influence of the tooth profile for loading conditions such that the rollers tend to cross the profile (*i.e.*, $s_{c,1} < s_{c,tp}$) has been explored. ϕ_{tp} proves to be a good parameter to analyse the tooth profile's influence in these conditions. The following section now explores the limit tension ratio $(T_s/T_t)_{lim}$ for each profile below which no mechanical solution is possible (see §II.2). Exploring these extreme loading conditions will demonstrate the interest of the second analysis tool: the pressure angle characteristic curve.

During a drive period, the meshing angles $\alpha_{s,t,j}$ and the number of links in contact change for a given sprocket. These parameters modify the dependence between $s_{c,1}$ and T_s/T_t (see §II.2 and eq.(II-31)), therefore modifying the limit tension ratio.
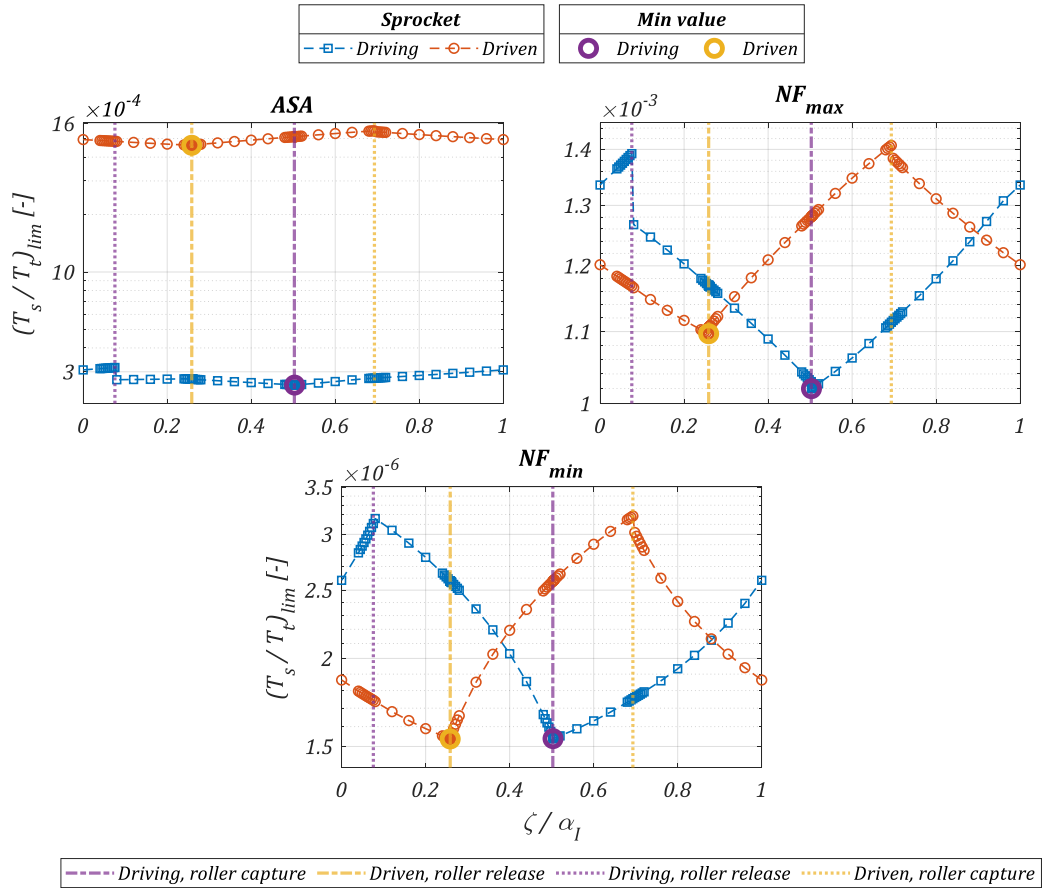
Figure IV-18: Limit tension ratio for each sub-position within a drive period

Figure IV-18 shows the significant variation of the limit tension ratio for all sub-positions within a drive period. For instance, for the NF_{min} profile, the limit ratio can vary up to 100% (from approximately $1.5e^{-6}$ to $3e^{-6}$). Discontinuities are visible at the roller capture and release events. They are a consequence of the compatibility between sub-models. The most favourable sub-positions (*i.e.*, that allow reaching the smaller tension ratio) are the same for all profiles. Indeed, all the conditions responsible for the variation of the limit ratio stem from the global kinematics, which is independent of the tooth profile geometry. For the driven (driving) sprocket, the most favourable sub-position is located immediately before (after) a new roller is released (captured). The influence of angles $\alpha_{t,j}$ therefore seems to be dominant on the limit tension ratio. These sub-positions correspond to $\zeta/\alpha_I \approx$ 0.5 and 0.26 for the driving and driven sprocket, respectively. The limit ratio varies greatly depending on the tooth profile considered. It can range from about $1e^{-3}$ for the NF_{max} profile to $1.5e^{-6}$ for the NF_{min}. In practice, this implies that the NF_{min} profile is able to withstand more severe loading conditions than the NF_{max}. The differences between driving or driven sprocket also depend on the profile. The ASA profile shows the greatest difference regarding this point with a driving sprocket able to endorse ratio about 5 times smaller than the driven (*i.e.*, about $3e^{-4}$ and $16e^{-4}$ for the driving and driven sprocket, respectively).

The differences between driving and driven sprockets can be analysed considering the relation between the location of roller 1 (*i.e.*, $s_{c,1}$) and the tension ration T_s/T_t (see §II.2) at a given sub-position. This relation is plotted in Figure IV-19 for the three profiles at the most favourable sub-position given above.
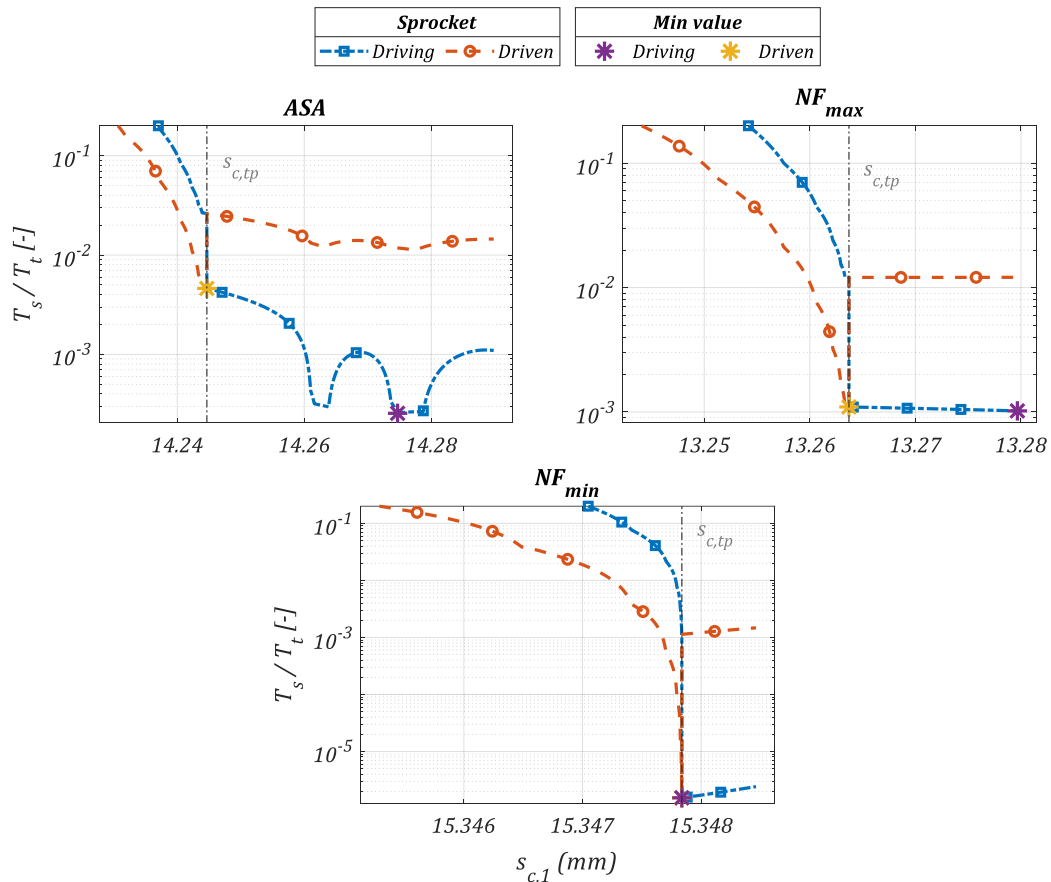
Figure IV-19: Relation between $s_{c,1}$ and T_s/T_t at the most favourable sub-position

Differences between driving and driven sprockets are caused by the friction correction angle δ. For a driving (driven) sprocket, the correction is positive (negative) before the tp (*i.e.*, $s_{c,1} < s_{c,tp}$) and negative (positive) after (*i.e.*, $s_{c,1} > s_{c,tp}$). The transition between the two extreme δ values occurs in the interval $\left[s_{c,tp} - a, s_{c,tp} + a\right]$.

As shown in Figure IV-18, the NF_{min} profile can reach ratios up to 100 times smaller than other profiles, mainly due to its small ϕ_{tp} value. Indeed, for values of $s_{c,1}$ before the transition point ($s_{c,1} < s_{c,tp}$), going closer to the tp allows reaching smaller ratios as all pressure angles tend to match ϕ_{tp}. Beyond the tp, the behaviour depends on the profile. For ASA and NF_{max}, the relation between $s_{c,1}$ and T_s/T_t is decreasing meaning that smaller ratios can be reached. On the contrary, for the NF_{min} profile, higher values of $s_{c,1}$ beyond the tp result in higher tension ratios. Due to the friction correction, driven sprockets reach their minimal tension ratio nearby the tp as the correction is not overcome even for profiles showing a decreasing relation beyond the tp (*e.g.*, ASA profile). Conversely, for the driving sprocket, friction correction favours cases with $s_{c,1} > s_{c,tp}$. Consequently, the ASA and NF_{max} profiles reach their minimal tension ratio beyond the transition point. For the NF_{min} profile, the minimum for the driving and driven sprocket are both reached by the tp (see Table IV-6). Contrary to the NF_{max} and NF_{min} profiles, the ASA profile shows considerable non-monotonic variation after the tp. For some ratios, up to 4 possible roller locations could therefore be suitable (see §II.3 for simultaneous $s_{c,1}$ solutions).

The minimal reachable tension ratios for all profiles are presented in Table IV-5. Table IV-6 gives the locations $\left(\bar{s}_{c,1}\right)_{lim}$ that allow reaching the minimal tension ratio. These locations are given relatively to the transition point $s_{c,tp}$ according to eq.(IV-3). Positive (negative) $\left(\bar{s}_{c,1}\right)_{lim}$ corresponds to the minimal ratio being reached after (before) the transition point.

$$\left(\bar{s}_{c,1}\right)_{lim} = s_{c,1} - s_{c,tp} \qquad\qquad \textbf{\textit{(IV-3)}}$$

	ASA	NF_{max}	NF_{min}
Driving	$2.55e^{-4}$	$1.02e^{-3}$	$1.54e^{-6}$
Driven	$4.61e^{-3}$	$1.10e^{-3}$	$1.54e^{-6}$

Table IV-5: Minimal tension ratio for driving and driven sprocket

	ASA	NF_{max}	NF_{min}
Driving	$3.00e^{-5}\ m$	$1.60e^{-5}\ m$	$2.63e^{-10}\ m$
Driven	$-4.37e^{-9}\ m$	$-1.53e^{-9}\ m$	$-1.08e^{-9}\ m$

Table IV-6: $\left(\bar{s}_{c,1}\right)_{lim}$ for ASA, NF_{max} and NF_{min} sprockets

It can be observed that the driven sprockets always reach their minimal ratios before the transition point (*i.e.*, $\left(\bar{s}_{c,1}\right)_{lim} < s_{c,tp}$) while the driving ones reach theirs before the tp. Therefore, the minimal ratio is always reached in the zone of negative friction correction. Moreover, driven sprockets always reach their minimum very close to the tp (*i.e.*, $\left(\bar{s}_{c,1}\right)_{lim} \approx 1e^{-9}m$) while it can be attained further for driving sprockets (see Figure IV-19).

Reaching the minimum ratio before or after the transition point has consequences for the locations of all the rollers in contact with the sprocket. According to the adjacent location characteristic curve (see §II.2), when the roller location $s_{c,1}$ is beyond the transition point, locations of following rollers tend to infinity. And the more the initial roller location exceeds s_{tp}, the more the rollers will climb the tooth flank until one eventually misses a tooth, resulting in a chain drop. Figure IV-20 shows the resulting

roller location for a driven (a) and a driving sprocket (b) at the minimal ratio configuration (both with ASA profile). For the driven profile, as $s_{c,1}$ is nearby the transition point, all the rollers remain approximately at the same location. For the driving one however, the location tends to infinity and the rollers climb the tooth flank.

(a)   **(b)**
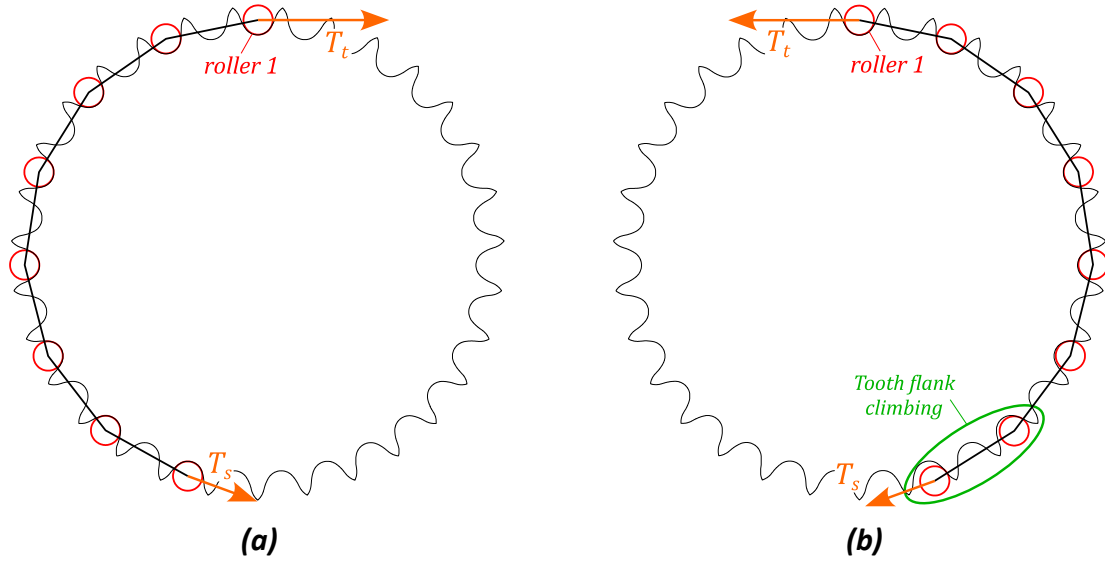
Figure IV-20: Roller location for the limit tension ratio (a) driven (b) driving ASA profile

It was mentioned in the previous part (§IV.2.1) that smaller tension ratios are reached for small pressure angle ϕ values. This angle is changed by the friction correction, explaining the differences between driving and driven sprockets. However, the pressure angle is mainly a consequence of the profile geometry. To appreciate the differences between tooth profiles, it is therefore useful to plot a second characteristic curve. In Figure IV-21, the pressure angle of roller $i + 1$ is plotted against the location of roller i (expressed using γ). For each possible roller location, the pressure angle characteristic curve shows the pressure angle of the following roller, therefore exhibiting its variation depending on the profile geometry.
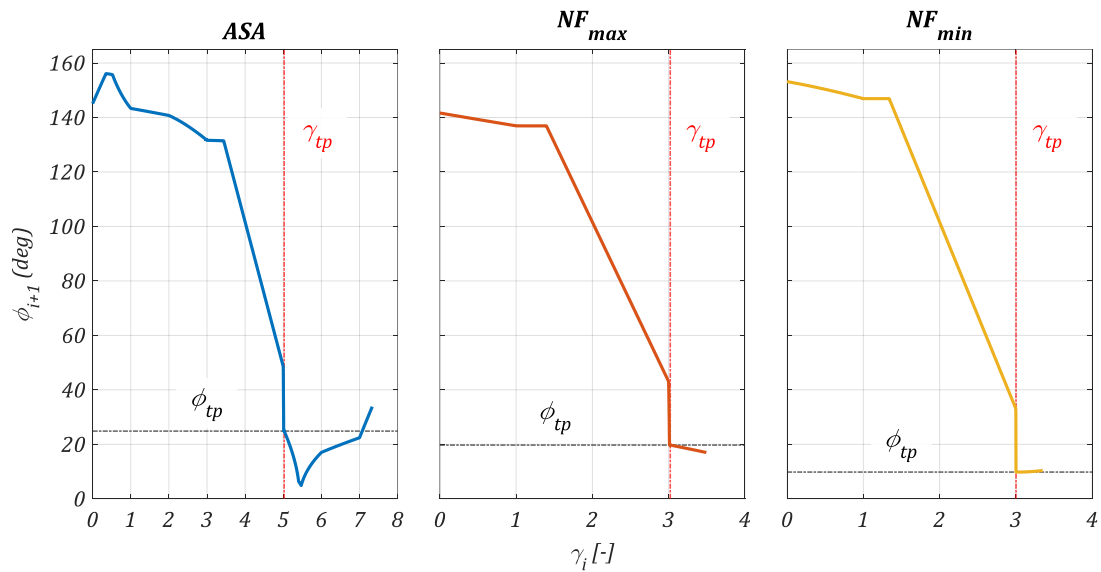
Figure IV-21: Pressure angle characteristic curves for ASA, NF_{max} and NF_{min} profiles

Going back to the pressure angle values presented in Table IV-4, the characteristic curve shows the symmetric property of the profiles studied. In particular, profiles with small ϕ_{tp} (*e.g.*, NF_{min}) also exhibit bigger pressure angles when the roller comes into contact with the opposite tooth flank.

This curve is not defined for all values of γ. Indeed, as for the adjacent roller location curve (see Figure II-21), for high γ_i values (*i.e.*, roller climbing the tooth flank), γ_{i+1} and therefore ϕ_{i+1} might not be defined.

The pressure angle at the transition point ϕ_{tp} can first be read on this curve, giving an indication on the profile's properties in terms of link tension, contact force and roller location (see §IV.2.1). Then, the curve shape, particularly after the transition point ($\gamma > \gamma_{tp}$) allows deducing the profile properties. For instance, it can be observed that the pressure angle increases after the tp for the NF_{min} profile. As a consequence, in terms of ϕ, there is no benefit for a roller to climb the tooth flank on this profile. This translates into a minimal ratio being reached by the transition point. Conversely, for the NF_{max} profile, the pressure angle keeps decreasing after the tp. This results in a limit ratio reached after the tp for a driving sprocket, as smaller ϕ values are obtained for a roller climbing the tooth flank. For ASA and NF_{max} driven sprockets, the benefit of climbing the tooth flank is unclear. Indeed, it allows reducing the pressure angle but along a positive friction correction. To explore these cases, the same characteristic curve is plotted in Figure IV-22 after adding the correction angle. The parameters used are still $|\delta(\infty)| = 5°$ and $a = 1e^{-10}m$.
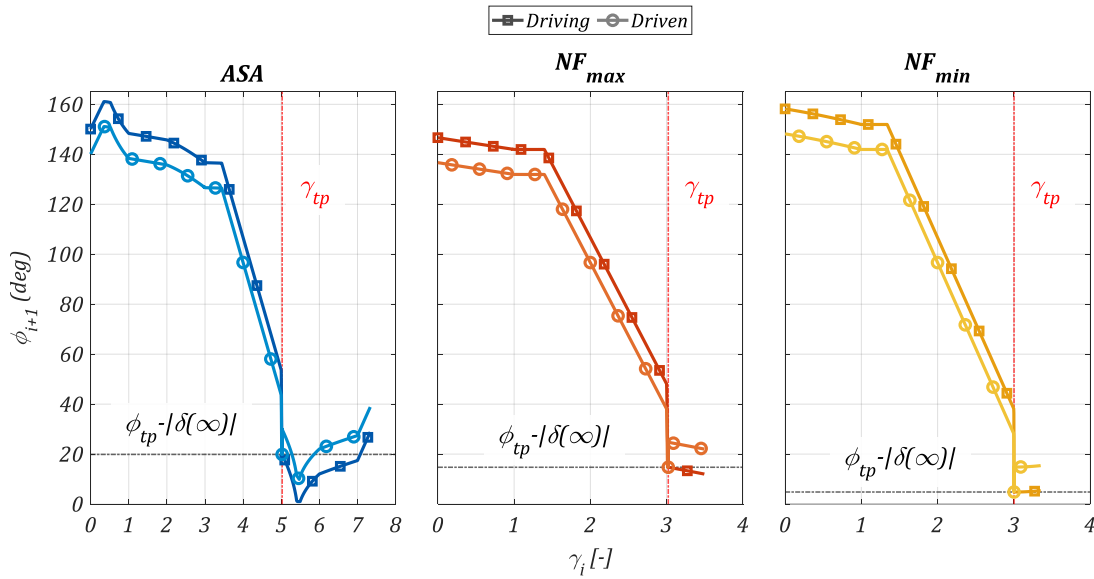
Figure IV-22: Pressure angle characteristic curves for ASA, NF_{max} and NF_{min} profile with friction correction

For the ASA profile, the corrected pressure angle $\phi - \delta$ can reach negative values for the smallest pressure angle immediately after the tp. A negative pressure angle value results in a sign switch in eq.(II-27), therefore translating into negative link tension. Such a specific condition would probably not occur on a regular chain drive. To prevent any perturbation, the value of the corrected pressure angle is bounded at 1°.

As a 5° correction angle was used, the driving and driven curves are always 10° apart. The correction sign switch is visible at the transition point. Both curves reached a corrected pressure angle of $\phi_{tp} - |\delta(\infty)|$ either immediately before or after the transition point. Based on this corrected curve, the case of a NF_{max} driven sprocket can be settled. The corrected curve shows that, even if the pressure angle

reduces after the tp, the decrease is not strong enough to overcome the positive correction resulting in a minimal pressure angle occurring at the tp. This explains why the minimal ratio was observed by the transition point (see Table IV-6). For a driven ASA sprocket, the interest of climbing the tooth flank cannot be clearly assessed. Indeed, it can be observed that the positive friction correction can be overcome as smaller pressure angles are possible after the tp even with the $+5°$ handicap. However, Figure IV-22 shows only the pressure angle for the roller $i + 1$, not for all the following ones. Therefore, even if one roller can reach a smaller pressure angle, the following ones might have a location such that their pressure angle is greater than the preceding one, potentially cancelling the benefit obtained. These complex effects can be appreciated by directly plotting the relation between $s_{c,1}$ and T_s/T_t as presented in Figure IV-19. For the example (ASA driven sprocket) considered, there is no advantage as the minimal ratio is reached by the tp. But for other cases, for instance with more rollers in contact with the driven sprocket or with a smaller friction correction, the relation would change and maybe result in another roller location for the limit ratio.

Apart from the question of the driven ASA profile, the analysis of the pressure angle characteristic curve allows deducing the behaviour of the profile under maximal load.

The effect of tooth profile geometry on a chain drive can be summarised as follows. When the loading conditions allow stable operations ($s_{c,1} < s_{c,tp}$), the pressure angle at the transition point ϕ_{tp} proves to be a good tool for analysing the profile's influence. Profiles with smaller ϕ_{tp} tend to withstand more load on each tooth, resulting in steeper slopes in the load variation (for both increase and decrease). The tooth profile also influences the limit tension ratio that a sprocket can support before chain drop occurs. Depending on the profile geometry, the rollers might tend to climb the tooth flank to reach smaller pressure angles. This phenomenon usually occurs for the driving sprocket as the negative friction correction intensifies the potential reduction of the pressure angle. Conversely, driven sprockets should reach their limit tension ratio nearby the transition point as the positive friction correction undergone when climbing the tooth flank usually cancels the possible benefit relating to the pressure angle. However, these conclusions depend on the correction angle $|\delta(\infty)|$. A smaller correction angle favours possible tooth flank climbing.

IV.2.3 Simplified analysis, the three sprocket behaviours

Based on the three sub-models presented by Lodge & Burgess [70] and considering the results of the previous parts, roller motions can be split into three different behaviours (see Figure IV-23).

- Inter-tp behaviour. When $s_{c,1} < s_{c,tp} - a$, all rollers are corrected with $\delta = +|\delta(\infty)| = +\text{atan}(\mu_\delta)$ for driving sprockets ($\delta = -|\delta(\infty)| = -\text{atan}(\mu_\delta)$ for driven ones). The roller locations tend more or less quickly to $s_{c,tp}^A$ depending on the loading conditions. In this zone, the behaviour of the model is similar to Kim & Johnson's model [52]. The GPLD model [2], [70], [81] is a first approximation of this behaviour.

- Static roller behaviour. When $s_{c,1} \in [s_{c,tp} - a, s_{c,tp} + a]$, all the rollers are corrected with the same $\delta \in [-\text{atan}(\mu_\delta), +\text{atan}(\mu_\delta)]$ depending on loading conditions. Moreover, as $s_{c,1}$ is very close to the transition point, all the roller locations stay almost the same. In this zone, the friction correction angle "adjusts" to the loading conditions with almost no consequences on roller location. The model is then similar to what Lodge & Burgess called the "static roller model" [70].

- Tooth climbing behaviour. When $s_{c,1} > s_{c,tp} + a$, all the rollers are corrected with $\delta = -|\delta(\infty)| = -\text{atan}(\mu_\delta)$ for driving sprockets ($\delta = +|\delta(\infty)| = +\text{atan}(\mu_\delta)$ for driven ones).

The roller locations tend to climb the tooth flank. In this zone, the behaviour resembles the "low slack tension" model again presented by Lodge & Burgess [70].

(a)

(b)
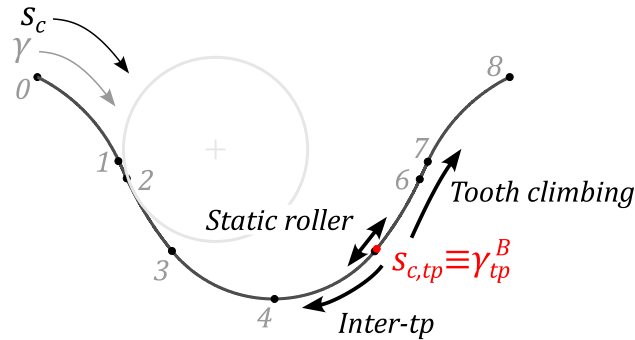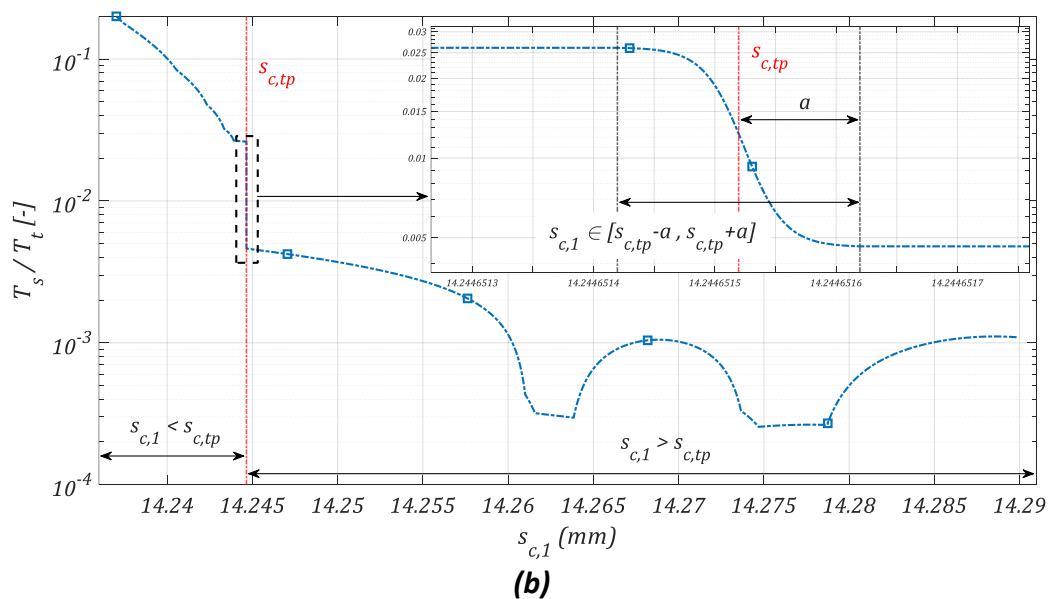
Figure IV-23: Three zones in the relation between roller location and tension ratio (driving ASA profile at the most favourable sub-position, see Figure IV-19)

The behaviour in which each sprocket lies depend on the loading conditions applied, and on the tooth profile used. Going toward small tension ratio (more extreme loading conditions), the sprocket first exhibits inter-tp behaviour. Then, as the ratio reduces, the rollers increasingly stay nearby the tp until they all stick to it in a static roller behaviour. Then, depending on the geometry and the sprocket being driving or driven, the roller may tend to climb the tooth flank in order to reach smaller tension ratios. However, as shown in §IV.2.2, the interest of the tooth climbing behaviour is not present for all profiles.

For driven sprockets, due to the negative friction correction undergone before the tp, the reachable tension ratios in inter-tp behaviour overlap those of the static roller one. The inter-tp behaviour also usually overlaps the tooth climbing behaviour. However, this last point depends on the profile geometry and, the friction correction angle (see Figure IV-24 and Figure IV-22). This results in simultaneous solutions (see Figure IV-24). As in this work, the solution with the smallest roller location is always preferred (see §II.3), the inter-tp branch is always chosen. This point was already addressed as choice between sub-models by Lodge and Burgess in [70] and the GPLD model (corresponding to the inter-tp behaviour) was also preferred.
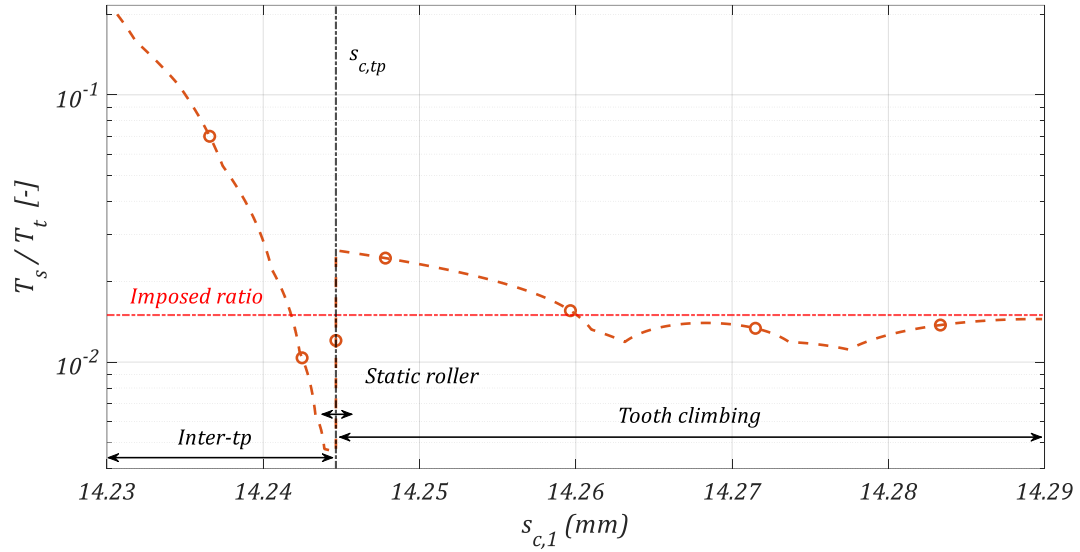
Figure IV-24: Three zones in the relation between roller location and tension ratio (Driven ASA profile at the most favourable sub-position, see Figure IV-19)

The three different behaviours are illustrated in Figure IV-25 for a driving torque of $C_I = 600N.m$ (the driven sprocket uses the NF_{min} profile to withstand the applied load). For this specific loading condition, the NF_{min} sprocket is situated in the inter-tp behaviour while the NF_{max} is in static roller behaviour and the ASA is in tooth climbing one.

$31/31$ (double pitch) ; Driving sprocket ; C_I =600N.m ; slack = 4%
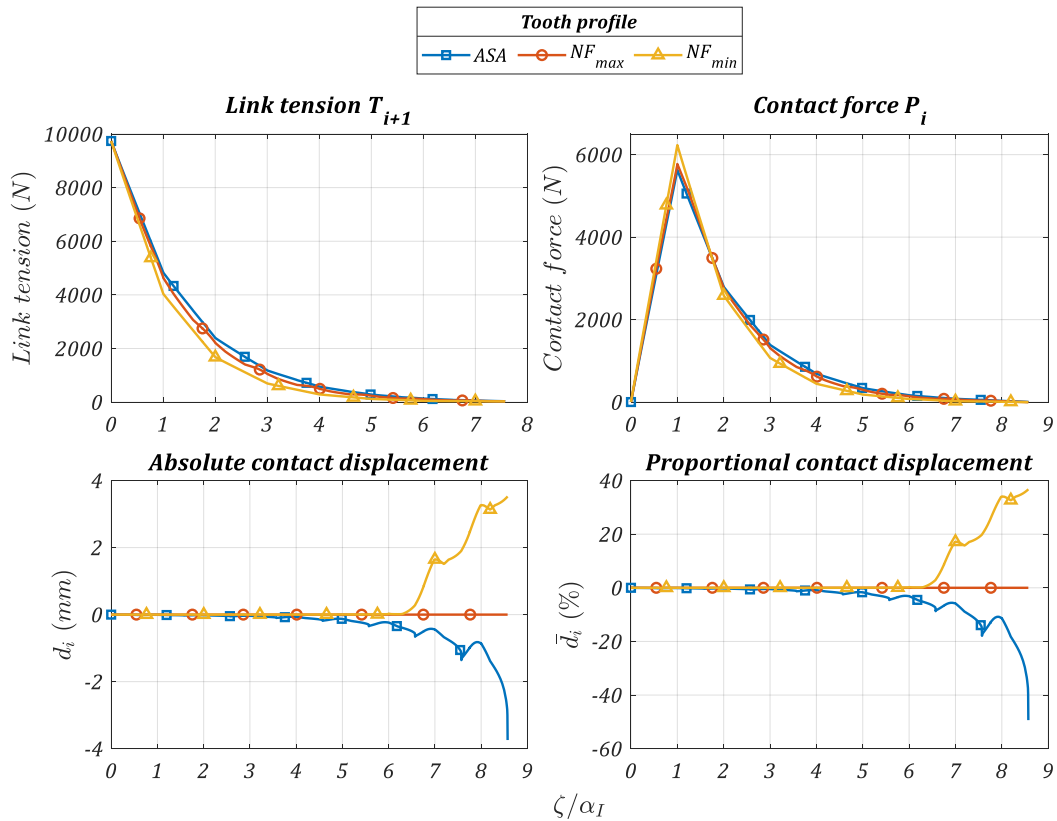
Figure IV-25: Link tension, contact force and roller location for $C_I = 600N.m$, driving sprocket

In the static roller behaviour, all the rollers are nearby the tp and the friction correction adjusts to the loading conditions. Therefore, two profiles are not discernible as the pressure angles (constant for all rollers in this case) adjusts to the same value for both profiles to match the loading conditions. An example is given in Figure IV-26 where both the ASA and NF_{max} profiles are in the static roller behaviour (still with NF_{min} driven sprocket).

31/31 (double pitch) ; Driving sprocket ; C_I =200N.m ; slack = 4%
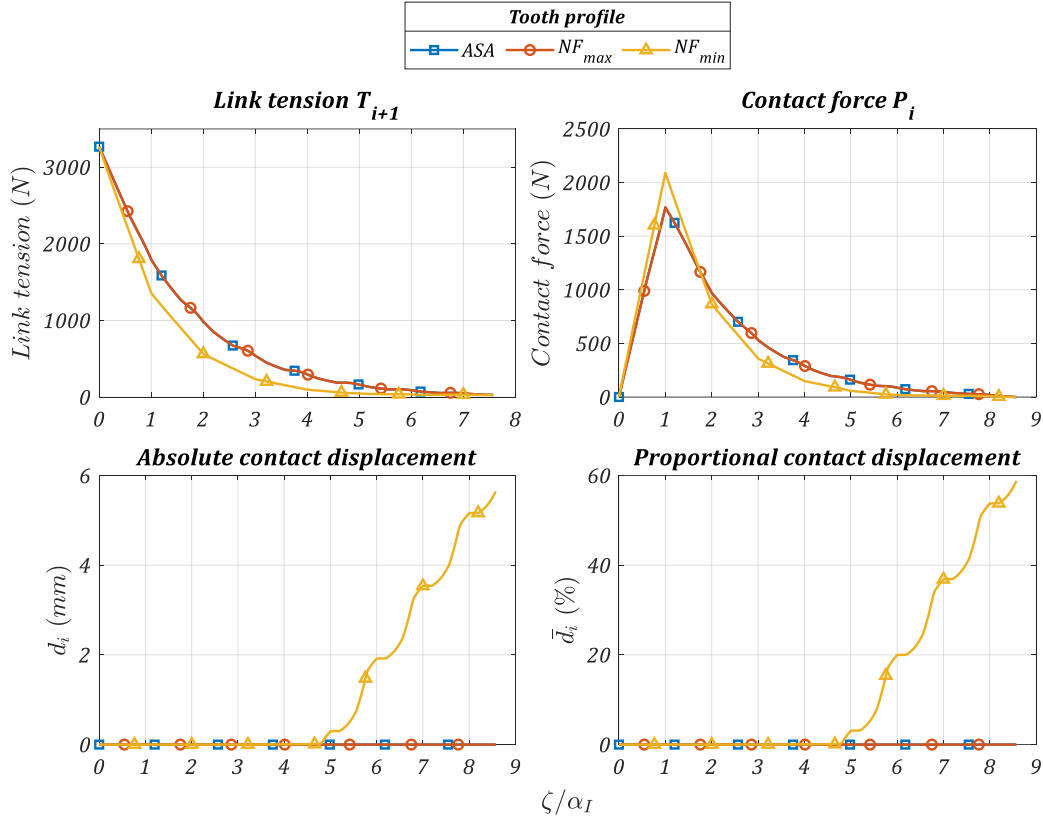
Figure IV-26: Link tension, contact force and roller location for $C_I = 200N.m$, driving sprocket

However, the zone of static roller behaviour depends on the profile used. Therefore, the NF_{max} profile is able to reach smaller ratios in static roller behaviour than the ASA as its ϕ_{tp} is also smaller.

It should also be noted that the existence of static roller behaviour depends on the chosen a parameter (tanh width). Indeed, for this behaviour to exist, the transition of δ between $-\text{atan}(\mu_\delta)$ and $+\text{atan}(\mu_\delta)$ (or the reverse for driving sprockets) must be able to occur within a "static roller zone" where the roller location remains approximately the same. This zone could for instance be defined as the first roller locations $s_{c,1}$ such that all the following rollers remain "close to the transition point". The comparison of the interval width obtained with a would give an indication of the existence of the static roller behaviour.

An example is carried out with an ASA 31 teeth double pitch sprocket in contact with 9 rollers. Rollers are considered "close to the tp" in a zone of $2\mu m$ width and centered at the tp, corresponding to the interval $[s_{c,tp} - 1\mu m, s_{c,tp} + 1\mu m]$. The interval obtained for $s_{c,1}$, ensuring that all the following rollers remain in the $2\mu m$ zone, is approximately $[s_{c,tp} - 1e^{-8}m, s_{c,tp} + 1e^{-8}m]$. The width of this resulting "static roller zone" for $s_{c,1}$ remains significantly bigger than $a = 1e^{-10}m$, resulting in the existence of the static roller behaviour. However, this analysis is difficult to generalise as it depends on the tooth profile and the number of links in contact with the sprocket. For more information about the value of a, see Appendix F.

This part was dedicated the introduction of analysis methods used to characterise tooth profile properties. The pressure angle at the transition point ϕ_{tp} was introduced. This parameter gives information about the profile's ability to support loads, with low ϕ_{tp} being associated with high loading capacity. The different slopes in link tension and contact force observed in §IV.1 can be analysed using this parameter. The limit tension ratio $(T_s/T_t)_{lim}$ of each tooth profile was then presented. Differences between profiles and between driving and driven sprockets were observed. Driven sprockets reach their minimal ratio nearby the transition point, while driving ones might tend to climb the tooth flank to reach smaller tension ratios (*e.g.*, ASA and NF_{max} profiles). Pressure angle characteristic curves, with and without friction correction, were introduced to characterise profile properties. These curves give information about the pressure angle evolution depending on roller location and represents tooth profile properties, such as the tendency to climb the tooth flank to reach small tension ratios.

Then, an analysis of the model based on three characteristic behaviours was presented (in a similar way to Lodge & Burgess in [70]). The three behaviours are inter-tp, static roller and tooth climbing. The appearance of each behaviour depends on the tooth profile used and the loading conditions applied.

In the following part, a typical track cycling drive is presented and the analysis methods proposed are applied to this specific case.

IV.3 Application to track cycling drives

The conclusions of the previous parts are now applied to the context of track cycling drives. These drives are characterised by large numbers of teeth at the driving sprocket (called chainring) compared to the driven one (called rear cog). The looseness of the slack strand is usually higher than in industrial contexts and the driving torque can reach up to $300N.m$ sustained for several drive rotations (see Chapter I).

A typical track cycling drive is considered. The numbers of teeth are $Z_I|Z_{II} = 60|15$. The slack strand is set at 11% (see drive parameters in Table IV-2). A typical track cycling chain is used (its characteristics are given in Table IV-8). Sprockets and chain pitches match at $12.7mm$ and $\Delta Y = -50mm$. The general aspect of the drive is presented in Figure IV-27 and the global kinematics, again obtained with $\psi_{t,I}\big|_{init} = 0$ is presented in Figure IV-28.

$Z_I|Z_{II}$	L	ΔY	$slack$	$|\delta(\infty)|$
60|15	≈ 385mm	$-50mm$	11%	5°

Table IV-7: **Parameters** *of the* $60|15$ *double pitch drive*

Pitch p	D_{roller}	m_{link}
$1/2'' = 12.7mm$	$7.75mm$	$3.6g$

Table IV-8: Characteristics of the typical track cycling chain
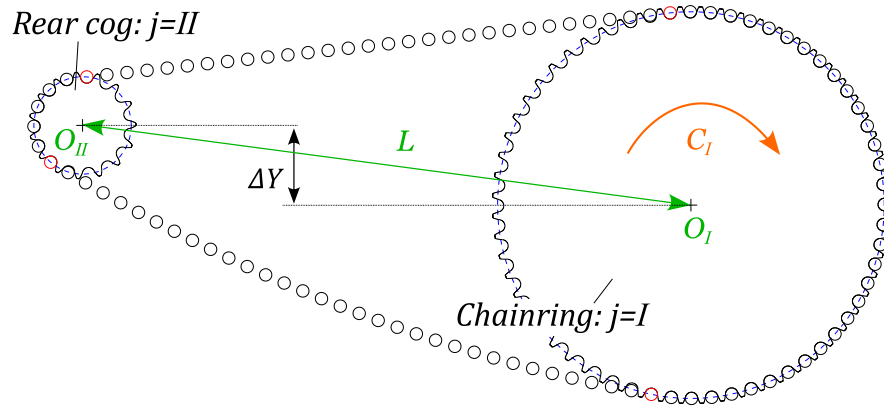
Figure IV-27: General view of the $60|15$ *track cycling drive (* $slack = 11\%$ *)*
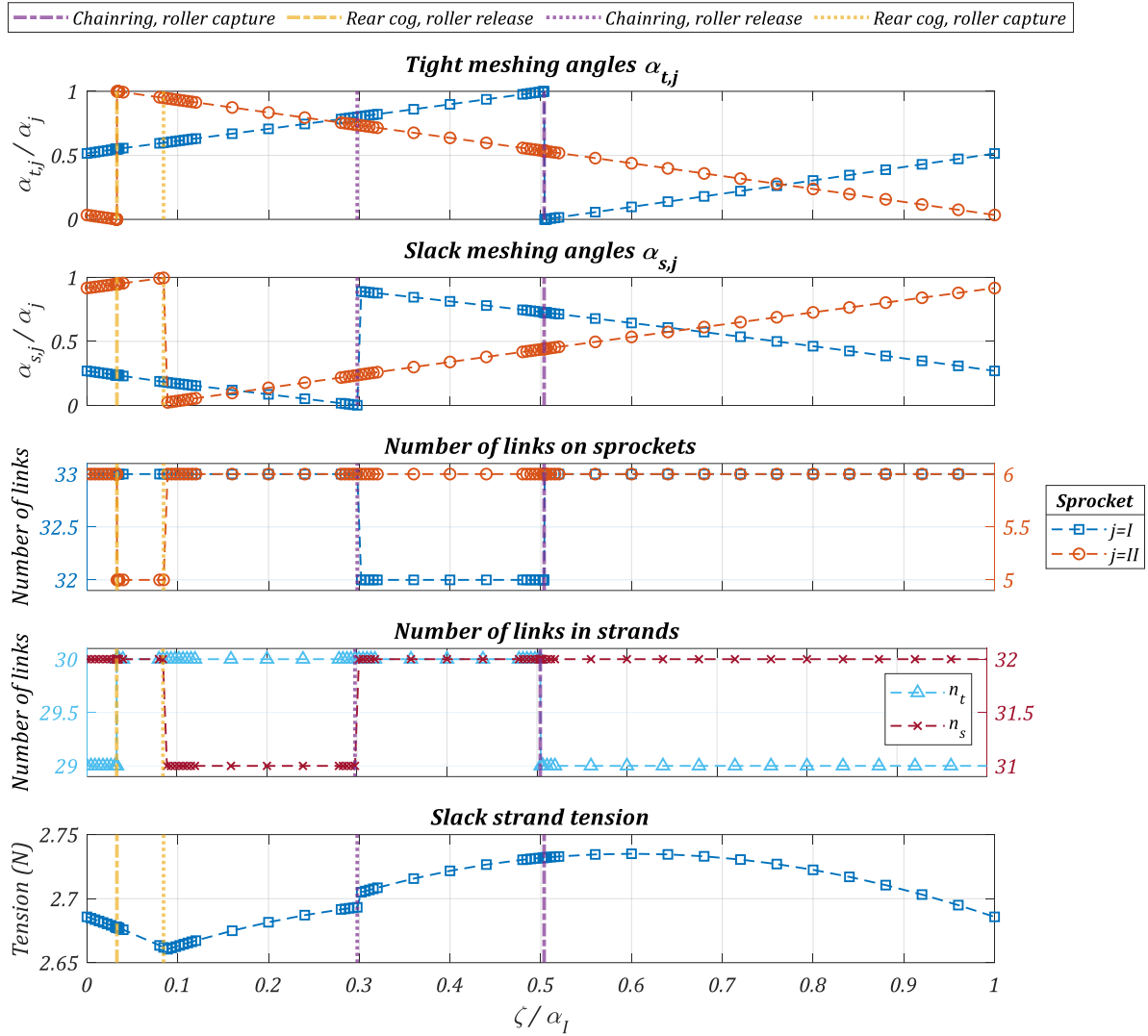
Figure IV-28: Global kinematics of the $60|15$ track cycling drive

As for the 31|31 drive, the number of links in contact with the driving (chainring) and driven (rear cog) sprocket vary. However, as the number of teeth differs between the chainring and rear cog, so do the number of links in contact n_j. The slack tension also varies (only $T_{s,I}$ is plotted as the slack tension is almost equal for both sprockets) and exhibits discontinuities at the event of roller capture and release relative to the slack strand. Unlike the symmetric 31|31 drive studied in §IV.1, the slack strand tension is not the same at the event of roller capture (release) by the chainring and release (capture) by the rear cog. This is due to the drive not being symmetric ($Z_I \neq Z_{II}$ and $\Delta Y \neq 0$). However, the main difference between industrial and track cycling drives comes from the magnitude of the slack strand tension. Indeed, as the track cycling chain is lighter, the resulting tension is smaller and only reaches about $2.7N$ in this example. As torques applied to track cycling drives are very high (up to $300N.m$ on the chainring maintained for several chainring revolutions), the resulting tension ratios applied to the sprockets are significantly lower than in the preceding industrial example. For the $60|15$ drive, a driving torque of $C_I = 300N.m$ results in a tension ratio $T_s/T_t = 1.2e^{-3}$. This ratio is typically within the limit ratio zone presented in Figure IV-19 and Table IV-5. Therefore, not all the profiles might be able to withstand the ratios encountered in track cycling applications.

However, limit ratios are specific to a given profile, number of teeth, and sub-position. It can therefore be fastidious to check the limit of each possible sprocket. A more general approach to quickly assess the capability of each sprocket depending of the profile used is presented in the following part.

IV.3.1   Limit tension ratio in stable working conditions

It was shown in the previous part (§IV.2) that the limit ratio is reached either with all rollers lying nearby the tp or with rollers climbing the tooth flank depending on the profile and sprocket being driving or driven. In a track cycling context, the risk of chain drop must be reduced. Therefore, tooth climbing behaviour (where rollers climb the tooth flank) in not desirable. As a consequence, the limit ratio in stable working conditions $(T_s/T_t)_{lim,tp}$ is defined as the smallest reachable tension ratio considering only inter-tp and static roller behaviour.

As shown before (see §IV.2), the minimal reachable ratio, excluding tooth climbing behaviour, is obtained in static roller with a negative friction correction $\delta = -|\delta(\infty)|$, for both driving and driven sprockets. When all the rollers lie nearby the tp, Figure IV-17 shows that the articulation angles α^* remains almost equal to the pitch angle α. This leads to the following approximate tension ratio expression for all the rollers stuck at the tp with a negative friction correction.

$$\frac{T_s}{T_t} = \prod_{i=1}^{n+1} \frac{\sin(\phi_i - |\delta(\infty)|)}{\sin(\phi_i - |\delta(\infty)| + \alpha_i^*)} \qquad \textbf{\textit{(IV-4)}}$$

with:
- n, the number of links in contact with the sprocket considered
- $\phi_i = \phi_{tp}$ for $i \in [\![2,n]\!]$
- $\alpha_i^* = \alpha$ for $i \in [\![2,n]\!]$

In eq.(IV-4), for the first and last roller in contact ($i = 1$ and $n + 1$), angles ϕ_i and α_i^* vary, therefore influencing the tension ratio. In order to obtain an expression independent of any sub-position related parameter, the effect of the first and last roller ($i = 1$ and $n + 1$) is considered to be equivalent to one articulation with angle $\phi_i = \phi_{tp}$ and $\alpha_i^* = \alpha$. Therefore, the expression for the limit ratio in stable working conditions is given in eq.(IV-5).

$$\left(\frac{T_s}{T_t}\right)_{lim,tp} = \left(\frac{\sin(\phi_{tp} - |\delta(\infty)|)}{\sin(\phi_{tp} - |\delta(\infty)| + \alpha)}\right)^N \qquad \textbf{\textit{(IV-5)}}$$

with:
- $N = \text{floor}(Z/2) - 1$, the equivalent number of links (floor designates a round down operation).

The equivalent number of links N can be adjusted to the application. In this case, it is set at $\text{floor}(Z/2) - 1$ to be representative of a rear cog in track cycling applications. Indeed, as the chainring is usually significantly bigger than the rear cog, the number of links in contact with the rear cog is smaller than $Z/2$ (see Figure IV-28).

Based on the definition given by Binder in [32] for the "pressure angle for a new chain", the pressure angle at the transition point can usually be approximated with the general expression given in eq. (IV-6).

$$\phi_{tp} = K - \frac{K'}{Z} \tag{IV-6}$$

with:

- K and K' numerical constants fitted for each tooth profile

Constants K and K', obtained for ASA, NF_{max} and NF_{min} sprockets of pitch $p = 12.7mm$ used with a chain of matching pitch, and $D_{roller} = 7.75mm$ are presented in Table IV-9.

	ASA	NF_{max}	NF_{min}
K (deg)	34.64	29.96	20
K' (deg)	123	137.1	135.5

Table IV-9: Constants K and K' for ASA, NF_{max} and NF_{min} profiles

Using eq. (IV-5) with the value of ϕ_{tp} calculated according to eq.(IV-6) allows plotting the limit tension ratio in stable working conditions as a function of the number of teeth (see Figure IV-29). A correction angle of $|\delta(\infty)| = 5°$ is used.
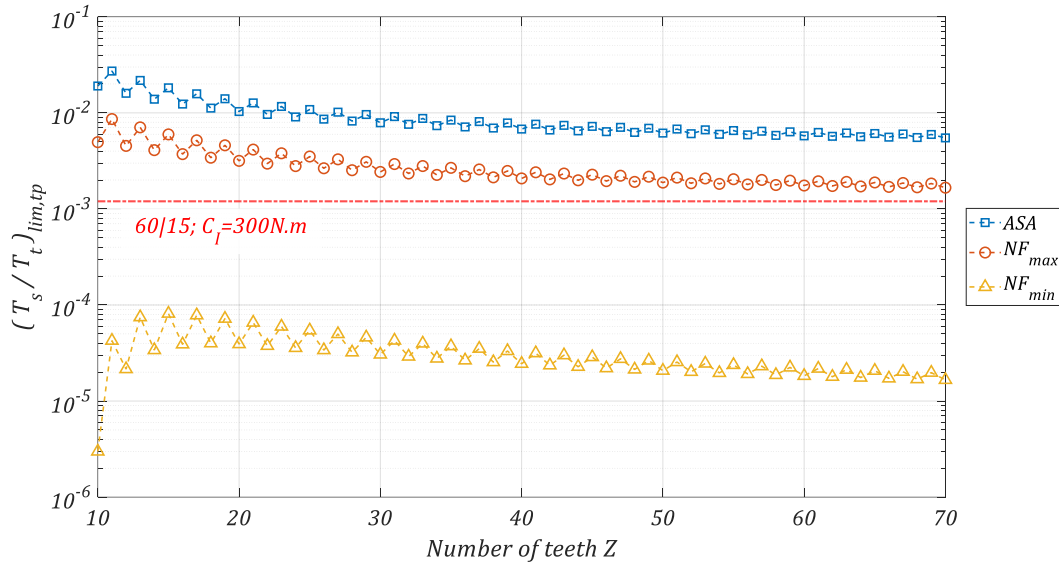
Figure IV-29: Limit tension ratio in stable working conditions for industrial profiles

The use of the equivalent number of links N (based on the floor function) causes oscillations for odd and even numbers of teeth. The order of magnitude of the tension ratio for the 60|15 drive with a driving torque $C_I = 300N.m$ is also represented.

The NF_{min} capacity to withstand more load than the other two profiles is clearly visible. The ASA profile carries lower load in stable working conditions due to its high ϕ_{tp}. Figure IV-29 shows that only the NF_{min} profile can be used in track cycling applications as the limit ratios are too high for the remaining profiles. Based on this assessment, and to study the influence of profile geometry on track cycling drives, three original tooth profile geometries are proposed. The definition of these new tooth geometries is based on the NF_{max} and NF_{min} ones (see Appendix A).

- The profiles are symmetric. Therefore, only one half is defined and the second one is deduced from symmetry about $(O, \vec{y})$, see Figure IV-30.

- The defined half is given by two tangent circle arcs (to ensure slope continuity). This configuration was chosen to match the standard (ISO 606 [31]). Moreover, it covers a great variety of geometries with a limited number of parameters.
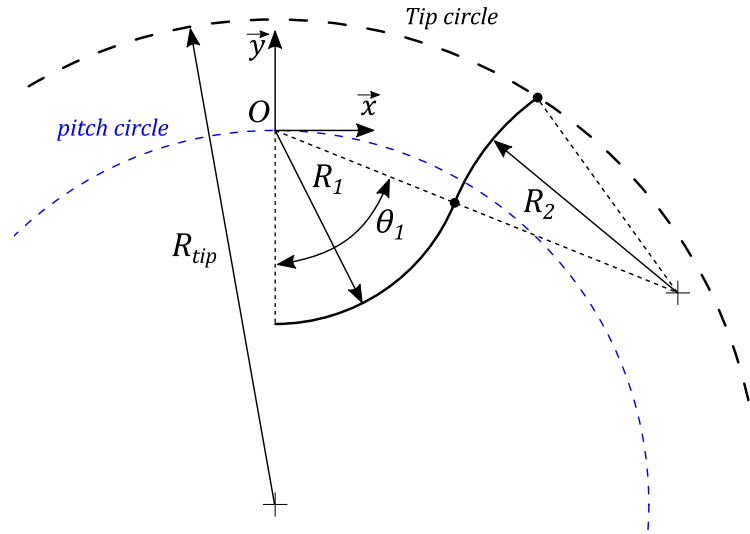
Figure IV-30: Definition of tooth profile with two circle sectors

As the two circle arcs must be tangent, the geometry is fully defined using only four parameters (see Figure IV-30)

- $R_1 = R_{tb}$, the radius of the first circle sector. This curve portion corresponds to the tooth bottom of the profile.
- θ_1, the sweep angle for the first circle sector.
- R_2, the radius of the second circle sector.
- R_{tip}, the tip radius of the profile.

The three profiles proposed are called *Cycling Profiles* and are denoted CP_1, CP_2 and CP_3. They are illustrated for $Z = 15$ in Figure IV-31 and their geometrical characteristics are presented in Table IV-10. These characteristics have been chosen in such way that the profiles proposed are able to withstand the low track cycling tension ratios. The tooth bottom radius R_1 goes from almost no clearance with the roller ($R_{roller} = 3.875mm$) for CP_1 to significant clearance for CP_3. Different definitions for angle θ_1 and radius R_2 are proposed based on the characteristics of the NF_{max} and NF_{min} profiles and from observations and measurements of real track cycling sprockets. The previous parts (§IV.1 and IV.2) showed that the profile properties are mainly influenced by ϕ_{tp} being a result of the inter-tp zone geometry. Therefore, and especially considering only stable working conditions (*i.e.*, no tooth climbing behaviour), the tooth flank definition beyond the tp does not seem to be a significant parameter. Based on this conclusion, all the *Cycling Profiles* are defined with the same tip radius. Its value corresponds to the mean tip radius of the NF_{min} and NF_{max} profiles.
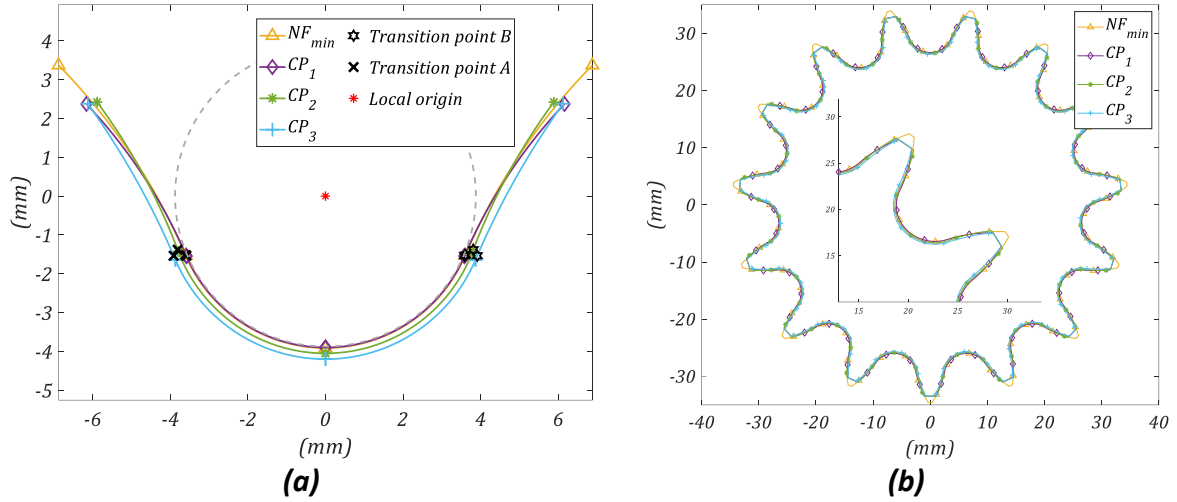
Figure IV-31: Comparison of NF_{min} and Cycling profiles: (a) in the local profile coordinate system, (b) for a whole sprocket ($Z = 15$, $p = 12.7mm$)

	CP_1	CP_2	CP_3
R_1 (mm)	3.9	4.05	4.2
θ_1 (deg)	$75 - 125/Z$	$75 - 85/Z$	$70 - 45/Z$
R_2 (mm)	$\frac{1}{2}Z + 6$	$Z + 1$	$2Z - 9$
R_{tip} (mm)		$2.023Z + 3.141$	

Table IV-10: Geometrical characteristics of the Cycling Profiles

	CP_1	CP_2	CP_3
K (deg)	15	15	19.96
K' (deg)	55.3	97.42	139.5

Table IV-11: Constants K and K' for cycling profiles $CP_{1,2,3}$

Constants K and K', for the calculation of ϕ_{tp}, are presented in Table IV-11. Parameter K constitutes the limit value for an infinite number of teeth while parameter K' characterises how fast ϕ_{tp} tends to K for high Z. Compared to the industrial profiles (see Table IV-9), the *Cycling Profiles* exhibit smaller values of K. Profile CP_1 has the smallest K' parameter of all the tested profiles and will therefore tend more rapidly to its limit pressure angle $\phi_{tp}(\infty) = K$. The evolution of the pressure angle at the transition point ϕ_{tp} depending on the number of teeth is given for all the tooth profiles in Figure IV-32.
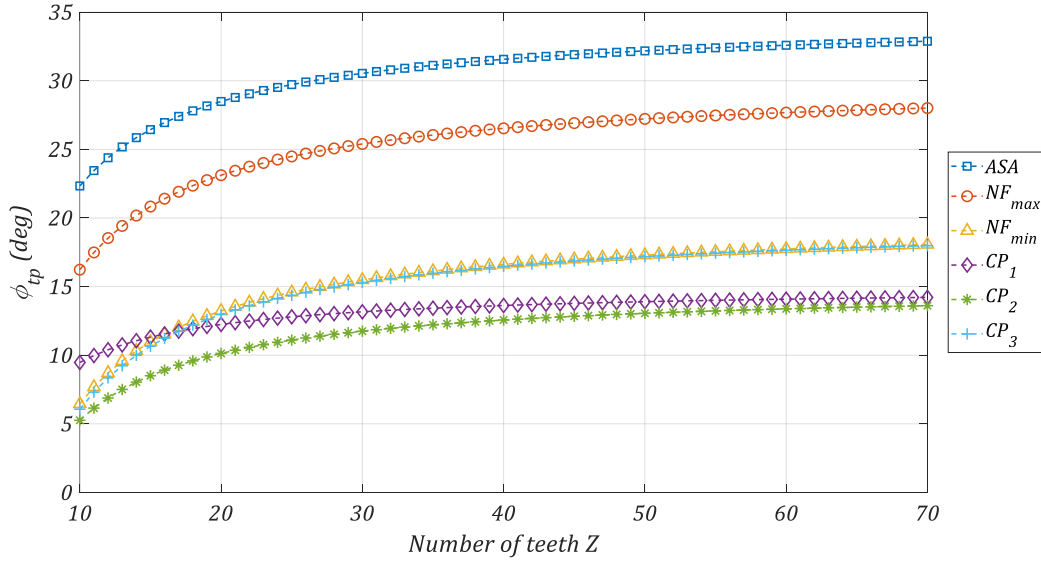
Figure IV-32: Evolution of ϕ_{tp} with the number of teeth

As prescribed by eq.(IV-6), all the profiles show increasing ϕ_{tp} with the number of teeth Z. Profiles NF_{max} and ASA show the larger ϕ_{tp} which is consistent with their high limit tension ratio in stable working conditions (see Figure IV-29). Despite the different K and K' parameters, the tooth profile hierarchy is usually respected as ϕ_{tp} ordering of the tooth profile families (*i.e.*, ASA, NF_{min}, CP_1, *etc.*) is similar regardless of the number of teeth (*e.g.*, profile CP_2 always has the smallest pressure angle, profile ASA always has the biggest). The only exception is the profile CP_1 whose curve crosses those of NF_{min} and CP_3 at about $Z = 17$ teeth. Due to its smaller K' parameter, it tends to reach its limit value more rapidly than the others. Consequently, its ϕ_{tp} is bigger than those of NF_{min}, CP_2 and CP_3 at $Z = 10$ but almost catches with CP_2 at 70 teeth. The pressure angles of all the *Cycling Profiles* are smaller than those of the NF_{min} one (except for CP_1 for small numbers of teeth). They should therefore be able to withstand small tension ratios. The evolution of the limit ratio in stable working conditions is shown in Figure IV-33 (calculated with a friction correction of $|\delta(\infty)| = 5°$). As expected, the low ϕ_{tp} values for the *Cycling Profiles* allow reaching small limit tension ratios in stable working conditions.
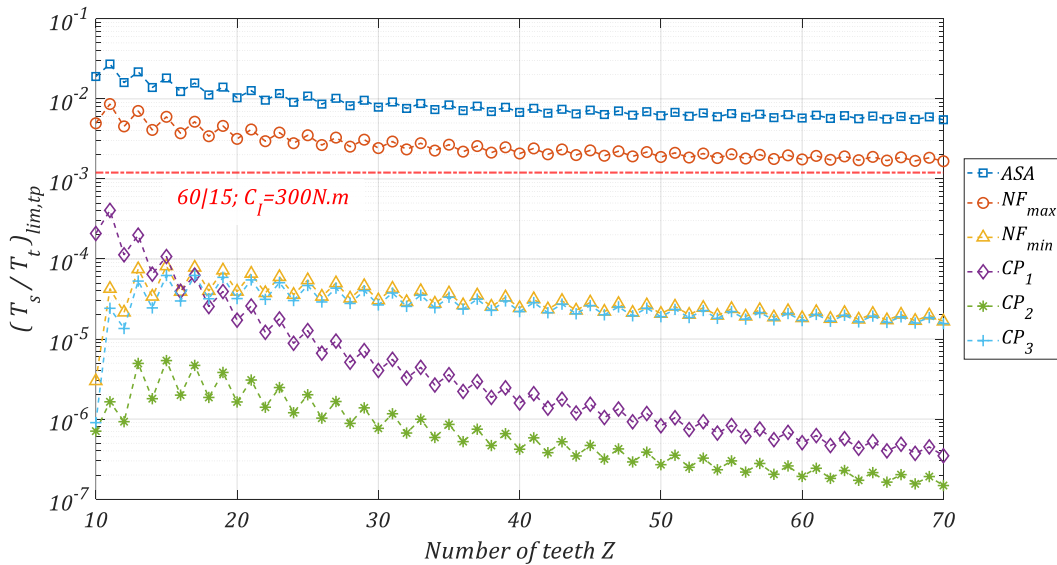
Figure IV-33: Limit ratio in stable working conditions for industrial and cycling profiles

It is interesting to note that profile families are generally consistent as the limit tension ratio in stable working conditions remains almost constant regarding to the number of teeth. Indeed, articulation angle α decreases as Z increases which counterbalances the increase in ϕ_{tp} shown in Figure IV-32. However, high numbers of teeth are generally associated with lower limit tension ratios. The evolution of the limit tension ratio according to the number of teeth is monotonic for the ASA, NF_{max} and CP_1 profiles. For the three remaining ones (NF_{min}, CP_2 and CP_3), the relation is non-monotonic as small numbers of teeth result in smaller limit tension ratios. The maximal limit ratio (sprocket carrying least load) occurs for $Z = 15$. The behaviour of the profile family CP_1 is quite different from the others as significant differences in limit tension ratio in stable working conditions are visible regarding to the number of teeth. A 70-tooth sprocket supports a ratio about 1000 times smaller than a $Z = 10$ sprocket (about $3e^{-7}$ versus $2e^{-4}$, respectively). The unusual behaviour is due to its small parameter K', as shown in Figure IV-32.

For the calculation of CP_2 at $Z = 10$, the corrected pressure angle $\phi_{tp} - \delta$ is set at the floor value of $1°$ (see Figure IV-22).

The relation between tooth profile geometry and limit tension ratio in stable working conditions can also be appreciated through parameter ϕ_{tp}. Figure IV-34 represents the relation between ϕ_{tp} and the limit tension ratio in stable working conditions. It allows quickly discriminating which profile is suitable for which application given the required limit tension ratio.
Figure IV-34 is calculated without the influence of friction ($|\delta(\infty)| = 0°$). The equivalent number of links N is set at $Z/2 - 1$.
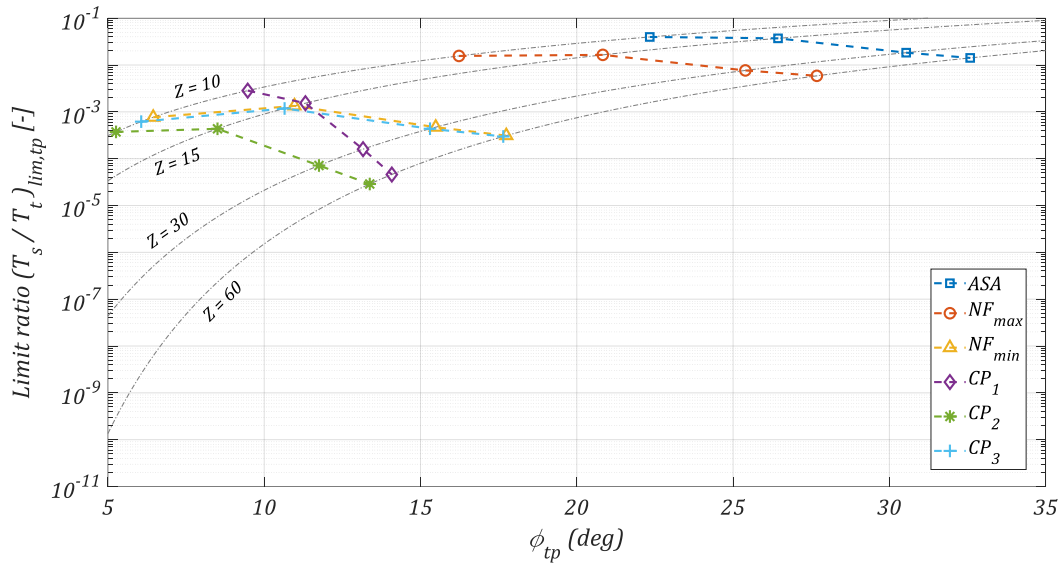
Figure IV-34: Relation between ϕ_{tp} and $(T_s/T_s)_{lim,tp}$

Points related to each profile family are presented. As in Figure IV-33, the discrimination between ASA and NF_{max} and the other profile families is clear. Except for CP_1 and CP_2, the relatively constant limit tension ratio regarding the number of teeth is also observed. The specific behaviour of the CP_1 profile is clearly visible with a significant drop in limit ratio as the number of teeth increases. Figure IV-34 and Figure IV-32 show that this drop is caused by ϕ_{tp} increasing more slowly than for the other profiles.

In the previous parts (§IV.1 and IV.2), it was shown that the properties of the tooth profiles (mainly ϕ_{tp}) can vary significantly with consequences on the behaviour of the chain drive (see §IV.1). Profiles NF_{min} and NF_{max} were defined as the two extreme acceptable geometries for standard ISO 606 [31].

However, the resulting properties were significantly different in terms of link tension, contact force, roller motion (see *e.g.*, Figure IV-7) and limit tension ratio (see §IV.2). Moreover, the ASA profile, whose definition lies between the NF_{min} and NF_{max} profiles (see Figure IV-3), also complies with the ISO 606 standard with an even greater difference in behaviour (tendency to climb the tooth flank, non-monotonic $s_{c,1}$-T_s/T_t relation). Therefore, the existing standards are not sufficient to ensure constant drive behaviour. Due to their specific geometry, the *Cycling Profiles* do not comply with the ISO 606 standard (see Appendix A for definitions of all the tooth profiles used in this manuscript).

IV.3.2 Tooth profile influence

The influence of the tooth profile is now tested on the 60|15 track cycling drive. The four profiles withstanding the severe tension ratios specific to the application are tested (NF_{min} and CP profiles). Figure IV-35 shows the link tension, contact force and roller location evolution for the chainring (*i.e.*, driving sprocket) with a driving torque $C_I = 50N.m$. The friction correction angle is still $|\delta(\infty)| = 5°$ and $a = 1e^{-10}m$.
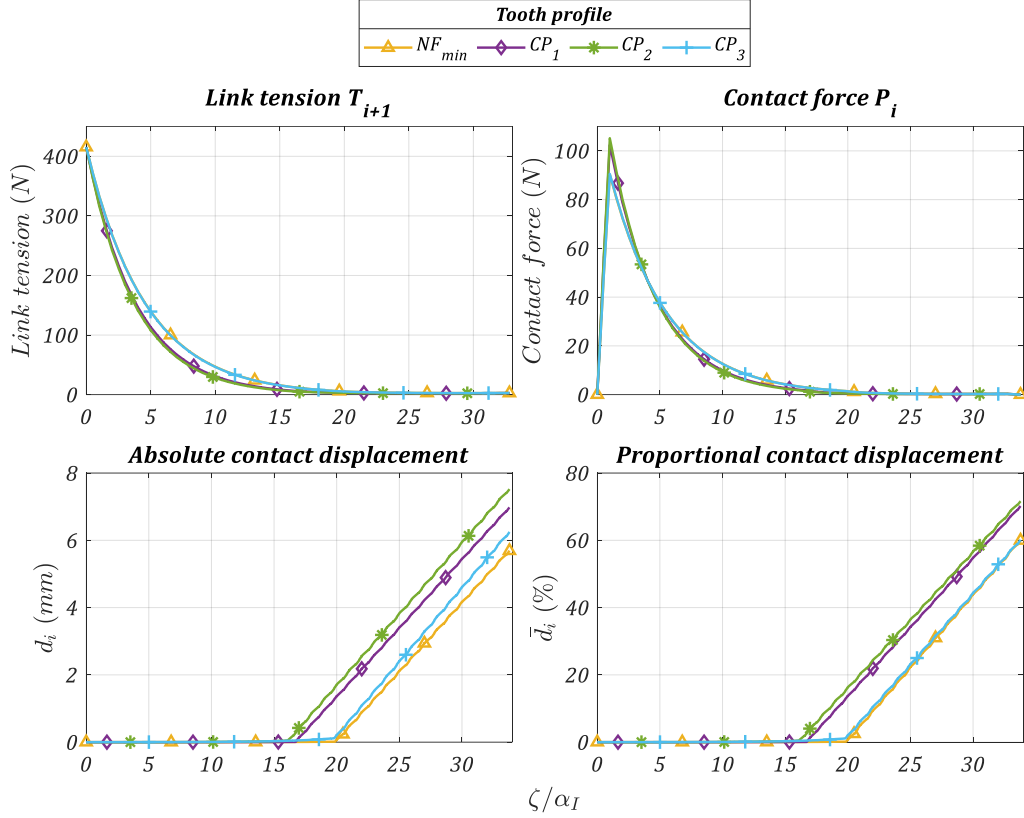
Figure IV-35: Link tension, contact force and roller location for $C_I = 50N.m$, chainring

As expected based on Figure IV-33, all the profiles present inter-tp behaviour as the ratio applied is smaller than $(T_s/T_t)_{lim,tp}$. The general shape of the curves is similar to what was obtained for industrial drives. The evolution appears smoother as the number of links in contact with the chainring ($n_I \in [\![32, 33]\!]$, see Figure IV-28) is higher than what was observed on the 31-tooth double pitch sprocket ($n_I \in [\![7, 8]\!]$, see Figure IV-2). However, slope breaks are still visible for each whole value of ζ/α_I, particularly on the roller location evolution. Two groups of profiles are visible. Profiles CP_1 and CP_2 show similar behaviours with the steepest slopes and therefore the longest roller motion ($\approx 70\%$ of the inter-tp distance). On the other hand, profiles NF_{min} and CP_3 also show similar behaviours with shallower slopes and shorter roller motion ($\approx 60\%$ of the inter-tp distance). The differences between absolute and proportional contact displacement are explained by the different inter-tp distances for each profile. Those distances are given in addition to the characteristic parameters of all profiles in Appendix A.

The results obtained for the rear cog (*i.e.*, driven sprocket), still with $C_I = 50N.m$ are presented in Figure IV-36.
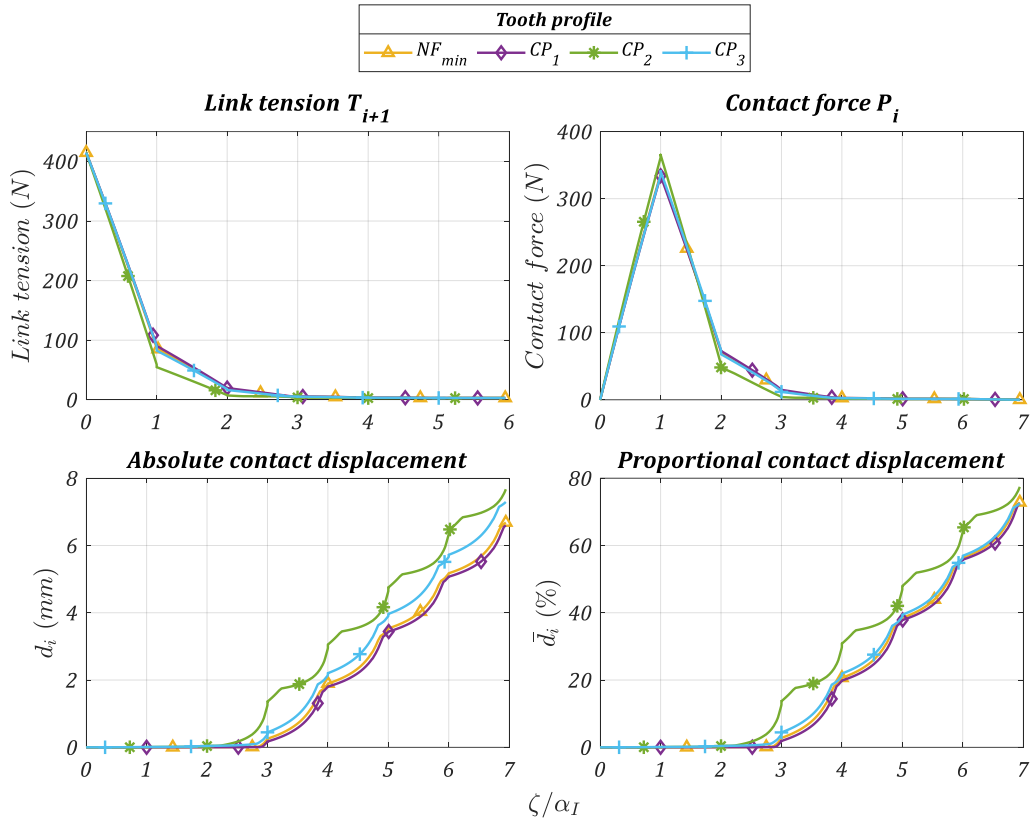
Figure IV-36: Link tension, contact force and roller location for $C_I = 50N.m$, rear cog

The two groups visible for the chainring (CP_1-CP_2 on one side and NF_{min}-CP_3 on the other) are not present for the rear cog. On the contrary, the CP_1 profile behaves like profiles NF_{min} and CP_3, leaving CP_2 with the steepest slopes and the longest roller motion. The change in the behaviour of the CP_1 profile between the chainring and rear cog is consistent with Figure IV-34 and Figure IV-32. These figures showed that, for small (high) numbers of teeth the ϕ_{tp} value for CP_1 is comparable to CP_3 and NF_{min} (CP_2). Although the final roller position is close for all profiles (about 70% of the inter-tp distance), a roller in contact with the CP_2 profile will undergo more displacement as this profile is more subject to oscillations. The differences between absolute and proportional contact displacement are still caused by different inter-tp distances. As fewer links are in contact with the rear cog ($n_{II} \in [\![5,6]\!]$, see Figure IV-28), the slope breaks at each whole value of ζ/α_I, are clearly visible in link tension and contact force. These breaks correspond to the roller release in the tight strand. Regarding roller location, apart from the slope breaks caused by roller release, each profile exhibits a specific oscillation pattern.

An example with a more severe driving torque of $C_I = 300N.m$ is presented in Figure IV-37.

$$60/15 \; ; \; Rear \; cog \; ; \; C_I = 300N.m \; ; \; slack = 11\%$$
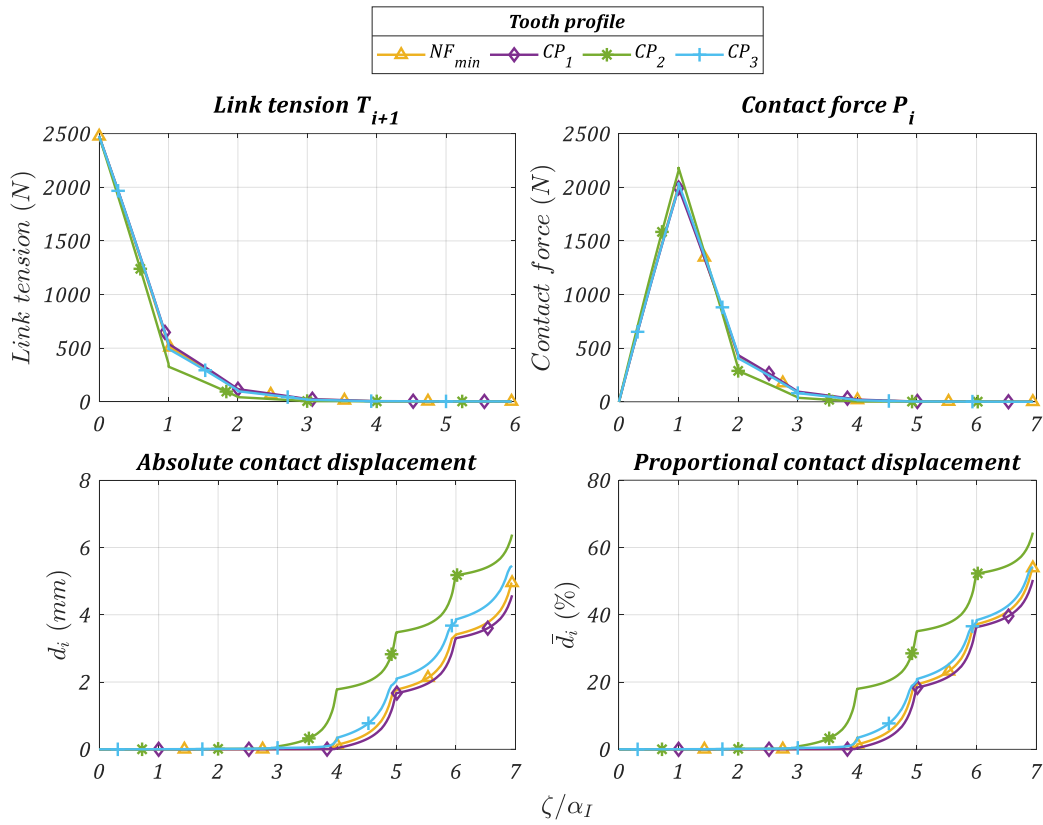
Figure IV-37: Link tension, contact force and roller location for $C_I = 300N.m$, rear cog

As observed for industrial drives, increasing the loading (*i.e.*, reducing the tension ratio) reduces roller motion. The maximal roller displacement reaches about 50% of the inter-tp distance for the CP_1, CP_3 and NF_{min} group and about 60% for the CP_2. The oscillation pattern of each profile tends to converge with only the roller release slope breaks affecting roller motion. Roller motion oscillation increases with the loading torque but no back-and-forth motion is observed in this example. Due to the small ϕ_{tp}, characteristic of cycling profiles, the first tooth (at $\zeta/\alpha_I = 1$) carries the majority of the load. For $C_I = 300N.m$, all the profiles show a maximum contact force at about $2000N$. This value decreases to about $400N$ for the second tooth ($\zeta/\alpha_I = 2$). The decrease continues causing the final teeth (closer to the slack strand) to bear almost no load ($P_i \approx 1.6N$ at $\zeta/\alpha_I = 5$). The same phenomenon is observed in link tension where almost no load is carried after $\zeta/\alpha_I = 4$.

Compared to what was observed for industrial drives, the general behaviour is similar. The slopes in link tension and contact force depend directly on parameter ϕ_{tp} and roller motion reduces for small tension ratios. However, as the ϕ_{tp} for *Cycling Profiles* are significantly lower than those for NF_{max} and ASA, the link tension and contact force undergo steeper slopes.

Considering energy efficiency, tooth profiles with low ϕ_{tp} (*e.g.*, profile CP_2) result in more roller displacement. However, these displacements are performed with lower forces as the decreasing slopes are steeper. On the contrary, with a higher ϕ_{tp} value, the rollers undergo less displacement but the loads are higher. Therefore, it is not possible to easily assess which profile will result in the best efficiency.

IV.4   Conclusion

This chapter analysed the influence of tooth profile geometry on both industrial and cycling chain drives. The QSCDM, introduced in Chapter II was used for all the calculations. Analysis methods were proposed to characterise the tooth profile properties to analyse their influence more quickly.

An industrial 31|31 drive was presented first. Link tension, contact force and roller location were shown for three industrial profiles (ASA, NF_{max} and NF_{min}). Each profile exhibited different increasing and decreasing slopes for the evolution of loads (link tension and contact force). Roller location was shown to be connected with loads as link tension and contact force decrease (increase) when the roller contacts the tight (slack) side of the tooth profile. Profiles with steeper slopes also exhibit longer roller motion (*e.g.*, NF_{max} profile). Driven sprockets exhibited steeper slopes than driving ones with the same profile. Consequently, the roller motion was also longer for driven sprockets. Increasing driving torque reduces roller motion. Oscillations both in loads and roller displacement were reported for all loading conditions. Such oscillations were not observed in the work of Kim & Johnson [52] and Naji & Marshek [2], [62]. In these works, only a single sprocket was considered instead of the whole drive in the QSCDM. These oscillations are explained by the variations in strand tensions resulting in variations of the tension ratios. For extreme cases, back-and-forth roller motion was reported. This non-monotonic variation is not compatible with the hypothesis stated for friction modelling. However, this phenomenon would require additional work in order to propose a suitable model. Nevertheless, the source of these oscillations in loads and roller motion were found in a more realistic model (the whole drive compared to a single sprocket). Consequently, these phenomena are probably more representative of what might happen in a real chain drive than the steady evolution showed in the literature (see §III.3.2 and *e.g.*, in [2], [52]).

The analysis of industrial drives gives a first assessment of the influence of tooth profile on chain drive behaviour. Based on these results, original analysis methods were presented. The pressure angle at the transition point ϕ_{tp} was introduced. This parameter is related to the increasing and decreasing slopes specific to each profile, the small ϕ_{tp} being associated with the steeper slopes. Then, the limit tension ratio that each profile is able to withstand was analysed. Depending on the sprocket being driving or driven, the location of the first roller $s_{c,1}$ at the limit ratio changes. The limit ratio was reached either with all the rollers lying at the transition point or climbing the tooth flank. To analyse the differences between profiles, the pressure angle characteristic curve, showing the evolution of ϕ_{i+1} as a function of γ_i, was presented. This curve captures the geometrical properties of a given profile. Considering correction due to friction, the behaviour at the limit tension ratio could be determined (except for the unclear case of driven ASA sprockets). At their limit ratio, all the rollers were demonstrated to lie nearby the transition point for driven sprockets. For driving ones, ASA et NF_{max} profiles reach their limit ratio with the rollers climbing the tooth flank, contrary to the NF_{min}. The influence of friction correction on this phenomenon was also addressed. Depending on the loading conditions, three behaviours of roller motion were proposed based on the sub-models described by Lodge & Burgess in [70]. For higher tension ratios, the rollers tend to cross the profile from tp^B to tp^A in the inter-tp behaviour. As the tension ratio decreases (the driving torque increases), rollers stay longer at tp^B until all lie almost immobile. When subjected to this behaviour, called static roller behaviour, the friction correction switches sign while the rollers stay nearby the transition point. Then, depending on the profile, even smaller ratios can be reached for rollers climbing the tooth flank in the roller climbing behaviour. The transition between each behaviour is progressive and occurs at specific ratios for each profile. The QSCDM therefore combines all the different approaches presented in the literature (GPLD, static roller and low slack tension, [2], [62], [70]).

The analysis methods developed were then applied to a typical track cycling drive. The limit tension ratio in stable working conditions was introduced. This ratio excludes the tooth climbing behaviour as

the risk of chain drop cannot be accepted in track cycling. It was shown that ϕ_{tp} is directly related to this limit ratio with the smaller ϕ_{tp} making it possible to reach the smaller ratios. Analysis of the limit ratio in stable working conditions showed that ASA and NF_{max} profiles cannot withstand the severe ratios encountered in track cycling drives. Original tooth profile geometries, the *Cycling Profiles,* were introduced. These profiles are built such that their ϕ_{tp} is small enough to overcome track cycling constraints. The influence of tooth profile geometry on track cycling drive was tested using the four profiles suitable for track cycling applications (NF_{min}, $CP_{1,2,3}$). The drive behaviour was similar to the results obtained with the industrial case. However, the very low ϕ_{tp} of the tested profiles caused the increasing and decreasing slopes to be even steeper. As a consequence, most of the load, both in link tension and contact force, is carried by the first roller/link.

Considering track cycling drive energy efficiency, the results obtained do not allow easily determining which profile will result in the smallest dissipation. Indeed, profiles with longer roller motion undergo this motion under lower loads than what was observed for profiles exhibiting the shorter roller motion. Moreover, each profile reacts differently to the varying tension ratio and exhibits its own oscillation pattern, likely with consequences on the resulting power losses. An analysis of chain drive efficiency considering the effect of roller motion is therefore necessary to determine which geometry results in the lowest power losses. The two last chapters of this thesis are dedicated to this analysis.

Chapter V

Chain drive efficiency: model and validation

It was shown in the previous chapter (Chapter IV) that the 2D geometry of the tooth profile influences drive behaviour, both for industrial and track cycling applications. Roller motion was modified depending on the tooth profile geometry considered so that the most energetic efficient profile could not be easily determined. Moreover, the author showed in [81] that dissipations due to roller motion could represent a significant part of chain drive losses. It is therefore necessary to explore this phenomenon.

This chapter is dedicated to the presentation and validation of an original Chain Drive Efficiency Model (CDEM). This efficiency model continues from the QSCDM introduced in Chapter II and uses the results obtained "per component" as input parameters.

The first part details the efficiency model. This model considers losses due to friction at interfaces between chain parts. This includes losses due to meshing and roller motion as both cause relative displacements between parts. Dissipations are assumed to occur only for articulations in contact with a sprocket. Moreover, the drive is assumed to be perfectly aligned and therefore no lateral contact between plates is considered. Coulomb friction is assumed at all chain interfaces.

Elements of validation of the efficiency model are then presented. Predictions are compared to experimental results from the literature considering industrial drives. Differences between the approach presented, considering additional losses due to roller motion, and previous models considering only meshing losses are highlighted. The results show that losses due to roller motion explain lower efficiency measurements at low torque. Then, measurements from a test rig developed in parallel with this thesis and dedicated to track cycling applications are used to validate the model's relevance for these specific drives. Model predictions and test rig results are compared for several tension settings, numbers of teeth and tooth profiles.

V.1 Chain Drive Efficiency Model

Meshing and roller losses were introduced in Chapter I, §I.4. Meshing losses are caused by the articulation movement undergone by each link during its meshing and un-meshing at a given sprocket. Roller losses are caused by the motion of the rollers along their associated tooth profile during contact with a sprocket. This motion was highlighted in Chapter IV and shown to be dependent on the tooth profile.

However, the physical phenomena responsible for the meshing and roller motion losses are similar as both are caused by friction at interfaces between chain parts. Therefore, no distinction between the two loss types is considered in the model. Instead, a new distinction based on the contribution of each interface is proposed.

The chain is considered to operate in a single plane (*i.e.*, 2D). Therefore, it is assumed that no lateral contact between plates occurs. Consequently, within a chain articulation (*i.e.*, set of pin, bush and roller, see Chapter II and Figure V-1), friction is assumed to occur only at three interfaces between parts: pin/bush, bush/roller and roller/profile (see Figure V-1.a). Coulomb friction [85] is assumed at all interfaces, each having a distinct friction coefficient (see Table V-1 below). Pins, bushes and rollers are assumed to be perfectly cylindrical. Their outer radius is denoted R_{pin}, R_{bush} and R_{roller} (see Figure V-1.b).

Losses are considered only for chain articulations in contact with a sprocket. Indeed, no relative motion between links occurs at the tight strand as it is assumed to be perfectly straight. Moreover, dissipations in the slack strand are neglected as link tension is usually very low (compared to tension in the tight strand) in track cycling applications, see Figure IV-28.

Until now, no consideration of rotational speed has been introduced as the chain drive model is quasi static. However, time considerations are needed for efficiency calculations. It is assumed that the chain drive operates under steady state conditions. The chainring rotational speed Ω_I is constant and given as input variable. Constant loadings conditions are given by a torque C_j applied either on the chainring or the rear cog.
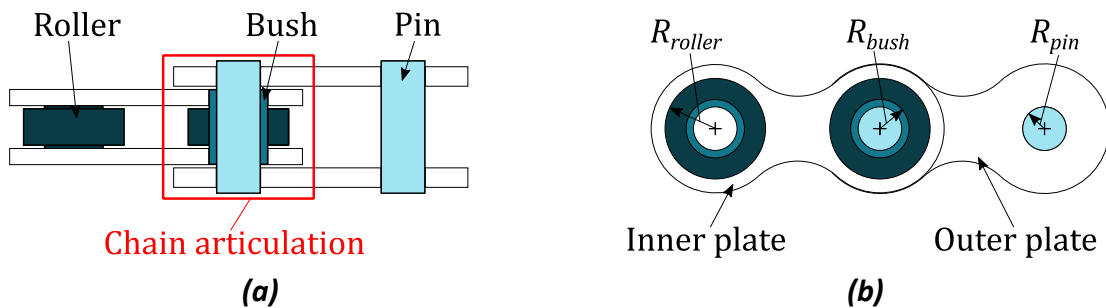
Figure V-1: (a) Chain drive articulation (b) Definition of R_{pin}, R_{bush} and R_{roller}

The Chain Drive Efficiency Model (CDEM) is used, continuing from the QSCDM introduced in Chapter II (see Figure V-2). Its input variables are the variation of loads (link tension T and contact force P), roller location (s_c) and relative link orientation (link angles α^*, ν and κ). All input variables are provided "per component" (see §II.3.2). Two kinematic cases (A and B, see below) are considered to calculate the roller rotation based on the roller/profile contact point displacement (given by s_c). Therefore, the final result of the efficiency model is an interval bounded by the two kinematic hypotheses.

In a regular roller chain, inner link (bush link) and outer link (pin link) alternate (see Figure V-3). Two types of articulation are defined from this alternance as their influence on dissipation differs (see Chapter I). These two types have been named differently in previous studies: forward/rear pin [32],

[76], open/narrow end forward (in the context of cranked link chains) [74], [75] and pin/bush articulation [70], [79]. In the following development, the denomination pin/bush articulation is used. A pin (bush) articulation corresponds to an articulation such that a pin (bush) link undergoes rotation during articulation due to meshing on the considered sprocket. From the standpoint of power loss, the meshing of a pin articulation mainly produces friction at the pin/bush interface. For bush articulation however, additional dissipations are caused at the bush/roller interface. Moreover, the loads at stake for each interface are also different depending on the type of articulation (see Chapter I and §V.1.1 below). Figure V-3.b shows a pin articulation during its meshing on the chainring and a bush articulation during its meshing on the rear cog.
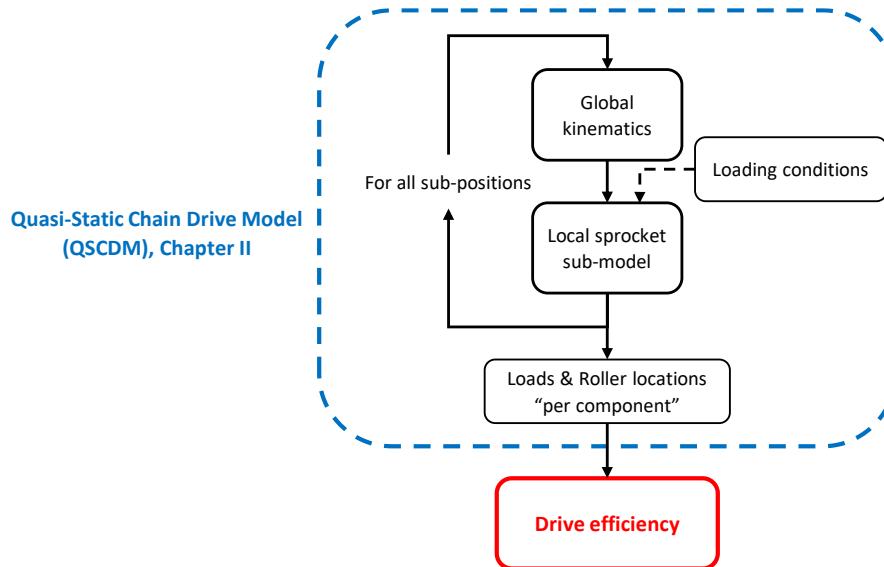
Figure V-2: Position of the chain drive efficiency model
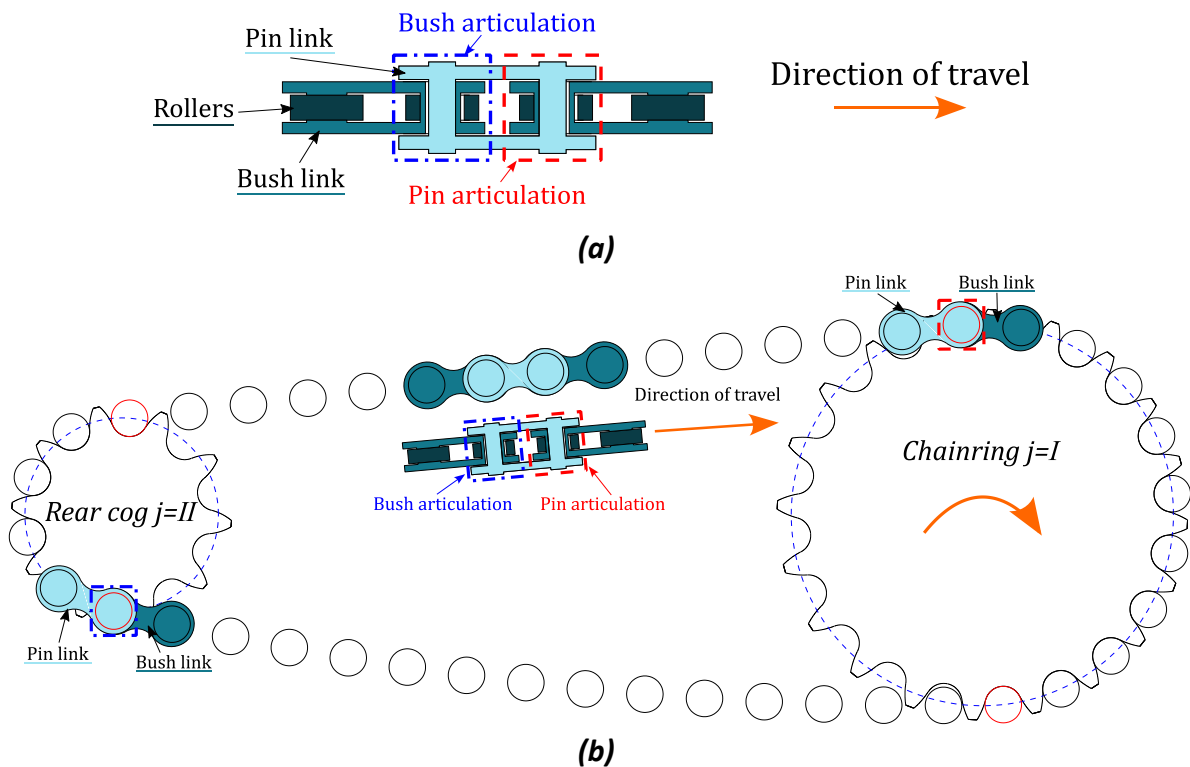
Figure V-3: (a) Pin and bush articulation (b) Meshing of pin articulation on the chainring and bush articulation on the rear cog

V.1.1 Loads and motion of chain articulations

For the following development, a chain drive articulation is considered (*i.e.*, set of pin, bush and roller, see Figure V-1). All input variables are given "per component" using index k according to Chapter II, §II.3.2.

The following parameters are taken from the chain drive model (see Figure V-4).

- P, the contact force between the profile and the roller of the articulation considered
- T_{fol} and T_{prev}, the tensions in the link following and preceding the articulation considered, respectively. fol and $prev$ stand for following and previous, respectively;
- κ, the tilting angle of the previous link (with respect to the local $\vec{x}$ axis, see Figure V-4);
- ν, the tilting angle of the following link (with respect to the local $\vec{x}$ axis, see Figure V-4);
- α^*, the angle between the following and the previous link;
- s_c, the curvilinear abscissa of the contact point between the roller and the tooth profile. To simplify notations, s_c is simply denoted s in this chapter.

The denomination T_{prev}/T_{fol} is close to that of T_i/T_{i+1} introduced in Chapter II. Indeed, both designate the previous and following links with respect to a given articulation. However, index i refers to spatial numbering (*i.e.*, "per position"). Therefore, each articulation changes index i at chainring roller capture. The $prev/fol$ refers to the same articulation during several drive periods in a "per component" perspective. Concretely, $prev/fol$ links are defined from $i/i + 1$ but changing index i at each chainring roller capture. P in the CDEM context is defined in a similar way from P_i in Chapter II.
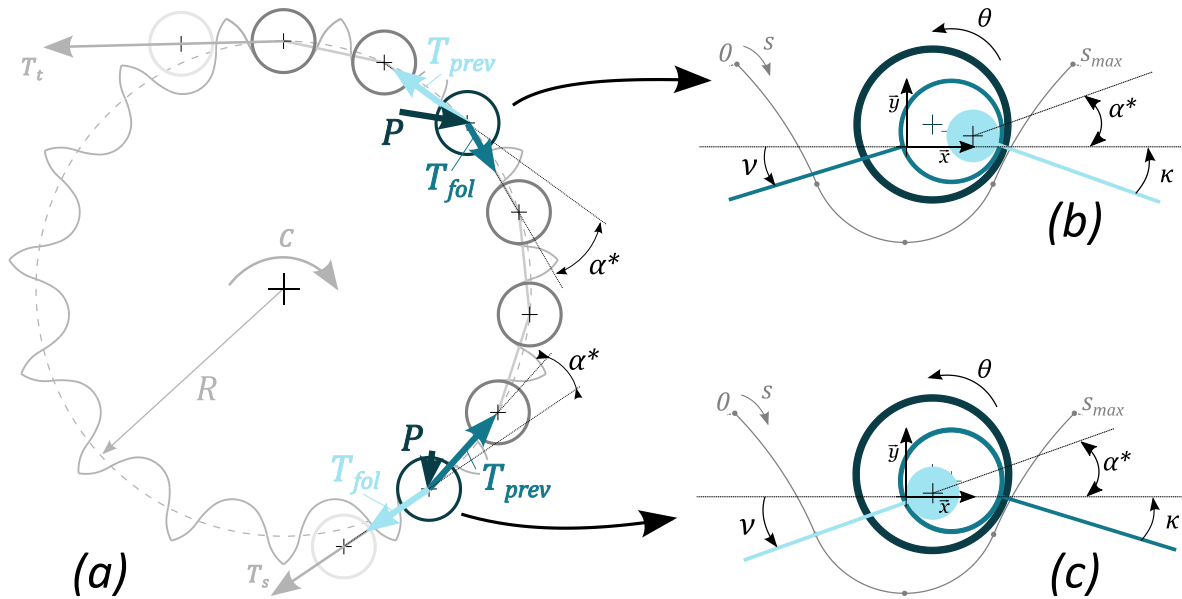
Figure V-4: (a) Loads applied on pin and bush articulations, (b) displacement parameters for pin articulation, (c) displacement parameters for bush articulation

Although connected by eq.(II-21), α^*, ν and κ are all used in the following development to facilitate understanding.

To calculate loss, it is necessary to know the motion of each chain part and the forces applied while the motions studied are performed. These two points are treated below.

a) Motion of parts

The motions of each chain part are defined by variables s_c, α^*, κ, ν and roller rotation angle θ (see Figure V-4.b-c). Except for roller rotation, the displacement of each chain part between sub-positions k and $k+1$ is given directly according to eq.(V-1).

$$\Delta s_k = s_{k+1} - s_k \qquad (a)$$

$$\Delta \alpha^*{}_k = \alpha^*{}_{k+1} - \alpha^*{}_k \qquad (b)$$

$$(V\text{-}1)$$

$$\Delta \nu_k = \nu_{k+1} - \nu_k \qquad (c)$$

$$\Delta \kappa_k = \kappa_{k+1} - \kappa_k \qquad (d)$$

The chain drive model proposed in Chapter II gives the location of the contact point between the roller and its corresponding tooth profile using variable s. However, no information is given about the rotation of the roller itself (angle θ in Figure V-4.b-c). This rotation must therefore be calculated providing kinematic hypotheses at the roller/profile contact.

The materials and lubrication conditions are likely to be similar at both the roller/profile and the bush/roller interfaces. However, the radius at the bush roller interface is smaller than at the roller/profile one (*e.g.,* $D_{roller} = 7.75mm$ and $D_{bush} = 5.1mm$ for usual track cycling chain). Therefore, for a given torque, sliding will occur first at the bush/roller interface. Consequently, the bush/roller interface cannot undergo rolling if the roller/profile interface is subjected to sliding.

Therefore, two extreme kinematic cases are considered:

- **Case A:** It is assumed that there is no sliding at the bush/roller interface. Therefore, the roller rolls without sliding on the tooth profile. This condition is sufficient to define roller rotation and therefore sliding occurs at the bush/roller interface.
  For this case, the roller kinematics implies the following equation between $\Delta\theta_k$ and Δs_k.

Case A: $$\Delta\theta_k = \frac{-\Delta s_k}{R_{roller}} \qquad (V\text{-}2)$$

- **Case B:** Sliding is assumed to occur at both roller/profile and bush/roller interfaces. For this case, no kinematic condition constrains roller rotation. It is therefore assumed that no rolling occurs at the bush/roller interface. As a consequence, the roller/profile contact point slides a distance Δs_k. Figure V-5 illustrates this change of orientation, the roller in sub-position k is represented by a dotted line while sub-position $k+1$ by a solid line. Excluding any unlikely self-rotation of the roller, this corresponds to the kinematic condition with the longest sliding distance.

  For case B, the roller rotation is expressed as follows.

Case B: $$\Delta\theta_k = \frac{\Delta s_k}{R_{curve}} \qquad (V\text{-}3)$$

  with:

- R_{curve} the profile curvature radius at the roller/profile contact point considered. R_{curve} can be positive or negative depending on whether the profile portion considered is convex or concave, respectively.

The calculation of $\Delta\theta_k$ can be more complex when the contact point changes curve portions. Details about these specific cases are given in Appendix H.
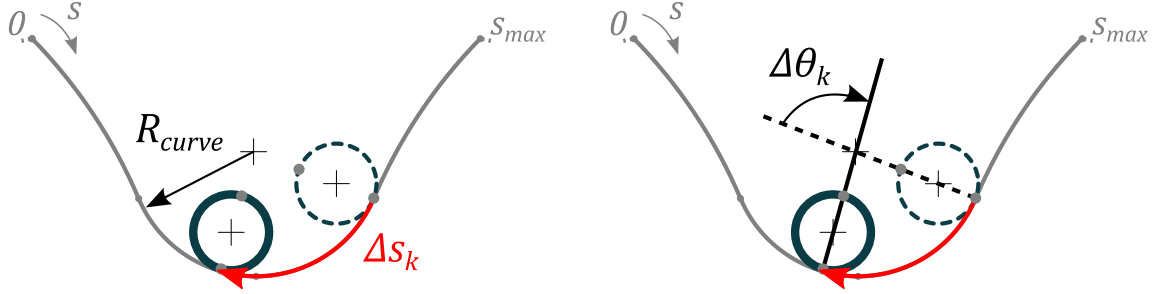
Figure V-5: Relation between Δs_k and $\Delta\theta_k$ for case B (sub-position k and $k+1$ in dashed and solid lines, respectively)

Cases A and B represent two extreme kinematic conditions: in case A, the sliding distance at the roller/profile contact point is null while it is maximal for case B (excluding roller self-rotation). For case B, sliding is assumed at both roller interfaces. Following Coulomb friction theory, the tangential force is therefore fixed at both interfaces and roller equilibrium cannot be achieved. However, no feedback loop is considered in the chain drive model between kinematics and loads. The roller kinematics as given by the chain drive model is therefore considered to be independent of any later assumption regarding kinematics (case A or B) or loads.

b) Forces

Between sub-position k and $k+1$, link tensions and roller/profile contact force are considered as constant. The value is assumed to be the mean between position k and $k+1$ (see eq.(V-4)).

$$\overline{P}_k = \frac{P_{k+1} + P_k}{2} \qquad (a)$$

$$\overline{T_{prev}}_k = \frac{T_{prev_{k+1}} + T_{prev_k}}{2} \qquad (b) \qquad \textbf{(V-4)}$$

$$\overline{T_{fol}}_k = \frac{T_{fol_{k+1}} + T_{fol_k}}{2} \qquad (c)$$

Assuming Coulomb friction with sliding at a given interface [85], the magnitudes of tangential and normal forces ($\overrightarrow{F_T}$ and $\overrightarrow{F_N}$, respectively) are linked by eq.(V-5) (see Figure V-6).

$$F_T = \mu F_N \qquad \textbf{(V-5)}$$

with:

- $F_T = \left\|\overrightarrow{F_T}\right\|$
- $F_N = \left\|\overrightarrow{F_N}\right\|$
- μ the sliding friction coefficient at the interface considered.

This equation can be rearranged using the total force $\vec{F}$ as follows.

$$F_T = F \frac{\mu}{\sqrt{1 + \mu^2}}$$

(V-6)

with:

- $F = \left\| \vec{F} \right\|$
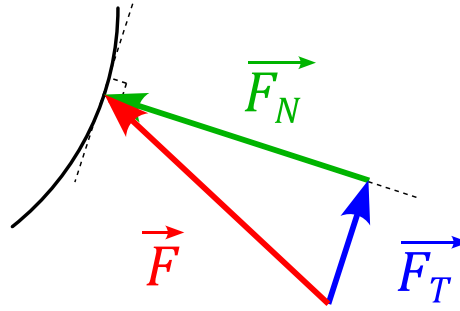
Figure V-6: Decomposition of total force

Returning to our application, T and P are magnitudes of total forces F. Therefore, the magnitudes of the forces producing work at each interface are given in Table V-1 according to eq.(V-6) (see Figure V-4).

Interface	Pin articulation	Bush articulation
Pin/bush	$\overline{T_{prev}}_k \cdot \dfrac{\mu_{pb}}{\sqrt{1 + \mu_{pb}^2}}$	$\overline{T_{fol}}_k \cdot \dfrac{\mu_{pb}}{\sqrt{1 + \mu_{pb}^2}}$
Bush/roller	$\overline{P}_k \cdot \dfrac{\mu_{br}}{\sqrt{1 + \mu_{br}^2}}$	
Roller/profile	$\overline{P}_k \cdot \dfrac{\mu_{rp}}{\sqrt{1 + \mu_{rp}^2}}$	

Table V-1: Magnitudes of tangential force at each interface for pin and bush articulations

with:

- μ_{pb}, the friction coefficient at the pin/bush interface
- μ_{br}, the friction coefficient at the bush/roller interface
- μ_{rp}, the friction coefficient at the roller/profile interface

Contact force P applies at the roller/profile interface. As dynamical effects are neglected, the bush/roller force also has a magnitude of P. For the bin/bush interface, the force to be considered is the tension in the neighbouring pin link. It therefore depends on the articulation being a pin or a bush one. For a pin articulation, T_{prev} is considered while T_{fol} is used for a bush one (see Table V-1).

V.1.2　Power losses calculation

The motion of each part constituting a chain articulation as well as the forces applied on it have been detailed. Both can now be combined to calculate the resulting power losses. The dissipated mechanical works for a pin articulation during its contact with a given sprocket are first detailed.

a) Pin articulation mechanical work

Figure V-7 shows motion parameters (*i.e.*, ν, κ, α^* and θ) and forces (T_{fol}, T_{prev} and P) on a pin articulation. The preceding link is a pin link (tension T_{prev}, orientation κ) and the following one is a bush link (tension T_{fol} and orientation ν).
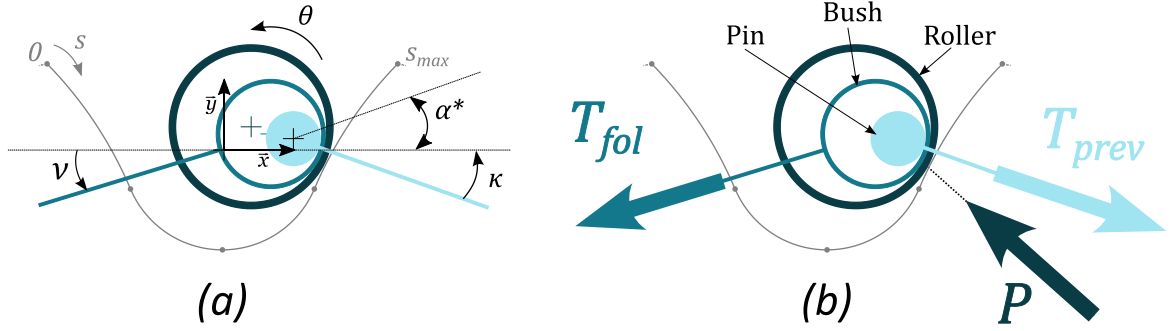
Figure V-7: (a) motion parameters and (b) forces on pin articulations

The losses undergone by a pin articulation are split into the contribution of each interface: pin/bush, bush/roller and roller/profile.

i. Pin/bush interface (pb)

The dissipated work at a given interface is calculated considering the product between the sliding distance and the tangential force (already introduced in Table V-1).
Between sub-positions k and $k + 1$, the pin/bush interface is subject to the following sliding distance (see notations in Figure V-7).

$$d_{sliding}\big|_{pb,pin\ art}^{k} = R_{pin}.|\Delta\alpha^*{}_k| \tag{V-7}$$

This motion occurs under the following tangential force (according to Table V-1).

$$F_T\big|_{pb,pin\ art}^{k} = \overline{T_{prev}}_k.\frac{\mu_{pb}}{\sqrt{1 + \mu_{pb}^2}} \tag{V-8}$$

The resulting work is then expressed as follows.

$$W\big|_{pb,pin\ art}^{k} = d_{sliding}\big|_{pb,pin\ art}^{k}.F_T\big|_{pb,pin\ art}^{k}$$

$$= R_{pin}.|\Delta\alpha^*{}_k|.\overline{T_{prev}}_k.\frac{\mu_{pb}}{\sqrt{1 + \mu_{pb}^2}} \tag{V-9}$$

Finally, the total work dissipated at the pin/bush interface during the contact with the sprocket (sprocket j) considered is obtained by summing eq.(V-9) from the sub-position of roller capture ($k = 1$) to the sub-position of roller release ($k = k_{max}$).

$$
\begin{aligned}
W|^j_{pb,pin\,art} &= \sum_{k=1}^{k_{max}-1} W|^k_{pb,pin\,art} \\[2mm]
&= \sum_{k=1}^{k_{max}-1} \overline{T_{prev}}_k \cdot \frac{\mu_{pb}}{\sqrt{1+\mu_{pb}^2}} \cdot R_{pin} \cdot |\Delta\alpha^*_k|
\end{aligned}
$$

<div align="right">(V-10)</div>

ii. Bush/roller interface (br)

At the bush/roller interface, the sliding distance is more complex. Indeed, between sub-positions k and $k+1$, the bush link (*i.e.*, following link, see Figure V-7) changes orientation by an amount $\Delta\nu_k$. Simultaneously, the roller orientation changes by an amount $\Delta\theta_k$. Therefore, the sliding distance is expressed as follows.

$$
d_{sliding}|^k_{br,pin\,art} = R_{bush} \cdot |\Delta\theta_k - \Delta\nu_k|
$$

<div align="right">(V-11)</div>

In eq.(V-11), $\Delta\theta_k$ is set to the appropriate value depending on the kinematic hypothesis considered (case A or case B).

According to Table V-1, the following expression stands for the tangential force.

$$
F_T|^k_{br,pin\,art} = \bar{P}_k \cdot \frac{\mu_{br}}{\sqrt{1+\mu_{br}^2}}
$$

<div align="right">(V-12)</div>

As with the previous interface, the total work dissipated at the bush/roller interface during the contact with sprocket j is given by eq.(V-13).

$$
W|^j_{br,pin\,art} = \sum_{k=1}^{k_{max}-1} \bar{P}_k \cdot \frac{\mu_{br}}{\sqrt{1+\mu_{br}^2}} \cdot R_{bush} \cdot |\Delta\theta_k - \Delta\nu_k|
$$

<div align="right">(V-13)</div>

It can be noted that the variation in pin link orientation does not influence the loss at the bush/roller interface (angle κ does not appear in eq.(V-13)).

iii. Roller/profile interface (rp)

At the roller/profile interface, the sliding distance between sub-positions k and $k+1$ also depends on the case considered (A or B) according to eq.(V-14). For case A, the pure rolling condition implies that no sliding occurs; as for case B the sliding distance reaches its maximum Δs_k.

Case A: $\qquad\qquad\qquad\qquad d_{sliding}|^k_{rp,pin\,art} = 0$ $\qquad\qquad\qquad$ (a)

Case B: $\qquad\qquad\qquad\qquad d_{sliding}|^k_{rp,pin\,art} = \Delta s_k$ $\qquad\qquad\qquad$ (b)

<div align="right">(V-14)</div>

According to Table V-1, the tangential force is given by the following equation.

$$F_T|^k_{rp,pin\ art} = \bar{P}_k . \frac{\mu_{rp}}{\sqrt{1 + \mu_{rp}^2}}$$ **(V-15)**

Consequently, the total work dissipated at the roller/profile interface during the articulation contact with sprocket j is given as follows, depending on the kinematic case considered.

Case A: $$W|^j_{rp,pin\ art} = 0$$ *(a)*

Case B: $$W|^j_{rp,pin\ art} = \sum_{k=1}^{k_{max}-1} \bar{P}_k . \frac{\mu_{rp}}{\sqrt{1 + \mu_{rp}^2}} . \Delta s_k$$ *(b)* **(V-16)**

As the sliding distance is null for case A (pure rolling), so it is for the total dissipated work.

Finally, the total work dissipated by a pin articulation during its contact with sprocket j is calculated as the sum of the dissipated works at each interface (pin/bush, bush/roller and roller/profile).

$$W|^j_{pin\ art} = W|^j_{pb,pin\ art} + W|^j_{br,pin\ art} + W|^j_{rp,pin\ art}$$ **(V-17)**

b) Bush articulation mechanical work

The same development is now given for a bush articulation. Motion parameters (*i.e.*, v, κ, α^* and θ) and forces (T_{fol}, T_{prev} and P) are shown in Figure V-8. Compared to a pin articulation, the pin and bush link are switched. The bush link is now the previous one, located with angle κ, and its tension force is T_{prev}.
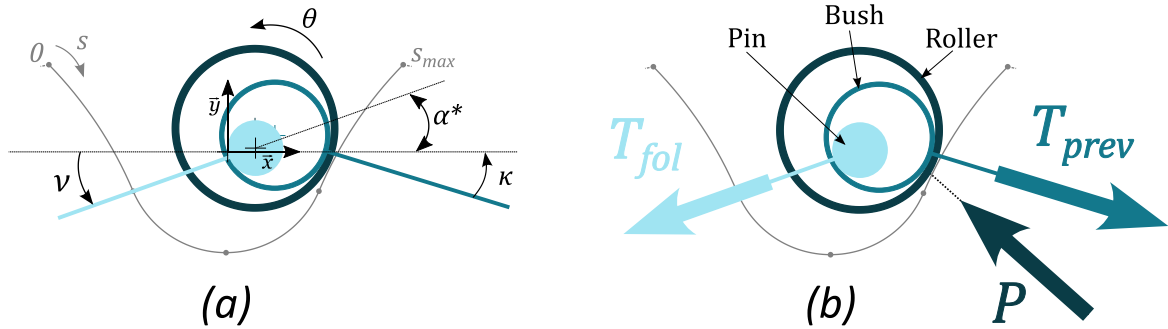
Figure V-8: (a) motion parameters and (b) forces on bush articulations

i. Pin/bush interface

The sliding distance at the pin/bush interface is identical to the pin articulation case (see eq.(V-7)).

$$d_{sliding}|^k_{pb,bush\ art} = R_{pin} . |\Delta \alpha^*_k|$$ **(V-18)**

The tangential force differs from the pin articulation case as the pin link is now the following one (see Figure V-8). Therefore, the tangential force is based on $\overline{T_{fol}}_k$ (see Table V-1).

$$F_T|^k_{pb,bush\ art} = \overline{T_{fol}}_k . \frac{\mu_{pb}}{\sqrt{1 + \mu_{pb}^2}}$$ **(V-19)**

The total dissipated work is therefore expressed as follows.

$$W|^j_{pb,bush\ art} = \sum_{k=1}^{k_{max}-1} \overline{T_{fol_k}} \times \frac{\mu_{pb}}{\sqrt{1+\mu_{pb}^2}} \times R_{pin} \times |\Delta\alpha^*_k| \tag{V-20}$$

ii. Bush/roller interface

For the bush/roller interface, the difference compared to the pin articulation case comes from the bush link now being the previous one. Its tilting variation is then given by κ resulting in the following expression for the sliding distance.

$$d_{sliding}|^k_{br,bush\ art} = R_{bush}.|\Delta\theta_k - \Delta\kappa_k| \tag{V-21}$$

As for the pin articulation case, $\Delta\theta_k$ is set to the appropriate value depending on the kinematic hypothesis considered (case A or case B).
According to Table V-1, the tangential force is the same as for the pin articulation case.

$$F_T|^k_{br,bush\ art} = \overline{P}_k.\frac{\mu_{br}}{\sqrt{1+\mu_{br}^2}} \tag{V-22}$$

The total dissipated work is given as follows.

$$W|^j_{br,bush\ art} = \sum_{k=1}^{k_{max}-1} \overline{P}_k.\frac{\mu_{br}}{\sqrt{1+\mu_{br}^2}}.R_{bush}.|\Delta\theta_k - \Delta\kappa_k| \tag{V-23}$$

iii. Roller/profile interface

For the roller/profile interface, the dissipated work is identical to the pin articulation case. It is therefore directly expressed in eq.(V-24) depending on the kinematic hypothesis (case A or B).

Case A: $\qquad\qquad W|^j_{rp,bush\ art} = 0 \qquad\qquad\qquad\qquad$ (a)

$$\qquad\qquad\qquad\qquad\qquad\qquad\qquad\qquad\qquad\qquad\qquad\qquad\qquad\qquad\text{(V-24)}$$

Case B: $\qquad W|^j_{rp,bush\ art} = \sum_{k=1}^{k_{max}-1} \overline{P}_k.\frac{\mu_{rp}}{\sqrt{1+\mu_{rp}^2}}.\Delta s_k \qquad$ (b)

As with the pin articulation case, the total work dissipated by a bush articulation during its contact with sprocket j is given by eq.(V-25).

$$W|^j_{bush\ art} = W|^j_{pb,bush\ art} + W|^j_{br,bush\ art} + W|^j_{rp,bush\ art} \tag{V-25}$$

c) Summary of dissipated works

Dissipated works at each articulation interface are summarised in Table V-2.

Interface		Pin articulation	Bush articulation
Pin/bush		$\overline{T_{prev_k}} \cdot \dfrac{\mu_{pb}}{\sqrt{1+\mu_{pb}^2}} \cdot R_{pin} \cdot |\Delta\alpha^*_k|$	$\overline{T_{fol_k}} \cdot \dfrac{\mu_{pb}}{\sqrt{1+\mu_{pb}^2}} \cdot R_{pin} \cdot |\Delta\alpha^*_k|$
Bush/roller	Case A	$\overline{P}_k \cdot \dfrac{\mu_{br}}{\sqrt{1+\mu_{br}^2}} \cdot R_{bush} \cdot \left| \dfrac{-\Delta s_k}{R_{roller}} - \Delta\boldsymbol{\nu_k} \right|$	$\overline{P}_k \cdot \dfrac{\mu_{br}}{\sqrt{1+\mu_{br}^2}} \cdot R_{bush} \cdot \left| \dfrac{-\Delta s_k}{R_{roller}} - \Delta\boldsymbol{\kappa_k} \right|$
	Case B	$\overline{P}_k \cdot \dfrac{\mu_{br}}{\sqrt{1+\mu_{br}^2}} \cdot R_{bush} \cdot \left| \dfrac{\Delta s_k}{R_{curve}} - \Delta\boldsymbol{\nu_k} \right|$	$\overline{P}_k \cdot \dfrac{\mu_{br}}{\sqrt{1+\mu_{br}^2}} \cdot R_{bush} \cdot \left| \dfrac{\Delta s_k}{R_{curve}} - \Delta\boldsymbol{\kappa_k} \right|$
Roller/profile	Case A	0	
	Case B	$\overline{P}_k \cdot \dfrac{\mu_{rp}}{\sqrt{1+\mu_{rp}^2}} \cdot \Delta s_k$	

Table V-2: Work dissipated in each chain articulation interface between sub-positions k and $k+1$

V.1.3   Dissipation over the entire drive

The mechanical work dissipated by a pin and a bush articulation during their contact with a given sprocket j was expressed. These results are now combined to calculate the efficiency of the drive.

Losses are considered only during the contact with sprockets. Therefore, during an entire drive rotation, a pin articulation undergoes the following dissipation ($j = I$ and II for the chainring and rear cog, respectively).

$$W|_{pin\ art} = W|_{pin\ art}^{j=I} + W|_{pin\ art}^{j=II} \qquad\qquad \textbf{(V-26)}$$

Similarly, the work dissipated by a bush articulation is given by eq.(V-27).

$$W|_{bush\ art} = W|_{bush\ art}^{j=I} + W|_{bush\ art}^{j=II} \qquad\qquad \textbf{(V-27)}$$

For a complete rotation of the drive, the total work dissipated by all the chain articulation is as follows.

$$W_{tot} = \frac{Nb_{link}}{2} \cdot \left(W|_{pin\ art} + W|_{bush\ art} \right) \qquad\qquad \textbf{(V-28)}$$

with:
- Nb_{link}, the total chain number of links. Nb_{link} is always an even number as cranked links are not studied in this work.

This amount of work is dissipated within a time Δt required for a complete drive rotation (see eq.(V-29)).

$$\Delta t = \frac{Nb_{link}}{Z_I} \cdot \frac{2\pi}{\Omega_I} \qquad\qquad \textbf{(V-29)}$$

with:

- Ω_I, the chainring rotational speed rad/s (given as input).

Therefore, the total power loss caused by the dissipation in all the chain articulations is given as follows.

$$P_{loss} = \frac{W_{tot}}{\Delta_t} = \frac{\left(W|_{pin\ art} + W|_{bush\ art}\right)}{2} \cdot \frac{\Omega_I Z_I}{2\pi} \qquad \textbf{(V-30)}$$

The energy efficiency of the drive is therefore:

$$\eta = \frac{C_I \Omega_I - P_{loss}}{C_I \Omega_I}$$

$$= 1 - \frac{Z_I \cdot \left(W|_{pin\ art} + W|_{bush\ art}\right)}{4\pi C_I} \qquad \textbf{(V-31)}$$

with:

- C_I, the mean chainring torque (for an entire drive rotation), either given as input or calculated using eq.(II-32).

The dissipated works depend on the kinematic case considered (case A or B). Therefore, using eq.(V-31), two efficiency values η_A and η_B are obtained, one for each kinematic case. Case B (sliding at both bush/roller and roller/profile interfaces) is the less favourable in terms of chain drive efficiency and therefore η_B is always the lower bound of the interval.

The chain drive model introduced in Chapter II is quasi static. Therefore, its results are independent of the drive rotational speed. The work dissipated in a chain articulation is calculated based on these speed free results. No notion of speed is added in the calculation of the dissipated work (see Table V-2, friction coefficients are assumed to be constant). The drive rotational speed appears in eq.(V-30) giving the power loss but cancels in eq.(V-31). In this model, the drive efficiency η is therefore independent from any speed consideration. This consequence of the quasi static chain drive model is supported by the experimental results of Lodge & Burgess [70] showing no significant effect of the rotational speed on efficiency. These tests were run for moderate speeds (up $150 rpm$) which is consistent with track cycling applications (see Figure V-10 below). For higher rotational speeds, the effect on power losses could be considered, for instance, by adding a physical model for the friction coefficients calculation (presented for instance in [86]). However, such a model was not used in this work.

The efficiency model can be easily adapted to study cranked link chains (*i.e.*, with only pin or bush articulations depending on the set-up direction). For such cases, eq.(V-28) should be modified to account for only the type of articulation considered (pin or bush).

For the rest of the manuscript, the chain drive efficiency model introduced in this part will be called the Chain Drive Efficiency Model (CDEM).

Further remarks:

Although not differentiated in the efficiency model presented, terms referring to meshing and roller losses can be identified in dissipated work expressions (see Table V-2). Indeed, angles between links mostly vary during link meshing and un-meshing and are essentially constant elsewhere (see Figure V-9 for α^* variation). Therefore, the terms $\Delta\alpha^*$, $\Delta\nu$ and $\Delta\kappa$ are mostly associated with meshing losses. On the other hand, the terms implying variation of the roller location Δs are associated with roller losses. Figure V-9 shows the variation of articulation angle α^* and the proportional contact displacement for the rear cog of the $60|15$ drive studied in §IV.3.2 at $C_I = 50 N.m$. It should be noted that the roller barely moves at the transition with the tight strand (from $\zeta/\alpha_I = 0$ to 1). Therefore, meshing and roller losses are mostly distinct in time. Indeed, meshing losses occur at link meshing and un-meshing while roller losses mostly occur in between. When the rollers do not reach the second transition point (*i.e.*, $\bar{d}_i < 100\%$) meshing and roller losses can coexist at transition with the slack strand. However, the load, and therefore the associated losses, at this point are usually significantly lower.
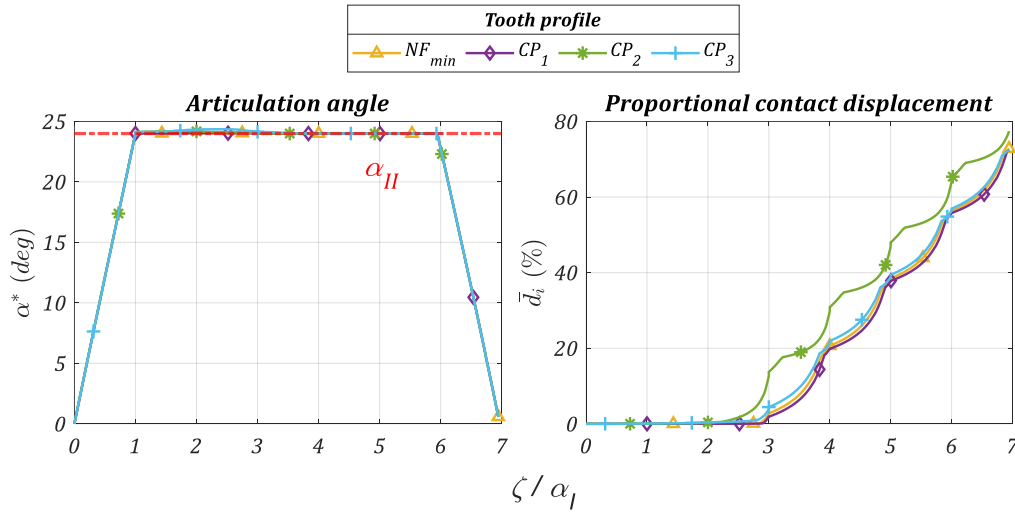
Figure V-9: Articulation angle and proportional roller displacement at the rear cog; $60|15$, $C_I = 50N.m$ (see §IV.3.2)

The model proposed is based on the numerical calculation of part motions and loads. Therefore, its results are dependent on the discretisation of the chain drive model. Considering the cyclic properties of the chain drive model (see Chapter II) the discretisation of "per component" variables directly depends on the number of sub-positions considered in the drive period studied. A study of the influence of this discretisation parameter on the efficiency predictions is presented in the Appendix I. It resulted in the adaptative pitch presented for example in Figure III-18. This adaptative pitch allows good representation of roller capture and release events (important to capture meshing losses) while limiting computation time. The influence of the friction correction angle δ and tanh parameter a (defined in Chapter II) on efficiency predictions were also tested. More information is presented in the Appendix I.

The Chain Drive Efficiency Model (CDEM) was introduced. This model unifies meshing and roller losses. It uses "per component" loads (link tension and roller/profile contact force) and roller location provided by the QSCDM (introduced in Chapter II). In accordance with the QSCDM, only 2D motions are considered. Coulomb friction is assumed at all the articulation interfaces considered (pin/bush, bush/roller and roller/profile). Roller rotation, not given by the chain drive model, is determined based on two extreme kinematic cases (denoted case A and B).

V.2 Elements of validation

The Chain Drive Efficiency Model (CDEM) was presented in the previous part. Its predictions are now compared to experimental measurements to assess the validity of the approach proposed. Results from the literature are first considered for industrial chain drives. Then results obtained using a dedicated track cycling test rig are compared with CDEM predictions.

V.2.1 Industrial drive: model and experiments from Lodge & Burgess [70]

The predictions of the Chain Drive Efficiency Model (CDEM) are compared to the work presented by Lodge & Burgess in [70]. In this paper, a model of chain drive efficiency was proposed considering only meshing losses at both the tight and slack strands. Experimental measurements were also conducted at several rotational speeds and used to validate the model. This comparison focusses on a 19|19 chain drive. It is specified in the paper that a Renold BS [11] chain of pitch $1/2''$ with 100 links was used but the tension setup and the tooth profile used were not mentioned.

To allow the comparison, the CDEM is set with the parameters given in Table III-4. The friction correction angle is $|\delta(\infty)| = 5°$ and the slack strand looseness is set at $slack = 7.25\%$ (details about this tension setting are given below). The chain characteristics are summarised in Table III-5 according to the manufacturer's catalogue [11] for a BS chain of $1/2''$. In addition, pin and bush diameters (not given in the catalogue) were measured on an ISO industrial chain of matching pitch. All the friction coefficients μ_{pb}, μ_{br} and μ_{rp} are assumed to be constant and equal to 0.11, as given in the paper for a lubricated steel/steel contact [70].

$Z_I|Z_{II}$	L	ΔY	$slack$	$|\delta(\infty)|$
19|19	$513.7mm$	0	7.25%	5°

Table V-3: Drive parameters for comparison with Lodge & Burgess [70]

Pitch p	D_{pin}	D_{bush}	D_{roller}	m_{link}
$12.7mm$	$4.42mm$	$6.37mm$	$8.51mm$	$8.89g$

Table V-4: Chain parameters from [11] for comparison with Lodge & Burgess [70]

It can be noted that the chain used is significantly heavier than a bicycle chain. The Renold BS chain has a mass of $8.89g/link$ compared to $3.6g/link$ for regular track cycling chain (see Table III-5 and Table V-5). This choice was made on purpose in the paper to favour losses in the slack strand (heavier links increase the slack strand tension).

In order to ensure comparison with the efficiency model presented by Lodge & Burgess [70], losses due to meshing had to be distinguished from the roller ones. Losses due to meshing are calculated considering only the losses occurring during the meshing and un-meshing period (*e.g.,* in the intervals $\zeta/\alpha_I \in [0,1]$ and $\zeta/\alpha_I \in [\zeta/\alpha_I|_{max} - 1, \zeta/\alpha_I|_{max}]$, in Figure V-9). As shown in Figure V-9, some roller losses can occur at the transition with the slack strand but their influence should be minimal as the loads are significantly lower than in the tight one. Knowing the CDEM meshing losses, the looseness setting $slack$ is chosen so that CDEM meshing loss predictions equal those of Lodge & Burgess's model for $C_{II} = 30N.m$ (*i.e.,* to fit the prediction of both models for the biggest torque, see Figure V-10). The value obtained ($slack = 7.25\%$) is higher than the 4 to 6% recommended from industrial drive [73] but still represents a realistic tension setting. The corresponding slack strand tension varies around $14.5N$.

Figure V-10 shows the comparison between the efficiency model of Lodge & Burgess, the experimental measurements performed by Lodge & Burgess, and the CDEM. The meshing losses, calculated as detailed above, are also shown. The interval between the two extreme efficiencies η_A and η_B is represented in the shaded area. As mentioned in §V.1.3, case B corresponds to the lower efficiency.
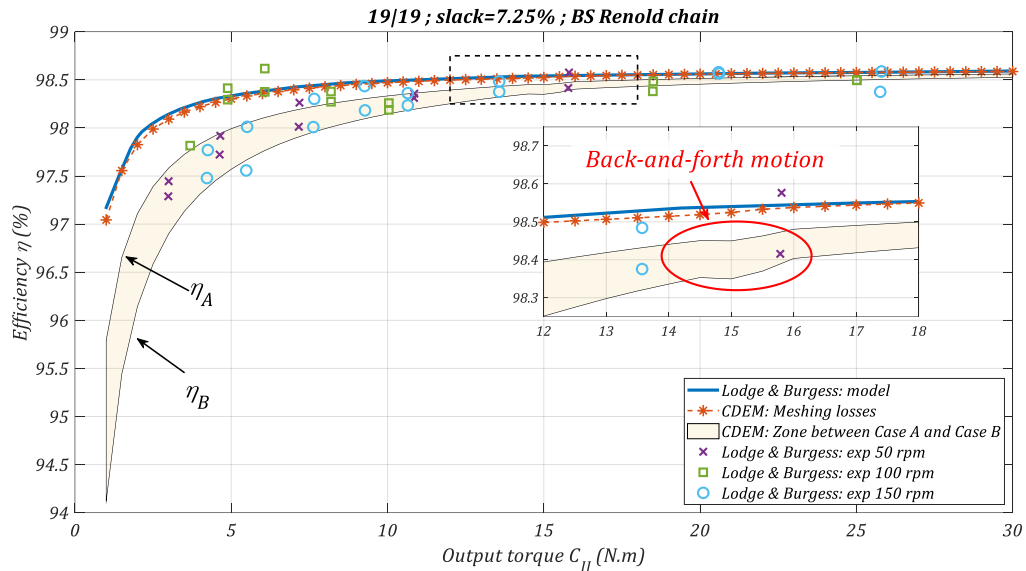
Figure V-10: Chain drive efficiency, comparison with Lodge & Burgess [70]

Both CDEM meshing losses and the model of Lodge & Burgess predict the same increase in chain drive efficiency with increasing output torques C_{II}. Considering only the meshing losses, this effect is explained as follows. The input power and the tight strand tension increase with torque. In the meantime, the slack strand tension remains the same (global kinematics is independent of the loading conditions). Therefore, the significance of the slack strand meshing losses decreases as torque increases, resulting in growing efficiency. Compared to the model of Lodge & Burgess, the whole CDEM (shaded area in Figure V-10) exhibits lower efficiency due to additional roller losses. The effect of roller losses is particularly significant for low torque. For instance, for $C_{II} = 1N.m$, the efficiency predicted considering only meshing losses is about 97% while the full CDEM predicts down to 94.1% (for case B) considering the effect of roller losses. However, with increasing torque, the effect of roller losses decreases as the predicted interval tends toward the meshing losses curve. Compared to the experimental measurements, Lodge & Burgess's efficiency model mostly overestimates the drive efficiency, especially for low torques. This overestimation was attributed in the paper [70] to vibrations and roller sprocket impacts. The CDEM shows better agreement with the experimental results. Indeed, the lower efficiency, due to roller losses, is in accordance with the experimental measurements at low torques. This result suggests that the losses responsible for the deviation of Lodge & Burgess's model from the experimental results could be caused by roller motion. It should be noted that the agreement with the $100rpm$ measurements is less convincing as the efficiencies are higher than those observed for 50 and $150rpm$ cases at low torque. However, the experimental results suggest that drive rotational speed is not a first order parameter on efficiency as no tendency with increasing speed is present.

An inflection in the CDEM predictions is visible at $C_{II} = 15N.m$. Efficiency stops momentarily to increase with growing torque before catching up with the original trend at about $C_{II} = 16N.m$. This inflection is not present in the meshing loss predictions. To investigate this phenomenon, Figure V-11 shows the roller motion at the driving sprocket for several output torques.
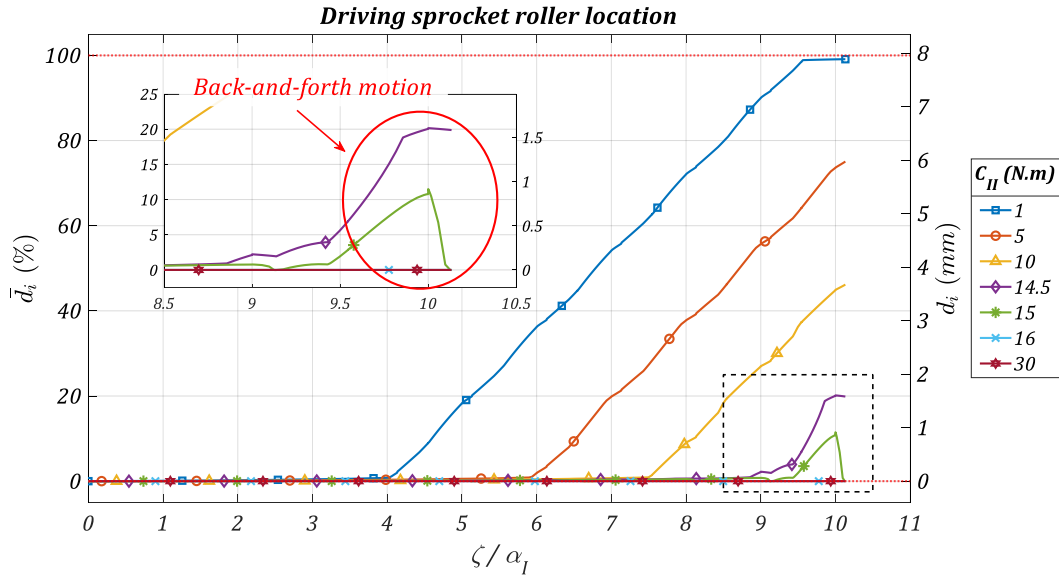
Figure V-11: Roller displacement for several torques, 19|19 drive, driving sprocket, ASA profile

As already shown in Chapter IV, rollers contact the driving sprocket nearby the transition point tp^B. The interval of tension ratios T_s/T_t explored is moderate as extreme values are about 0.36 and 0.018 for $C_{II} = 1$ and $30N.m$, respectively (see Chapter IV for orders of magnitude of tension ratios). This results in the driving sprocket being in the inter-tp regime (rollers tending to cross the profile toward tp^A) up to $C_{II} = 16N.m$ before reaching the static roller regime (see Figure V-11). The tooth climbing regime is not reached as rollers are still immobile at tp^B for $C_{II} = 30N.m$. Consequently, the curves are superimposed for small ζ/α_I and become distinguishable when the rollers leave the transition point. As the output torque C_{II} increases, the rollers tend to stay longer nearby the transition point. The inflexion, noticed in the efficiency predictions, corresponds to the transition from the inter-tp regime to the static roller one. Figure V-11 shows that this transition occurs between $C_{II} = 14.5$ and $16N.m$ as the rollers all remain immobile at the transition point for $C_{II} = 16N.m$. During the transition, back-and-forth roller motion occurs, particularly for $C_{II} = 15N.m$. This additional roller motion causes additional losses and explains the inflection in the efficiency predictions.

The increase of efficiency with growing torques, already reported in [70], is therefore related to two distinct effects. As the tight strand tension increases (to match the increasing torque requirement), the constant losses due to meshing at the slack strand become less significant compared to the input power (increasing with torque). At the same time, the increasing torque reduces roller motion and related roller losses. As it considers both meshing and roller losses, the CDEM therefore predicts a stronger effect of torque on chain drive efficiency compared to the model of Lodge & Burgess (see Figure V-10). More details about these points are given in the following chapter (see Chapter VI).

The comparison of CDEM with the results of Lodge & Burgess [70] shows that both models are in agreement. Considering additional roller losses, the CDEM justifies the drop in efficiency at low torque that could not be explained by models based only on meshing losses. It was shown that temporarily inflection could occur in the increasing relation between torque and efficiency. Such inflection is caused by the appearance of back-and-forth roller motion causing additional roller displacement and losses.

The new efficiency model is now tested against experimental results from a test rig dedicated to efficiency measurements of track cycling drives.

V.2.2 Track cycling drive: dedicated test rig measurements

A test rig dedicated to measurements of track cycling drive efficiency was developed at the LaMCoS[1] laboratory (see Figure V-12.a). This test rig mimics a track cycling drive. Two shafts, representing the chainring and rear cog axis are instrumented with torque transducers measuring both torque and rotational speed. No derailleur system is present. Rotational speed is imposed on Shaft 1 while resistive torque is imposed on Shaft 2 (see Figure V-12.b). The power is delivered and absorbed by two servo motors. Bearings are mounted between the drive and torque transducers. Consequently, comparing the power between the two shafts gives a measure of the efficiency of the tested drive plus the losses of the bearings and torque transducers. Therefore, only relative results are presented (comparison between drives) as the absolute drive losses cannot be easily determined. The centre distance L as well as the vertical shift ΔY can be set to match track bike dimensions. Any chainring or rear cog matching the track cycling standards can be tested.
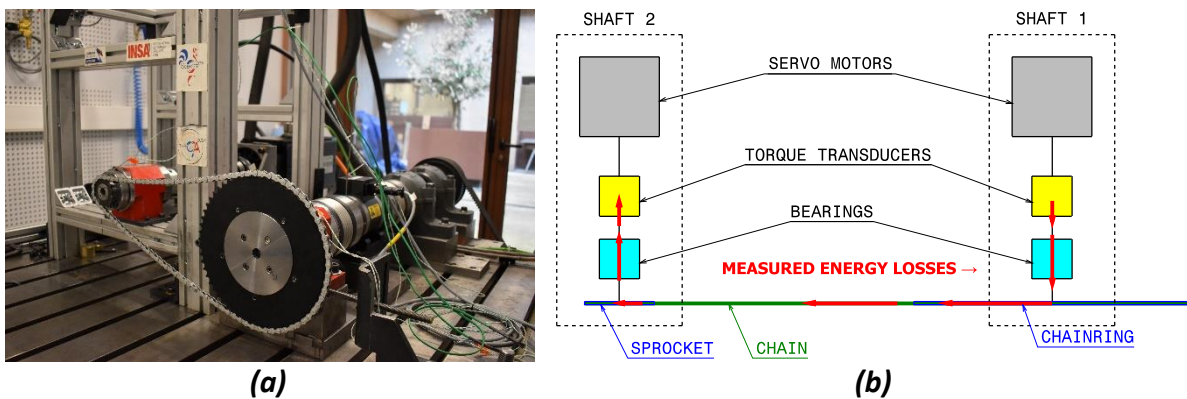
Figure V-12: Track cycling efficiency test rig (a) general view (b) diagram

For the results presented, the vertical shift ΔY is always set at $-50mm$ to reproduce real track bike dimensions [92]. The centre distance L is adjusted for each test to match the tension setting requirements. On the test rig, a representation of the chain tension is obtained by measuring the deflection at the middle of the tight strand under a mass of $1kg$. The deflection is measured perpendicularly to the tight common tangent direction (see Figure V-13.a). The measurement is carried out with unloaded drive. The tight strand is considered (instead of the slack one) as measurements are easier to carry out (the calliper can be put on the top of the strand, *etc*.) which ensures better precision and repeatability. The order of magnitude of the values obtained should be comparable to the slack strand deflections computed by the model (see Chapter II, §II.1.2) as the unloaded drive allows the strand looseness to pass indifferently from the tight or slack strand.

All the tests are performed using track cycling chains with their original lubricant. The characteristics of the chains used are given in Table V-5.

Pitch p	D_{pin}	D_{bush}	D_{roller}	m_{link}
$12.7mm$	$3.6mm$	$5.10mm$	$7.75mm$	$3.6g$

Table V-5: Track cycling chain dimensions for experimental measurements and model calculations

Calculations using the CDEM are all performed with a friction correction angle $|\delta(\infty)| = 5°$ and vertical shift $\Delta Y = -50mm$. All the friction coefficients (μ_{pb}, μ_{br} and μ_{rp}) are assumed to be constant and

equal to 0.11, similarly to the previous case. The chain dimensions are identical to these used on the test rig (see Table V-5).

(a) **(b)**
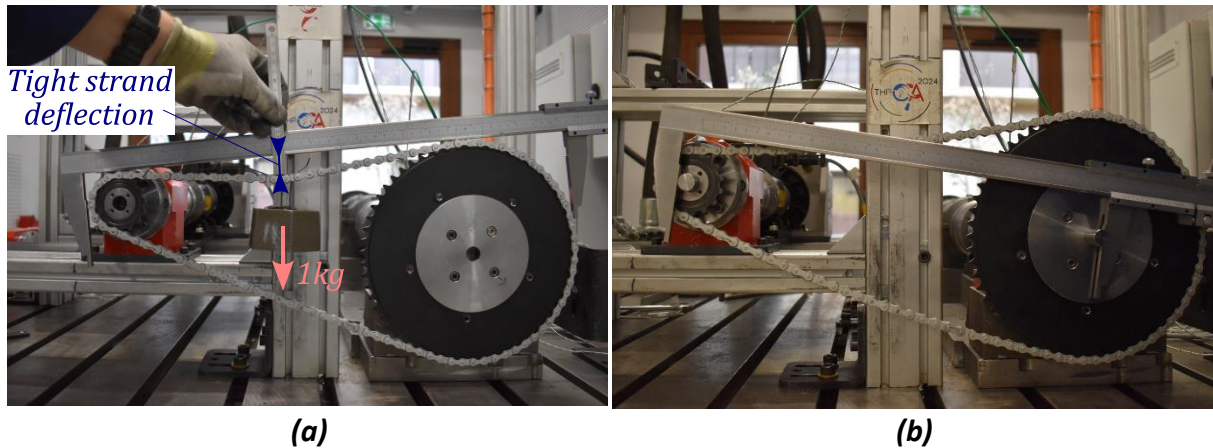
Figure V-13: Measurements of (a) tight strand deflection (b) centre distance L

Unless stated otherwise, comparisons between test rig results and CDEM are carried out using a real track cycling tooth profile called "*Reference*". The chainring and rear cog have been manufactured following this profile and used on the test rig. The precise 2D geometry of this profile was given to the author allowing efficiency calculations. The ϕ_{tp} parameter of this real track cycling profile is comparable to the values presented for the *Cycling Profiles* (see §IV.3). This confirms the conclusions of Chapter IV regarding specifying constraints on tooth profiles for track cycling applications.
The geometry of this *Reference* tooth profile is not given in this manuscript for confidentiality reasons.

All the experiments presented are representative of track cycling applications. Severe loading conditions are imposed with low slack strand tension (see m_{link} in Table V-5) resulting in low tension ratios. In this work, the author formatted the results obtained from the test rig. However, he did not develop the test rig itself or perform the measurements presented. The test rig results are presented here for the purpose of validating the chain drive efficiency model.

a) Influence of chain tension

The comparison of CDEM predictions with the test rig results is first conducted regarding the influence of the tension setting on the drive efficiency.

Several tension settings were tested on the test rig with the regular 60|15 drive presented in Chapter IV (see §IV.3). The tight strand deflection passed from $5mm$ for the tightest setting to 30 for the loosest. In terms of centre distance, this corresponds to 385.5 to 387.4mm. The tested chain had 100 links. The chainring and rear cog used the *Reference* profile. The influence of chain tension was tested for two loading conditions (denoted LC_1 and LC_2) described in Table V-6. The first condition (LC_1) shows reduced output torque (on Shaft 2) compared to LC_2. LC_2 also exhibits higher rotation speeds. These conditions have been chosen to be representative of real track cycling applications. LC_2 is representative of a high intensity sprint while LC_1 mimics endurance races.

Loading conditions (LC)	C_{II} ($N.m$)	Ω_I (rpm)	Input power P_I (W)
LC_1	13	90	490
LC_2	30	130	1634

Table V-6: Tested loading conditions for comparison between experiments and model results

Figure V-14 illustrates the two extreme tension settings (*i.e.*, tight strand deflections of 5 and $30mm$) using the drive arrangements predicted by the QSCDM for equivalent configurations. One can note that the number of links in contact with the chainring decreases as the slack strand became looser (strand tips are shown in red).

(a)   *(b)*
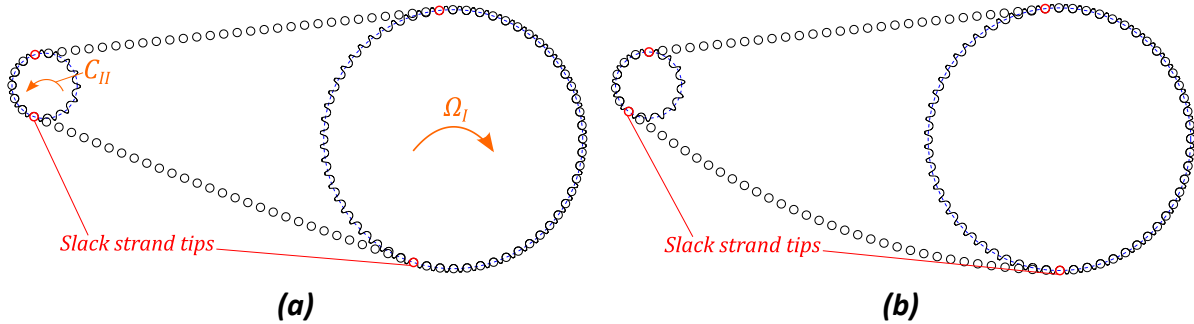
Figure V-14: $60|15$ *drives (a)* $slack = 2\%$ *(b)* $slack = 20\%$ *(with profile* CP_1*). Both figures have the same scale.*

The total losses measured by the test rig (losses from the drive and from the bearings) are presented in Figure V-15. The tests were performed by sessions of 25 minutes with efficiency measurements at 5, 15 and 25 minutes. Each tension setting (*i.e.*, tight strand deflection value) was tested during 6 sessions (*i.e.*, 18 efficiency measurements). The minimal and maximal values as well as the standard deviation are also represented in Figure V-15.
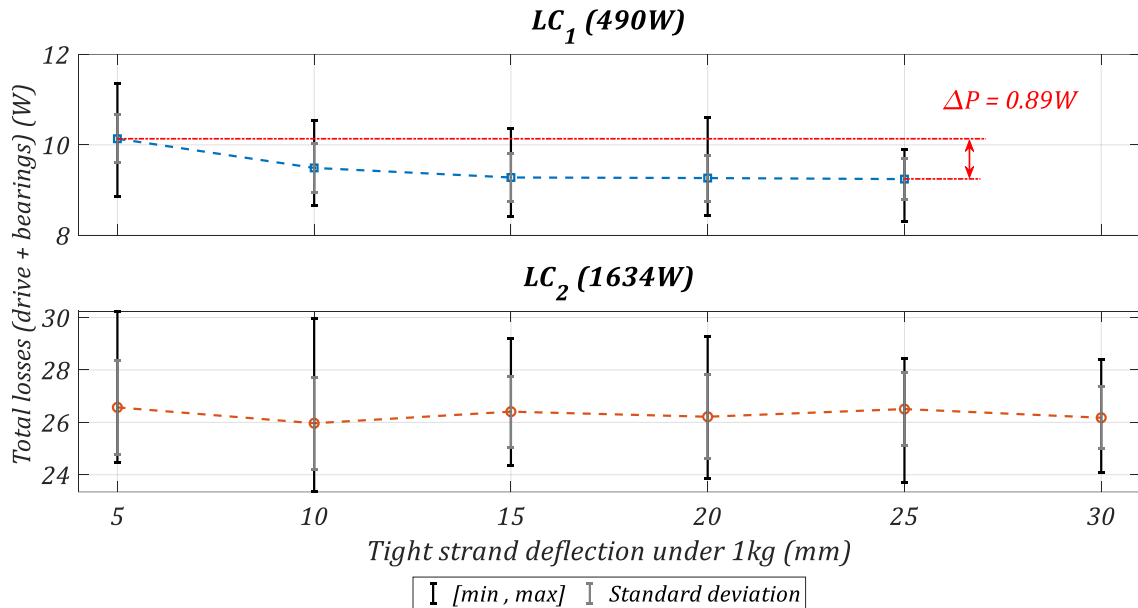
Figure V-15: Total power losses measured by the test rig for tension settings

Tighter settings correspond to small tight strand deflections (left of the graph) while looser settings are on the right of the graph.

For LC_1, as expected, the total losses decrease as the tension setting became looser. Starting from $15mm$ of tight strand deflection, the losses seem to reach a plateau where additional strand looseness does not result in less dissipation. On the contrary, between 5 and $10mm$ deflection, the effect of the tension setting is more significant. Between the tightest and the loosest settings, the mean difference in power losses reaches $\Delta P = 0.89W$ (see eq.(V-32)). For LC_2 however, no significant effect is visible. It must be noted that the dispersion at this loading condition is higher. Indeed, more than $1600W$ are

transmitted which increases the uncertainties related to the torque transducer. For LC_2 the standard deviation reaches about $1.5W$.

$$\Delta P = P_{tighest\ setting} - P_{loosest\ setting} \qquad \textbf{(V-32)}$$

with:

- $P_{tighest\ setting}$, the power losses obtained for the tightest tension setting (*i.e.*, smallest tight strand deflection or *slack* parameter).
- $P_{loosest\ setting}$, the power losses obtained for the loosest tension setting (*i.e.*, highest tight strand deflection or *slack* parameter).

To perform comparisons with these experimental results, the CDEM is tested with the parameters given in Table V-7. The *Reference* tooth profile geometry is used for all calculations. The values of L are chosen to obtain slack strand looseness ranging from 2% (tightest setting) to 20% (loosest setting). The range of explored tensions should be wider with the model than with the test rig. Indeed, $slack =$ 2% roughly corresponds to a tight strand deflection of $\frac{2}{100} \times 383 \times \frac{1}{2} = 3.8mm$ and $slack = 20\%$ should correspond to about $39mm$ (compare with from 5 to $30mm$ with the test rig). However, this comparison between the measured deflection and the computed one can only be carried out for an order of magnitude. Indeed, the chain drive model neglects roller/profile clearance for global kinematics (see Chapter II). Therefore, its centre distance predictions are underestimated as roller/profile but also chain articulation clearances must be overcome to reach the required tension (these clearances are neglected in the model, see Chapter II). Therefore, the centre distances L predicted by the model are systematically lower than that applied on the test rig to obtain a similar tension setting.

$Z_I | Z_{II}$	L	ΔY	$slack$	$|\delta(\infty)|$
60|15	$386.1 \rightarrow 383.0mm$	$-50mm$	$2 \rightarrow 20\%$	$5°$

Table V-7: Drive parameters of the model for comparison of tension influence with test rig measurements

The obtained drive efficiencies are represented in Figure V-16. The solid curves show the mean efficiency values and shaded areas show the interval $[\eta_B, \eta_A]$.
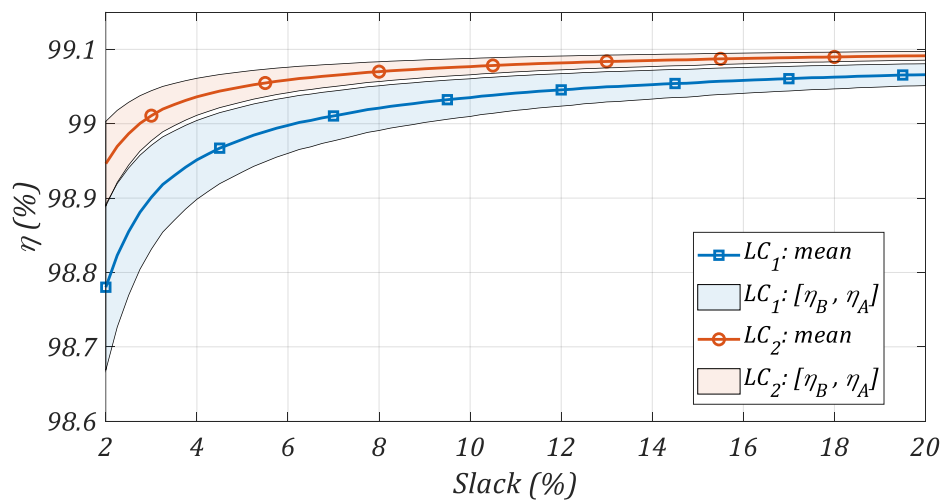
Figure V-16: Efficiency as a function of the slack setting for LC_1 and LC_2

In accordance with the experimental measurements for LC_1, efficiency increases for higher $slack$ values (*i.e.,* looser tension settings). Indeed, as the looseness increases, the slack strand tension decreases from about $13N$ to about $1.5N$ (for $slack = 2\%$ and $slack = 20\%$, respectively). Therefore, the associated losses are also reduced. Moreover, the decrease of slack strand tension also reduces the tension ratio T_s/T_t which tends to limit roller motion (see Chapter IV) and therefore the associated losses. Furthermore, consistently with the results shown in Figure V-10, the predicted efficiency is higher for LC_2 as the torque applied is greater ($C_{II} = 30N.m$ against 13 for LC_1). The interval $[\eta_B, \eta_A]$ also narrows as fewer roller motions occur as the torque increases.

The consequence of these efficiency values in terms of power dissipated by the chain drive are represented in Figure V-17. Power loss differences between the tightest ($slack = 2\%$) and the loosest ($slack = 20\%$) settings ΔP are given (see eq.(V-32)).

Comparison of the ΔP predictions between test rig measurements and CDEM predictions are summarised in Table V-8 for LC_1 and LC_2.
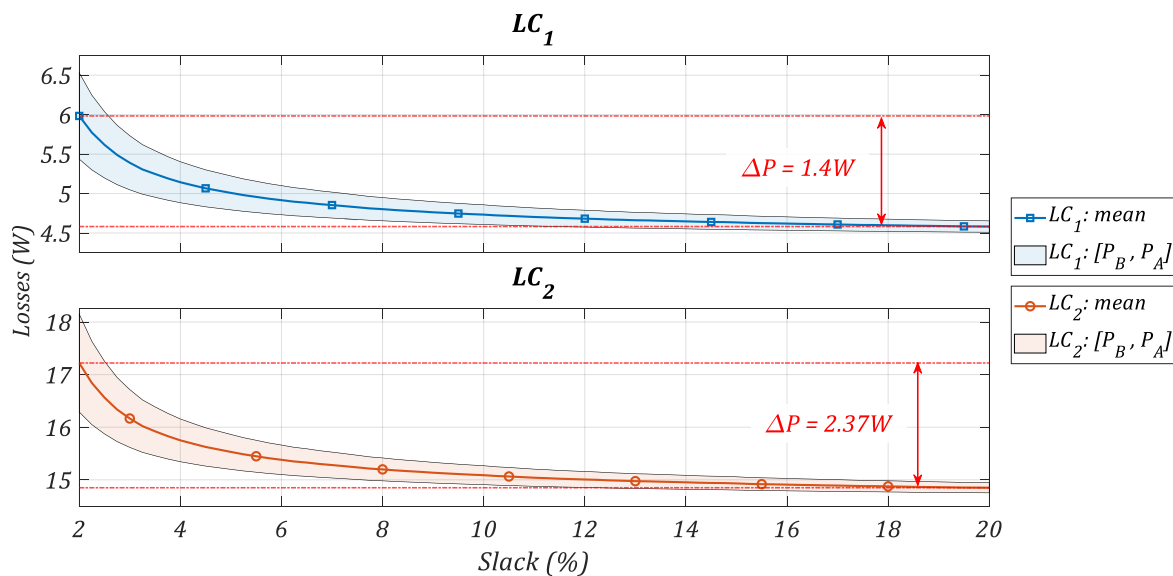
Figure V-17: Dissipated losses predictions depending on the $slack$ setting for LC_1 and LC_2

	Test rig experimental results	Model predictions
LC_1	$0.89W$	$1.4W$
LC_2	Non-significant	$2.37W$

Table V-8: Influence of tension setting: Comparison of ΔP between experimental measurements and CDEM predictions

According to the CDEM predictions, losses are reduced for higher $slack$ settings for both loading conditions (LC_1 and LC_2). Consistently with the experimental measurements, the dissipated losses tend to an asymptote for high $slack$ settings. The strong reduction in losses measured by the test rig between 5 and $10mm$ deflection (see Figure V-15) is also visible between $slack = 2$ and $\approx 6\%$ in the model predictions (see Figure V-17). A difference of $\Delta P = 1.4W$ is predicted by the model between the two extreme tension settings (*i.e.,* $slack = 2$ and 20%). This difference is consistent with the measurement of $0.89W$ by the test rig. Moreover, the interval of tension setting explored by the model is probably wider than that explored with the test rig. This wider interval will tend to increase the predicted ΔP, especially at low $slack$ settings (high tension) where small looseness variations cause high efficiency differences. For LC_2, due to the higher transmitted power, the model predicts a

difference of dissipated power of $2.37W$ between the two extreme settings. This difference was not observed in the test rig results. However, the predictions of the CDEM are within the order of magnitude of the measurement dispersions. Therefore, the predicted relation between the tension setting and drive losses is difficult to measure with the sensors available.

Although the prediction of ΔP is higher for LC_2 than for LC_1, its relative influence compared to the losses of the drive is significantly lower. ΔP reaches $1.4W$ compared to a loss of about $5.5W$ for LC_1. For LC_2, the drive losses represent about $16W$ with $\Delta P = 2.37W$ for LC_2. Therefore, the influence of the $slack$ setting decreases as torque increases.

For LC_1, CDEM predictions and experimental results agree on the asymptotical relation between tension setting and losses. Differences of dissipated power between the two extreme settings ΔP are also in accordance. The model prediction is higher but this difference could be explained by the difficulties of representing the same tension setting for both the test rig and the numerical model.
For LC_2 no significant results were observed in the test rig measurements. However, CDEM predictions show that the effect should lie within the test rig uncertainties. Indeed, the dispersion of the experimental results increases with the power transmitted.

b) Effect of numbers of sprockets teeth: comparison of $60|15$ and $52|13$ drives

The second comparison between the CDEM prediction and the test rig results is carried out considering efficiency results for different numbers of teeth. Two configurations with the same gear ratio $Z_I/Z_{II} = 4$ are considered: $Z_I|Z_{II} = 60|15$ and $52|13$. Sprocket size differences can be appreciated in Figure V-18 showing drive arrangements predicted by the QSCDM.

<div align="center">(a)   (b)</div>
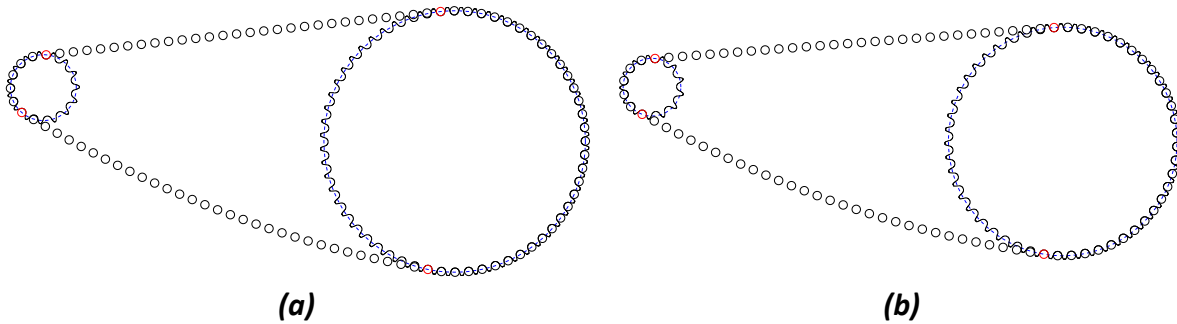
Figure V-18: (a) $60|15$ drive (b) $52|13$ drive, both with a looseness setting of $slack = 11\%$ (with Profile CP_1). Both figures have the same scale.

The comparison between the two drives is still carried out for the two loading conditions given in Table V-6. A chainring and a rear cog both corresponding to the *Reference* tooth profile were used for all the tests. The test rig centre distance L is chosen to obtain a tension setting representative of a typical track cycling drive (tight strand deflexion under $1kg$ mass of $\approx 20mm$). The resulting centre distances varied from 381 to $386mm$. It can be noted that the tight strand deflection considered lies at the plateau where differences in $slack$ settings have minimal consequences on efficiency (see Figure V-15). Chains of 100 and 94 links were used for the 60|15 and 52|13 drives, respectively.
The total losses (drive + bearings) measured by the test rig are presented in Figure V-19. The mean values are given with the minimal and maximal measurements and the standard deviation. As for the previous case, the results were obtained by performing 25-minute tests of each configuration with efficiency measurements at 5, 15 and 25 minutes. 3 and 4 sessions were performed for 52|13 and 60|15 at LC_1, respectively (corresponding to a total of 9 and 12 measurements, respectively). For LC_2, 8 sessions were performed for both configurations (24 measurements) in order to reduce uncertainties.
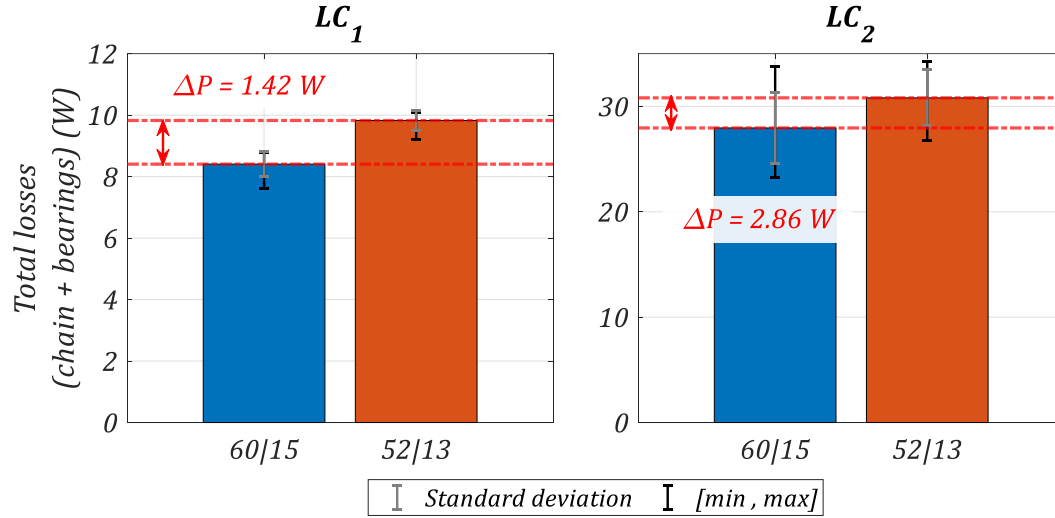
Figure V-19: Total power losses measured by the test rig for $60|15$ and $52|13$ drives for both Loading Conditions (LC_1 and LC_2)

As with the previous case, higher losses are measured for LC_2 which come along increasing test rig uncertainties (higher standard deviation and $[min , max]$ interval, see Figure V-19). For both loading conditions, the mean losses obtained with the 60|15 drive are lower than those obtained with the 52|13 one. The difference ΔP between 60|15 and 52|13 drives (see eq.(V-33)) reaches $1.42W$ for LC_1 and $2.86W$ for LC_2. These results confirm previous measurements from the literature showing that efficiency is higher for bigger sprockets [70], [76], [93].

$$\Delta P = P_{52|13} - P_{60|15} \qquad\qquad \textbf{(V-33)}$$

with:

- $P_{52|13}$, the power losses obtained for the 52|13 drive
- $P_{60|15}$, the power losses obtained for the 60|15 drive

Comparison with the CDEM predictions is carried out with the following parameters. The slack strand looseness is set at $slack = 11\%$ to obtain a comparable tension setting. As with the test rig tests, the number of links are 100 and 94 for the 60|15 and 52|13 drive, respectively. The *Reference* profile is used for all the calculations allowing direct comparisons with the experimental measurements. A summary of the drive parameters used is given in Table V-9.

$Z_I|Z_{II}$	L	ΔY	$slack$	$|\delta(\infty)|$
52|13	$381.3mm$	$-50mm$	11%	5°
60|15	$385.8mm$			

Table V-9: Drive parameters for the comparison of $52|13$ and $60|15$ drives

The results obtained are presented in Figure V-20. Predicted efficiencies as well as drive losses are shown for each configuration. Error bars give the values of efficiency η and power losses P for cases A and B. The main bars represent the mean of both cases. Differences in power losses ΔP between 60|15 and 52|13 (see eq.(V-33)) configurations are also shown.

Efficiency model: comparison of 52|13 and 60|15 for two Loading Conditions ($LC_{1,2}$)
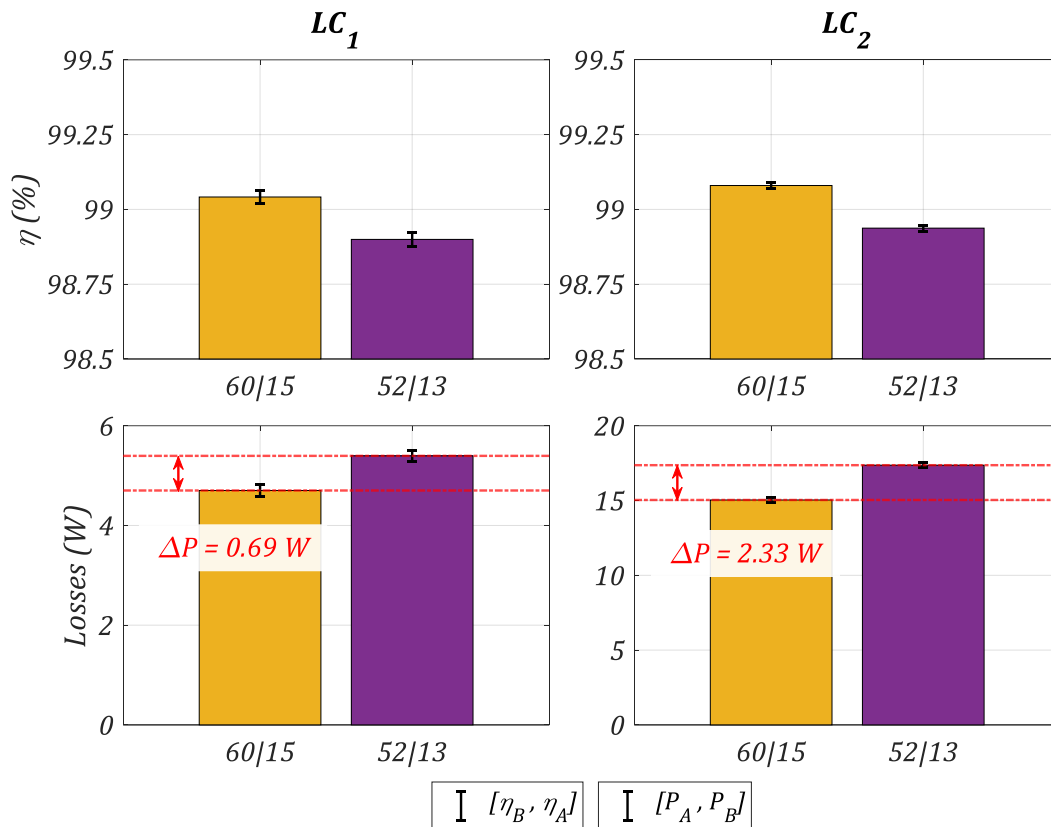
Figure V-20: Model predictions for $60|15$ and $52|13$ drives for both Loading Conditions (LC_1 and LC_2)

For both loading conditions, the predicted efficiencies are higher for the 60|15 drive. Moreover, efficiencies are also higher for LC_2 (with more torque) than for LC_1 and the $[\eta_B, \eta_A]$ interval is reduced (see Figure V-16). Consequently, in accordance with the test rig results, loss predictions are higher for the 52|13 drive.

Loss differences ΔP measured by the test rig and calculated with the CDEM are given in Table V-10.

	Test rig experimental results	CDEM predictions
LC_1	$1.42W$	$0.69W$
LC_2	$2.86W$	$2.33W$

Table V-10: Comparison of ΔP between experimental measurements and model predictions for different sprocket sizes

Test rig results and CDEM predictions agreed that the 60|15 drive is always more efficient than the 52|13 (physical explanations about this point are given in Chapter VI). Moreover, the orders of magnitude of the ΔP are similar for the CDEM and the test rig. However, model predictions in terms of ΔP are lower than test rig measurements. This is particularly true for LC_1 where the prediction is about half the measured value. For LC_2, the model prediction is within the test rig error bars (see Figure V-19).

It is possible that the *slack* settings used for the CDEM were looser than the test rig ones. Indeed, as mentioned above, tension settings are difficult to compare between the CDEM and the test rig. This could explain the lower ΔP predictions as increasing the slack strand tension (*i.e.*, reducing the strand deflection) would automatically increase the drive losses and therefore the differences between 52|13 and 60|15 (see Figure V-15). As this effect decreases with increasing torque (see Figure V-16) this could explain why the CDEM predictions for ΔP are better for LC_2 than for LC_1. However, the *slack* setting

tested should lie at the plateau where this effect should not be very significant. It is also possible that the assumed friction coefficients (0.11 for all interfaces) are too low and that more dissipative contacts occur for the drive tested, resulting in higher ΔP.

Nevertheless, test rig measurements and model predictions both agreed that bigger sprockets exhibit higher efficiency. This result is consistent with the literature as it has already been reported both experimentally [70], [76], [93] and by models [70], [74], [76], [93]. Moreover, the order of magnitudes obtained for loss differences ΔP are consistent between test rig measurements and model predictions, suggesting that no important phenomenon has been neglected.

c) Influence of chainring tooth profile

The final comparison between CDEM calculations and test rig results is carried out by testing the influence of the chainring tooth profile. Three chainrings from the market (denoted Chainring 1, 2 and 3) are compared, using the test rig, to the *Reference* chainring. All the tests are performed at Loading Condition LC_1 (see Table V-6) using a 60|15 drive configuration. A 15 tooth *Reference* rear cog was used for all tests. Parameters of the chains used corresponded to Table V-5 with 100 links (see Figure V-21). The drive centre distance was again set to obtain a strand deflection under $1kg$ mass of $\approx 20mm$. Slight differences in tight strand deflection were observed between chainring tooth profiles for a given centre distance L. Therefore, each drive was set with its specific centre distance to obtain the required tension setting (the values of L obtained ranged from 384 to $386mm$). However, as the tension setting lies in the plateau reported in Figure V-15, the consequences on the efficiencies measured should not be significant.

Manual interventions had to be performed on the test rig between the trials of the different chainrings. Due to these interventions, sensor offsets were modified causing the magnitude of total losses measured by the test rig to be different for each chainring. However, the *Reference* chainring was tested after each intervention. Therefore, a test with the *Reference* chainring is available for each chainring tested (*i.e.*, Chainring 1,2 and 3) in the same test rig conditions. Consequently, the results are given directly in Figure V-22 relatively to the reference case (*Reference* chainring and rear cog). The difference ΔP corresponds to the losses obtained with a given chainring compared to those obtained with the *Reference* one according to eq.(V-34).
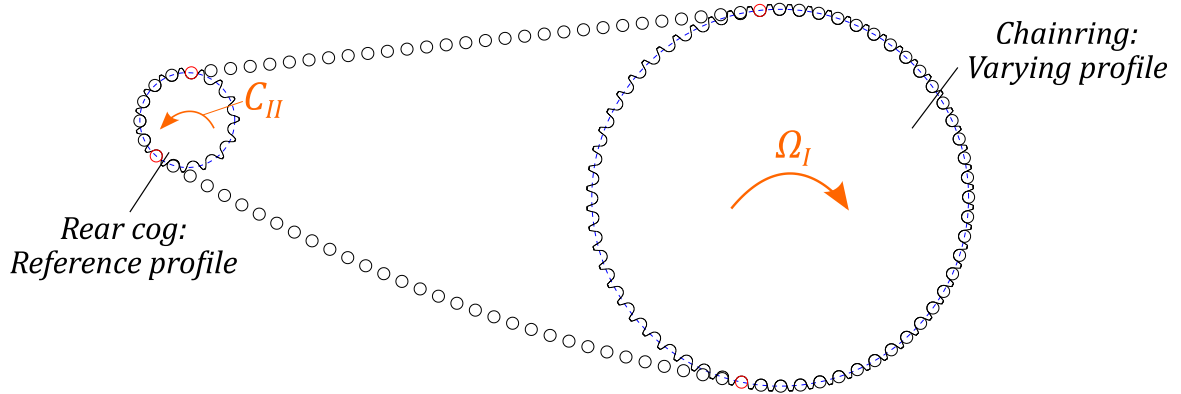
Figure V-21: Illustration of chainring influence tests

$$\Delta P = P_{Chainring\ i} - P_{Ref} \qquad \text{(V-34)}$$

with:

- $P_{chainring\ i}$, the total losses measured using Chainring i

- P_{ref}, the total losses measured using the *Reference* chainring

Tests were performed in sessions of 25 minutes with measurements at 5, 15 and 25 minutes. Each comparison with the *Reference* configuration was carried out on 12 measurements (4 sessions of 3 measurements). The minimal and maximal values as well as the standard deviation are indicated in Figure V-22.
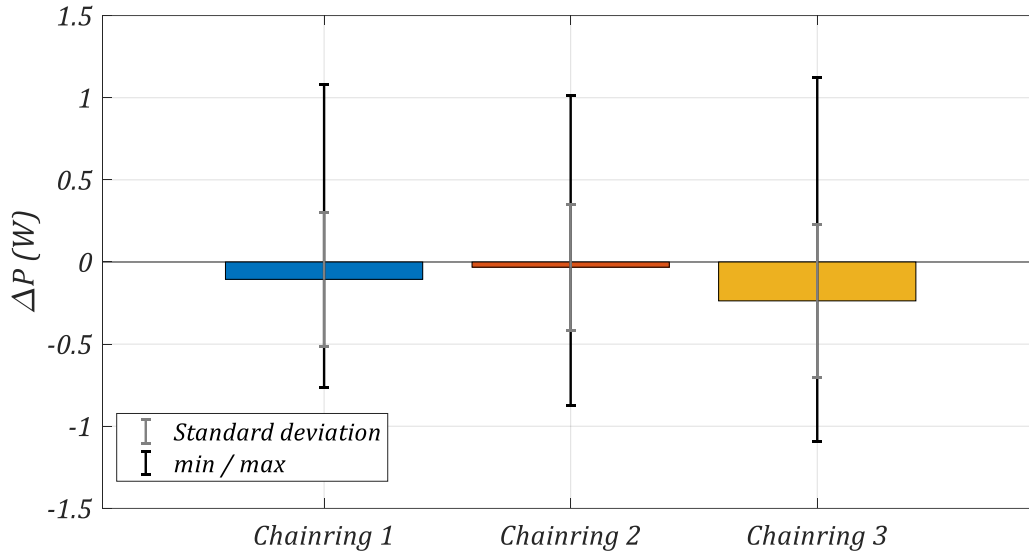
Figure V-22: Test rig measurements for the three chainrings tested relatively to the Reference case

The measured ΔP are negative, suggesting better efficiency with the tested chainring than for the reference case (*Reference* chainring and rear cog, see eq.(V-34)). However, all ΔP are included in the standard deviations. Therefore, the tests concluded that there were no significant differences between the three chainrings tested and the *Reference* one.

Except for the *Reference* tooth profile (denoted "Ref" in Figure V-23), the precise 2D geometries of the chainrings tested (Chainrings 1,2 and 3 in Figure V-22) are not known by the author. To perform comparisons with the model results, the influence of the chainring tooth profile is assessed by testing the four profiles able to withstand track cycling constraints: NF_{min}, CP_1, CP_2 and CP_3 (see §IV.3). The calculations are performed for LC_1 (see Table V-6) using the drive parameters given in Table V-9 for 60|15 drive. The chain parameters can be found in Table V-5 with 100 links. Drive efficiency as well as relative losses ΔP (see eq.(V-34)) compared to the reference case are given in Figure V-23. The intervals obtained using case A and case B are represented. For the relative losses, intervals $[\Delta P_{min}, \Delta P_{max}]$ (see Figure V-23) are calculated assuming that cases A and B could occur indifferently for each configuration (see eq.(V-35)).

$$\Delta P_{min} = P_{ref}\big|_A - P_{profile}\big|_B \qquad (a)$$
$$\Delta P_{max} = P_{ref}\big|_B - P_{profile}\big|_A \qquad (b)$$

(V-35)

with:

- $P_{ref}\big|_{A,B}$, the dissipation obtained with the *Reference* geometry for case A or B
- $P_{profile}\big|_{A,B}$, The dissipation obtained using the tested profile (NF_{min}, CP_1, CP_2 or CP_3) for case A or B
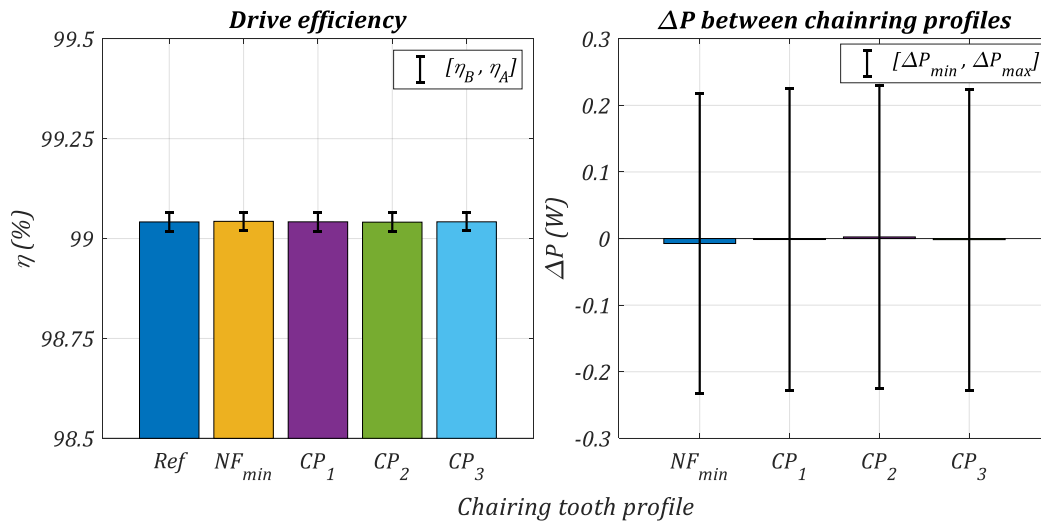
Figure V-23: Influence of chainring tooth profile according to the CDEM predictions

The drive efficiencies predicted by the CDEM are identical for all the chainrings tested. Consequently, the ΔP values are negligible and included in the $[\Delta P_{min}, \Delta P_{max}]$ intervals. Therefore, the model also concluded that the chainring tooth profile had a negligible effect on drive efficiency.

The CDEM can be used to explain the similar efficiencies for all the chainrings tested. Indeed, using a similar method as indicated in §V.2.1, the computed losses are split between roller and meshing losses and between the chainring and the rear cog contribution. The proportions obtained for a CP_1 chainring are presented in Figure V-24 and Table V-11 ($j = I$ and II for the chainring and rear cog, respectively). Losses due the roller motion are denoted 'roller' while those due to meshing are denoted 'mesh'.
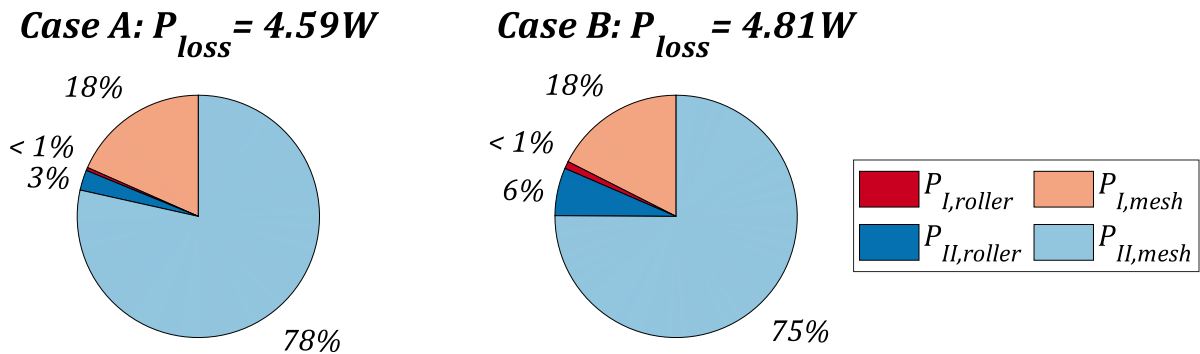
Figure V-24: Loss contributions for the $60|15$ drive, LC1, CP_1 chainring and Reference rear cog

	$P_{I,roller}$	$P_{I,mesh}$	$P_{II,roller}$	$P_{II,mesh}$
Case A	< 1%	18%	3%	78%
Case B			6%	75%

Table V-11: Loss contributions for the $60|15$ drive, LC1, CP_1 chainring and Reference rear cog

First, it is observed that the total predicted losses are higher for case B than for case A ($4.81W$ and $4.59W$, respectively). This was expected considering the less favourable hypotheses of case B. Meshing losses are caused by parameters depending on the global kinematics: tight strand tension T_t, pitch angle $\alpha_{I,II}$, *etc.* They are therefore identical for all the chainrings. Thus, changing the chainring tooth

profile influences only the losses attributed to roller motion at the chainring. However, results show that this loss type contribution represents less than 1% (both for cases A and B). In these conditions, the negligible influence of chainring geometry seems consistent. This low proportion of roller motion related losses is due to the low tension ratio (about $6.2e^{-3}$) resulting in small roller motion. Moreover, this motion occurs under moderate loading due to the rapid decrease in both link tension T and contact force P undergone using track cycling profiles (see *e.g.*, Figure IV-36). More details about this point will be given in the following chapter (Chapter VI).

The remaining proportions show that meshing losses are by far the greatest contributor in this loading condition. 18% of the losses are due to the chainring meshing losses while between 75 to 78% are caused by the rear cog meshing losses. This difference between chainring and rear cog meshing are directly related to the pitch angle α_j [32], [70], [76]. Indeed, the rear cog pitch angle is significantly higher than the chainring one due to its smaller number of teeth ($\alpha_I = 24°$ and $\alpha_{II} = 6°$ in this example), resulting in a greater sliding distance. The results also show that roller losses at the rear cog are more significant than those at the chainring.

No significant influence of the chainring geometry was reported on the test rig measurements. Although direct comparisons using the tested tooth profile geometries could be performed, analysis of the model results prove that the chainring geometry is not a significant parameter under the loading condition tested. The CDEM prediction therefore seems correct. Moreover, the model proves to be an efficient tool for analysing and explaining the test rig results.

Comparisons with experimental results, both from the literature and from a dedicated test rig were carried out. In both cases, the CDEM predictions agreed with experimental the measurements, therefore demonstrating the relevance of the approach presented.

V.3 Conclusion

This chapter was dedicated to the introduction and validation of the Chain Drive Efficiency Model (CDEM). This model calculates chain drive efficiency considering meshing losses and losses due to roller motions along their corresponding tooth profile.

The efficiency model was first introduced. This model considers all losses due to friction at the chain interfaces. This includes meshing losses and losses caused by roller motion along their associated tooth profile. It is intended to be used with the QSCDM presented in Chapter II as it uses loads (link tension and roller/profile contact force) and roller location "per component" as inputs. The hypotheses are the same as those of the chain drive model: only planar motions (2D) are considered without any influence of dynamical effects (quasi-static). The chain is assumed to be perfectly aligned and therefore friction is considered only at the pin/bush, bush/roller and roller/profile interfaces (no lateral contact occurs with plates). Coulomb friction is assumed at all interfaces. Differences between pin and bush articulations are considered. The results per component provided by the chain drive model (introduced in Chapter II) give only the evolution of the roller/profile contact location. Therefore, additional kinematic hypotheses are stated to determine roller rotation. Two extreme cases, meant to represent the best and worst possible conditions, were considered. In case A, rolling without sliding occurs at the roller/profile interface while sliding occur at the bush/roller one. In case B, sliding occur at both the bush/roller and roller/profile interfaces. The contact hypotheses assumed for this efficiency model are different from those of Kim & Johnson's tension model [52] in which rolling at the bush/roller interface was considered simultaneously to sliding at the roller/profile one. As a consequence of the two kinematic cases considered, the predicted efficiency is given in the form of an interval $[\eta_B, \eta_A]$.

The CDEM predictions were then compared to experimental results, both from the literature and from a dedicated test rig. Predictions agreed with the experimental measurements of Lodge & Burgess [70] for an industrial drive. The results showed that lower efficiencies observed at low torque, which could not be explained by a model considering only meshing losses (like that presented by Lodge & Burgess), seemed to be caused by roller motion losses. This comparison demonstrates the interest of the model presented. The predictions of the CDEM were then compared to experimental measurements from a test rig dedicated to track cycling applications. For a high transmitted power (about $1600W$), the variability in the experimental results made comparisons difficult. However, for lower power (about $490W$), the trends found with the CDEM and the test rig were in accordance. The model and experimental measurements agreed on the asymptotic relation between chain tension and drive efficiency. The interest of using bigger sprockets was also found by both approaches and the magnitude of model predictions in terms of saved power was consistent with the experimental results. Finally, the model and experiments agreed on the negligeable influence of the chainring tooth profile. For this last case, the model proves to be a good tool for explaining numerical results as it provides information about the significant loss mechanisms.

The validation process showed that the influence of the parameters tested (*e.g.*, torque, chain tension, *etc*.) is usually more significant than the width of the interval $[\eta_B, \eta_A]$. Therefore, considering two kinematic hypotheses does not prevent conclusions to be drawn with the CDEM.

The Chain Drive Efficiency Model (CDEM) was introduced and validated. It will now be used to explore the efficiency of track cycling drives and identify the parameters with the greatest impact.

Chapter VI

Parametric study of chain drive efficiency

The previous chapter introduced a Chain Drive Efficiency Model (CDEM). The latter considers both roller and meshing losses and has the ability to consider different tooth profile geometry. Using the model introduced, this chapter presents a parametric analysis of chain drive efficiency. Only track cycling cases are considered. They are characterised by low slack strand tensions (about $3N$) and high input torques (up to $300N.m$ at the chainring sustained for several drive rotations), resulting in small tension ratios (about $1e^{-3}$ for $300N.m$). An example of such a drive is presented in Chapter IV. Only the four profiles able to withstand track cycling constraints are considered: NF_{min}, CP_1, CP_2 and CP_3. The first part is dedicated to the full characterisation of a regular 60|15 drive. To do so, the influence of torque and tension setting on the efficiency of such a drive is studied. It is shown that the action of both parameters can be combined into a single third one: the tension ratio. The evolution of loss mechanisms for several ratios is then analysed. Total losses are split between roller and meshing contributions to determine which phenomenon is dominant for track cycling drives. In addition, calculations are carried out for different tooth profiles to study their influence on drive efficiency. A key tooth profile parameter explaining the differences between geometries is identified.

Then, the analysis is extended to other drive configurations. To do so, parameters related to the drive architecture are explored. The influence of the number of sprocket teeth is characterised for several applied torques. Application to drives with constant gear ratio Z_I/Z_{II} is presented (*e.g.*, 44|11 and 60|15 drives with a gear ratio of 4). The influence of chain pitch is then tested for standards directly above and below the reference $1/2''$ pitch used in cycling applications. Changing the chain pitch usually occurs with the modification of chain part dimensions (*i.e.*, change of pin, bush and roller diameters) [11]. To properly separate the effect of this change of dimension from the pitch change, hypothetical cases with pin, bush and roller dimensions equal to those of a reference $1/2''$ chain are studied. Then, the influence of the friction coefficient is assessed. Losses are also split between the contribution of each interface (pin/bush, bush/roller and roller/profile) in order to identify the main contributors.

Finally, an analysis of chain drive efficiency based on Design Of Experiments (DOE) is proposed. This analysis summarises the effect of all the parameters considered in this chapter (*i.e.*, torque, tension setting, sprocket sizes, chain pitch and friction coefficient). It gives a global point of view to easily identify which parameters have the greatest influence. Interactions between parameters are also identified. Based on this analysis, guidelines for future efficiency optimisation are given.

Parameters used for efficiency calculations

In this chapter, unless otherwise stated, all calculations are carried out for $|\delta(\infty)| = 5°$ and $a = 0.1nm = 1e^{-10}m$. As with the validation process, the friction coefficients at pin/bush, bush roller and roller profile interfaces (*i.e.*, μ_{pb}, μ_{br} and μ_{rp}, respectively) are assumed to be constant and all equal to a global friction coefficient $\bar{\mu} = 0.11$ [70]. By default, a $1/2''$ chain is considered with the dimensions given in Table VI-1. The vertical shift is constant: $\Delta Y = -50mm$. The numbers of chain links are always even and chosen so that the centre distance L obtained is adjusted to obtain the required tension setting $slack$, with the smallest value above $L = 380mm$. These constraints are chosen to match the geometrical properties of a real track bicycle [92]. In the previous chapter (see Chapter V), torques were given for the rear cog to match the test rig conditions. In this chapter however, torque values C_I are given for the chainring (*i.e.*, torque applied by the athlete). Values are therefore generally higher due to the gear ratio Z_I/Z_{II}.

Pitch p	D_{pin}	D_{bush}	D_{roller}	m_{link}
$12.7mm$	$3.6mm$	$5.10mm$	$7.75mm$	$3.6g$

Table VI-1: Regular track cycling chain parameters

VI.1   60|15 drive: characterisation and tooth profile analysis

This part is dedicated to the characterisation of a regular 60|15 track cycling drive. The influence of torque (*i.e.*, chainring torque C_l) and tension setting $slack$ on drive efficiency is explored. It is shown that they can be simultaneously analysed using the tension ratio T_s/T_t. Then, the underlying mechanisms explaining the evolution of efficiency depending on the tension ratio are analysed. To simultaneously explore the influence of tooth profile geometry, calculations are carried out using the four profiles suitable for track cycling applications (see Chapter IV, Figure IV-33): NF_{min}, CP_1, CP_2 and CP_3.

Profile parameters are recalled in Table VI-1. All the profiles studied are defined using two circle arcs 1 and 2 (see Appendix A for profile definition). R_1 is the radius of the tooth bottom circle arc (to be compared with $R_{roller} = 3.875mm$) and R_2 is the radius on the second arc.

	CP_1	CP_2	CP_3	NF_{min}[1]
K (**deg**)	15	15	19.96	20
K' (**deg**)	55.3	97.42	139.5	135.5
R_1 (**mm**)	3.9	4.05	4.2	3.91
θ_1 (**deg**)	$75 - 125/Z$	$75 - 85/Z$	$70 - 45/Z$	$70 - 45/Z$
R_2 (**mm**)	$\frac{1}{2}Z + 6$	$Z + 1$	$2Z - 9$	$0.93(Z + 2)$
R_{tip} (**mm**)	$2.023Z + 3.141$			$R_{pitch} + 4.0625$

Table VI-2: Tooth profiles parameters for NF_{min}, CP_1, CP_2 and CP_3

Used in eq.(IV-6), parameters K and K' result in the ϕ_{tp} values presented in Figure IV-32. Profiles NF_{min} and CP_3 showed similar pressure angles. Profile CP_2 had the smallest ϕ_{tp} for all the numbers of teeth tested. Below 15 teeth, profile CP_3 has the biggest pressure angle. Its value then decreases toward that of CP_2, leaving the NF_{min} and CP_3 profiles with the highest ϕ_{tp} above 17 teeth. Regarding the tooth bottom radius R_1, CP_1 has the smallest one close to the NF_{min} value. Profile CP_2 and CP_3 exhibit higher radii. Each profile then shows different values for R_2 and R_{tip} (see Table IV-10). However, the transition points lie close to the border between the two circle arcs for all the profiles (see Appendix A and Figure VI-1). Therefore, parameters R_2 and R_{tip} should not influence profile behaviour as no roller will contact the tooth flanks higher than both transition points. Indeed, these profiles are considered in this chapter because they do not reach the tooth climbing regime for usual track cycling loading conditions (conversely to NF_{max} and ASA). Consequently, for all the calculations presented in this chapter, all the profiles present roller motion in inter-tp or static roller behaviour (see Chapter IV).

---

[1] For $p = 12.7mm$ and $D_{roller} = 7.75mm$
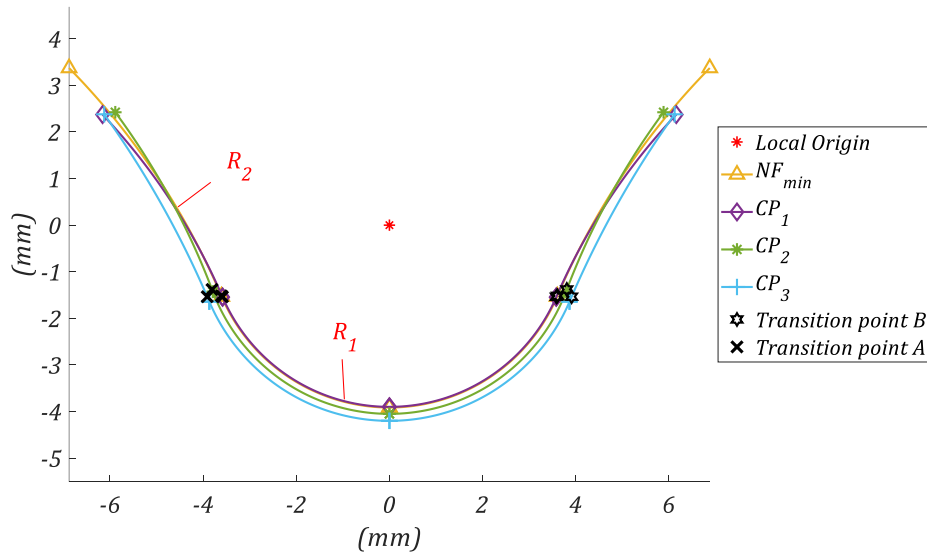
Figure VI-1: Profiles NF_{min} and Cycling Profiles in local coordinate system with transition points A and B ($Z = 15$, $p = 12.7mm$)

VI.1.1 Influence of torque and tension setting. Common approach of tension ratio

a) Efficiency depending on torque

The influence of torque is studied first. Calculations are carried out for the usual 60|15 drive with a tension setting $slack = 11\%$. The centre distance L is set to the smallest value above $380mm$ allowing to obtain the prescribed tension setting. This results in a chain with 100 links. The slack tension is about $2.7N$ in these conditions (see Figure IV-28). Torques ranging from 5 to $300N.m$ are considered to match track cycling conditions. The conditions imposed result in chainring tension ratio $T_{s,I}/T_t$ ranging from about $6.1e^{-2}$ for $C_I = 5N.m$ to about $1.1e^{-3}$ for $300N.m$.

A summary of the drive parameters is given in Table VI-3.

$Z_I|Z_{II}$.	$slack$ (%)	L (mm)	Nb_{link}	$T_{s,I}$ (N)	C_I ($N.m$)	$T_{s,I}/T_t$
60|15	11	> 380	100	≈ 2.7	$5 \rightarrow 300$	$6.1e^{-2} \rightarrow 1.1e^{-3}$

Table VI-3: Drive characteristics for the influence of chainring torque C_I

The efficiencies obtained are first presented only for the NF_{min} profile in Figure VI-2. The mean efficiency between cases A and B is represented by a solid line while the interval $[\eta_B, \eta_A]$ is represented by a shaded area.
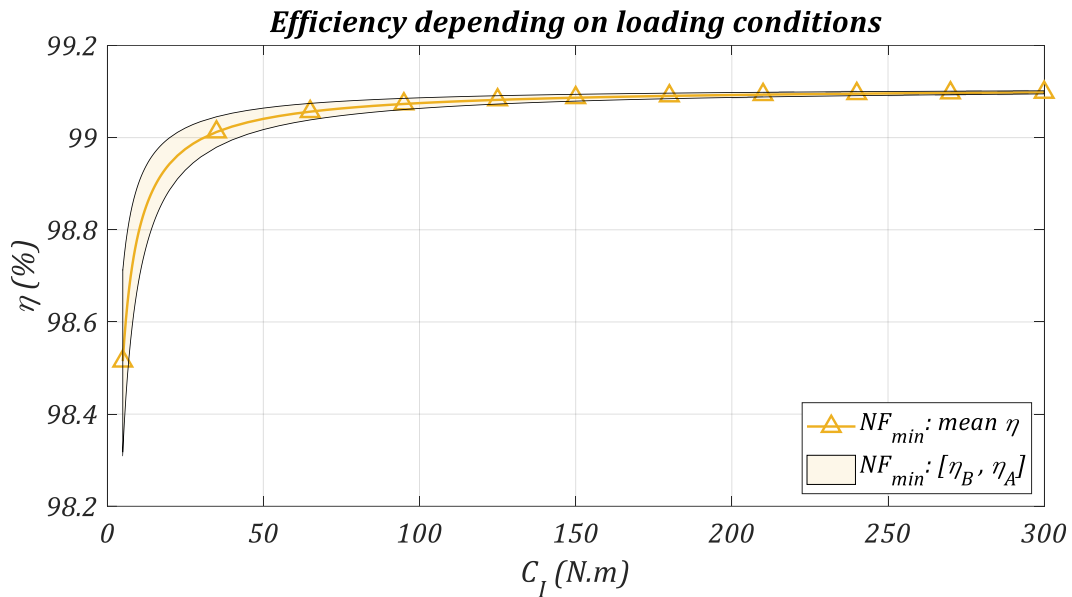
Figure VI-2: Influence of torque on efficiency for the NF_{min} profile. $60|15$, $slack = 11\%$

As observed during the CDEM validation (renvoi §V.2), efficiency increases with increasing torque. This relation is explained by two effects. First, the decreasing influence of the slack strand meshing losses. Indeed, these losses are independent from the chainring torque, contrary to the tight strand ones. Second, the roller motion reduces for higher torque (relation between roller motion and loading conditions are presented in Chapter IV). Details on each loss type contribution is given in the following section (see §VI.1.2). The effect is more significant at low torques before efficiency asymptotically converges for higher loading conditions. Mean efficiency ranges from about 98.5% at $C_I = 5N.m$ to 99.09% at $300N.m$. The increase slows significantly starting from $50N.m$ where efficiency already reaches 99.04% and a plateau is attained approximately at $C_I = 100N.m$ where 99.07% is obtained. The variation between cases A and B can be appreciated. The interval drastically reduces with increasing torque. The difference is about 0.4% at $5N.m$ but becomes almost negligible for higher torques (about 0.005% between cases A and B at $C_I = 300N.m$)

The influence of tooth profile is shown in Figure VI-3.a where mean efficiency is plotted for the four profiles studied (intervals between cases A and B are not shown for readability reasons). The second plot (Figure VI-3.b) shows the difference between each profile efficiency and the NF_{min} one.
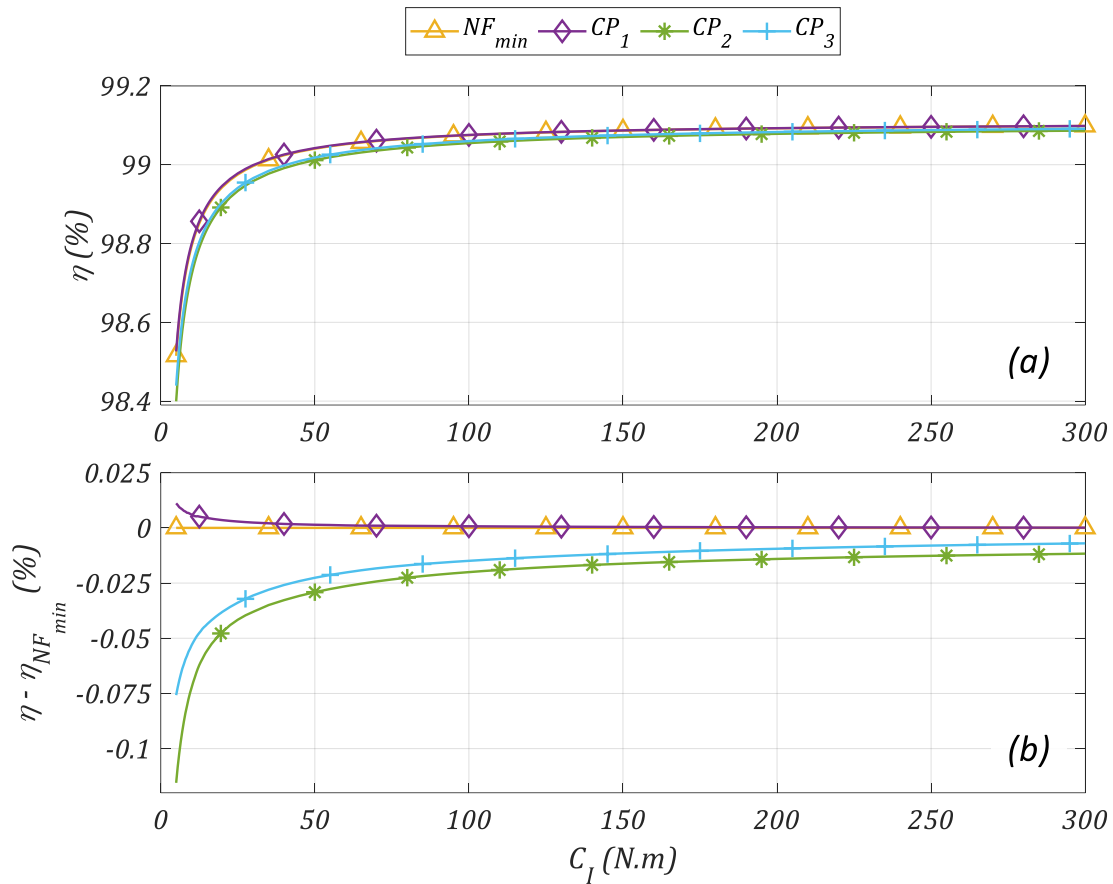
Figure VI-3: Influence of torque on efficiency, comparison of profiles. (a) Absolute values (b) Comparison with NF_{min}. $60|15$, $slack = 11\%$

All the profiles show the same trend of increasing efficiency with higher chainring torque. The plateau starting approximately at $C_I = 100N.m$ is also observed for all profiles. Profiles NF_{min} and CP_1 show almost the same behaviour. Profiles CP_2 and CP_3 exhibit efficiencies below the two other ones. Overall, the differences between profiles are small. The highest gap is observed at $5N.m$ between profiles CP_1 and CP_2 and reaches 0.13%. At $\Omega_I = 100rpm$ (about $52W$ at the chainring) this difference would result in saving $0.7W$ using CP_1 instead of CP_2. Moreover, as with the difference between cases A and B, the differences between profiles decrease with higher torque. At $50N.m$, the gap between CP_1 and CP_2 is 0.03% which results in $0.16W$ assuming $\Omega_I = 100rpm$ ($524W$ of power produced by the cyclist at the chainring). Therefore, even if the power is usually higher for greater torques, differences between profiles decrease quicker and the potential gain related to power losses becomes negligible for high torques.

b) Efficiency depending on tension setting

The effect of tension setting is now studied on the $60|15$ drive. Slack strand looseness from 2 to 20% are tested. Four chainring torques are studied as summarised in Table VI-4.

$Z_I|Z_{II}$.	$slack$ (%)	L (mm)	Nb_{link}	$T_{s,I}$ (N)	C_I (N.m)	$T_{s,I}/T_t$
60|15	$2 \rightarrow 20$	> 380	100	$\approx 13.3 \rightarrow 1.6$	5, 50, 100 and 300	$2.4e^{-1} \rightarrow 6.6e^{-4}$

Table VI-4: Drive characteristics for the influence of tension setting slack

The results are first presented only for the NF_{min} profile in Figure VI-4. The $[\eta_B, \eta_A]$ interval is still shown in the shaded area and the mean value by the solid line.
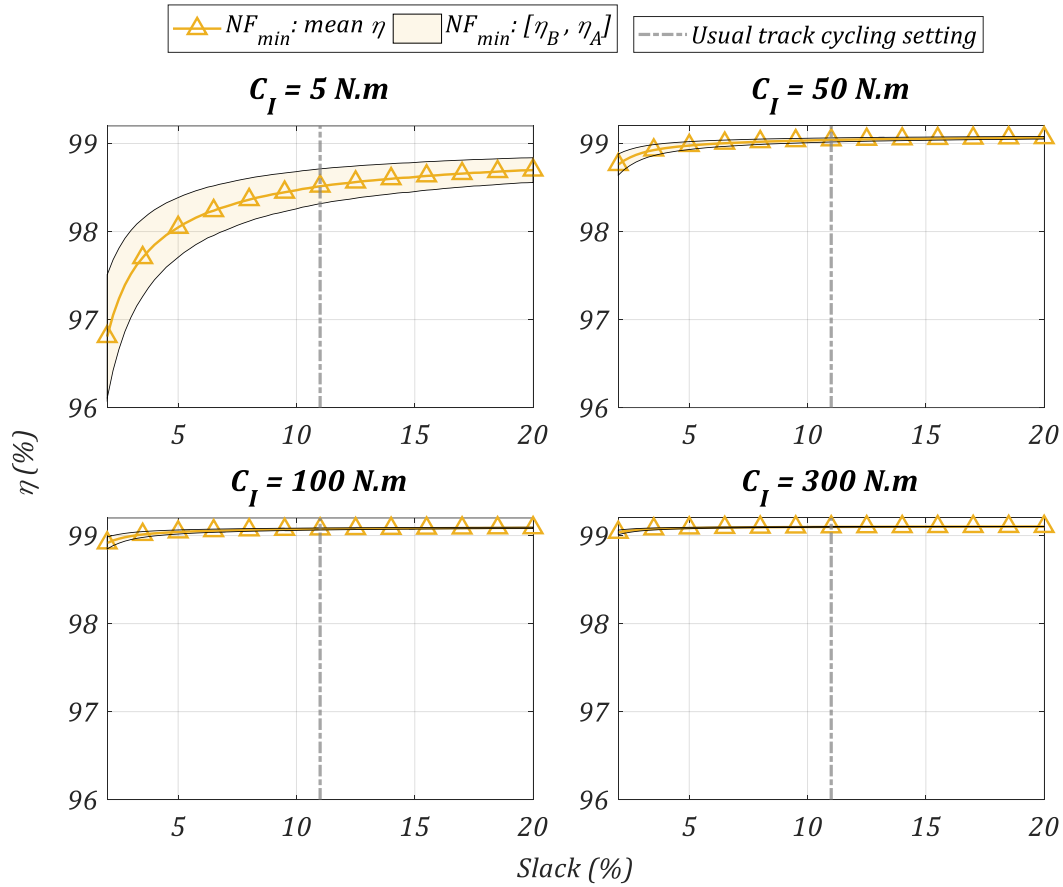
Figure VI-4: Influence of tension setting on efficiency for the NF_{min} profile. $60|15$, $C_I = 5, 50, 100$ and $300\ N.m$

As shown during the validation process (see §V.2), efficiency is higher for looser settings (high $slack$ values). This effect is caused by the reduction of roller and slack strand meshing losses. The reduction of roller losses manifests through the narrowing of the $[\eta_B, \eta_A]$ interval with growing torque. As for the slack strand meshing losses, they are directly related to the slack strand tension which decreases for looser settings (*i.e.*, higher $slack$). The slack tension is about $13.3N$ at 2% and falls to approximately $1.6N$ at 20% (see Table VI-4). To a lesser extent, lower slack tension results in lower tight tension for a given torque, which also reduces losses. The curve shapes are similar to what has been observed for the influence of torque (see Figure VI-2). Efficiency increases quickly for small $slack$ settings (*i.e.*, tight drives) before reaching a plateau at about 7.5%. Therefore, as the torque increases, the influence of the slack setting decreases. It is very significant at $C_I = 5N.m$ where a difference of about 1.9% is observed between the tightest and the loosest setting (*i.e.*, between $slack = 2$ and 20%). For $50N.m$, the effect decreases to 0.3% and 0.07% at $300N.m$. Assuming $\Omega_I = 100rpm$, these differences represent 1, 1.5 and 2.2W, respectively. Therefore, although the difference in efficiency decreases, the resulting power losses increase with increasing torque (assuming constant rotational speed). However, track cycling drives usually already lie at the plateau at $slack \approx 11\%$. Potential gains are therefore limited. Moreover, the risk of chain drop ultimately rises with increasing looseness as the tension ratio is reduced (see §IV.2). For all the results presented in Figure VI-4, the chainring tension ratio goes from 0.24 for $C_I = 5N.m$ at $slack = 2\%$ to $6.6e^{-4}$ for $C_I = 300N.m$ at $slack = 20\%$ (see Table VI-4).

Differences between profiles are presented in Figure VI-5 for $C_I = 5$ and $300 N.m$.
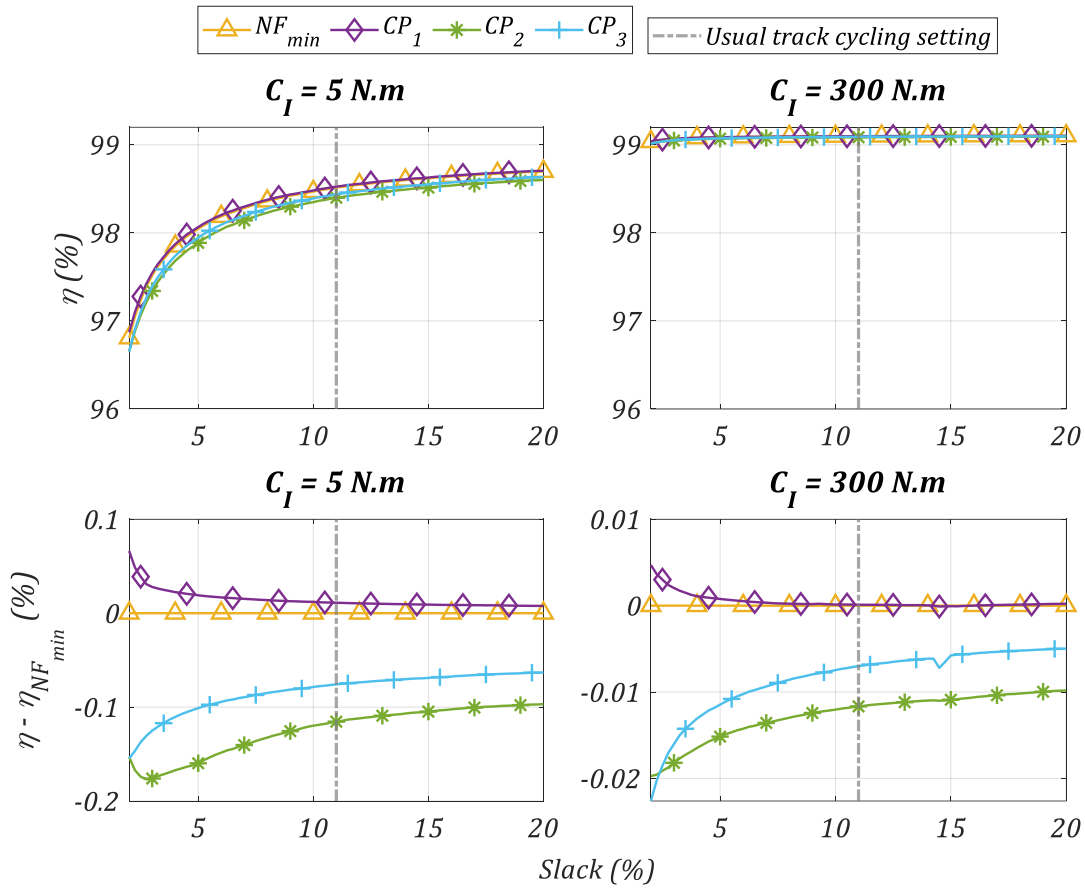
Figure VI-5: Influence of slack on efficiency, comparison of profiles comparison. $60|15$, $C_I = 5, 50, 100$ and $200 N.m$

The results are close to what has been observed with the influence of torque (see Figure VI-3). All the profiles show the same increasing relation with the tension setting. Similarly, the effect is reduced in the same way for all profiles by increasing torques (see Figure VI-5 for $C_I = 300 N.m$). The ranking between profiles (in terms of efficiency) is the same as in Figure VI-3 with CP_1 being the most efficient profile closely followed by NF_{min}. CP_3 and CP_2 follow respectively. The potential gains between CP_1 and CP_2 profiles are maximal for the lower tension ratio ($C_I = 5 N.m$, $slack = 2\%$) and reach 0.22%. However, this condition is also the least efficient as it combines low torque and high looseness setting.

It is noteworthy that the inflection in the CP_3 curve at $C_I = 300 N.m$ for $slack = 14.5\%$. This inflection is caused by the emergence of back-and-forth roller motion at the transition between inter-tp and static roller behaviour. A similar phenomenon was presented in the validation process (see §V.2). The motion quickly disappears as the efficiency at $slack = 15\%$ already converges with the original tendency.

c) The tension ratio perspective

The influence of torque C_I and tension setting $slack$ have been shown. Both phenomena exhibit similar shapes with a strong increase before reaching a plateau. However, variations of both the slack setting and the chainring torque result in a variation of the ratio between the tight and slack tensions. Indeed, increasing the strand looseness (*i.e.*, parameter $slack$) reduces the slack tension. Similarly, increasing the chainring torque results in higher tight tension to match the torque requirements. It was shown in

Chapter IV that the tension ratio is fundamental for understanding the drive behaviour. In the inter-tp regime, smaller tension ratios are associated with less roller motion as the drive behaviour tends to the static roller one (no tooth climbing behaviour occurs for the profiles studied). Therefore, an analysis of the previous results considering the tension ratio is now presented.

In the following, tension ratio designates the ratio of slack to tight strand tensions calculated at the chainring (*i.e.*, slack tension $T_{s,I}$ is considered). The slack tension at the rear cog is usually almost equal so this ratio is representative of both sprocket behaviours.

The mean value of chainring tension ratio $T_{s,I}/T_t$ is calculated for all cases presented in the previous section. Each case is plotted in Figure VI-6 showing mean drive efficiency as a function of the chainring tension ratio for the NF_{min} profile. Points obtained by varying the tension setting for constant torque are denoted 'Constant torque' while those obtained with a fixed slack setting ($slack = 11\%$) and varying torques are denoted 'Constant slack'. In Figure VI-6, the x-axis is in logarithmic scale and is reversed. Therefore, low tension ratios (severe loading conditions) are at the right-hand side of the figure. Conversely, high ratios (moderate loading conditions) are at the left-hand side.
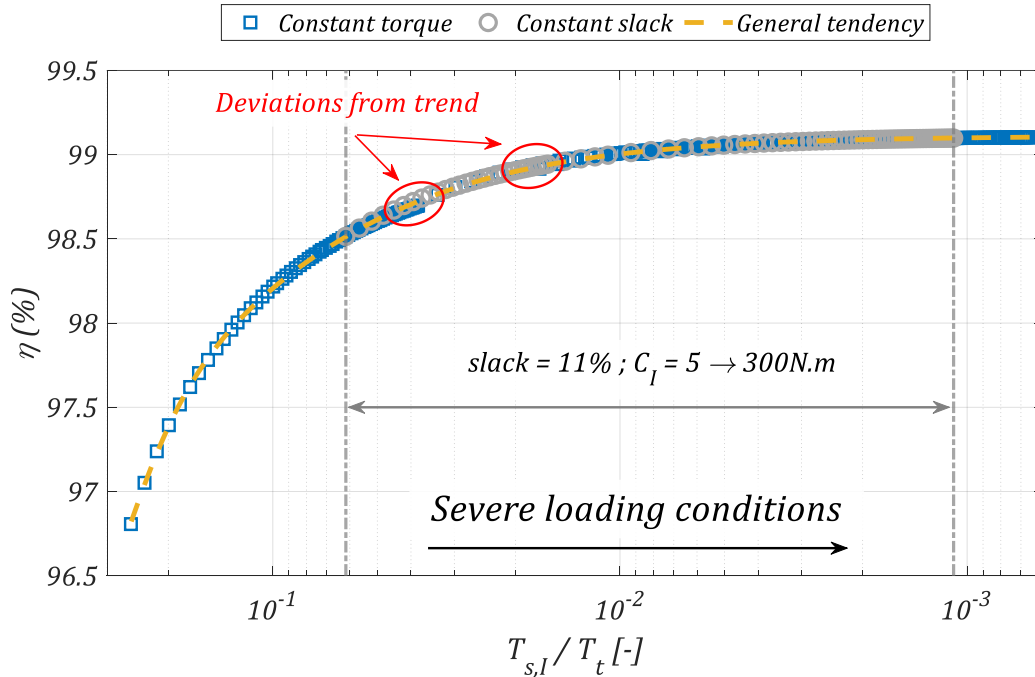
Figure VI-6: Efficiency depending on chainring tension ratio for the NF_{min} profile (reversed x-axis)

Cases with low chainring torque (*e.g.*, $C_I = 5N.m$) are visible at the left-hand side of the figure (high tension ratio of about 0.2 to $5e^{-2}$). They overlap between $4e^{-2}$ and $5e^{-2}$ with the constant slack calculations. Lower ratios are obtained with a chainring torque $C_I = 300N.m$. The smallest ratio corresponds to $C_I = 300N.m$ with the loosest tension setting $slack = 20\%$.
The points obtained illustrate a clear trend showing the same asymptotic shapes as what was observed for the influence of torque and tension. The rapid increase is present for high ratios (moderate loadings) before the efficiency reaches a plateau for low ratios.
The general trend presented in Figure VI-6 is obtained with the best fit of a degree 5 polynomial.

However, the arrangement around the common trend is not perfect as points with similar ratios do not display exactly the same efficiency. This phenomenon is observed in particular between $4e^{-2}$ and

$5e^{-2}$ and around $2e^{-2}$. These variations are caused by slight differences in roller motions obtained depending on the ratio being reached for different values of torque C_I and tension setting $slack$. A deeper analysis of the differences observed around $T_{s,I}/T_t = 2e^{-2}$ is presented in Appendix J.

VI.1.2   Analysis of the influence of tension ratio on chain drive efficiency

As with the NF_{min}, general trends are obtained for each tooth profile using the best fit of a degree 5 polynomial on the mean efficiency between cases A and B. These tendencies are plotted for all the profiles tested in Figure VI-7 and show growing efficiency with decreasing tension ratio.
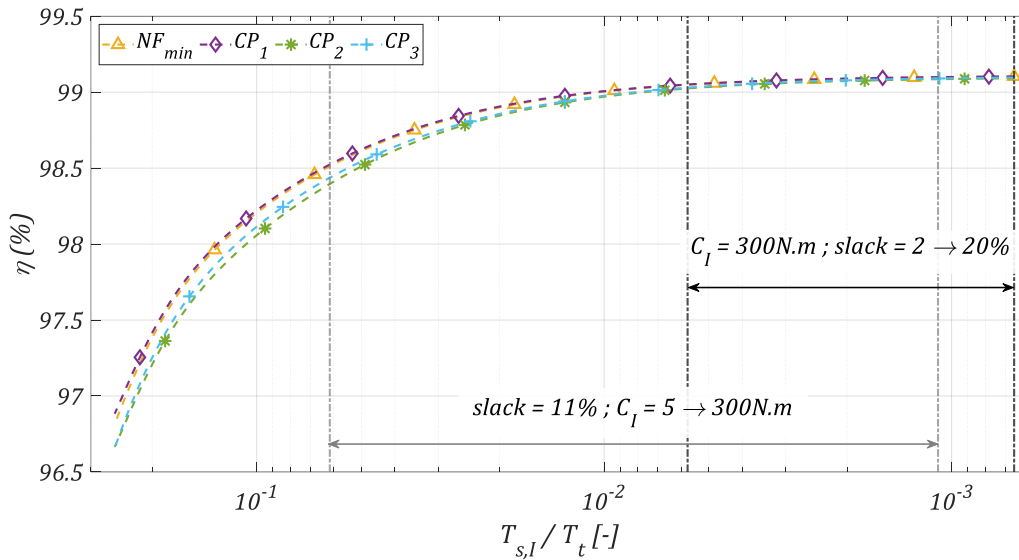
Figure VI-7: Efficiency depending on chainring tension ratio, profile comparisons

The efficiency ranking between profiles is similar to what was observed in Figure VI-3 and Figure VI-5 for torque and tension setting variation, respectively. Profile CP_1 exhibits the highest efficiency followed closely by NF_{min}. Profiles CP_3 and CP_2 are behind. The results obtained in the previous section (§VI.1.1) can therefore be analysed simultaneously using the tension ratio. The magnitude of the effect studied (variation of tension setting $slack$ or torque C_I) depends on the tension ratios explored. Therefore, the calculation at, for instance, $slack = 11\%$ for various torques (see Figure VI-2), showed higher efficiency variation than those obtained for constant chainring torque at $C_I = 300N.m$ as the tension ratio range explored was smaller and also restricted to small ratios (see Figure VI-7).

Now that both influences of tension and torque have been included in the tension ratio parameter, the reasons explaining increasing efficiency with decreasing ratio can be detailed. To do so, a closer look is given to three specific ratios. The highest and the lowest considered in the calculations carried-out and a ratio meant to represent a usual track cycling drive. The drive configuration for each ratio is detailed in Table VI-5.

	$Z_I \| Z_{II}$	$T_{s,I}/T_t$	C_I (N.m)	slack (%)
High ratio		0.25	5	2
Usual track cycling	60|15	$6.5e^{-3}$	50	11
Low ratio		$6.6e^{-4}$	300	20

Table VI-5: Drive parameters for the three studied chainring tension ratios

It was shown in Chapter IV that roller motion decreases as the chainring torque increases (*i.e.*, the tension ratio decreases). Figure VI-8 and Table VI-6 illustrate the consequences of this variation in terms of contribution of each loss type (*i.e.*, meshing and roller losses) for the chainring and rear cog (designated using subscript *I* and *II*, respectively).

		$P_{I,roller}$ (%)	$P_{I,mesh}$ (%)	$P_{II,roller}$ (%)	$P_{II,mesh}$ (%)	η (%)
High ratio	*Case A*	5	12	31	**53**	97.5
	Case B	7	7	50	**35**	96.1
Usual track cycling	*Case A*	< 1	18	3	**78**	99.1
	Case B	< 1	17	7	**75**	99
Low ratio	*Case A*	< 1	19	< 1	**81**	99.1
	Case B					

Table VI-6: Cases A and B, split between roller and meshing losses at the chainring and rear cog (I and II, respectively) for various tension ratios
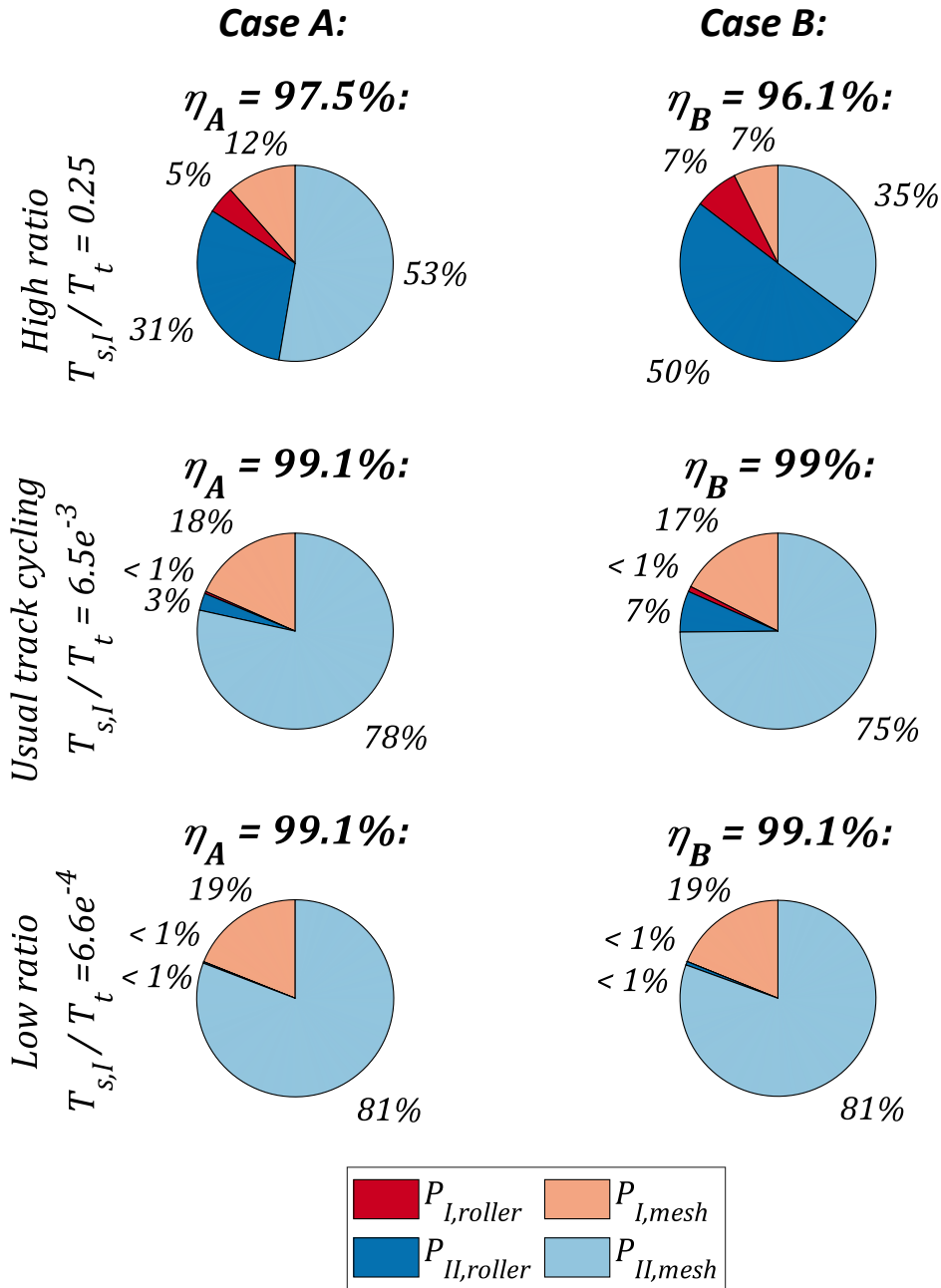
Figure VI-8: Cases A and B, split between roller and meshing losses at the chainring and rear cog (I and II, respectively) for various tension ratios.

For high ratios (moderate loading conditions), the proportion of losses caused by roller motion is very significant compared to the meshing losses. It ranges from 36% for case A to 57% for case B. Indeed, the roller motion is considerable for these ratios, resulting in significant losses. However, as the tension ratio reduces, rollers tend to stay longer nearby the transition point (see Figure VI-9). Moreover, the relative contact force P_i/T_t also reduces with the tension ratio (see Figure VI-9). The combination of both effects lowers the influence of roller losses. Efficiency therefore increases as meshing losses gradually become the only significant source of dissipation. For a usual track cycling drive, the proportion of roller losses increases from 3 to 7% depending on case A and B, respectively. Following the same trend, roller losses are almost non-existant for the lowest ratio. The significant proportion roller losses for high ratios are consistent with the preliminary study proposed by the author in [81]. However, the exploration of smaller ratios more representative of track cycling applications shows that

the significance of roller losses quickly decreases. As presented in the preceding chapter (see §V.2.2), the rear cog is responsible for most of the losses at all ratios as it always produces at least 81% of the total dissipation. It should be noted that efficiency is always lower for case B compared to case A. This indicates that the magnitude of meshing losses is the same for case A and B and that only roller losses increase, resulting in a decrease in the proportion of meshing loss.
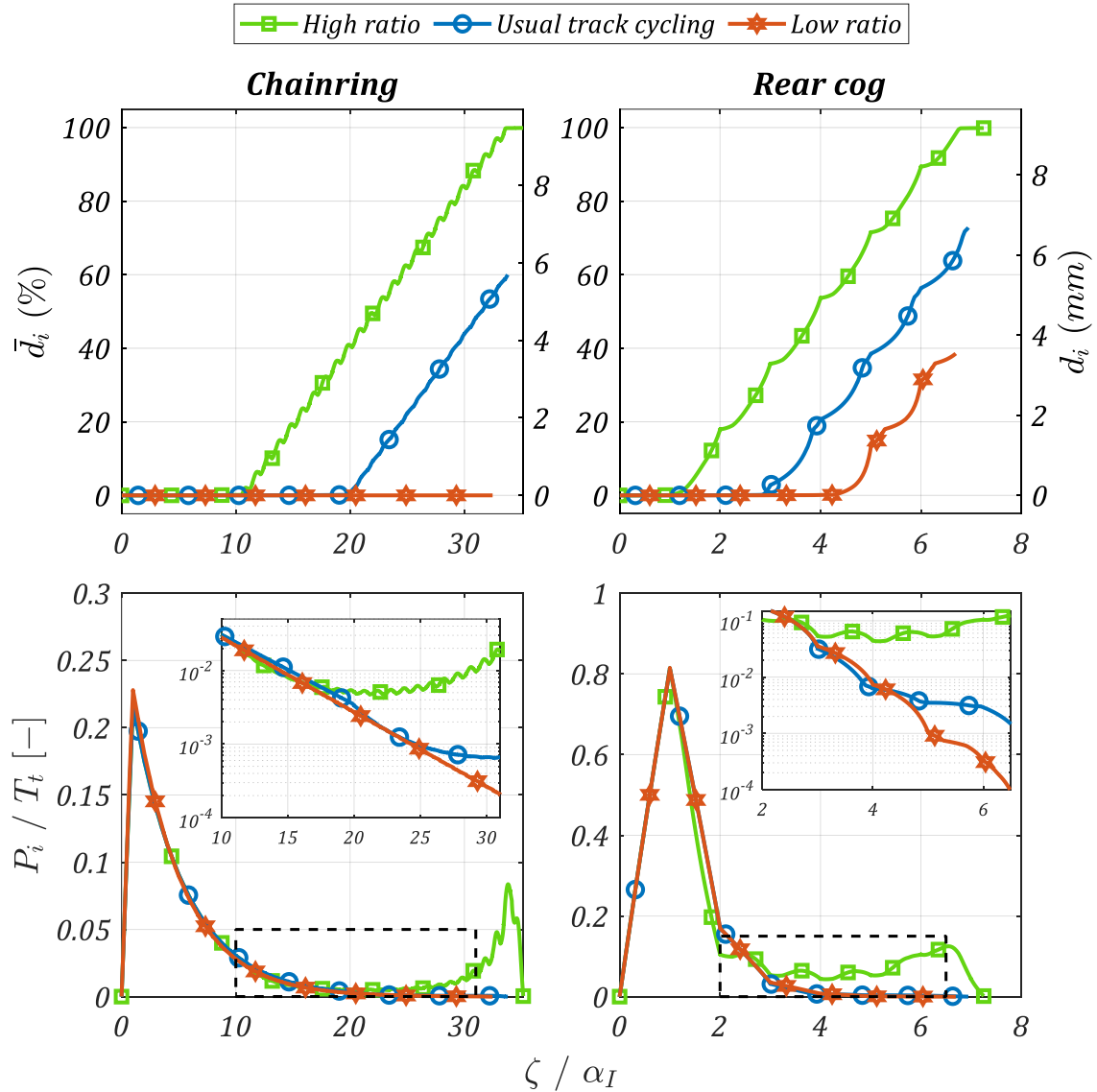
Figure VI-9: Roller motion and roller profile contact force for high, usual track cycling, and low ratios

A first factor explaining the increase in efficiency with decreasing ratio was explored: the reduction of roller losses. However, a second one, independent of roller losses, also plays a role. As introduced by Lodge & Burgess in [70] and earlier in this manuscript, the meshing losses at the tight strand gradually become dominant as their relative influence increases with decreasing tension ratios. This increase is illustrated in Figure VI-10 and Table VI-7 showing a split in the proportion of loss between losses due to roller motion and tight and slack strand meshing.
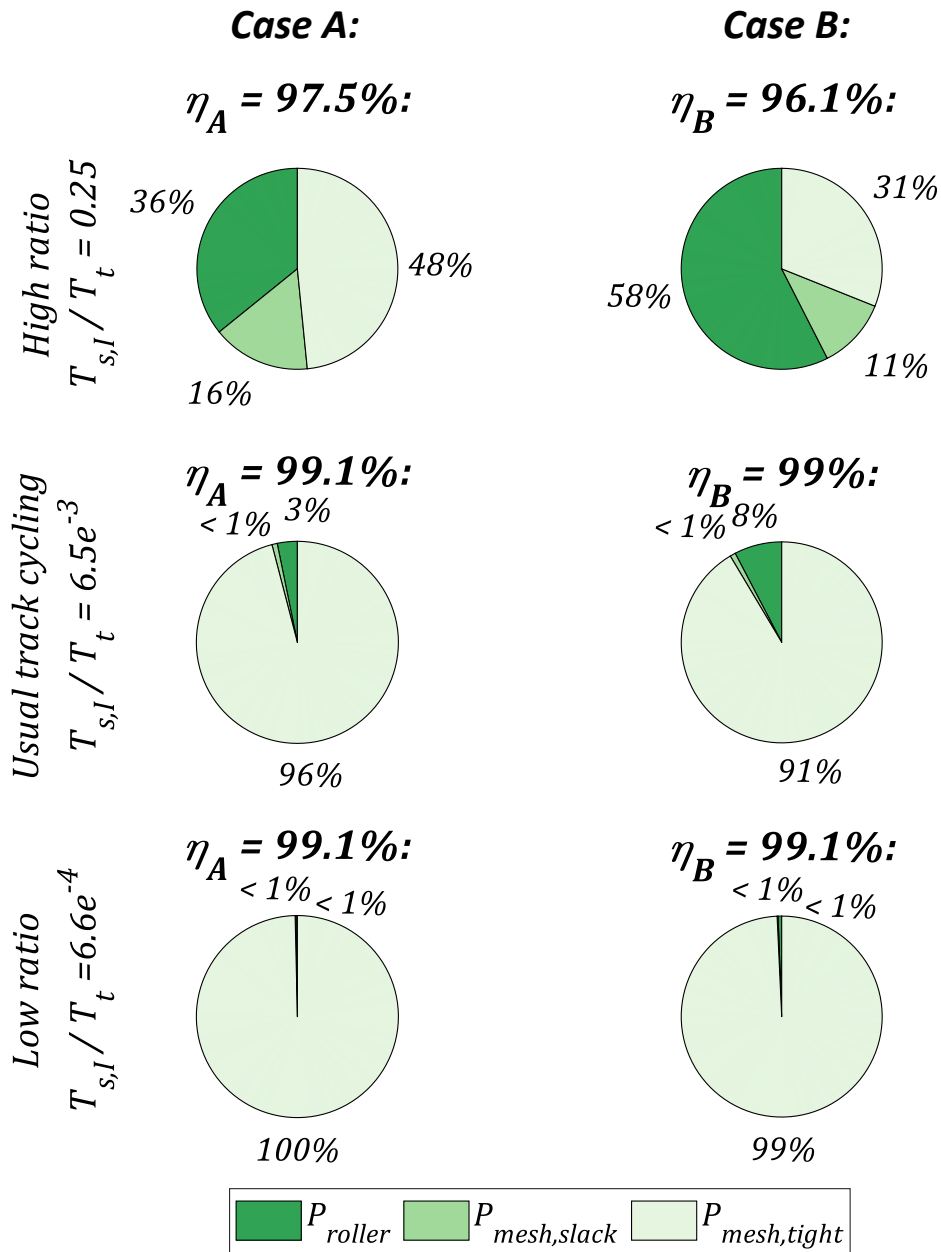
Figure VI-10: Cases A and B, split between roller and meshing losses at the tight and slack strands for various tension ratios

		P_{roller} (%)	$P_{mesh,slack}$ (%)	$P_{mesh,tight}$ (%)	η (%)
High ratio	Case A	36	16	**48**	97.5
	Case B	58	11	**31**	96.1
Usual track cycling	Case A	3		**96**	99.1
	Case B	8	< 1%	**91**	99
Low ratio	Case A			**100**	
	Case B	< 1	< 1%	**99**	99.1

Table VI-7: Cases A and B, split between roller and meshing losses at the tight and slack strands for various tension ratios

Consistently with Figure VI-8, the proportion of roller losses decreases with decreasing tension ratio. However, this second splitting method allows appreciating the contribution of tight strand meshing losses compared to the slack ones. The growing importance of tight strand meshing losses with decreasing tension ratios is clear. Indeed, meshing losses are directly dependent on the associated strand tension. Therefore, as the tight tension becomes dominant compared to the slack one (*i.e.*, tension ratio reduces), the tight meshing losses increase in significance. For high ratios, tight meshing losses are significant but have the same order of magnitude as the other contributions: meshing at the slack strand and losses due to roller motion. For a usual track cycling drive, tight meshing losses are responsible for 91 to 96% of the total dissipation. For extreme loadings (lowest tension ratios) all other loss types are negligible.

The two phenomena explaining the increasing drive efficiency with decreasing tension ratio have been detailed.

- First, roller motion decreases for lower ratios, resulting in this type of loss type becoming negligeable for severe loadings. Meshing losses are therefore the predominant type of dissipation for usual track cycling applications. This point could not be assessed with efficiency models based only on meshing losses such as in [70], [74]–[76], [94].
- Secondly, among the meshing losses, those caused at the slack strand become less significant as the tension ratio decreases. This results in the tight strand meshing losses becoming the most significant sources of loss for usual track cycling applications. This point was already mentioned by Lodge & Burgess [70] and Kidd [76] with an efficiency model based only on meshing losses.

The analysis carried out also explains the limited influence of tooth profile. Indeed, tooth profile geometry influences only roller losses as the meshing phenomenon is common to every geometry. Therefore, the tooth profile geometry influences only efficiency for conditions where roller losses make a significant contribution such as high tension ratios. For lower tension ratios, as roller losses decrease in significance, so does the influence of tooth profile. However, only track cycling profiles were tested. These profiles have relatively similar properties to withstand the specific constraints of their application, accentuating the small tooth profile influence. It would be interesting to test the influence of industrial tooth profiles (ASA and NF_{max}) on efficiency compared to *e.g.*, NF_{min} as their properties exhibit more discrepancies compared to the *Cycling Profiles*. However, the efficiency of industrial drives is beyond the scope of this thesis and is left for future works.

Nevertheless, an answer can be given to the question formulated at the end of Chapter IV: is it more efficient to favour roller motion under small loads (with a low ϕ_{tp} value) compared to less roller motion but undergo under higher loads (with higher ϕ_{tp}).
As shown in Figure VI-7, the most efficient tooth profile among those tested is CP_1, followed by NF_{min}. These profiles do not have the smallest ϕ_{tp} (see Table VI-2 and Figure IV-32). They are however those with the smallest tooth bottom radii (R_1 in Table VI-2) which results in smaller absolute roller displacement d_i for the same proportional displacement $\bar{d}_i$. From this analysis, the tooth bottom radius therefore seems to be the dominant parameter for assessing the influence of tooth profile on drive efficiency.

This part was dedicated to the effect of chainring torque C_I and tension setting $slack$ on drive efficiency. At the same time, four tooth profile geometries were tested.

First, the effect of torque was considered. The results show that efficiency increases while the interval $[\eta_B, \eta_A]$ reduces with rising torques. These results are consistent with modelling and experimental studies in the literature [70], [76], [84], [94]. Starting at about $C_I = 100 N.m$, efficiency reaches a plateau where the influence of further torque increases become almost negligible. The effect of the tension setting exhibits higher efficiency for high $slack$ values (*i.e.,* looser tension settings). An asymptotical behaviour is also reported with the plateau starting at about $slack = 7.5\%$. This result situates the typical track cycling setting ($slack = 11\%$) in the zone of optimal efficiency. Moreover, it ensures that a slight variation around the chosen setting will not lead to an excessive effect on drive losses. This result is consistent with the test rig measurements presented in §V.2.2. Then, it was shown that the similar asymptotical variation observed for the effect of both chainring torque and tension setting can be analysed considering a third parameter: the tension ratio (*i.e.,* the ratio of slack to tight strand tension). The relation between drive efficiency and tension ratio shows the same asymptotic shape with lower ratios (*i.e.,* more severe loading conditions) being associated with higher efficiencies. This indicates that two drives with the same ratio have approximately the same efficiency regardless of this ratio being reached *e.g.,* with small torque and tight tension setting or with high torque and loose setting.

Mechanisms underlying the asymptotic relation between efficiency and tension ratio were then explored. Two main reasons were identified. First, it was shown that losses due to roller motion decrease for lower ratios. This phenomenon is caused by a limitation of roller motion and a reduction of the relative contact force P_i/T_t. Secondly, the slack strand meshing losses decrease in significance as the slack tension becomes negligible compared to the tight one. This last point was already reported in the literature [70], [76]. Due to a combination of these two effects (*i.e.,* the reduction of both roller and slack strand meshing losses), the tight strand meshing losses become dominant for low tension ratios and therefore for a typical track cycling drive.

The influence of 2D tooth profile geometry was also tested. As the profile geometry only modifies roller losses, its influence reduces with the magnitude of this type of loss. Therefore, the results show that efficiency is almost independent of tooth profile for low ratios typical of track cycling drives. The small differences show that ϕ_{tp} is not a dominant parameter for assessing profile efficiency properties. The tooth bottom radius seems to be the only influential parameter, as profiles with smaller roller/profile clearances exhibit higher efficiencies. This effect is probably caused by the reduced distance travelled by a roller while crossing the tooth profile.

VI.2 Influence of number of teeth, pitch and friction coefficient

This part extends the analysis to drives other than the regular 60|15 one. Therefore, parameters related to the architecture of the chain drive are explored. The influence of sprockets numbers of teeth is analysed first. Then, the influence of chain pitch is studied. Finally, the consequence of the variations of the global fiction coefficient $\bar{\mu}$ are explored and the losses are split between the contributions of each interface (pin/bush, bush/roller, and roller/profile). Only the NF_{min} geometry is considered. Indeed, the previous part showed that tooth profile does not change the general drive behaviour in terms of efficiency (*i.e.*, the effects of torque and tensions setting were similar for all profiles). Moreover, the influence of tooth profile was shown to be minimal for typical track cycling drives.

VI.2.1 Tooth number

To assess the influence of number of teeth on chain drive efficiency, a wide variety of $Z_I|Z_{II}$ configurations are tested. The boundaries are chosen considering the geometrical limitations of a track bike. Indeed, to prevent collision with the chain stays (see Figure VI-11), the number of chainring teeth Z_I is limited to 70. On the other hand, rear cogs with fewer than $Z_{II} = 11$ teeth are not considered as the resulting pitch circle is smaller than the hub screw. Their manufacturing is therefore more difficult. Moreover, the polygonal effect is very significant for such small numbers of teeth so their use is not recommended by manufacturers (see Chapter I). The maximal (minimal) number of rear cog (chainring) teeth is chosen to obtain realistic gear ratios. Finally, Z_I ranges between $[\![40,70]\!]$ while Z_{II} varies between $[\![11,25]\!]$.
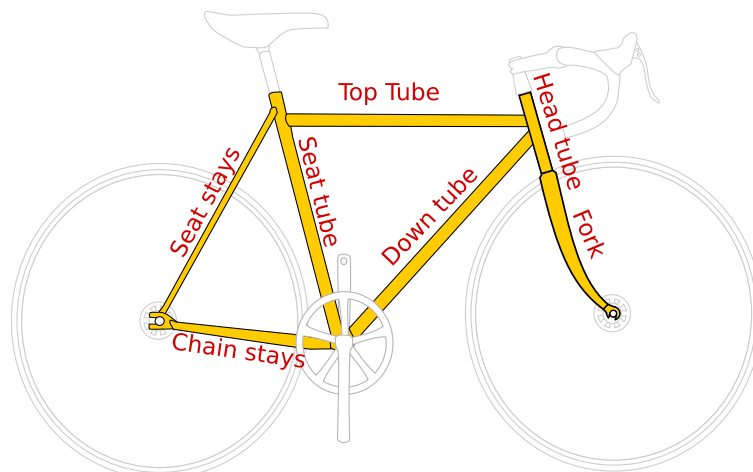
Figure VI-11: Bicycle frame diagram [95]

The tension setting is set at $slack = 11\%$ for all drives resulting in about $3N$ of slack strand tension. The numbers of chain links are even and chosen to match the tension requirements with the smallest centre distance above $L = 380mm$ and $\Delta Y = -50mm$. The 40|11 drive is, for instance, tested with 86 links and $L = 381.5mm$. For the 70|25 drive, 110 links are considered with $L = 385.1mm$. Calculations are carried out for three driving torques: $C_I = 5N.m, 50N.m$ and $300N.m$. $C_I = 50N.m$ represents a typical track cycling drive. $C_I = 300N.m$ accounts for the extreme loading conditions encountered in high intensity sprints or during race starts. Finally, $C_I = 5N.m$ is chosen to explore the consequences of the number of sprocket teeth for less severe conditions.

Figure VI-12 shows the mean efficiencies between cases A and B depending on the number of sprocket teeth.
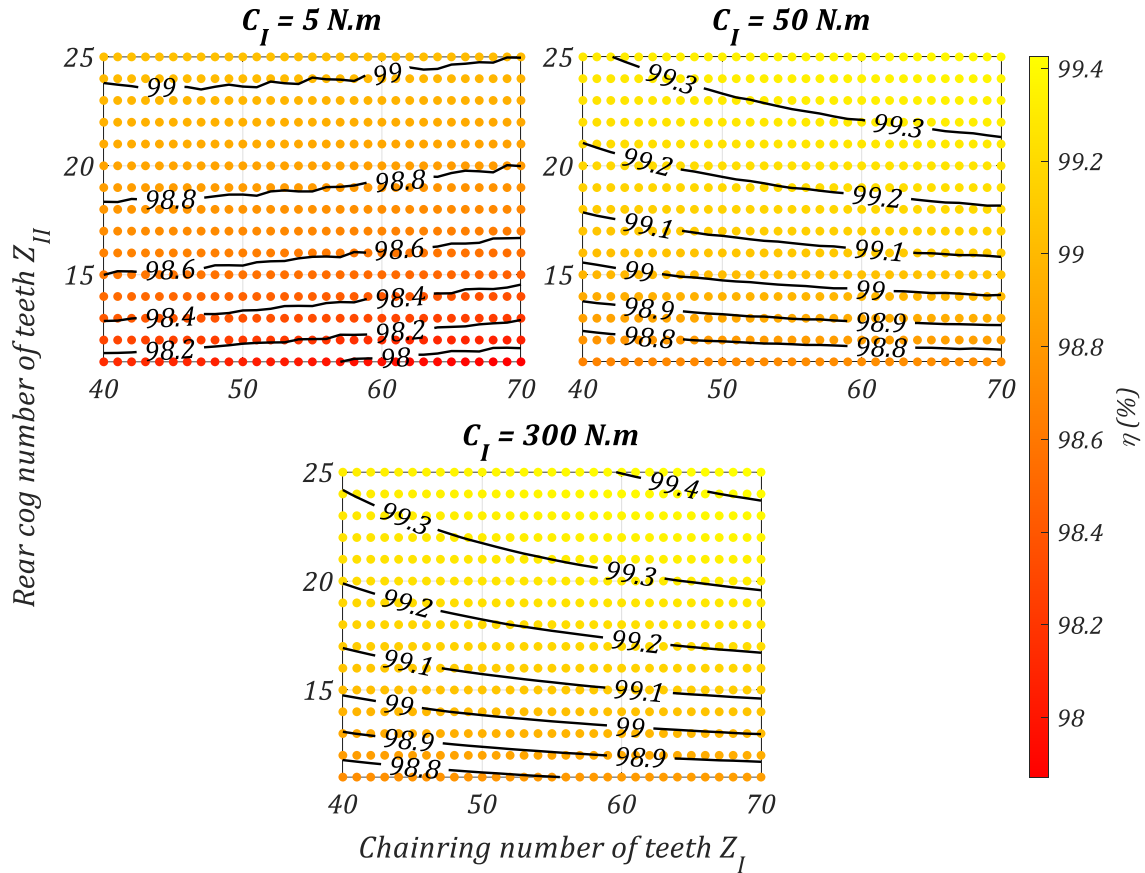
Figure VI-12: Efficiency depending on the number of teeth for various torques

Efficiencies increase with greater chainring torque which is consistent with the analysis presented in the previous part (see §VI.1). Isolines indicate which number of teeth between the chainring and the rear cog is the most influential. For every torque, the influence of the number of rear cog teeth is more significant than the chainring one (isolines are almost horizontal). This is particularly true for high numbers of chainring teeth. This positive effect is explained by the reduction of the pitch angle α_{II} for higher numbers of teeth (see Figure VI-13.a). This reduction limits the meshing losses associated with the rear cog which results in higher efficiencies. The effect of the number of chainring teeth is less straightforward as it depends on the torque considered. Higher numbers of teeth result in more efficient drives for high torques ($C_I = 50$ and $300 N.m$) while the effect is detrimental for low torques ($C_I = 5 N.m$, except for low Z_I and high Z_{II}). Indeed, increasing the number of chainring teeth reduces the tight strand tension (for constant torque, see Figure VI-13.b). This reduction has two main effects. First, the tight strand meshing losses reduce as they directly depend on this tension. Secondly, the tension ratio rises as the slack tension remains approximately constant. This rise tends to increase the proportion of roller and slack meshing losses which reduces efficiency. The overall behaviour resulting from these two contrary effects indeed depends on the chainring torque. For high torques, the tension ratio varies between $8.5e^{-4}$ to $1.3e^{-3}$ for $C_I = 300 N.m$ (see Figure VI-13.c) and ranges from $5e^{-3}$ to $7.5e^{-3}$ for $C_I = 50 N.m$. These values are located at the plateau described in the previous part (see Figure VI-7). Therefore, the efficiency reduction due to the increase of tension ratio increase is negligible and the effect of increasing the number of chainring teeth is positive. At $C_I = 5 N.m$ however, the tension ratio varies between about $4.5e^{-2}$ and $7e^{-2}$ (see Figure VI-13.d). For such ratios,

Figure VI-7 indicates that the efficiency decrease is much more significant. Therefore, the overall effect is detrimental.

It must also be noted that increasing the number of chainring teeth reduces the pitch angle α_I. However, at the same time, the number of chain articulations performed during a given amount of time increases (Z_I articulations are performed for each chainring rotation). Both effects are opposite. Their influence will be clarified in the following section.
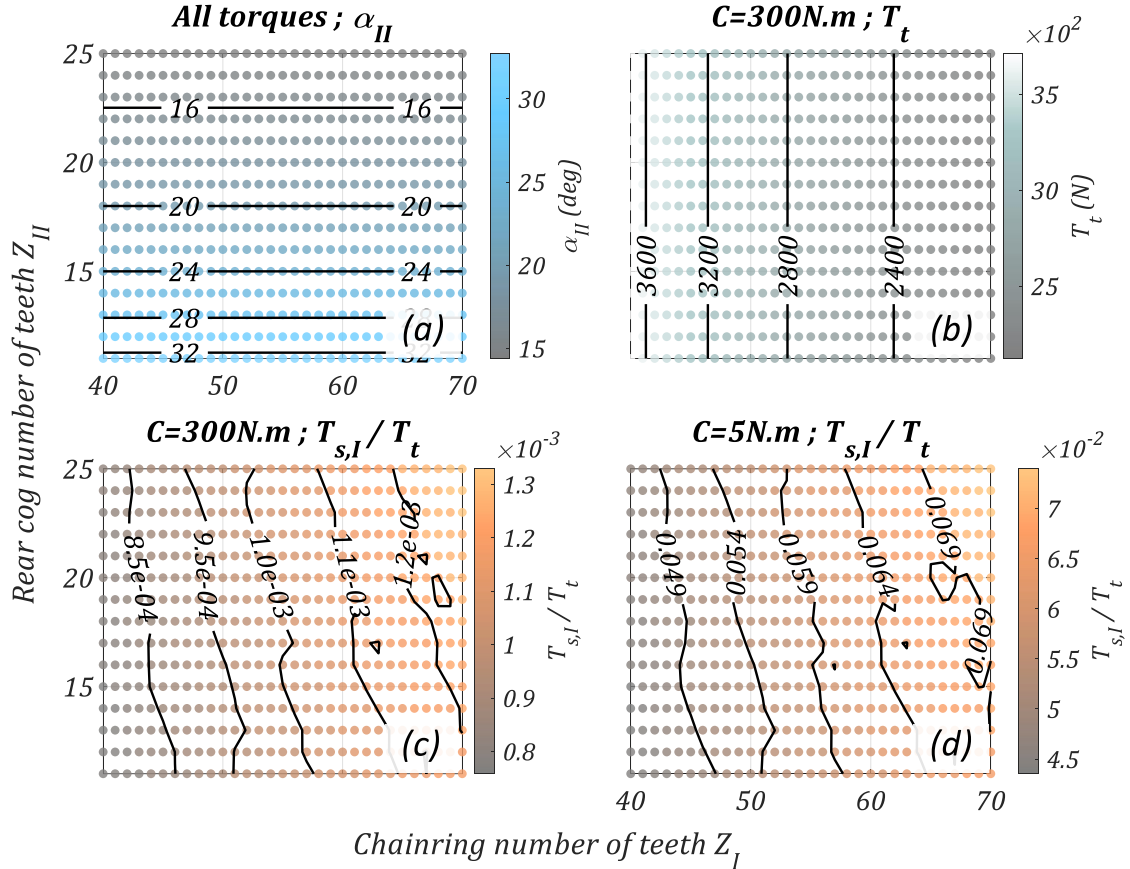
Figure VI-13: (a) rear cog pitch angle α_{II}, (b) Tight strand tension $C_I = 300N.m$, (c) Tension ratio for $C_I = 300N.m$, (d) Tension ratio for $C_I = 5N.m$

In track cycling applications, the choice of number of teeth is mostly dictated by the gear ratio (*i.e.*, Z_I/Z_{II}) which greatly influences the athlete's sensations and performances. The gear ratio is chosen by the athlete according to his physical characteristics which make any change difficult. Therefore, it makes more sense to compare drives with identical gear ratios as a potential change should not modify the athlete's sensations. Thus, all the drives with a gear ratio of 4 are extracted from the previous results (*i.e.*, Figure VI-12) and presented in Figure VI-14. The results are shown for $C_I = 5N.m, 50N.m$ and $300N.m$. Similar results for gear ratio of 3 and 5 are presented in Appendix K.
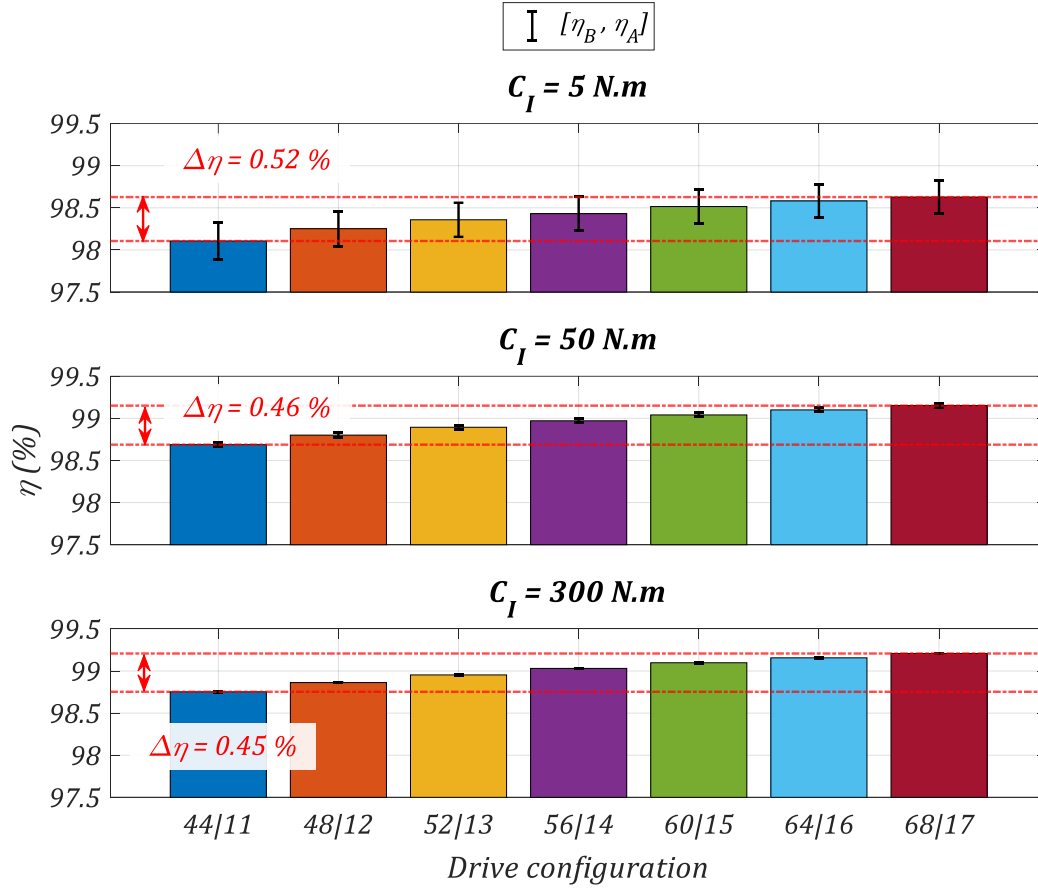
Figure VI-14: Effect of tooth number on efficiency for drives of gear ratio 4

The interest of increasing sprocket sizes is present for every torque condition, even for $C_I = 5N.m$. Indeed, despite the slightly detrimental effect of increasing Z_I at low torques, the increase of Z_{II} is more significant, resulting in more efficient drives. The interest of increasing sprocket size is usually greater for small sprockets than for larger ones. More efficiency is saved, for instance, between 44|11 and 48|12 than between 64|16 and 68|17. The effect also decreases with increasing torque but remains relatively significant. Assuming $\Omega_I = 100rpm$, the power losses saved between a 44|11 and a 68|17 drive are about 0.27, 2.4 and 14W for $C_I = 5N.m$, $50N.m$ and $300N.m$, respectively.

The effect of the number of sprocket teeth is significant and can be explained by the following factors.

- Increasing the number of chainring teeth results in reducing the tight strand tension for a given torque.
- For both sprockets, increasing the number of teeth reduces the articulation angle.

Both factors result in reduced meshing losses which are dominant for track cycling drives (except for very low torques, see Figure VI-8 and Figure VI-10). Therefore, the positive effect of the number of teeth on drive efficiency is present regardless of the torque applied.

The increase in tooth number is restricted by the pitch radius reaching bicycle geometrical limitations. However, a reduction in articulation angle α_j can be achieved independently of the pitch radius, by changing the chain pitch. The effect of this parameter is explored in the next section.

VI.2.2   Chain pitch

In cycling applications, a pitch $p = 1/2'' = 12.7mm$ is used. For this pitch, dedicated chains are proposed by the manufacturers. Cycle plates are usually thinner than industrial ones to achieve weight reductions. In industrial applications, other pitches are used and in particular the standard directly below and above $1/2''$: $3/8'' = 9.525mm$ and $5/8'' = 15.875mm$, are designated as short and long pitch, respectively. The influence of these different pitches on drive efficiency is explored in this section. No cycling chains for these pitches are widely commercialised. Therefore, the pin, bush and roller dimensions of industrial chains will be used (see Table VI-8 below). As mentioned in §I.1.2, the British team used a $3/8''$ chain at the last Tokyo Olympic games [27]. However, the precise pin, bush and roller dimensions are not known by the author. Only drives with a gear ratio of 4 are considered.

When changing the pitch, all other chain dimensions (*i.e.*, pin, bush and roller diameters) are also modified accordingly. However, these dimensions also influence power losses and consequently drive efficiency. To isolate the effect of chain pitch and chain dimension changes, two cases are considered for short pitch: $3/8''$ and long pitch: $5/8''$. Calculations using Real Chain Dimensions (denoted RCD) according to the chosen pitch are carried out. Additionally, calculations changing only the chain pitch and keeping other chain dimensions identical to the usual $1/2''$ track cycling chain (Everything Else Unchanged, EEU) are also performed. Figure VI-15 illustrates views of EEU and RCD chain links. The differences for an entire drive are illustrated in Figure VI-16, showing the same number of teeth for EEU and RCD. The parameters (*i.e.*, dimensions and mass) of each chain considered in this section are summarised in Table VI-8.
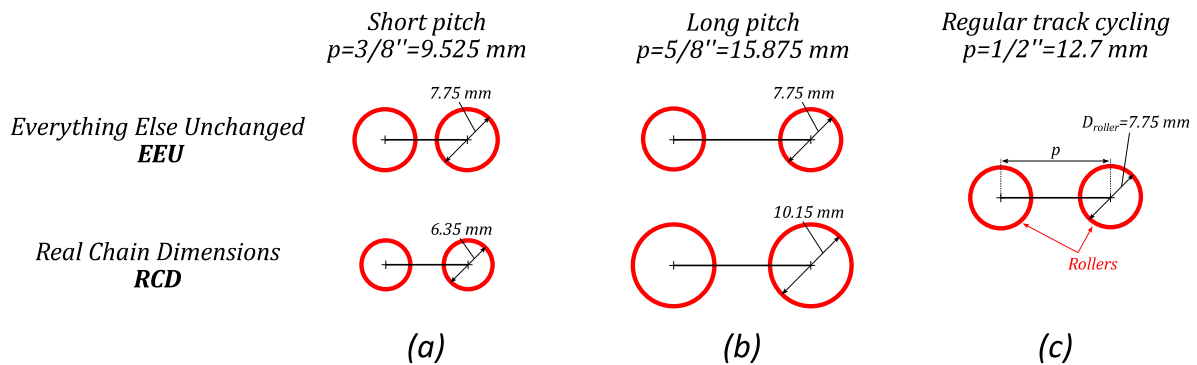
Figure VI-15: Views of EEU and RCD chain links (a) $p = 3/8''$ (b) $p = 5/8''$ (c) $p = 1/2''$. All scales are the same.
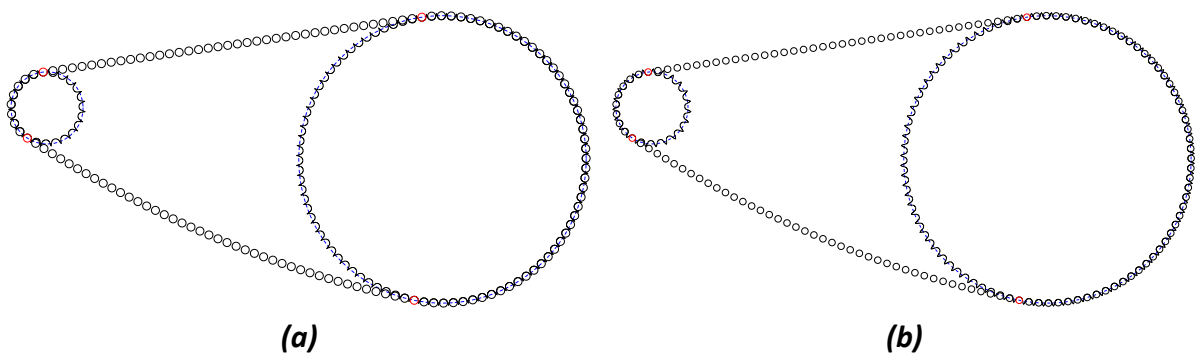
Figure VI-16: $92|23$ drives, $p = 3/8''$ (a) EEU (b) RCD. Both figures have the same scale.

	p (inch)	p (mm)	D_{pin} (mm)	D_{bush} (mm)	D_{roller} (mm)	m_{link} (g)	$\bar{m}$ (g/mm)
Regular track cycling chain	1/2	12.7	3.66	5.1	7.75	3.6	0.28
Short pitch EEU	3/8	9.525				2.7	
Long pitch EEU	5/8	15.875				4.5	
Short pitch RCD	3/8	9.525	3.25	4.75	6.35	3	0.31
Long pitch RCD	5/8	15.875	5.05	7.05	10.15	6.5	0.41

Table VI-8: Chain parameters for different pitches

For $3/8''$ and $5/8''$ chains, the pin and roller diameters are taken from industrial standards corresponding to the pitch considered [11]. The bush diameters, not provided in the catalogue, were measured on industrial chains with matching pitch (ISO n°- 06 B-1 and 10 B-1 for $3/8''$ and $5/8''$, respectively [96]). The RCD link masses are estimated using a CAD[2] software assuming standard steel for every piece. The link masses for EEU chains are calculated from the $1/2''$ mass proportional to the chain pitch. The slack tensions obtained with the EEU chains should therefore be similar to the reference case (*i.e.*, $1/2''$).

Part dimensions are smaller for smaller pitch chains. Thus, the $3/8''$ chain has the smallest dimensions for pin, bush and roller diameter followed by the $1/2''$ and the $5/8''$. Link mass is also reduced with reduced pitch. However, the linear mass density follows a different trend (see Table VI-8). The usual track cycling chain exhibits the lowest, just below the $3/8''$ and the $5/8''$ chains. This indicates that weight saving measures could probably be carried out on $3/8''$ and $5/8''$ chains before any eventual track cycling use.

Different chain pitches are compared for equivalent pitch radii. To determine the equivalent number of teeth, Z_{II} is first set to obtain the closest possible pitch circle compared to the reference case according to eq.(VI-1). Then, the number of chainring teeth is taken as $Z_I = 4Z_{II}$ to ensure a similar gear ratio. The number of teeth obtained does not necessarily agree with the closest pitch circle obtained with eq.(VI-1). Therefore, pitch circle radii are not exactly similar for all pitches but correspond to the closest equivalent drive possible.

$$Z' = \mathrm{round}\left(\frac{\pi}{\mathrm{asin}\left(\frac{p'}{p} . \sin\left(\frac{\pi}{Z} \right) \right)} \right) \qquad \textbf{\textit{(VI-1)}}$$

with:

- round, function giving the nearest integer
- Z', the number of teeth with the new pitch p'
- p and Z the original pitch and number of teeth, respectively

---

[2] CAD: Computer Aided Design

Comparisons are carried out based on three drives of gear ratio 4. The smallest one (44|11 for $p = 1/2''$), the largest one (68|17 for $p = 1/2''$), and the usual track drive (60|15 for $p = 1/2''$). Pitch circle dimensions and number of teeth for each pitch are presented in Table VI-9.

$p = 1/2''$	$Z_I\|Z_{II}$	44|11	60|15	67|18
	$R_I\ (mm)$	89.01	121.33	137.50
	$R_{II}\ (mm)$	22.54	30.54	34.56
$p = 3/8''$	$Z_I\|Z_{II}$	60|15	80|20	92|23
	$R_I\ (mm)$	91.00	121.31	139.49
	$R_{II}\ (mm)$	22.91	30.44	34.98
$p = 5/8''$	$Z_I\|Z_{II}$	36|9	48|12	56|14
	$R_I\ (mm)$	91.07	121.36	141.56
	$R_{II}\ (mm)$	23.21	30.67	35.67

Table VI-9: Drive dimensions for several pitches

NF_{min} sprockets adapted for each case (defined by pitch and roller diameter) are generated following the ISO 606 [31] standard as detailed in the Appendix A. The results for $C_I = 50N.m$ are presented in Figure VI-17.
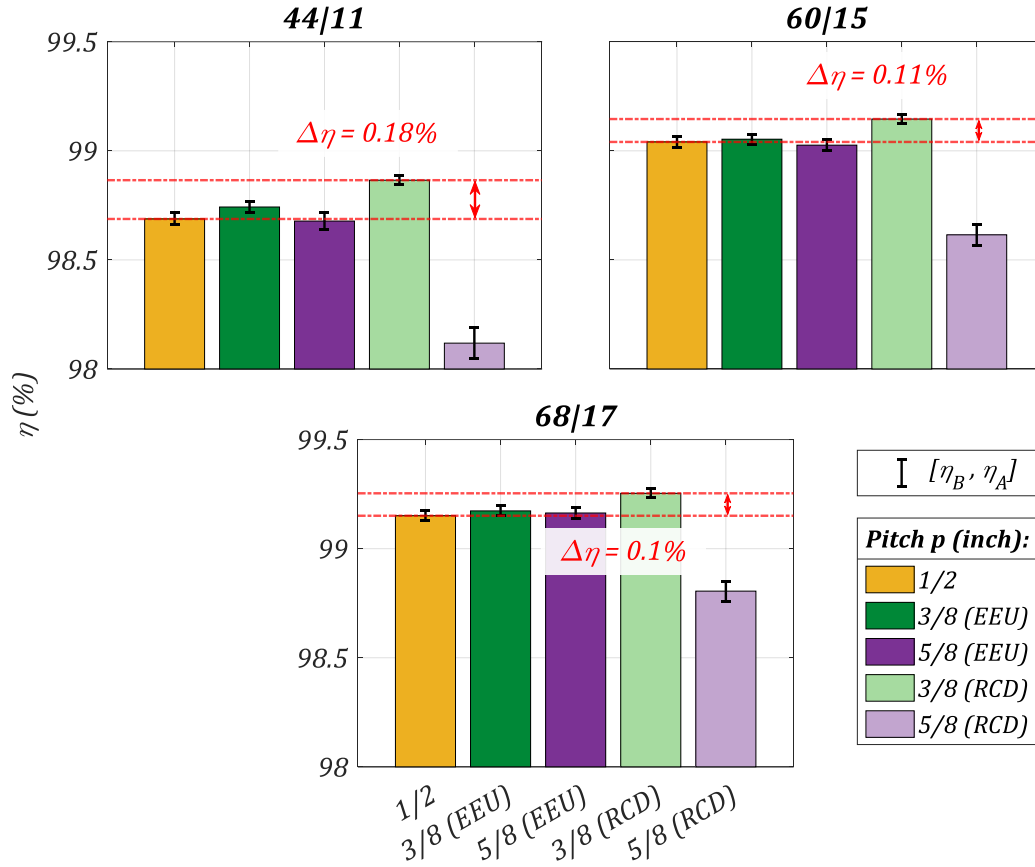
Figure VI-17: Effect of chain pitch on efficiency for $C_I = 50 N.m$

Efficiency predictions follow the same trend for all the pitch radii tested (based on 44|11, 60|15 and 68|17 drives for $p = 12.7mm$). Except for the 44|11 case discussed below, no significant differences between the $1/2''$ and EEU cases are reported. Differences arise for the RCD cases where $3/8''$ and $5/8''$ show the best and worst efficiency for all radii, respectively. This indicates that pitch change, although resulting in a modification of the pitch angle α_j does not result in changed efficiency. Indeed, while changing the drive pitch, the number of articulations performed in a given amount of time also changes with an effect tending to counterbalance α_j change. Reducing (increasing) the drive pitch results in decreasing (expanding) the pitch angle but also increasing (reducing) the number of articulations performed for one chainring rotation. Figure VI-17 shows that the overall effect is negligible for the drives tested.

Deeper analysis of $44|11$ *like drives*

In addition to the effects already mentioned, roller motion is also modified by different tooth profiles and roller diameters. Similarly to the deviation from the general trend caused by roller motions in §VI.1.1 (see Appendix J), roller motions also influence the results here and their effect is difficult to dissociate from others. Therefore, the significant efficiency increases for the $3/8''$ EEU case on the 44|11 based drive is associated with less oscillations in chainring roller motion and shorter roller/sprocket contact at the rear cog (see Figure VI-18). These different roller motions translate into a shorter $[\eta_B, \eta_A]$ interval (see Figure VI-17). The same remark applies for the 68|17 based drives where the $5/8''$ EEU case results in better efficiency than the reference one. Moreover, the drive pitch radii are each slightly different, and depend on the chain pitches, which also induces a variation of efficiency.
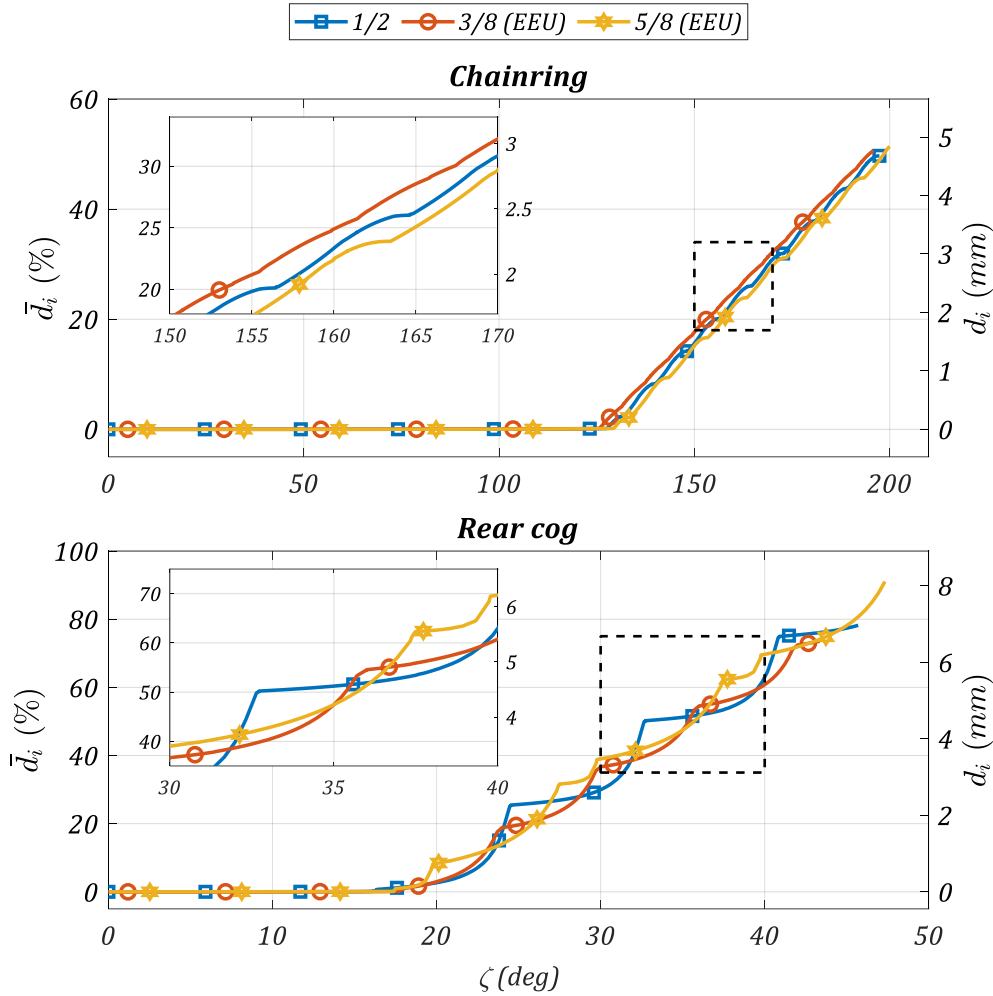
Figure VI-18: Roller motion for $44|11$ based drives, $C_I = 50N.m$

Overall, for the pitch radii tested, the main effect is visible for the RCD cases. For these cases, the influence is mainly a consequence of changing part dimensions. Indeed, for shorter (longer) pitches, pin, bush and roller diameters are reduced (increased) resulting in smaller (larger) sliding distances (see §V.1) and therefore smaller (larger) associated losses. This effect is significant and results in efficiency gains from 0.1 to 0.18% depending on the pitch radii (see Figure VI-17). Still assuming $\Omega_I = 100rpm$, 0.94, 0.58 or 0.52W could be saved for 44|11, 60|15 and 67|18 based drives, respectively (compared to the reference case with $p = 1/2'' = 12.7mm$).

The results for $C_I = 300N.m$ are presented in Figure VI-19.
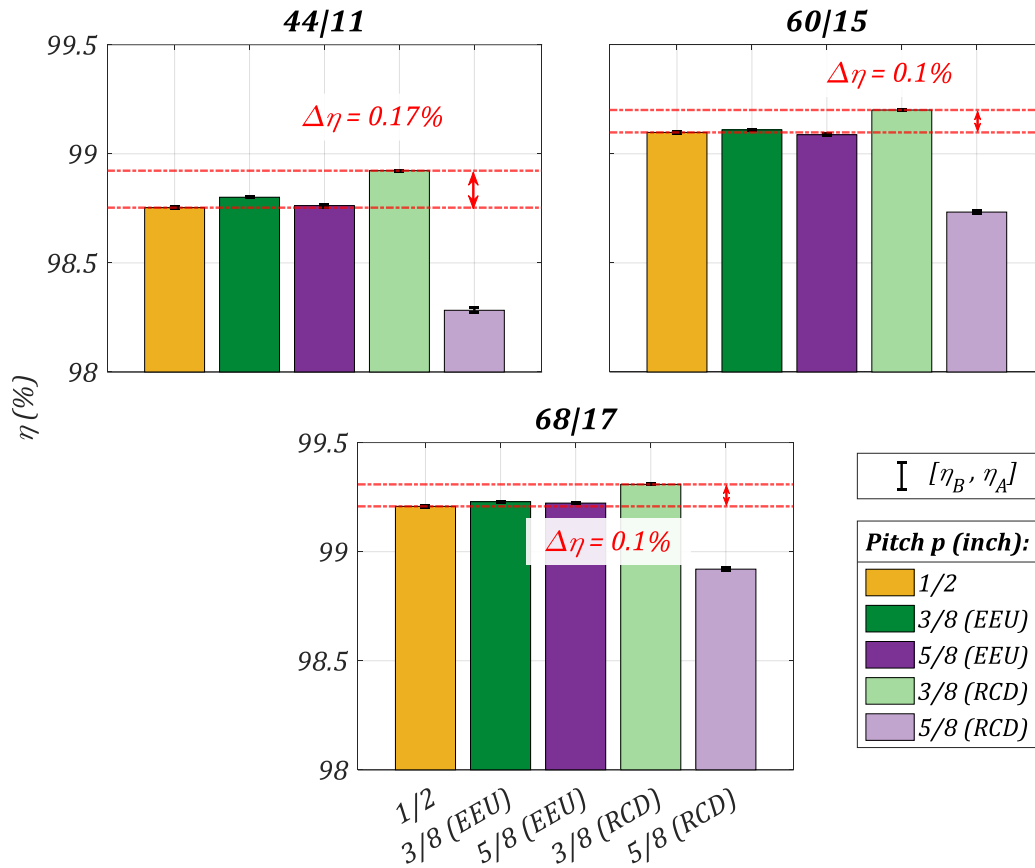
Figure VI-19: Effect of chain pitch on efficiency for $C_I = 300N.m$

As with the effect of sprocket size, the influence of pitch variation is largely maintained for high torques. This was not the case, for instance, for the influence of the tension setting $slack$. The same conclusions as in Figure VI-17 can be drawn for $C_I = 300N.m$. The principal effect of pitch change comes from the modification of chain dimensions as the efficiencies obtained for EEU cases are similar to the reference case ($p = 1/2''$). Assuming $\Omega_I = 100rpm$, the power losses saved reaches 5 and $3W$ for 44|11 and 60|15 or 68|17 based drives, respectively (same power loss save for 60|15 and 68|17).

Combining the potential gains obtained using the effects of pitch and sprocket size, a usual 60|15 drive with $p = 1/2''$ could be replaced by a 92|23 one with $p = 3/8''$ resulting in an efficiency saving of 0.19% and 0.21% for $C_I = 50$ and $300N.m$, respectively. Still assuming $\Omega_I = 100rpm$, this represents a significant save of about $1W$ and $6.6W$, respectively.

VI.2.3   Friction coefficient

This section is dedicated to the influence of friction coefficients. The drive efficiency model introduced different coefficients for each interface: pin/bush (μ_{bp}), bush/roller (μ_{br}) and roller/profile (μ_{rp}). In this chapter, all the coefficients are assumed to be equal and constant. The global value was chosen at $\bar{\mu} = 0.11$ [70].

a) Modification of $\bar{\mu}$

First, the influence of the global friction coefficient $\bar{\mu}$ on drive efficiency is tested. Its value is changed independently from the friction correction angle $|\delta(\infty)|$. Indeed, the theory of friction correction is based on the roller/profile friction coefficient. However, experimental evidence of the reduction of the effect of friction on load evolution with, for example, more efficient drive lubrication, does not yet exist.

Therefore, a constant correction angle is considered. It equals the only value supported experimentally by the studies of Naji & Marshek [62]: $|\delta(\infty)| = 5°$ (*i.e.*, μ_δ is distinct from μ_{rp}).

Calculations are still carried out for the usual 60|15 drive with a tension setting $slack = 11\%$. The global friction coefficient varies between $[0.09 , 0.13]$ which represents about $\pm 20\%$ of variation around the assumed value of $\bar{\mu} = 0.11$.
The results for $C_I = 5N.m$, $50N.m$ and $300N.m$ are presented in Figure VI-20. Solid lines show the mean efficiency between cases A and B. The interval $[\eta_B, \eta_A]$ is represented in shaded areas.
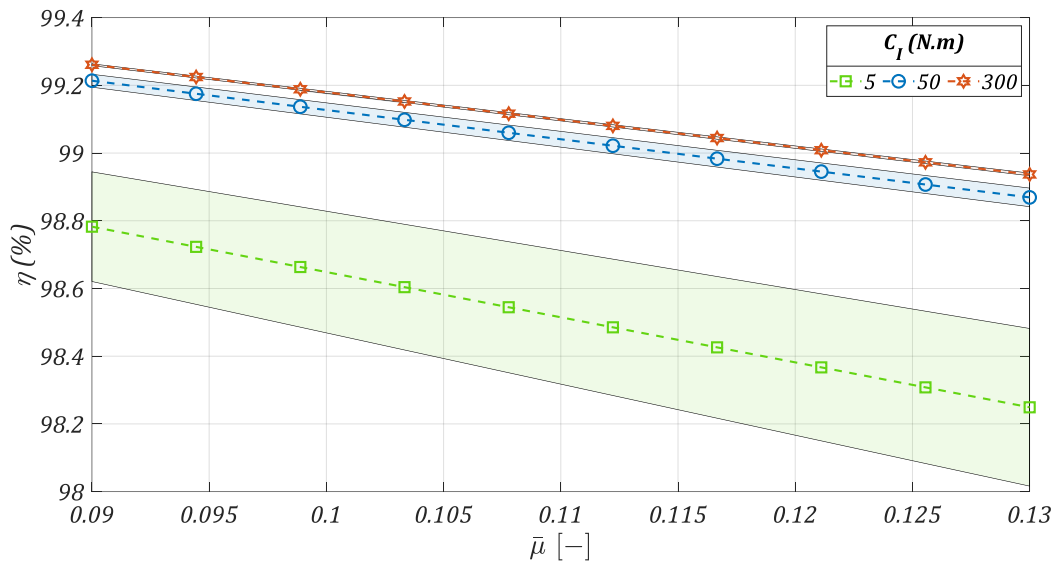
Figure VI-20: Effect of global friction coefficient $\bar{\mu}$ on efficiency for various torques. $\mathbf{60|15}$, $\boldsymbol{p = 12.7mm}$

As expected, efficiency decreases with increasing $\bar{\mu}$ which is consistent with physical intuition. Moreover, the decrease is linear. Indeed, §V.1 (see Table V-2) shows that losses are proportional to the friction coefficient (Coulomb friction is assumed). Therefore, power losses and ultimately drive efficiency (see eqs.(V-30) and (V-31)) also vary linearly with the global friction coefficient $\bar{\mu}$. The effect is relatively significant for all torques. The differences in efficiency between the best and worst cases (*i.e.*, $\bar{\mu} = 0.09$ and 0.13, respectively) reach about 0.53%, 0.34% and 0.32% for $C_I = 5N.m$, $50N.m$ and $300N.m$, respectively. This results, in terms of power losses, in 0.28, 1.78 and $10.1W$ for $C_I = 5N.m$, $50N.m$ and $300N.m$, respectively (still assuming $\Omega_I = 100rpm$). The reduction of the interval $[\eta_B, \eta_A]$ with increasing torques (already mentioned *e.g.*, in Figure VI-2) is clearly visible.

As for chain pitch and number of teeth, the effect largely persists for high torques as it influences the meshing losses that are dominant for severe loading conditions.

b) Contribution of each chain interface

The effect of friction coefficient on drive efficiency is considerable for all loading conditions. Friction coefficients could be reduced by using adapted lubricants or surface treatments. This optimisation trail is very interesting as it does not require the athlete to change any physiological or psychological habits. However, tribological improvements are usually achieved for precise contact conditions. These conditions depend on (non-exhaustive list) materials, roughness, clearance and sliding speeds. It is therefore likely that the optimal lubricant for, for instance, the pin/bush interface does not perfectly suit the other ones (*i.e.*, bush/roller and roller/profile). In this context, knowing which interface is responsible for most of the losses is important in order to determine which conditions to focus on. To this end, Figure VI-21 and Table VI-10 show the contribution of each interface to global losses for $C_I = 5N.m$, $50N.m$ and $300N.m$. The calculations are still performed for a $60|15$ drive with $slack = 11\%$.

		$P_{pin/bush}$ (%)	$P_{bush/roller}$ (%)	$P_{roller/profile}$ (%)	η (%)
$C_I = 5N.m$	Case A	**61**	39	0	98.7
	Case B	**47**	28	25	98.3
$C_I = 50N.m$	Case A	**75**	25	0	99.1
	Case B	**71**	24	5	99
$C_I = 300N.m$	Case A	**77**	23	0	99.1
	Case B	**76**	23	< 1	

*Table VI-10: Cases A and B, split between chain interfaces (pin/bush, bush/roller and roller/profile). **60|15**, $p = 12.7mm$*
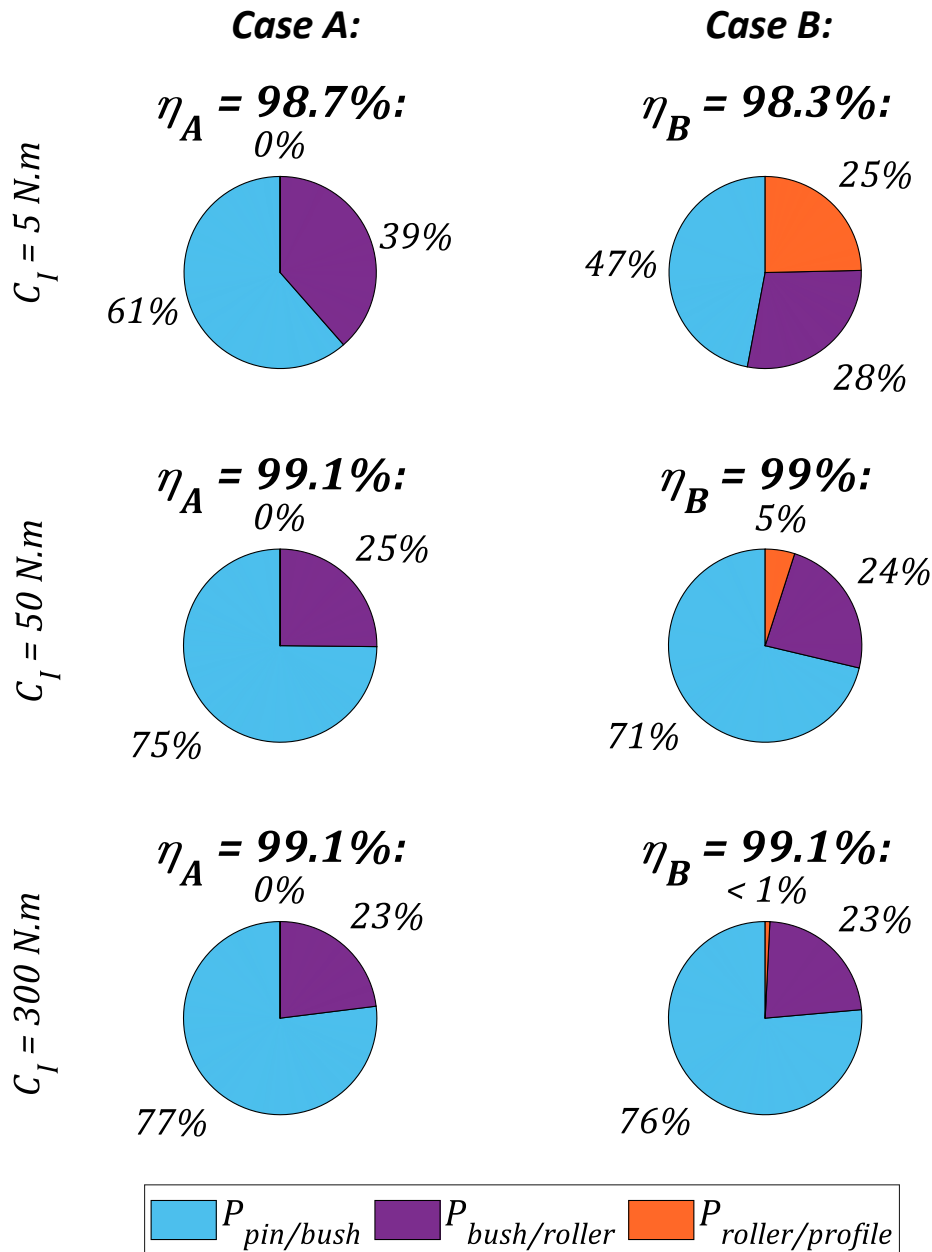
Figure VI-21: Cases A and B, split between chain interfaces (pin/bush, bush/roller and roller/profile). $60|15$, $p = 12.7mm$

The contribution of the roller/profile interface is always null for case A as rolling without sliding is assumed (see §V.1). As with the pie charts presented in §VI.1.2 (see Figure VI-8 and Figure VI-10), lower efficiency for case B indicates that total losses are higher. For this example, the pin/bush interface represents the same amount of loss for case A and B and the smaller proportion is only a consequence of higher overall losses for case B.

As the applied torque increases, the tension ratio reduces and tight strand meshing losses progressively become preponderant, as shown in §VI.1.2. During meshing losses, dissipations occur at the pin/bush interface for both pin and bush articulations. Additional dissipation occurs at the bush/roller interface for bush articulation. Therefore, the pin/bush interface is always the largest loss contributor. As torque increases and meshing losses become the only significant source of loss, the pin/bush contribution tends to about 3/4, leaving the last quarter for bush/roller interface.

Based on this assessment, any tribological optimisation (either lubrication or surface treatment) should preferentially be dedicated to the pin/bush interface. However, this comes with the challenge of reaching this interface. Indeed, as clearances are small, it can be difficult to ensure that sufficient lubricant is supplied in the heart of the chain articulation.

This part was dedicated to the analysis of parameters related to the architecture of the drive. Calculations were carried out only for the NF_{min} tooth profile as the previous part (see §VI.1) showed that tooth profile geometry does not greatly influence losses for track cycling drives.

The influence of the number of sprocket teeth was first analysed. Extreme numbers of teeth were chosen based on the geometrical limitations of track bicycles [92]. Chainring and rear cog showed different influences. For the chainring, the conclusions change depending on the applied torque. Indeed, increasing its number of teeth reduces the tight strand tension and therefore reduces the tension ratio. This causes a reduction of tight strand meshing losses but increases the proportion of roller and slack meshing losses. For low torques, the overall effect is negative while it is positive for high torques. However, the effect of the number of rear cog teeth is always more significant. Increasing Z_{II} results in better drive efficiency thanks to reduced pitch angle. Therefore, for drives with a constant Z_I/Z_{II} ratio, the overall effect of bigger sprockets is always positive.

In order to further reduce the pitch angle while maintaining acceptable sprocket size, the effect of chain pitch was then explored. Standard pitches directly above and below the usual $1/2''$ one were considered. However, changing sprocket pitch usually entails modifying the dimensions of the chain parts (*e.g.*, pin, bush and roller diameters). To separate this effect from the pitch change, EEU (Everything Else Unchanged) cases were considered. For these cases, only chain pitch was modified while the other chain dimensions were kept constant. The results showed that smaller pitch indeed reduces losses. However, significant differences were reported only for RCD cases, showing that the effect is mainly due to modified chain dimensions. This highlighted that reducing only the pitch angle for constant sprocket size (*i.e.*, EEU cases) does not greatly modify chain efficiency as the number of articulations experience in a given amount of time also increases.

Finally, the effect of the global friction coefficient $\bar{\mu}$ was explored. Consistent with the assumption of Coulomb friction, the evolution of drive efficiency depending on $\bar{\mu}$ is linear. Efficiency variations for a modification of about 20% of the friction coefficient were given. Then, the losses were split between each chain interface (pin/bush, bush/roller and roller/profile). The breakdown showed that the pin/bush interface is responsible for most of the losses ($3/4$ for $C_I > 50N.m$). This indicates that any potential optimisation of lubricant properties should be carried out based on the tribological conditions (*i.e.*, sliding speed, roughness, *etc*.) encountered at this interface.

The first two parts of this chapter explored the influence of numerous parameters on chain drive efficiency. In the following part, the Design Of Experiments (DOE) methodology is used to compare each influence.

VI.3 Comparison of parameter influences using Design Of Experiments

In this chapter, the dependency of chain drive efficiency on numerous parameters has been explored. However, each parameter has mainly been studied alone while keeping the others constant. Therefore, potential interactions between parameters were difficult to appreciate. Moreover, it was not easy to compare each contribution which made it difficult to determine on which ones the effort of optimisation should focus. In order to answer these questions, the Chain Drive Efficiency Model (CDEM) is analysed using a Design Of Experiments (DOE) methodology. This tool allows the identifying the contribution of each factor as well as the potential interactions with minimal calculations.
The DOE is used to explore the contribution of 6 parameters:

- $\bar{\mu}$, the global friction coefficient
- $slack$, the tension setting
- C_I, the torque applied on the chainring
- R_{II}, the rear cog pitch radius
- R_I, the chainring pitch radius
- p, the drive pitch (identical pitch for sprockets and chain)

Although §VI.1 showed that the effect of tension setting $slack$ and chainring torque C_I both depend on the tension ratio, the two parameters are considered here to retain easily interpretable variables. §VI.2 showed that the effect of the number of sprocket teeth mainly reduces to a pitch circle radius modification. Therefore, the numbers of teeth are determined based on the last three parameters: R_{II}, R_I and p. For 3/8 and 5/8″ pitches, chains with real dimensions (*i.e.*, RDC in §VI.2.2) are used (EEU cases are not considered, see Table VI-8). Only discreet values of pitch p are considered. The ranges explored for each factor are given in Table VI-11.

$\bar{\mu}$	$slack$ (%)	C_I ($N.m$)	R_{II} (mm)	R_I (mm)	p ($inch$)
$[0.09\,,0.13]$	$[4\,,20]$	$[5\,,300]$	$[22.5\,,42.6]$	$[80.9\,,141.5]$	$[\![3\,,5]\!] \times 1/8$

Table VI-11: Ranges of DOE factors

The intervals are essentially identical to the boundaries set in the previous parts except for the tension setting $slack$. Indeed, for drives with a larger pitch (*e.g.*, 5/8″) and a small number of teeth, the variation of instantaneous mid-span movement (see §II.1.2) within a drive period is larger. Consequently, too small $slack$ values are not always reachable (this point was already addressed in §III.1.2). The lower bound of the $slack$ setting is therefore increased to 4%. Radii R_{II} and R_I are chosen to include 11 teeth rear cog with $p = 1/2″$ and 56 teeth chainring with $p = 3/8″$ (see Table VI-9).

Unless stated otherwise, in this part i and j are used for factor indexation (see Table VI-12) and k is the number of the DOE trials (*e.g.*, Table VI-14 below).

VI.3.1 Fractional factorial design

The aim of the DOE is to characterise the influence of different factors on a given response: in this case drive efficiency η. As the factors usually have different units and variation ranges, non-dimensional coded units x_i are introduced in order to compare factor variation within the same scale. Coded units vary between -1 and 1. $x_i = -1$ corresponds to the lowest value explored for factor i while $x_i = 1$ corresponds to the highest one. Conversion between the coded and original values is carried out according to eq.(VI-2).

$$x_i = \frac{2(A_i - \bar{A}_i)}{A_{i,max} - A_{i,min}} \qquad \textit{(VI-2)}$$

with:

- $A_{i,max}$, the maximal value of factor i
- $A_{i,min}$, the minimal value of factor i
- $\bar{A}_i = \frac{A_{i,max} + A_{i,min}}{2}$, the mean value of factor i (see Table VI-12)

Table VI-12 gives the index i associated with each of the six factors considered. Conversions between coded units and usual values (calculated using eq.(VI-2)) are also given. In this section, the coded level of each factor can be designated either using their index i or directly by the name of the factor (*e.g.*, $x_{i=1}$ or $x_{\bar{\mu}}$, see Table VI-12).

Factor	i	$x_i = -1$ $A_{i,min}$	$x_i = 0$ $\bar{A}$	$x_i = 1$ $A_{i,max}$
$\bar{\mu}$	**1**	0.09	0.11	0.13
$slack$ (%)	**2**	4	12	20
C_I ($N.m$)	**3**	5	152.5	300
R_{II} (mm)	**4**	22.5	32.55	42.6
R_I (mm)	**5**	80.9	111.2	141.5
p ($inch$)	**6**	3/8	1/2	5/8

Table VI-12: Index i and conversion between coded and usual values for each factor

Without information about the function relating the coded variables x_i and the chain drive efficiency η, a general function is assumed as follows [97].

$$\eta = f(x_1, x_2, x_3, \dots) \qquad \textit{(VI-3)}$$

A Taylor-Mac Laurin series expansion of the function is usually considered. Assuming the derivatives to be constant, the expansion is expressed as a polynomial [97], [98]. Its expression is given by eq.(VI-4). The output of the polynomial function is usually denoted Y. In that case, it corresponds to the prediction of chain drive efficiency η according to the polynomial.

$$\eta = Y = E_0 + \sum_{i=1}^{nb_{fact}} E_i x_i + \sum_{i=1}^{nb_{fact}} E_{ij} x_i x_j \left(1 - \delta_{ij}\right) + \sum_{i=1}^{nb_{fact}} E_{ii} X_i^2 + \cdots \qquad \textbf{\textit{(VI-4)}}$$

with:

- $\delta_{ij} = \begin{cases} 0 \ if \ i \neq j \\ 1 \ if \ i = j \end{cases}$, the Kronecker delta
- $E_0, E_i, E_{ij}, E_{ii}, \ldots$, the coefficients of the polynomial
- nb_{fact}, the number of factors
- X_i^2 defined below in eq.(VI-5)

Coefficient E_0 gives the mean value of the polynomial. Coefficients E_i characterise the linear effect of factor i on the output value Y. Coefficients E_{ij} characterise the potential interactions between factors. Coefficients E_{ii} characterise the quadratic effect of factor i. The development can be extended with the same principle to higher degrees.

Coefficients E will later be determined to fit the polynomial model on CDEM results (in a least square sense, see §VI.3.2). For cases where factor levels are equally spaced with the same number of observations per level factor (conditions fulfil here), the coded level can be chosen so that the effect calculations become non-correlated (*i.e.*, orthogonal). This enables calculating a given coefficient E_i without having to consider all the others, see for instance eqs.(VI-7) and (VI-8) below. Such coded levels adapted to each specific case can be found in [99]. In particular for this study, quadratic coefficients E_{ii} are multiplied with the coded variable X_i^2, determined based on x_i according to eq.(VI-12).

$$X_i^2 = 3x_i^2 - 2 \qquad \textbf{\textit{(VI-5)}}$$

The idea of the DOE analysis is to determine the main polynomial coefficients using carefully chosen trials. Then the analysis of the sign and magnitude of each coefficient (called effect) can be carried out to assess the contribution of each factor (E_i, E_{ii} and E_{ij}) on chain drive efficiency.

For our application, the previous parts showed that the effect of the factors considered are highly non-linear (*e.g.*, influence of chainring torque C_I, see VI.1.1). Therefore, it is interesting to study quadratic contributions E_{ii} as they are likely to be significant. To do so, three levels of coded units ($x_i = -1$, 0 and 1) must be considered. With 6 factors having three levels each, the total number of possible level combinations is $3^6 = 729$. It means that 729 trials must be carried out to calculate the 729 polynomial coefficients (*i.e.*, E_i, E_{ij}, E_{ii}, *etc.*) corresponding to the effects of all factors and all interactions. It is called full factorial design 3^6 (6 factors with 3 levels each) and results in a perfect fit of the polynomial model on the trials. In this design, among the 729 coefficients, 6 correspond to main effects (E_i, order 1), 6 to quadratic effects (E_{ii}, order 2) and 15 to linear interaction between two factors (E_{ij}, order 2), see Table VI-13. The remaining coefficients are associated with higher orders (*i.e.*, ≥ 3).

However, it is likely that the high order actions have limited influence on the final results (*e.g.*, order-6 interaction E_{123456}). Therefore, to reduce the number of trials and consequently the computational cost, a fractional factorial design is used. Fractional DOE is a variation of the basic factorial DOE in which only a subset of the trials is used to determine only polynomial coefficients of interest. Doing so, several polynomial coefficients are determined simultaneously with no possibility to separate each contribution (*i.e.*, actions are called aliased). It is then important to carefully choose which coefficients to alias. Low order effects (*e.g.*, effect of order one E_i) are usually aliased with higher order ones (*e.g.*, order five).

Order 0	E_0	1
Order 1 (E_i)	$\bar{\mu}$, $slack$, C_I, R_{II}, R_I, p	6
Order 2, quadratic (E_{ii})	$\bar{\mu}^2$, $slack^2$, C_I^2, R_{II}^2, R_I^2, p^2	6
Order 2, interaction (E_{ij})	$\bar{\mu}.slack$, $\bar{\mu}.C_I$, $\bar{\mu}.R_{II}$, $\bar{\mu}.R_I$, $\bar{\mu}.p$ $slack.C_I$, $slack.R_{II}$, $slack.R_I$, $slack.p$, $C_I.R_{II}$, $C_I.R_I$, $C_I.p$ $R_{II}.R_I$, $R_{II}.p$ $R_I.p$	15

Table VI-13: Actions with order ≤ 2 for six 3-level factors

In this study, it is assumed that only the 28 actions with order ≤ 2 are significant (see Table VI-13). Therefore, a factorial plan 3^{6-1} is used with the alias generator $\mathbf{0 = 123456}$ [97], [98]. This generator indicates that coefficient E_0 will be aliased with two other coefficients: E_{123456} and $E_{1^2 2^2 3^2 4^2 5^2 6^2}$ (*i.e.,* interaction between the 6 linear and 6 quadratic terms, respectively). The resulting fractional design ensures that all actions with order ≤ 2 are aliased with ones of a strictly higher order, assumed as non-significant. Using this fractional design reduces the number of trials to $3^{6-1} = 243$.

Coded units for each trial are arranged into the 243×6 trial matrix in which each line gives the values associated with the trial considered. This orthogonal matrix is called test matrix and is given in Appendix L. Index k is introduced to number the trials between 1 and $nb_{trial} = 243$.

Coded units for trials $k = 55$ and $k = 177$ are given as examples in Table VI-14. The conversion into factor values is given in Table VI-15.

k	$x_{\bar{\mu}}$	x_{slack}	x_{C_I}	$x_{R_{II}}$	x_{R_I}	x_p
55	-1	-1	-1	1	-1	1
177	1	0	0	-1	1	-1

Table VI-14: Coded units for trials 55 and 177

k	$\bar{\mu}$	$slack$ (%)	C_I (N.m)	R_{II} (mm)	R_I (mm)	p (inch)
55	0.09	4	5	42.6	80.9	5/8
177	0.13	11	152.5	22.5	141.5	3/8

Table VI-15: Factor values for trials 55 and 177

The number of chainring and rear cog teeth Z_j are calculated from the values of factors R_I, R_{II} and p according to eq.(VI-7).

$$Z_j = \text{round}\left(\frac{\pi}{\text{asin}\left(\frac{p}{2R_j}\right)}\right) \tag{VI-6}$$

with:

- $j = I$ for the chainring and II for the rear cog

Due to the discrete nature of the numbers of teeth (required to be integers), the real pitch circle radii are slightly different from the value prescribed by the coded units. Therefore, the real pitch radius of

two trials with the same x_{R_j} are different for different pitches. The gap between the R_j factor values and the real pitch radii is larger for bigger pitches.

The number of chain links and centre distance L are then determined to find the smallest L value higher than $380mm$ allowing to match the tension setting requirement given by factor $slack$. The vertical shift is still $\Delta Y = -50mm$. General views of the drives obtained for $k = 55$ and 177 are shown in Figure VI-22.

<center>

(a)   *(b)*

</center>
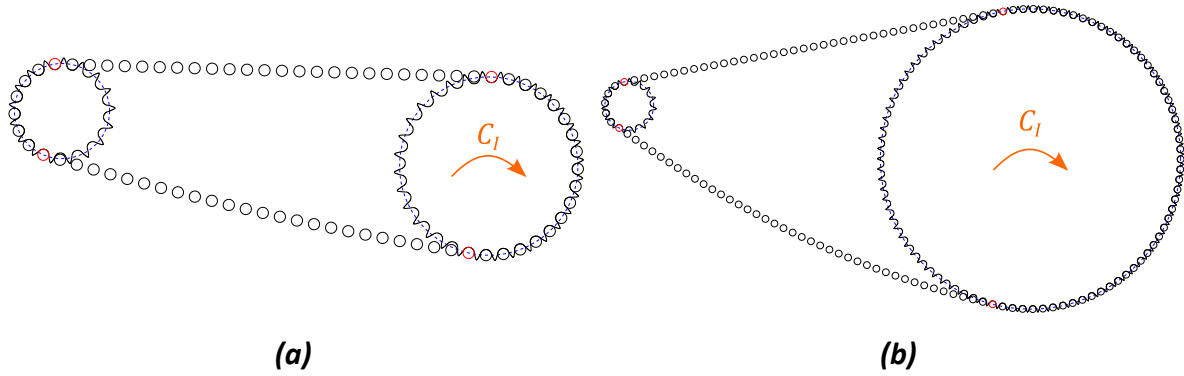
Figure VI-22: General views (a) $k = 55$ (b) $k = 177$. Both figures have the same scale.

The simulation of the CDEM is then carried out with the prescribed chainring torque C_I and efficiency is calculated considering the given global friction coefficient $\bar{\mu}$. The results obtained for all the trials are arranged in a column vector $\boldsymbol{\eta_{CDEM}}$ where $\boldsymbol{\eta_{CDEM}}(k)$ gives the mean efficiency $(\eta_A + \eta_B)/2$ predicted by the CDEM for trial k. Vector $\boldsymbol{\eta_{CDEM}}$ is also given in Appendix L.

VI.3.2 Results of the polynomial model

Equations given in this section are adapted from [98]–[100].

The polynomial model introduced in eq.(VI-4) is fitted on the CDEM results of the 243 trials $\boldsymbol{\eta_{CDEM}}$. To do so, the effect of the 28 actions of interest E_0, E_i, E_{ii} and E_{ij} are calculated. Thanks to the carefully chosen orthogonal polynomial basis (mentioned above), each effect can be calculated independently of the others. Intermediate variable M is calculated first according to eq.(VI-7).

$$E_0: \qquad M_0 = \sum_{k=1}^{nb_{trial}} \boldsymbol{\eta_{CDEM}}(k) \qquad\qquad \textit{(a)}$$

$$E_i: \qquad M_i = \sum_{k=1}^{nb_{trial}} x_{i,k}\boldsymbol{\eta_{CDEM}}(k) \qquad\qquad \textit{(b)}$$

(VI-7)

$$E_{ij}: \qquad M_{ij} = \sum_{k=1}^{nb_{trial}} x_{i,k}x_{j,k}\boldsymbol{\eta_{CDEM}}(k) \qquad\qquad \textit{(c)}$$

$$E_{ii}: \qquad M_{ii} = \sum_{k=1}^{nb_{trial}} X_{i,k}\boldsymbol{\eta_{CDEM}}(k) \qquad\qquad \textit{(d)}$$

with:

- $x_{i,k}/X_{i,k}$ the coded level for factor i at trial k

The polynomial coefficients (called effects) are calculated according to eq.(VI-8) from the values of M.

E_0:
$$E_0 = \frac{M_0}{nb_{trial}} \qquad (a)$$

E_i:
$$E_i = \frac{M_i}{\sum_{k=1}^{nb_{trial}} x_{i,k}^2} \qquad (b)$$

E_{ij}:
$$E_{ij} = \frac{M_{ij}}{\sum_{k=1}^{nb_{trial}} \left(x_{i,k} x_{j,k}\right)^2} \qquad (c)$$

E_{ii}:
$$E_{ii} = \frac{M_{ii}}{\sum_{k=1}^{nb_{trial}} X_{i,k}^2} \qquad (d)$$

(VI-8)

The analysis of the effects obtained is carried out in the following section (see §VI.3.3).
From the effects E the sum of squares SS attributed to each of the 28 actions considered are computed using eq.(VI-9). The sum of squares on the entire results $\boldsymbol{\eta}_{CDEM}$ is also computed according to eq.(VI-10).

E_i: $SS_i = E_i M_i$ (a)

E_{ij}: $SS_{ij} = E_{ij} M_{ij}$ (b)   **(VI-9)**

E_{ii} $SS_{ii} = E_{ii} M_{ii}$ (c)

$$SS_{tot} = \sum_{k=1}^{nb_{trial}} (\boldsymbol{\eta}_{CDEM}(k) - \overline{\eta_{CDEM}})^2 \qquad \textbf{(VI-10)}$$

with:

- $\overline{\eta_{CDEM}}$, the mean value of results vector $\boldsymbol{\eta}_{CDEM}$

The variance V associated to each action is obtained from the sum of squares SS according to eq.(VI-11). For the 28 actions considered, variances and sum of squares are equal due to the associated degree of freedom dof being one.

E_i: $V_i = SS_i/dof_i$ (a)

E_{ij}: $V_{ij} = SS_{ij}/dof_{ij}$ (b)   **(VI-11)**

E_{ii} $V_{ii} = SS_{ii}/dof_{ii}$ (c)

with:

- $dof_i = dof_{ij} = dof_{ii} = 1$ for the 28 actions considered.

Among the 28 actions considered, to evaluate, which ones are the most significant and even which ones are non-significant, an analysis of variance (ANOVA, see [99], [100]) is conducted. This analysis consists in calculating the ratio between the variance due to each factor considered (*i.e.,* V_i, V_{ij} or V_{ii}) and the residual variance due to neglected actions. In this case, the residual sum of squares SS_{res} (attributed to the neglected actions with order ≥ 3) is calculated from SS_{tot} and the SS attributed to

each of the 28 actions considered (eq.(VI-9)). Then, the associated variance V_{res} is calculated using eq.(VI-12). This variance accounts for all the actions neglected *a priori* in the analysis (*i.e.*, actions with order ≥ 3).

$$V_{res} = \frac{SS_{res}}{dof_{res}} = \frac{\left(V_{tot} - \sum_{i=1}^{nb_{fact}} V_i - \sum_{i,j=1}^{nb_{fact}} V_{ij} - \sum_{i=1}^{nb_{fact}} V_{ii}\right)}{dof_{res}} \quad \text{(VI-12)}$$

with:

- $dof_{res} = 243 - 28 = 215$

Then a Fisher-Snedecor test [99], [100] is carried out for each of the 28 actions considered. This test consists by comparing the ratio V/V_{res} with a reference value which ultimately gives a probability that the action considered is more significant than the neglected ones.

Figure VI-23 shows the certainty (in %) that each action is more influential than the residual constituted by all the actions neglected *a priori* (*i.e.*, actions with order ≥ 3).
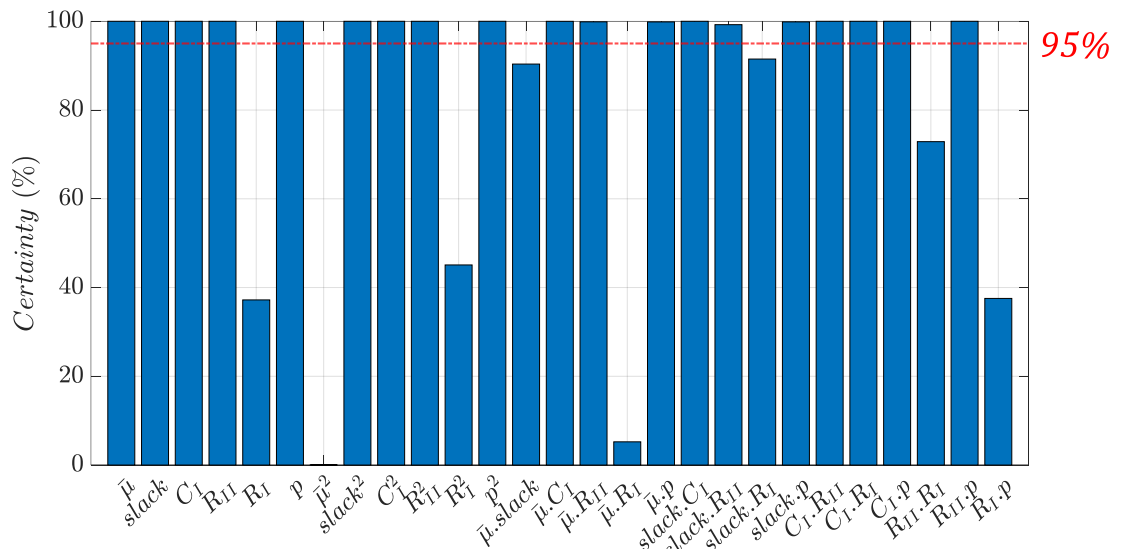
Figure VI-23: Certainty of action significance compared to the residual variance according to the Fisher-Snedecor test [99], [100]

Actions with a certainty level lower than 95% are considered to be non-influential and will be neglected for the rest of the analysis. According to Figure VI-23, actions: R_I, $\bar{\mu}^2$, R_I^2, $\bar{\mu}.slack$, $\bar{\mu}.R_I$, $slack.R_I$, $R_I.R_{II}$ and $R_I.p$ are rejected. The variance attributed to each of these actions have then been added to the residual variance V_{res} (see eq.(VI-12)). The Fisher-Snedecor has been carried out again to ensure that all the remaining actions are above the 95% limit even with the increased residual variance. After this second test, no other actions had to be rejected. Among the 243 actions studied, the 19 remaining ones after the Feshier-Snedecor test account for 93% of the global sum of squares SS_{tot} (see eq.(VI-10)).

The non-significance of action $\bar{\mu}^2$ was expected as efficiency is proportional to the global friction coefficient $\bar{\mu}$, as highlighted in §VI.2.3.

It is interesting to note that the effects of R_I and most of its related interactions (except $C_I.R_I$) are non-significant. Indeed, Z_I was shown to have an influence on efficiency in §VI.2.1. However, this effect was shown to be detrimental to efficiency for low torques and positive for high torques. The effect of chainring torque C_I is likely to be similar, as shown in §VI.1.1. It is therefore possible that the effect of

R_I is hidden in the effect of C_I. Moreover, back-and-forth roller motions occur for some trials, particularly with low $slack$ settings (tight drives). This phenomenon, present for high and low torques, might have contributed to blurring the R_I effect.

A polynomial model is created according to eq.(VI-4) considering only the 19 remaining actions (polynomial coefficients obtained are given in Figure VI-28.a below). Its predictions are compared to the chain drive efficiency model calculations $\boldsymbol{\eta_{CDEM}}$ for the 243 trials. The results are shown in Figure VI-24.
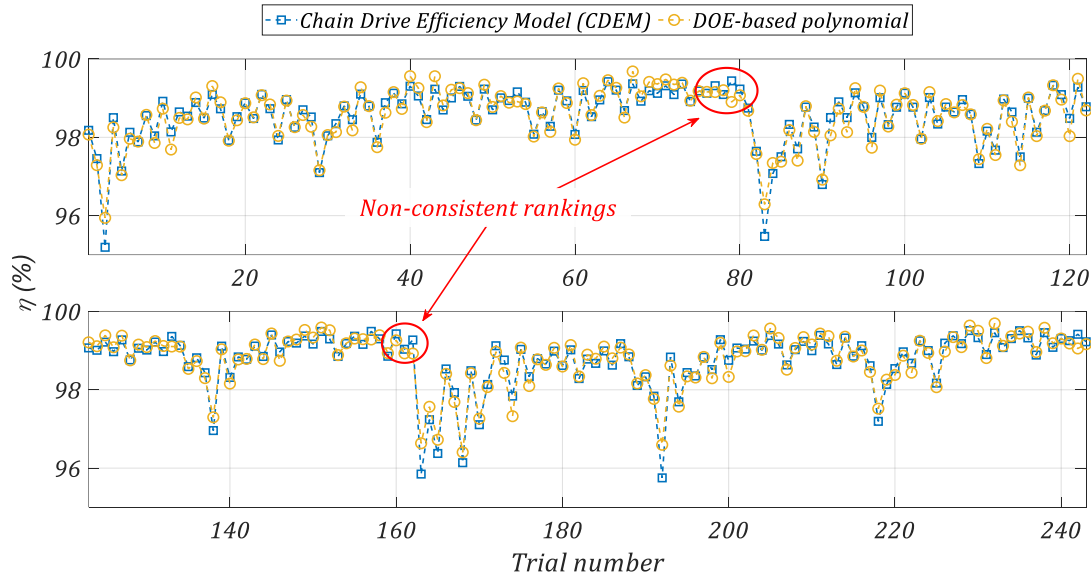
Figure VI-24: CDEM and DOE-based polynomial predictions for the 243 trials on the fractional design

The predictions of the DOE based polynomial model are consistent with the results of the CDEM. This supports the variance analysis as the polynomial model is based only on the 19 most influential actions determined using the Fisher-Snedecor test. It is important to note that the efficiency ranking between trials is generally identical for both models (*i.e.*, if a trial k exhibits higher efficiency than another trial k' according to the CDEM, so it is for the DOE-based polynomial). This point shows that the DOE based model can be used to determine if a given drive configuration is more efficient than another one. However, the ranking is not respected for some trials, particularly close to trial 79 (see Figure VI-25).
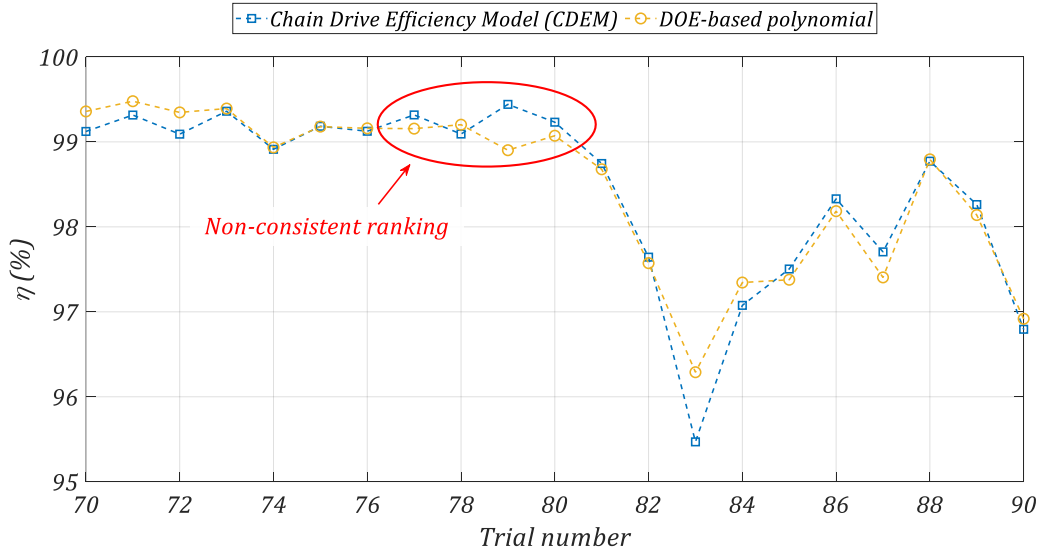
Figure VI-25: Zoom in on the non-consistent ranking for trials 77 to 80

Trials 73 to 81 all have the same values for C_I, R_I and R_{II} ($x_{C_I} = 1$, $x_{R_I} = -1$ and $x_{R_{II}} = 1$) but a different pitch p and tension setting $slack$. It is likely that the varying chain pitch p resulted in different pitch radii (see eq.(VI-6)) between trials, explaining the discrepancies with the Chain Drive Efficiency Model (CDEM).

The differences between the CDEM and the DOE-based polynomial model are represented according to eq (VI-13) in Figure VI-26.

$$|\Delta\eta| = |\eta_{CDEM} - \eta_{DOE\ polynomial}| \qquad \textbf{(VI-13)}$$
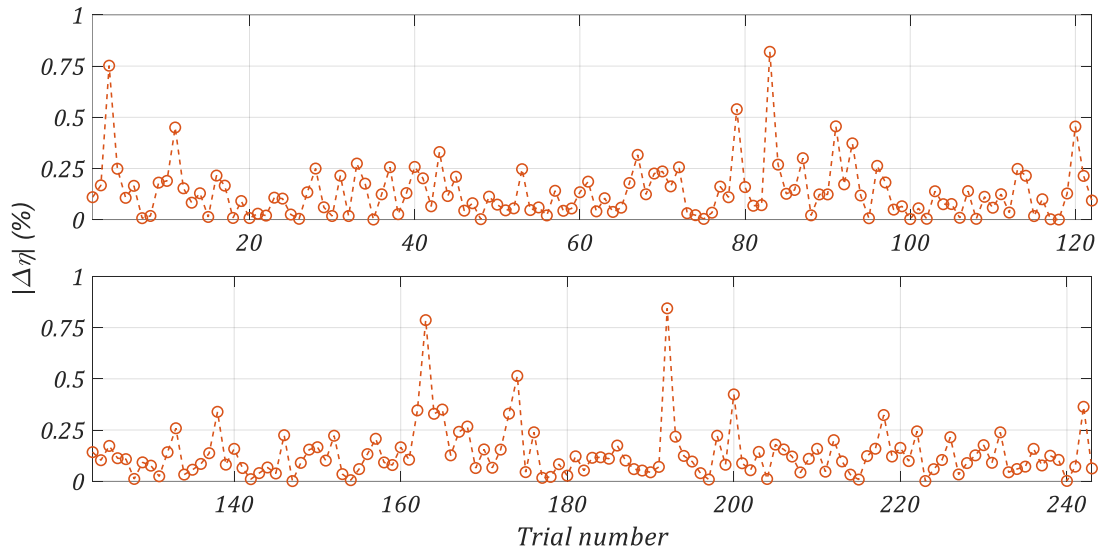
Figure VI-26: Absolute difference between the CDEM and the DOE-based polynomial model for the 243 trials of the fractional design

The biggest gaps ($|\Delta\eta > 0.5\%|$) occur for trials with the lowest efficiency predictions. These trials all correspond to cases with a high chain pitch (*i.e.*, $p = 5/8''$). Excluding these cases, the gaps are usually lower than 0.25%. This gap of 0.25% between the prediction of the chain drive efficiency model and

the DOE-based one is usually higher than the effects of each parameter studied in this chapter (*e.g.*, the variation due to chain pitch was of the order of 0.1% in §VI.2.2).

The DOE-based polynomial is also tested in 25 trials with random coded values in the interval $[-1\,,1]$ (x_p is randomly taken between -1, 0 and 1). The comparison is shown in Figure VI-27.
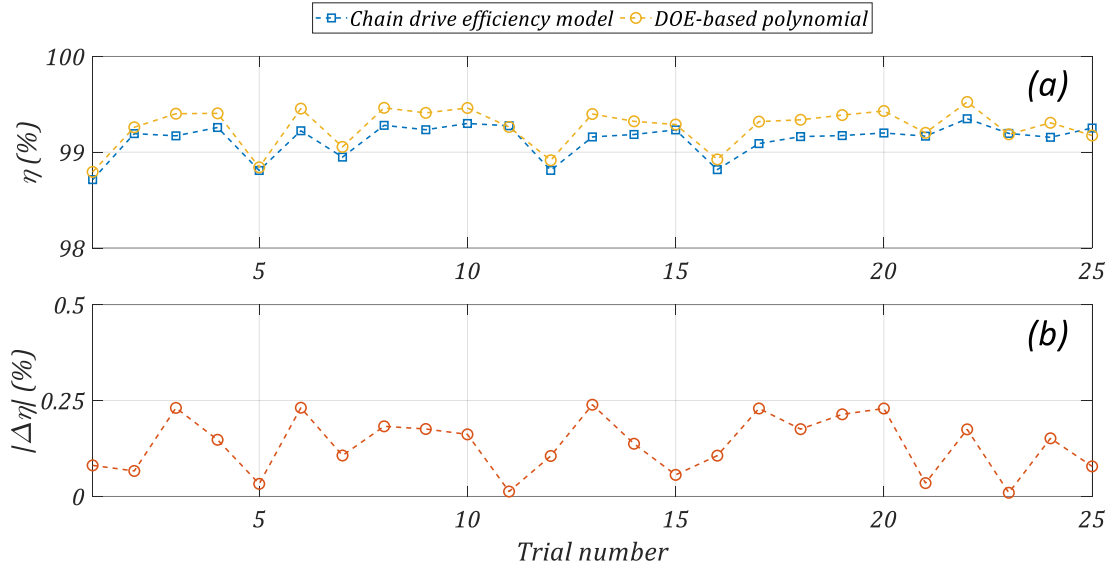
Figure VI-27: Comparison between predictions of the CDEM and polynomial DOE-based model for the 25 random trials. (a) efficiency predictions (b) absolute difference

Except for the last cases (number 23 to 25), the tendencies are also similar between both models. The absolute differences $|\Delta\eta|$ are always less than 0.25%. It can be noted that the predictions of the DOE-based polynomial model are almost systematically higher than the CDEM ones. This indicates that the $729 - 19 = 710$ actions neglected either *a priori* (*i.e.*, order ≥ 3) or after the Fisher-Snedecor test (see Figure VI-23) overall have a detrimental effect on efficiency.

From the comparisons between the DOE-based polynomial model and the CDEM, it was observed that the hierarchies between drive configurations are usually similar for both models. Therefore, the polynomial model usually allows quickly determining if a given drive configuration is more or less efficient than another. Missing hierarchies might be caused by pitch radius variations between trials with same x_{R_j} values but with different chain pitches. The efficiency predictions of the polynomial model generally overestimate drive efficiency. The absolute difference is typically of the order of 0.1%. The difference has the same magnitude as the effect explored in this chapter. Therefore, the DOE-based polynomial model is not accurate enough to replace the CDEM. However, as the hierarchies are identical, analysis of the polynomial coefficients E (called effects) gives an interesting view of the general trends of chain drive efficiency variation. These trends are analysed in the following section.

VI.3.3 Analysis of polynomial coefficients *E*

This part is dedicated to the analysis of the polynomial coefficients E. The coefficients are called effects and characterise the influence of each action on drive efficiency.

According to eq.(VI-8), the effect of the significant actions (according to the Fisher-Snedecor test) are presented in Figure VI-28.a. The magnitude of effects E alone does not characterise the influence of the relative actions as the intervals ranged by each factor are different. To identify the actions with the

greatest influence on drive efficiency, the proportions of the sum of squares $\overline{SS} = SS/SS_{tot}$ (expressed in percentage) attributed to each action are also plotted in Figure VI-28.b. Higher $\overline{SS}$ are associated with greater influence on efficiency.
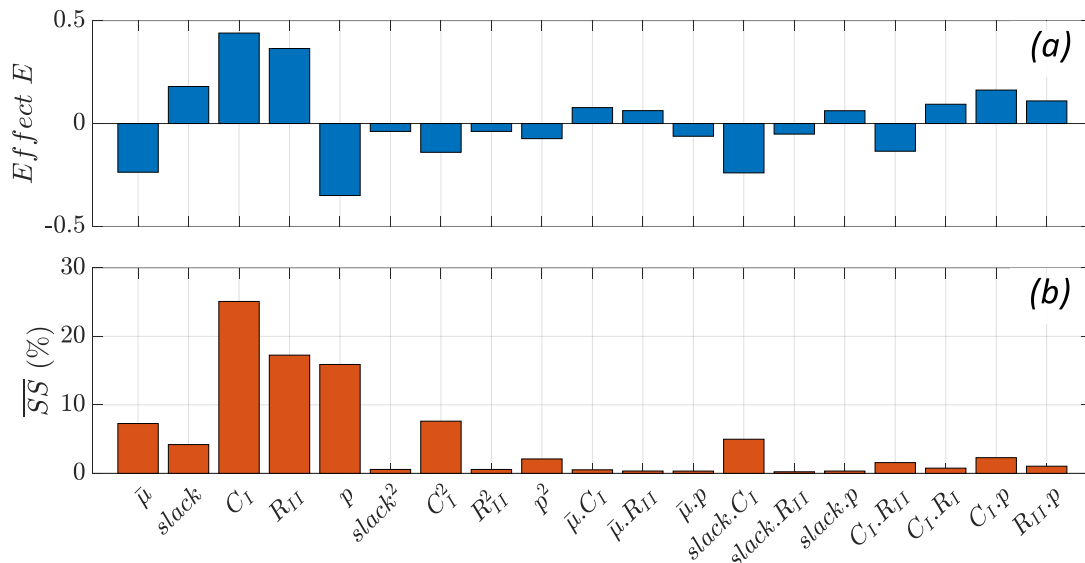
Figure VI-28: (a) Effect E (b) Sum of squares proportion $\overline{SS}$ for significant actions

The sign of the effects gives the direction of influence of the action considered. For instance, the negative effect of the global friction coefficient $\bar{\mu}$ indicates that higher friction coefficients result in lower drive efficiency. The effect of chain pitch p is also negative as the chain efficiency decreases for a higher pitch. These results are consistent with the previous part (see §VI.2). On the contrary, the effect of chainring torque C_I, tension setting $slack$ and rear cog radius R_{II} are positive. This indicates that the larger these factors are, the higher the drive efficiency. These results are also consistent with previous parts (see §VI.1 and §VI.2). The DOE provides the additional information of the proportional sum of squares $\overline{SS}$ which enables easier comparison of the influence of each factor. From the proportional sum of squares, Figure VI-28.b shows that the chainring torque is the most influential factor (representing about 25% of SS_{tot}). This indicates that a large part of drive efficiency is determined by the torque applied by the athlete. The rear cog radius and chain pitch follow with proportional sum of squares of about 17 and 16%, respectively. This assessment supports the idea of using a rear cog as large as possible as the effect on drive efficiency is substantial. Moreover, this modification can be made relatively easily as it is possible to preserve the drive ratio by also adjusting the chainring size. The chain pitch also plays an important role. However, this effect must be tempered as the variation is mostly between $5/8''$ and $1/2''$ chains (see quadratic analysis below), resulting in limited perspective for cycling applications. Among linear actions, the friction coefficient follows with $\overline{SS} \approx 7\%$. This indicates that this factor is not very influential. Finally, the tension setting $slack$ represents about 4% of $\overline{SS}$ showing its limited influence compared to other factors.

Linear actions account for the most part of the efficiency variation as they represent about 70% of SS_{tot}. However, some quadratic actions also exhibit considerable influence. This is particularly the case for C_I^2 and p^2. Interactions between first order actions also play a role as they account for about 10% of $\overline{SS}$. Analysing the sign of these effects might be difficult. Therefore, dedicated tools are used below to facilitate interpretation.

a) Analysis of quadratic effect

Figure VI-29 shows effect plots for the six main factors. These plots are built from the mean efficiency values for each coded unit x_i being at -1, 0 and 1. Each point therefore results from a mean of 81 trials.
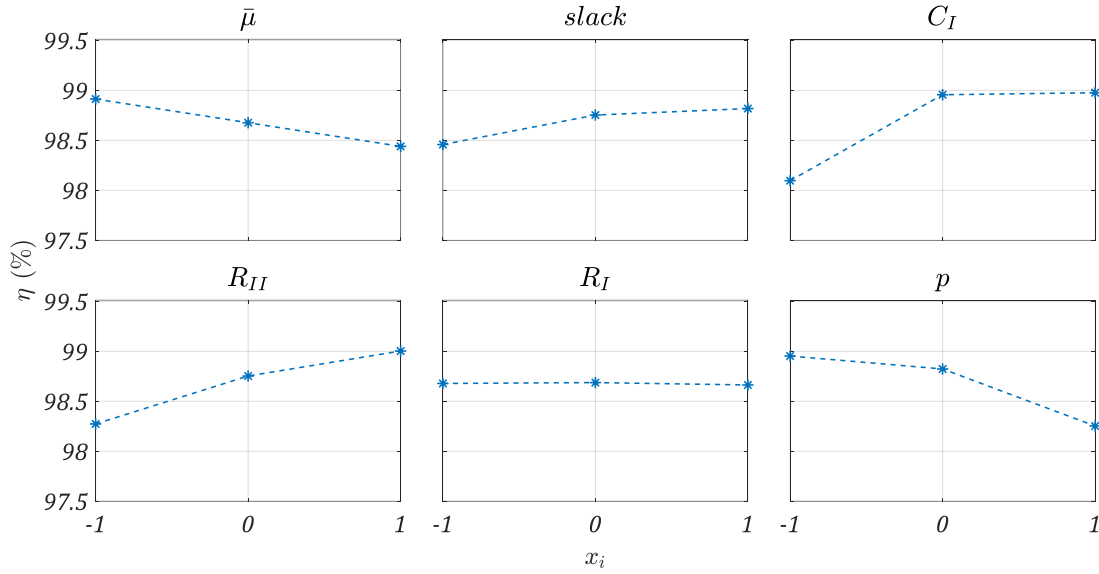
Figure VI-29: Effect plot for the six main factors

The plot for $\bar{\mu}$ shows the detrimental effect of this factor on drive efficiency (*i.e.*, the higher the global friction coefficient the lower the efficiency). This is consistent with the effect $E_{\bar{\mu}} < 0$ shown in Figure VI-28. Moreover, the relation is linear, consistently with action $\bar{\mu}^2$ being negligible according to the Fisher-Snedecor test. The second plot is for the $slack$ parameter. This time, efficiency increases for higher $slack$ values corresponding to the positive effect E_{slack} in Figure VI-28. However, the relation is not linear as the effect is less significant between $x_{slack} = 0$ and 1 than between -1 and 0. This deviation from linearity is characterised by the effect $slack^2$. The same behaviour is observed for C_I with an even stronger deviation from linearity. Indeed, the high significance of C_I^2 effect ($\overline{SS} \approx 7.6\%$) induced a strong decrease of the chainring torque effect for high torques. Almost the entirety of the torque effect lies between $x_{C_I} = -1$ and 0 (*i.e.*, $C_I = 5$ to $152.5 N.m$, see Table VI-12) while between $x_{C_I} = 0$ and -1, the effect is almost inexistant. These results are consistent with the analysis presented in §VI.1 showing that efficiency as a function of tension ratio quickly reached a plateau for low ratios (*i.e.*, high torques and/or low-tension settings). The effect of the rear cog radius R_{II} is positive (*i.e.*, higher radii associated with higher efficiencies) and almost linear. For the chainring radius R_I, the mean efficiencies are identical for all values of x_{R_I}. This indicates an absence of correlation with the drive efficiency which is consistent with the Fisher-Snedecor test showing that this factor is negligible. Finally, the chain pitch p plot shows that higher pitches reduce drive efficiency. The quadratic effect is also significant. Therefore, most of the influence attributed to this factor in Figure VI-29 occurs between $x_p = 1$ and 0 (*i.e.*, $p = 5/8$ to $1/2''$). Much less influence is visible for further reduction of the chain pitch.

b) Analysis of interactions

Interaction plots help to interpret the sign of the effects E_{ij}. These plots characterise the reciprocal actions between two parameters. They show the mean response of a parameter discriminated by the value of the second one. To study, for instance, the interaction between $slack$ and C_I, the effect of $slack$ is plotted for $x_{C_I} = -1$ or 1 (each point therefore results from the mean value of 27 trials). The comparison of the two slopes obtained gives information on the interaction effect. Plots for the three most significant interactions (in terms of $\overline{SS}$) are presented in Figure VI-30.
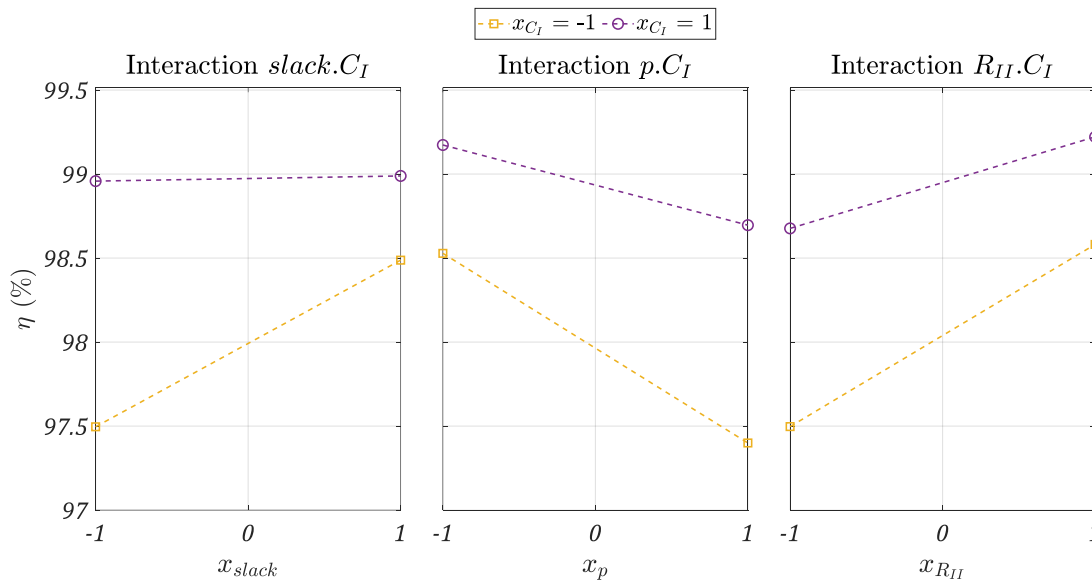
Figure VI-30: Examples of interaction plots

The interaction between $slack$ and C_I is described first. For $x_{C_I} = -1$, the effect of $slack$ is considerable as indicated by the slope. On average, 1% of efficiency is saved between $x_{slack} = -1$ and 1 (with $x_{C_I} = -1$). However, for high torques (*i.e.*, $x_{C_I} = 1$), the effect greatly reduces as indicated by the almost constant line. This indicates that interaction $slack.C_I$ tends to reduce the influence of tension setting $slack$ for high chainring torques C_I. The interaction can also be interpreted the other way round, *i.e.*, the influence of the chainring torque is reduced for loose tension settings. Therefore, the negative effect $E_{slack.C_I}$ indicates a reduction of both effects with a high product of both coded values x_{slack} and x_{C_I}. This strong interaction is still consistent with §VI.1 and the efficiency plateau for low tension ratios. For the interaction $C_I.p$ between the chainring torque and the chain pitch, the slope variation between $x_{C_I} = -1$ and 1 is less significant. However, it indicates that the increase of efficiency for a smaller chain pitch is less significant for high torques than for smaller ones. The same conclusion can be drawn for the interaction between R_{II} and C_I. Indeed, the slope characterising the effect of R_{II} diminishes for $x_{C_I} = 1$ compared to $x_{C_I} = -1$. Overall, the three interactions studied show that all the effects, no matter their sign, are reduced for high chainring torque. Among the six factors, the number of rear cog teeth R_{II} best preserves its effect at high torques C_I. Conversely, high torques almost completely cancels the effect of the tension setting $slack$.

Finally, it can be noted that the values calculated for $x_{C_I} = 1$ are systematically higher than those for $x_{C_I} = -1$. This once again shows that high torques favour better efficiency and that this factor is preponderant.

c) Conclusions and guidelines for efficiency optimisation

The Design Of Experiments (DOE) tool was used to analyse the effects of all the factors of chain drive efficiency considered. Six factors were studied: the global friction coefficient $\bar{\mu}$, the tension setting $slack$, the chainring torque C_I, the chainring and rear cog pitch radii R_I and R_{II}, and the chain pitch p. Each factor had three levels to characterise the non-linear effects. A 3^{6-1} fractional design was used to limit the computational cost of the analysis. This choice was made to ensure that the 28 actions with order ≤ 2 of interest were mixed up (*i.e.*, aliased) with actions of strictly superior order.

An analysis of the variance (ANOVA, [99], [100]) attributed to each factor has been carried out. Comparison with the residual variance through a Fisher-Snedecor resulted in considering only 19 actions accounting for about 93% of the total sum of squares. The effect of the chainring pitch radius was shown to be negligeable. The predictions of a polynomial model based on the 19 influential actions were compared to those of the Chain Drive Efficiency Model (CDEM). The ability of the DEO-based polynomial model to preserve efficiency rankings between drive configurations was demonstrated. However, the absolute predictions of the polynomial model are not accurate enough to represent an alternative to the CDEM.

The analysis of the effects was then carried out. The analysis confirmed the conclusions of the previous parts. Higher chainring torque, tension setting and rear cog pitch radius favour better drive efficiency. On the other hand, friction coefficient and chain pitch show the opposite effect (*i.e.*, higher values result in lower efficiency). Analysis of the quadratic effects showed that the influence of chainring torque and chain pitch are highly non-linear. Finally, the interactions between factors were explored. The results showed that high chainring torque values tend to reduce the effect of all the other factors, particularly the tension setting $slack$. The interest of the DOE analysis lies in ranking the effects by significance.

The following conclusions are drawn for each factor by descending order of the sum of squares proportion.

1. Chainring torque C_I: This factor is the most influential parameter for chain drive efficiency. However, its effect is highly non-linear which causes its influence to be concentrated on low torques.
2. Rear cog pitch radius R_{II}: The quadratic effect of R_{II} as well as its interaction with C_I are moderate. Therefore, its influence is mainly preserved for any radius and regardless of the torque applied.
3. Chain pitch p: The quadratic effect of p is significant. Therefore, the potential gain of changing a $1/2''$ chain for a $3/8''$ one is less significant than suggested by the high proportional variance of factor p.
4. Global friction coefficient $\bar{\mu}$: Lower values obviously result in better efficiency. Neither quadratic effect nor interaction with other factors are highly significant. This indicates that the potential gains resulting from smaller friction coefficients are mainly independent from any other parameters.
5. Tension setting $slack$: Its influence is non-linear and highly corelated with the chainring torque C_I consistently with §VI.1.
6. Chainring pitch radius R_I: Its effect was shown to be negligeable by the Fisher-Snedecor analysis. Indeed, §VI.2.1 shows that the chainring size is less influential than the rear cog one (due to the higher number of chainring teeth for track cycling applications) and that it depends on the torque applied. The appearance of back-and-forth roller motion for some trials might also have influenced this conclusion.

Based on this analysis, the following guidelines for optimising track cycling drives can be drawn up. When possible, depending on the athlete's physical qualities, power generation through torque instead of rotational speed should be favoured. This can be achieved by increasing the gear ratio Z_I/Z_{II}. The rear cog radius should be increased as much as possible. The chainring radius can also be increased to ensure a similar gear ratio without detrimental repercussions. However, the potential consequences of using bigger sprockets on other bicycle losses such as aerodynamic drag should be investigated to ensure that the overall benefit for the whole bicycle-athlete system is positive. The chain pitch p should also be reduced as smaller pin, bush and roller dimensions result in better efficiency due to the limited sliding distances. However, such modification can be costly as it requires new compatible chains and sprockets. Increasing sprocket size and reducing chain pitch would probably increase the mass of the chain drive. For endurance races where the speed is mainly constant, this effect should be negligible. However, for shorter races such as sprints and team sprints, optimisation between drive mass and efficiency should be considered. It is also worth noticing that the minimum bike weight of 6.8 kg imposed by UCI [101] is often reached by adding ballast. In such context, larger drives could be used without adversely affecting the overall weight of the bike. Finally, studies on lubrication and surface treatment should not be neglected although the effect is less significant than the other factors. Indeed, the limited interaction with other parameters ensures that all the gains made through lower friction coefficients would not influence the other drive parameters. Moreover, from the athlete's point of view, changing this parameter is mostly transparent. No major optimisation possibilities appear for the tension setting $slack$. Indeed, its effect is not dominant and the current settings are already situated on the efficiency plateau, therefore limiting any potential gain.

VI.4   Conclusion

This chapter was dedicated to the study of roller chain drive efficiency. The influence of numerous factors was tested, from the torque applied by the athlete on the chainring to the number of teeth and chain pitch. Roller motions were considered and differences between tooth profile geometries studied. First, the efficiency of a regular 60|15 track cycling drive was characterised. To do so, the influence of the chainring torque C_I and tension setting $slack$ was detailed for several tooth profile geometries. The results showed that the influence of C_I and $slack$ were similar for all the profiles tested. Efficiency increases and the interval $[\eta_B, \eta_A]$ decreases with increasing chainring torque. Above about $C_I = 100 N.m$, efficiency reaches a plateau where it remains constant for higher torques. The same behaviour was observed for the influence of the tension setting $slack$. Efficiency rises with the $slack$ setting (*i.e.*, for looser tension setting) and a plateau of efficiency is reached at about $slack = 7.5\%$. The influences of both factors were then studied considering a third one: the tension ratio. A more general curve of efficiency depending on tension ratio was built. This curve is punctuated by changes of torques and/or tension setting. Efficiency increases for lower ratios and reaches a plateau at about $T_{s,I}/T_t = 2e^{-2}$. Mechanisms explaining the increased efficiency with lower ratios were then detailed. It was shown that roller losses decrease for lower ratios. Moreover, the influence of slack strand meshing losses also decreases as the slack tension becomes negligible compared to the tight one. Therefore, for typical track cycling drives with low tension ratios T_s/T_t, tight strand meshing losses are largely preponderant. Differences between profiles were shown to be minor. However, it seems that profiles with smaller tooth bottom radii exhibit slightly better efficiencies. As the trends observed were similar for all tooth profiles, the rest of the chapter focused only on NF_{min} geometry.

The analysis was then extended to drive configurations other than the 60|15 one. Influences of parameters related to the architecture of the drive were explored. The effect of the number of sprocket teeth was detailed considering the pitch radius limitations imposed by track bikes. It was shown that the influence of the number of chainring teeth depends on the torque applied. Its effect on efficiency is detrimental for low torque while it is positive for high ones. However, for any torque value, the effect of the number of rear cog teeth is dominant compared to the chainring one and results in higher efficiencies for higher Z_{II}. This effect is attributed to the reduction of the pitch angle α_j resulting in less meshing losses. Overall, for a constant gear ratio Z_I/Z_{II}, increasing the number of sprocket teeth results in higher efficiency regardless of the torque applied. The effect of chain pitch was then explored. The idea of changing the chain pitch was tested to assess the influence of further pitch angle reduction while limiting sprocket size. The effect of modified chain dimensions (*e.g.*, pin, bush and roller diameters) inherent to pitch change was separated from the pitch modification itself. EEU (Everything Else Unchanged) cases were considered where pin, bush and roller dimensions are similar to the reference $1/2''$ one with only the pitch being changed. EEU cases showed similar efficiency to that of the reference $1/2''$ drive. However, Real Chain Dimension (RCD) cases showed that smaller pitches are associated with higher efficiency due to reduced sliding distances. This analysis showed that changing the pitch angle without modification of pitch radius R_j does not influence chain efficiency. Indeed, reduced pitch angles are counterbalanced by more chain articulations for a given amount of time. Then, the effect of the global friction coefficient $\bar{\mu}$ was explored. The potential gains of lower coefficients were quantified. Moreover, contribution of each chain interface was presented. This breakdown showed that the pin/bush interface is responsible for most of the losses. Potential lubricant optimisation should therefore focus on the tribological conditions (*i.e.*, sliding speed, roughness, *etc.*) encountered at this interface.

Finally, an analysis the Chain Drive Efficiency Model (CDEM) using a Design Of Experiments (DOE) was presented. All the parameters explored in the chapter were considered: chainring torque, tension setting, sprocket sizes, chain pitch and friction coefficient. This analysis aimed at facilitating the

comparison of each factor's influence in order to identify the most influential optimisation possibilities. This tool also allowed exploring interactions between factors. A fractional factorial design was used to limit the computation cost of the analysis. A Fisher-Snedecor test [99], [100] was conducted to identify 19 actions responsible for about 93% of the sum of squares. The results showed that the chainring torque C_I is the main factor influencing drive efficiency, followed by the rear cog radius R_{II} and the chain pitch p. The effect of the chainring radius R_I was negligible. Based on these assessments, guidelines for optimisation of chain drive efficiency were given. However, in the context of high-level track cycling, future studies should consider the implication of any change to the chain drive on the global athlete-bicycle system. Indeed, care must be taken that potential side effects do not cancel the gains obtained from better drive efficiency (*e.g.*, weight increase, modification of aerodynamic properties, *etc*.).

General conclusion

The main objective of this study was to explore roller chain drive efficiency in the context of track cycling. It was also proposed to consider the influence of losses caused by the motion of rollers along their corresponding tooth profile. To achieve this, an efficiency model was developed, based on previous works, in two mains steps. First, a Quasi-Static Chain Drive Model (QSCDM) is proposed to calculate roller locations as well as the evolution of loads (*i.e.*, link tensions and roller/profile contact forces). Then, based on these results, a Chain Drive Efficiency Model (CDEM) is introduced to calculate drive efficiency.

The Quasi-Static Chain Drive Model (QSCDM) was first introduced. This model is based on previous studies and reuses modelling components from the literature. It assumed that the chain operates in a single plane (2D). All dynamical effects are neglected and chain parts are assumed to be rigid (*i.e.*, part deformations are neglected). The drive kinematics is determined using two dedicated sub-models for the tight and slack strands. Kinematics is assumed to be independent of the external loading conditions (*e.g.*, applied torque) and also of the driving and driven sprockets tooth profile geometries. Loads and roller locations are calculated using a local sprocket sub-model. This sub-model uses the kinematic results and can be used with different tooth profile geometries. The effect of friction is modelled using a correction angle δ which introduces differences between driving and driven sprockets. Compatibility issues between the different sub-models (*e.g.*, strand and local sprocket sub-models) as well as challenges raised by the numerical resolution were addressed. The QSCDM was built considering the track cycling context, thereby justifying, for instance, the quasi-static approach (light chains and moderate rotational speeds). However, it can be used for industrial chain drives whose characteristics meet the model hypotheses.

Elements of validation of the QSCDM were then presented. Model predictions were tested using both numerical results and experimental measurements from the literature. Comparisons with numerical results from Kim & Johnson [52] and Troedsson & Vedmar [67] supported the hypotheses stated for the QSCDM. Indeed, the simpler tension model (compared to Kim & Jonhson) as well as the rigid solids assumption (contrary to Troedsson & Vedmar) did not significantly impact the predictions. Comparisons were carried out for industrial chain drives as similar results relating to track cycling do not yet exist in the literature.

The QSCDM was then used to explore the influence of tooth profile geometry on drive behaviour (*i.e.*, loads and roller location evolution). Industrial and track cycling drives were considered. For industrial drives, significant differences were reported between geometries extracted from ASA [32] and ISO [31] standards. Based on the industrial results, methods for analysing the influence of tooth profile were proposed. The pressure angle at the transition point ϕ_{tp} was introduced as a key factor to asses tooth profile influence. Tooth profiles with a low ϕ_{tp} were associated with high load carrying capacity resulting in strong decrease of link tension and roller/profile contact force. Three main sprocket behaviours, inspired by the sub-models proposed by Lodge & Burgess [70], were introduced: inter-tp, static roller and tooth climbing. These behaviours allow easier analysis of roller location evolution depending on the loading conditions applied. The tools developed were then applied to track cycling chain drives, characterised by low slack over tight tension ratio T_s/T_t. It was shown that the specific constraints for this application could only be overcome by dedicated tooth profiles. This led to the introduction of original geometries adapted to the cycling context: the *Cycling Profiles.*

Then, the Chain Drive Efficiency Model (CDEM) was introduced. It calculates drive efficiency based on the results supply by the QSCDM. Two extreme kinematic cases A and B were considered to asses roller rotation based on roller location along its associated profile. Consequently, the result of the CDEM is an interval $[\eta_B , \eta_A]$. Validation of the efficiency predictions was also proposed. Results from the literature on industrial drives showed that the losses caused by roller motion might explain lower efficiencies for small external torques. Comparisons with experimental measurements carried out, in the laboratory, using a test rig dedicated to track cycling drives were also presented.

Finally, the CDEM was used to conduct a parametric study of track cycling chain drive efficiency. The influence of tooth profile geometry was shown to be minimal in this context, probably due to the high similarities between profiles. These similarities are explained by the extreme constraints imposed by track cycling applications that all *Cycling Profiles* must cope with. Apart from tooth profile geometry, the influence of tension setting, applied torque, chain pitch, sprocket number of teeth and friction coefficient were explored. An analysis based on the Design Of Experiments (DOE) methodology was also proposed to compare the effect of each parameter. Based on the results, guidelines for optimisation of track cycling chain drives were given.

This research work left several pending questions that point to interesting perspectives. In the short term, the following points could be explored:

- The optimisation guidelines given through the DOE analysis require experimental measurements to verify the predicted gains. Moreover, potential side effects for the efficiency of the global cyclist-bicycle system (outside the scope of this thesis) should be explored before implementing these solutions. For instance, increased sprocket size should improve chain drive efficiency. However, the drive weight could also increase and potential aerodynamic consequences might occur. These effects need to be clarified to ensure that the overall outcome is positive.
- The application of the CDEM model to industrial cases might provide interesting results. Indeed, the lower tension ratios encountered allow the use of tooth profiles with more property variations compared to track cycling. The influence on drive efficiency might therefore be greater for instance between a *Cycling Profile CP* and the ASA profile. Moreover, the question of increasing efficiency is receiving more attention due to the upcoming energetic transition. In this context, the models developed could be interesting tools to introduce efficiency as a selection criterion in industrial context.
- The sprocket sub-model part of the QSCDM can be easily adapted to consider small variations of chain pitch p_{chain} compared to the sprocket one $p_{sprocket}$. This ability could be used to explore the influence of wear (which translates in pin-link pitch elongation) and continue the work initiated by Naji & Marshek [6]. Similarly, the influence of the deviations from nominal dimensions mentioned in §I.3 could be estimated.

Other questions require substantial work and therefore constitute long-term perspectives.

- In specific conditions, back-and-forth roller motions were predicted by the QSCDM with consequences on drive efficiency. It could be interesting to verify the physical existence of this phenomenon by trying to measure such motion experimentally. To do so, drive configurations with significant slack strand tension variations should be studied. Such drives could be characterised by heavy chain, long pitch and small numbers of sprocket teeth.
- Understanding the influence of friction on the evolution of loads (link tensions and roller/profile contact forces) can be improved. In this study it was modelled using a correction

angle δ. However, this approach is based on few experimental measurements. Particularly, it would be interesting to test experimentally if lubricating conditions at the roller/profile interface significantly influence differences between the driving and driven sprockets. In other terms, are μ_δ and μ_{rp} the same parameter?

- Finally, studying the influence of dynamical effects, particularly strand vibrations, on drive efficiency would be very interesting. Especially in the cycling context where the torque applied at the pedals usually undergoes considerable variation within a chainring revolution. This acyclic torque might significantly influence strand vibration with potential consequences on drive efficiency.

Appendix

Appendix A **Tooth profiles definition**

All tooth profiles considered in this manuscript are symmetrical. Therefore, only one half is defined. Then, the second one can be deduced by symmetry with respect to $(O, \vec{y})$ (see Figure A-1).

A.1 Tooth profile definitions

a) *ASA tooth profile definition*

The definition of the ASA tooth profile can be found in [32], [64]. It is given as follows.
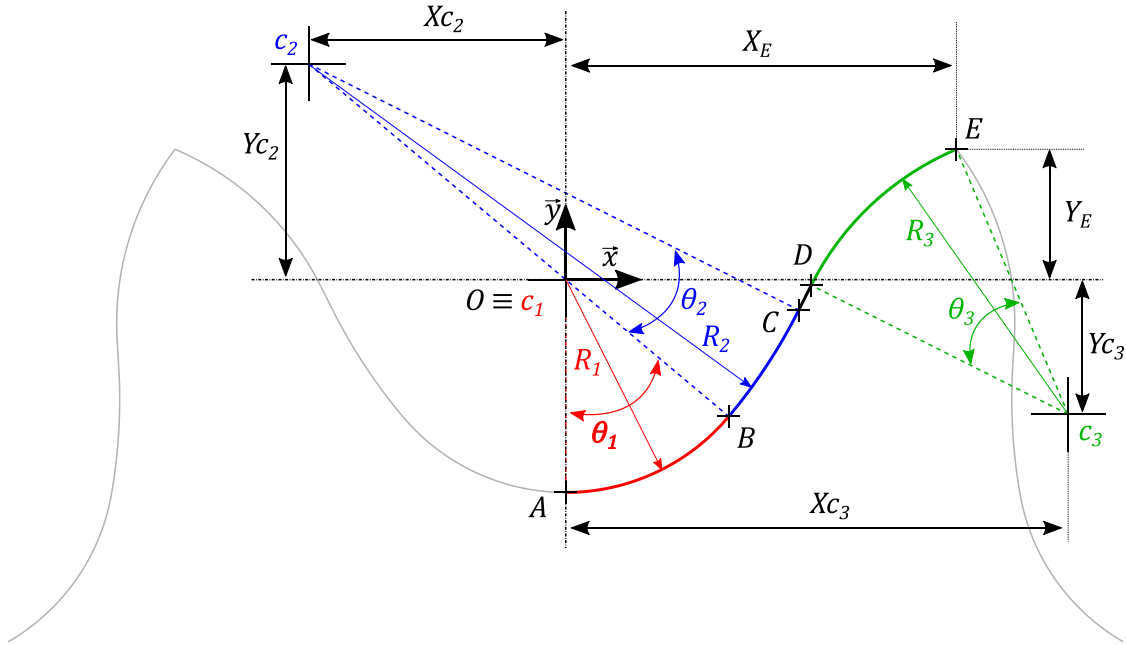
Figure A-1: Definition of the ASA tooth profile [32], [64]

In Figure A-1, the ASA tooth profile is defined using four curve portions:

- Between A and B, the first circle arc defines the tooth bottom. This arc is also called *seating curve*. Its centre coincides with the local origin O and its radius is strictly superior to the roller radius R_{roller}. Its parameters are: centre c_1, radius R_1, central angle θ_1.
- Between B and C, a second circle arc is called the *working curve* (centre c_2, radius R_2, central angle θ_2.)
- Points C and D are linked by a line called the *straight portion*
- Between D and E a last circle arc called the *topping curve* defines the tooth tip (centre c_3, radius R_3, central angle θ_3.)

Curve portion parameters are given as functions of the sprocket pitch p, the number of teeth Z and the diameter of the roller to be used with the profile considered D_{roller}. The pitch angle $\alpha = \frac{2\pi}{Z} = \frac{360°}{Z}$ is also used as an intermediate variable. The radii R_i and central angles θ_i of each circle arc are summarised in Table A-1. Additional parameters needed to fully define the profile are given in Table A-2.

i	R_i	θ_i
1	$0.5025D_{roller} + 0.0015 \times (0.0254)$	$55° - \dfrac{60°}{Z}$
2	$1.3025D_{roller} + 0.0015 \times (0.0254)$	$18° - \dfrac{56°}{Z}$
3	$D_{roller} \times \left(0.8\cos(\theta_2) + 1.24\cos\left(17° - \dfrac{64°}{Z}\right) - 1.3025 \right)$ $- 0.0015 \times (0.0254)$	Function of other parameters (see Table A-2)

Table A-1: Radii R_i and central angles θ_i

H (Intermediate variable)	$\sqrt{R_3^2 - \left(1.24D_{roller} - \dfrac{p}{2}\right)^2}$
X_E	$\dfrac{p}{2}\cos\left(\dfrac{\alpha}{2}\right) + H\sin\left(\dfrac{\alpha}{2}\right)$
Y_E	$-\dfrac{p}{2}\sin\left(\dfrac{\alpha}{2}\right) + H\cos\left(\dfrac{\alpha}{2}\right)$
X_{c_2}	$-0.8D_{roller}\cos(90° - \theta_1)$
Y_{c_2}	$0.8D_{roller}\sin(90° - \theta_1)$
X_{c_3}	$1.24D_{roller}\cos\left(\dfrac{\alpha}{2}\right)$
Y_{c_3}	$-1.24D_{roller}\sin\left(\dfrac{\alpha}{2}\right)$

Table A-2: Other characteristic point coordinates, see Figure A-1

In [32], two main pressure angles values are given for the ASA profile:

- First, the tooth pressure angle for new chain $\phi_{new\ chain}$. This angle is calculated assuming that rollers $i-1$ and i are seated and that the roller/profile contact point (for roller i) lies at point B (see Figure A-1).

$$\phi_{new\ chain} = 35° - \frac{120°}{Z} \qquad \text{(A-1)}$$

- The minimal pressure angle ϕ_{min} is meant to account for rollers climbing the tooth flank. Its value is calculated still assuming rollers $i-1$ and i to be seated. However, this time the contact point is considered to lie at point C (see Figure A-1).

$$\phi_{min} = 17° - \frac{64°}{Z} \qquad \text{(A-2)}$$

These angles can be compared to the expression for ϕ_{tp} obtained using the QSCDM, see Table A-6 below.

b) NF tooth profiles definition

NF tooth profiles are defined by the ISO 606 standard [31] using two tangent circles arcs. These profiles are defined by four parameters (see Figure A-2):

- R_1, θ_1 the radius and central angle of the first circle arc (tooth bottom)
- R_2, the radius of the second circle arc
- R_{tip}, the tip radius

The centre of the first circle arc is the local origin O.

The four parameters are functions of the sprocket pitch p, the number of teeth Z and the diameter of the roller to be used with the profile considered D_{roller}. The pitch diameter $D_p = \frac{p}{\sin(\alpha/2)}$ is also used as intermediate variable.
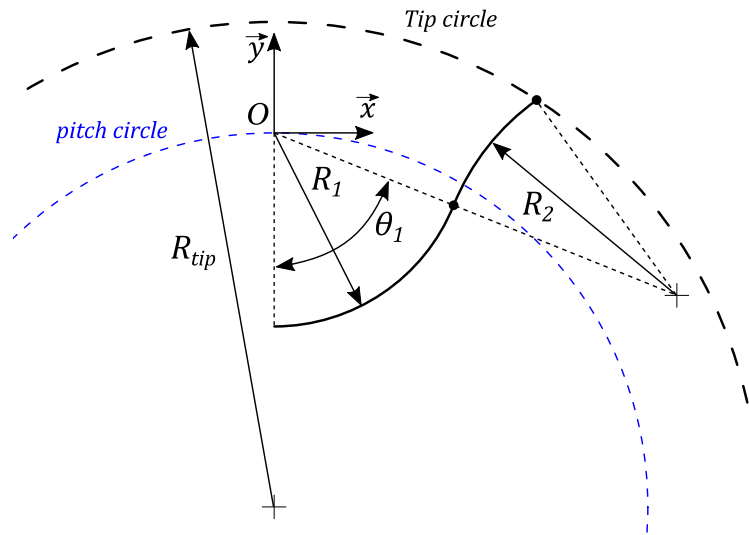
Figure A-2: Definition of tooth profile with two circle sectors

	NF_{min}	NF_{max}
R_1	$0.505 D_{roller}$	$0.505 D_{roller} + 0.069 (D_{roller})^{\frac{1}{3}}$
θ_1	$70° - \dfrac{45°}{Z}$	$60° - \dfrac{45°}{Z}$
R_2	$0.12 D_{roller}(Z+2)$	$0.008 D_{roller}(Z^2 + 180)$
R_{tip}	$\dfrac{1}{2}\left(D_p + 1.25p - D_{roller}\right)$	$\dfrac{1}{2}\left(D_p + p\left(1 - \dfrac{1.6}{Z}\right) - D_{roller}\right)$

Table A-3: Parameters of NF_{max} and NF_{min} tooth profile

Note: For the calculation of R_1 for the NF_{max} profile, D_{roller} must be given in mm.

c) Cycling profiles definition

The cycling profiles are defined similarly to the NF ones (see Figure A-2) according to the parameters given in Table A-4. Compared to the ASA and the NF profiles, the *Cycling Profiles* are only parametrised by the number of teeth Z. Therefore, their definition is only suitable for cycling applications (*i.e.*, $p = 1/2'' = 12.7mm$ and $D_{roller} = 7.75mm$).

	CP_1	CP_2	CP_3
$R_1\ (mm)$	3.9	4.05	4.2
$\theta_1\ (deg)$	$75 - 125/Z$	$75 - 85/Z$	$70 - 45/Z$
$R_2\ (mm)$	$\frac{1}{2}Z + 6$	$Z + 1$	$2Z - 9$
$R_{tip}\ (mm)$		$2.023Z + 3.141$	

Table A-4: Definition of the Cycling Profiles CP

A.2 Profile characteristic parameters

Table A-5 gives the transition point coordinates and inter-tp distance for each tooth profile family. Values are given for $Z = 15$, 30 and 60 teeth, $p = 1/2'' = 12.7mm$ and $D_{roller} = 7.75mm$.
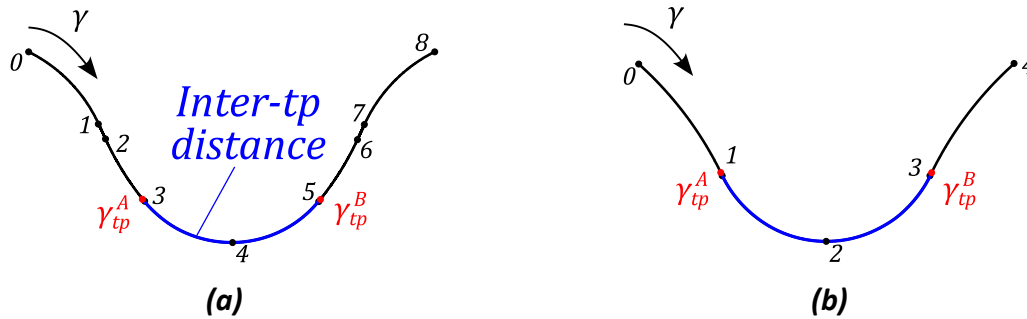
Figure A-3: Inter-tp distance for (a) ASA (b) two-circle tooth profile

	Z	γ_{tp}^A	γ_{tp}^B	Inter-tp distance (mm)
ASA	15	2.9703	5.0297	7.15
	30	2.9755	5.0245	7.42
	60	2.9777	5.0223	7.55
NF_{min}	15	0.9978	3.0022	9.18
	30	0.9977	3.0023	9.39
	60	0.9976	3.0024	9.49
NF_{max}	15	0.9775	3.0225	8.25
	30	0.9787	3.0213	8.47
	60	0.9793	3.0207	8.58
CP_1	15	0.9982	3.018	9.09
	30	0.9984	3.0016	9.66
	60	0.9985	3.0015	9.94
CP_2	15	0.9880	3.0120	9.91
	30	0.9887	3.0113	10.30
	60	0.9891	3.0109	10.50
CP_3	15	0.9752	3.0248	10.05
	30	0.9753	3.0247	10.28
	60	0.9758	3.0242	10.39

Table A-5: Transition point coordinates and inter-tp distances

Table A-6 gives parameters K and K' for all tooth profiles. They are used in eq.(A-3) to calculate the pressure angle at the transition point $\phi_{tp}\big|_B = \phi_{tp}$ (see Chapter IV).

	K (deg)	K' (deg)
ASA	34.64	123
NF_{max}	29.96	137.1
NF_{min}	20	135.5
CP_1	15	55.3
CP_2	15	97.42
CP_3	19.96	139.5

Table A-6: Parameters K and K'

$$\phi_{tp} = K - \frac{K'}{Z}$$
(A-3)

Compared to the expression $\phi_{new\ chain}$ for an ASA profile given in [32] (see eq.(A-1)), the expression given by the QSCDM for ϕ_{tp} is close. The differences are probably due to the different hypotheses stated (roller seated and assumed contact point for $\phi_{new\ chain}$). This indicates that a good approximation of ϕ_{tp} can be obtained only by geometrical mean (with hypotheses similar to $\phi_{new\ chain}$) at the stage of tooth profile conception without any numerical analysis.

A.3 Characteristic curve library

Examples of roller location characteristic curves are given for ASA and NF profiles in Figure A-4 and CP profiles in Figure A-5 for $Z = 15$, 30 and 60 teeth. For s_c and s_r, curves are centred on the curvilinear abscissa of the bottom of the tooth profile s_0 (tooth profile point such tat $y = 0$). For symmetrical profiles (all profiles here), this point corresponds to $\gamma = Nb_{portion}/2$ (*i.e.*, $\gamma = 4$ for ASA and $\gamma = 2$ for the others).
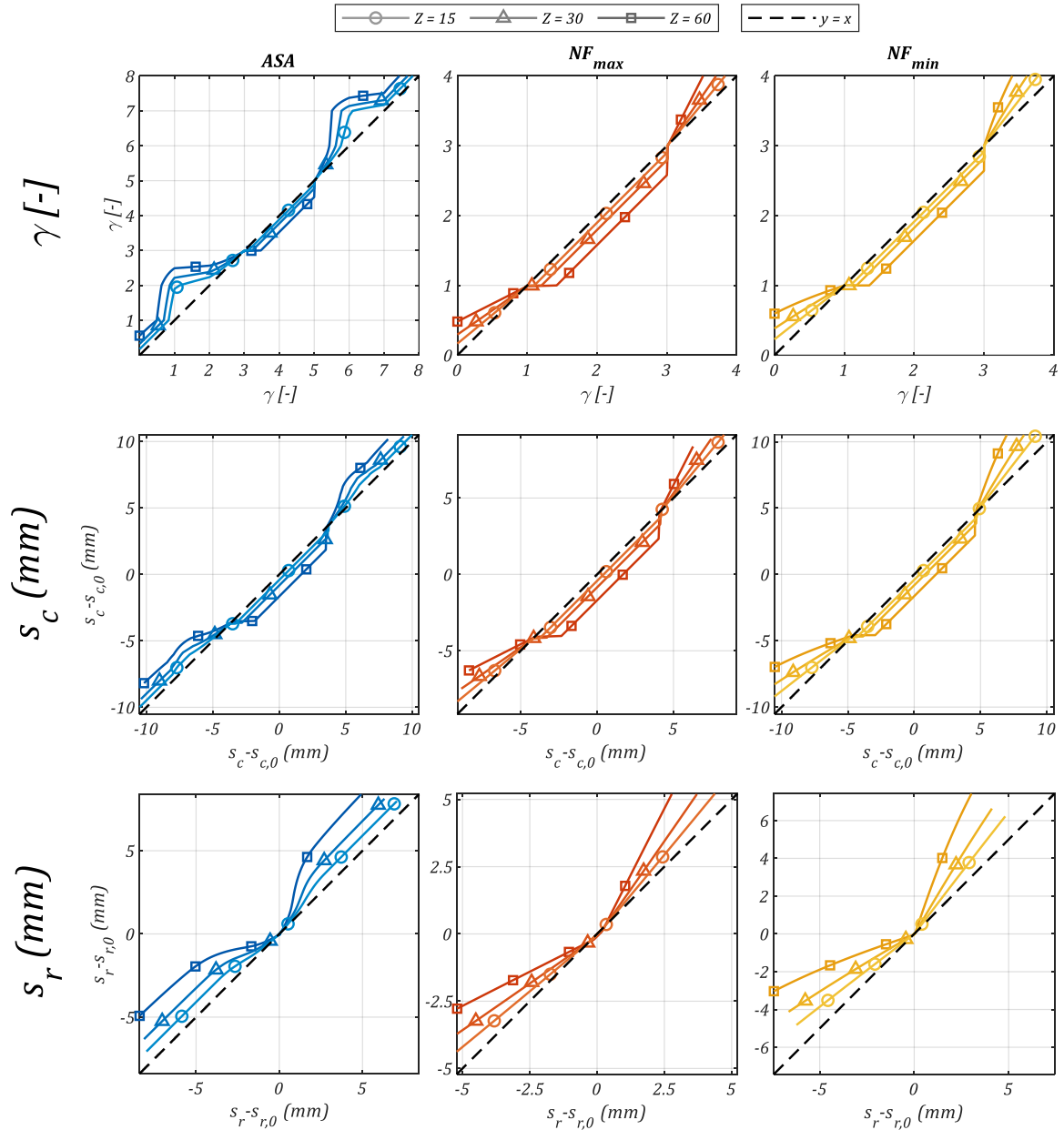
Figure A-4: Roller location characteristic curves for ASA and NF tooth profiles
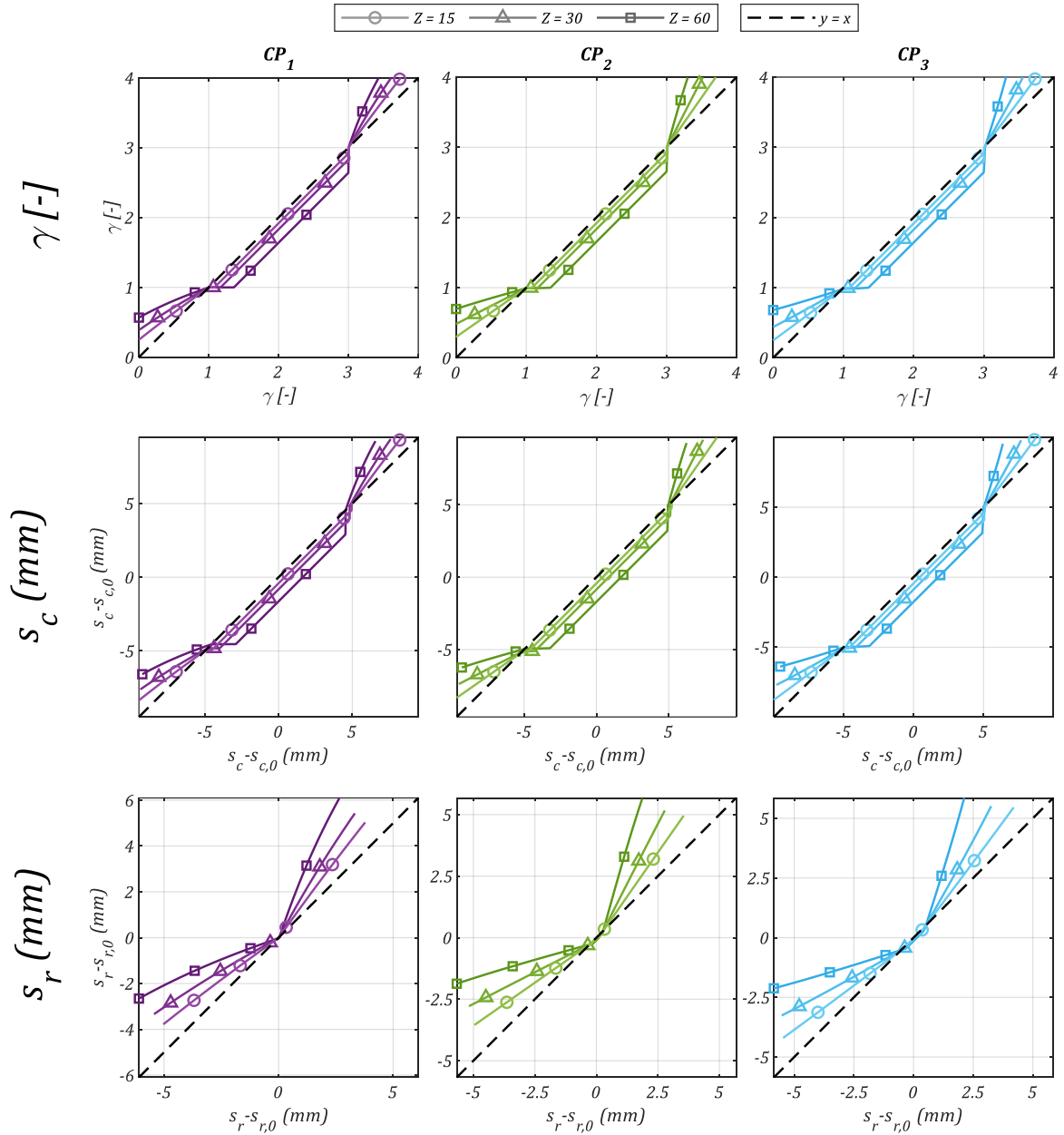
Figure A-5: Roller location characteristic curves for CP tooth profiles

Figure A-6 shows examples of pressure angle characteristic curves for all tooth profiles. Lower pressure angles near the transition point (*i.e.*, near $\gamma = 3$, see Table A-5), reached by the *Cycling Profiles*, compared to ASA and NF_{max}, are visible.
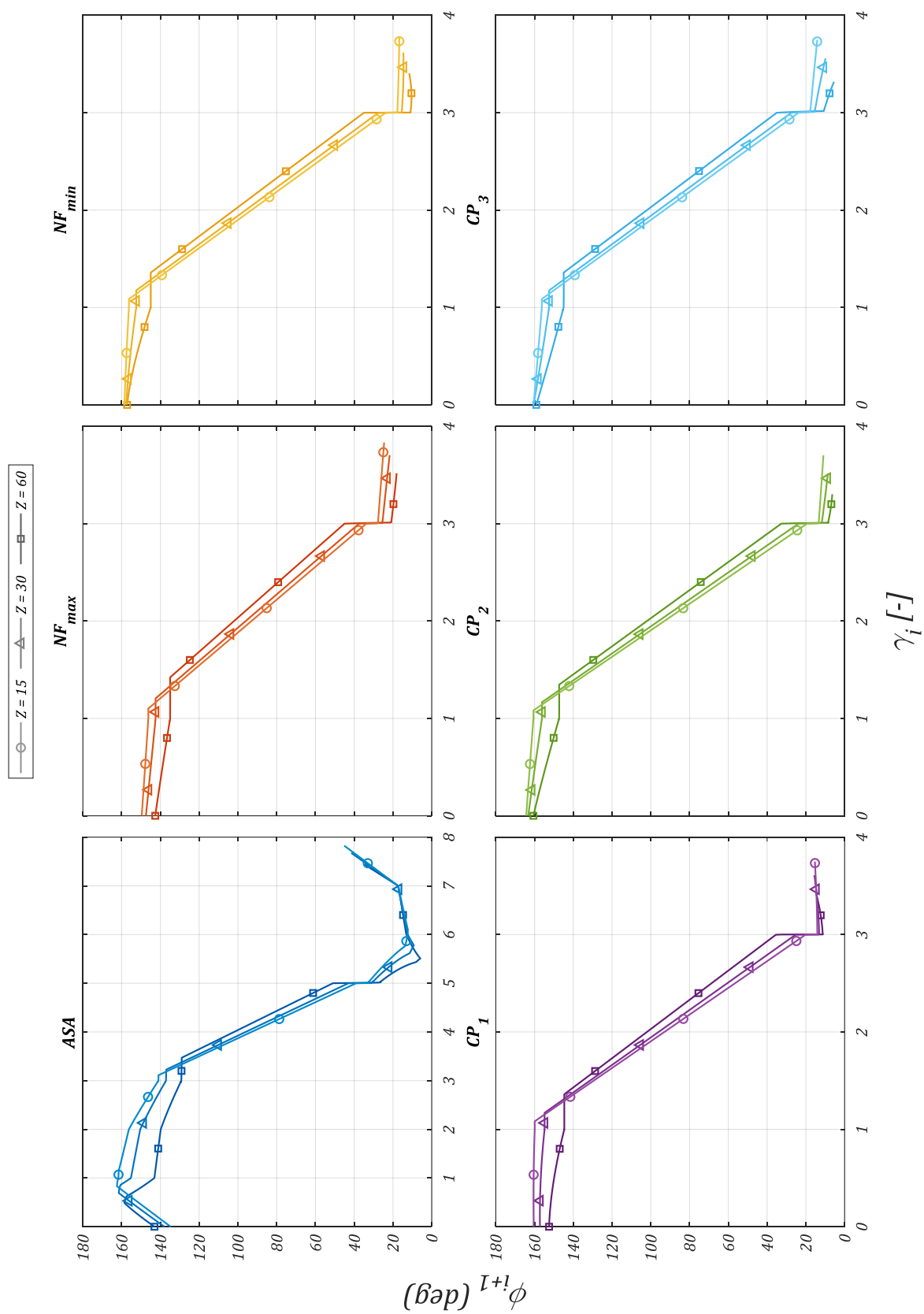
Figure A-6: Roller location characteristic curves for Cycling Profiles (CP)

Appendix B **Calculation of roller centre trajectory**

From the definition of the tooth profile, the roller centre trajectory is calculated from the roller radius. The problem here is to find the parallel to the tooth profile shifted by R_{roller} toward the "inside" of the profile (*i.e.*, toward O_i, see Figure B-2 below). To ease the notations, a quick definition of the curve portions (circle arc or line) is first given in §B.1.

B.1 **Curve portion definition**
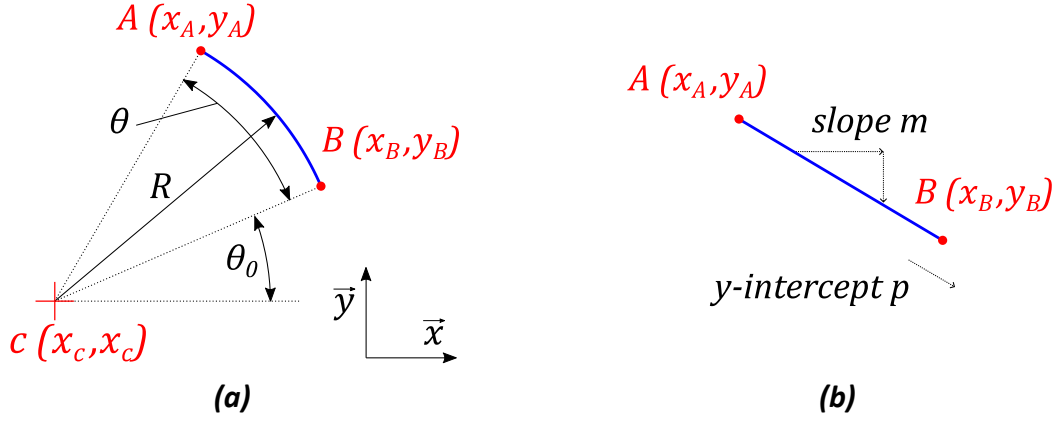
Figure B-1: Definition of (a) circle arc (b) line

In Figure B-1:

- A circle arc (see Figure B-1.a) is defined by its centre c, and the two extreme points A and B. Knowing these three points, additional parameters are calculated (see eqs.(B-1) to (B-3)):
    - The radius R
    - The central angle θ
    - The tilting angle θ_0

$$R = \begin{cases} \sqrt{(x_A - x_c)^2 + (y_A - y_c)^2} \\ \sqrt{(x_B - x_c)^2 + (y_B - y_c)^2} \end{cases} \tag{B-1}$$

$$\theta = \left(\overrightarrow{cB}, \overrightarrow{cA} \right) \tag{B-2}$$

$$\theta_0 = \left(\vec{x}, \overrightarrow{cB} \right) \tag{B-3}$$

- Similarly, a line (see Figure B-1.b) is defined by its two extreme points A and B. From these two points, it is possible to compute the slope m and the y-intercept p.

$$m = \frac{y_B - y_A}{x_B - x_A} \tag{B-4}$$

$$p = \begin{cases} y_A - mx_A \\ y_B - mx_B \end{cases} \tag{B-5}$$

For both circle arcs and lines, point A is the extreme point with the smallest x coordinate (always at the left-hand side according to the coordinate axis given in Figure B-1.a).

In any tooth profile definition, curve portion are continuously connected. Therefore, the B point of the first portion coincides with the A point of the second one (see connection between curve portion 1 and 2 in Figure B-2.a).

B.2   Roller centre trajectory

This part now details the procedure used for the calculation of the roller centre trajectory. Similarly to the tooth profile, the roller centre trajectory is defined using circle arcs and straight lines still according to the definitions given in §B.1.

First, it is assumed that two straight portions cannot be adjacent. Indeed, as the tooth profile must ensure continuous slopes, two adjacent straight portions can be assembled in a single one. Taking advantage of this property, the circle arcs are treated first.

The parallel of each circle arc is defined as another circle arc with the same centre and central angle. The radius is determined as $R_i \pm R_{roller}$. The sign depending on the circle arc being concave or convex (see eqs.(B-6)).

- A concave curve has a decreasing derivative (*e.g.*, Figure B-2.a).
- A convex curve has an increasing derivative (*e.g.*, Figure B-2.b).
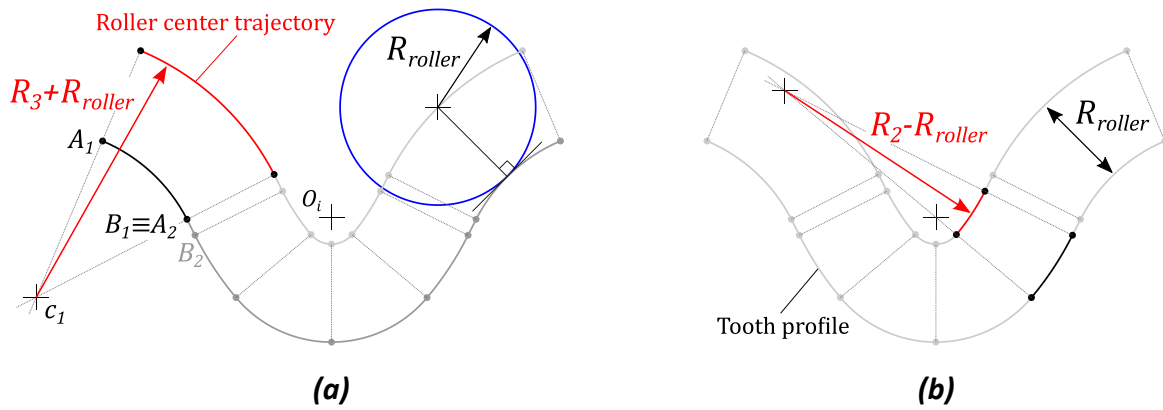
Figure B-2: Roller centre trajectory for (a) concave and (b) convex circle arc

Concave:	$R_i' = R_i + R_{roller}$	(a)
Convex:	$R_i' = R_i - R_{roller}$	(b)

(B-6)

with:

- R_i, the circle arc radius for curve portion i at the tooth profile
- R_i', the circle arc radius for curve portion i at the roller centre trajectory

Points A' and B' for the circle arcs of the roller centre trajectory are determined using R_i' and following directions $\overrightarrow{cA}$ and $\overrightarrow{cB}$, respectively (see Figure B-1.a Figure B-2.a).

Once all the circle arcs have been processed, the lines are re-defined between the extreme points A' and B' (see Figure B-3).
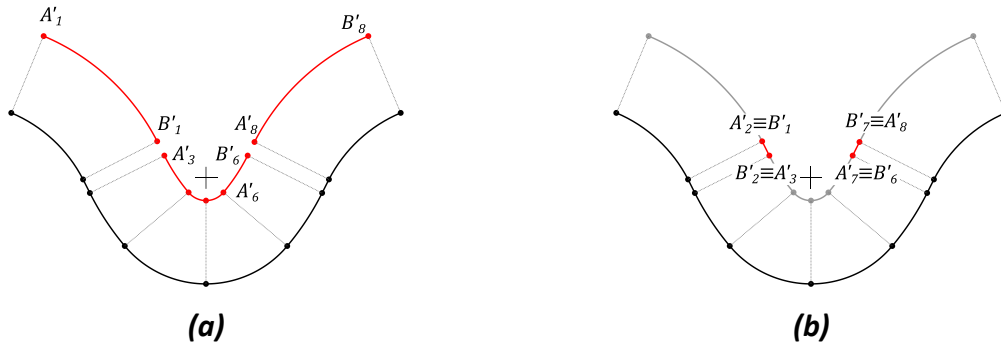
Figure B-3: Calculation of the roller centre trajectory (a) circle arcs (b) lines

The two steps of the procedure are therefore:

1. Create the parallel to each circle arc whose radius is calculated according to eq.(B-6)
2. Create the parallel to each line between the corresponding A' and B' points according to Figure B-3

Appendix C **Conversion between equivalent roller location coordinates**

C.1   Conversion between γ, s_r and s_c

Parameters used to describe circle arcs and lines are given in Appendix B.

In this appendix, the whole and fractional parts of γ are used. They are represented by $\lfloor \gamma \rfloor$ and $\{\gamma\}$, respectively according to eq.(C-1).

$$\gamma = \lfloor \gamma \rfloor + \{\gamma\} \qquad\qquad \textbf{(C-1)}$$

with:

- $\lfloor \gamma \rfloor \in \mathbb{N}$
- $\{\gamma\} \in [0,1[$

Conversion from γ to s_c or γ to s_r follows the same procedure. One just has to consider the parameters of the tooth profile or the roller centre trajectory to obtain s_c and s_r respectively. The same goes for conversions from s_c to γ and s_r to γ. Therefore, conversion procedures are only given from γ to s (without subscript) and from s to γ.

Definition of the roller location coordinates γ, s_c and s_r are given in Figure C-1.a. Curve portions are numbered from 1 to $Nb_{portion}$ with index k. Curve portion i goes from $\gamma = k - 1$ to $\gamma = k$ (see Figure C-1.a). Figure C-1.b shows that γ is proportional to the sweeping angle ρ for circle arc and to x for line.
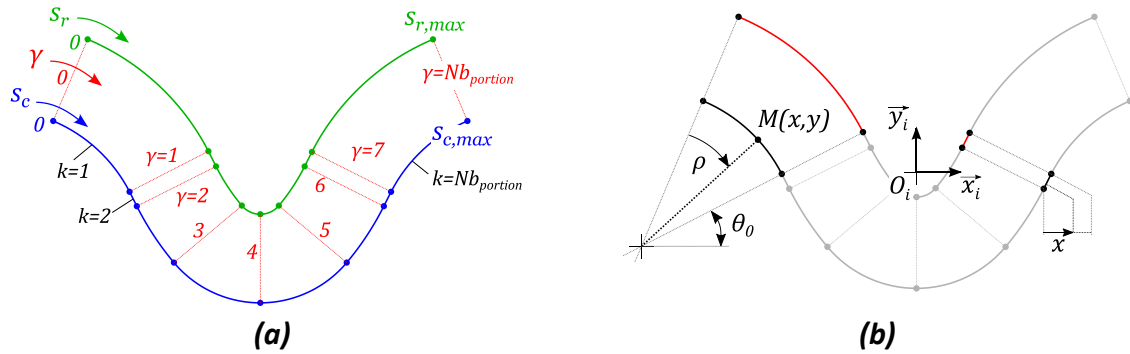
Figure C-1: (a) Roller location coordinates (b) proportionality of γ for circle arc and line

a)   Conversion form γ to s

Starting from a coordinate γ, the equivalent s value is calculated with two steps. First, s_{whole}, the curvilinear abscissa corresponding to $\lfloor \gamma \rfloor$ is calculated following eqs.(C-2) and (C-3).

$$s_{whole} = \sum_{k=1}^{\lfloor \gamma \rfloor} l_{portion}^k \qquad\qquad \textbf{(C-2)}$$

with:

- $l_{portion}^k$, the length of portion k, calculated according to eqs.(C-3).

Circle arc: $$l_{portion}^{k} = R_k \theta_k \tag{a}$$

$$\text{(C-3)}$$

Line: $$l_{portion}^{k} = \left(x_B^k - x_A^k\right)\sqrt{1 + m_k^2} \tag{b}$$

with:

- R_k, θ_k, radius and central angle of curve portion k (in case of circle arc), respectively
- x_B^k, x_A^k and m_k the x-coordinate of points A, B and the line slope for curve portion k (in case of line), respectively

Then, s_{frac}, the length along the curve considered between $\lfloor \gamma \rfloor$ and γ is calculated according to eqs.(C-4).

Circle arc: $$s_{frac} = \{\gamma\} R_{\lfloor \gamma \rfloor + 1} \theta_{\lfloor \gamma \rfloor + 1} \tag{a}$$

$$\text{(C-4)}$$

Line: $$s_{frac} = \{\gamma\} \left(x_B^{\lfloor \gamma \rfloor + 1} - x_A^{\lfloor \gamma \rfloor + 1}\right)\sqrt{1 + m_{\lfloor \gamma \rfloor + 1}^2} \tag{b}$$

Finally, the equivalent s value is calculated according to eq.(C-5).

$$s = s_{whole} + s_{frac} \tag{C-5}$$

b) Conversion from s to γ

First, comparison between s and the curvilinear abscissa of the points of transition between curve portions is carried out until a value of $\lfloor \gamma \rfloor$ fulfilling eq.(C-6) is found.

$$s_A^{\lfloor \gamma \rfloor + 1} \leq s \leq s_B^{\lfloor \gamma \rfloor + 1} \tag{C-6}$$

From $\lfloor \gamma \rfloor$, s_{frac} is calculated following eq.(C-7).

$$s_{frac} = s - s_A^{\lfloor \gamma \rfloor + 1} \tag{C-7}$$

The s_{frac} value obtained is used to calculate $\{\gamma\}$ according to eqs.(C-8)

Circle arc: $$\{\gamma\} = \frac{s_{frac}}{R_{\lfloor \gamma \rfloor + 1} \theta_{\lfloor \gamma \rfloor + 1}} \tag{a}$$

$$\text{(C-8)}$$

Line: $$\{\gamma\} = \frac{s_{frac}}{\left[\left(x_B^{\lfloor \gamma \rfloor + 1} - x_A^{\lfloor \gamma \rfloor + 1}\right)\sqrt{1 + m_{\lfloor \gamma \rfloor + 1}^2}\right]} \tag{b}$$

Finally, γ is obtained from $\lfloor \gamma \rfloor$ and $\{\gamma\}$ according to eq.(C-1).

C.2 Conversion between γ and (x, y)

Roller location can also be given in coordinates (x, y). These coordinates are associated with a local tooth profile coordinate system $(O_i, \vec{x_i}, \vec{y_i})$, see Figure C-1.b.

a) Conversion from γ to $M(x, y)$

Knowing the γ, the equivalent coordinates (x, y) are calculated according to eqs.(C-9) depending on curve portion $\lfloor \gamma \rfloor + 1$ being a circle arc or a line.

$$
\text{Circle arc:} \quad
\begin{cases}
x = x_c^{\lfloor \gamma \rfloor + 1} + R_{\lfloor \gamma \rfloor + 1} \cos\left(\theta(1 - \{\gamma\}) + \theta_0^{\lfloor \gamma \rfloor + 1}\right) \\
y = y_c^{\lfloor \gamma \rfloor + 1} + R_{\lfloor \gamma \rfloor + 1} \sin\left(\theta(1 - \{\gamma\}) + \theta_0^{\lfloor \gamma \rfloor + 1}\right)
\end{cases}
\quad (a)
$$

$$\text{(C-9)}$$

$$
\text{Line:} \quad
\begin{cases}
x = x_A^{\lfloor \gamma \rfloor + 1} + \{\gamma\}\left(x_B^{\lfloor \gamma \rfloor + 1} - x_A^{\lfloor \gamma \rfloor + 1}\right) \\
y = m_{\lfloor \gamma \rfloor + 1} x + p_{\lfloor \gamma \rfloor + 1}
\end{cases}
\quad (b)
$$

with:

- (x_C, y_C), the centre coordinates of circle arc $\lfloor \gamma \rfloor + 1$ (see Figure B-1.a)
- $R_{\lfloor \gamma \rfloor + 1}$, $\theta_{\lfloor \gamma \rfloor + 1}$ and $\theta_0^{\lfloor \gamma \rfloor + 1}$, the radius, central angle and tilting angle of the circle arc $\lfloor \gamma \rfloor + 1$, respectively (see Figure B-1.a and Figure C-1.b)
- $x_B^{\lfloor \gamma \rfloor + 1}$, $x_A^{\lfloor \gamma \rfloor + 1}$, $m_{\lfloor \gamma \rfloor + 1}$ and $p_{\lfloor \gamma \rfloor + 1}$ the x-coordinate of points A and B, the line slope and the y-intercept for curve portion $\lfloor \gamma \rfloor + 1$, respectively

Depending on the curve considered (tooth profile or roller centre trajectory), coordinates (x, y) can specify the location of the roller centre or the roller/profile contact point.

b) Conversion from $M(x, y)$ to γ

Comparisons between x-coordinates of points A and B of each curve portion (see Figure B-) and x are carried out in order to determine $\lfloor \gamma \rfloor$ according to eq.(C-10).

$$x_A^{\lfloor \gamma \rfloor + 1} \leq x \leq x_A^{\lfloor \gamma \rfloor + 1} \qquad \text{(C-10)}$$

Once $\lfloor \gamma \rfloor$ is known, $\{\gamma\}$ is calculated according to eqs.(C-11) (see Figure C-1.b).

$$
\text{Circle arc:} \qquad \{\gamma\} = \frac{\rho}{\theta_{\lfloor \gamma \rfloor + 1}} \qquad (a)
$$

$$\text{(C-11)}$$

$$
\text{Line:} \qquad \{\gamma\} = \frac{x - x_A^{\lfloor \gamma \rfloor + 1}}{x_B^{\lfloor \gamma \rfloor + 1} - x_A^{\lfloor \gamma \rfloor + 1}} \qquad (b)
$$

with:

- $\rho = \left(\overrightarrow{c_{\lfloor \gamma \rfloor + 1} B_{\lfloor \gamma \rfloor + 1}}, \overrightarrow{c_{\lfloor \gamma \rfloor + 1} M}\right)$, see Figure C-

Finally, γ is obtained from $\lfloor \gamma \rfloor$ and $\{\gamma\}$ according to eq.(C-1).

Appendix D **Adjacent roller location**

D.1 **General procedure**

This appendix presents the procedure used to calculate the coordinate γ_{i+1} of roller $i + 1$ knowing γ_i, the coordinate of roller i. The procedure presented is based on the previous works by Naji & Marshek [64] and Kim & Johnson [52]. Notations introduced in Appendix B and Appendix C are used.

As a first step, the roller centre coordinate (x_i, y_i), in the local coordinate system $\vec{x_i}, \vec{y_i}$, are calculated from γ_i following §C.2.

Then, from (x_i, y_i), coordinates (x_i', y_i') of the centre of a hypothetic roller in contact with the adjacent tooth profile with the same γ coordinate are calculated using eq.(D-1). (x_i', y_i') are still expressed in the local coordinate system $\vec{x_i}, \vec{y_i}$ (see Figure D-1.a).

$$\begin{cases} x_i' = x_i \cos(\alpha) - \left(R_p + y_i\right) \sin(\alpha) \\ y_i' = \left(R_p + y_i\right) \cos(\alpha) + x_i \sin(\alpha) - R_p \end{cases} \qquad \textbf{(D-1)}$$

with:

- $\alpha = 2\pi/Z$, the pitch angle of the sprocket considered
- $R_p = \dfrac{p_{sprocket}}{2\sin(\alpha/2)}$, the pitch radius of the sprocket considered

From (x_i', y_i'), the problem reduces to find the intersection between the roller centre trajectory of tooth profile i and a circle of radius p_{chain} centred in (x_i', y_i'). If the tooth profile has been defined following the constraints stated in Chapter II, no more than one intersection can exist (see Figure D-1.b).

<div align="center">

(a)   **(b)**
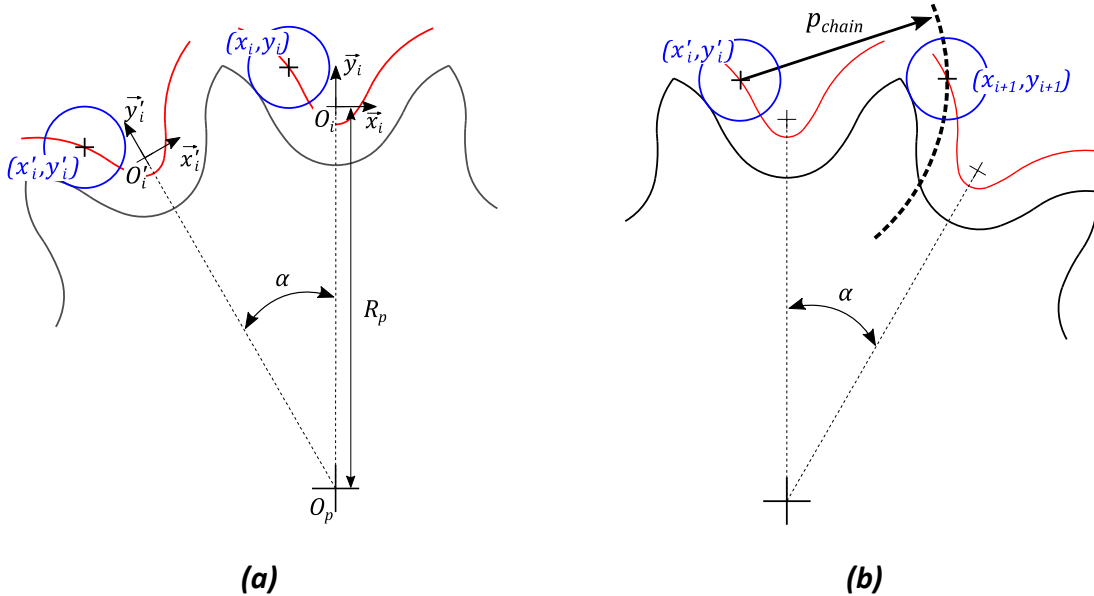
Figure D-1: (a) Calculation of (x_i', y_i') from (x_i, y_i) (b) Calculation of (x_{i+1}, y_{i+1}) from (x_i', y_i')

</div>

To find the intersection, it is necessary to determine on which curve portion the roller $i + 1$ lies (located by x_{i+1} and y_{i+1}. To do so, eq.(D-2) defines distances d between (x_i', y_i') and the points A and B of each curve portion (see Figure B-1).

$$\begin{cases} d_{A,k} = \sqrt{\left(x_A^k - x_i'\right)^2 + \left(y_A^k - y_i'\right)^2} \\ d_{B,k} = \sqrt{\left(x_B^k - x_i'\right)^2 + \left(y_B^k - y_i'\right)^2} \end{cases} \qquad \textbf{(D-2)}$$

The index k of the curve portion of interest must fulfil eq.(D-3).

$$\left(d_{A,k} - p_{chain}\right)\left(d_{B,k} - p_{chain}\right) \le 0 \qquad \textbf{(D-3)}$$

Then, depending on portion k being a circle arc or a line, the coordinates (x_{i+1}, y_{i+1}) of the adjacent roller can be found analytically. Solution for circle/circle and circle/line intersections are given in §D.2 or §D.3, respectively.

Finally, coordinates (x_{i+1}, y_{i+1}) are converted into equivalent roller location γ_{i+1} still following §C.2.

The procedure can therefore be summarised as follows:

1. Calculate (x_i, y_i) from γ_i.
2. Calculate the equivalent coordinate (x_i', y_i') of an hypothetic roller with the same coordinate γ in contact with the adjacent tooth profile.
3. Solve analytically the intersection between the roller centre trajectory and the circle of centre (x_i', y_i') and radius p_{chain}. The solution gives (x_{i+1}, y_{i+1}).
4. Calculate γ_{i+1} from (x_{i+1}, y_{i+1}).

Finally, it can be noted that the procedure can be inversed to determine the coordinates of the preceding roller (*i.e.*, γ_{i-1} from γ_i).

D.2 Intersection between two circles

The procedure detailed here is based on [102].

The problem outline is to analytically find the coordinates of the intersection points between two given circles. In the general case, two circles can have either two, one or no intersection points. However, as the circle arc considered fulfils eq.(D-3), the case of interest is the first one (two intersection points).

The problem of finding the intersection points of two circles (denoted 1 and 2) can be expressed by the following equation system for x and y given in eqs.(D-4).

$$\begin{cases} (x - X_1)^2 + (y - Y_1)^2 = R_1{}^2 \\ (x - X_2)^2 + (y - Y_2)^2 = R_2{}^2 \end{cases} \tag{D-4}$$

with:

- X_1 and Y_1, the coordinates of the first circle centre
- R_1, the radius of the first circle
- X_2 and Y_2, the coordinates of the second circle centre
- R_2, the radius of the second circle

The system can be written equivalently in a coordinate system with (X_1, Y_1) as origin, see eqs.(D-5).

$$\begin{cases} x^2 + y^2 = R_1{}^2 \\ (x - X_2')^2 + (y - Y_2')^2 = R_2{}^2 \end{cases} \tag{D-5}$$

Eqs.(D-5) is equivalent to eqs.(D-6).

$$\begin{cases} x^2 + y^2 = R_1{}^2 & (a) \\ ax + by = c & (b) \end{cases} \tag{D-6}$$

with:

- $a = 2.X_2'$
- $b = 2.Y_2'$
- $c = R_1{}^2 + X_2'^2 + Y_2'^2 + R_2{}^2$
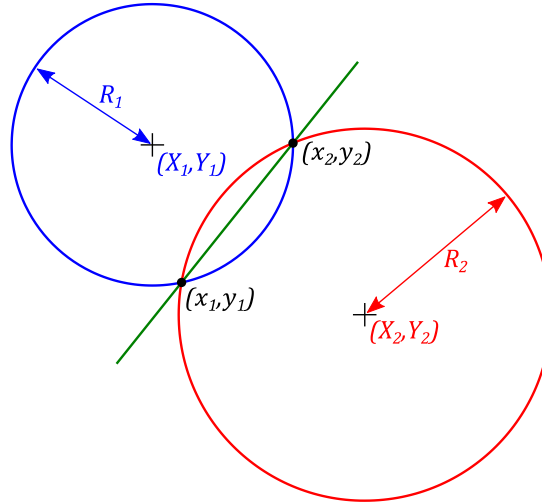
Figure D-2: Intersection points of two circles

Eq.(D-6.b) is characteristic of the straight-line connecting the two intersection points (x_1, y_1) and (x_2, y_2), see Figure D-2.

Substituting y^2 according to eq.(D-6.a) into the square of eq.(D-6.b) leads to a new quadratic equation for x, see eq.(D-7).

$$x^2(a^2 + b^2) + x(-2ac) + (c^2 - b^2 R_1{}^2) = 0 \qquad \text{(D-7)}$$

The discriminant for eq.(D-7) is given by eq.(D-8).

$$\Delta = (-2ac)^2 - 4(a^2 + b^2)(c^2 - b^2 R_1{}^2) \qquad \text{(D-8)}$$

Δ in eq.(D-8) is always positive as it is assumed that there are two distinct intersection points. The x-coordinate for both intersection points are then given by eq.(D-9).

$$x_{1,2} = \frac{2ac \pm \sqrt{\Delta}}{2(a^2 + b^2)} \qquad \text{(D-9)}$$

The corresponding y-coordinates are given, using eq.(D-6.b), in eq.(D-10).

$$y_{1,2} = \frac{c - ax_{1,2}}{b} \qquad \text{(D-10)}$$

Thus, the solving procedure for the problem of circle intersection is as follows:

1. Write the equation system in the coordinate system with (X_1, Y_1) as origin
2. Solve the problem using eqs.(D-6) to (D-10)
3. Move back the solution $(x_{1,2}, y_{1,2})$ into the original coordinate system

Finally, among the two intersection points, only one is of interest for the problem of consecutive roller location. Therefore, a final test to determine which point lies in the considered circle arc must be carried out.

D.3 Intersection between a circle and a line

As for the problem with two circles, the intersection between a straight line and a circle can either take place at zero, one or two distinct points. Similarly, considering eq.(D-3) only the two-intersection point case is considered.
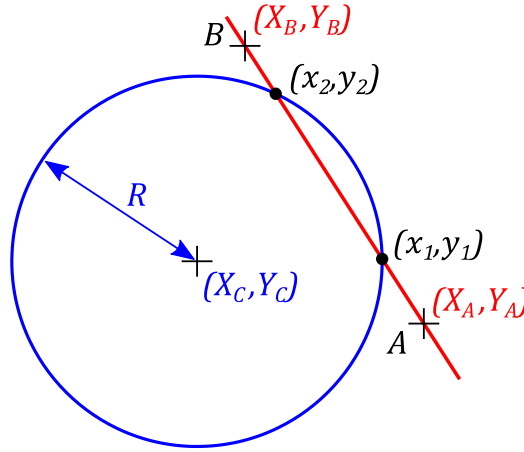
Figure D-3: Intersection points between a circle and a line

Knowing A and B, two distinct points on the straight line (see Figure D-3), the intersection problem can be expressed with the equation system for x and y given in eqs.(D-11).

$$\begin{cases} y = mx + p & \text{(a)} \\ (x - X_C)^2 + (y - Y_C)^2 = R^2 & \text{(b)} \end{cases} \quad \text{(D-11)}$$

with:

- $m = \frac{Y_B - Y_A}{X_B - X_A}$ and $p = Y_B - mX_B$, the parameters of the straight-line equation
- X_C and Y_C, the circle centre coordinates
- R, the circle radius

Substituting eq.(D-11.a) into eq.(D-11.b) leads to the quadradic equation for x given in eq.(D-12).

$$ax^2 + bx + c = 0 \quad \text{(D-12)}$$

with:

- $a = 1 + m^2$
- $b = -2X_C + 2mp - 2mY_C$
- $c = X_C{}^2 + p^2 - 2pY_C + Y_C{}^2 - R^2$

The coordinates of the two intersection points are therefore given by eqs.(D-13).

$$\begin{cases} x_{1,2} = \dfrac{-b \pm \sqrt{\Delta}}{2a} & \text{(a)} \\ y_{1,2} = mx_{1,2} + p & \text{(b)} \end{cases} \quad \text{(D-13)}$$

with $\Delta = b^2 - 4ac$, the discriminant of eq.(D-12).

As for the intersection of circles, the solution of practical use is the one lying into the interval of interest.

Appendix E **Calculation of the mid-span movement**

This appendix details the numerical procedure used to calculate the mid-span movement and ultimately the $slack$ parameter (see Chapter II).

It is assumed that the maximal slack strand deflection is obtained when the slack strand trajectory is constrained in such way that it forms two straight parts connected at the link where the hypothetic load is applied (see Figure E-1). Therefore, for each roller of the slack strand, the corresponding two lines trajectory is computed by finding the intersection of two circles Figure E-1):

- Circle of centre E_I and radius $i_{ms}.p$
- Circle of centre E_{II} and radius $(n_s - i_{ms}).p$

with:

- $i_{ms} \in [\![1, n_s - 1]\!]$

Note: Index i_{ms} is different from the spatial index i used for rollers and links numbering.
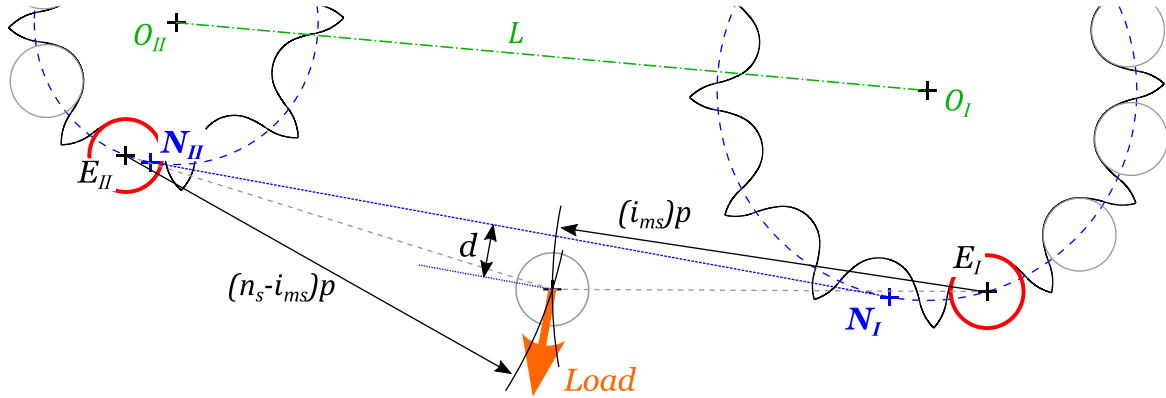
Figure E-1: Calculation of the mid-span movement d

Once the intersection point is found, the distance $d_{i_{ms}}$ to the common tangent is calculated (Figure E-). The process is repeated for all i_{ms}. The mid-span movement for sub-position m is considered to be twice the biggest found deflection $d = \max(d_{i_{ms}})$. This leads to eq.(E-1) giving the expression of the instantaneous $slack_m$ parameter (*i.e.*, for a given drive sub-position m). The final $slack$ is calculated as a mean for ten linearly spaced sub-position as detailed in Chapter II.

$$slack_m = \frac{2d}{L} \qquad\qquad \text{(E-1)}$$

It must be noted that this geometric method does not consider possible collision between the stretched strand and the sprockets. Indeed, for high looseness, a slack strand stretched upward might collide a sprocket. For such case, the theoretical two-line trajectory, assumed for mid-span calculation cannot be reached (see Figure E-2). The theoretical mid-span movement would therefore be higher than what could be measured for a real drive in identical conditions. Moreover, the calculated geometric deflection is the limit theoretically obtained for an infinite force pulling the strand. The deflection observed on a real drive would necessarily be smaller.

However, the theoretical deflection computed geometrically can be compared as an order of magnitude with a deflection observed on real drives (see for instance Chapter V).
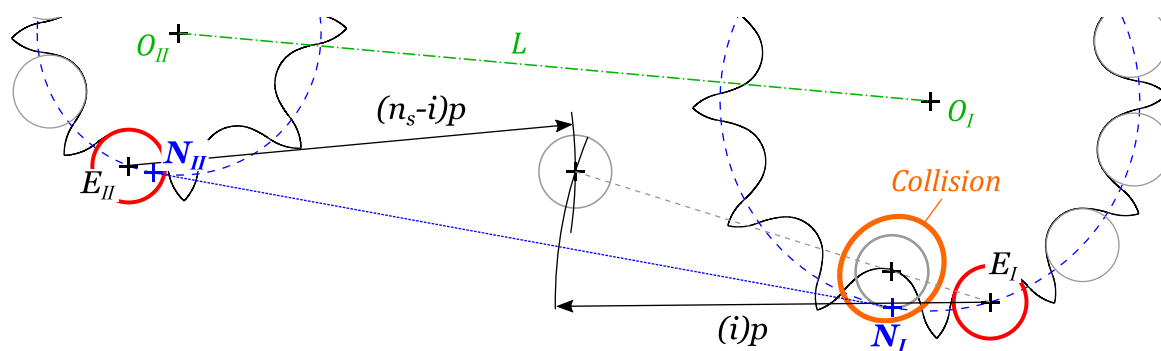
Figure E-2: Possible collision between the stretched slack strand and the sprockets

Appendix F **Choice of a (transition of friction correction parameter)**

The tanh function is introduced in Chapter II to calculate the friction correction angle δ. It allows to continuously join the two extreme values $\pm \operatorname{atan}(\mu_\delta)$. The tanh function depends on the parameter a giving the width of the transition zone. The choice of this parameter changes the relation between δ and $s_{c,1}$ (see eq.(II-28)) therefore influencing the relation between $s_{c,1}$ and the loading conditions (illustration of this relation is given in Figure II-27). a is a numerical parameter, therefore, its value is chosen so that it does not influence the results obtained.

Due to the connection between the global kinematics (which considers all the roller centres on the pitch circles) and the local sprocket sub-model (considering precise roller location along the tooth profile), the slack strand tensions $T_{s,j}$ change discontinuously when a roller is added or removed to the slack strand (see for instance Figure III-18). These discontinuities pass from the slack tension to the tension ratio applied on the sprockets. Combined with the modification of δ, these discontinuities can be amplified resulting in significant jumps in the roller location evolution predicted. Depending on the value of a, the amplitude of these discontinuities varies (see evolution of s_c "per component" in Figure F-1).
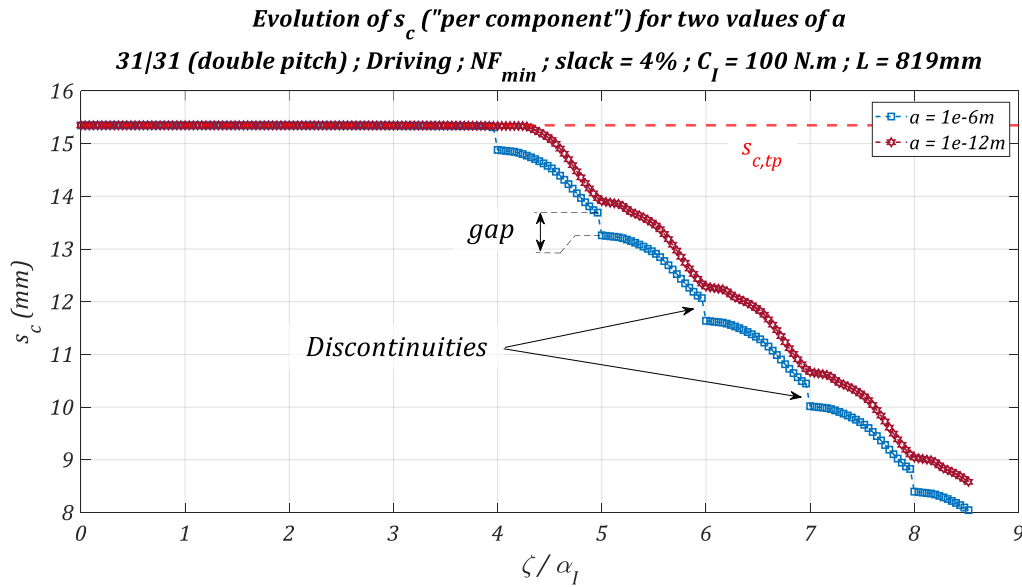
Figure F-1: Examples of discontinuities in s_c evolution for the driving sprocket

The value of a is chosen so that it does not affect the amplitude of the discontinuities. Figure F-2 shows the maximal gap (defined in Figure F-1) on the roller location s_c depending on the torque applied on the driving sprocket for several values of a (from $a = 1e^{-6}m$ to $a = 1e^{-12}m$). Two drives are studied (as in Chapter IV). A 31|31 double pitch industrial drive ($slack = 4\%$) and a 60|15 cycling drive ($slack = 11\%$), both with the profile NF_{min}. All calculations are performed with $|\delta(\infty)| = 5°$.
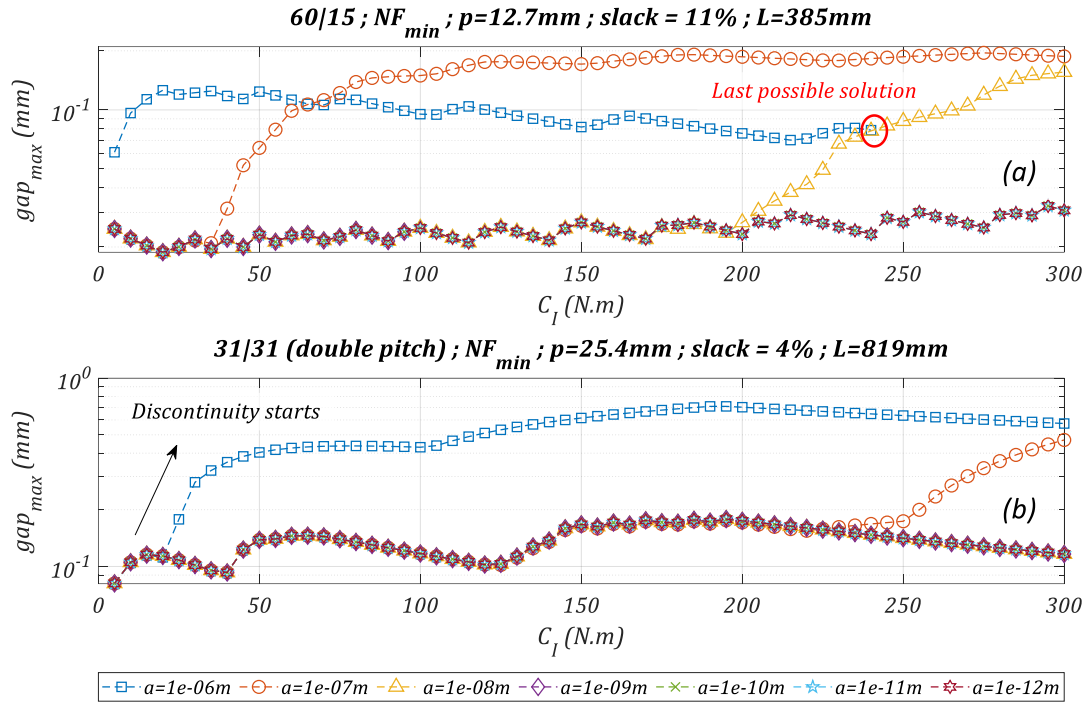
Figure F-2: Evolution of the maximal gap depending on parameter a, (a) cycling (b) industrial drives

For the cycling drive (Figure F-2.a), the $a = 1e^{-6}m$ curve stops at $C_I = 240N.m$ as no solution was found beyond (*i.e.*, the value of a also influences the limit tension ratio). Emergence of discontinuities are characterised by rapid increase of the gap. For both cases, large values of a induce the apparition of discontinuities. For the industrial drive (Figure F-2.b), no effect is reported for value smaller than $1e^{-7}m$ (for the explored torque range), $1e^{-8}$ for the cycling drive.

The influence of the parameter a varies depending on the profile used and the loading conditions. Therefore, to be sure to always lie on the plateau where variable a has no effect, a value of $a = 1e^{-10}m$ is chosen for the entire manuscript (unless otherwise stated).

The influence of a on drive efficiency calculated by the CDEM is detailed in Appendix I

Appendix G **Back-and-forth roller motion**

It was shown in Chapter IV that un-monotonous roller motion called back-and-forth roller motion can appear. This appendix explores the underlying causes behind this specific phenomenon.

The conclusions of Chapter IV, in terms of roller motion, can be summarised as follows. Going from high to low tension ratios, a sprocket goes through three behaviours:

- The inter-tp behaviour where rollers tend to cross the profile from tp^B to tp^A
- The static roller behaviour where rollers are (quasi) immobile at tp^B
- The tooth climbing behaviour where rollers climb the tooth flank beyond tp^B to reach smaller pressure angles ϕ

a) Inter-tp behaviour

Between each sub-position, angles α_s and α_t vary which modifies the relation between T_s/T_t and $s_{c,1}$ (see Chapter II). Moreover, the constant torque condition, imposed in Chapter IV, changes the tension ratio required which also modifies the location of the first roller $s_{c,1}$. In the absence of tension ratio variation, Kim & Johnson show in [52] that the resulting roller motion is monotonous from tp^B to tp^A.

To explore the influence of the varying tension ratio, the constant torque condition is replaced by a constant tensions one. Figure G-1 gives an example for the case presented in Chapter IV with $C_I = 50N.m$ (see Figure IV-7). The tight and strand tensions are set to 830 and $30N$, respectively to closely match the loading conditions. This results in the driving torque C_I varying between 49.40 and $50.50N.m$.
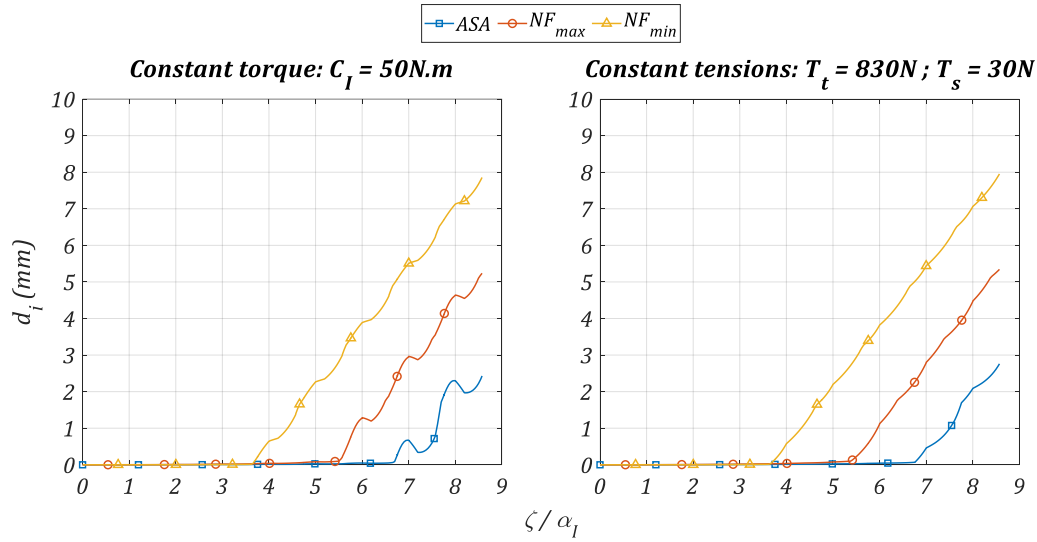
Figure G-1: Comparison between roller motion with constant torque or constant tensions conditions (based on Figure IV-7, $C_I = 50N.m$)

Back-and-forth roller motions disappear for the constant tensions case (consistently with the results of Kim & Johnson in [52]). This shows that the tension ratio variation causes back-and-forth roller motion in the inter-tp behaviour. It is interesting to note that the absolute distance d_i reached is similar for both cases which confirms that the loading conditions are similar.

b) Tooth climbing behaviour

In the tooth climbing behaviour, removing the tension ratio variation using the constant tensions conditions is not sufficient to prevent back-and-forth roller motion. This might be caused by the variation of slopes in curve illustrating the relation between $s_{c,1}$ and T_s/T_t. The slopes usually shallower after the transition points (*i.e.*, for $s_{c,1} > s_{c,tp}$). The most complex slope variation is observed for the ASA profile (see Figure II-29).

Figure G-2 shows a comparison between constant torque and constant tensions for the $C_I = 600N.m$ case (renvoi Figure IV-25). The tight and slack tensions are set to $T_t = 9622N$ and $T_s = 30N$. This results in the driving torque C_I varying between 592.7 and $605.2N.m$. The loading conditions are such that the ASA sprocket is in the tooth climbing behaviour, while the NF_{max} one is in static roller and the NF_{min} is in inter-tp. It is observed that the constant tensions conditions remove back and forth motion for the NF_{min} sprocket (*i.e.*, inter-tp behaviour) but not for the ASA one (tooth climbing behaviour).
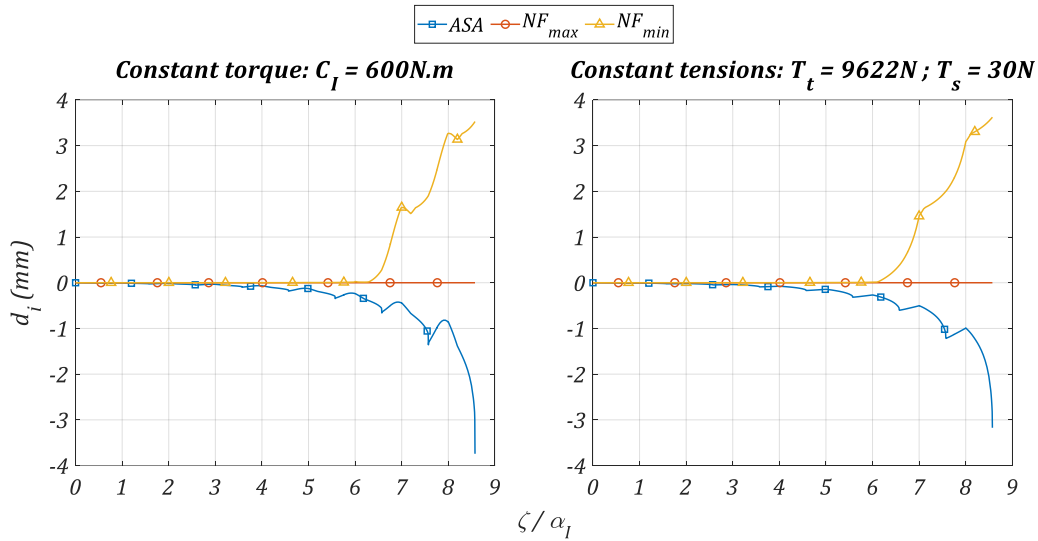
Figure G-2: Comparison between roller motion with constant torque or constant tensions conditions (based on Figure IV-25, $C_I = 600N.m$)

Figure G-3 shows a comparison of constant torque and constant tensions cases based on the $C_I = 600N.m$ configuration. It confirms that link tension T, contact force P and roller motions d and $\bar{d}$ are similar.

31/31 (double pitch) ; Driving sprocket ; C_I =600N.m ; slack = 4%

(a)
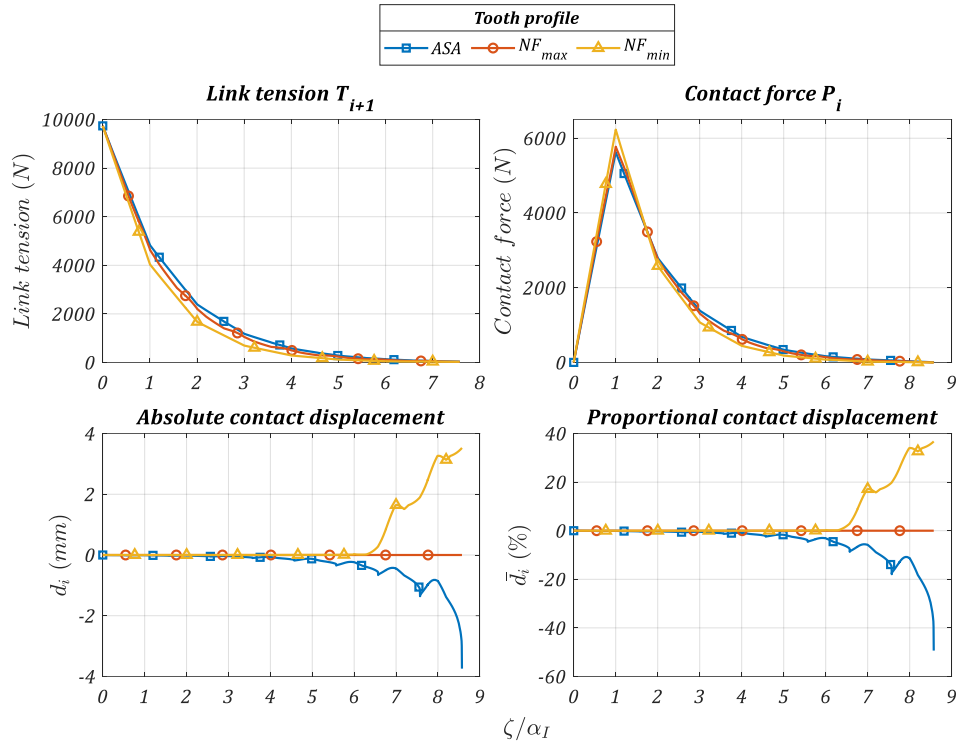
31/31 (double pitch) ; Driving sprocket ; T_s =30N ; T_t =9622N ; slack = 4%
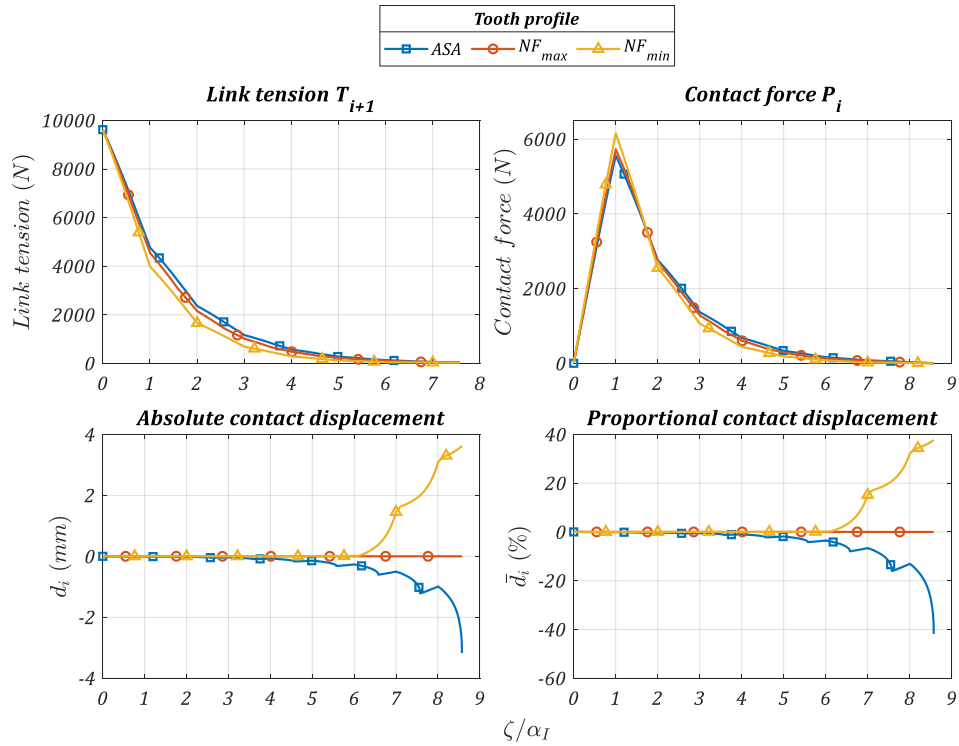
(b)

Figure G-3: Comparison between (a) constant torque and (b) constant tensions cases (based on Figure IV-25, $C_I = 600N.m$)

Appendix H **Calculation of $\Delta\theta$**

The variation of roller orientation $\Delta\theta_k$ between sub-positions k and $k+1$ is calculated from Δs_k (see Chapter V). For case B (*i.e.,* sliding at both bush/roller and roller/profile interfaces), the relation between $\Delta\theta$ and Δs is given by eq.(H-1) (see Chapter V).

$$\text{Case B:} \qquad\qquad \Delta\theta_k = \frac{\Delta s_k}{R_{curve}} \qquad\qquad \textbf{(H-1)}$$

with:

- R_{curve} the profile curvature radius at the roller/profile contact point considered. R_{curve} can be positive or negative depending on whether the profile portion considered is convex or concave, respectively.

However, it is possible that the variation of curvilinear abscissa Δs_k occurs between two curve portions. In the case of one portion being concave ($R_{curve} < 0$) and the second one being convex ($R_{curve} > 0$), the sigh of $\Delta\theta_k$ must be clarified.

This case typically arises for two-circle profiles (*i.e., NF* and CP profiles) where the transition point tp^B lies in the second circle arc (being concave). In the inter-tp regime, roller location goes from tp^B, in the concave circle arc, toward tp^A through the tooth bottom which is a convex circle arc (examples of transition point coordinates are given in Appendix A).

In the following, it is assumed that the roller tracked is in contact with a curve portion denoted 1 at sub-position k before transitioning to a second curve portion 2 for sub-position $k+1$. Therefore, Δs_k can be split in two contributions according to eq.(H-2).

$$\Delta s_k = \Delta s_{k,1} + \Delta s_{k,2} \qquad\qquad \textbf{(H-2)}$$

with:

- $\Delta s_{k,1}$, the variation of curvilinear abscissa in portion 1
- $\Delta s_{k,2}$, the variation of curvilinear abscissa in portion 2

On both curve portions, the variation of curvilinear abscissa results in a variation of roller orientation $\Delta\theta_{k,1}$ and $\Delta\theta_{k,2}$ calculated according to eq.(H-3) (adapted from eq.(H-1)).

$$\Delta\theta_{k,i} = \frac{\Delta s_{k,i}}{R_{curve,i}} \qquad\qquad \textbf{(H-3)}$$

with:

- $\Delta s_{k,i}$, the variation of curvilinear abscissa in portion i
- $R_{curve,i}$, the curvature radius of portion i (infinite for a line portion)

The global variation of roller orientation $\Delta\theta_k$ is calculated as the sum of the absolute value of each contribution. The sign is taken as the sign of the biggest contributor (between $\Delta\theta_{k,1}$ and $\Delta\theta_{k,2}$). The

hypothesis stated is that possible compensation with $\Delta\xi$ and $\Delta\nu$ (see eq.(V-11) and eq.(V-21)) is more likely to happen for the portion with the biggest $\Delta\theta_{k,i}$. This translates into eq.(H-4).

$$\Delta\theta_k = \text{sgn}\left(\sum_{i=1}^{2}\Delta\theta_{k,i}\right)\sum_{i=1}^{2}\left|\Delta\theta_{k,i}\right| \qquad \textbf{(H-4)}$$

with:

- sgn, the sign function such that $\text{sgn}(x) = \begin{cases} -1 & if\ x < 0 \\ 0 & if\ x = 0 \\ 1 & if\ x > 0 \end{cases}$

The influence of this hypothesis on the drive efficiency obtained reduces as the number of sub-positions considered increases which cause the values of Δs_k and $\Delta\theta_k$ to reduce. Its influence is therefore included into the influence of the discretisation explored in Appendix I.

Appendix I **Influence of ζ discretisation, δ, and a on efficiency η**

This appendix explores the influence of various parameters on the efficiency η predict by the Chain Drive Efficiency Model (CDEM, see Chapter V). All calculations are carried out for the classical track cycling drive 60|15. Unless otherwise stated, NF_{min} tooth profile is used for the chainring and the rear cog. The first part (§I.1) proposes a sensibly study of drive efficiency to the chosen numerical discretisation. The two followings (§I.2 and §I.3) explore the influence of $|\delta(\infty)|$ and a on the efficiency results (§I.2 and §I.3, respectively). They show that this manuscript conclusions are largely independent of these parameters.

I.1   **Influence of ζ discretisation on η**

This appendix explores the influence of the discretisation pitch on the results of the CDEM. The number of sub-positions k_{max} considered for efficiency calculation directly depends on the discretisation of ζ within the drive period explored in the QSCDM (see Chapter II). The influence of this discretisation is therefore tested. Calculation parameters are set according to Table I-1. Different looseness settings $slack$ are considered. Similarly to Chapter VI, the centre distance L is set to the smallest value above $380mm$ that satisfies the $slack$ setting considered. The chainring torque is set at $C_I = 5N.m$ which is the case with highest influence of roller losses (see Chapter VI). It was chosen to vary the looseness setting $slack$ as this parameter shows the most noticeable influence of ζ discretisation on drive efficiency.

$Z_I|Z_{II}$	$slack$ (%)	L (mm)	Nb_{link}	C_I $(N.m)$	$|\delta(\infty)|$	a (m)
60|15	$2 \rightarrow 20$	> 380	100	5	5°	$1e^{-10}$

Table I-1: Drive parameter for the influence of ζ discretisation on drive efficiency

For the conditions explored (typical track cycling drive), meshing losses are dominant (see Chapter VI). It is therefore necessary to precisely capture the meshing and un-meshing process at both the chainring and the rear cog to ensure reliable efficiency prediction.

To limit the number of sub-positions explored by the QSCDM, the discretisation pitch is refined only around the event of roller capture and release (associated to meshing losses). These events are characterised by discontinuities in the evolution of angles $\psi_{s,t,j}$ and number of links $n_{s,t,j}$ (see for instance §III.1.1). When refined, the interval in which the discontinuities occur is subdivided in 9 smaller intervals (see Figure I-1).
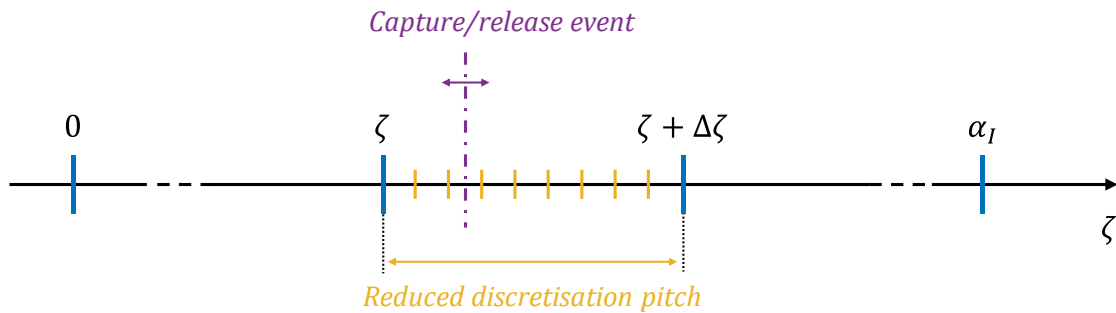
Figure I-1: Reduced discretisation pitch around capture/release events

Depending on the cases, refinement is carried out around all the events of roller capture/release or only around some of them. Indeed, it is known that meshing losses are mostly caused at the tight strand and by the sprocket with the smallest tooth number (see Chapter I and Chapter VI). Therefore, it is interesting to change only the discretisation pitch around the most influent (in terms of power losses) meshing/un-meshing events. Table I-2 details the three possible refinements considered here.

All	Driving (chainring) and driven (rear cog) meshing/un-meshing
Tight	Driving (chainring) meshing and driven (rear cog) un-meshing
Small teeth	$Z_I > Z_{II}$: Driving (chainring) meshing
	$Z_I \leq Z_{II}$: Driven (rear cog) meshing

Table I-2: Definition of all, tight and small teeth refinement

Table I-3 details different refinement strategies. Case 1 corresponds to 25 evenly spaced points per period. Case 6 exhibits the highest number of points. It must be noted that refinements introduced in Table I-2 can be combined. For instance, for case 3 (see Table I-3), discretisation pitch is first reduced around all the capture and release events before a second refinement is carried out only for those of the tight strand.

Case 1	25 points per period
Case 2	25 points per period + *all*
Case 3	25 points per period + *all* + *tight*
Case 4	25 points per period + *all* + *tight* + *small teeth*
Case 5	25 points per period + *all* + *all* + *tight* + *small teeth*
Case 6	25 points per period + *all* + *all* + *all* + *tight* + *small teeth*

Table I-3: Discretisation characteristics of the six tested cases

Figure I-2 shows the obtained values of ζ as a function of the sub-position index m for the 60|15, $slack = 11\%$ drive. The refinements at each capture/release events are clearly visible. Consistently with Table I-3, for instance for case 6, the discretisation pitch is minimal (*i.e.*, the curve slope in Figure I-2) around the roller release from the rear cog as this event correspond to the tight strand for the smallest sprocket. The interest of the non-uniform pitch is also visible. Indeed, using a uniform discretisation with the smallest pitch (from case 6 around roller release from the rear) would result is a significantly higher number of sub-positions (more than 1 000 000 for the example of Figure I-2). Therefore, the variable pitch allows important precision around events of interest without too significant consequences on the computational cost.
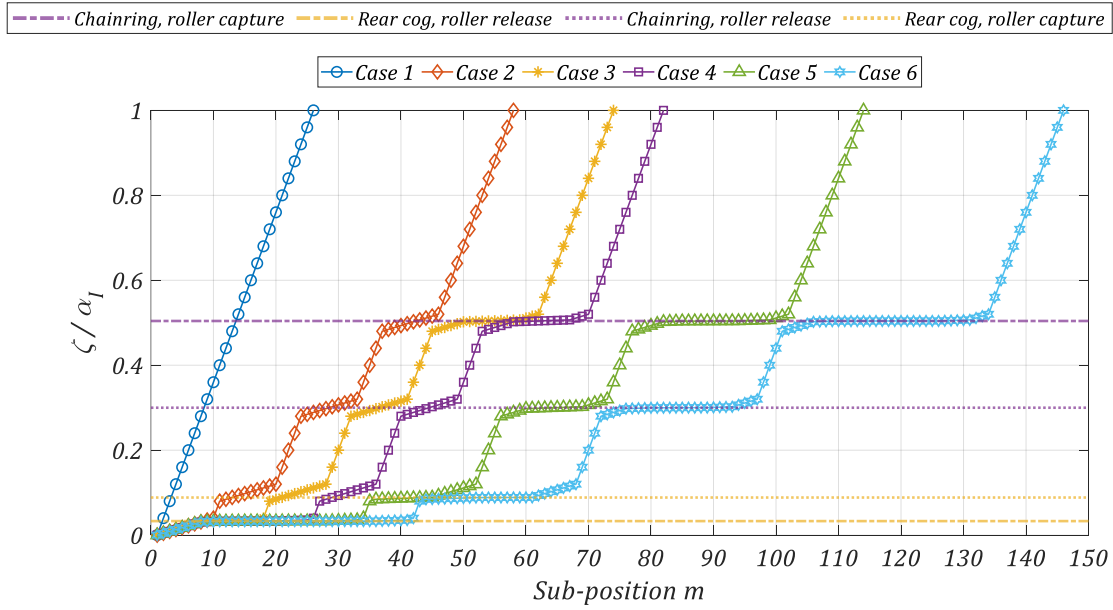
Figure I-2: Evolution of ζ as a function of m for each discretisation case ($60|15$, $C_I = 5N.m$, slack $= 11\%$)

Figure I-3 shows the influence of the considered ζ discretisation on the relation between $slack$ setting and efficiency η (only cases 1, 4 and 6 are plotted for visibility reasons). Curves show mean efficiency between cases A and B (see Chapter V). It is observed that efficiencies predicted with case 1 are always higher than those obtained with cases 4 and 6. Moreover, an oscillation pattern is visible. Efficiencies predicted with case 1 gradually diverge from the ones predicted with case 6 before discontinuously catching back. This is consistent with a discretisation issue of the meshing/un-meshing phenomenon. No significant variation is visible for case 6 which suggests that the lower discretisation pitch around roller capture/release is sufficient to ensure independence of ζ discretisation on η. Evolution for cases 4 and 6 are similar which suggest that sufficient discretisation might be reached before case 6.
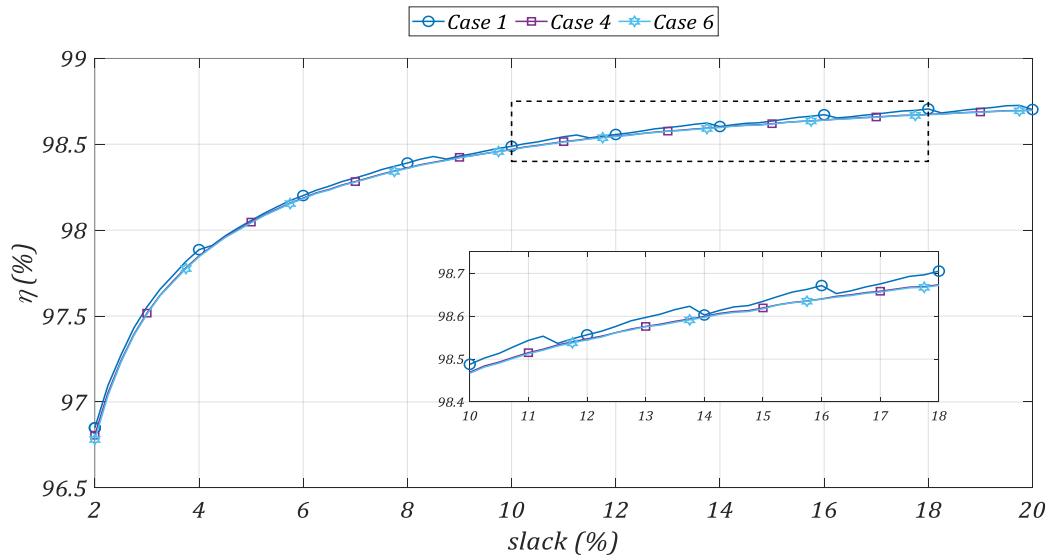
Figure I-3: Comparison of mean efficiency (between cases A and B) for cases 1, 4 and 6

Figure I-4.a shows the efficiency difference between each case and case 6 considered to be the reference (still in mean efficiency between cases A and B). The mean numbers of considered sub-

positions $\overline{nb}_{pos}$ for one drive period are also presented in Figure I-4.b. This number is calculated as the mean of nb_{pos} for all slack settings (between from $slack = 2$ to 20%). This number is not constant for all $slack$ settings as capture/release events might occurs in the same interval resulting in lower number of sub-positions per drive period.
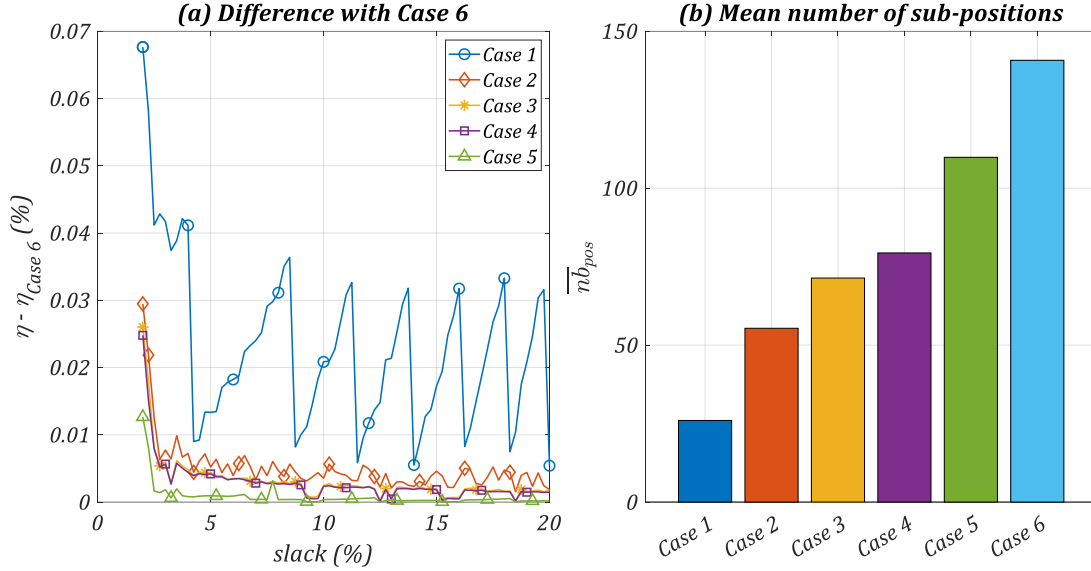
Figure I-4: (a) Efficiency difference with case 6 (b) Mean number of sub-positions within a drive period

The oscillations observed in Figure I-3 for case 1 are clearly visible in Figure I-4.a. Oscillations of lower amplitude are still visible for case 2. Starting from case 3 the difference with case 6 is always lower that 0.005% except for low $slack$ values where it can reach 0.02%. Figure I-4.b shows that an important increase in sub-position number occurs between case 4 and case 6 (due to the additional *all* discretisation, see Table I-3). From these results, case 4 seemed to be the best compromise between precision and computational cost. With this discretisation, the typical calculation time was about 8 minutes for each drive configuration (*i.e.*, to solve the QSCDM and the CDEM). Case 4 is therefore used in the entire manuscript resulting in the adaptative discretisation pitch visible for instance in Figure III-18 or Figure IV-2.

I.2 Influence of δ on η

This appendix explores the influence of the friction correction angle δ on drive efficiency. The classical 60|15 is still considered with the parameters given in Table I-4. Three values of $|\delta(\infty)|$ are tested: 3°, 5° and 7° (5° was used for all the calculations presented in this manuscript). The looseness setting is set at $slack = 11\%$ and the chainring torque C_I varies between 5 and $300 N.m$. Except for Figure I-8 below, the NF_{min} tooth profile is used for all calculations. ζ discretisation is set according the case 4 in §I.1.

Efficiency as a function of chainring torque C_I is presented in Figure I-5.a. Differences with the case $|\delta(\infty)| = 5°$ are shown in Figure I-5.b.

$Z_I|Z_{II}$	$slack$ (%)	L (mm)	Nb_{link}	C_I $(N.m)$	$|\delta(\infty)|$	a (m)
60|15	11	> 380	100	$5 \rightarrow 300$	**3, 5 and 7**	$1e^{-10}$

Table I-4: Drive parameters for the influence of δ on drive efficiency

Figure I-5: (a) Influence of $|\delta(\infty)|$ on drive efficiency (b) Differences with $|\delta(\infty)| = 5°$

The relation between chainring torque C_I and drive efficiency is similar for all correction angles. Particularly, the drive efficiency increases with larger chainring torques C_I is comparable for all cases. Efficiency is higher for lower correction angles. The difference reduces with increasing torques and seems to reach an asymptote at a value lower than $\pm 0.01\%$ of difference for high torques (see Figure I-5.b).

The causes of these differences are shown in Figure I-6 which gives the evolution of the roller losses at the chainring and the rear cog. The total meshing losses are also given.
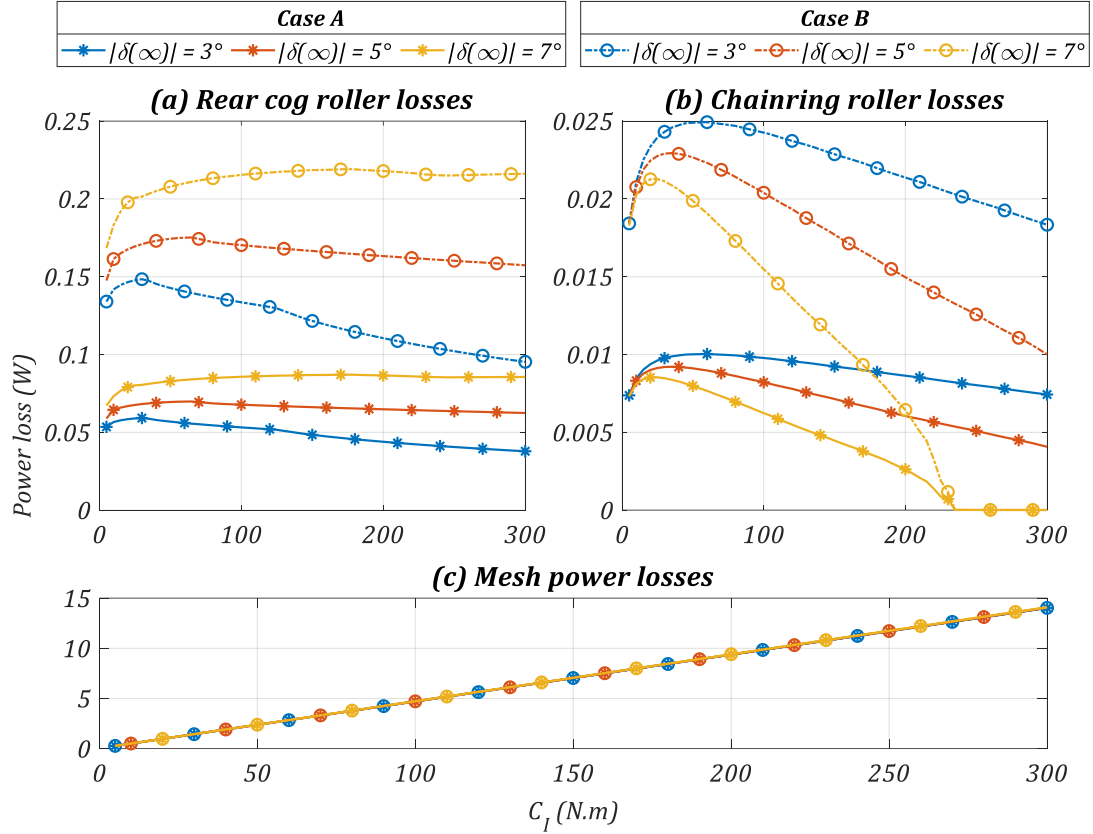
***Figure I-6:** Influence of $|\delta(\infty)|$ on different loss sources: roller losses at (a) the rear cog (b) the chainring and (c) total meshing losses*

First, losses for case B (circles in Figure I-6) are always higher than the corresponding ones for case A which is consistent with the underlying kinematic hypothesis (see Chapter V). Results show that lower correction angles increase roller losses at the chainring while they reduce those at the rear cog. Indeed, for the chainring, in the inter-tp behaviour, the friction correction tends to increase ϕ which reduces roller motion and therefore roller losses (see Chapter IV and Chapter VI). For the rear cog the effect is opposite as the friction correction reduces ϕ in the inter-tp behaviour. However, the roller losses at the rear cog are significantly higher than those at the chainring (about ten times higher, scales are different in Figure I-6). Therefore, lower correction angles overall result in less roller losses and therefore better efficiency.

Figure I-6.c confirms that meshing losses are independent of the friction correction angle and the kinematic case (A or B). The scale also recalls that meshing losses are largely dominant for such drives.

An example of resulting roller motions for $C_I = 250N.m$ is given in Figure I-7. One can notice that the chainring is in static roller behaviour for $|\delta(\infty)| = 7°$ which is consistent with the related roller loss being null in Figure I-6.b.
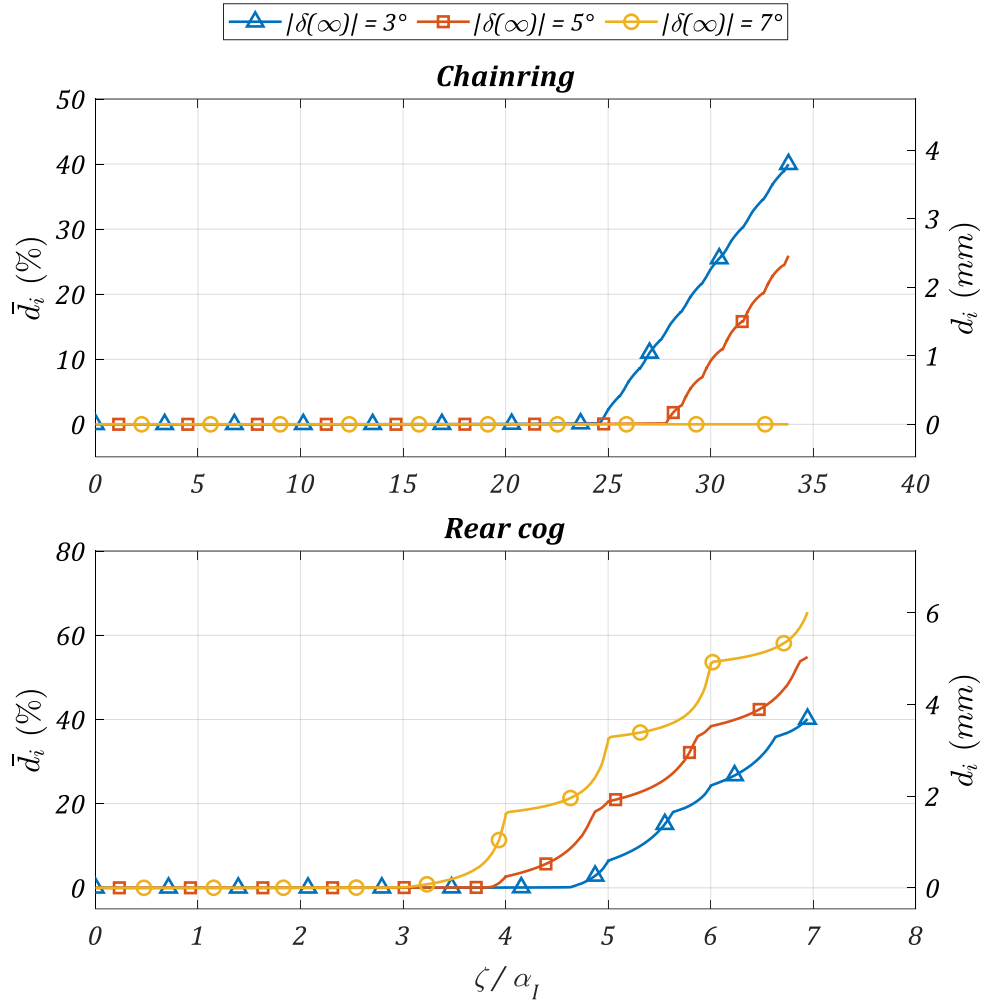
Figure I-7: Influence of $|\delta(\infty)|$ on chainring and rear cog roller motions for $C_I = 250N.m$

Considering only NF_{min} tooth profile, it was shown that the influence of δ mainly reduces to an efficiency shift (see Figure I-5). However, it is important to verify that all tooth profiles are shifted the same way so that the efficiency hierarchy is independent of the δ value considered. Figure I-8 shows a comparison of efficiency (relatively to the NF_{min}) as a function of chainring torque for the four profiles suitable for track cycling application (i.e., NF_{min}, CP_1, CP_2 and CP_3). Figure I-8.b is similar to Figure VI-3.b.
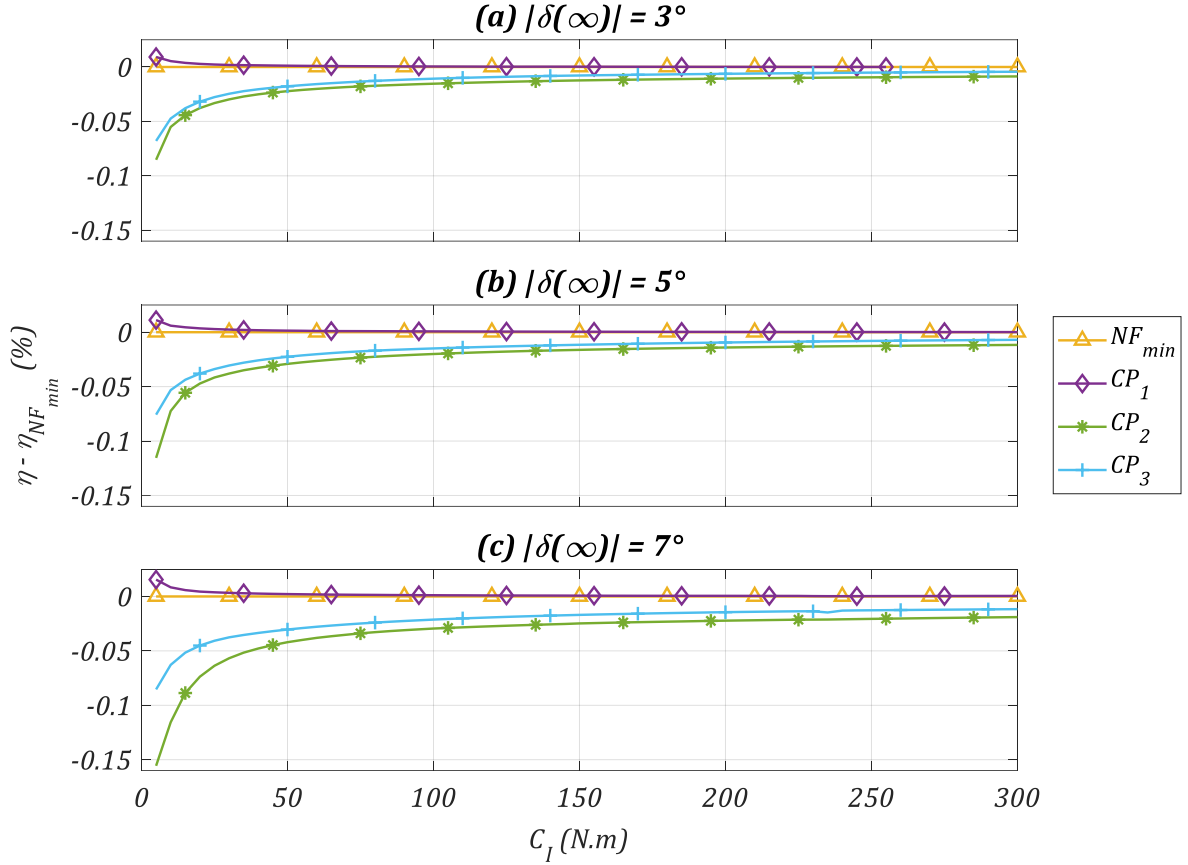
***Figure I-8: Comparison between tooth profiles (a)** $|\delta(\infty)| = 3°$ **(b)** $|\delta(\infty)| = 5°$ **(c)** $|\delta(\infty)| = 7°$*

Consistently with Figure I-6 showing that roller losses are increased by larger values of $|\delta(\infty)|$, the differences between tooth profiles are amplified for larger $|\delta(\infty)|$. However, the tooth profile hierarchy is similar regardless of the friction correction. CP_1 is still the most efficient profile due to its low tooth bottom radius (see Table A-4) followed by NF_{min}, CP_2 and CP_3. However, it can be noted that for CP_1 and $|\delta(\infty)| = 3°$, no solution could be found beyond $C_I = 255 N.m$. Indeed, the values of $|\delta(\infty)|$ change the profile capacity to withstand loads. This shows that the margin of CP_1 profile in terms of loading capacities is lower than for the other profiles.

This part shows that the conclusions regarding efficiency are largely independent of the $|\delta(\infty)|$ value considered. However, this parameter changes the magnitude of the losses. The values of $|\delta(\infty)| = 5°$ is supported by the experimental study of Naji & Marshek [62] regarding loads evolution. It could also be fitted along with $\bar{\mu}$ (see Chapter VI) on efficiency measurements.

I.3 Influence of a on η

The influence of parameter a on drive efficiency is finally tested. The 60|15 drive with NF_{min} tooth profile is still considered with the parameters given in Table I-5. The ζ discretisation is still according to case 4 in §I.1.

Figure I-9 shows drive efficiency as a function of the chainring torque C_I for values of a between $1e^{-6}$ and $1e^{-12}m$ ($a = 1e^{-10}m$ was used for all the calculations of this manuscript, see Appendix F).

$Z_I|Z_{II}$	$slack$ (%)	L (mm)	Nb_{link}	C_I $(N.m)$	$|\delta(\infty)|$	a (m)
60|15	11	> 380	100	$5 \rightarrow 300$	5	$1e^{-6} \rightarrow 1e^{-12}$

Table I-5: Drive parameters for the influence of δ on drive efficiency
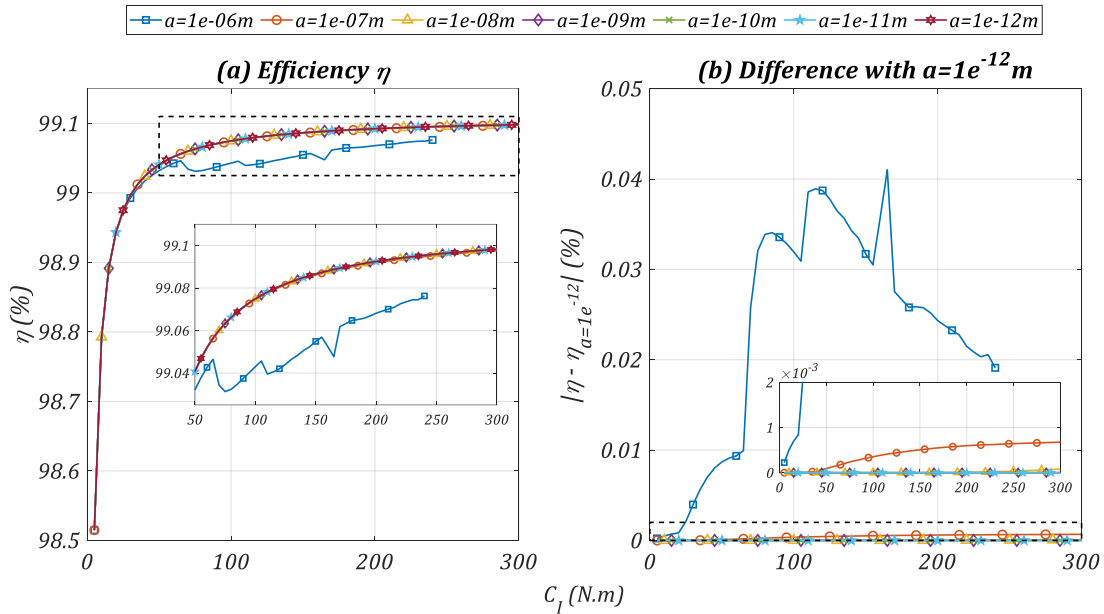
Figure I-9: (a) Influence of a on drive efficiency (b) Differences with $a = 1e^{-12}m$

Except for $a = 1e^{-6}m$, all efficiencies are similar regardless of a. Figure I-9.b shows that differences in efficiency starts with the discontinuities in roller motion reported in Appendix F. The influence is important for $a = 1e^{-6}m$ but becomes negligible beyond. For $a = 1e^{-7}m$, differences with other a values are visible but are smaller than 0.001% (see Figure I-9.b) which is largely lower than the efficiency differences reported in Chapter VI (lowest differences are of the order of 0.1%). Indeed, values of a influence roller motion and therefore roller losses that quickly reduce in significance with rising torque. Therefore, for track cycling drive, starting from $1e^{-8}m$, the influence of a on drive efficiency is negligible.

The curve for $a = 1e^{-6}m$ stops at $C_I = 240N.m$ as no solutions was found beyond for similar reasons as in Appendix F.

Appendix J Efficiency variations for similar tension ratios

Chapter VI showed that a correlation exists between drive efficiency η and tension ratio $T_{s,I}/T_t$. However, small deviations were observed around the common trend recalled in Figure J-1 (similar to Figure VI-6). This appendix explores the cases around $T_{s,I}/T_t = 2^{-2}$.
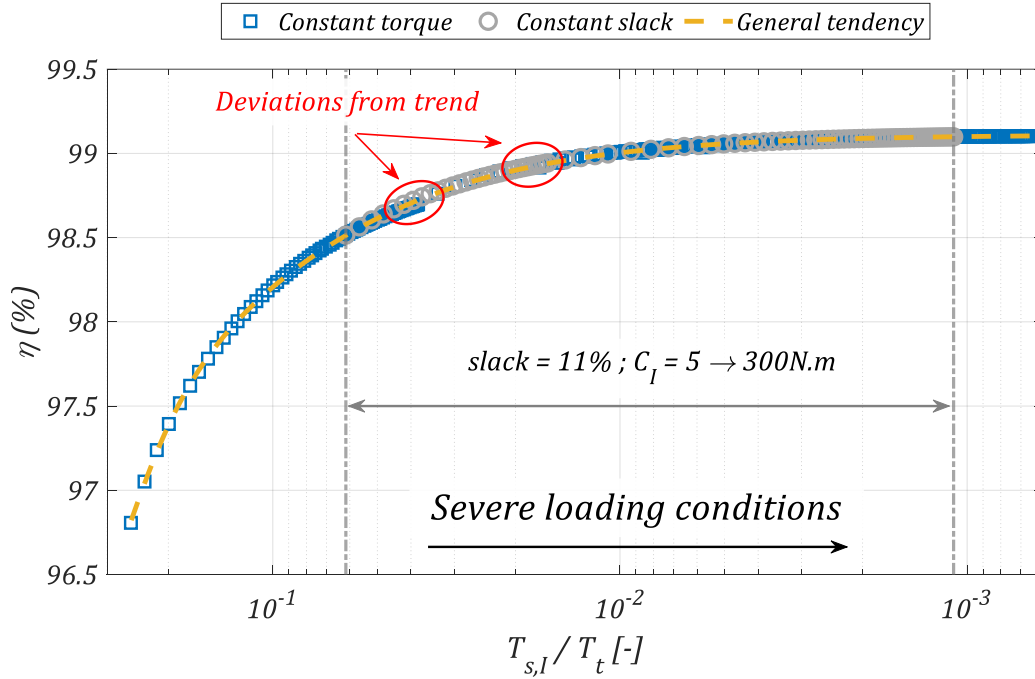
Figure J-1: Efficiency depending on chainring tension ratio for the NF_{min} profile (reversed x-axis)

A zoom-in view of the preceding curve around $2e^{-2}$ is presented in Figure J-2 (in linear scale). Each marker corresponds to a calculated drive configuration. Marker types highlight the context of each calculation and particularly the chainring torque and tension setting considered. Squares show the drive configurations obtained by varying the $slack$ setting with constant torque $C_I = 100N.m$. Circles represent varying $slack$ with $C_I = 50N.m$. Stars represent constant $slack = 11\%$ and varying torques. Three cases 1, 2 and 3 are extracted from each sub-family (*i.e.*, squares, circles and stars). A deeper analysis is carried out for these cases to explain efficiency deviations. The drive parameters are given in Table J-1.

	$Z_I\|Z_{II}$	Tooth profile	$T_{s,I}/T_t$	C_I $(N.m)$	$slack$ $(\%)$
Case 1			0.0171	100	2
Case 2	60|15	NF_{min}	0.0167	50	4
Case 3			0.0170	19	11

Table J-1: Drive parameters for cases 1, 2 and 3
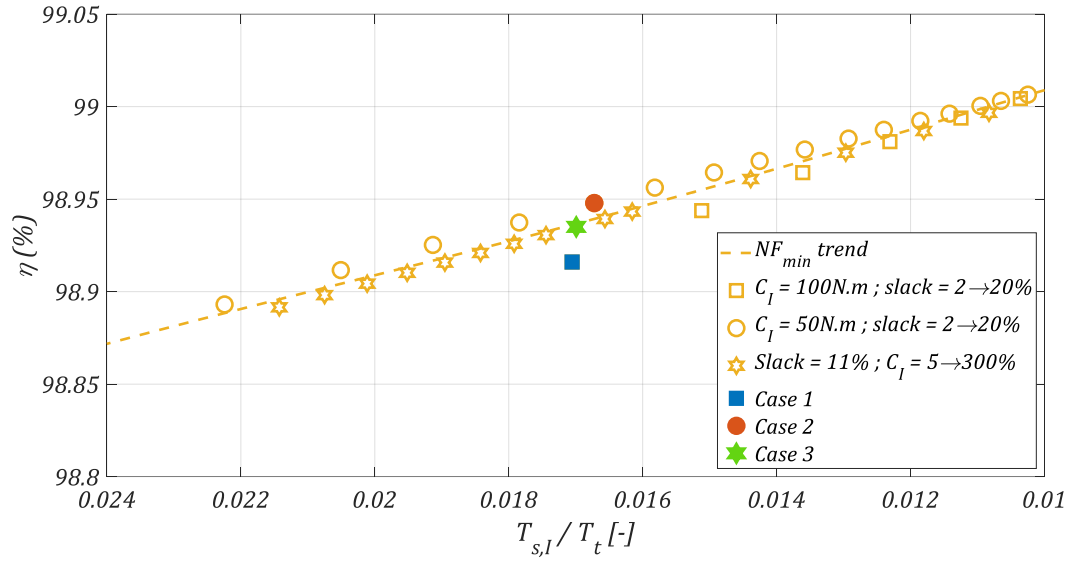
Figure J-2: Efficiency depending on chainring tension ratio for NF_{min} profile. Zoom-in around $T_{s,I}/T_t = 2e^{-2}$
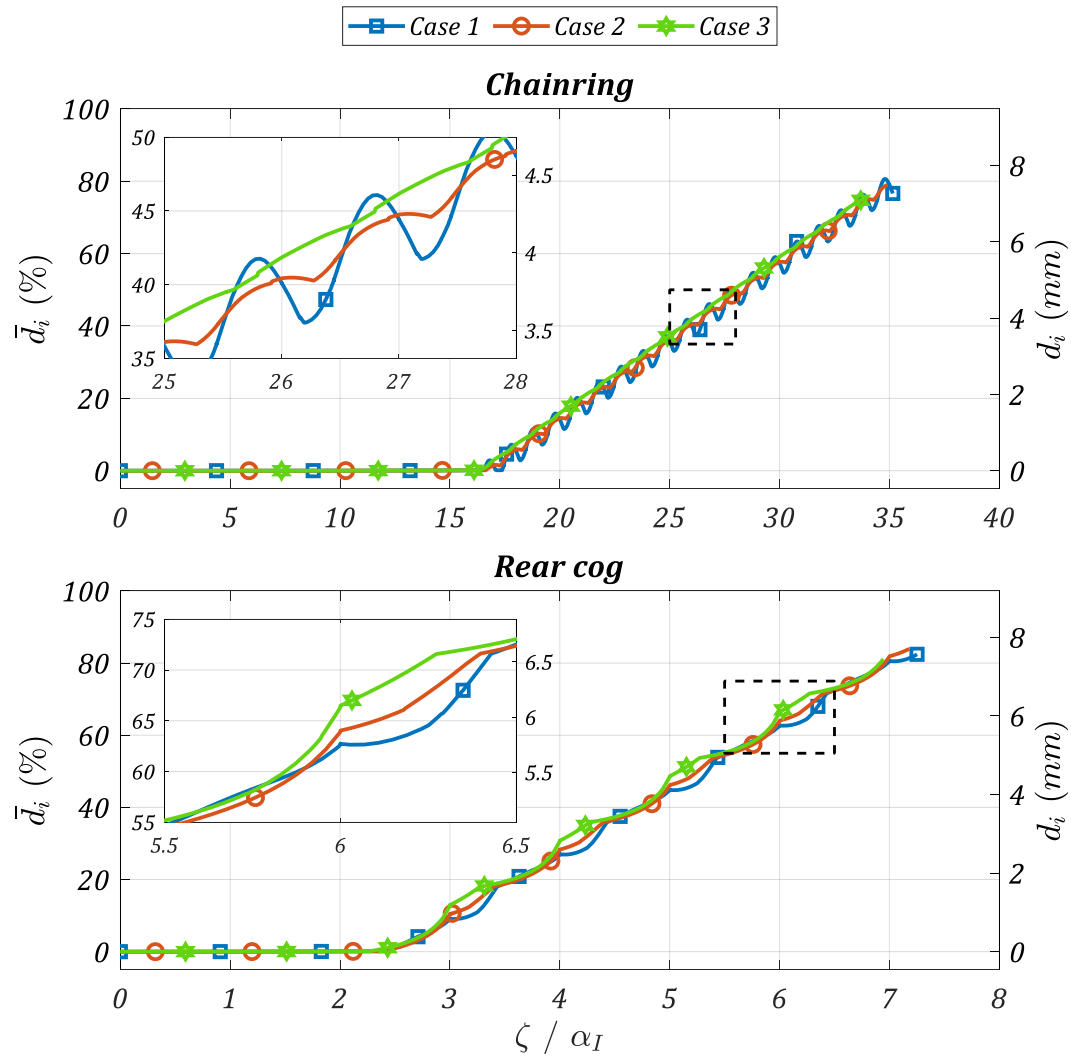
Figure J-3: Chainring and rear cog roller motions for Cases 1, 2 and 3

The three cases studied show similar tension ratios but each ratio is reached with different torque and tension settings. Case 1, which shows lower efficiency, corresponds to a relatively high torque ($C_I = 100N.m$) with a tight tension setting ($slack = 2\%$). On the contrary, case 3 exhibits a lower chainring torque ($19N.m$) but a looser tension setting ($slack = 11\%$). Case 2 lies in between the two preceding ones and results in the highest efficiency. Chainring and rear cog roller motion for the three cases are presented in Figure J-3.

Roller motions are comparable and show similar trends for all cases. For both the chainring and rear cog, rollers leave the transition point (*i.e.*, $\bar{d}_i = 0\%$) at the same time for all cases and reach between 75 to 80% of the inter-tp distance. However, differences between each case are visible. First, for cases with a tighter tension setting (*i.e.*, lower $slack$ value), the wrapping angle is larger, resulting in rollers staying longer in contact with both sprockets (see Figure J-4). Therefore, case 3 ($slack = 11\%$) exhibits rollers leaving the chainring and the rear cog sooner than for other cases, resulting in lower roller losses. Moreover, for case 1 (with the tightest tension setting), significant back-and-forth roller motion is visible at the chainring. Small back-and-forth roller motions are also visible, still at the chainring, for case 2. The differences between cases translate into variations of efficiency. Therefore case 1 exhibits the lowest efficiency due to back-and-forth roller motion at the chainring and to its rollers contacting each sprocket for more time compared to the other cases. Similarly, case 3 shows the best efficiency as rollers leave each sprocket sooner and no back-and-forth roller motion occurs.

Wrapping angle

(a)   **(b)**
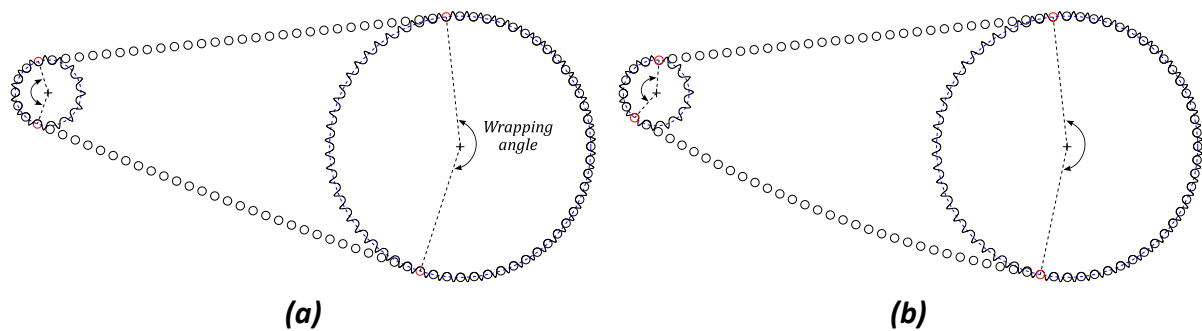
Figure J-4: General aspect and wrapping angle for: (a) case 1, (b) case 3. Both figures have the same scale.

Therefore, the tension ratio influences the general drive behaviour resulting in a strong corelation with efficiency. However, each different drive has its particularity resulting in differences in roller motion. These differences cause dispersion around the general trend between drive efficiency and tension ratio.

Appendix K **Influence of the numbers of sprockets teeth for constant gear ratios**

Chapter VI explored the influence of the numbers of sprockets teeth on drive efficiency. The interest of studying drives with an identical gear ratio Z_I/Z_{II} was highlighted and an example for all the possible drives (considering the geometrical limitations of track bikes) with a gear ratio of 4 was given. Figure K-1 and Figure K-2 illustrates the variation of efficiency for drives for a gear ratio of 3 and 5, respectively. Figure K-1 shows more drives than Figure K-2 as the lower gear ratio enables more choices with the boundaries considered. Comparison of Figure K-1 and Figure K-2 illustrates the preeminent effect of the number of rear cog teeth compared to the chainring one. Indeed, efficiencies are generally higher for drives with a gear ratio of 3 compared to 5 due to the higher number of rear cog teeth. Overall, the trend given in §VI.2.1 for drives for a gear ratio of 4 is still observed with drives with higher numbers of sprockets teeth being the more energetic efficient.
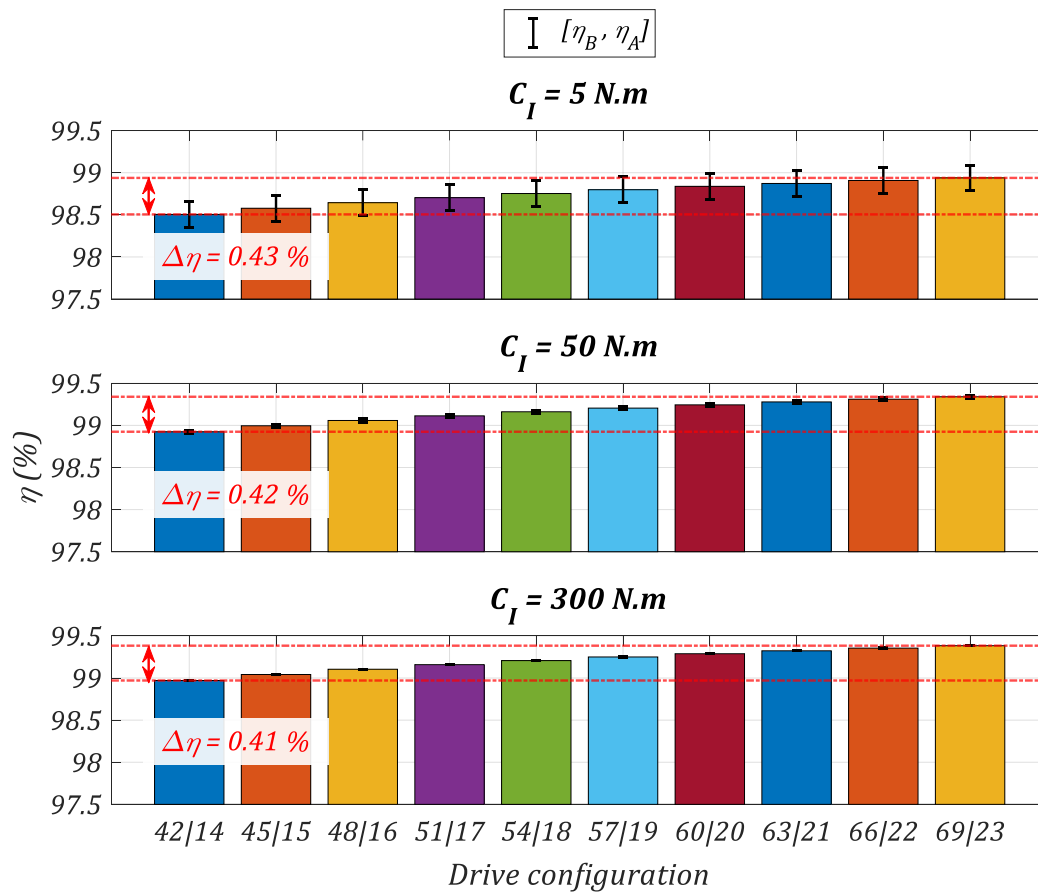
Figure K-1: Effect of tooth number on efficiency for drives of gear ratio 3
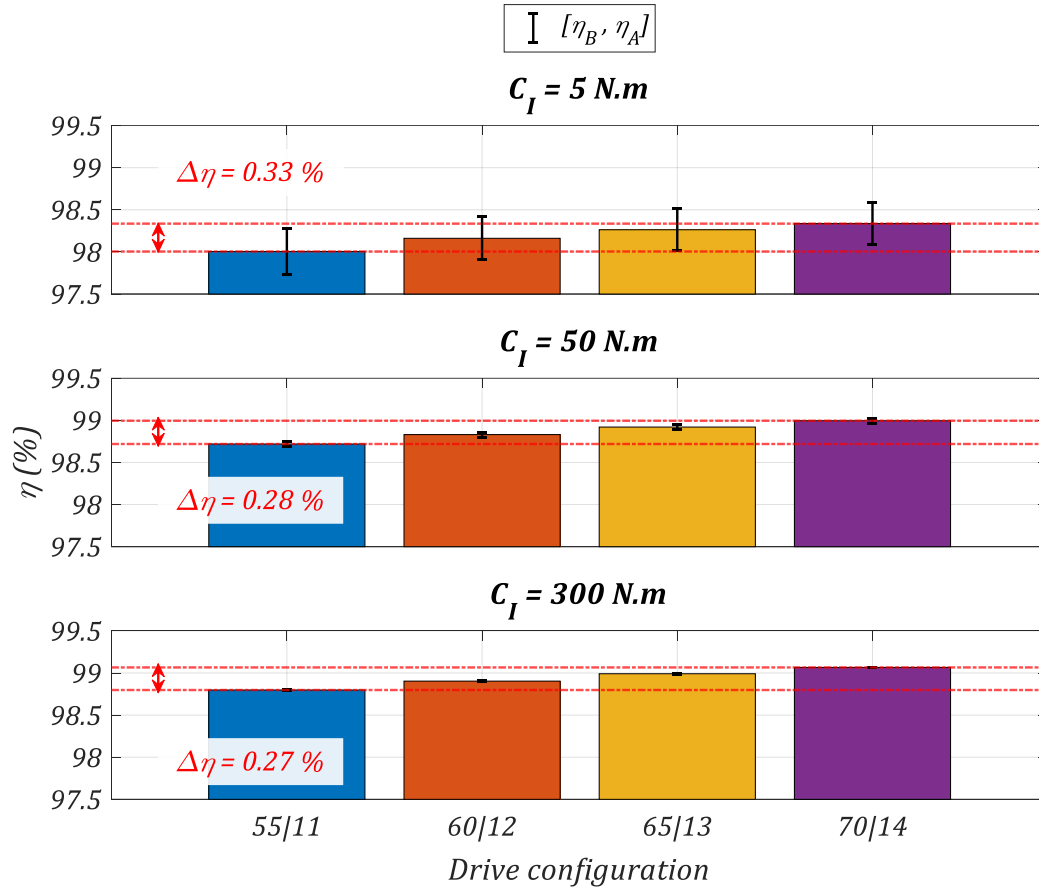
Figure K-2: Effect of tooth number on efficiency for drives of gear ratio 5

Appendix L DOE matrices

L.1 Trial matrix:

k	$x_{\bar{\mu}}$	x_{slack}	x_{C_I}	$x_{R_{II}}$	x_{R_I}	x_p
1	-1	-1	-1	-1	-1	-1
2	0	-1	-1	-1	-1	0
3	1	-1	-1	-1	-1	1
4	-1	0	-1	-1	-1	0
5	0	0	-1	-1	-1	1
6	1	0	-1	-1	-1	-1
7	-1	1	-1	-1	-1	1
8	0	1	-1	-1	-1	-1
9	1	1	-1	-1	-1	0
10	-1	-1	0	-1	-1	0
11	0	-1	0	-1	-1	1
12	1	-1	0	-1	-1	-1
13	-1	0	0	-1	-1	1
14	0	0	0	-1	-1	-1
15	1	0	0	-1	-1	0
16	-1	1	0	-1	-1	-1
17	0	1	0	-1	-1	0
18	1	1	0	-1	-1	1
19	-1	-1	1	-1	-1	1
20	0	-1	1	-1	-1	-1
21	1	-1	1	-1	-1	0
22	-1	0	1	-1	-1	-1
23	0	0	1	-1	-1	0
24	1	0	1	-1	-1	1
25	-1	1	1	-1	-1	0
26	0	1	1	-1	-1	1
27	1	1	1	-1	-1	-1
28	-1	-1	-1	0	-1	0
29	0	-1	-1	0	-1	1
30	1	-1	-1	0	-1	-1
31	-1	0	-1	0	-1	1
32	0	0	-1	0	-1	-1
33	1	0	-1	0	-1	0
34	-1	1	-1	0	-1	-1
35	0	1	-1	0	-1	0
36	1	1	-1	0	-1	1
37	-1	-1	0	0	-1	1
38	0	-1	0	0	-1	-1
39	1	-1	0	0	-1	0
40	-1	0	0	0	-1	-1
41	0	0	0	0	-1	0
42	1	0	0	0	-1	1
43	-1	1	0	0	-1	0
44	0	1	0	0	-1	1
45	1	1	0	0	-1	-1
46	-1	-1	1	0	-1	-1
47	0	-1	1	0	-1	0
48	1	-1	1	0	-1	1
49	-1	0	1	0	-1	0
50	0	0	1	0	-1	1
51	1	0	1	0	-1	-1
52	-1	1	1	0	-1	1
53	0	1	1	0	-1	-1
54	1	1	1	0	-1	0
55	-1	-1	-1	1	-1	1
56	0	-1	-1	1	-1	-1
57	1	-1	-1	1	-1	0
58	-1	0	-1	1	-1	-1
59	0	0	-1	1	-1	0
60	1	0	-1	1	-1	1
61	-1	1	-1	1	-1	0
62	0	1	-1	1	-1	1
63	1	1	-1	1	-1	-1
64	-1	-1	0	1	-1	-1
65	0	-1	0	1	-1	0
66	1	-1	0	1	-1	1
67	-1	0	0	1	-1	0
68	0	0	0	1	-1	1
69	1	0	0	1	-1	-1
70	-1	1	0	1	-1	1
71	0	1	0	1	-1	-1
72	1	1	0	1	-1	0
73	-1	-1	1	1	-1	0
74	0	-1	1	1	-1	1
75	1	-1	1	1	-1	-1
76	-1	0	1	1	-1	1
77	0	0	1	1	-1	-1
78	1	0	1	1	-1	0
79	-1	1	1	1	-1	-1
80	0	1	1	1	-1	0
81	1	1	1	1	-1	1
82	-1	-1	-1	-1	0	0
83	0	-1	-1	-1	0	1
84	1	-1	-1	-1	0	-1
85	-1	0	-1	-1	0	1
86	0	0	-1	-1	0	-1
87	1	0	-1	-1	0	0
88	-1	1	-1	-1	0	-1
89	0	1	-1	-1	0	0
90	1	1	-1	-1	0	1
91	-1	-1	0	-1	0	1
92	0	-1	0	-1	0	-1
93	1	-1	0	-1	0	0
94	-1	0	0	-1	0	-1
95	0	0	0	-1	0	0
96	1	0	0	-1	0	1
97	-1	1	0	-1	0	0
98	0	1	0	-1	0	1
99	1	1	0	-1	0	-1
100	-1	-1	1	-1	0	-1
101	0	-1	1	-1	0	0
102	1	-1	1	-1	0	1
103	-1	0	1	-1	0	0
104	0	0	1	-1	0	1
105	1	0	1	-1	0	-1
106	-1	1	1	-1	0	1
107	0	1	1	-1	0	-1
108	1	1	1	-1	0	0
109	-1	-1	-1	0	0	1
110	0	-1	-1	0	0	-1
111	1	-1	-1	0	0	0
112	-1	0	-1	0	0	-1
113	0	0	-1	0	0	0
114	1	0	-1	0	0	1
115	-1	1	-1	0	0	0
116	0	1	-1	0	0	1
117	1	1	-1	0	0	-1
118	-1	-1	0	0	0	-1
119	0	-1	0	0	0	0
120	1	-1	0	0	0	1
121	-1	0	0	0	0	0
122	0	0	0	0	0	1
123	1	0	0	0	0	-1
124	-1	1	0	0	0	1
125	0	1	0	0	0	-1
126	1	1	0	0	0	0

127	-1	-1	1	0	0	0
128	0	-1	1	0	0	1
129	1	-1	1	0	0	-1
130	-1	0	1	0	0	1
131	0	0	1	0	0	-1
132	1	0	1	0	0	0
133	-1	1	1	0	0	-1
134	0	1	1	0	0	0
135	1	1	1	0	0	1
136	-1	-1	-1	1	0	-1
137	0	-1	-1	1	0	0
138	1	-1	-1	1	0	1
139	-1	0	-1	1	0	0
140	0	0	-1	1	0	1
141	1	0	-1	1	0	-1
142	-1	1	-1	1	0	1
143	0	1	-1	1	0	-1
144	1	1	-1	1	0	0
145	-1	-1	0	1	0	0
146	0	-1	0	1	0	1
147	1	-1	0	1	0	-1
148	-1	0	0	1	0	1
149	0	0	0	1	0	-1
150	1	0	0	1	0	0
151	-1	1	0	1	0	-1
152	0	1	0	1	0	0
153	1	1	0	1	0	1
154	-1	-1	1	1	0	1
155	0	-1	1	1	0	-1
156	1	-1	1	1	0	0
157	-1	0	1	1	0	-1
158	0	0	1	1	0	0
159	1	0	1	1	0	1
160	-1	1	1	1	0	0
161	0	1	1	1	0	1
162	1	1	1	1	0	-1
163	-1	-1	-1	-1	1	1
164	0	-1	-1	-1	1	-1
165	1	-1	-1	-1	1	0
166	-1	0	-1	-1	1	-1
167	0	0	-1	-1	1	0
168	1	0	-1	-1	1	1
169	-1	1	-1	-1	1	0
170	0	1	-1	-1	1	1
171	1	1	-1	-1	1	-1
172	-1	-1	0	-1	1	-1
173	0	-1	0	-1	1	0
174	1	-1	0	-1	1	1
175	-1	0	0	-1	1	0
176	0	0	0	-1	1	1
177	1	0	0	-1	1	-1
178	-1	1	0	-1	1	1
179	0	1	0	-1	1	-1
180	1	1	0	-1	1	0
181	-1	-1	1	-1	1	0
182	0	-1	1	-1	1	1
183	1	-1	1	-1	1	-1
184	-1	0	1	-1	1	1
185	0	0	1	-1	1	-1
186	1	0	1	-1	1	0
187	-1	1	1	-1	1	-1
188	0	1	1	-1	1	0
189	1	1	1	-1	1	1
190	-1	-1	-1	0	1	-1
191	0	-1	-1	0	1	0
192	1	-1	-1	0	1	1
193	-1	0	-1	0	1	0
194	0	0	-1	0	1	1
195	1	0	-1	0	1	-1
196	-1	1	-1	0	1	1
197	0	1	-1	0	1	-1
198	1	1	-1	0	1	0
199	-1	-1	0	0	1	0
200	0	-1	0	0	1	1
201	1	-1	0	0	1	-1
202	-1	0	0	0	1	1
203	0	0	0	0	1	-1
204	1	0	0	0	1	0
205	-1	1	0	0	1	-1
206	0	1	0	0	1	0
207	1	1	0	0	1	1
208	-1	-1	1	0	1	1
209	0	-1	1	0	1	-1
210	1	-1	1	0	1	0
211	-1	0	1	0	1	-1
212	0	0	1	0	1	0
213	1	0	1	0	1	1
214	-1	1	1	0	1	0
215	0	1	1	0	1	1
216	1	1	1	0	1	-1
217	-1	-1	-1	1	1	0
218	0	-1	-1	1	1	1
219	1	-1	-1	1	1	-1
220	-1	0	-1	1	1	1
221	0	0	-1	1	1	-1
222	1	0	-1	1	1	0
223	-1	1	-1	1	1	-1
224	0	1	-1	1	1	0
225	1	1	-1	1	1	1
226	-1	-1	0	1	1	1
227	0	-1	0	1	1	-1
228	1	-1	0	1	1	0
229	-1	0	0	1	1	-1
230	0	0	0	1	1	0
231	1	0	0	1	1	1
232	-1	1	0	1	1	0
233	0	1	0	1	1	1
234	1	1	0	1	1	-1
235	-1	-1	1	1	1	-1
236	0	-1	1	1	1	0
237	1	-1	1	1	1	1
238	-1	0	1	1	1	0
239	0	0	1	1	1	1
240	1	0	1	1	1	-1
241	-1	1	1	1	1	1
242	0	1	1	1	1	-1
243	1	1	1	1	1	0

L.2   Results vector η_{CDEM}:

k	$\eta_{CDEM}(k)$
1	98,179
2	97,457
3	95,192
4	98,502
5	97,139
6	98,129
7	97,883
8	98,555
9	98,037
10	98,920
11	98,138
12	98,648
13	98,541
14	98,888
15	98,491
16	99,094
17	98,728
18	97,922
19	98,527
20	98,879
21	98,480
22	99,096
23	98,731
24	97,933
25	98,962
26	98,254
27	98,703
28	98,520
29	97,099
30	98,040
31	98,348
32	98,801
33	98,450
34	99,103
35	98,797
36	97,872
37	98,884
38	99,127
39	98,855
40	99,304
41	99,055
42	98,453
43	99,229
44	98,698
45	99,005
46	99,299
47	99,048
48	98,439
49	99,231
50	98,702
51	99,007
52	98,939
53	99,160
54	98,896
55	98,079
56	98,657
57	98,281
58	99,205
59	98,931
60	98,072

k	$\eta_{CDEM}(k)$
61	99,196
62	98,527
63	98,955
64	99,420
65	99,205
66	98,683
67	99,365
68	98,922
69	99,190
70	99,123
71	99,316
72	99,091
73	99,361
74	98,913
75	99,184
76	99,125
77	99,317
78	99,093
79	99,441
80	99,232
81	98,746
82	97,644
83	95,470
84	97,076
85	97,504
86	98,330
87	97,705
88	98,773
89	98,262
90	96,795
91	98,505
92	98,905
93	98,504
94	99,136
95	98,784
96	97,997
97	99,012
98	98,324
99	98,768
100	99,128
101	98,770
102	97,957
103	99,016
104	98,338
105	98,772
106	98,646
107	98,963
108	98,591
109	97,330
110	98,158
111	97,671
112	98,977
113	98,645
114	97,501
115	98,999
116	98,130
117	98,682
118	99,328
119	99,090
120	98,484
121	99,281
122	98,780

k	$\eta_{CDEM}(k)$
123	99,070
124	99,010
125	99,217
126	98,973
127	99,274
128	98,763
129	99,062
130	99,015
131	99,220
132	98,976
133	99,363
134	99,135
135	98,591
136	98,817
137	98,435
138	96,959
139	99,115
140	98,316
141	98,839
142	98,778
143	99,116
144	98,851
145	99,400
146	98,965
147	99,233
148	99,193
149	99,373
150	99,167
151	99,490
152	99,299
153	98,851
154	99,182
155	99,368
156	99,160
157	99,492
158	99,301
159	98,857
160	99,429
161	99,035
162	99,272
163	95,848
164	97,237
165	96,374
166	98,532
167	97,930
168	96,138
169	98,487
170	97,108
171	98,136
172	99,125
173	98,761
174	97,840
175	99,033
176	98,335
177	98,796
178	98,658
179	98,988
180	98,621
181	99,020
182	98,287
183	98,784
184	98,675

k	$\eta_{CDEM}(k)$
185	98,993
186	98,630
187	99,178
188	98,843
189	98,110
190	98,331
191	97,838
192	95,751
193	98,835
194	97,693
195	98,439
196	98,353
197	98,830
198	98,516
199	99,280
200	98,753
201	99,067
202	99,039
203	99,244
204	99,009
205	99,386
206	99,167
207	98,635
208	99,024
209	99,236
210	98,998
211	99,389
212	99,171
213	98,645
214	99,324
215	98,858
216	99,126
217	98,615
218	97,195
219	98,139
220	98,541
221	98,969
222	98,680
223	99,251
224	99,001
225	98,170
226	99,192
227	99,379
228	99,178
229	99,513
230	99,331
231	98,900
232	99,457
233	99,078
234	99,307
235	99,508
236	99,325
237	98,887
238	99,459
239	99,084
240	99,310
241	99,254
242	99,418
243	99,226

Résumé étendu en français

This thesis has been written in English. Therefore, an extended summary in French is presented below. It describes the main outlines of this research work.

Ce manuscrit de thèse a été rédigé en anglais. En conséquence, un résumé étendu, reprenant les principaux points de ce travail de recherche, est présenté en français ci-dessous.

I. Introduction

L'importante compétition entre cyclistes sur piste de très haut niveau pousse les travaux de recherches à explorer toutes les possibilités d'optimisations. Dans ce contexte, le rendement énergétique des transmissions par chaine à rouleaux est étudié dans le but d'améliorer la compréhension des pertes de puissance et de proposer des possibilités d'optimisations.

Le travail de recherche présenté dans ce manuscrit propose une étude du rendement des transmissions par chaine en prenant en compte l'influence des pertes provoqués par le mouvement des rouleaux le long de leur profil de dent associé. L'influence de la géométrie de denture utilisée pour le pignon menant (plateau) et le pignon mené (pignon) est également prise en compte.

Pour ce faire, un premier modèle permettant de calculer les charges (*i.e.*, tension dans les maillons et force de contact rouleau/profil) est présenté (appelé QSCDM[1]). Un second modèle dédié au calcul du rendement d'une transmission par chaine est ensuite proposé (appelé CDEM[2]). Sur la base de ces deux outils, l'influence de la géométrie de denture sur le fonctionnement d'une transmission par chaine est d'abord étudiée. Enfin, une étudie du rendement des transmissions par chaine de cyclisme sur piste est proposée.

---

[1] Quasi-Static Chain Drive Model (QSCDM) : Modèle de transmission par chaine quasi-statique
[2] Chain Drive Efficiency Model (CDEM) : Modèle de rendement de transmission par chaine

II.   Contexte et étude bibliographique

Ce chapitre est consacré à l'introduction du contexte de l'étude et à l'analyse de la littérature.

Dans un premier temps, les spécificités des transmissions par chaine en cyclisme sur piste sont détaillées. Celles-ci sont principalement : des chaînes légères ($3.6\ g/maillon^3$), des vitesses de rotation modérées (jusqu'à $130 tr/min$ au plateau) et des couples importants (jusqu'à $300 N.m$ au plateau maintenus durant plusieurs rotations). Ces contraintes ont conduit à une approche de modélisation quasi-statique.

Une vue d'ensemble de la transmission par chaine à rouleaux est ensuite donnée. La définition des pignons standards (selon les normes ASA [32] et ISO 606 [31]) est détaillée. Les profils de denture en résultant sont désignés ASA et $NF_{min/max}$ dans le manuscrit. L'effet polygonal, un phénomène inhérent à toute transmission par chaîne, est présenté. Ce phénomène est important à prendre en compte lors de l'étude du fonctionnement des transmissions par chaine car il introduit une erreur de transmission qui se traduit par une relation complexe entre les vitesses instantanées du pignon menant (plateau) et du pignon mené (pignon). La littérature sur le sujet est détaillée. Elle montre que les modèles cinématiques utilisant des mécanismes à quatre barres constituent une approche intéressante lorsque les effets dynamiques sont négligés.

Les évolutions successives des modèles de tension quasi-statique (dédiés au calcul des tensions dans les maillons et des forces de contact entre rouleaux et pignons) sont ensuite présentées. Les modèles successifs ont permis d'améliorer l'interdépendance entre les charges et les positionnements des rouleaux. Cependant, ce lien est introduit avec des défis numériques qui se traduisent par des modèles à forte intensité de calcul. Les résultats de ces modèles successifs sont en accord avec les mesures de tension de maillons, effectuées dans des conditions représentatives de transmissions industrielles (principalement Naji & Marshek [62] et Stephenson *et al.* [72]).

Enfin, les modèles et mesures expérimentales antérieurs, consacrés à l'efficacité des transmissions par chaine sont présentés. La plupart des modèles sont basés sur les pertes d'engrènement causées par l'articulation entre maillons consécutifs pendant l'engrènement et le désengrènement. Ces modèles concordent généralement avec les données expérimentales, à l'exception notable des couples faibles. Récemment, l'auteur a souligné que les pertes causées par le mouvement des rouleaux le long de leur profil de dent associé pouvaient avoir une influence significative sur l'efficacité de la transmission. L'importance des pertes causées par les rouleaux soulève également la question du profil de denture, qui pourrait modifier l'évolution du mouvement des rouleaux.

Objectifs de la thèse

Compte tenu des travaux antérieurs sur le sujet, l'objectif principal de cette thèse est d'étudier l'efficacité des transmissions par chaine en tenant compte de l'influence des pertes causées par le mouvement des rouleaux le long de leur profil de denture associé. Pour ce faire, un modèle paramétrique d'efficacité de transmissions par chaine est développé. Le modèle sera capable de prendre en compte différentes géométries de profils de denture provenant de normes ou créées pour l'étude (*e.g.*, ASA, NF_{min} et NF_{max}). Il sera utilisé pour tester l'influence de divers paramètres tels que les réglages de tension, les conditions de charge (*i.e.*, le couple appliqué), le pas de la chaîne, les nombre de dents des pignons, *etc*.

---

[3] A comparer à environ $7.6 g/maillon$ pour des chaines industrielles de pas identique [11].

La modélisation du rendement se fera en deux étapes. Tout d'abord, un modèle quasi statique de transmission par chaine (QSCDM) sera présenté. Par rapport aux travaux précédents, sa formulation est générale et permet de prendre en compte n'importe quelle géométrie de denture. Ce premier modèle calculera les charges (*i.e.*, les tensions dans les maillons et les forces de contact entre rouleaux et pignons) et les déplacements (*i.e.*, le mouvement des rouleaux et les orientations des maillons). Des éléments des études précédentes de Lodge & Burgess [70], Troedsson & Vedmar [67] et Kim & Johnson [52] seront réutilisés. Une architecture originale basée sur des sous-modèles dédiés aux brins tendu et mou et aux pignons est proposée pour faciliter la résolution numérique et donc limiter les éventuels problèmes signalés par Troedsson & Vedmar [67]. La validation sera présentée sur la base d'entraînements industriels. Le modèle quasi-statique (QSCDM) sera ensuite utilisé pour étudier l'influence du profil de denture sur le comportement de transmissions par chaine industrielles et cyclistes (évolution des charges, mouvement des rouleaux, *etc.*). Dans un second temps, un modèle de rendement de transmission par chaine (CDEM) sera présenté. Par rapport aux études précédentes, l'influence des pertes causées par le mouvement des rouleaux est prise en compte. Combiné au modèle de transmission par chaine quasi statique (QSCDM), il calculera le rendement d'une transmission en prenant en compte le mouvement des rouleaux et la géométrie de denture. Enfin, le CDEM sera utilisé pour réaliser une étude paramétrique de l'efficacité des transmissions par chaines de vélo de piste en tenant compte de l'influence des pertes de rouleaux. A partir des résultats obtenus, des lignes directrices pour des optimisations possibles seront discutées.

Compte tenu de l'application en cyclisme sur piste (chaine légère, vitesse modérée, *etc.*), les effets dynamiques, y compris les vibrations des brins, seront négligés. Cependant, le modèle quasi-statique proposé (QSCDM) est général et peut être appliqué à n'importe quelle transmission à deux pignons tant que les hypothèses sont respectées (*e.g.*, les effets dynamiques peuvent être négligés). Il peut donc être utilisé pour les transmissions industrielles à vitesse de rotation modérée. Étant donné que la littérature sur le modèle de tension quasi-statique est principalement constituée d'exemples industriels, le QSCDM sera validé sur de tels transmissions industrielles. Le même raisonnement s'applique au modèle d'efficacité (CDEM). Ce dernier sera toutefois utilisé pour mener une étude paramétrique uniquement sur les transmissions de cyclisme sur piste.

III. Modèle quasi-statique de transmission par chaine (QSCDM[4])

Dans ce chapitre, le modèle de transmission par chaine quasi statique (QSCDM) est présenté. Ce modèle 2D permet d'étudier une transmission par chaîne, en considérant les connexions entre les brins et les pignons, chacun étant représenté par un sous-modèle spécifique. Les calculs peuvent être effectués en utilisant différentes géométries de denture. La résolution est effectuée en deux étapes successives. Tout d'abord, la cinématique globale (*i.e.*, les trajectoires des brins, et le nombre de maillons dans chaque sous-modèle) est déterminée. Ses résultats sont ensuite utilisés par le sous-modèle local de pignon.

La cinématique globale de la transmission est détaillée en premier. Cette dernière est supposée être indépendante des conditions de charge (*i.e.*, du couple appliqué) et du profil de denture des pignons. Les jeux entre rouleaux et fonds de dent sont également négligés de tel sorte que le centre de chaque rouleau en contact avec un pignon se trouve sur le cercle primitif. Un sous modèle est utilisé pour chaque brin (brin tendu et brin mou). Le brin tendu est supposé être parfaitement rectiligne et sa modélisation est basée sur un mécanisme 4-barres. La dépendance entre la rotation du plateau et du pignon peut ainsi être exprimée et prise en compte. Le sous-modèle de brin mou est basé sur des travaux précédent [67], [70]. Il suppose que la tension est uniquement causée par l'effet de la gravité. Les deux sous-modèles sont utilisés au sein d'une procédure numérique originale. Une fois la solution obtenue, les trajectoires des brins sont connues. Cela permet de connaitre les angles $\alpha_{t,s,j}$ ainsi que les tensions appliquées par le brin mou sur chaque pignon $T_{s,j}$. Ces données sont nécessaires pour utiliser le sous-modèle local du pignon.

Le sous-modèle local utilisé pour les pignons est ensuite détaillé. Il permet de calculer simultanément les charges (*i.e.*, les tensions dans les maillons et les forces de contact entre rouleaux et pignons) ainsi que l'emplacement des rouleaux le long du profil de denture. En effet, il est montré que les charges et les positions de rouleaux sont liées. Les positions successives des rouleaux le long de leur profil sont calculées en considérant que les centres de deux rouleaux consécutifs doivent être distant d'un pas de chaine (l'allongement sous charge est négligé [2]). En utilisant la relation ainsi obtenue, une courbe caractéristique appelée courbe caractéristique des positions de rouleaux est construite [52], [67]. Elle représente les positions du rouleau $i + 1$ (notée γ_{i+1}) en fonction de celle du rouleau i (notée γ_i). Les points stables de cette courbe (*i.e.*, point pour lesquels les positions i et $i + 1$ sont identiques) sont appelés points de transitions. Ils sont au nombre de deux et sont appelées tp^A et tp^B. Il est montré qu'une relation directe existe entre l'emplacement des rouleaux le long de leur profil et le chargement imposé sur la transmission (*e.g.*, le couple appliqué). Cette relation fait appel à des angles caractéristiques entre les directions de maillons consécutifs (α^*, ξ and ν) et entre les forces de tension T et de contact P (angle de pression ϕ). Le frottement est introduit en utilisant un angle de correction δ selon une approche similaire à celle de Naji & Marshek [2]. Les problèmes de compatibilité aux interfaces entre les brins et les sous-modèles locaux de pignon sont également abordés.

La procédure générale de résolution de l'ensemble du QSCDM est introduite. La cinématique globale est résolue en premier, avant que ses résultats ne soient utilisés dans le sous-modèle local de pignon. Les conditions de chargement peuvent être spécifiées, de manière équivalente, soit par un couple appliqué sur l'un ou l'autre des pignons soit par la tension du brin tendu. Cette approche séquentielle (*i.e.*, cinématique globale puis sous-modèle de pignon) permet de résoudre facilement chaque sous-

---

[4] Quasi-Static Chain Drive Model (QSCDM) : Modèle quasi-statique de transmission par chaine

modèle mais introduit des questions de compatibilité. Une seule période d'engrènement (correspondant à une rotation des pignons menant et mené d'un angle α_I et α_{II} respectivement) est étudiée. Cette dernière est découpée en sous-positions sur lesquelles la procédure de résolution est appliquée. Cependant, la résolution donne une distribution spatiale des résultats « per position ». Une dernière étape est donc nécessaire afin d'obtenir les charges et les mouvements de rouleaux en suivant un composant donné (*e.g.*, un maillon ou un rouleau). Ces résultats sont appelés « per component ». La méthode permettant de déterminer les résultats « per component » à partir de ceux « per position » est détaillée. Enfin, les cas où plusieurs positions de rouleaux $s_{c,1}$ conviennent sont traités.

IV.   Eléments de validation du QSCDM

Ce chapitre est consacré à la validation du modèle quasi statique de transmission par chaine (QSCDM) présenté plus haut. La validation est menée sur différentes sous-parties du modèle et finalement sur l'ensemble du QSCDM.

La cinématique globale est tout d'abord examinée. La comparaison du sous-modèle de brin tendu est en accord avec les prévisions analytiques de Fuglede & Thomsen [1]. Les prédictions des positions de capture et de libération des rouleaux sont similaires, de même que la vitesse de rotation et l'accélération du pignon. Comparée à une étude analytique, la procédure numérique présentée a l'avantage d'être plus souple à l'ajout de nouvelles hypothèses. Le sous-modèle du brin mou est ensuite analysé et comparé aux résultats connus de la courbe caténaire (ou chainette) [89]. Son comportement se montre cohérent. Une application à un exemple de transmission par chaine donne également des résultats cohérents.

Le sous-modèle local de pignon est ensuite analysé en deux étapes. Tout d'abord, des prédictions de positions de rouleaux, indépendamment de l'impact sur les charges, sont considérées. Une comparaison des courbes caractéristiques des positions de rouleaux est proposée avec les résultats de Kim & Johnson [52]. Le calcul des angles entre maillons est ensuite confronté aux mesures graphiques de Binder [32] et aux prévisions numériques de Naji & Marshek [64]. La comparaison a montré des tendances similaires malgré de faibles variations imputées aux différentes hypothèses considérées dans chacune des études.

Dans un second temps, la relation entre les positions des rouleaux et les charges, telle que prédite par le sous-modèle de pignon local, est étudiée. Le sous-modèle est testé seul, sans lien avec la cinématique globale. Les prédictions sont confrontées au modèle de Lodge & Burgess [70] et aux résultats expérimentaux de Stephenson *et al.* [72]. En raison de la spécificité des cas étudiés (trajectoires de brins contraintes par des rails de guidage/tendeurs), l'évolution des angles d'engrènement $\alpha_{s,t,j}$ ne peut être calculée. Les résultats sont donc présentés « per position ». Les comparaisons sont menées pour des prédictions de tension de maillons et montrent des résultats cohérents. Comparé au modèle de Lodge & Burgess, qui suppose une variation instantanée de la position du rouleau, le modèle proposé permet de saisir le changement progressif entre les deux points de transition (entre tp^B sur le côté tendu de la denture et tp^A sur le côté mou). Les prédictions « per component » sont ensuite comparées au modèle de Kim & Johnson [52] sur l'étude du cas classique d'une transmission $Z_I|Z_{II} = 31|31$ avec chaine à pas double. Les deux modèles s'accordent sur l'évolution de la tension des maillons et de la position des rouleaux. Cette concordance suggère que le frottement aux interfaces axe/bague et bague/rouleau (pris en compte par Kim & Johnson mais négligé dans ce manuscrit) n'influence pas de manière significative le comportement de la transmission. L'approche de l'angle de correction, utilisée dans ce manuscrit, semble donc suffisante pour modéliser l'effet du frottement.

L'ensemble du QSCDM (*i.e.*, la cinématique globale et le sous-modèle de pignon) est ensuite confronté aux résultats du modèle présenté par Troedsson & Vedmar [67]. Malgré des incertitudes sur la géométrie de denture ainsi que les caractéristiques de la chaine utilisée pour les calculs de Troedsson & Vedmar, les prédictions sont en accord. Ce résultat confirme l'hypothèse selon laquelle les déformations des pièces, et plus particulièrement l'allongement des maillons, n'influencent pas de manière significative le comportement de la transmission (c'est-à-dire les charges et les positions des rouleaux). De même, le choix de négliger la gravité dans le sous-modèle de pignon est appuyé.

Dans ce chapitre, l'ensemble du QSCDM ainsi que les sous-modèles qui le constituent sont comparés avec succès aux résultats de la littérature, provenant à la fois de modèles numériques et de mesures expérimentales. Bien qu'elles soient destinées à l'étude des transmissions de cyclisme sur piste, les hypothèses du modèle sont suffisamment générales pour couvrir des cas industriels. Grâce à cette flexibilité, le modèle a été validé à l'aide de la littérature sur des transmissions par chaine industrielles, car aucun résultat approprié n'a pu être trouvé pour les transmissions cyclistes. La proximité entre les transmissions industrielles testées et les cas de cyclisme (*e.g.*, effet dynamique négligeable) garantit la validation pour une utilisation spécifique au cyclisme sur piste.

V.   Comportement des transmissions par chaine, influence du profil de denture sur des cas industriels et de cyclisme sur piste

Ce chapitre analyse l'influence de la géométrie du profil de denture sur les transmissions par chaine industrielles et cyclistes. Le QSCDM, présenté au §III, est utilisé pour tous les calculs. Des méthodes d'analyse sont proposées pour caractériser les propriétés du profil de denture. Ces dernières permettent de rapidement caractériser l'influence du profil.

Une transmission industrielle 31|31 (à pas double) est d'abord considérée. Les tensions dans les maillons, les force de contact et les positions des rouleaux sont calculés pour trois profils industriels (ASA, NF_{max} et NF_{min}). Chaque profil présente des pentes différentes lors des croissances et décroissances d'efforts (tension dans les maillons et force de contact) observées durant le contact des composants avec un pignon. Les positions des rouleaux sont couplées avec les charges : la tension dans les maillons et la force de contact diminuent (augmentent) lorsque le rouleau entre en contact avec le côté tendu (mou) du profil de la denture. Les profils avec des pentes plus importantes présentent également un mouvement de rouleau plus long (par exemple, le profilNF_{min}). Les pignons menés présentent des pentes plus importantes que les pignons menants avec le même profil. Par conséquent, le mouvement des rouleaux est également plus long pour les pignons menés. L'augmentation du couple appliqué réduit le mouvement des rouleaux. Des oscillations, à la fois dans les charges et le déplacement des rouleaux, sont présentes pour toutes les conditions de chargement. De telles oscillations n'ont pas été observées dans les travaux de Kim & Johnson [52] et de Naji & Marshek [2], [62]. Dans ces précédents travaux, un seul pignon était considéré au lieu de la transmission complète dans le QSCDM. Ces oscillations s'expliquent par les variations de tension des brins (T_s and T_t pour le brin mou et tendu respectivement) qui entraînent des variations du rapport de tension T_s/T_t. Dans les cas extrêmes, les mouvements de rouleaux effectuent des va et vient le long du profil de denture (avec de multiples changements de direction). Cette évolution non monotone n'est pas compatible avec l'hypothèse énoncée pour la modélisation du frottement. Toutefois, ce phénomène nécessiterait des travaux supplémentaires afin de proposer un modèle approprié. Néanmoins, les oscillations des charges et du mouvement des rouleaux trouvent leur source dans un modèle plus réaliste (modélisation d'une transmission complète par rapport à un seul pignon). Par conséquent, ces phénomènes sont probablement plus représentatifs de ce qui pourrait se produire dans une transmission par chaine réelle que l'évolution régulière décrite dans la littérature (*e.g.*, [1, 3]).

L'analyse des transmissions industrielles donne une première évaluation de l'influence du profil de denture sur le comportement des transmissions par chaîne. Sur la base de ces résultats, des méthodes d'analyse originales sont présentées. L'angle de pression au point de transition ϕ_{tp} est introduit. Ce paramètre est lié aux pentes croissantes et décroissantes propres à chaque profil. Les petits ϕ_{tp} sont associés aux pentes les plus importantes. Ensuite, le rapport de tension limite que chaque profil est capable de supporter est analysé. La position $s_{c,1}$ du premier rouleau pour un pignon soumis au rapport limite change pour un pignon menant ou mené. Le rapport limite est atteint soit lorsque tous les rouleaux se trouvent au point de transition, soit lorsqu'ils grimpent sur le flanc de la dent. Pour analyser les différences entre les profils, la courbe caractéristique de l'angle de pression, montrant l'évolution de ϕ_{i+1} en fonction de γ_i, est proposée. Cette courbe reflète les propriétés géométriques d'un profil donné. En tenant compte de la correction due au frottement, le comportement au rapport de tension limite peut être déterminé (sauf pour le cas plus complexe d'un pignon mené avec un profil ASA). Pour les pignons menants, tous les rouleaux se situent près du point de transition tp^B au ratio

de tension limite. Pour les pignons menés, les profils ASA et NF_{max} atteignent leur rapport limite avec des rouleaux grimpant sur le flanc de la denture à l'inverse du NF_{min} qui l'atteint avec tous les rouleaux immobiles au point de transmission (de la même manière que pour le pignon menant). L'influence de l'angle de correction δ sur ce phénomène est également étudiée. En se basant sur ces résultats, et en reprenant l'idée de sous modèle introduite par Lodge & Burgess [70], trois comportements du mouvement des rouleaux sont proposés en fonction de la charge appliquée sur le pignon considéré. Pour un rapport de tension T_s/T_t plus élevé (*i.e.*, chargements moins sévères), les rouleaux ont tendance à traverser le profil, du tp^B vers le tp^A, dans le comportement appelé inter-tp. Lorsque le rapport de tension diminue (*i.e.*, le couple appliqué augmente), les rouleaux restent plus longtemps au tp^B jusqu'à ce qu'ils soient presque immobiles. Lorsqu'ils sont soumis à ce comportement, appelé comportement rouleaux statiques, la correction due au frottement change de signe tandis que les rouleaux restent proches du point de transition tp^B. Ensuite, en fonction du profil, des rapports encore plus faibles peuvent être atteints pour des rouleaux grimpant sur le flanc de la dent, dans le comportement appelé rouleau grimpant. La transition entre chaque comportement est progressive et se produit à des rapports spécifiques pour chaque profil. Le QSCDM unifie donc les différentes approches présentées dans la littérature (GPLD, *static roller* et *low slack tension*, [1, 4, 8]).

Les méthodes d'analyse développées sont ensuite appliquées à une transmission 60|15 typique en cyclisme sur piste. Le rapport de tension limite dans des conditions de fonctionnement stables est introduit. Ce rapport exclut le comportement de rouleaux grimpants car le risque de saut de chaine ne peut pas être couru en cyclisme sur piste (pour des raisons de sécurité des athlètes). Une expression analytique simplifiée, et basée sur le paramètre ϕ_{tp}, permettant de calculer ce rapport est proposée. Il est montré que ϕ_{tp} est directement lié à ce rapport limite, les plus petits ϕ_{tp} permettant d'atteindre les rapports les plus faibles. L'analyse du rapport limite dans des conditions de fonctionnement stables montre que les profils ASA et NF_{max} ne peuvent pas supporter les rapports sévères (*i.e.*, très faible, de l'ordre de $1e^{-3}$) rencontrés dans les transmissions de cyclisme sur piste. Des géométries originales de profils de denture, les profils cyclistes (appelés CP), sont introduites. Ces profils sont construits de telle sorte que leur ϕ_{tp} soit suffisamment petit pour faire face aux contraintes spécifiques au cyclisme sur piste. L'influence de la géométrie du profil de denture sur le comportement de la transmission en cyclisme sur piste est ensuite testée en utilisant les quatre profils adaptés à cette application (NF_{min}, $CP_{1,2,3}$). Le comportement de la transmission est similaire aux résultats obtenus pour le cas industriel. Cependant, le très faible ϕ_{tp} des profils testés a pour conséquence des pentes croissantes et décroissantes encore plus importantes. En conséquence, la majeure partie de la charge, tant en tension dans les maillons qu'en force de contact, est supportée par le premier rouleau/maillon.

Si l'on considère l'efficacité énergétique des transmissions de cyclisme sur piste, les résultats obtenus ne permettent pas de déterminer facilement quel profil entraînera la plus faible dissipation. En effet, les profils ayant un mouvement de rouleaux plus important subissent ce mouvement sous des charges plus faibles que ce qui a été observé pour les profils présentant un mouvement de rouleau plus court. En outre, chaque profil réagit différemment aux variations du rapport de tension. Cela influe sur les mouvements de rouleaux et donc sur les pertes de puissance qui en résultent. Une analyse du rendement des transmissions par chaine prenant en compte l'effet du mouvement des rouleaux est donc nécessaire pour déterminer quelle géométrie entraîne les pertes de puissance les plus faibles. Les deux derniers chapitres de cette thèse sont consacrés à cette analyse.

VI. Modèle de rendement (CDEM[5]) : développement et validation

Ce chapitre est consacré à l'introduction et à la validation du modèle de rendement de transmission par chaine (CDEM). Ce modèle calcule le rendement d'une transmission par chaine en tenant compte des pertes d'engrènement et des pertes dues aux mouvements des rouleaux le long de leur profil de denture associé.

Le modèle de rendement est d'abord présenté. Ce modèle prend en compte toutes les pertes dues aux frottements entre les différents composants d'une chaine. Cela inclut les pertes dues à l'engrènement et les pertes causées par les mouvements des rouleaux le long de leur profil de denture correspondant. LE CDEM fonctionne avec le QSCDM présenté au chapitre II (§III) car il utilise les charges (tension dans les maillons et force de contact entre le rouleau et le profil) et l'emplacement des rouleaux « per component » comme données d'entrée. Les hypothèses sont identiques à celles du modèle du QSCDM : seuls les mouvements plans (2D) sont considérés sans aucune influence des effets dynamiques (quasi-statique). La chaine est supposée parfaitement alignée et le frottement n'est donc pris en compte qu'aux interfaces axe/bague, bague/rouleau et rouleau/profil (aucun contact latéral avec les plaques n'est considéré). Des frottements de Coulomb sont supposés à toutes les interfaces. Les différences entre les articulations d'axes (*pin articulation*) et de bagues (*bush articulation*) sont prises en compte. Les résultats « per component » fournis par le modèle de transmission par chaine (présenté au chapitre II, voir §III) ne donnent que l'évolution de l'emplacement du contact rouleau/profil. Par conséquent, des hypothèses cinématiques supplémentaires sont formulées pour déterminer la rotation propre du rouleau. Deux cas extrêmes, censés représenter les meilleures et les pires conditions possibles, sont envisagés. Dans le cas A, du roulement sans glissement se produit à l'interface rouleau/profil, tandis que du glissement se produit à l'interface bague/rouleau. Dans le cas B, le glissement se produit à la fois aux interfaces bague/rouleau et rouleau/profil. Les hypothèses de contact retenues pour ce modèle de rendement sont différentes de celles du modèle de tension de Kim & Johnson [52] où le roulement à l'interface bague/rouleau était considéré comme simultané au glissement à l'interface rouleau/profil. En conséquence des deux cas cinématiques considérés, le rendement prédit est donné sous la forme d'un intervalle $[\eta_B, \eta_A]$.

Les prévisions du CDEM sont ensuite comparées aux résultats expérimentaux, provenant à la fois de la littérature et d'un banc d'essai dédié. Les prédictions sont en accord avec les mesures expérimentales de Lodge & Burgess [70] sur des transmissions industrielles. Les résultats montrent que les faibles rendements observés à faible couple, qui ne pouvaient pas être expliqués par un modèle ne prenant en compte que les pertes d'engrènement (comme celui présenté par Lodge & Burgess), semblent être causés par les pertes dues au mouvement des rouleaux. Cette comparaison démontre l'intérêt du modèle présenté. Les prédictions du CDEM sont ensuite comparées aux mesures expérimentales d'un banc d'essai dédié aux applications de cyclisme sur piste. Ce banc a été développé au LaMCoS[6], simultanément à ces travaux de recherche. Pour une puissance transmise élevée (environ $1600W$), la variabilité des résultats expérimentaux rend la comparaison difficile. Cependant, pour une puissance plus faible (environ $490W$), les tendances observées avec le CDEM et le banc d'essai sont conformes. Le modèle et les mesures expérimentales s'accordent sur la relation asymptotique entre la tension de la chaine et le rendement de la transmission. L'intérêt d'utiliser des pignons plus grands a également été mis en évidence par les deux approches et les prédictions du modèle en termes de puissance

---

[5] Chain Drive Efficiency Model (CDEM) : Modèle de rendement de transmission par chaine
[6] LaMCoS : Laboratoire de Mécanique des Contact et des Structure. http://lamcos.insa-lyon.fr/?L=2

économisée sont cohérentes avec les résultats expérimentaux. Enfin, le modèle et les expériences s'accordent sur l'influence négligeable du profil de denture du plateau. Dans ce dernier cas, le modèle s'avère être un bon outil pour expliquer les résultats numériques. En effet, ce dernier montre que les pertes causées par le mouvement des rouleaux au plateau sont négligeables (par rapport aux pertes d'engrènement et dues au mouvement des rouleaux au pignon) pour des applications en cyclisme sur piste. Or, les différences entre profils de denture se manifestent uniquement sur les pertes causées par les rouleaux, d'où le résultat mesuré (pas d'influence du fabriquant de plateau sur le rendement de la transmission).

Le processus de validation a montré que l'influence des paramètres testés (*e.g.*, le couple, la tension de la chaîne, *etc*.) est généralement plus importante que la largeur de l'intervalle $[\eta_B, \eta_A]$. Par conséquent, la prise en compte de deux hypothèses cinématiques n'empêche pas de tirer des conclusions avec le CDEM.
Le modèle d'efficacité de la transmission par chaine (CDEM) a été présenté et validé. Dans la suite, Il est utilisé pour explorer le rendement des transmissions de cyclisme sur piste afin d'identifier les paramètres les plus influents.

VII. Etude paramétrique du rendement des transmissions de cyclisme sur piste

Ce chapitre est consacré à l'étude du rendement des transmissions par chaine à rouleaux. L'influence de nombreux facteurs est testée, depuis le couple appliqué par l'athlète sur le plateau jusqu'au nombre de dents et au pas de la chaîne. Les mouvements des rouleaux sont pris en compte et les différences entre les géométries des profils de denture sont étudiées.

Dans un premier temps, le rendement d'une transmission 60|15, classique du cyclisme sur piste, est caractérisé. Pour ce faire, les influences du couple C_I appliqué au plateau ainsi que du réglage de la tension $slack$ sont détaillées pour plusieurs profils de denture. Les résultats montrent que les influences de C_I et $slack$ sont similaires pour tous les profils testés. Le rendement augmente et l'intervalle $[\eta_B, \eta_A]$ se réduit avec l'augmentation du couple du plateau. Au-dessus d'environ $C_I = 100N.m$, le rendement atteint un plateau où il reste constant pour des couples plus élevés. Le même comportement est observé pour l'influence du réglage de la tension $slack$. Le rendement augmente pour les paramètres $slack$ plus importants (*i.e.*, pour un réglage de tension plus lâche) et un plateau de rendement est atteint à environ $slack = 7.5\%$. L'influence de ces deux facteurs est ensuite étudiée en tenant compte d'un troisième facteur : le rapport de tension. Une courbe plus générale du rendement en fonction du rapport de tension est proposée. Cette courbe peut être parcourue par des changements de couples C_I et/ou de réglages de tension $slack$. Le rendement augmente pour des rapports plus faibles et atteint un plateau à environ $T_{s,I}/T_t = 2e^{-2}$. Les mécanismes expliquant l'augmentation du rendement pour des rapports plus faibles sont ensuite détaillés. Il est montré que les pertes au niveau des rouleaux diminuent pour des rapports plus faibles. De plus, l'influence des pertes d'engrènement au brin mou diminue également car la tension du brin mou devient négligeable par rapport à celle du brin tendu. Par conséquent, pour les transmissions typiques du cyclisme sur piste avec des rapports de tension T_s/T_t faibles, les pertes d'engrènement associées au brin tendu sont largement prépondérantes. Les différences entre les profils se révèlent être mineures. Toutefois, il semble que les profils ayant des rayons de fond de dent plus petits présentent des rendements légèrement supérieurs. En conséquence, le profil CP_1 (avec le rayon de fond de dent le plus faible) est le plus efficace.

Plus généralement, les tendances observées étant similaires pour tous les profils de denture, la suite du chapitre n'a été menée que sur la géométrie NF_{min}.

L'analyse est ensuite étendue à des configurations de transmission autres que la 60|15. L'influence des paramètres liés à l'architecture de la transmission est étudiée. L'effet du nombre de dents des pignons est détaillé en tenant compte des limitations de rayon imposées par les dimensions des vélos de piste. Il est démontré que l'influence du nombre de dents du plateau dépend du couple appliqué. Son effet sur le rendement est préjudiciable pour les couples faibles alors qu'il est positif pour les couples élevés. Cependant, indépendamment du couple appliqué, l'effet du nombre de dents du pignon arrière est prépondérant par rapport à celui du plateau et se traduit par des rendements plus élevés pour des Z_{II} plus élevés. Cet effet est attribué à la réduction de l'angle d'articulation α_j qui se traduit par une réduction des pertes d'engrènement. Globalement, pour un rapport d'engrènement Z_I/Z_{II} constant, l'augmentation du nombre de dents des pignons se traduit par un rendement plus élevé, quel que soit le couple appliqué. L'effet du pas de la chaine est ensuite étudié. L'idée de modifier le pas de la chaine est testée pour évaluer l'influence d'une réduction supplémentaire de l'angle d'engrènement tout en limitant l'encombrement des pignons. La modification du pas de la chaine s'accompagne de modification des autres dimensions (notamment les diamètres d'axe, de bague et rouleau). Le changement de ces diamètres influe également sur le rendement de la transmission. Cet

effet doit donc être séparé du changement de pas seul. Pour ce faire, des cas EEU (*Everything Else Unchanged*, toute choses égales par ailleurs) pour lesquels le pas seul est modifié sont étudiés (les dimensions des axes, bagues et rouleaux sont similaires à celles de la chaine de pas $1/2''$). Les cas EEU montrent un rendement similaire à celui de la transmission $1/2''$ de référence. Des cas RCD (*Real Chain Dimension*, dimensions réelles) sont également considérés. Les résultats montrent que les rendements RCD sont meilleurs pour les pas plus faibles. L'effet est donc indépendant de la réduction de pas et est attribué aux réductions des distances de glissement pour les pas plus faibles (les diamètres d'axes, de bague et de rouleaux réduisent avec les pas de chaine). Cette analyse montre que la modification de l'angle d'engrènement sans modification du rayon primitif R_j n'influence pas le rendement de la transmission. En effet, les angles d'engrènement réduits sont compensés par un plus grand nombre d'articulations de la chaine pour une durée donnée. Ensuite, l'effet du coefficient de frottement global $\bar{\mu}$ est exploré. L'influence de coefficients de frottement plus faibles ou plus forts est quantifiée. De plus, la contribution de chaque interface de la chaine (*i.e.*, axe/bague, bague/rouleau et rouleau/profil) à la dissipation globale est présentée. Cette décomposition montre que l'interface axe/bague est responsable de la majeure partie des pertes. Une potentielle optimisation du lubrifiant utilisé doit donc se concentrer sur les conditions tribologiques (vitesse de glissement, rugosité, *etc*.) rencontrées à cette interface.

Enfin, une analyse du modèle de rendement de transmission par chaine (CDEM) à l'aide d'un plan d'expérience (Design Of Experiments, DOE) est présentée. Tous les paramètres étudiés dans ce chapitre sont pris en compte : couple au plateau, réglage de la tension, taille des pignons, pas de la chaine et coefficient de frottement. Le but de cette analyse est de faciliter la comparaison de l'influence de chaque facteur afin d'identifier les possibilités d'optimisation les plus importantes. Cet outil permet également d'explorer les interactions entre les facteurs. Un plan fractionnaire est utilisé pour limiter le temps de calcul de l'analyse. Un test de Fisher-Snedecor [99], [100] est effectué pour identifier 19 actions responsables d'environ 93% de la somme des carrés des écarts à la moyenne (Sum of Square, SS). Les résultats montrent que le couple appliqué au plateau C_I est le principal facteur influençant le rendement de transmission, suivi du rayon du pignon arrière R_{II} et du pas de chaine p. L'effet du rayon du plateau R_I s'avère négligeable. Sur la base de ces résultats, des lignes directrices pour l'optimisation du rendement des transmissions par chaine sont données. Toutefois, les recommandations données prennent uniquement en compte le rendement de la transmission. Dans le contexte du cyclisme sur piste de haut niveau, les études futures devraient prendre en compte l'implication de toute modification de la transmission par chaine sur le système global athlète-vélo. En effet, il faut veiller à ce que de potentiels effets indésirables n'annihilent pas les gains liés à un meilleur rendement de la transmission (*e.g.*, augmentation du poids, modification des propriétés aérodynamiques, *etc*.)

VIII. Conclusion

L'objectif principal de cette thèse était d'étudier le rendement des transmissions par chaine à rouleaux dans le contexte du cyclisme sur piste. Il a également été proposé de prendre en compte l'influence des pertes causées par le mouvement des rouleaux le long de leur profil de denture correspondant. Pour ce faire, un modèle de rendement a été développé, sur la base de travaux antérieurs, en deux étapes principales. Tout d'abord, un modèle de transmission par chaine quasi-statique (QSCDM) est proposé pour calculer le positionnement des rouleaux ainsi que l'évolution des charges (*i.e.*, les tensions dans les maillons et les forces de contact entre le rouleau et le profil). Ensuite, sur la base de ces résultats, un modèle de rendement de la transmission par chaine (CDEM) est introduit pour calculer le rendement de la transmission.

Le modèle quasi-statique de transmission par chaine (QSCDM) a d'abord été présenté. Ce modèle s'inspire d'études antérieures et réutilise les éléments de modélisation de la littérature. Il suppose que la chaine fonctionne dans un seul plan (2D). Tous les effets dynamiques sont négligés et les pièces de la chaine sont supposées rigides (*i.e.*, les déformations des pièces sont négligées). La cinématique de transmission est déterminée à l'aide de deux sous-modèles dédiés aux brins tendu et mou. La cinématique est supposée être indépendante des conditions de chargement (*e.g.*, le couple appliqué) et également des profils de denture des pignons utilisés. Les charges et l'emplacement des rouleaux sont calculés à l'aide d'un sous-modèle local de pignon. Ce sous-modèle utilise les résultats cinématiques et peut être utilisé avec différents profils de denture. L'effet du frottement est modélisé à l'aide d'un angle de correction δ qui introduit des différences entre pignons menants et pignons menés. Les problèmes de compatibilité entre les différents sous-modèles (*e.g.*, les sous-modèles de brin et de pignon local) ainsi que les défis posés par la résolution numérique sont abordés. Le QSCDM est construit en tenant compte du contexte du cyclisme sur piste qui justifie par exemple l'approche quasi-statique (chaînes légères et vitesses de rotation modérées). Cependant, il peut être utilisé pour des transmissions par chaine industrielle dont les caractéristiques répondent aux hypothèses du modèle.

Les éléments de validation du QSCDM ont ensuite été présentés. Les prédictions du modèle ont été confrontées à la fois à des résultats numériques et à des mesures expérimentales tirées de la littérature. Les comparaisons avec les résultats numériques de Kim & Johnson [52] et Troedsson & Vedmar [67] ont confirmé les hypothèses formulées pour le QSCDM. En effet, le modèle de tension plus simple (par rapport à Kim & Jonhson) ainsi que l'hypothèse de solides rigides (à l'inverse de Troedsson & Vedmar) n'ont pas d'impact significatif sur les prédictions. Les comparaisons ont été effectuées pour des transmissions par chaine industrielle, car il n'existe pas encore de résultats similaires dans le contexte du cyclisme sur piste dans la littérature.

Le QSCDM a ensuite été utilisé pour étudier l'influence de la géométrie du profil de denture sur le comportement de la transmission (*i.e.*, les charges et l'évolution de la position des rouleaux). Des transmissions industrielles et de cyclisme sur piste ont été étudiées. Pour les transmissions industrielles, des différences significatives ont été signalées entre les géométries extraites des normes ASA [32] et ISO [31]. Sur la base des résultats industriels, des méthodes d'analyse de l'influence du profil de denture ont été proposées. L'angle de pression au point de transition ϕ_{tp} a été introduit comme facteur clé pour évaluer l'influence du profil de denture. Les profils de denture à faible ϕ_{tp} ont été associés à une capacité de charge élevée entraînant une forte décroissance de la tension de maillon et des forces de contact rouleau/profil. Les premières dents portant une forte majorité de la charge. Trois comportements de pignons principaux, inspirés des sous-modèles proposés par Lodge & Burgess

[70], ont été introduits : inter-tp, rouleau statique et rouleau grimpant. Ces comportements facilitent l'analyse de l'évolution de la position du rouleau en fonction des conditions de chargement appliquées. Les outils développés ont ensuite été appliqués aux transmissions par chaine de cyclisme sur piste, caractérisées par un faible ratio entre les tensions de brin mou et tendu T_s/T_t. Il a été montré que les contraintes spécifiques à cette application ne pouvaient être satisfaites que par des profils de denture spécifiques. Cela a conduit à l'introduction de géométries originales adaptées au contexte du cyclisme : les profils de cyclisme CP.

Ensuite, le modèle de rendement de transmission par chaine (CDEM) a été introduit. Ce modèle calcule le rendement d'une transmission sur la base des résultats fournis par le QSCDM. Deux cas cinématiques extrêmes A et B sont considérés pour évaluer la rotation du rouleau en fonction de sa position le long de son profil associé. Par conséquent, le résultat du CDEM est un intervalle $[\eta_B , \eta_A]$. Une validation des prédictions de rendement a également été proposée. Les résultats de la littérature pour les transmissions industrielles montrent que les pertes causées par le mouvement des rouleaux pourraient expliquer les rendements plus faibles pour les petits couples. Une comparaison avec des mesures expérimentales réalisées à l'aide d'un banc d'essai dédié aux transmissions de cyclisme sur piste a également été présentée.

Enfin, le CDEM a été utilisé pour réaliser une étude paramétrique du rendement de la transmission par chaine du cyclisme sur piste. L'influence de la géométrie du profil de denture s'est révélée minime dans ce contexte, probablement en raison des grandes similitudes entre les profils. Ces similitudes s'expliquent par les contraintes extrêmes imposées par les applications de cyclisme sur piste auxquelles tous les profils doivent faire face. Outre la géométrie du profil de denture, l'influence du réglage de la tension, du couple appliqué, du pas de la chaîne, des nombres de dents et du coefficient de frottement a été étudiée. Une analyse basée sur les plans d'expériences (DOE) a également été proposée pour comparer l'effet de chaque paramètre. Sur la base des résultats, des lignes directrices pour l'optimisation des transmissions par chaine du cyclisme sur piste ont été données.

Ce travail de recherche a laissé plusieurs questions en suspens qui ouvrent des perspectives intéressantes. À court terme, les points suivants pourraient être explorés :

- Les possibilités d'optimisation données par l'analyse DOE nécessitent des mesures expérimentales pour vérifier les gains prédits. De plus, les effets secondaires potentiels sur le rendement du système global cycliste-vélo (en dehors du champ d'application de cette thèse) devraient être explorés avant de mettre en œuvre ces solutions. Par exemple, l'augmentation de la taille des pignons devrait améliorer le rendement de la transmission par chaîne. Cependant, le poids de la transmission pourrait également augmenter et des conséquences aérodynamiques potentielles pourraient apparaître. Ces effets doivent être clarifiés pour s'assurer que le résultat global soit positif.

- L'application du modèle CDEM à des cas industriels pourrait donner des résultats intéressants. En effet, les rapports de tension plus faibles rencontrés permettent d'utiliser des profils de denture dont les propriétés varient davantage par rapport au cyclisme sur piste. Les variations de rendement pourraient donc être plus importantes, par exemple, entre un profil cycliste CP et un profil ASA.

- Le sous-modèle de pignon, qui fait partie du QSCDM, peut facilement être adapté pour prendre en compte une faible variation du pas de la chaine p_{chaine} par rapport au pas du pignon p_{pignon}. Cette capacité pourrait être utilisée pour explorer l'influence de l'usure (qui se traduit par un allongement du pas de la chaine) et poursuivre le travail initié par Naji & Marshek [6].

D'autres questions nécessitent des travaux importants et constituent donc des perspectives à long terme.

- Dans des conditions spécifiques, le QSCDM a prédit des mouvements de va-et-vient des rouleaux, avec des conséquences sur le rendement de la transmission. Il pourrait être intéressant de vérifier l'existence physique de ce phénomène en essayant de mesurer ce mouvement expérimentalement. Pour ce faire, il conviendrait d'étudier les configurations de transmission présentant une variation importante de la tension du brin mou. Ces transmissions pourraient être caractérisées par une chaine lourde, un pas long et des nombres de dent faibles.

- La compréhension de l'influence du frottement sur l'évolution des charges (tensions dans les maillons et forces de contact entre le rouleau et le profile) peut être améliorée. Dans cette étude, elle a été modélisée à l'aide d'un angle de correction δ, mais cette approche repose sur peu de mesures expérimentales. En particulier, il serait intéressant de tester expérimentalement si les conditions de lubrification à l'interface rouleau/profil influencent significativement les différences entre le pignon menant et le pignon mené. En d'autres termes, μ_δ et μ_{rp}[7] sont-ils le même paramètre ?

- Enfin, il serait très intéressant d'étudier l'influence des effets dynamiques, particulièrement les vibrations des brins. D'autant plus dans le contexte du cyclisme sur piste ou le couple appliqué sur les pédales varie fortement au cours d'une révolution de plateau. Cet acyclisme pourrait avoir une influence significative sur les vibrations de brins et potentiellement sur le rendement de la transmission.

---

[7] μ_δ est relié à l'influence du frottement sur la distribution des charges alors que μ_{rp} est le coefficient de frottement entre rouleau et profil utilisé pour le calcul du rendement. Dans ces travaux, il a été supposé que ces deux paramètres sont indépendant.

References

[1]   N. Fuglede and J. J. Thomsen, "Kinematics of roller chain drives - Exact and approximate analysis," *Mech. Mach. Theory*, vol. 100, pp. 17–32, 2016, doi: 10.1016/j.mechmachtheory.2016.01.009.

[2]   M. R. Naji and K. M. Marshek, "Analysis of sprocket load distribution," *Mech. Mach. Theory*, vol. 18, no. 5, pp. 349–356, 1983, doi: 10.1016/0094-114X(83)90130-1.

[3]   Public domain, "The sketch (drawing) of roller chain, Leonardo da Vinci." https://commons.wikimedia.org/wiki/File:The_sketch_(drawing)_of_roller_chain,_Leonardo_ da_Vinci.jpg (accessed May 22, 2023).

[4]   R. Roletschek, "Kettenvergleich," 2005. https://commons.wikimedia.org/wiki/File:Kettenvergleich.jpg (accessed May 22, 2023).

[5]   Renold, "History of Renold Compagny." https://www.renold.com/company/history/ (accessed May 22, 2023).

[6]   M. R. Naji and K. M. Marshek, "The effects of the pitch difference on the load distribution of a roller chain drive," *Mech. Mach. Theory*, vol. 24, no. 5, pp. 351–362, 1989, doi: 10.1016/0094-114X(89)90065-7.

[7]   R. Tandler, N. Bohn, U. Gabbert, and E. Woschke, "Experimental investigations of the internal friction in automotive bush chain drive systems," *Tribol. Int.*, vol. 140, no. July, p. 105871, 2019, doi: 10.1016/j.triboint.2019.105871.

[8]   R. Tandler, N. Bohn, U. Gabbert, and E. Woschke, "Analytical wear model and its application for the wear simulation in automotive bush chain drive systems," *Wear*, vol. 446–447, no. January, p. 203193, 2020, doi: 10.1016/j.wear.2020.203193.

[9]   C. U. Kim, J. Y. Chung, and J. Il Song, "Dynamic analysis of long heavy-duty roller chain for bucket elevator of continuous ship unloader," *Adv. Mech. Eng.*, vol. 9, no. 8, pp. 1–11, 2017, doi: 10.1177/1687814017723296.

[10]   X. Ma, X. Shi, and J. Zhang, "Modeling and experimental investigation on the vibration of main drive chain in escalator," *INTER-NOISE 2019 MADRID - 48th Int. Congr. Exhib. Noise Control Eng.*, 2019.

[11]   Renold, "Catalogue des produits," 2017. https://www.renoldfrance.com/media/2037843/fr-renold-tcat-2017-web.pdf (accessed Jun. 28, 2023).

[12]   J. Huo, S. Yu, J. Yang, and T. Li, "Static and dynamic characteristics of the chain drive system of a heavy duty apron feeder," *Open Mech. Eng. J.*, vol. 7, no. 1, pp. 121–128, 2013, doi: 10.2174/1874155X01307010121.

[13]   Marc Carémantrant, "L'arrivé du RER NG se précise," *Rail passion*, vol. n°-305, no. Mars 2023, pp. 14–16, 2023.

[14]   M. CIVIERO, M. MARCHI, and A. LAGOMARSINI, "Bicycle sprocket and sprocket assembly comprising such a sprocket," EP3689731A1, 2020 [Online]. Available: https://worldwide.espacenet.com/patent/search?q=pn%3DEP3689731A1

References

[15] Y. FUKUNAGA, "Bicycle sprocket," US2018073620A1, 2018 [Online]. Available: https://worldwide.espacenet.com/patent/search?q=pn%3DUS10138991B2

[16] T. Iwai, N. Tetsu, and Yoshida Toyoshi, "Bicycle sprocket, sprocket assembly, rear sprocket assembly, and drive train of bicycle," US2020346713A1, 2020 [Online]. Available: https://worldwide.espacenet.com/patent/search?q=pn%3DTW201825346A

[17] V. Campagnolo, "Bicycle chain sprocket," US5782712A, 1998 [Online]. Available: https://worldwide.espacenet.com/patent/search?q=pn%3DUS5782712A

[18] P. Esquibel, "Multi-speed sprocket assembly," US8550944B2, 2013 [Online]. Available: https://worldwide.espacenet.com/patent/search?q=pn%3DUS2010081531A1

[19] J. Hanke, "Single sprocket," US11378171B2, 2022 [Online]. Available: https://worldwide.espacenet.com/patent/search?q=pn%3DUS11378171B2

[20] Zero Friction Cycling, "Lubricant testing." https://zerofrictioncycling.com.au/lubetesting/ (accessed May 15, 2023).

[21] Bike radar, "Chain lube buyer's guide: what's the best chain lube for your bike?" https://www.bikeradar.com/advice/buyers-guides/chain-lubes/ (accessed May 15, 2023).

[22] CeramicSpeed and Friction Facts, "OVERSIZED PULLY WHEEL SYSTEM," 2018. https://www.ceramicspeed.com/media/3503/oversized-pulleys.pdf (accessed Jun. 28, 2023).

[23] Keithonearth, "Derailleur Bicycle Drivetrain," 2009. https://commons.wikimedia.org/wiki/File:Derailleur_Bicycle_Drivetrain.svg (accessed May 22, 2023).

[24] Public domain, "Western Wheel Works bicycle, 1892." https://commons.wikimedia.org/wiki/File:Western_Wheel_Works_bicycle,_1892.jpg (accessed May 22, 2023).

[25] J. D. Palmer, L. Lobmeyer, and M. Fowler, "Drive sprocket," US11603906B2, 2023 [Online]. Available: https://worldwide.espacenet.com/patent/search?q=pn%3DUS11603906B2

[26] J. D. Palmer, L. Lobmeyer, and M. Fowler, "Drive sprocket," GB2597910A, 2022 [Online]. Available: https://worldwide.espacenet.com/patent/search?q=pn%3DGB2597910A

[27] Cycling news, "Team GB to use small-pitch chains worth £450 in Tokyo Olympics track events." https://www.cyclingnews.com/news/team-gb-to-use-small-pitch-chains-worth-pound450-in-tokyo-olympics-velodrome/ (accessed May 24, 2023).

[28] I. O. Commitee, "Cycling: History of cycling Track at the Olympic Games," 2015. https://web.archive.org/web/20200926125930/https://stillmed.olympic.org/AssetsDocs/OSC Section/pdf/QR_sports_summer/Sports_olympiques_cyclisme_sur_piste_eng.pdf (accessed Jun. 06, 2023).

[29] BBC Sport, "Tokyo Olympics: Cycling Track - Men's Sprint results." https://www.bbc.com/sport/olympics/58023546 (accessed May 22, 2023).

[30] ISO, "ISO 9633:2001; Cycle chains — Characteristics and test methods." 2001. [Online]. Available: https://www.iso.org/fr/standard/23532.html

[31]   ISO, "ISO 606:2015; Short-pitch transmission precision roller and bush chains, attachments and associated chain sprockets." 2015. [Online]. Available: https://www.iso.org/fr/standard/61232.html

[32]   R. C. Binder, *Mechanics of the Roller Chain Drive: Based on Mathematical Studies by R. C. Binder*. Prentice-Hall, 1956.

[33]   B. KOHLER and E. SZTRYGLER, "Chaînes mécaniques," *Fonct. Compos. mécaniques*, vol. base docum, no. ref. article : b5650, Feb. 1989, doi: 10.51257/a-v1-b5650.

[34]   Renold, "Roller chain designer guide," 2023. https://www.renold.com/upload/renoldswitzerland/roller_chain_designer_guide.pdf (accessed Sep. 25, 2023).

[35]   S. Mahalingam, "Polygonal action in chain drives," *J. Franklin Inst.*, vol. 265, no. 1, pp. 23–28, 1958, doi: 10.1016/0016-0032(58)90665-3.

[36]   R. A. Morrison, "Polygonal Action in Roller Chain Drives," *Mach. Des.*, pp. 155–159, 1952.

[37]   G. Bouillon and G. V. Tordion, "On polygonal action in roller chain drives," *J. Manuf. Sci. Eng. Trans. ASME*, vol. 87, no. 2, pp. 243–251, 1965, doi: 10.1115/1.3670804.

[38]   N. Fuglede, "Kinematics and Dynamics of Roller Chain Drives," Technical University of Denmark, 2014.

[39]   E. I. Radzimovsky, "Eliminating Pulsations in Chain Drives," *Prod. Eng.*, vol. 26, no. 7, pp. 153–157, 1955.

[40]   R. C. Binder and G. G. Mize, "Strand vibrations in a roller-chain drive," *J. Franklin Inst.*, vol. 247, no. 1, 1949, doi: 10.1016/0016-0032(49)90897-2.

[41]   R. C. Binder and W. V. Covert, "Impact between chain roller and sprocket in a chain drive," *J. Franklin Inst.*, vol. 245, no. 4, pp. 319–329, 1948, doi: 10.1016/0016-0032(48)90931-4.

[42]   R. A. Sack, "Transverse oscillations in travelling strings," *Br. J. Appl. Phys.*, vol. 5, no. 6, pp. 224–226, 1954, doi: 10.1088/0508-3443/5/6/307.

[43]   S. Mahalingam, "Transverse vibrations of power transmission chains," *Br. J. Appl. Phys.*, vol. 8, no. 4, pp. 145–148, 1957, doi: 10.1088/0508-3443/8/4/303.

[44]   S. R. Turnbull, "The Dynamic behaviour of roller chain drives," University of Newcastle, 1974.

[45]   S. W. Nicol and J. N. Fawcett, "REDUCTION OF NOISE AND VIBRATION IN ROLLER CHAIN DRIVES.," *Inst Mech Eng Proc*, vol. 191, no. 39, 1977, doi: 10.1243/pime_proc_1977_191_044_02.

[46]   J. N. Fawcett and S. W. Nicol, "Influence of Lubrication on Tooth-Roller Impacts in Chain Drives.," *Inst Mech Eng Proc*, vol. 191, no. 21, pp. 271–275, 1977, doi: 10.1243/pime_proc_1977_191_033_02.

[47]   J. N. Fawcett, "A theoretical investigation of the vibration of roller chain drives," in *ASME Proc. World Cong. Theory Mach. Mech.*, 1979, no. 2, pp. 1482–1485.

References

[48]   J. N. Fawcett and S. W. Nicol, "Vibration of a Roller Chain Drive Operating at Constant Speed and Load.," *Proc. - Inst. Mech. Eng.*, vol. 194, pp. 97–101, 1980, doi: 10.1243/PIME_PROC_1980_194_012_02.

[49]   J. N. Fawcett, "Chain and Belt Drives - A Review," *Shock Vib. Dig.*, vol. 13, pp. 5–12, 1981.

[50]   E. W. Chen, J. Wang, K. Zhong, Y. Lu, and H. Wei, "Vibration dissipation of an axially traveling string with boundary damping," *J. Vibroengineering*, vol. 19, no. 8, pp. 5780–5795, 2017, doi: 10.21595/jve.2017.18651.

[51]   G. E. Choi, W., & Johnson, "Transverse vibration of roller chain drive with tensioner," *International Design Engineering Technical Conferences and Computers and Information in Engineering Conference*, vol. 11795. pp. 19–28, 1993.

[52]   M. S. Kim and G. E. Johnson, "Mechanics of roller chain-sprocket contact: a general modelling stragegy," in *American Society of Mechanical Engineers, Design Engineering Division (Publication) DE*, 1992, vol. 43 pt 2, pp. 689–695.

[53]   S. L. Pedersen, "Simulation and Analysis of Roller Chain Drive Systems," Technical University od Denmark (DTU), 2004.

[54]   H. Zheng, Y. Y. Wang, and K. P. Quek, "A refined numerical simulation on dynamic behavior of roller chain drives," *Shock Vib.*, vol. 11, no. 5–6, pp. 573–584, 2004, doi: 10.1155/2004/548172.

[55]   G. Hippmann, M. Arnold, M. Schittenhelm, and C. D. Simulation, "Efficient Simulation of Bush and Roller Chain Drives," *Multibody Dyn. 2005, ECCOMAS Themat. Conf.*, no. June, pp. 21–24, 2005.

[56]   C. Pereira, J. Ambrosio, and A. Ramalho, "Contact mechanics in a roller chain drive using a multibody approach," *11th Pan-American Congr. Appl. Mech.*, no. 1994, 2010.

[57]   J. Ambrosio, C. Malça, and A. Ramalho, "Planar roller chain drive dynamics using a cylindrical contact force model," *Mech. Based Des. Struct. Mach.*, vol. 44, no. 1–2, pp. 109–122, Apr. 2016, doi: 10.1080/15397734.2015.1087319.

[58]   M. Omar, "Multibody dynamics formulation for modeling and simulation of roller chain using spatial operator," in *MATEC Web of Conferences*, 2016, vol. 51. doi: 10.1051/matecconf/20165101003.

[59]   M. A. Omar, "Chain drive simulation using spatial multibody dynamics," *Adv. Mech. Eng.*, vol. 2014, 2014, doi: 10.1155/2014/378030.

[60]   A. Kubo, M. Sonada, and T. Saitoh, "Sprocket for chain," US7128673B2, 2006 [Online]. Available: https://worldwide.espacenet.com/patent/search?q=pn%3DJP2005030501A

[61]   S. Sakura, A. Hirai, and M. Sonada, "Chain transmission device," US7691020B2, 2010 [Online]. Available: https://worldwide.espacenet.com/patent/search?q=pn%3DUS7691020B2

[62]   M. R. Naji and K. M. Marshek, "Experimental determination of the roller chain load distribution," *J. Mech. Des. Trans. ASME*, vol. 105, no. 3, pp. 331–338, 1983, doi: 10.1115/1.3267365.

[63]   B. H. Eldiwany and K. M. Marshek, "Experimental load distributions for double pitch steel roller

chains on polymer sprockets," *Mech. Mach. Theory*, vol. 24, no. 5, pp. 335–349, 1989, doi: 10.1016/0094-114X(89)90064-5.

[64]   M. R. Naji and K. M. Marshek, "Analysis of roller chain sprocket pressure angles," *Mech. Mach. Theory*, vol. 19, no. 2, pp. 197–203, 1984, doi: 10.1016/0094-114X(84)90042-9.

[65]   M. R. Naji and K. M. Marshek, "The effects of the pitch difference on the load distribution of a roller chain drive," *Mech. Mach. Theory*, vol. 24, no. 5, pp. 351–362, 1989, doi: 10.1016/0094-114X(89)90065-7.

[66]   T. VERNE, "Simulation et Analyse du Comportement des Transmissions par Chaine à Rouleaux," INSA Lyon, 1994.

[67]   I. Troedsson and L. Vedmar, "A method to determine the static load distribution in a chain drive," *J. Mech. Des. Trans. ASME*, vol. 121, no. 3, pp. 402–408, 1999, doi: 10.1115/1.2829475.

[68]   I. Troedsson and L. Vedmar, "A method to determine the dynamic load distribution in a chain drive," *Proc. Inst. Mech. Eng. Part C J. Mech. Eng. Sci.*, vol. 215, no. 5, pp. 569–579, 2001, doi: 10.1243/0954406011520959.

[69]   I. Troedsson and L. Vedmar, "A method to determine the static load distribution in a chain drive," *Proc. Inst. Mech. Eng. Part C J. Mech. Eng. Sci.*, vol. 215, no. 5, pp. 569–579, 2001, doi: 10.1243/0954406011520959.

[70]   C. J. Lodge and S. C. Burgess, "A model of the tension and transmission efficiency of a bush roller chain," *Proc. Inst. Mech. Eng. Part C J. Mech. Eng. Sci.*, vol. 216, no. 4, pp. 385–394, 2002, doi: 10.1243/0954406021525179.

[71]   C. J. Lodge, "Theoretical and experimental studies of the mechanical bahaviour of roller chains," University of Bristol, 2022. doi: 10.1088/1361-6404/ac2881.

[72]   R. Stephenson, D. Glennie, J. N. Fawcett, and J. M. Hale, "A method of measuring the dynamic loads in high-speed timing chains," *Proc. Inst. Mech. Eng. Part D J. Automob. Eng.*, vol. 214, no. 2, pp. 217–226, 2000, doi: 10.1177/095440700021400211.

[73]   Diamond   Chain   Company,   "Technical   Engineering,"   2022. https://www.norfolkbearings.com/products/diamond/DIAMONDTechnicalEngineering.pdf (accessed Jun. 28, 2023).

[74]   N. E. Hollingworth and D. A. Hills, "Theoretical efficiency of a cranked link chain drive," *Proc. Inst. Mech. Eng. Part C J. Mech. Eng. Sci.*, vol. 200, no. 5, pp. 375–377, 1986, doi: 10.1243/PIME_PROC_1986_200_141_02.

[75]   N. E. Hollingworth and D. A. Hills, "Forces in a heavy-duty drive chain during articulation," *Proc. Inst. Mech. Eng. Part C J. Mech. Eng. Sci.*, vol. 200, no. 5, pp. 367–374, 1986, doi: 10.1243/PIME_PROC_1986_200_140_02.

[76]   M. D. Kidd, N. E. Loch, and R. L. Reuben, "Bicycle chain efficiency," Heriot-Watt University, Scotland, 2000. doi: 10.1201/9781003078098-37.

[77]   J. B. Spicer, C. J. K. Richardson, M. J. Ehrlich, J. R. Bernstein, M. Fukuda, and M. Terada, "Effects of frictional loss on bicycle chain drive efficiency," *J. Mech. Des. Trans. ASME*, vol. 123, no. 4, pp. 598–605, 2001, doi: 10.1115/1.1412848.

[78] J. B. Spicer, "Effects of the nonlinear elastic behavior of bicycle chain on transmission efficiency," *J. Appl. Mech. Trans. ASME*, vol. 80, no. 2, p. 021005, Mar. 2013, doi: https://doi.org/10.1115/1.4007431.

[79] S. P. Zhang and T. O. Tak, "Efficiency estimation of roller chain power transmission system," *Appl. Sci.*, vol. 10, no. 21, pp. 1–13, 2020, doi: 10.3390/app10217729.

[80] M. Sgamma, F. Bucchi, and F. Frendo, "A phenomenological model for chain transmissions efficiency," *IOP Conf. Ser. Mater. Sci. Eng.*, vol. 1038, no. 1, p. 012060, 2021, doi: 10.1088/1757-899x/1038/1/012060.

[81] G. Lanaspeze, B. Guilbert, L. Manin, and F. Ville, "Preliminary modelling of power losses in roller chain drive: application to single speed cycling," *Mech. Ind.*, vol. 23, p. 27, Nov. 2022, doi: 10.1051/meca/2022026.

[82] C. J. Lodge and S. C. Burgess, "An investigation into the selection of optimum chain and sprocket size," *J. Eng. Des.*, vol. 15, no. 6, pp. 563–580, 2004, doi: 10.1080/09544820410001731128.

[83] G. C. Barnaby, J. Yon, and S. C. Burgess, "Sprocket Size Optimization for Derailleur Racing Bicycles," *J. Sci. Cycl.*, vol. 9, no. 2, p. 36, 2020.

[84] G. C. Barnaby, S. Burgess, and J. Yon, "Mapping whole-event drive losses: the impact of race profile and rider input on transmission efficiency in cycling," *J. Sci. Cycl.*, vol. 10, no. 2, pp. 1–6, 2021.

[85] E. Popova and V. L. Popov, "The research works of Coulomb and Amontons and generalized laws of friction," *Friction*, vol. 3, no. 2, pp. 183–190, 2015, doi: 10.1007/s40544-015-0074-6.

[86] Y. Diab, F. Ville, and P. Velex, "Prediction of Power Losses Due to Tooth Friction in Gears," *Tribol. Trans.*, vol. 49, no. 2, 2006, doi: 10.1080/05698190600614874.

[87] R. Wragge-Morley, J. Yon, R. Lock, B. Alexander, and S. Burgess, "A novel pendulum test for measuring roller chain efficiency," *Meas. Sci. Technol.*, vol. 29, no. 7, May 2018, doi: 10.1088/1361-6501/aaa239.

[88] A. Egorov, K. Kozlov, and V. Belogusev, "A method for evaluation of the chain drive efficiency," *J. Appl. Eng. Sci.*, vol. 13, no. 4, 2015, doi: 10.5937/jaes13-9170.

[89] A. Bodin, "La chaînette," 2012. http://math.univ-lille1.fr/~bodin/geometrie/ch_chainette.pdf (accessed Mar. 08, 2023).

[90] S. Mahalingam, "Polygonal action in chain drives.pdf," *J. Franklin Inst.*, vol. 265, no. 1, pp. 23–28, 1958, doi: https://doi.org/10.1016/0016-0032(58)90665-3.

[91] Wipperman, "Main Catalogue 2015. Industrial Chains, Sprockets and Accesories," 2015. https://wippermann.s3.amazonaws.com/dokumente/en/product-catalogs/main-catalogue-wippermann-cat-2015-en.pdf (accessed Jun. 28, 2023).

[92] LOOK, "LOOK T20 dimmensions." https://www.lookcycle.com/fr-fr/produits/velos/piste/t20/t20-speed-version-kit-cadre (accessed May 13, 2023).

[93] J. B. Spicer, "Effects of the nonlinear elastic behavior of bicycle chain on transmission efficiency," *J. Appl. Mech. Trans. ASME*, vol. 80, no. 2, 2013, doi: 10.1115/1.4007431.

[94]   J. B. Spicer, C. J. K. Richardson, M. J. Ehrlich, J. R. Bernstein, M. Fukuda, and M. Terada, "Effects of frictional loss on bicycle chain drive efficiency," *J. Mech. Des. Trans. ASME*, vol. 123, no. 4, pp. 598–605, 2001, doi: 10.1115/1.1412848.

[95]   Keithonearth, "Bicycle Frame Diagram," 2008. https://commons.wikimedia.org/wiki/File:Bicycle_Frame_Diagram-en.svg (accessed May 25, 2023).

[96]   Norelem, "Chaînes à rouleaux simples DIN ISO 606, plaques arrondies." https://www.norelem.fr/fr/fr/Produits/THE-BIG-GREEN-BOOK/norelem-actionne-Systèmes-et-composants-pour-la-construction-de-machines-et-d-installations/22000-Éléments-de-transmission/Chaînes-et-pignons/22200-Chaînes-à-rouleaux-simples-DIN-ISO-606-plaques-arr (accessed May 26, 2023).

[97]   J. Goupy, "Les plans d'experiences," *Rev. Modul.*, no. 34, 2006.

[98]   Douglas C. Montgomery, *Design and analysis of experiments, 8th edition*, vol. 32, no. 1. 2013. doi: 10.1002/ep.11743.

[99]   N. R. Draper and H. Smith, "Applied Regression Analysis, 3rd Edition," *John Wiley & Sons, Inc.* p. 736, 1998.

[100]   D. Dean, A., Voss, *Design and Analysis of Experiments*, vol. 77, no. 12. 2000. doi: https://doi.org/10.1007/b97673.

[101]   UCI, "Clarification Guide of The UCI Technical Regulations - 05/10/2021," 2021. https://assets.ctfassets.net/761l7gh5x5an/7s1ma6mVAVlFwi8rRgy0Iw/1bef531dd9e9f534c34ff016c68e3c72/Clarification_Guide_of_the_UCI_Technical_Regulation_-_20211005_-_ENG.pdf (accessed Oct. 10, 2023).

[102]   D. Roegel, "Intersection de deux cercles dans le plan Une solution," 2001. https://members.loria.fr/DRoegel/loc/note0001.pdf (accessed Apr. 27, 2023).

FOLIO ADMINISTRATIF

THESE DE L'INSA LYON, MEMBRE DE L'UNIVERSITE DE LYON

NOM : LANASPEZE   DATE de SOUTENANCE : 29/09/2023

Prénoms : Gabriel Jean Marie

TITRE : Contribution to roller chain drive quasi-static modelling for efficiency optimisation. Application to track cycling.

NATURE : Doctorat
                                                                        Numéro d'ordre : 2023ISAL0066

Ecole doctorale : MEGA, n°162
Spécialité : Génie mécanique

RESUME :

L'importante compétition entre cyclistes sur piste de très haut niveau pousse les travaux de recherches à explorer toutes les possibilités d'optimisations. Dans ce contexte, le rendement énergétique des transmissions par chaine à rouleaux est étudié dans le but d'améliorer la compréhension des puissances dissipées et d'en déduire des possibilités d'optimisations.
Dans les transmissions par chaine, les pertes sont majoritairement causées par l'engrènement/dégrènement des maillons sur les pignons. Toutefois, une étude préliminaire a montré que les pertes dues au mouvement des rouleaux le long de leur profil de dent ont une influence significative. Le but de ce travail est donc d'explorer ce phénomène.
Un modèle 2D quasi-statique est tout d'abord présenté. La cinématique générale (comprenant les erreurs de transmission) est déterminée en utilisant des sous-modèles spécifiques aux brins tendu et mou. Un modèle local de pignon est ensuite introduit afin de calculer les tensions dans les maillons ainsi que les forces de contact entre rouleaux et pignons. Le modèle peut être utilisé avec différentes géométries de denture.
Après un processus de validation, le modèle quasi-statique est utilisé pour étudier l'influence du profil de denture sur les évolutions corrélées des charges et des positions de rouleaux. Des différences significatives sont observées. L'application du modèle à une transmission de cyclisme sur piste montre que des géométries de denture dédiées sont indispensables pour faire face aux contraintes spécifiques induites par cette utilisation.
Un second modèle est ensuite proposé. En se basant sur les résultats du modèle quasi-statique, il calcule le rendement d'une transmission en prenant en compte les pertes causées par l'engrènement ainsi que les mouvements de rouleaux. Des comparaisons avec des résultats expérimentaux sont menées pour valider l'approche proposée.
Le modèle de rendement est ensuite utilisé pour mener une étude paramétrique sur des transmissions par chaines de cyclisme sur piste. L'influence de plusieurs paramètres est explorée : géométrie de denture, couple appliqué, réglage de la tension, nombres de dent des pignons, pas de la chaine et coefficient de frottement. Les interactions entre paramètres sont identifiées. En se basant sur les résultats, des lignes directrices pour de futures optimisations sont proposées.

MOTS-CLÉS : Transmission mécanique, chaine à rouleaux, cinématique, modèle de tension, géométrie de denture, mouvement de rouleau, pertes de puissance, rendement

Laboratoire (s) de recherche :
                                   LaMCoS - INSA Lyon

Directeurs / directrice de thèse :

            Lionel MANIN – INSA Lyon, Fabrice VILLE – INSA Lyon, Bérengère GUILBERT – INSA Lyon

Présidente de jury :
                              Marie-Christine BAIETTO

Composition du jury :

            Stuart BURGESS, Franck RENAUD, Marie-Christine BAIETTO,
            Christophe CLANET, Bérengère GUILBERT, Fabrice VILLE